

Titre: On-line assessment and numerical modeling of thermal fatigue and oxidation damages in turbine airfoils under simulated service conditions
Title:

Auteur: Stéphane Gendron
Author:

Date: 1996

Type: Mémoire ou thèse / Dissertation or Thesis

Référence: Gendron, S. (1996). On-line assessment and numerical modeling of thermal fatigue and oxidation damages in turbine airfoils under simulated service conditions [Thèse de doctorat, École Polytechnique de Montréal]. PolyPublie.
Citation: <https://publications.polymtl.ca/8959/>

 **Document en libre accès dans PolyPublie**
Open Access document in PolyPublie

URL de PolyPublie: <https://publications.polymtl.ca/8959/>
PolyPublie URL:

Directeurs de recherche:
Advisors:

Programme: Non spécifié
Program:

UNIVERSITÉ DE MONTRÉAL

**ON-LINE ASSESSMENT AND NUMERICAL MODELLING
OF THERMAL FATIGUE AND OXIDATION DAMAGES
IN TURBINE AIRFOILS UNDER SIMULATED SERVICE CONDITIONS**

STÉPHANE GENDRON

DÉPARTEMENT DE MÉTALLURGIE ET DE GÉNIE DES MATÉRIAUX
ÉCOLE POLYTECHNIQUE DE MONTRÉAL

THÈSE PRÉSENTÉE EN VUE DE L'OBTENTION
DU DIPLÔME DE PHILOSOPHIAE DOCTOR (Ph.D.)
(MÉTALLURGIE ET GÉNIE DES MATÉRIAUX)
DÉCEMBRE 1996

© Stéphane Gendron, 1996.



National Library
of Canada

Bibliothèque nationale
du Canada

Acquisitions and
Bibliographic Services

Acquisitions et
services bibliographiques

395 Wellington Street
Ottawa ON K1A 0N4
Canada

395, rue Wellington
Ottawa ON K1A 0N4
Canada

Your file Votre référence

Our file Notre référence

The author has granted a non-exclusive licence allowing the National Library of Canada to reproduce, loan, distribute or sell copies of this thesis in microform, paper or electronic formats.

L'auteur a accordé une licence non exclusive permettant à la Bibliothèque nationale du Canada de reproduire, prêter, distribuer ou vendre des copies de cette thèse sous la forme de microfiche/film, de reproduction sur papier ou sur format électronique.

The author retains ownership of the copyright in this thesis. Neither the thesis nor substantial extracts from it may be printed or otherwise reproduced without the author's permission.

L'auteur conserve la propriété du droit d'auteur qui protège cette thèse. Ni la thèse ni des extraits substantiels de celle-ci ne doivent être imprimés ou autrement reproduits sans son autorisation.

0-612-26420-3

Canada

UNIVERSITÉ DE MONTRÉAL
ÉCOLE POLYTECHNIQUE DE MONTRÉAL

Cette thèse intitulée:

**ON-LINE ASSESSMENT AND NUMERICAL MODELLING
OF THERMAL FATIGUE AND OXIDATION DAMAGES
IN TURBINE AIRFOILS UNDER SIMULATED SERVICE CONDITIONS**

présentée par: GENDRON Stéphane

en vue de l'obtention du diplôme de: Philosophiae Doctor

a été dûment acceptée par le jury d'examen constitué de:

M. VERREMAN Yves, Ph.D., président

M. MARCHAND Norman J., Sc.D., membre et co-directeur de recherche

M. AJERSCH Frank, Ph.D., membre et co-directeur de recherche

M. PATNAIK Prakash C., Ph.D., membre

Mme BERNARD Marie, Ph.D., membre

À ma très chère femme, Lucie
À mes enfants

À ma mère, mon père, ma soeur
À ma belle famille

Et à mes amies et amis

REMERCIEMENTS

Je tiens tout d'abord à remercier mon premier co-directeur de thèse, Dr Norman Marchand, de m'avoir proposé un projet si intéressant et enrichissant à la fois. Son grand soutien tant technique que moral tout au long de ce projet m'ont permis de me dépasser et de persévérer jusqu'au bout. J'aimerais remercier également Dr Jean-Pierre Immarigeon, superviseur technique des travaux effectués à l'Institut de Recherche en Aérospatial du CNRC (IRA), pour ses nombreux conseils et son implication constante dans le projet. Je suis reconnaissant envers mon deuxième co-directeur de thèse, Dr Frank Ajersch pour avoir dirigé ma carrière dans le domaine des applications à haute température, ainsi qu'envers les membres du jury, Dr Prakash Patnaik, Dr Marie Bernard et Dr Yves Verreman pour leurs critiques constructives. J'ai beaucoup apprécié les discussions avec Dr Ashok Koul, Dr Michael Schütze, Dr Christophe Korn et M. Roger Pelletier, qui m'ont inspiré sur divers aspects du projet.

Je veux souligner ici l'aide technique des personnes suivantes sans laquelle le projet n'aurait pas atteint la même envergure. Il s'agit de M. Paul-Éric Bélanger, Dr Jerzy Kacprzyński, Dr Wiesław Beres et M. Sébastien Boire-Lavigne pour les analyses thermo-mécaniques par éléments finis, et des technologues Tak Terada, Ray Dainty, Dave Morphy et Dave Chow pour leur travail de laboratoire à l'IRA. La présentation physique de cette thèse n'aurait pas la même allure sans la minutieuse et laborieuse contribution de Mme Lucie Lalonde chez qui j'admire la patience et la compréhension en tant qu'épouse d'un homme trop distrait par son travail.

La réalisation du projet a été entièrement financé par le Département de la Défense Nationale Canada (Financement FA 220788-NRC 22) à qui je dois par le fait même plusieurs années de salaire.

RÉSUMÉ

Cette thèse décrit un projet portant sur le problème de la fatigue thermique dans les aubes de turbines à gaz utilisées en aviation. Les buts du projet étaient de développer et de valider une méthode capable de prédire la vie en fatigue thermique ainsi que l'endommagement associé à l'oxydation cyclique de ces composantes. Le projet comporte deux volets. Le premier volet traite de l'aspect expérimental qui vise à reproduire et à évaluer l'endommagement dans des échantillons soumis à des conditions semblables à celles prévalant dans une turbine à gaz. Le deuxième volet, d'ordre numérique, tente de déterminer le cumul de dommage en fatigue et en oxydation propre à ces échantillons, afin d'obtenir leur vie utile à partir de leur histoire thermomécanique.

Plus précisément au sujet du volet expérimental, huit essais de fatigue thermique ont été menés à l'aide d'une chambre de combustion, sur des échantillons en René 80, revêtus ou non. Les échantillons de géométrie à double bord, dont les rayons imitent ceux des bords d'attaque et de fuite des ailettes réelles, ont été commercialement obtenus par solidification directionnelle (SD). Le revêtement appliqué, le Codep B-1, est un alliage riche en aluminium, produit par cémentation. Les échantillons ont été exposés en alternance à un jet de gaz chaud à haute vitesse (1323°C, MACH 0.4) produit par la chambre de combustion et un jet d'air froid (à température ambiante), parallèle au premier, pendant au plus 3000 cycles thermiques.

L'initiation et la propagation de fissures développées en fatigue thermique aux bords d'attaque des échantillons ont été suivies en cours d'essai, grâce à une technique électrique consistant à imposer un courant alternatif dans les échantillons et à mesurer la chute de potentiel associée. La vie à l'initiation des échantillons non revêtus ainsi

mesurée se situe autour de 760 ± 20 cycles, alors que le même matériau revêtu démontre une vie inférieure jouant autour de 300 ± 100 cycles. La résolution de la technique électrique est de $200 \mu\text{m}$ ou moins ce qui implique que les vies mesurées grâce à cette technique correspondent au nombre de cycles nécessaires pour initier une fissure courte de $200 \mu\text{m}$ environ. La vitesse de propagation a été établie à environ $2 \mu\text{m}/\text{cycle}$, en tenant compte du taux de récession de la surface de l'alliage dû à l'oxydation cyclique. Quelques essais ont été arrêtés après détection de fissure.

L'étude métallographique des échantillons provenant des tests interrompus, a révélé la présence de quelques pics d'oxydes de moins de $100 \mu\text{m}$ (valeur de l'ordre de grandeur de la résolution de la technique électrique de détection de fissure), qui se sont formés préférentiellement dans les zones interdendritiques, aux carbures débouchant à la surface du bord d'attaque et aux joints de grains des revêtements. Les pics ont été retrouvés aux endroits les plus contraints et où la température n'est pas la plus haute. Cette observation tend à prouver que les pics d'oxydes ne résultent que de l'oxydation de microfissures initiées préférentiellement en fatigue à ces sites. Des fissures majeures se sont ensuite propagées entre les dendrites où des carbures fragilisants se trouvent concentrés. Les têtes de fissure sont toutes sévèrement oxydées. Bien que le mécanisme de propagation ne soit pas encore bien connu, le rôle de la fragilisation de la zone en tête de fissure due à la diffusion de l'oxygène dissout dans le métal est d'une grande importance dans le processus de fissuration, comme il a été reconnu dans plusieurs modèles d'interaction d'endommagements fatigue-oxydation. En plus des fissures, d'importantes pertes de métal causées par les conditions d'oxydation cycliques ont été observées aux bords d'attaque au niveau de la partie directement exposée au jet de gaz chaud, que les échantillons soient revêtus ou non. Ailleurs, où la température n'excède pas 1090°C , les revêtements se sont révélés protecteurs.

Dans le volet numérique du projet, la distribution de température a été calculée

à partir du code d'éléments finis ABAQUS et de valeurs expérimentales des coefficients de transfert de chaleur par convection et par radiation. L'écart moyen entre les températures calculées et mesurées durant le régime permanent du cycle thermique est de seulement 35°C en moyenne, et de 15°C en tête du bord d'attaque, où la température atteint une valeur maximale de 1164°C.

À partir des résultats de l'analyse thermique et des propriétés mécaniques du matériau, la distribution des contraintes dans les échantillons fut aussi calculée par éléments finis en employant un modèle thermo-élastoplastique ainsi qu'un modèle thermo-élasto-viscoplastique. Le deuxième modèle est basé sur le code de Walker qui a été modifié pour tenir compte de l'orthogonalité des propriétés élastiques du René 80 (SD). Ce dernier modèle fut employé pour calculer de façon plus précise la déformation viscoplastique ainsi que la relaxation dans les éléments du bord d'attaque exposés aux conditions thermo-mécaniques les plus sévères.

Selon l'étude thermo-élastoplastique menée à terme, les fissures sont apparues là où la température est élevée et où les contraintes sont maximales. Plus précisément, la contrainte qui plafonnent en tension à la fin du cycle de chauffage, suivi du pic en tension durant le refroidissement, sont considérés comme étant la force motrice de la fissuration sous conditions de fatigue-oxydation. L'endommagement associé au plateau en tension et au pic en tension a été estimé séparément au moyen de quatre lois de cumul d'endommagement fatigue-oxydation à haute température. La vie résultante a été établie en supposant une simple loi de cumul linéaire. Les paramètres de ces lois, qui décrivent le mieux les données expérimentales sur la fatigue à haute température du René 80 polycristallin, furent obtenus par itération numérique. La distribution des vies prédites le long du bord d'attaque se compare très bien à celle des fissures dans les échantillons testés dans la chambre de combustion. Les vies prédites aux endroits les plus sévèrement sollicités le long du bord d'attaque sont d'un à deux ordres de grandeur

en dessous des vies mesurées avec la technique de chute de potentiel. Ceci n'est pas étonnant, comme les données employées à la détermination des paramètres proviennent d'essais de fatigue sur le René 80 polycristallin, impliquant des joints de grains orientés perpendiculairement à la contrainte principale (ce qui réduit la vie de façon significative), contrairement au René 80 (SD) employé dans ce projet, dont les joints de grains sont orientés dans le même sens que la contrainte principale. Un modèle (développé par Neu et Sehitoglu) qui tient compte des conditions thermo-mécaniques impliquées en fatigue thermique, dont le déphasage entre déformations de nature thermique et mécanique, a été utilisé pour voir l'effet du cyclage thermique sur la vie en fatigue mais aussi pour estimer l'influence de l'endommagement en fluage qui est complètement négligé par les lois de cumuls fatigue-oxydation à haute température. Ce modèle a permis de démontrer que le fluage n'a pas d'influence sur la vie en fatigue pour les temps de maintien à haute température expérimentés durant les essais de fatigue thermique, mais plutôt que l'effet de l'environnement est dominant. De plus, les vies calculées selon les deux classes de modèle sont très semblables, ce qui semble valider l'approche basée sur les lois de fatigue-oxydation à haute température, telle que proposée dans l'aspect numérique de ce projet de modélisation de la vie en fatigue thermique.

La perte d'alliage, notée importante au bord d'attaque et qui est principalement due à l'oxydation cyclique, fut aussi modélisée. Un algorithme tenant compte de la succession des principaux mécanismes d'oxydation impliqués durant le cyclage thermique a été développé. Les mécanismes considérés sont la formation d'une couche d'oxyde protecteur, l'écaillage des couches d'oxydes durant le refroidissement du substrat métallique, l'appauvrissement de l'alliage en éléments actifs, la transition de l'oxydation externe vers l'oxydation interne, et la consommation de la zone appauvrie. En dépit des nombreuses hypothèses simplificatrices apportées pour résoudre ce problème complexe, les pertes d'alliages prédites le long du bord d'attaque ne diffèrent que d'au plus 10% des résultats expérimentaux.

ABSTRACT

This thesis describes a project on the problem of thermal fatigue cracking in aircraft engine turbine blades and vanes. The goals of the project were to develop and validate a methodology for thermal fatigue life prediction and oxidation damage of these components. The project was divided into an experimental phase, which consisted in reproducing and assessing damage accumulation in airfoil-like specimens tested under well simulated service conditions, and to a numerical or modelling phase which consisted in establishing the thermal fatigue life and the oxidation damage from the knowledge of the thermal and mechanical histories of the critical elements in the specimens. On the experimental side, eight thermal fatigue tests were conducted on double-edge wedge (DEW) specimens made of DS René 80 (coated and uncoated) in a burner rig. The DEW specimens were alternately exposed to a hot gas stream (at 1323°C and MACH 0.4) and a cold air jet (at ambient temperature), up to 3000 times.

Initiation and growth of leading edge cracks in the DEW specimens were measured on-line during testing using an advanced alternating current - potential drop (ACPD) technique. Under the test conditions considered, fatigue life of bare DS René 80 was determined to be 760 ± 20 cycles. The same material coated with Codep B-1 exhibited a shorter life to crack initiation which ranged around 300 ± 100 cycles. The resolution of the technique was established to be of 200 μm or less which implies that the measured lives correspond to the number of cycles necessary to initiate a short crack of less than 200 μm . The crack growth after correction for metal loss due to erosion was established to be about 2 $\mu\text{m}/\text{cycle}$. Some tests were stopped after crack detection.

Metallography of specimens of interrupted tests revealed the presence of some

oxide spikes of less than 100 μm (approximately the resolution of the ACPD technique) which had preferentially formed in interdendritic zones or at carbides at the surface of the bare specimens and in grain boundaries of the coating. However, these oxide protuberances were only found where the temperature is moderate and the stresses are very high, as opposed to locations where the temperature is very high. This indicates that these spikes result from the oxidation of fatigue microcracks. Well defined cracks propagated along interdendritic regions where embrittling MC carbides are segregated. The crack tips were heavily oxidized. The mechanism of crack propagation is not clear but the embrittlement of the material in front of the crack tip by oxygen diffusion is believed to play an important role which was taken into account in the damage modelling section of the thesis. Important metal losses of few millimetres due to severe cyclic oxidation conditions were also observed at the leading edge of both bare and coated specimens in the area directly exposed to the hot gas stream. The coating had a good oxidation resistance effect when the substrate temperature did not exceed 1090°C.

A numerical analysis was carried out where the specimen temperature distribution was computed with the ABAQUS-FE code using experimentally determined values of convective heat transfer coefficients and the radiation heat transfer conditions. The computed temperatures of the hot section of the specimen were within 35°C of measured temperatures during steady state (15°C at the leading edge tip), which can reach a maximum temperature of 1164°C at the leading edge. From the knowledge of the temperature distribution in the specimen and the mechanical properties, the stress distribution was also computed by finite element analysis using a thermo-elastoplastic deformation model. A thermo-elasto-viscoplastic analysis based on a modified version of the model of Walker was also used to obtain more realistic values of the inelastic strain and stress relaxation in the most stressed location along the leading edge. Cracks appear where both temperatures and principal tensile stresses are high. Cracks were only observed at locations along the leading edge. It appears that a peak of tensile stress

normal to the crack growth direction develops at the end of the temperature rise, followed by stress relaxation during the hold time at high temperature. Both the tensile stress peak and plateau values at elevated temperature were considered to be the driving force for thermal fatigue damage and were used to estimate life to failure of elements along the leading edge of specimens from four high-temperature fatigue-oxidation damage accumulation models. The parameters of the models were obtained by fitting the results of isothermal fatigue tests conducted on polycrystalline René 80 at high temperature in air. The distribution of the predicted life compares very well to that of cracks along the leading edge, but life predictions were one to two orders of magnitude below the life to crack initiation measured from the ACPD technique. Contrary to the case of the DS material tested in the burner rig, the presence of transvers grain boundaries for the case of the polycrystalline material used to calibrate the models could explain this difference. A thermo-mechanical fatigue model which considers the phasing between the temperature and the mechanical strain as well as the oxidation-fatigue and creep-fatigue damages interactions, demonstrated that the creep damage effect can be neglected for the hold time at high temperature normally found in the thermal fatigue tests carried out in the burner rig. The same order of magnitude of life expectancy was obtained with this model as with the more limited isothermal fatigue-oxidation models.

The alloy surface recession or metal consumption resulting from cyclic oxidation was also modelled. An algorithm, which takes into consideration the sequence of the principal oxidation processes, was developed for this task. The model takes into account external protective oxidation, oxide scale spalling, alloy depletion in the active elements which form the protective oxide scale, transition from external to internal oxidation, and consumption of the depleted zone resulting in alloy surface recession. Despite the assumptions made to simplify this complex problem, the predicted alloy surface recession along the leading edge was found to be in very good agreement with experimental profiles (within less than 10%).

CONDENSÉ EN FRANÇAIS

Cette thèse décrit un projet portant sur le problème de la fatigue thermique dans les aubes de turbines à gaz utilisées en aviation. Les buts du projet étaient de développer et de valider une méthode capable de prédire la vie en fatigue thermique ainsi que l'endommagement associé à l'oxydation cyclique de ces composantes. Le projet comporte deux volets. Le premier volet traite de l'aspect expérimental qui vise à reproduire et à évaluer l'endommagement dans des échantillons soumis à des conditions semblables à celles prévalant dans une turbine à gaz. Le deuxième volet, d'ordre numérique, tente de déterminer le cumul de dommage en fatigue et en oxydation propre à ces échantillons, afin d'obtenir leur vie utile à partir de leur histoire thermomécanique.

Plus précisément au sujet du volet expérimental, huit essais de fatigue thermique ont été menés à l'aide d'une chambre de combustion, sur des échantillons en René 80, revêtus ou non. Les échantillons de géométrie à double bord, dont les rayons imitent ceux des bords d'attaque et de fuite des ailettes réelles, ont été commercialement obtenus par solidification directionnelle (SD). Le revêtement appliqué, le Codep B-1, est un alliage riche en aluminium, produit par cémentation. Les échantillons ont été exposés en alternance à un jet de gaz chaud à haute vitesse (1323°C, MACH 0.4) produit par la chambre de combustion et un jet d'air froid (à température ambiante), parallèle au premier, pendant au plus 3000 cycles thermiques.

L'initiation et la propagation de fissures développées en fatigue thermique aux bords d'attaque des échantillons ont été suivies en cours d'essai, grâce à une technique électrique consistant à imposer un courant alternatif dans les échantillons et à mesurer la chute de potentiel associée. La vie à l'initiation des échantillons non revêtus ainsi

mesurée se situe autour de 760 ± 20 cycles, alors que le même matériau revêtu démontre une vie inférieure jouant autour de 300 ± 100 cycles. La résolution de la technique électrique est de $200 \mu\text{m}$ ou moins ce qui implique que les vies mesurées grâce à cette technique correspondent au nombre de cycles nécessaires pour initier une fissure courte de $200 \mu\text{m}$ environ. La vitesse de propagation a été établie à environ $2 \mu\text{m}/\text{cycle}$, en tenant compte du taux de récession de la surface de l'alliage dû à l'oxydation cyclique. Quelques essais ont été arrêtés après détection de fissure.

L'étude métallographique des échantillons provenant des tests interrompus, a révélé la présence de quelques pics d'oxydes de moins de $100 \mu\text{m}$ (valeur de l'ordre de grandeur de la résolution de la technique électrique de détection de fissure), qui se sont formés préférentiellement dans les zones interdendritiques, aux carbures débouchant à la surface du bord d'attaque et aux joints de grains des revêtements. Les pics ont été retrouvés aux endroits les plus contraints et où la température n'est pas la plus haute. Cette observation tend à prouver que les pics d'oxydes ne résultent que de l'oxydation de microfissures initiées préférentiellement en fatigue à ces sites. Des fissures majeures se sont ensuite propagées entre les dendrites où des carbures fragilisants se trouvent concentrés. Les têtes de fissure sont toutes sévèrement oxydées. Bien que le mécanisme de propagation ne soit pas encore bien connu, le rôle de la fragilisation de la zone en tête de fissure due à la diffusion de l'oxygène dissout dans le métal est d'une grande importance dans le processus de fissuration, comme il a été reconnu dans plusieurs modèles d'interaction d'endommagements fatigue-oxydation.

En plus des fissures, d'importantes pertes de métal causées par les conditions d'oxydation cycliques ont été observées aux bords d'attaque au niveau de la partie directement exposée au jet de gaz chaud, que les échantillons soient revêtus ou non. Ailleurs, où la température n'excède pas 1090°C , les revêtements se sont révélés protecteurs. Plus particulièrement, dans le cas des échantillons non revêtus, la nature et

la morphologie de la couche d'oxyde formée le long du bord d'attaque varient en fonction de la variation de la température et de l'expansion thermique. Dans les zones de l'échantillon qui ne sont pas directement exposées au jet de gaz chaud, où la température et l'expansion thermique sont relativement modérées, une couche d'oxydes $\text{Cr}_2\text{O}_3\text{-Al}_2\text{O}_3$ compacte et protectrice se forme. Dans la zone directement exposée au jet, où la température et l'expansion thermique sont élevées, la couche protectrice s'est écaillée donnant lieu à la formation d'une couche d'oxyde riche en nickel ainsi qu'à d'importantes pertes d'alliage de l'ordre de 2 mm après 2500-3000 cycles.

Pour les échantillons revêtus, une couche d'oxyde Al_2O_3 compacte et protectrice s'est formée aux endroits où la température et l'expansion thermique sont modérées. Dans la zone exposée directement aux gaz chauds et où les contraintes thermiques dans le substrat sont les plus élevées, le revêtement présente des protubérances d'oxydes résultant de l'oxydation de fissures causées par fatigue thermique au niveau des joints de grain du revêtement. L'apparition des protubérances d'oxydes a donné lieu à la destruction accélérée et localisée du revêtement, provoquant une piquûration précoce du substrat. Des fissures de fatigue thermique se sont ensuite développées à la base de ces piquûres qui agissent comme des concentrateurs de contrainte.

L'endommagement par fatigue thermique et par oxydation cyclique tel que rencontré au niveau des ailettes de turbine à gaz fut reproduit sur des échantillons grâce à la chambre de combustion. Cet instrument de laboratoire est donc capable de simuler les conditions de service en terme de température, de vitesse et de chimie des gaz de combustion.

Dans le volet numérique du projet, la distribution de température a été calculée à partir du code d'éléments finis ABAQUS et de valeurs expérimentales des coefficients de transfert de chaleur par convection et par radiation. L'écart moyen entre les

températures calculées et mesurées durant le régime permanent du cycle thermique est de seulement 35°C en moyenne, et de 15°C en tête du bord d'attaque, où la température atteint une valeur maximale de 1164°C.

Les coefficients de transfert de chaleur par convection ont été déterminés par bilan d'énergie à partir des mesures de températures de surface des échantillons. Les mesures de température ont été effectuées avec des thermocouples dont la jonction fut soudées au fond de trous machinés dans les échantillons et avec un pyromètre optique. Ces techniques de mesure sont complémentaires dans le sens que les thermocouples permettent les mesures aux bords d'attaque et de fuite contrairement au pyromètre optique alors que ce dernier permet des mesures locales très variées sur les surfaces planes. L'écart entre les coefficients déterminés par les deux techniques de mesure est de 20% ou moins ce qui est très raisonnable compte tenu de la difficulté expérimentale et analytique du problème.

À partir des résultats de l'analyse thermique et des propriétés mécaniques du matériau, la distribution des contraintes dans les échantillons fut aussi calculée par éléments finis en employant un modèle thermo-élastoplastique ainsi qu'un modèle thermo-élasto-viscoplastique. Le deuxième modèle est basé sur le code de Walker qui a été modifié pour tenir compte de l'orthogonalité des propriétés élastiques du René 80 (SD). Ce dernier modèle fut employé pour calculer de façon plus précise la déformation viscoplastique ainsi que la relaxation dans les éléments du bord d'attaque exposés aux conditions thermo-mécaniques les plus sévères. Au bout de dix cycles thermiques simulés, l'amplitude de la déformation plastique calculée avec ce modèle plus raffiné est dix fois plus importante que celle prédite à partir du modèle thermo-élastoplastique. La contrainte de tension développée durant le cycle de chauffage atteint une valeur maximale de 110 MPa selon le modèle thermo-élasto-viscoplastique, ce qui s'approche de la valeur obtenue par le modèle thermo-élastoplastique qui néglige par

contre la relaxation de la contrainte vers la fin du cycle de chauffage.

Selon l'étude thermo-élastoplastique menée à terme, les fissures sont apparues là où la température est élevée et où les contraintes sont maximales. Plus précisément, la contrainte qui plafonne en tension à la fin du cycle de chauffage, suivi du pic en tension durant le refroidissement, sont considérés comme étant la force motrice de la fissuration sous conditions de fatigue-oxydation. L'endommagement associé au plateau en tension et au pic en tension a été estimé séparément au moyen de quatre lois de cumul d'endommagement fatigue-oxydation à haute température. La vie résultante a été établie en supposant une simple loi de cumul linéaire. Les paramètres de ces lois, qui décrivent le mieux les données expérimentales sur la fatigue à haute température du René 80 polycristallin, furent obtenus par itération numérique. La distribution des vies prédites le long du bord d'attaque se compare très bien à celle des fissures dans les échantillons testés dans la chambre de combustion. Les vies prédites aux endroits les plus sévèrement sollicités le long du bord d'attaque sont d'un à deux ordres de grandeur en dessous des vies mesurées avec la technique de chute de potentiel. Ceci n'est pas étonnant, comme les données employées à la détermination des paramètres proviennent d'essais de fatigue sur le René 80 polycristallin, impliquant des joints de grains orientés perpendiculairement à la contrainte principale (ce qui réduit la vie de façon significative), contrairement au René 80 (SD) employé dans ce projet, dont les joints de grains sont orientés dans le même sens que la contrainte principale. Un modèle (développé par Neu et Sehitoglu) qui tient compte des conditions thermo-mécaniques impliquées en fatigue thermique, dont le déphasage entre déformations de nature thermique et mécanique, a été utilisé pour voir l'effet du cyclage thermique sur la vie en fatigue mais aussi pour estimer l'influence de l'endommagement en fluage qui est complètement négligé par les lois de cumuls fatigue-oxydation à haute température. Ce modèle a permis de démontrer que le fluage n'a pas d'influence sur la vie en fatigue pour les temps de maintien à haute température expérimentés durant les essais de fatigue

thermique, mais plutôt que l'effet de l'environnement est dominant. De plus, les vies calculées selon les deux classes de modèle sont très semblables, ce qui semble valider l'approche basée sur les lois de fatigue-oxydation à haute température, telle que proposée dans l'aspect numérique de ce projet de modélisation de la vie en fatigue thermique.

La perte d'alliage, notée importante au bord d'attaque et qui est principalement due à l'oxydation cyclique, fut aussi modélisée. Un algorithme tenant compte de la succession des principaux mécanismes d'oxydation impliqués durant le cyclage thermique a été développé. Les mécanismes considérés sont la formation d'une couche d'oxyde protecteur, l'écaillage des couches d'oxydes durant le refroidissement du substrat métallique, l'appauvrissement de l'alliage en éléments actifs, la transition de l'oxydation externe vers l'oxydation interne, et la consommation de la zone appauvrie.

Plusieurs hypothèses ont été formulées afin de simplifier ce problème complexe. Premièrement, l'alliage René 80 et le revêtement codep B-1 sont ramenés à un système ternaire Ni-Cr-Al. Plus précisément, le substrat est considéré comme étant un alliage Ni-Cr avec 22% at. de Cr capable de former une couche d'oxyde protectrice de Cr_2O_3 , tant que la cinétique d'appauvrissement en Cr dans substrat n'atteint pas une vitesse critique. De même, le revêtement codep B-1 est considéré comme un alliage Ni-Al avec 60% at. d'Al pouvant former une couche d'oxyde protectrice d' Al_2O_3 . Lorsque l'alliage ou le revêtement est appauvrit en Cr ou en Al à une vitesse telle que la formation d'une couche d'oxyde protectrice n'est plus possible, la zone appauvrie est considérée être composée de Ni avec des traces de Cr ou d'Al (selon le cas) dont la cinétique d'oxydation associée à la formation d'une couche d'oxyde NiO est rapide et donne lieu à la récession de la surface de l'alliage. La vitesse de croissance des couches d'oxydes est modélisée par une loi de cinétique d'oxydation parabolique dont les paramètres ont été établis à partir d'études expérimentales sur le René 80 ainsi que les alliages Ni-Cr et Ni-Al. L'appauvrissement en Cr et Al du substrat et du revêtement résultant de la

diffusion de ces éléments vers la couche d'oxyde a été déterminé par la résolution des équations de Fick par la technique des différences finies. Le coefficient de diffusion du Cr ainsi que l'énergie d'activation déterminés expérimentalement pour un superalliage à base de nickel très semblable au René 80 furent employés dans ces équations. Les critères de transition entre l'oxydation externe associée à la formation d'une couche d'oxyde protectrice et l'oxydation interne donnant lieu à la récession de la couche de l'alliage appauvrie en Cr ou en Al sont établis par les lois de la thermodynamique et de la cinétiques. Le critère thermodynamique stipule que l'oxydation de la couche appauvrie n'a lieu que lorsque l'activité du Cr ou de l'Al à la surface de l'alliage est si faible que l'oxyde de NiO est plus stable que l'oxyde de Cr ou d'Al. Le critère cinétique établit que l'oxydation interne se produit lorsque la vitesse de diffusion du Cr et de l'Al est inférieure à celle nécessaire à la formation d'une couche d'oxyde protecteur. Ce critère cinétique est rencontré lorsque la composition de base en Cr ou en Al est inférieure à environ 12% at. sous des conditions d'oxydation isotherme ou lorsque la couche d'oxyde protecteur est écaillée sous des conditions de cyclage thermique. L'écaillage de la couche d'oxyde est causé par le développement de contraintes de compression critiques lors du cycle de refroidissement qui donnent lieu à la rupture supposée toujours survenir à l'interface oxyde-métal. Le critère de rupture choisi est celui développé par Schütze qui stipule que pour une déformation en compression de la couche d'oxyde imposée par la contraction du substrat métallique, la couche d'oxyde s'écaille lorsqu'elle atteint une épaisseur critique. L'effet des porosités, des micro-fissures, de la sinuosité de l'interface oxyde-métal a été négligé dans l'établissement de ce critère. L'influence du rayon de courbure du bord d'attaque sur les processus d'oxydation, de diffusion et d'écaillage a aussi été négligée.

En dépit des nombreuses hypothèses simplificatrices posées, les pertes d'alliages prédites le long du bord d'attaque des échantillons non-revêtus ne diffèrent que d'au plus 10% des pertes telles que mesurées dans la zone du bord d'attaque exposée aux

conditions thermo-mécaniques les plus sévères. Dans le cas des échantillons revêtus, l'algorithme de modélisation du processus d'oxydation cyclique a permis de prédire une destruction complète du revêtement après 200 cycles thermiques dans la zone du bord d'attaque exposée à des températures excédant 1000°C telle qu'observée expérimentalement.

Basé sur les réalisations du projet décrit dans cette thèse, on peut constater que l'objectif principal qui visait à développer une méthodologie pour prédire l'endommagement par fatigue thermique et par oxydation cyclique dans les ailettes de turbines à gaz a été atteint. Cependant, la validation de cette méthodologie a comporté des lacunes au niveau de la modélisation de la vie en fatigue. Le manque de données expérimentales sur le comportement en fatigue à haute température du René 80 obtenu par solidification directionnelle (René 80 SD) plutôt que par solidification conventionnelle en est la principale cause. De plus, la technique de détection de l'initiation des fissures était la chute de contrainte pour les essais de fatigue isothermes servant à la calibration des modèles de prédictions alors qu'une technique de chute de potentiel électrique de détection était employée lors des essais de fatigue thermique dans la chambre de combustion, ce qui implique une sensibilité différente de détection. Il est donc recommandé à partir de ces constats de réaliser des essais de fatigue isothermes et thermo-mécaniques sur le René 80 SD et d'utiliser la même technique de chute de potentiel électrique afin de calibrer les modèles de prédiction de vie, de sorte qu'une validation de la méthodologie convenable soit réalisée. Ultiment, la méthodologie pourrait être étendue à la prédiction de l'endommagement par fatigue thermique, par fluage et par oxydation cyclique des ailettes en service.

CONTENTS

REMERCIEMENTS	v
RÉSUMÉ	vi
ABSTRACT	x
CONDENSÉ EN FRANÇAIS	xiii
LIST OF TABLES	xxvi
LIST OF FIGURES	xxviii
LIST OF APPENDIXES	xxxviii
LIST OF ABBREVIATIONS AND SYMBOLS	xl
1. INTRODUCTION	1
1.1 Background	1
1.2 Project Objectives and Approach	1
2. LITERATURE REVIEW OF METALLURGY, THERMAL FATIGUE AND OXIDATION DAMAGES MODELLING FOR BARE AND COATED SUPERALLOYS	5
2.1 Chemical and Physical Metallurgy of Ni-Base Superalloys and Aluminide Coatings	6

2.2 Thermal Fatigue Damage Modelling	9
2.2.1 Mechanisms	11
2.2.1.1 Crack Initiation	11
2.2.1.2 Crack Propagation	13
2.2.2 Fatigue-Oxidation Life Prediction Models	17
2.2.2.1 Coffin	17
2.2.2.2 Ostergren	22
2.2.2.3 Antolovich et al.	24
2.2.2.4 Romanoski et al.	29
2.2.2.5 Reuchet and Rémy	34
2.2.2.6 Neu-Sehitoglu	37
2.3 Oxidation Damage Modelling	44
2.3.1 Chemical Nature of the Oxide Scale	45
2.3.2 Oxide Scale Growth Kinetics	46
2.3.2.1 Uniform Oxidation	46
2.3.2.2 Localized Oxidation	52
2.3.3 Alloy Surface Recession Kinetics	54
2.3.4 Alloy Depletion Profile	56
2.3.5 Transition from External to Internal Oxidation	60
2.3.6 Cyclic Oxidation	63
3. EXPERIMENTAL PROGRAM	69
3.1 Thermal Fatigue Testing in the Burner Rig	70
3.1.1 Material and Specimen Geometry	70
3.1.2 Burner Rig Description and Instrumentation	71
3.1.2.1 Burner Rig Installation	71
3.1.2.2 Data Acquisition System	73
3.1.3 Experimental Conditions	74

3.1.4	Testing Procedure	76
3.2	Specimen Temperature Measurement Techniques	77
3.2.1	Thin-wire Thermocouple	77
3.2.2	Optical Pyrometry	78
3.3	Damage Assessment Techniques	79
3.3.1	Metallography Damage Assessment	79
3.3.2	On-line Crack Growth Assessment	80
4.	EXPERIMENTAL RESULTS	84
4.1	Damage Assessment from Metallographic Analysis	85
4.1.1	Evolution of the Microstructure	85
4.1.1.1	Virgin Specimens	85
4.1.1.2	Tested Specimens	87
4.1.2	Thermal Fatigue Cracking Damage	91
4.1.2.1	Crack Initiation	91
4.1.2.2	Crack Propagation	93
4.1.2.3	Length and Position of Cracks and Oxide Spikes	95
4.1.3	Oxidation Damage	100
4.1.3.1	Uncoated Specimens	100
4.1.3.2	Coated Specimens	102
4.1.4	Comparison of the Results to Airfoil Damage Occuring in Other Burner Rigs and in Real Engines	104
4.1.5	Conclusions	105
4.2	On-line Crack Growth Assessment	108
4.2.1	Potential Drop Evolution	108
4.2.2	Crack Initiation	111
4.2.3	Crack Growth Rate	112
4.2.4	Resolution of the Technique	118

4.2.5 Conclusions	120
5. THERMO-MECHANICAL ANALYSIS AND DAMAGE MODELING ..	121
5.1. Thermal Analysis	122
5.1.1 Temperature Measurements	122
5.1.1.1 Thin-wire Thermocouple Measurements	123
5.1.1.2 Optical Pyrometry Measurements	128
5.1.2 Temperature Computation	129
5.1.2.1 Conductive Heat Transfer	129
5.1.2.2 Radiation Heat Transfer	130
5.1.2.3 Convective Heat Transfer	132
5.1.2.4 Computation of Transient Temperatures During Cycling	148
5.1.3 Conclusions	152
5.2 Mechanical Analysis	153
5.2.1 Computation Methodology	154
5.2.1.1 Thermo-elastoplastic Analysis	157
5.2.1.2 Thermo-elasto-viscoplastic Analysis	163
5.2.2 Results of the Computation	169
5.2.2.1 Thermo-elastoplastic Behaviour	169
5.2.2.2 Thermo-elasto-viscoplastic Behaviour	173
5.2.3 Conclusions	175
5.3 Thermal Fatigue Damage Modelling	177
5.3.1 Theoretical and Experimental Validities of the Models	178
5.3.1.1 Theoretical Validity	178
5.3.1.2 Experimental Validity	184
5.3.2 Prediction of Thermal Fatigue Life from Burner Rig Conditions	191

5.3.2.1 Methodology for the Determination of the Constants for IF Life Prediction Models	192
5.3.2.2 Life Prediction Results	195
5.3.2.3 Comparison of Predicted and Experimental Life	199
5.3.3 Conclusions	206
5.4 Oxidation Damage Modelling	210
5.4.1 Algorithm for Modelling Alloy Depletion Profile and Alloy Surface Recession	211
5.4.2 Prediction of the Alloy Depletion profiles and Alloy Surface Recession Under Burner Rig Conditions	214
5.4.2.1 Alloy Depletion Profiles	215
5.4.2.2 Alloy Surface Recession	218
5.4.3 Conclusions	221
6. GENERAL CONCLUSIONS	223
7. RECOMMENDATIONS	233
REFERENCES	235
FIGURES	246
APPENDIXES	364

LIST OF TABLES

Table 2.1 Effect of hold time in IF tests on CC René 80 to 871°C	21
Table 2.2 Constant k_{p0} ' and activation energy Q for oxidation of dilute and rich Ni-Cr and Ni-Al alloys	49
Table 2.3 Values of the parameters of the parabolic kinetic Equations 48-51 of oxidation DS René 80 at 1050 °C	51
Table 2.4 Equivalent volume of Ni, the alloy René 80 and their oxides	55
Table 2.5 Mechanical properties of principal Ni, Cr, Al oxides	66
Table 3.1 List of the Thermal Fatigue Tests Carried Out on DS René 80 (DEW) Specimens in the Burner Rig	75
Table 4.1 Evolution of the Metallurgical Parameters of DS René 80 during TF Testing	90
Table 4.2 Length and Position of Oxide Spikes in TF Specimens	96
Table 4.3 Length and Position of Cracks in TF Specimens	98
Table 4.4 Thermal Fatigue Results	119
Table 5.1 Specimen Temperatures Measured by Thermocouples During Steady-state as a Function of Gas Temperature	125
Table 5.2 Computed Surface Temperatures as a Function of Gas Temperature T/C	127
Table 5.3 Characteristics of the Hot Gas Stream	136
Table 5.4 Experimental Heat-transfer Coefficients for Gas Stream Temperature Varying from 800 to 1200°C	143
Table 5.5 Geometric Factors (GF) for Gas Stream Temperature Varying from 800 to 1200°C	143
Table 5.6 Experimental Heat-transfer Coefficients for Gas Stream at 1300°C . . .	146
Table 5.7 Comparison of GF and h Values Obtained by Thermocouple	

and Pyrometry Measurements at $T_g = 1323^\circ\text{C}$	147
Table 5.8 Elastic properties established for DS René 80	160
Table 5.9 Yield stress and maximum stress obtained from cyclic stress-strain curves for CCR80	162
Table 5.10 Constants of the exponential form of the Walker model for B1900+Hf	168
Table 5.11 Summary of oxidation-fatigue models	180
Table 5.12 Life prediction relative error, RE, for different models and data sets obtained for IF tests on CC René 80	187
Table 5.13 Values of the model constants and exponents determined from data sets obtained for isothermal fatigue tests carried out at 871°C and at 982°C on CC René 80	190
Table 5.14 Minimal fatigue lives of elements at the leading edge of the DEW specimen as computed from different models and from the results of two mechanical analyses	197
Table 5.15 Corrected life predictions, $N_f(\text{ACPD,DS})$, computed from different models versus experimental life for initiation of a short crack, $N_{i, \text{exp}}$, obtained in the BR	205
Table 5.16 Measured Maximal Surface Recession along the Leading Edge of DEW Specimens after Testing in the Burner Rig Compared to Predicted Values	220

LIST OF FIGURES

Figure 1.1 Flow chart process of thermal fatigue modelling damage accumulation in turbine blades and vanes	247
Figure 2.1 Strain versus time and temperature under OP, IP and CCWD TMF testing conditions	248
Figure 2.2 Dependence of strain-controlled LCF life on maximum cyclic tensile stress for various orientation in DS René 120	249
Figure 2.3 Fatigue oxidation crack growth mechanism A	250
Figure 2.4 Fatigue-oxidation crack growth mechanism B	251
Figure 2.5 Cyclic strain softening behaviour at different frequencies	252
Figure 2.6 Comparison of frequency-modified elastic and plastic strain range vs cycles to failure with test results	253
Figure 2.7 Schematic hysteresis loops, stress and strain vs time records for different cycling conditions	254
Figure 2.8 Experimental fatigue lives ($N_{f\text{exp}}$) obtained from IF tests on CC René 80 compared with lives ($N_{f\text{cal}}$) calculated with Equation 15	255
Figure 2.9 Schematic illustration of the mechanism of incremental decohesion along a grain boundary	256
Figure 2.10 Schematic diagram of oxide growth with repeated rupture	257
Figure 2.11 Schematic diagram of the oxide composition and morphology formed at the surface of Cr-Al rich (a) and dilute (b) Ni-Cr-Al alloys	258
Figure 2.12 Schematic of an oxide scale formed at the surface of a metallic substrate	259
Figure 2.13 Solute content effect on the parabolic rate constant k_p' for (a) the Ni-Cr and (b) Ni-Al alloys at different temperatures	260
Figure 2.14 Kinetics of oxidation of DS René 80 at 1050 °C for the leading edge	

(LE), the flat surface (FS) and the trailing edge of a DEW specimen	261
Figure 2.15 Penetrating oxide spike associated with the preferential oxidation of a carbide, a grain boundary or an interdendritic zone next to the surface of the substrate	262
Figure 2.16 Definition of nodal points used in the finite difference method for solving the alloy depletion profile during oxidation	263
Figure 3.1 Double edge-wedge (DEW) specimen geometry meant to reproduce leading edge and trailing edge radii of real airfoils	264
Figure 3.2 IAR burner rig test facility instrumented for thermal fatigue test . . .	265
Figure 3.3 Schematic cutaway view of the combustor of the IAR burner rig . . .	266
Figure 3.4 Hardware configuration of the burner rig controls and data acquisition system	267
Figure 3.5 Design of the specimen holder which is fixed to the pneumatic carrier in the burner rig	268
Figure 3.6 Schematic of the instrumented shell-like specimen showing the 13 locations where thin-wire thermocouples were spot-welded inside the specimen .	269
Figure 3.7 Polished leading edge section through the DEW specimen showing the embedded thermocouple inside its metal (310 SS) sheath	270
Figure 3.8 Drawing of the different sections cut off the specimens for the metallography	271
Figure 3.9 Drawing of the double edge-wedge cast specimen with the indication of the current probes location and the potential probes locations	272
Figure 4.1 Metallographic aspect of the virgin material of an uncoated DEW specimen	273
Figure 4.2 Micrographs of the virgin material from a longitudinal section through a coated DEW specimen	275
Figure 4.3 Thickness of the coating and of the interdiffusion zone around the specimen cross-section	276

Figure 4.4 γ precipitates aligned and elongated perpendicularly to the principal stress near a crack tip	277
Figure 4.5 Columnar grains precipitated at grain boundaries in the coating exposed to 780 thermal cycles	278
Figure 4.6 Oxide spikes: (a) formed at the interdendritic regions, (b) formed at a carbide; (c) formed at microstructural heterogeneities	279
Figure 4.7 Oxide spikes blunted by lateral oxidation	281
Figure 4.8 Two sharp oxide spikes at the root of a notch, machined 0.3 mm deep and 0.5 mm wide at the leading edge, before testing	282
Figure 4.9 Oxide fingers formed into the columnar grains in the coating	283
Figure 4.10 Small cracks initiated at the root of crevices (pits) in the substrate of a coated specimen	284
Figure 4.11 Crack propagated at the leading edge of a specimen exposed to 2500 short thermal cycles	285
Figure 4.12 Crack propagated at the leading edge of a specimen exposed to 2140 long thermal cycles	287
Figure 4.13 Crack propagated at the root of a large crevice at the leading edge of a coated specimen exposed to 2500 short thermal cycles	289
Figure 4.14 Full scale photograph (in a) and macrography (in b) of the SRC bare specimen exposed to 3000 thermal cycles in the burner rig, showing eight cracks and important material losses at the leading edge	290
Figure 4.15 In the protective oxidation zones (labelled A in Figure 4.14) a continuous external oxide scale, normally composed of a Cr_2O_3 external layer and of an Al_2O_3 sub-layer formed	291
Figure 4.16 In the transition zones, the protective oxide scale spalls off which leads to the formation of a porous non-protective nickel-rich oxide scale	292
Figure 4.17 In the spalled oxide zone, the substrate is drastically consumed . . .	293
Figure 4.18 Material loss (y_A) along the leading edge of SRC and SRD	

specimens after testing in the burner rig	294
Figure 4.19 Full scale photograph (in a) and macrography (in b) of the SRF coated specimen exposed to 2500 thermal cycles in the burner rig, showing numerous cracks and an irregular leading edge	295
Figure 4.20 Measured evolution of the potential drop during a typical thermal cycle	296
Figure 4.21 Evolution of the electrical resistivity of a typical nickel-based superalloy (Udimet 700) with temperature	297
Figure 4.22 Evolution of the potential drop (measured during the steady state portion of thermal cycles) during TF testing SRA	298
Figure 4.23 Evolution of the potential drop (measured during the steady state portion of thermal cycles) during TF testing SRD	299
Figure 4.24 Evolution of the potential drop (measured during the steady state portion of thermal cycles) during TF testing SRB	300
Figure 4.25 Evolution of the potential drop (measured during the steady state portion of thermal cycles) during TF testing SRC	301
Figure 4.26 Evolution of the potential drop (measured during the steady state portion of thermal cycles) during TF testing SRF	302
Figure 5.1 Representative temperature profile during thermal cycling in rig as established by thermocouples embedded within the body of the DEW specimen .	303
Figure 5.2 Model of the in-plane longitudinal section through the leading edge of the specimen used in conjunction with Equation 94 to calculate the local surface temperature and the thermal gradient at the surface	304
Figure 5.3 Distribution of surface temperature along the mid-section of the DEW specimen corresponding to the axis of the hot gas stream	305
Figure 5.4 Thermal conductivity and specific heat of René 80 as a function of temperature	306
Figure 5.5 Measured temperatures (corrected for radiation) and computed velocity	

profiles within the hot gas stream produced by the rig	307
Figure 5.6 Surface elemental volume of size $dx.dy.dz$ over which the energy balance is derived from different locations over the surface of the DEW specimen in accordance with the coordinate system shown	308
Figure 5.7 Profile of experimental geometric factors (GF) and their corresponding heat-transfer coefficients along chordwise section of specimen in the axis of the hot gas stream	309
Figure 5.8 Photograph of DEW specimen after one thermal cycle in the test rig showing oxidation pattern characteristic of flow separation at the transition between the flat and wedged portion of the specimen	310
Figure 5.9 Heat-transfer coefficient profile at the leading edge along the longitudinal axis z during the heating and cooling	311
Figure 5.10 Mesh and axes system used in the thermal FE-analysis	312
Figure 5.11 Computed temperature history at different locations of the leading edge tip of the DEW specimen during thermal cycling in the burner rig	313
Figure 5.12 Computed temperature profile along the leading edge tip of the DEW specimen at different times during thermal cycling	314
Figure 5.13 Computed isotherms in the DEW specimen (in the plane $y-z$, see Figure 5.10) at the end of the heating and cooling thermal cycling, compared to typical spalled off oxide patterns observed in specimens after 2500 thermal cycles	315
Figure 5.14 Computed isotherms in the mid-section of the DEW specimen (in the plane $x-y$, see Figure 5.10) at the end of the heating cycle	316
Figure 5.15 Computed surface temperature profile along the chordwise mid-section of the DEW specimen at the end of the heating cycle, compared to measured temperatures obtained by optical pyrometry	317
Figure 5.16 Mesh and axes system used in the mechanical FE-analysis	318
Figure 5.17 Cyclic stress-strain (σ - ϵ) curve for CCR80 at 980°C	319

- Figure 5.18** Computed temperature (T) and principal stress (σ_{33} or σ_z) histories at three highly stressed locations along the leading edge tip of the DEW specimen (axis z in Figure 5.16) during thermal cycling in the burner rig 320
- Figure 5.19** Isotherms, schematic loads and real von Mises stress distributions (plane 2-3) in the DEW specimen during heating 321
- Figure 5.20** Isotherms, schematic loads and real von Mises stress distributions (plane 2-3) in the DEW specimen during cooling 323
- Figure 5.21** Computed temperature (T) and principal stress (σ_{33} or σ_z) distributions along the leading edge tip (axis z in Figure 5.16) at the end of the heating cycle (time = 150 s) and 4 seconds after the beginning of the cooling cycle (time = 154 s). Oxide spikes (a_o) and crack (a) locations along the leading edge are concentrated where the maximal temperatures and stresses were observed 325
- Figure 5.22** Computed variation of the different strains during one thermal cycle at the most stressed location of the leading edge of the DEW specimen ($z = 29.75$ mm) 326
- Figure 5.23** Computed stress-strain variation during one thermal cycle in the burner rig at the most stressed location of the leading edge of the DEW specimen ($z = 29.75$ mm). The stress and the strain are expressed as the principal stress (σ_{33} or σ_z) and the principal thermal strain (ϵ_{33}^{th}), respectively 327
- Figure 5.24** Computed stress-strain variation during one thermal cycle in the burner rig at the most stressed location of the leading edge of the DEW specimen ($z = 29.75$ mm). The stress and the strain are expressed as the principal stress (σ_{33} or σ_z) and the elastic strain (ϵ_{33}^e), respectively 328
- Figure 5.25** Computed stress-strain variation during one thermal cycle in the burner rig at the most stressed location of the leading edge of the DEW specimen ($z = 29.75$ mm). The stress and the strain are expressed as the principal stress (σ_{33} or σ_z) and the plastic strain (ϵ_{33}^p), respectively 329

- Figure 5.26** Experimental monotonic stress-strain curve of CCR80 tested at 980°C and at constant strain rate $3.33 \times 10^{-5} \text{ s}^{-1}$ compared to computed curve from the modified elasto-viscoplastic model of Walker using the constitutive parameters of B1900+Hf 330
- Figure 5.27** Stress-strain loops (10 thermal cycles in the burner rig) computed with the thermo-elasto-viscoplastic model of Walker, at the location exposed to the most severe thermo-mechanical condition along the leading edge of the DEW specimen ($z = 38.25 \text{ mm}$). The stress and the strain are expressed as the principal stress (σ_{33} or σ_z) and the plastic strain (ϵ_{33}^p), respectively 331
- Figure 5.28** Comparison of life predicted with the Coffin's Models ($\Delta\epsilon_e$ and $\Delta\epsilon_p$) with experimental life obtained for isothermal fatigue tests carried out under continuous cycling at 871°C on CC René 80 332
- Figure 5.29** Comparison of life predicted with the Ostergren's Model with experimental life obtained for isothermal fatigue tests carried out under continuous cycling at 871°C on CC René 80 333
- Figure 5.30** Comparison of life predicted with the Antolovich et al.'s Model with experimental life obtained for isothermal fatigue tests carried out under continuous cycling at 871°C on CC René 80 334
- Figure 5.31** Comparison of life predicted with the Romanoski et al.'s Model with experimental life obtained for isothermal fatigue tests carried out under continuous cycling at 871°C on CC René 80 335
- Figure 5.32** Comparison of life predicted with the Coffin's Model ($\Delta\epsilon_e$) with experimental life obtained for isothermal fatigue tests carried out under tensile and/or compressive strain hold time at 871°C on CC René 80 336
- Figure 5.33** Comparison of life predicted with the Coffin's Models ($\Delta\epsilon_p$) with experimental life obtained for isothermal fatigue tests carried out under tensile and/or compressive strain hold time at 871°C on CC René 80 337
- Figure 5.34** Comparison of life predicted with the Ostergren's Model with

experimental life obtained for isothermal fatigue tests carried out under tensile and/or compressive strain hold time at 871°C on CC René 80	338
Figure 5.35 Comparison of life predicted with the Antolovich et al.'s Model with experimental life obtained for isothermal fatigue tests carried out under tensile and/or compressive strain hold time at 871°C on CC René 80	339
Figure 5.36 Comparison of life predicted with the Romanoski et al.'s Model with experimental life obtained for isothermal fatigue tests carried out under tensile and/or compressive strain hold time at 871°C on CC René 80	340
Figure 5.37 Computed temperature (T) and principal stress (σ_{33} or σ_z) variation at position $z = 29.75$ mm along the leading edge of the DEW specimen during thermal cycling in the burner rig	341
Figure 5.38 Distribution of the principal stress (σ_z), the temperature (T) and the probability (P) of crack initiation after $N_{f, min}$ cycles (computed from the models of Coffin) compared to oxide spikes (a_o) and cracks (a) along the leading edge . .	342
Figure 5.39 Distribution of the principal stress (σ_z), the temperature (T) and the probability (P) of crack initiation after $N_{f, min}$ cycles (computed from the model of Ostergren) compared to oxide spikes (a_o) and cracks (a) along the leading edge .	343
Figure 5.40 Distribution of the principal stress (σ_z), the temperature (T) and the probability (P) of crack initiation after $N_{f, min}$ cycles (computed from the model of Antolovich et al.) compared to oxide spikes (a_o) and cracks (a) along the leading edge	344
Figure 5.41 Distribution of the principal stress (σ_z), the temperature (T) and the probability (P) of crack initiation after $N_{f, min}$ cycles (computed from the model of Romanoski et al.) compared to oxide spikes (a_o) and cracks (a) along the leading edge	345
Figure 5.42 Algorithm for Modelling Alloy Depletion Profile and Alloy Surface Recession	346
Figure 5.43 Computed variation of the Cr content at the metallic surface	

of Ni-Cr alloys with various Cr nominal contents, during isothermal oxidation at 1164°C	347
Figure 5.44 Computed Cr content profile in the depleted zone of a Ni-22at%Cr alloy exposed to different number of typical thermal cycles in the burner rig with a maximum alloy temperature of 1164°C ($z = 46.25$ mm)	348
Figure 5.45 Computed Cr and Al content profile ($N_{Cr} + N_{Al}$) in the depleted zone of an uncoated DSR80 alloy exposed to 1.7 thermal cycles in the burner rig with a maximum alloy temperature of 1164°C ($z = 46.75$ mm)	349
Figure 5.46 Computed Cr and Al content profile ($N_{Cr} + N_{Al}$) in the depleted zone of a coated DSR80 alloy exposed to 25 thermal cycles in the burner rig with a maximum alloy temperature of 1164°C ($z = 46.75$ mm)	350
Figure 5.47 Computed variation of the Cr content (N_{Cr}) at different depths in the depleted zone of a Ni-22at%Cr alloy during thermal cycling in a burner rig with a maximum alloy temperature of 1164°C ($z = 46.75$ mm)	351
Figure 5.48 Computed variation of the Cr and Al content ($N_{Cr} + N_{Al}$) at the metallic surface of the uncoated DSR80 alloy at different longitudinal positions along the leading edge of DEW specimens during thermal cycling in a burner rig	352
Figure 5.49 (a) Computed variation of the Cr and Al content ($N_{Cr} + N_{Al}$) at different depths in the depleted zone of the coated DSR80 alloy at the longitudinal position $z = 46.75$ mm along the leading edge of DEW specimens during thermal cycling in a burner rig (the maximum alloy temperature reaches 1164°C at this position). (b) detailed variation of the Cr and Al content ($N_{Cr}' + N_{Al}'$) at the metallic surface of the coating	353
Figure 5.50 Effect of alloy surface recession on the computed variation of the Cr content (N_{Cr}') at the surface of a Ni-22at%Cr alloy during thermal cycling in a burner rig with a maximum alloy temperature of 1164°C ($z = 46.75$ mm)	355
Figure 5.51 Effect of alloy surface recession on computed variation of the Cr	

and Al content ($N_{Cr} + N_{Al}$) at the surface of the uncoated DSR80 alloy at the longitudinal position $z = 46.75$ mm 356

Figure 5.52 Computed alloy surface recession (y_A) of an uncoated and a coated DSR80 alloy at two positions along the leading edge of DEW specimens during thermal cycling in a burner rig: (a) $z = 46.75$ mm with a maximum alloy temperature of 1164°C ; (b) $z = 25.50$ mm with a maximum alloy temperature of 936°C 357

Figure 5.53 Computed alloy surface recession (y_A) along the leading edge (axis z) of uncoated DEW specimens in DRS80 during thermal cycling in a burner rig with (a) short periods of 150 s in the hot gas stream (case of tests SRA, SRB, SRC, SRF, refer to Subsection 4.1), and with (b) long periods of 390 s in the hot stream (case of the test SRD) 359

Figure 5.54 Measured vs computed alloy surface recession (y_A) along the leading edge (axis z) of uncoated DEW specimens of DRS80 after testing in a burner rig with (a and c) short periods of 150 s in the hot gas stream (test SRC), and with (b and d) long periods of 390 s in the hot stream (test SRD) 361

LIST OF APPENDIXES

APPENDIX A	DETAILED THERMAL FATIGUE TESTING PROCEDURE IN BURNER RIG	365
APPENDIX B	DESCRIPTION OF THE CGM5 CRACK GROWTH MONITOR	377
APPENDIX C	PROGRAMMING OF THE MICRISTAR	390
APPENDIX D	AUTONICKEL PLATING PROCEDURE	400
APPENDIX E	PLOTTING OF THE POTENTIAL DROP VS NUMBER OF CYCLES FROM MEASURED PD DURING THERMAL FATIGUE TESTS	403
APPENDIX F	DETERMINATION OF THE RADIATION HEAT TRANSFER PARAMETERS	408
APPENDIX G	EVALUATION OF THE EFFECT OF CONDUCTION AND RADIATION HEAT LOSSES FROM JUNCTION OF A THERMOCOUPLE ON GAS TEMPERATURE MEASUREMENT	417
APPENDIX H	PROGRAMS FOR ASSISTANCE IN THERMAL ANALYSIS APPLIED TO THE DEW SPECIMEN IN THE BURNER RIG	425

APPENDIX I	GENERALISATION OF THE WALKER SUBROUTINE FOR ISOTROPIC MATERIALS TO THE CASE OF ORTHOTROPIC MATERIALS	467
APPENDIX J	PROGRAMS FOR THE DETERMINATION OF THE OPTIMAL FATIGUE-OXIDATION DAMAGE MODEL PARAMETERS	515
APPENDIX K	PROGRAMS FOR THE DETERMINATION OF THERMAL FATIGUE LIFE FROM IF AND TMF DAMAGE MODELS	535
APPENDIX L	PROGRAMS FOR THE DETERMINATION OF THE DEPLETION PROFILE AND THE ALLOY RECESSION INTERFACE IN UNCOATED AND COATED Ni-BASE ALLOYS	545

LIST OF ABBREVIATIONS AND SYMBOLS

a	crack length
a_i	spatial resolution of the crack growth monitor
a_i	crack length at initiation
a_f	crack length to failure
a_{final}	crack length at the end of a fatigue test
a_s	penetrating oxide spike depth measured from the surface of the metal
a_A	chemical activity of A in the alloy A-B
a_B	chemical activity of B in the alloy A-B
a_{AO}	chemical activity of the oxide AO in the oxide scale
a_{BO}	chemical activity of the oxide BO in the oxide scale
A	area
α	thermal expansion coefficient
ACPD	Alternating Current Potential Drop
BEI	Backscattered Electrons Imaging
BR	Burner Rig
C	stiffness matrix
C_B	Concentration of B in the alloy A-B
C_p	specific heat
CO or C	Coating
CC	Conventional Casting
CCWD	CounterClockWise Diamond
$CF_{k_p'}$	Correction Factor to establish the effective k_p' from the constant k_p' evaluated at T_{max} during thermal cycling
CG	Columnar Grain

CGM5	Crack Growth Monitor version 5
D	continuum Damage variable
D^{fat}	fatigue Damage variable
D^{ox}	oxidation Damage variable
D^{creep}	creep Damage variable
D_B	coefficient of diffusion or diffusivity of B in the alloy A-B
D_{B0}	frequency factor for the diffusivity of B in the alloy A-B
d	diameter
$da_{\text{ox},c}$	oxidation penetration of the carbides during one cycle
$da_{\text{ox},M}$	oxidation penetration of the matrix during one cycle
d_s	penetrating oxide spike depth measured from the external oxide surface
$d_{s,f}$	critical oxide spike length
da/dN	crack growth rate
$(da/dN)_e$	crack shortening rate caused by erosion
$(da/dN)_m$	measured crack growth rate
$(da/dN)_{\text{tf}}$	crack tip extension rate caused by thermal fatigue
d_γ	average size of the gamma prime precipitates
δ	skin depth
δ_{ij}	Kronecker delta
Δa	crack extention
$\Delta \epsilon$	strain range
ΔG_{AO}	free energy of formation of the oxide AO
ΔG_{BO}	free energy of formation of the oxide BO
$\Delta G^\circ_{\text{AO}}$	standard free energy of formation of the oxide AO
$\Delta G^\circ_{\text{BO}}$	standard free energy of formation of the oxide BO
ΔH	activation energy
ΔPD	Potential Drop variation

$\Delta\sigma_{\text{eff}}$	effective stress range ($\sigma - \sigma_{\text{th}}$)
Δt	cycle period
Δt	increment of time
ΔT	Temperature variation
Δy	increment of depth in the metallic substrate
DCPD	Direct Current Potential Drop
DEW	Double Edge - Wedge
DS	Directional Solidification
DSR80	René 80 DS
E	Young's modulus
ε	emissivity
ε	true strain
$\dot{\varepsilon}$	strain rate
ε_{min}	minimum strain
ε_{max}	maximum strain
ε_e	elastic strain
$\varepsilon_{\text{mech}}$	mechanical strain
ε_{net}	net or total strain
ε_p or ε^I	plastic or inelastic strain
ε_{th}	thermal strain
EDM	Electro Discharge Machining
EDX	Energy-Dispersive X-ray spectrometry
f	AC frequency
f	yield surface function in the space of stress
f_c^*	effective fraction of carbides on the crack path
F_{i-j}	radiation shape factor related to elements i and j
FCC	Face-Centred-Cubic lattice structure
FE	Finite Elements

FS	Flat Surface of an airfoil
G	shear modulus
G	thermal Gradient
γ_0	fracture surface energy of the interface metal-oxide
GF	geometric factor expressed as the local h to mean h ratio
h	local convective heat transfer coefficient
h_0	mean convective heat transfer coefficient
HCF	High Cycle Fatigue
HD	Hard Disk
IF	Isothermal Fatigue
IP	In-Phase
$J_{B(m)}$	flux of B in the alloy
$J_{B(ox)}$	flux of B in the oxide scale
K	viscous drag stress or friction stress
k	thermal conductivity
k_p	metal consumption parabolic rate constant
k_e'	rate of evaporation of the oxide scale
k_p'	parabolic oxidation rate constant
k_p^*	equivalent parabolic oxidation rate constant
k_s'	oxidation rate constant for the spike penetration
l_d'	average arm spacing of the primary dendrites
l_d''	average arm spacing of the secondary dendrites
l_{MC}	average length of needles that compose the MC carbides
λ	plastic multiplier
LCF	Low Cycle Fatigue
LE	Leading Edge of an airfoil
LEFM	Linear Elastic Fracture Mechanics
\dot{m}	mass flow

M_g	gas velocity expressed in MACH
μ_r	relative permeability
n	exponent of the oxidation kinetics law
n'	cyclic hardening exponent
N	Number of cycles
N_a	number of cycles to crack arrest
N_A	molar fraction or content of the noble element A in alloy A-B
N_B	molar fraction or content of the active element B in alloy A-B
N_B'	molar fraction of B at the oxide-metal interface
N_B^0	nominal content of the element B in alloy A-B
N_B^{eq}	molar fraction of B in the metal at equilibrium between the oxide scale and the metallic substrate
N_B^{tr}	critical content in B for the transition from internal to external oxidation of the active element B in the alloy A-B
N_i	life to crack initiation
N_f	life to failure
N_{final}	total number of cycles carried out during a fatigue test
$N_{f\,cal}$	predicted (calculated) fatigue life
$N_{f\,exp}$	experimental fatigue life
N_f^{fat}	fatigue life
N_f^{ox}	oxidation life
N_f^{creep}	creep life
N_t	transition fatigue life
Nu	Nusselt number
ν	kinematic viscosity
ν	poisson's ratio
ν	cycle frequency
ν_{eff}	effective cycle frequency

ω	deviatoric back stress
Ω	back stress
OP	Out-of-Phase
p_{O_2}	partial pressure of oxygen
PD	Potential Drop
Pr	Prandlt number
ϕ^{ox}	TMF phasing function in the fatigue-oxidation damage model of Neu-Sehitoglu
Φ^{ox}	TMF phasing factor in the fatigue-oxidation damage model of Neu-Sehitoglu
φ	plastic rate multiplier
q	heat flux
q_k	conduction heat flux
q_r	radiation heat flux
q_h	convection heat flux
Q	heat rate
Q	activation energy
R	correlation factor
R	gas constant
R or R_σ	stress Ratio ($\sigma_{min}/\sigma_{max}$)
R_ϵ	strain Ratio ($\epsilon_{min}/\epsilon_{max}$)
$R_{ACPD/SD}$	Ratio of the life determined from the ACPD and the SD techniques
$R_{DS/CC}$	Ratio of the life of DS and CC structures with the same alloy composition
Re	Reynolds number
RAM	Random Access Memory
RE	Relative Error
ρ	density

ρ	electrical resistivity
S	compliance matrix
S	deviatoric of the total stress
σ	constant of Stefan-Boltzmann
σ	true stress
σ_{eff}	effective stress
σ_{eq}	von Mises stress
σ_{gb}	cohesive strength of a grain boundary
σ_H	hydrostatic stress
σ_{min}	minimum stress
σ_{max}	maximum stress
σ_{open}	crack opening stress
σ_{th}	threshold stress for microcrack extension
σ_y	yield stress
Σ	effective stress
Σ_{eq}	equivalent effective stress
SC	Single Crystal
SD	Stress Drop
SEM	Scanning Electron Microscope
SS	Steady State
STD	Standard Deviation
t	oxide scale thickness
t	time
t_e	time of preoxidation
t_h	total hold time during a period
t_{hC}	hold time during Compression
t_{hT}	hold time during Tension
T	Temperature

T_0	initial Temperature
T_g	corrected gas Temperature
T_j	Temperature of the element "j" of the surroundings
T_s	surface Temperature
T/C	hot gas stream Temperature as measured by the thermocouple of control in the BR
TE	Trailing Edge of an airfoil
TF	Thermal Fatigue
Th	Thermocouple measurement
TMF	Thermo-Mechanical Fatigue
TSF	Thermal-Stress Fatigue
U	local gas velocity
U_g	mean gas velocity
US	Unsteady State
V_m	molar volume
\bar{V}_m	equivalent volume of the metal
\bar{V}_{ox}	equivalent volume of the oxide
W_T	effective tensile work
x	oxide scale thickness
x_0	stabilized oxide scale thickness
x_c	critical oxide scale thickness for its rupture
ϵ_c^P	critical oxide scale strain for its rupture under compression
x_t	cumulative oxide scale thickness
X	deviatoric of the internal stress
y	consumed metal thickness
y_A	recession of the alloy A-B surface depleted in B during oxidation

1. INTRODUCTION

1.1 Background

In high performance aero engines, the thermally induced stresses associated with engine start-up and shutdown, in combination with cyclic mechanical loads, are responsible for thermal fatigue damage accumulation in turbine blades and vanes which leads to cracking and eventually to failure. This form of damage is life limiting for these components in many high performance engines. Thermal fatigue also implies repeated cracking and spalling of the protective oxide scale causing accelerated oxidation, instability of the component geometry and reduction of engine efficiency. The thermal fatigue life of blades and vanes is very difficult to predict because of the numerous variables that influence damage accumulation. The variables include the material properties, the component geometry and the nature of the thermal cycle. For blades, the superimposed mechanical loads arising from rotation can have a significant effect. The complexity of the problem is enhanced by synergistic interactions between crack initiation and growth and the processes of surface degradation by cyclic oxidation and erosion which are conditioned by hot gas chemistry and dynamics, and by cyclic thermal expansion of the components. The task of validating thermal fatigue life prediction models for blades and vanes is complex because the thermal history and life to crack initiation for blades and vanes are not generally well known.

1.2 Project Objectives and Approach

This project was initiated by École Polytechnique of Montréal, in collaboration

with NRC's Institute for Aerospace Research (IAR) in order to develop and validate a methodology for thermal fatigue and oxidation damage prediction for turbine blades and vanes. Both experimental and numerical aspects of damage modelling were addressed simultaneously by IAR and École Polytechnique. The approach followed for this undertaking is summarized in the flow chart shown in Figure 1.1, where the experimental and analytical tasks of the project are identified separately with solid and dashed lines, respectively.

On the experimental side, a test facility located in the laboratories of the IAR was instrumented and used to conduct thermal fatigue tests cracking on airfoil-like specimens under well simulated service conditions. The facility is an automated high velocity-low pressure burner rig capable of subjecting the specimens (or real turbine airfoils, blades and vanes, if necessary) to cyclic heating and cooling representative of thermal cycles experienced by blades and vanes in engines. The standard specimen for the thermal fatigue test has a double edge - wedge (DEW) geometry meant to simulate the complex geometry of blades and vanes. The specimen material is DS René 80 (also designated as DSR80), a typical cast nickel-base superalloy for blades and vanes in aero engines produced by directional solidification (DS). Some specimens are coated with Codep B-1, an aluminide coating applied to improve the resistance of these components to oxidation and corrosion.

In a typical test, the specimen is heated in the high velocity hot gas jet produced by the rig for a period of time sufficient to achieve steady state temperatures across the airfoil. The specimen is then withdrawn from the hot gasses and is placed into a secondary gas jet at room temperature for forced air cooling. This heating and cooling is meant to reproduce the temperature variations experienced by blades and vanes during start up (take off) conditions and shutting down (landing) of engines. These large temperature excursions are known to be highly damaging to blades and vanes, from the

point of view of thermal fatigue damage accumulation and cyclic oxidation. The initiation of cracks at the leading edge of the specimen and the rate of propagation of these cracks were monitored in-situ, using a high resolution alternating current-potential drop (ACPD) technique, which was calibrated against measured crack length of the specimen. In this technique, an alternating current of constant amplitude and frequency is applied across the specimen. The change in potential drop associated with the change of impedance of the specimen arising from the formation of cracks was measured during testing, using AC-PD probes attached to the specimen and a crack growth monitor specially designed for this purpose. Oxidation damage, which mainly translates into material losses, was assessed by quantitative metallography of the specimen exposed to different numbers of cycles.

The temperature history of the specimen was established by finite element (FE) analysis using the ABAQUS code using thermo-physical properties of the material obtained from the literature, and measured values of surface emissivity and convective heat transfer coefficients. The heat transfer coefficients were determined from energy balances using measurements of specimen surface temperatures, gas velocity and temperature profiles. The cyclic stress-strain history of the specimen was computed from its thermal history, also with the help of the ABAQUS code, using a thermo-elastoplastic deformation model in first approximation and a thermo-elasto-viscoplastic model in order to obtain more realistic results. Fatigue life and material losses were then determined from different fatigue-oxidation damage models chosen to best describe the dominant mode of damage accumulation, as determined by metallographic analysis. The constants for the deformation model, the fatigue and oxidation damages models were determined from uniaxial isothermal fatigue and oxidation data found in the literature.

The validation of the damage accumulation modelling approach adopted in this

project was finally achieved by comparing the predicted life and alloy surface recession with experimental life and material loss obtained from thermal fatigue tests carried out in the burner rig.

The present thesis reports in detail the experimental and the numerical aspects of the project in six following Sections. A review of the metallurgy of nickel-base superalloys and aluminide coatings as well as on thermal fatigue and oxidation damages modelling is presented in Section 2. Section 3 and 4 respectively present the experimental method and results of the thermal fatigue testing program in the burner rig. The discussion and numerical analysis of the results are presented in Section 5. Finally, the general conclusions and the recommendations followed from the project are summarised in Section 6 and 7.

2. L I T E R A T U R E R E V I E W O F M E T A L L U R G Y , T H E R M A L F A T I G U E A N D O X I D A T I O N D A M A G E S M O D E L L I N G F O R B A R E A N D C O A T E D S U P E R A L L O Y S

This Section presents a literature review of the metallurgy , the thermal fatigue and oxidation damages modelling applicable to nickel-base superalloys and aluminide coatings, with particular attention to DS René 80 alloy, bare and coated with Codep B-1, which was chosen for the thermal fatigue testing program in the burner rig.

2.1 Chemical and Physical Metallurgy of Ni-Base Superalloys and Aluminide Coatings, [1]

The elements, which compose the chemistry of Ni-base superalloys, as DS René 80_(*) (also designated as DSR80), can be regrouped in three classes according to their respective role:

- 1° FCC Phase (γ) Formers: These elements are Ni, Cr, Co, Mo, W, Hf and make up the nickel-rich face-centred-cubic (FCC) austenitic (γ) matrix of DSR80. The FCC atomic structure confers to the alloy a relatively good toughness while solid-solution strengthening of the matrix is insured by the presence of Cr, Mo and W atoms, as they have a larger atomic diameter than Ni and which make cross-slip more difficult by reducing the stacking-fault energy.
- 2° Gamma Prime (γ') Precipitates Formers: In the γ matrix, Al, Ti and Hf tend to form very fine and coherent $(\text{Ni,Co})_3\text{X}$ γ' precipitates which give the alloy its extraordinary strength over a wide range of temperature. With its FCC structure, this ductile phase has no embrittling effect on the alloy. These precipitates are obtained by controlling the alloy chemistry and heat treatment during the alloy elaboration.
- 3° Grain Boundaries Formers: With their very odd atomic diameter, B, C

*: Nominal alloy composition:

In wt%:	14.0 Cr, 9.5 Co, 4.8 Ti, 4.0 Mo, 4.0 W, 3.0 Al, 0.75 Hf, 0.08 C, 0.02 Zr, 0.015 B, Bal. Ni;
In at%:	15.50 Cr, 9.28 Co, 5.77 Ti, 2.40 Mo, 1.25 W, 6.40 Al, 0.242 Hf, 0.383 C, 0.013 Zr, 0.080 B, Bal. Ni.

and Zr are mainly found at the grain boundaries where they improve the strength and the creep resistance of the alloy.

A subclassification of these elements can be made:

- a) Carbides Formers: This subclass includes Cr, Mo, W, Ti that preferentially react with C to form complex carbides with different morphologies and stoichiometries (MC , $M_{23}C_6$, M_6C). Under well controlled heat treatment, these types of carbides are obtained which result in extra alloy strengthening, especially at grain boundaries.
- b) Al and Cr Oxides Formers: The presence of proper amount of Al and Cr in the alloy allows the formation of compact and adherent Al_2O_3 and Cr_2O_3 oxide scales at the alloy surface, providing excellent protection against severe oxidation and hot corrosion damage.

As mentioned in Section 1, the DSR80 alloy is obtained by directional solidification. Contrary to the conventional casting method, which results in an alloy microstructure with equiaxial grains distribution, the directional solidification technique provides a structure with columnar grains oriented parallel to the longitudinal axis of the airfoils, which considerably increases the creep and fatigue life. Although, the DS technique allows to get the $\langle 0,0,1 \rangle$ crystallographic direction (associated to the lowest elastic modulus in FCC lattice structures) oriented in the longitudinal direction of the airfoil. This helps to increase life to rupture of DS alloys by lowering the thermal stresses associated with the elastic strains in this direction. Each grain are composed of dendrites which are Ni-rich trees-like structures found in the matrix, composed of primary arms oriented in the direction of solidification and sometime of secondary arms perpendicular to the primary ones. The Ni-rich dendrites result from solute segregation

between the dendrite arms during the fast directional solidification process. Higher concentration of impurities and carbides are found between the dendrite arms due to this segregation.

Even if the Al content in DSR80 is sufficient to form a protective Al_2O_3 oxide layer, at least under isothermal conditions, this may be not the case under thermal cycling conditions, for which the Al and Cr alloy depletion next to the oxide scale is more severe and rapid. Additional aluminium can be introduced into the surface layer by a cementation technique. The resulting Al rich layer at the alloy surface results in a β -aluminide coating, such as the Codep B-1 coating used on DSR80 in the present thermal fatigue study. By controlling the diffusion processing conditions, different thicknesses, Al-content and grain sizes can be obtained, which affect oxidation and thermal fatigue resistance of the components.

2.2 Thermal Fatigue Damage Modelling

Contrary to pure fatigue at low temperature, isothermal fatigue (IF), thermal fatigue (TF) and thermo-mechanical fatigue (TMF) of high temperature components in aero engine always involve interactions between fatigue and oxidation mechanisms, except in very high vacuum or in very pure inert atmosphere or when cracking is internal. Interactions between mechanisms are very complex and not yet well understood. The modelling task suffers from this lack of knowledge and is reflected by the widespread assumptions made to simplify or just to define the problem. This subsection reviews the possible mechanisms of fatigue-oxidation interactions and the main models proposed up to date. A creep-fatigue model is also studied.

In this thesis, the thermal fatigue (TF) terminology of Spera [2] is employed. According to this author, "Thermal Fatigue is the gradual deterioration and eventual cracking of a material by alternate heating and cooling during which free thermal expansion is partially or completely constrained". Thus two conditions are required for having thermal fatigue: 1° the temperature must vary with time, in opposition to isothermal fatigue (IF) and, 2° the thermal expansion must be constrained.

Thermal expansion constraint can be grouped in two categories: external and internal. External constraint arises from static or cyclic external forces applied at the boundary of a body during heating and cooling. This category of TF condition, also called Thermo-Mechanical Fatigue (TMF), is met in service, such as in the case of blades attached to the rotor in turbines which are submitted to centrifugal loads arising from rotation, in addition to the thermal loads arising from start-up and shut-down of the engine. In laboratory, TMF is simulated by independently imposing mechanical strain cycling and thermal cycling. Different phasings between the mechanical strain and thermal strain cycling can be applied. The two extreme phasing cases, Out-of-Phase

(OP) and In-Phase (IP), are graphically represented in Figure 2.1. Under OP conditions, the maximum thermal strain is reached during the time when the mechanical strain is minimum, whereas in IP conditions, the minima and the maxima of the two different natures of strain are in phase. An intermediate phasing case, which occurs more frequently in practice, is called Counterclockwise Diamond (CCWD) and is illustrated in Figure 2.1. In all cases, the net strain, ϵ_{net} , is given by the sum of the thermal and mechanical strain components, ϵ_{th} and ϵ_{mech} :

$$\epsilon_{net} = \epsilon_{th} + \epsilon_{mech} = \alpha (T - T_0) + \epsilon_{mech} \quad (1)$$

where α is the thermal expansion coefficient and T_0 is the initial temperature.

Internal constraint results in some elements of a body when their adjacent elements are at different temperatures and do not get the same thermal expansions. This TF condition, called Thermal-Stress Fatigue (TSF), is inevitable in high-temperature service devices when the surface temperature of the components of complex geometry vary rapidly during each start-up and shut-down operation. This is the case for turbine airfoils in aeroengines (especially the first stage stationary vanes in direct contact with the hot gas streams produced by the combustors) and for the DEW specimens thermally cycled under simulated service conditions in the burner rig.

2.2.1 Mechanisms

Complex interactions between fatigue-oxidation mechanisms are involved during the crack initiation and propagation. The following subsections will attempt to summarize the most probable mechanisms supported by numerous studies reported in the literature.

2.2.1.1 Crack Initiation

Oxidation influences crack nucleation from both physical and chemical considerations. At the physical level, oxidation modifies the surface morphology by introducing a general roughness, especially under thermal cycling conditions [101]. Preferential oxidation at grain boundaries in conventionally cast (CC) materials, in interdendritic zones for directionally solidified (DS) columnar grain (CG) and single crystal (SC) superalloys, at slip bands and at carbides protrusions at the surface of components all lead to the formation of oxide spikes. These discontinuities can act as stress concentration sites and are certainly preferential sites for crack initiation, as shown in many investigations, for various CC, CG and SC cobalt-based and nickel-based superalloys (René 80, IN-100, MAR-M247, MAR-M509, CMSX-2, René N4) [3-34]. The oxide spikes kinetics is described in Subsection 2.3.2.2 (see Equation 52). The extrusions, intrusions and steps formed at the surface by slip bands were also observed to act as crack initiation sites after they become oxidized [12, 18, 35, 36]. In some DS superalloys micropores produced during casting also act as initiation sites [25, 33, 34].

At the chemical level, monatomic oxygen and/or nitrogen diffuses into the metal and changes its chemical and mechanical properties. The metal-oxygen or metal-nitrogen bonds are less resistant to fracture than metallic bonds. The reduction in

ductility and the embrittlement associated with air-metal reaction are well established in numerous studies on pure nickel, nickel-base and cobalt-base superalloys oxidized before and during tensile and creep testing [37-40]. One of the most remarkable demonstrations of these effects was the study of Bricknell and Woodford on ultra pure nickel preexposed to air at high temperature (up to 1000°C) or in a vacuum of 10^{-5} torr and tensile tested in air or in pure argon from 25°C to 1000°C [37]. The study concluded that pure nickel is embrittled by air leading to intergranular fracture and severe loss in tensile ductility around 800°C. This problem is common to all the nickel-base alloys where oxygen is believed to cause embrittlement, even at very low partial pressure ($\sim 10^{-7}$ torr), by pinning grain boundaries at high temperature [38, 40]. At very low oxygen pressure, transgranular brittle fracture was also observed [38]. Oxygen embrittlement was also reported in DS René 80 [17], for which the grain boundary pinning mechanism is obviously not possible. In this case, and in the case of transgranular crack propagation, diffusion at the carbide-matrix interface may be responsible for the observed embrittlement. Oxygen diffusion into the matrix may also be involved, due to the titanium content in the alloy which increases the oxygen solubility [41]. The oxygen diffusion through the dislocation network and the oxygen binding at the dislocations can affect its mobility, and consequently the ductility and the toughness of the matrix, as also observed for carbon and other solute atoms (addition elements and impurities such as O, N) in steels. This ductility reduction, associated with solute-dislocation interactions is identified to be the Portevin-Le Châtelier effect [42].

Another mechanism responsible for the reduction of the ductility of the substrate is the oxidation of the slip bands intersecting the crack tip or the surface of the metal which certainly reduces or eliminates the gliding along these bands [12, 18, 35, 36].

2.2.1.2 Crack Propagation

In conventionally cast (CC) nickel-base superalloys (equiaxed grain microstructure) cracks are found to progress intergranularly [4, 5-8, 11-16, 18, 19, 21, 22, 32] and in some cases transgranularly [5-7, 14, 15, 22]. It was also found that sometimes they propagate intergranularly in the initial stage followed by a transgranular progression in a direction mostly normal to the principal tensile stress [3, 27]. In columnar-grained (CG) and single-crystal (SC) superalloys obtained by directional solidification (DS), cracks propagate across the primary dendrites and between the arms of the secondary dendrites where embrittling micropores, impurities and carbides are segregated [17, 20, 25, 33], when the tensile load is applied in the DS axis direction or within 45° of this axis. Comparison of fatigue life of CC and DS superalloys with the same chemical composition, showed the superiority of DS materials when tested under strain-controlled low cycle fatigue (LCF), thermal fatigue (TF) and thermo-mechanical fatigue (TMF) conditions and DS specimens loaded in the DS axis direction (or with an angle below 45°) [20, 25, 33, 43]. The inferiority of CC superalloys can be attributed to the grain boundaries perpendicular to the load direction which offers an easy crack growth path, contrary to primary dendrites and columnar grains in DS superalloys [20, 33]. This is supported by fatigue life obtained at high temperature for CG René 120 loaded at 90° of the DS axis direction (also called transverse loading) resulting in fracture along the grain boundaries, similar to the life obtained for CC René 120 also fractured intergranularly [33].

One can suppose that the shorter life of CC materials compared to that of DS materials of the same chemical composition may be explained by the difference of the value of the Young's modulus (E) of the two classes of materials because under strain-controlled cycling, the stress range and the maximum stress are proportional to E for a given strain range [25, 33]. In DS materials, the effect of anisotropy of the elastic

modulus can be rationalized by plotting the maximum stress (instead of the strain range) against life [17, 20, 25, 33, 44, 45]. According to the previous hypothesis, fatigue data of a DS and CC material plotted this way should collapse into one master curve. This is what can be observed with σ_{\max} - N_f plots (Figure 2.2) of CC and DS René 120 fatigue data obtained at 650°C under various DS axis orientation [33]. In this Figure, the fatigue data of the same alloy composition obtained at 982°C also collapsed into one curve, except for equiaxed and transversal DS orientation which collapsed on a lower curve [33]. From this result, it can be concluded that the difference between fatigue life of CC and DS materials tested under controlled strain amplitude is due to the elastic anisotropy effect at intermediate temperatures but, at high temperature, the difference is most likely caused by the orientation of grain boundaries relatively to the loading direction [33].

The validity of this conclusion can be interpreted by a review of micromechanisms of crack growth process involving environmental interaction. Two mechanisms are generally recognized in the literature. The first mechanism (A) involves successive fracture of the metal in front of the oxide spike tip which becomes embrittled by inward oxygen diffusion and the subsequent oxidation of the fresh metallic crack surfaces (see Figure 2.3). The partial or total fracture of the oxide spike associated with crack opening displacement accelerates oxygen transport to the spike tip by pipe diffusion. The hydrostatic stress increases oxygen diffusion into the metal by decreasing the activation energy and by multiplying fast diffusion paths such as dislocation framework. This mechanism has been accepted by many investigators [3, 4, 12-14, 16, 18, 19, 22-25].

Other researchers [22, 24, 26-30] have proposed a second mechanism (B) which involves successive steps of oxide growth until a critical thickness (x_c) is reached. At this point the oxide cracks leading to local exposure of fresh metal. This mechanism

results in two types of oxide intrusions, as described by Sehitoglu [26] who is probably one of the first to propose and experimentally confirm this mechanism (see Figure 2.4). The first type (Type I) is characterized by a continuous oxide layer with no visible stratification in the oxide, whereas the second oxide intrusion type (Type II) is wider and is characterized by stratified oxide growth. This results in successive oxide scale cracking and detachment from the substrate, when the oxide layer reaches a critical thickness, and is followed by fast oxide growth on the freshly exposed metallic surface. It can be noted that some authors do not exclude the existence of both variants of this mechanism. Boismier and Sehitoglu [27, 28] who observed Type I oxide intrusions formed in MAR-M247, a nickel-base superalloy, surrounded by a γ' depletion zone, assumed that oxide scale cracking can extend into the depleted zone, also considered a damaged zone. The γ' depleted zone is a consequence of outward diffusion of Al, Cr, Ti elements which are the γ' forming elements.

The type of oxide intrusion depends on the alloy system, the testing conditions (IF, TF, TMF) and parameters such as the temperature range, the strain rate, the strain range and the temperature-strain phasing [26-30]. With the temperature-strain phasing, the principal parameter which controls oxide scale cracking is the total mechanical strain of the substrate, more specifically the tensile strain for Type I oxide scale failure and the compressive strain for Type II oxide scale failure. This point is discussed in more detail in Subsection 2.3.6.

It has thus been shown that oxidation has a deleterious effect on life due to the embrittling effect of oxygen (mechanism A) and to the local oxide scale breaking and by spalling or local cyclic oxidation (mechanism B). Two additional mechanical effects of oxidation on crack growth rate have not yet been introduced. The first is the crack tip or oxide spike tip blunting caused by lateral oxidation. Similar to crack tip blunting associated with its plastic deformation [46], the lateral oxidation of the crack tip

increases the tip radius which causes a reduction of the stress concentration factor defined by Inglis [47]. Crack growth slows down and, in some cases, the crack propagation stops. The second effect of oxidation on crack growth rate is the crack closure obstruction associated with oxide scale build up on the metallic surfaces of the crack which is similar to the effect of the plastic zone formed along the crack surfaces that Newman proposed in his crack-closure model [48].

An LEFM analysis combined with an appropriate oxidation kinetics expression should allow the determination of the crack opening stress, σ_{open} , the ΔK_{eff} and the crack growth rate as defined by Paris et al. [49, 50]. However, it should be noted that the beneficial effect of crack tip blunting and closure on crack growth rate resulting from oxidation are in general outranked by the deleterious embrittling effect of oxygen penetration.

2.2.2 Fatigue-Oxidation Life Prediction Models

Many models have been suggested to predict the life of components subjected to fatigue and oxidation damages. In this subsection, six models are reviewed. They are all based on one of the two interaction fatigue-oxidation mechanisms presented in the last subsection. Some models are based on linear interactions, others on more complex synergistic non-linear interactions. Some are obtained from modified empirical relations which apply to fatigue at low temperature, others are developed with a mechanistic approach. In particular, this subsection presents for each model, the mechanism(s), the assumptions, the fracture criteria, the variables considered, the mathematical definition, the experimental methodology for the determination of the model parameters, the correlations between predicted and experimental lives as well as the range of testing conditions (IF, TF, TMF, temperature, strain range, cycling frequency...) for which the model have been validated.

2.2.2.1 Coffin [5, 7, 8]

Coffin introduced the cycling frequency into the low-temperature Coffin-Manson and Basquin Laws [51, 52] in order to illustrate the detrimental effect of environment on fatigue life for high temperature IF conditions. The cycling frequency variable captures the competition between the time dependent oxidation-damage and the cycle-dependent fatigue damage processes. At very high frequencies, the cycling period Δt is very short, leaving no time for diffusion controlled oxidation and oxygen embrittlement of the crack tip during each cycle.

In the low cycle fatigue (LCF) regime, the empirical formulation for the modified Coffin-Manson Law:

$$\Delta \varepsilon_p = C_2 N_f^{-\beta} v^{(1-k)\beta} \quad (2)$$

correlates the life or number of cycles to failure, N_f , to the plastic deformation range $\Delta \varepsilon_p$ and to the continuous cycling frequency, v , while in the high cycle fatigue (HCF) regime, the modified Basquin Law:

$$\Delta \varepsilon_e = \frac{\Delta \sigma}{E} = \frac{A'}{E} N_f^{-\beta'} v^{k'_1} \quad (3)$$

correlates the fatigue life to the elastic deformation range, $\Delta \varepsilon_e$, or stress range, $\Delta \sigma$ and to the frequency of cycling. By adding the two relations, the relation between the life and the total strain range can be obtained:

$$\Delta \varepsilon = \frac{A'}{E} N_f^{-\beta'} v^{k'_1} + C_2 N_f^{-\beta} v^{(1-k)\beta} \quad (4)$$

Here, A' , β' and k'_1 are the constants related to the material fatigue strength properties and C_2 , β and k are the constants related to the material fatigue ductility properties. As all the exponents are positive with $k < 1$ and $\beta > \beta'$, the life is proportional to the frequency, thus N_f is inversely proportional to the cycle period Δt . The definition of the continuous cycling frequency ($v = 1/\Delta t$) can be modified to consider the effect of a hold period during cycling. The new expression of the frequency is often called the effective frequency, v_{eff} , and given by [7]:

$$v_{eff} = \frac{1}{\Delta t + t_h} \quad (5)$$

The transition fatigue life N_t , defined to be the point of life at which strength and ductility properties equally contribute to fatigue resistance is found by combining Equations 2 and 3:

$$N_t = \left(\frac{A'}{C_2 E} \right)^{\frac{1}{\beta' - \beta}} v^{(k_1' - \beta(1-k)) / (\beta' - \beta)} \quad (6)$$

Thus, the transition fatigue life depends on the balance between the strength and the ductility properties of the material. For instance, cast nickel-base superalloys, which have high strength and low ductility, usually have a low transition life that can be below 100 cycles. N_t is of great importance to determine whether Equation (58) or (59) is more appropriate to predict life, according to the order of magnitude of the life expected. Coffin also found that the transition fatigue life given by Equation 6 is a more rational definition for the transition between LCF and HCF regimes than the conventional definition which set the transition around 10^4 to 10^5 , regardless of the material properties [7].

To illustrate the capabilities of the model, the results of a strain controlled LCF test program on CC René 80 conducted at 871°C are considered [5]. The material was cycled at several continuous frequencies ($v = 0.034$ -36.2 cycle/minute or cpm) and total strain ranges ($\Delta\epsilon = 0.4$ -1.1%). The fatigue life to failure, N_f , was determined when the stress drop due to the presence of cracks was detected, as shown in Figure 2.5 where the stress range is plotted against the number of cycles. In this figure, the continuous decrease in stress range at constant frequency before failure is associated with cyclic softening of the material. Note also that the stress range curve is shifted with the frequency. These phenomena associated with stress relaxation were considered in the predictive life Equations (2 to 4) by using the plastic strain range and the stress range evaluated at the mid-life $N_f/2$. The parameters of the equations obtained through multiple regression analysis have the following values: $A' = 469100$, $E = 22.4 \times 10^6$ psi, $\beta' = 0.191$, $k_1' = 0.112$, $C_2 = 0.761$, $\beta = 0.934$ and $k = 1.180$, when the stress is expressed in psi, the strain is expressed in mm/mm or in./in. (not in %) and the frequency is in cpm. Note that k is larger than unity which is abnormal [5]. This

result can be justified by the fact that the shortest life obtained was 275 which is higher than the transition life computed to be equal to 125 cycles at 1 cpm. This indicates that the material was tested more in the HCF regime and that the frequency modified elastic strain range law (Equation 3) should be used to fit the data. This also indicates that for lives around 1000 cycles and over, the fracture has a brittle character and must be governed by the stress range. The frequency plastic strain range Law (Equation 2) should not be used in this regime, as reflected by the large deviation of the life predicted with this Equation from the experimental life ($\pm 35\%$), compared to that obtained when Equation 3 is employed ($\pm 17\%$) (see Figure 2.6).

In another study carried out by Lord and Coffin [6], the effect of hold time on the LCF behaviour of CC René 80, tested in the same conditions as for the study reported above [5], was investigated. Schematic hysteresis loops, stress and strain vs time records for continuous cycling, equal hold times in tension and compression, tensile strain hold periods, and compressive strain hold periods are illustrated in Figure 2.7. Note that during the hold time, the stress relaxes due to the high testing temperature involved (871°C). The stress relaxation causes the maximum and the mean stress to shift. Table 2.1 summarizes the test results. It is surprising to see that the fatigue life globally increases with the total hold time ($t_h = t_{h\text{Tension}} + t_{h\text{Compression}}$) and that for a given hold time, the hold time in compression has a more detrimental effect on N_f than the hold time in tension. These results can certainly not be correlated by the frequency modified strain range laws using the extended definition of the frequency given by Equation 5 as this method predicts the fatigue life to be inversely proportional to the hold time, whether the hold time is imposed in compression or in tension during cycling. It seems that the effect of hold time on the maximum and the mean stress are directly related to the life and that this effect is much more important than the environmental effect. Coffin's relations have to be modified to take into consideration these new observations.

Table 2.1 Effect of hold time in IF tests on CC René 80 to 871°C, $\Delta\epsilon_p = 0.32\%$ (after [6]).

Hold Conditions	Hold Time (min)	$\Delta\epsilon$ (%)	$\Delta\sigma$ (MPa)	σ_{\max} (MPa)	N_f (cycles)
Tension	5	1.06	1093.9	482.2	450
Compression	5	1.04	1040.4	743.3	225
Tens. & Comp.	2.5	0.82	1143.2	579.9	280
Tension	30	0.92	1129.4	395.6	600
Compression	30	0.96	1139.8	729.6	170
Tens. & Comp.	15	0.71	1034.2	608.1	350

Concerning the effect of temperature on the parameters of Coffin's models, the fatigue strength constant, A' , and the elastic modulus, E , decrease with increasing temperature and the fatigue ductility constant C_2 increases with temperature [7]. The fatigue ductility exponent, β , increases at higher temperature whereas β' is not significantly affected by temperature variation [7]. Consequently, the fatigue life, N_f , and the transition fatigue life, N_t , shift to lower values when the temperature is raised.

2.2.2.2 Ostergren [9]

A relation similar to the frequency modified Coffin-Manson Law was proposed by Ostergren to consider the effect of hold time and frequency on fatigue life prediction for elevated temperature, strain-controlled LCF conditions. Ostergren used an energetic approach and postulated that the life in LCF is mostly spent in crack propagation and that damage is driven by plastic work instead of the plastic deformation. Assuming that the crack closure effect is important, the stress range under the crack opening stress σ_{open} does not contribute to the crack propagation and the effective tensile work (W_T) is proportional to the area in the σ - ϵ hysteresis loop over the σ_{open} :

$$W_T \propto (\sigma_T - \sigma_{open}) \Delta \epsilon_p \quad (7)$$

To simplify, Ostergren approximated W_T by $\sigma_T \cdot \Delta \epsilon_p$, with $\sigma_T = \sigma_{max}$ and $\sigma_{open} = 0$. Ostergren then substituted the plastic strain range by the simplified expression of the plastic work in the frequency modified Coffin-Manson Law (Equation 2) and found that the expression:

$$\sigma_T \Delta \epsilon_p N_f^{\beta} v^{(k-1)\beta} = C \quad (8)$$

can fit the LCF data very well for various materials (304SS, CrMoV, René 80, IN738), cycling frequencies (0.002-20 cpm), for hold times in tension (t_{hT}) and in compression (t_{hC}) (0-30 minutes) and for temperatures between 538 and 871°C.

In order to bring out hold time effect in his equation, Ostergren introduced two definitions of the effective frequency. When the time-dependant damage is independent of the wave shape of stress, the extended v_{eff} defined by Equation 5 in the last subsection of the Coffin Model can be used, with $t_h = t_{hT} + t_{hC}$. In the case where tensile creep deformation is detrimental and compressive creep deformation is beneficial, the effective frequency is defined by:

$$\begin{aligned}
 v_{eff} &= \frac{1}{\Delta t + t_{hT} - t_{hc}} & \text{for } t_{hT} > t_{hc} \\
 \text{and} \\
 v_{eff} &= \frac{1}{\Delta t} & \text{for } t_{hT} \leq t_{hc}
 \end{aligned} \tag{9}$$

For the superalloy René 80, the data obtained by Lord and Coffin [6] and reported in the last subsection (Table 2.1) is well fitted when using the following values:

$$C = 7.310 \text{ ksi} \cdot \text{cycle}^{\beta} \cdot \text{min}^{(1-k)\beta}$$

$$\beta = 0.565$$

$$k = 0.964$$

with a corresponding relative error $RE = 10.4\%$ for predicted N_f . It is surprising to see how this model can handle such a wide range of hold times in tension and in compression. The success of the model can largely be attributed to the use of the maximum stress which controls the crack growth in the brittle fracture regime and which takes into consideration the effect of relaxation during the hold periods.

Moreover, a very interesting study from Cook et al. [10] demonstrated that the Ostergren approach can be applied to predict lives of a superalloy (René 80 for instance) tested under TMF conditions (in-phase, out of phase and clockwise diamond ϵ -T cyclic phasing, with two temperature ranges, 760-871°C and 871-982°C). As the maximum temperature in a TMF cycle is assumed to be the most damaging, the constants of the Ostergren Model are determined from LCF tests at this maximum temperature. Predicted lives correlated surprisingly well the experimental TMF data with the majority of the values falling within ± 2 scatterband. This promising and relatively simple approach needs to be evaluated more extensively with other data on nickel-base superalloys.

2.2.2.3 Antolovich et al. [11-14, 16, 18, 19]

An extensive study of the high temperature LCF behaviour of some superalloys in air was carried out by Antolovich and co-workers [11-22] in order to determine the complex cyclic deformation-oxidation mechanisms and to propose a mechanistically-based life prediction model. The materials tested were René 77, Nimonic 90, Waspalloy, MAR M-002, DS René 80 and CC René 80. The IF tests were conducted at 760°C, 871°C, 927°C and 982°C at $R_e = 0.05$ most of the time (sometime fully reversed, $R_e = -1$), with a nominal ramp rate of either 0.5%/min or 50%/min and with a 90 seconds hold time imposed at either maximum or minimum strain for some tests. Some specimens were preoxidized 100 hours at 982°C either stress free or at a stress of 97 MPa. Failure was defined to be met when a significant stress drop was detected during testing, as this event was followed by a rapid crack growth and total failure of the specimen.

Based on metallographic observations of the specimens for which the tests were stopped just after stress drop detection, the authors claimed that cracks propagate from oxide spikes formed preferentially at the grain boundaries, when the oxide spikes reach a critical length, $d_{x,f}$. The failure can be considered effective when the metal in front of the oxide spike tip cracks after it has been embrittled by oxygen penetration along the grain boundary (mechanism A, Subsection 2.2.1.2). Or failure could correspond to the moment when the oxide spike loses coherency within the base metal and becomes a well-defined crack (mechanism B, Subsection 2.2.1.2). However, in both cases, the crack initiation depends on the size of the oxide spike and the magnitude of the stress. Intuitively, the failure criterion proposed by Antolovich et al. [53-55, 5-14, 16, 18, 19],

takes the form of:

$$\sigma_{\max} d_s^p = K_0 \quad (10)$$

where σ_{\max} is the maximum stress during cycling, K_0 is a material constant and p is an exponent. It can be noted that the left term is similar to a stress intensity factor when $p = 1/2$ and the right term is a constant that could be linked to the toughness of the embrittled metal or of the oxide at the oxide spike tip, depending on the nature of the operating mechanism (A or B). By plotting the LOG values of σ_{\max} and d_s measured when the stress starts to drop due to crack propagation, the values of K_0 and p are obtained by linear regression. The exponent p was found to be very close to $1/4$ [13, 14].

Before crack propagation, the oxide spike grows at a rate represented by an oxidation-kinetic power law as defined by Equation 8 of Subsection 2.3.2.2:

$$d_s = (n k'_s t)^{\frac{1}{n}} \quad (11)$$

where n is the exponent representative of the oxidation mechanism and k'_s is the oxidation rate constant for the oxide spike penetration which varies according to an Arrhenius expression, as defined by Equation 3 of Subsection 2.3.2.1:

$$k'_s = k'_{s0} \exp\left(\frac{-Q}{RT}\right) \quad (12)$$

The constants were obtained by metallographic analysis of oxide spikes measured for various times and temperatures: $n = 2$, the activation energy, $Q = 9$ kcal/mol and $2k'_{s0} = 1.66$ m²/s for CC René 80 in the temperature and time ranges of 760°C-982°C and 16-500 h, respectively. The value of $n = 2$ indicates a parabolic oxide spike growth rate which is unusual for a grain boundary which should be associated with $n = 4$, as Fisher theoretically found [56] and Reger and Rémy observed in IN-100 [4].

The life to failure, N_f , can be found by combining the kinetic power law (Equation 11) and the failure criterion (Equation 10). Converting the time of the oxidation kinetic law into the number of cycles with $t_f = N_f(\Delta t + t_h) = N_f(1/v + t_h)$ gives:

$$(\sigma_{\max})^{\frac{n}{p}} \left(\frac{1}{v} + t_h \right) N_f = K_1 \exp\left(\frac{Q}{RT}\right) \quad (13)$$

with:

$$K_1 = \frac{K_0^{\frac{n}{p}}}{n k'_s} \quad (14)$$

Here v is the continuous cycling frequency. By rewriting Equation 13, the fatigue life to failure is directly given by:

$$N_f = K_1 \left(\frac{v}{1 + v t_h} \right) \exp\left(\frac{Q}{RT}\right) (\sigma_{\max})^{-\frac{n}{p}} \quad (15)$$

In this Equation, the stress can be replaced by the plastic deformation range using the cycling flow rate_(*) for $R = -1$ which gives:

$$N_f = K_2 \left(\frac{v}{1 + v t_h} \right) \exp\left(\frac{Q}{RT}\right) (\Delta \epsilon_p)^{-\frac{n}{p} n'} \quad (16)$$

It is interesting to note that the resulting Equation 16 has the same formulation as that of the Coffin's frequency modified fatigue life (Equation 2), where the exponent β

*: The cycling flow rate can be defined by using the following Equation: $\sigma_{\text{cyclic}} = \sigma_0(\Delta \epsilon_p/2)^{n'}$, where σ_{cyclic} is the maximum stress, $\Delta \epsilon_p$ is the plastic strain amplitude, both obtained from a stabilised cyclic stress-strain curves, σ_0 is the cyclic strength coefficient and n' is the cyclic hardening exponent [46].

corresponds to $p/(n-n')$, $k = 0$, and where the temperature is explicitly expressed. By taking a typical range of the cyclic hardening exponent $n' = 0.15-0.20$, and the values of $p = 1/4$ and $n = 2$ as found by Antolovich et al. [13, 14], one gets $\beta = 0.6-0.8$ which is a range of the Coffin-Manson exponent commonly observed.

In Figure 2.8, experimental lives, obtained for CC René 80 at 871°C and 982°C and various frequencies [14], are compared with lives predicted with Equation 15. The correlation is poor with an error of $\pm 70\%$ at 871°C and of $\pm 1250\%$ at 992°C. As the relation between σ_{max} and $d_{s,f}$ fits the experimental observations very well, the lack of prediction capability of the Antolovich et al. model can be attributed to an incorrect relation between the fatigue life and the frequency. For example, in the model of Coffin with the life expressed as a function of the frequency, the frequency exponent $(1-k)$ is negative and close to 0, whereas in the relation of Antolovich written in the similar form (Equation 16), the frequency exponent is equal to unity.

When the form of the frequency modified Coffin's Law for Equation 16 is used, the predicted error is even worse than that found when the normal form of the Antolovich's model (Equation 15) is used. This shows that it is not found convenient to convert the Antolovich et al. life prediction Equation in a Coffin-Manson expression, as these authors attempted in [12-14, 18, 19].

This result also confirms that the maximum stress controls the fracture as previously discussed for brittle fracture in the last subsection. Also, the effect of cyclic softening_(c) and stress relaxation on N_f is well accounted for by the use of σ_{max} in the

*: This phenomenon was extensively studied by Antolovich et al. [12-15, 18] who found from TEM observations that cyclic softening was attributed to γ' coarsening and dislocation networks build-up on the γ' which reduce the matrix-precipitate strain energy.

life prediction model of Antolovich et al. which is not the case with $\Delta\epsilon_p$. The maximum stress can also implicitly rationalize the effect on life of anisotropic elastic properties of DS materials tested under strain-controlled conditions. This important effect was discussed in more details in Subsection 2.2.1.2.

According to Antolovich and his co-workers [12, 13, 15, 18], specimens preoxidized 100 hours at 982°C showed moderate life reduction for stress free exposure and radical life reduction by stress exposure (by a factor of 2 to 3 orders of magnitude). The life of the preoxidized specimens was equal or better than for the unexposed specimens when the surface layers were machined away, proving that the major effect of prior exposure was to introduce damage in the near surface region rather than to introduce detrimental phase changes in the bulk.

Antolovich et al. [13] proposed to consider the effect of preoxidation by introducing the time of exposure, t_e , (regardless of the stress) into the fatigue life prediction equations by the mean of the term $\{t_e + (1/v + t_h)N_f\}$. This is somewhat simplified and a more realistic relation should be defined.

2.2.2.4 Romanoski et al. [3]

In 1988, Romanoski, Antolovich and Pelloux proposed a model for life prediction for nickel-base superalloys (uncoated IN-100 and coated René 80, both obtained by CC) under high-temperature LCF conditions [3]. Using metallographic analysis, they established that crack initiation occurs very early in the fatigue life of the material component, probably during the first cycle. They observed that cracks propagate along transverse grain boundaries but also sometime transgranularly with the crack plane mostly normal to the direction of the applied stress. Romanoski demonstrated that grain boundary decohesion precedes the formation of the bulk oxidation product [4]. The decohesion arises from degradation of the grain boundary strength as a result of preferential oxygen diffusion in the boundaries. Although the oxide wedging effect on the mechanical driving force of crack growth is acknowledged, this effect is neglected in their present model. Failure was defined when stress drops by 10% relative to the initial value of stress, after which the crack starts to propagate rapidly until total failure.

From experimental results, it was observed that failure occurs for a particular combination of crack size and maximum stress, suggesting a quasi-fracture mechanics failure criterion:

$$\alpha \sigma_{\max} (\pi a_f)^p = K' \quad (17)$$

where α is a geometric factor, σ_{\max} is the maximum applied stress, a_f is the crack length before the rapid crack propagation stage, and K' is a material constant proportional to the material toughness. The value of p was assumed to be $\frac{1}{2}$ as defined in the stress intensity factor.

Concerning crack growth, it is assumed to proceed by incremental decohesion of the material or by crack extension, Δa , in each cycle, along a predominantly

intergranular path. The crack extension is defined by the depth at which the cohesive strength of the grain boundary, σ_{gb} , degraded by oxygen diffusion is lower or equal to the maximum effective stress across the grain boundary, as illustrated in Figure 2.9.

The crack extension, Δa , is assumed to be constant for a given maximum effective stress and cycle period Δt . Thus, the crack growth rate can be defined as:

$$\frac{da}{dN} = A \Delta \sigma_{eff}^m = A (\sigma_{max} - \sigma_{th})^m \quad (18)$$

where A and m are constants and $\Delta \sigma_{eff}$ is the effective stress range which considers a threshold stress, σ_{th} , for microcrack extension. Note that, in this formulation, the frequency is not explicitly acknowledged and is then included in the constant A . Concerning the threshold stress, the physical meaning of this parameter is not clear. The authors think that σ_{th} corresponds to the threshold stress for bulk cyclic plasticity. On the other hand, this threshold could also be related to the crack opening stress σ_{open} associated to the closure effect of oxidation products or to the lowest cohesive strength of the grain boundary saturated in oxygen, $\sigma_{gb} ([O] \text{ sat})$, see Figure 2.9. Assuming that the cohesive strength of the grain boundary, σ_{gb} , varies linearly with the oxygen concentration and assuming that the oxygen concentration along the grain boundary is a function of the distance x from the crack tip to the power $1/m$ (with $m \geq 1$), as analytically and experimentally determined by Martin and Perrailon [57], the cohesive strength of the grain boundary in front of the crack tip can be approximated by:

$$\sigma_{gb}(x) = \sigma_{gb}([O]_{sat}) + R x^{\frac{1}{m}} \quad (19)$$

where R is a function of the material, the environment and the cyclic period, Δt_c . The crack extension, Δa , for one cycle is defined by x in Equation 19 when $\sigma_{gb} = \sigma_{max}$:

$$\sigma_{max} = \sigma_{gb}([O]_{sat}) + R \Delta a^{\frac{1}{m}} \quad (20)$$

From this expression, the crack growth rate is given by:

$$\frac{da}{dN} = \Delta a = \frac{1}{R^m} (\sigma_{max} - \sigma_{gb}([O]_{sat}))^m \quad (21)$$

By comparing this Equation with Equation 18, one gets that $A = 1/R^m$ and $\sigma_{th} = \sigma_{gb}([O]_{sat})$.

This result is a possible interpretation of the significance of the threshold stress in the expression for the crack growth rate. It should be noted that the crack growth rate is not expressed as a function of the crack length, a , as it is in a conventional Paris correlation [49]. The authors considered that, as over most of the life, the observed cracks are mechanically small and should not influence the crack growth rate.

* Here, if it is assumed that Δa is proportional to $\Delta t^{1/n}$ or $v^{-1/n}$, then the parameter $R \propto \Delta t^{-1/n}$ or $R \propto v^{1/n}$, where n is an exponent ≥ 1 , related to the kinetics of diffusion of oxygen at the grain boundary, which is similar to the exponent n , related to the kinetics of oxidation of a grain boundary, as defined in Subsection 2.3.2.2.

The crack growth rate defined by Equation 18 can also be integrated to determine the fatigue life, N_f :

$$\int_{N_i}^{N_f} dN = \int_{a_i}^{a_f} \frac{da}{A (\sigma_{\max} - \sigma_{th})^m} \quad (22)$$

where a_i is the crack length at initiation and N_i is the number of cycles to crack initiation. In the development presented by Romanoski et al., both a_i and N_i are taken as zero for the case where the specimen surfaces are polished and not preoxidized before testing and the crack initiation is known to represent a very small fraction of the total life mostly spent in propagation. After integration, the life N_f is:

$$N_f = \frac{a_f}{A (\sigma_{\max} - \sigma_{th})^m} \quad (23)$$

Here a_f was already defined by the failure criterion, Equation 17 which after substitution in the fatigue life expression above, gives:

$$N_f = \frac{(K_f')^2}{\alpha^2 \pi A \sigma_{\max}^2 (\sigma_{\max} - \sigma_{th})^m} \quad (24)$$

Combining the constants into one:

$$N_f = \frac{K_f^2}{\sigma_{\max}^2 (\sigma_{\max} - \sigma_{th})^m} \quad (25)$$

At this point, the value of m has to be determined experimentally. The exponent m which best fits the LCF data for uncoated IN-100 and coated René 80, tested at 925°C and 1000°C, respectively, has the integer value $m = 2$. The values of σ_{th} and K_f for both alloys are then determined by finding the value of σ_{th} which minimizes the variance in

K_f for each data set. Here, K_f is given by:

$$K_f = \sigma_{\max} (\sigma_{\max} - \sigma_{th}) N_f^{\frac{1}{2}} \quad (26)$$

For IN-100, $\sigma_{th} = 121.6$ MPa, $K_f = 1.92 \times 10^6$ MPa².cycle^{1/2} and for René 80, $\sigma_{th} = 129.6$ MPa, $K_f = 1.04 \times 10^6$ MPa².cycle^{1/2}. Using these values, a very high correlation was obtained: $R \geq 0.986$.

Unfortunately, the Model of Romanoski et al. was not developed to predict the effect of temperature, frequency, hold time on fatigue life, and its validity was assessed for LCF conditions only.

2.2.2.5 Reuchet and Rémy [24]

In Reuchet and Rémy's Model [24] for life prediction in high temperature LCF conditions, the fatigue-oxidation interactions are simply considered to be linear. This means that the crack advance resulting from crack opening under cyclic stress (or fatigue damage) is superimposed on the crack advance due to oxidation at the crack tip. Thus, the crack growth rate is given by:

$$\frac{da}{dN} = \left(\frac{da}{dN} \right)_{fat} + \left(\frac{da}{dN} \right)_{ox} \quad (27)$$

Such a linear interaction has also been proposed by Chaboche [58] for fatigue-creep damage interactions.

The contribution of fatigue to the crack growth rate is expressed by the equation borrowed from Tomkins [59]:

$$\left(\frac{da}{dN} \right)_{fat} = \alpha \Delta \epsilon_p \left[\frac{1}{\cos\left(\frac{\pi}{2} \frac{\sigma_{max}}{\sigma_f}\right)} - 1 \right] a = B a \quad (28)$$

where α is a geometric factor which is equal to $(1.12 \cdot 2/\pi)^2 \approx 0.51$ for the case of a semi-circular crack in a LCF specimen geometry, σ_f is the tensile fracture stress, and all the other symbols have their usual meaning. The oxidation contribution to the crack growth rate is expressed by means of the model developed by Reuchet and Rémy [24], which considers the oxidation of the matrix and the carbides met along the crack path_(*)

* Usually along grain boundaries or between dendrite arms in superalloys.

separately, as their kinetic laws differ:

$$\left(\frac{da}{dN}\right)_{ox} = \left(\frac{da}{dN}\right)_{ox,M} (1 - f_c^*) + \left(\frac{da}{dN}\right)_{ox,c} f_c^* \quad (29)$$

where f_c^* is the effective fraction of carbides in the crack path. The oxidation penetration of the matrix $da_{ox,M}$ during one cycle of period Δt is given by:

$$\left(\frac{da}{dN}\right)_{ox,M} = n k_M^{\frac{1}{n}} \left[1 + k_{cyc0} \frac{\Delta \epsilon_p}{2} \right] \Delta t^{\frac{1}{n}} \quad (30)$$

and the oxidation penetration of the carbides $da_{ox,c}$ during one cycle of period Δt is expressed by:

$$\left(\frac{da}{dN}\right)_{ox,c} = 4 k_{c0}^{\frac{1}{4}} \exp\left(\frac{V_m \sigma_{max}}{12 RT}\right) \Delta t^{\frac{1}{4}} \quad (31)$$

where k_M is the oxidation rate constant of the undeformed matrix, k_{cyc0} is a constant of proportionality between the oxidation kinetics and the plastic deformation; k_{c0} is the oxidation rate constant of a carbide particle without stress, and V_m is a constant related to the molar volume of the carbides. The $V_m \cdot \sigma_{max}$ term takes into consideration the effect of hydrostatic stress on the activation energy of diffusion and is also presented in Subsection 2.3.6 (Equation 77).

Originally, Reuchet and Rémy [24] assumed a parabolic oxidation kinetics for the matrix with the exponent of Δt equal to $\frac{1}{2}$, whereas Equation 30 uses an exponent with the general form of $1/n$. This modification was made because the kinetics of oxidation of the matrix at the grain boundary under cyclic conditions has been shown to follow a kinetics law with $n = 4$, in IN-100 [4], similar to the kinetic law carbide oxidation [4]. When the oxidation kinetics of the G.B. follows a parabolic law, as Antolovich et al. found for René 80 [13, 14], the value of $n = 2$. The value of n could depend on the material and on the experimental conditions and has to be determined

carefully. It should also be noted that if the oxidation of the matrix takes place at the grain boundary and the local kinetics of oxidation is independent of cyclic straining and $k_{\text{cyc}0} = 0$ [4]. It is recognized that the kinetics of oxidation is largely influenced by the substrate deformation which causes oxide scale cracking and spalling, especially when the oxide scale becomes thicker (see Subsection 2.3.6).

The crack growth rate Equation 27 can be integrated to find the fatigue life:

$$N_f = \frac{1}{B} \ln \left[\frac{B a_f}{\left(\frac{da}{dN} \right)_{ox}} + 1 \right] \quad (32)$$

where B and $(da/dN)_{ox}$ are defined in Equations 28 and 29 respectively, and where the oxidation is assumed to control the crack growth rate when the crack is very small (at $N = 0$, $a \rightarrow 0$). After experimental determination of the parameters_(*), Equation 32 was used to predict life of the MAR-M509 superalloy at 20°C and 900°C in vacuum. Calculated and experimental fatigue lives were in reasonable agreement within a factor of two. Predicted lives were found to be conservative at low strain (long life), and too optimistic at high strain (short life).

* From fatigue tests conducted at high frequency or in vacuum or at low temperature for the Tomkins' Model, and at high temperature-low frequency in air for the oxidation model.

2.2.2.6 Neu-Sehitoglu [26-30]

The Neu-Sehitoglu Model, developed for life prediction under IF, TF and TMF conditions (with various temperature deformation phasing, strain rates...) is capable of handling oxidation-fatigue and creep-fatigue damage interactions assuming linear interactions, such that the total damage D is obtained by the sum of damage caused by each damage mode:

$$D = D^{fat} + D^{ox} + D^{creep} \quad (33)$$

The continuum damage variable D is the variable proposed by Kachanov to formulate his creep damage law, and also used by Lemaitre and Chaboche to develop more complex creep and creep-fatigue damage evolution laws [60]. D represents a scalar which varies from 0, for a defect free material, to 1, for a fully damaged material ($0 \leq D \leq 1$). The variable is a scalar instead of being a tensor because the microscopic damage effects are assumed isotropic in the material. In any section of the material, the isotropic variable D represents the fraction of the section that cannot support stress more precisely. The effective stress σ_{eff} is then defined as follows:

$$\sigma_{eff} = \frac{\sigma}{1 - D} \quad (34)$$

which can be used to consider the effect of damage on stress redistribution in the material.

Assuming linear damage accumulation ($D = N/N_f$), Equation 33 can also be

rewritten in terms of the failure life, N_f :

$$\frac{1}{N_f} = \frac{1}{N_f^{fat}} + \frac{1}{N_f^{ox}} + \frac{1}{N_f^{creep}} \quad (35)$$

In this equation, the life dominated by pure fatigue, N_f^{fat} , is established with the strain-life relation of Manson and Hirshberg [54]. The life dominated by creep damage is calculated with the creep-fatigue model of Neu-Sehitoglu. This model is briefly presented at the end of this Subsection 2.2.2.6. Attention can be now focused on the life term dominated by oxidation damage under fatigue conditions, N_f^{ox} , as defined by the Neu-Sehitoglu's model [26-30].

This model is based on the formation of oxide intrusions in the metallic substrate. The model is described by repeated local oxide scale growth and rupture by normal cracking of the scale followed by oxide scale detachment from the substrate when the oxide scale thickness reaches a critical value, \bar{x}_c . Two types of oxide intrusion are observed: Type I where the oxide scale only cracks locally at the end of the oxide intrusion, leaving a continuous oxide layer along the fracture surfaces of the resulting crack and Type II, where the oxide scale cracks and also detaches from the surface, leaving a multilayer or stratified wide oxide intrusion. The mechanism of formation of the two oxide intrusion types is well described in Figure 2.4.

The Neu-Sehitoglu model can apply to both types of intrusions. The model first considers the oxide growth rate to be given as:

$$\frac{dx}{dN} = \frac{dx}{dt} \Delta t \quad (36)$$

where x is the oxide thickness and Δt is the cyclic period. The oxide growth rate can be defined by a parabolic oxidation law up to time when the oxide scale thickness

reaches the critical value x_c , represented in the same form as Equations 45 and 46 of Subsection 2.3.2.1:

$$x = \sqrt{k_p t} \quad \text{or} \quad \frac{dx}{dt} = \frac{k_p}{2x} \quad (37)$$

where k_p is the parabolic oxidation rate constant_(*). Since k_p is a function of the diffusion of the oxide forming elements, and that the temperature varies during TF or TMF conditions, an equivalent parabolic rate constant k_p^* , representing the oxidation kinetics over one thermal cycle, has to be used, as defined in Subsection 2.3.6 (Equation 78).

When $x \rightarrow x_c$, the oxide scale fractures, the oxidation rate becomes very high each time the substrate surface becomes exposed. Figure 2.10 shows the series of parabolic curves which schematically describes repeated oxide growth and rupture. The overall evolution of the effective total oxide growth is described by:

$$x = B \frac{k_p^*}{\bar{x}_c} t^\beta \quad (38)$$

where \bar{x}_c is defined as the average value of the critical oxide thickness at rupture, and B and β are constants. Differentiating Equation 38 with respect to time and using Equation 36, we obtain the effective growth rate:

$$\frac{dx}{dN} = B \frac{k_p^*}{\bar{x}_c} \beta N^{\beta-1} \Delta t^\beta \quad (39)$$

Here, the average critical oxide thickness at rupture, \bar{x}_c , is a function of the mechanical strain range $\Delta \epsilon_{\text{mech}}$, the phasing of temperature and mechanical strain, and the strain rate.

* Note that the symbolism defined in Subsection 2.3 is used instead of the original notation used by Neu-Sehitoglu.

Based on experimental measurements for various TMF conditions, the expression of \bar{x}_c as a function of these parameters was found to be of the form:

$$\bar{x}_c = \frac{\delta_0}{\Delta \epsilon_{mech}^2 \Phi^{ox} \dot{\epsilon}^a} \quad (40)$$

where Φ^{ox} is a phasing factor, a is a material constant and δ_0 is a measure of oxide ductility.

The phasing factor Φ^{ox} is a function of the ratio of the thermal and mechanical strain rates ($\dot{\epsilon}_{th}/\dot{\epsilon}_{mech}$). The value of Φ^{ox} ranges from 0 when no environmental damage happens to 1 when the coupling of environment and phasing are the most detrimental to life. Such an extremely detrimental condition is observed for out-of-phase TMF phasing ($\dot{\epsilon}_{th}/\dot{\epsilon}_{mech} = -1$) which gives the smallest critical oxide thickness at rupture. The expression of Φ^{ox} which best reproduces the data is obtained by integrating a function ϕ^{ox} of the ratio ($\dot{\epsilon}_{th}/\dot{\epsilon}_{mech}$) over the cycle period Δt , as this ratio can vary during cycling:

$$\Phi^{ox} = \frac{1}{\Delta t} \int_0^{\Delta t} \phi^{ox} dt \quad (41)$$

with:

$$\phi^{ox} = \exp \left[-\frac{1}{2} \left(\frac{(\dot{\epsilon}_{th}/\dot{\epsilon}_{mech}) + 1}{\xi^{ox}} \right)^2 \right] \quad (42)$$

The parameter ξ^{ox} is a measure of the relative amount of damage associated with the various phasing (that is out-of-phase {OP}, in-phase {IP}, isothermal {no phasing}, intermediate phasings...)

Now that the different parameters of the effective total oxide growth rate equation are defined, it can be integrated to obtain the oxidation life term ($1/N_t^{ox}$) of Equation 35:

$$\frac{1}{N_f^{ox}} = \left[\frac{x_f \delta_0}{B \Phi^{ox} k_p^*} \right]^{-1/\beta} \frac{2 (\Delta e_{mech})^{(2/\beta) + 1}}{\dot{\epsilon}^{1 - (a/\beta)}} \quad (43)$$

where x_f corresponds to the depth of the total effective oxide intrusion_{cr}, which reaches a critical value leading to rapid crack growth (driven by the static load) and to failure. It should be noted that in this oxidation life prediction, the cyclic period is expressed by the combination of the mechanical strain range and strain rate such that $\Delta t = 2 \cdot \Delta e_{mech} / \dot{\epsilon}$.

As for the oxidation-fatigue damage model, the creep-fatigue model incorporates the effect of the thermo-mechanical phasing on life through an effective phasing parameter expressed as a function of the ratio of the thermal and mechanical strain rates. An Arrhenius expression is used assuming that the creep damage process is thermally activated. The triaxiality of the principal stress tensor is considered in terms of a linear relation between the two invariants of the tensor (i.e. the hydrostatic stress and the von Mises stress). The resulting effective stress is normalised with the drag stress (or viscous stress related to plastic flow), expressed as a function of temperature. Finally, in order to consider the effect of the variation of the temperature, the stress tensor and the thermo-mechanical strains on creep-fatigue life, the model can determine the damage accumulation for one cycle ($D^{creep} = 1/N_f^{creep}$) by integrating the damage accumulation as shown in Equation 44:

$$\frac{1}{N_f^{creep}} = \frac{1}{\Delta t} \int_0^{\Delta t} \exp \left[-\frac{1}{2} \left(\frac{(\dot{\epsilon}_{th} / \dot{\epsilon}_{mech}) - 1}{\xi^{creep}} \right)^2 \right] A \exp \left(\frac{-\Delta H}{RT} \right) \left(\frac{\alpha_1 \sigma_{eq} + \alpha_2 \sigma_R}{K} \right)^n dt \quad (44)$$

assuming linear damage accumulation during cycling. In this equation:

ϵ_{th} is the thermal strain;

ϵ_{mech} is the mechanical strain;

* Which can be considered as a crack caused by cyclic oxidation.

ξ^{creep} is a constant in the phasing function term;

A is the frequency constant associated to the creep damage process;

ΔH is the activation energy for the creep damage mechanism;

R is the gas constant;

T is the temperature in K;

σ_{eq} is the von Mises stress;

σ_H is the hydrostatic stress;

α_i are scaling factors;

K is the drag stress;

m is an exponent;

Δt is the cycle period;

t is the time.

The current fatigue-oxidation and creep-fatigue models of Neu-Sehitoglu have numerous constants to be experimentally established. The constants of the fatigue term ($1/N_f^{\text{fat}}$) can be determined at room temperature from standard fatigue tests or from the literature. The determination of the constants for the oxidation term ($1/N_f^{\text{ox}}$) requires:

- oxidation tests at different temperatures with unstressed specimens in order to obtain k_p^* and the oxidation activation energy Q ;
- isothermal fatigue tests at high temperature and at two different strain rates where oxidation-fatigue damage is dominant in order to determine B , β , x_f , a ;
- thermo-mechanical tests with two or three thermal to mechanical strain rate ratios (at least in-phase and out-of-phase) where fatigue-oxidation damage is dominant in order to determine ξ^{ox} and δ_0 .

The determination of the constants for the creep term ($1/N_f^{\text{creep}}$) requires:

- creep tests to determine ΔH ;
- isothermal fatigue tests at high temperature, at two different strain rates and stress ratios (R) where creep-fatigue damage is dominant, in order to determine A, m, α_1 , α_2 ;
- thermo-mechanical tests with two or three thermal to mechanical strain rate ratios (at least in-phase and out-of-phase) and where creep-fatigue damage dominates, in order to find ξ^{creep} ;

In total, a dozen of experiments have to be carried out if the oxidation and creep test results are found in the literature. The constants ξ^{ox} , B, x_p , A and m are determined from experimentally measured lives whereas, a, δ_0 , k_p^* and Q are obtained from metallographic analysis of the test specimens.

The predictive capacities of the Neu-Sehitoglu Models have been tested for different types of material, an aluminium alloy (Al 2xxx-T4), a steel (1070) and a superalloy (MAR-M247), over a wide range of conditions which include TMF OP ($\dot{\epsilon}_{\text{th}}/\dot{\epsilon}_{\text{mech}} = -1$) and TMF IP ($\dot{\epsilon}_{\text{th}}/\dot{\epsilon}_{\text{mech}} = 1$) [26-30]. Predictions were generally found to be very satisfactory.

2.3 Oxidation Damage Modelling

Oxidation plays an important role in thermal fatigue damage, as discussed in the last Subsection 2.2. Notably, localized oxidation arising at grain boundaries, at interdendritic zones and at carbides interfaces, causes stress concentration and reduces the life to crack initiation. On the other hand, uniform oxidation of components cyclically exposed to corrosive hot gases produced by engines combustors also causes important metal losses. Uniform oxidation modifies leading and trailing edges radii as well as the curvature of blades and vanes. This noticeably reduces engine efficiency and increases engine maintenance costs.

Oxidation of a nickel-base superalloy such as René 80, bare or coated, under thermal cycling conditions in a burner rig involves a complex succession of mechanisms: growth of an external protective oxide scale, alloy depletion of the most active elements, transition from external to internal oxidation, and consumption of the base metal resulting from its oxidation. The repeated spalling of the oxide scales associated to the cyclic contraction of the substrate during cooling significantly accelerates the base metal consumption or metal losses.

This subsection attempts to establish the equations and the parameters which best describe the principal mechanisms involved during oxidation and which will be used in Subsection 5.4 to develop a model or algorithm for the computation of the equivalent thickness of the base metal consumed.

2.3.1 Chemical Nature of the Oxide Scale

In the early stage of oxidation, the alloy in contact with air combines with oxygen to form a mono-molecular layer of oxide at its surface. As the oxidation proceeds, the oxide scale builds up and further oxygen-alloy reactions can occur at the alloy-oxide or oxide-gas interfaces through cation outward diffusion or oxygen inward diffusion. The diffusivity of the ions is strongly affected by the temperature and also by the chemical nature of the cations of the alloy. In the case of René 80, the chemical composition (given in Subsection 2.1) is complex and the oxide formed at its surface is composed of multilayers of complex mixes of alumina-chromium oxide, $\text{Al}_2\text{O}_3\text{-Cr}_2\text{O}_3$, spinels, $\text{Ni}(\text{Cr,Al})_2\text{O}_4$ and nickel oxide, $(\text{Ni,Cr,Al})\text{O}$, which also includes traces of other elements of the alloy (see Subsection 4.1). The aluminium-rich Codep B-1 coating used on some DEW specimens is rapidly oxidized to form a compact alumina-rich oxide scale which includes some chromium oxide and other impurities.

In order to simplify the problem, the constituents of the alloy can be separated into two groups: the noble elements and the active elements. The noble elements, represented by Ni, Co, Mo, have a moderate affinity for oxygen to form an oxide (moderately negative free energy of reaction) as compared to the active elements, represented by Cr, Ti, W, Al, Hf, C, Zr, B. A further simplification, based on their proportion in each group, consists of considering the alloy and the coating to be a Ni-Cr-Al alloy where the Ni represents the noble elements and Cr-Al represent the active elements. In this alloy system, the nature of the oxide scale depends of the content of the more active elements Cr-Al in the alloy, as illustrated in Figure 2.11.

In Cr-Al rich alloys (Figure 2.11a), an external scale, usually composed of a layer of chromium oxide (Cr_2O_3) and a sub-layer of alumina (Al_2O_3), forms at the surface of these alloys [61, 62]. During the oxide scale growth, the zone in the alloy next to the

interface is depleted in Cr and Al, leaving the typical concentration profiles as shown in Figure 2.11. Note that the original (or initial) alloy surface before oxidation corresponds to the alloy-oxide interface meaning that there is no alloy surface recession in this case.

In Cr-Al poor alloys (Figure 2.11b), an outer layer of nickel oxide (NiO) and a sublayer of NiO containing spinel islands ($\text{Ni}(\text{Cr,Al})_2\text{O}_4$) form at the surface of the alloy [61, 62]. The zone next to the alloy-oxide interface is completely depleted in Cr and Al and is composed of almost pure Ni with precipitates of alumina and chromium oxide, ($\text{Al}_2\text{O}_3\text{-Cr}_2\text{O}_3$). In dilute alloys, the content in active elements is too low to provide a continuous scale. In this case, the precipitates of $\text{Al}_2\text{O}_3\text{-Cr}_2\text{O}_3$ are formed in the depleted zone as a result of oxygen diffusion in the metal and reaction with the solutes, known as internal oxidation. As the depleted zone (mainly composed of pure nickel) oxidizes to produce the outer layer of NiO, the metal is consumed causing the alloy surface recession relative to the original surface, as opposed to the Cr-Al rich alloys. The presence of the spinels islands in the NiO sublayer results from the reaction of the NiO with the precipitates of $\text{Al}_2\text{O}_3\text{-Cr}_2\text{O}_3$ as the oxidation of the depleted zone progresses.

2.3.2 Oxide Scale Growth Kinetics

2.3.2.1 Uniform Oxidation

Usually, at high temperature, the rate of growth of the oxide scale dx/dt , which is directly related to the oxidation kinetics, is controlled by diffusion of the species in the oxide scale and is then inversely proportional to the scale thickness x (Figure 2.12) [62]:

$$\frac{dx}{dt} = \frac{k_p'}{x} \quad (45)$$

which leads to:

$$x^2 = 2 k_p' t \quad (46)$$

after integration. Here k_p' is a parabolic oxidation rate constant related to the coefficients of diffusion of oxygen and/or cations into the oxide scale. Since diffusion is a thermally activated process, k_p' varies with temperature according to the general Arrhenius expression:

$$k_p' = k_{p0}' \exp\left(\frac{-Q}{RT}\right) \quad (47)$$

In this Equation, k_{p0}' is a constant and Q is the activation energy associated with the diffusion process.

The variation of the value of k_p' for different compositions of alloy, combined with the study of the morphology of the different oxides produced, gives a valuable information on the effect of solute content on the oxidation kinetics. Figure 2.13 shows the variation of k_p' as a function of the nominal composition of the Ni-Cr and Ni-Al alloys for temperature ranging from 800° to 1200°C [63, 64]. For both systems, as the Cr and Al content of the alloy increases from 0 to about 12 at%, the rate constant increases relatively to that of pure Ni. After 12 at%, the rate constant suddenly falls by one to two order of magnitudes to values similar to the rate constant of pure Cr and Al. The high values of the rate constants of the diluted alloys are associated to the high diffusivity of cations in the NiO oxide scale and the increase of rate is related to the additional cation vacancies provided by solute. As the proportion of Al_2O_3 or Cr_2O_3 precipitates increases in the NiO scale, they considerably reduce the Ni cation flux

through the scale and the rate constant consequently drops. The low oxidation rate observed in alloys with solute contents of more than 12 at% is due to the formation of a compact and continuous oxide scale of alumina or chromium oxide which have very low vacancies concentration, thus causing considerably slow ionic migration through the oxide scale. Oxidation of dilute alloys is relatively rapid, which implies that the Cr and Al depleted zone, mainly composed of Ni, is consumed, whereas oxidation of Cr or Al rich alloys is very slow due to the partial alloy depletion of the active species without alloy consumption or alloy surface recession. For this reason, alumina and chromium oxide scales are considered to be protective against oxidation and many high temperature commercial alloys contain more than 12 at% of Cr and Al. The critical content in B, represented by N_B^r , which defines the transition from internal to external oxidation of the active element B is then very important to control in alloy design for high temperature applications. The Cr and Al contents being respectively of 15.5 and 6.5 at% in René 80 (22 at% in total), the alloy can be considered to be well protected by a continuous Al_2O_3 - Cr_2O_3 duplex scale, at least under isothermal conditions. The addition of aluminide coating obtained by diffusing Al into the surface guaranties an excellent protection (for the Codep B-1 coating, the amount of Al must be between 55 and 60 at%, see Subsection 2.1).

The constant k_{p0}' and the activation energy Q corresponding to the oxidation kinetics of dilute and rich alloys, delimited by the transition content N_B^r , were determined from Figure 2.13. Table 2.2 gives the values of these constants for both Ni-Cr and Ni-Al alloys. The appropriate oxide density was used to convert the units of the parabolic rate constants based from oxide mass gain ($g^2/cm^4/s$) to oxide scale thickness gain ($\mu m^2/s$).

Table 2.2 Constant k_{p0}' and activation energy Q for oxidation of dilute and rich Ni-Cr and Ni-Al alloys

Ni-Cr Alloy			
	k_{p0}' ($\text{g}^2/\text{cm}^4/\text{s}$)	k_{p0}' ($\mu\text{m}^2/\text{s}$)	Q (kJ/mole)
$N_{\text{Cr}} < 0.12$ (NiO)	0.007294	7729	165.1
$N_{\text{Cr}} \geq 0.12$ (Cr_2O_3)	0.001179	2172.6	185.6
Ni-Al Alloy			
	k_{p0}' ($\text{g}^2/\text{cm}^4/\text{s}$)	k_{p0}' ($\mu\text{m}^2/\text{s}$)	Q (kJ/mole)
$N_{\text{Al}} < 0.12$ (NiO)	0.05366	56870	195.1
$N_{\text{Al}} \geq 0.12$ (Al_2O_3)	0.05333	168000	237.5

The graphs in Figure 2.13 give a good idea of the order of magnitude of the parabolic rate constant of the René 80 alloy over a wide range of temperature but the doping effect of the numerous elements which are not present in Ni-Cr-Al alloys is very difficult to extrapolate accurately from the rate constants of the simpler alloys. It is preferable to get experimental values proper to René 80. In order to determine the value of the parabolic rate constant, k_p' , the scale thickness, x , has to be measured as a function of time of exposition to hot gases. Then x^2 is plotted against time and k_p' can be deduced from the slope of this graph.

Experimental results sometimes deviate from the parabolic expression 46 because other factors can affect the kinetics of oxidation, such as oxide evaporation and the radius of curvature of components. The chromium oxide is sensitive to evaporation at high temperature ($T > 1000^\circ\text{C}$) which is responsible for the acceleration of the oxidation

rates of the chromium oxide forming alloys. This was observed for MAR-M247 [65] and DS René 80 [66] for which the oxidation kinetics was determined in air at 1050 °C, for the leading edge (LE), the flat surface (FS) and the trailing edge of a double edge-wedge (DEW) specimen. Figure 2.14 shows the change in oxide scale thickness for DS René 80 as a function of time. The rate of oxidation is high at the beginning, then it slows down and becomes zero which corresponds to the plateau in the graph. In fact, if the evaporation rate is taken into consideration in Equation 45, the rate of oxide growth dx/dt , as observed for DS René 80, can be well described by [62]:

$$\frac{dx}{dt} = \frac{k'_p}{x} - k'_e \quad (48)$$

where the second term added is the rate of evaporation k'_e . When integrated, Equation 48 becomes:

$$t = \frac{k'_p}{k_e'^2} \left[-\frac{k'_e}{k'_p} x - \ln \left(1 - \frac{k'_e}{k'_p} x \right) \right] \quad (49)$$

When the scale is thin, the scale builds up because the diffusion is rapid compared to the rate of evaporation but as the scale becomes thicker, the rate of evaporation is more important and becomes equal to the growth rate. In this situation, the scale thickness stays stable ($dx/dt = 0$) and is limited to a thickness x_0 . The stabilization of x is clearly illustrated in Figure 2.14 where x_0 is indicated for data obtained from the flat portion (FS) of the DEW specimen. From Equation 48, x_0 can be defined as the value of x for which dx/dt equals zero:

$$x_0 = \frac{k'_p}{k'_e} \quad (50)$$

and Equation 49 can be rewritten as to be:

$$t = \frac{x_0}{k_e'} \left[-\frac{x}{x_0} - \ln \left(1 - \frac{x}{x_0} \right) \right] \quad (51)$$

Knowing x_0 , the rate of evaporation k_e' is then easy to calculate from experimental data by determining the slope of the graph of the time versus the term of Equation 51 between brackets. Table 2.3 summarizes the values of x_0 , k_e' and k_p' at different locations of the DEW specimen in DS René 80 at 1050 °C, while Figure 2.14 illustrates the calculated variation in scale thickness compared to the measurements. Table 2.3 also gives the corresponding value of k_{pO}' determined from the Arrhenius expression of the parabolic oxidation rate constant (Equation 47) and assuming that the activation energy for the oxidation of René 80 is the same as that of Cr-rich Ni-Cr alloys ($Q = 185.6$ kJ/mole, see Table 2.2).

Table 2.3 Values of the parameters of the paralinear kinetic Equations 48-51 of oxidation DS René 80 at 1050 °C.

Specimen Location	x_0 (μm)	k_e' ($\mu\text{m/hr}$)	k_p' ($\mu\text{m}^2/\text{hr}$)	k_{pO}' ($\mu\text{m}^2/\text{hr}$)
LE	28	0.28	7.8	1.66×10^8
FS	35	1.25	44	9.38×10^8
TE	26	0.26	6.8	1.45×10^8

While it is intuitively believed that the rate of evaporation should not vary with the radius of curvature, values of k_e' in Table 2.3 show an opposite result. The presence of TiO_2 which sometimes covers the external layer of Cr_2O_3 , also results in a variation of the chemical composition of the layer. Consequently, the change of chromium

activity can explain the observed evaporation rate. Values of the parabolic rate constant k_p' also vary significantly. Preferential diffusion of certain species is affected by the scale growth stresses induced by the convex geometry of the edges and can principally explain the variation of both k_p' and k_e' . Smaller range of k_p' values (12-19 $\mu\text{m}^2/\text{hr}$) can be found if k_e' is set to the average value of 0.5 $\mu\text{m}/\text{hr}$, but the curve fitting of the data is not as good.

Since the kinetics of oxidation was obtained from a discontinuous method, the experimental errors may not be the same from each specimen and it is difficult to get very accurately x_0 , k_p' and k_e' from these results. Also, the curve fitting is not perfect but is much more convenient than the fitting with an empirical power law.

Another factor which affects normal parabolic growth rate is the repeated cracking and spalling of the oxide scale caused by differential thermal expansion and contraction between the oxide and the metallic substrate during thermal cycling. Repeated scale breakdowns reset the scale thickness to small values, if not 0, which accelerate the global oxidation rate given by Equation 45. This point will be discussed in Subsection 2.3.6.

2.3.2.2 Localized Oxidation

Localized oxidation usually takes place at grain boundaries, interdendritic zones and carbides. In this subsection, preferential oxidation of these specific locations will be considered as penetrating oxide spikes, as illustrated in Figure 2.15.

Local oxidation kinetics is described with the following simple power law:

$$d_s^n = n k_s' t \quad (52)$$

where:

d_s is the penetrating oxide spike depth measured from the external oxide surface,

k_s' is the oxidation rate constant for the spike penetration,

n is the exponent representative of the oxidation mechanism.

The exponent n varies from 1 to 6 depending of the controlling mechanism of oxidation. When the oxidation kinetics is controlled by reaction rate at the metal-oxide or oxide-gas interfaces, $n = 1$, [62]. When it is controlled by diffusion of the cations or the anions through the oxide scale in one direction, $n = 2$, [62]. When the diffusion occurs in two directions like along grain boundaries, it is usually observed that $n = 4$, [56], and when the diffusion takes place at interfaces, as between a carbide precipitate and the substrate, $n = 6$, [67].

In MAR-M247 [65] and in DS René 80 [66], the preferential sites of oxidation are principally at the carbides, as found by Litz et al., [68]. Their oxidation kinetics was determined in air at 1050 °C as a function of the position along the periphery of a DEW specimen. It was found for DS René 80 that $n = 2.01$ which means the oxidation process is controlled by diffusion in one direction through the oxide formed from the carbides, while for MAR-M247, it seems that $n = 6$, i.e. the carbides oxidation is controlled by interfacial diffusion. Reger and Rémy [4] found that $n = 4$ for the oxidation kinetics of the carbides and the interdendritic zones in IN-100. They also found that, for short time exposure, only the carbides were oxidized while for long exposures, the oxidation of the interdendritic zones was dominant. These results show that the controlling mechanism of carbides oxidation can vary from an alloy to another

and the exponent, n , has to be experimentally determined.

For instance, the constant k_s' was determined for DS René 80 to be $14 \mu\text{m}^2/\text{hr}$, at 1050°C [66]. Under thermal fatigue conditions, it was found that the cyclic deformation of the oxide induced by the substrate during thermal fatigue has no effect on the preferential oxidation kinetics [4]. In other words, the oxide scale cracking and scalloping does not seem to affect the oxidation rate of the carbides and of the interdendritic zones.

2.3.3 Alloy Surface Recession Kinetics

In Ni-Cr-Al alloy systems with a nominal solute composition of $N_B^0 < N_B^{\text{tr}}$ (where B represents Cr or Al), the internal oxidation of B creates a totally depleted zone composed of pure Ni which is consumed during its oxidation. In this case and not in the case where $N_B^0 \geq N_B^{\text{tr}}$ (which implies the formation of a protective scale and only alloy depletion in B), the NiO oxide scale thickness x can be related to the thickness of metal consumed, translated by the alloy surface recession, y , as defined in Figure 2.12. While the relation between x and y is simply given by the ratio of the equivalent volumes of scale and metal_(s), \bar{V}_{ox} and \bar{V}_m :

$$\frac{y}{x} = \frac{\bar{V}_m}{\bar{V}_{\text{ox}}} \quad (53)$$

the Equations 45 and 46 can be expressed in terms of y :

*: The equivalent volume of an alloy is the same as the molar volume V_m , which both represent the volume of one mole of metallic atoms of the alloy. The equivalent volume of an oxide B_xO_y is the volume of one mole of cations in the oxide whereas its molar volume is defined as to be the volume of one mole of B_xO_y . Note that, if the stoichiometric index x is different of 1, the equivalent volume and the molar volume of B_xO_y are not the same.

$$\frac{dy}{dt} = \left(\frac{\bar{V}_m}{\bar{V}_{ox}} \right)^2 \frac{k'_p}{y} \quad (54)$$

$$y^2 = 2 \left(\frac{\bar{V}_m}{\bar{V}_{ox}} \right)^2 k'_p t \quad (55)$$

The parabolic rate constant for the metal consumption, k_p , can be defined from the constant k'_p and the equivalent volumes as:

$$k_p = \left(\frac{\bar{V}_m}{\bar{V}_{ox}} \right)^2 k'_p \quad (56)$$

and thus the Equations 54 and 55 can be rewritten as following:

$$\frac{dy}{dt} = \frac{k_p}{y} \quad (57)$$

$$y^2 = 2 k_p t \quad (58)$$

The equivalent volumes for pure nickel and the alloy René 80, as well as for the principal oxides formed at their surface, are given in Table 2.4

Table 2.4 Equivalent volume (in cm³/mole) of Ni, the alloy René 80 and their oxides.

\bar{V}_{Ni}	$\bar{V}_{René\ 80}$	\bar{V}_{NiO}	$\bar{V}_{Cr_2O_3}$	$\bar{V}_{Al_2O_3}$
8.39	7.02	13.8	14.6	12.8

2.3.4 Alloy Depletion Profile

In alloys rich in active elements B ($N_B^0 \geq N_B^u$), the external oxidation of B leads to the depletion of the alloy next its surface. The content profile in the depleted zone of the alloy depends on the diffusion of B which is well described by the Fick's second law:

$$\frac{\partial N_B}{\partial t} = D_B \frac{\partial^2 N_B}{\partial y^2} \quad (59)$$

or

$$\frac{\partial C_B}{\partial t} = D_B \frac{\partial^2 C_B}{\partial y^2} \quad (60)$$

where:

N_B is the molar fraction of B in the alloy;

C_B is the concentration of B in the alloy (in mole of B/unit of volume);

D_B is the diffusivity of B in the alloy or diffusion coefficient;

y is the axis in the alloy with the alloy-oxide interface taken as the origin; and

t is the time.

The complete solution of this differential problem requires that the initial and boundary conditions are defined. Usually, the initial condition is formulated as:

$$t = 0 \quad N_B = N_B^0 \quad \text{for } y \geq 0$$

and the boundary condition, as:

$$t > 0 \quad J_{B(m)} = J_{B(ox)} \quad \text{for } y = 0.$$

In other words, initially the concentration profile is flat and equal to the nominal composition N_B^0 of the alloy, and the flux of B in the alloy $J_{B(m)}$ must be equal to the

flux of B in the oxide scale $J_{B(ox)}$, at the alloy-oxide interface ($y = 0$), assuming that the oxidation kinetics is controlled by ionic diffusion in the oxide scale and not by diffusion of B in the alloy. The flux in the alloy at the interface is related to the concentration gradient according to the Fick's first law:

$$J_{B(m)} = -D_B \frac{\partial C_B}{\partial y} = -\frac{D_B}{\bar{V}_m} \frac{\partial N_B}{\partial y} \quad (61)$$

where the equivalent volume of the alloy \bar{V}_m is used to convert the molar fraction N_B in terms of concentration C_B . The flux in the oxide at the interface is related to the rate of oxide scale growth dx/dt as following:

$$J_{B(ox)} = \frac{1}{\bar{V}_{ox}} \frac{dx}{dt} = \frac{1}{\bar{V}_{ox}} \frac{k'_p(BO)}{x} \quad (62)$$

where the equivalent volume of the oxide \bar{V}_{ox} convert the volume of oxide produced during the interval of time, dt , in terms of mole of cations B.

The analytical solution to the Fick's second law for the conditions previously presented is a complex error function which gives the depletion profile according to the diffusion coefficient D_B and the parabolic rate constant k'_p . The analytical solution does not apply when the initial and boundary conditions are more complex than what supposed initially. For instance, if the initial profile in the alloy is not flat such as in a coated surface or if the oxide scale breaks during oxidation causing an abrupt increase in the B flux at the alloy-oxide interface, the analytical solution does not exist. In such cases, a numerical method is required. The finite difference method was used for solving these more complex situations, as was done for solving similar problems of heat conduction which involve changing convection boundary conditions [69]. In a one-dimensional problem, the method consists of dividing the substrate into increments, Δy , along the y -axis, from the substrate surface to a given depth, as shown in Figure 2.16.

The nodal points are designated by an integer, m , starting from 0 at the surface to N , the total number of increments. We need to calculate the molar fraction of B, N_B , at each nodal point, m , and for each increment of time, Δt .

In Fick's second law, the second partial derivative can be approximated by:

$$\frac{\partial^2 N_B}{\partial y^2} \approx \frac{NB(m+1) + NB(m-1) - 2NB(m)}{(\Delta y)^2} \quad (63)$$

and the time derivative can be approximated by:

$$\frac{\partial N_B}{\partial t} \approx \frac{NBP(m) - NB(m)}{\Delta t} \quad (64)$$

where:

$NB(m)$ is the molar fraction of B at the nodal point, m , and at time, t , and

$NBP(m)$ is the molar fraction of B at the nodal point, m , and at time, $t + \Delta t$.

For the interior nodes ($m > 0$), Fick's law can now be rewritten in terms of these finite-difference approximations as:

$$\frac{NBP(m) - NB(m)}{\Delta t} = D_B \left[\frac{NB(m+1) + NB(m-1) - 2NB(m)}{(\Delta y)^2} \right] \quad (65)$$

Thus, the molar fraction of B at the various nodes, m , after each increment of time, Δt , can be calculated from the previous values of the $NB(m)$ by isolating $NBP(m)$ in Equation 65:

$$NBP(m) = Fi[NB(m+1) + NB(m-1)] + (1 - 2Fi)NB(m) \quad (66)$$

where Fi is an dimensionless number regrouping D_B , Δt and Δy as follows:

$$Fi = \frac{D_B \Delta t}{(\Delta y)^2} \quad (67)$$

At the boundary node ($m = 0$), the boundary condition described by Equation 61 can be expressed with a finite-difference approximation as:

$$J_B = -\frac{D_B}{\bar{V}_m} \left[\frac{NB(1) - NB(0)}{\Delta y} \right] \quad (68)$$

and the Fick's law at the boundary node can be expressed by:

$$NBP(0) = Fi \left[-2 Bo + 2 NB(1) + \left(\frac{1}{Fi} - 2 \right) NB(0) \right] \quad (69)$$

where Bo is another dimensionless number regrouping the following parameters:

$$Bo = \frac{\bar{V}_m J_B \Delta y}{D_B} \quad (70)$$

The accuracy of the solution found with the finite-difference Equations 66 and 72 depends on the magnitude of the spacial and temporal increments, Δy and Δt . The smaller the value of these increments, the more accurate is the solution. On the other hand, too small increments increase the computation time and the risk of roundoff errors. With too large increments, the solution does not converge, according to the following convergence criterion:

$$Fi = \frac{D_B \Delta t}{(\Delta y)^2} \leq \frac{1}{2} \quad (71)$$

Respecting these restrictions, the spacial and temporal increments, Δy and Δt , have been set to 10 μm and 1 s.

In these Equations, the parabolic oxidation rate constant and the coefficient of

diffusion of Cr and Al in René 80 have to be determined as a function of temperature, using an Arrhenius expression. The parameters of the Arrhenius expression for the parabolic oxidation rate constant of René 80 were determined in Subsection 2.3.2.1 from experimental data found in the literature, whereas the parameters for the coefficient of diffusion of Cr and Al are not available for this alloy. The diffusion parameters which best apply to René 80 are those found for diffusion of Cr in the Ni-19.8wt%Cr-2.5wt%Ti-1.0wt%Al alloy obtained between 900 and 1200°C, from [70]. In this case, the frequency factor $D_{Cr0} = 0.5 \text{ cm}^2/\text{s}$ and the activation energy $Q = 267.8 \text{ kJ/mole}$.

2.3.5 Transition from External to Internal Oxidation

Two conditions, one thermodynamic and the other kinetic, are essential to achieve external oxidation of the more active element B of the alloy A-B. External oxidation of B implies that a protective oxide scale of BO is formed at the surface of the alloy [62]. Otherwise the transition from external to internal oxidation of B occurs causing the complete depletion of B in the alloy near the alloy-oxide interface and its rapid oxidation through the production of a less protective AO oxide scale, as discussed in Subsection 2.3.1, [62].

The activity of B (a_B) in the alloy near the interface has to be high enough so that the BO oxide is more stable than the AO oxide, i.e. the free energy of BO must be more negative than that of AO. The order of magnitude of the activity of B in the alloy can be determined from the equilibrium between AO and BO oxides. The free energy of formation of AO and BO, ΔG_{AO} and ΔG_{BO} , are given by the two following Equations:

$$2uA + O_2 \rightleftharpoons 2A_uO$$

$$\Delta G_{AO} = \Delta G_{AO}^{\circ} + RT \ln \left(\frac{a_{AO}^2}{a_A^{2u} p_{O_2}} \right) \quad (72)$$

$$2vB + O_2 \rightleftharpoons 2B_vO$$

$$\Delta G_{BO} = \Delta G_{BO}^{\circ} + RT \ln \left(\frac{a_{BO}^2}{a_B^{2v} p_{O_2}} \right) \quad (73)$$

where, respectively:

u and v are the cations to oxygen ratio of the stoichiometric A_uO and B_vO oxides symbolized by AO and BO in the equations and in the text for simplification; ΔG_{AO}° and ΔG_{BO}° are the standard free energy of formation of AO and BO oxides and;

a_A , a_B , a_{AO} and a_{BO} represent the activity of the species A, B, AO and BO; p_{O_2} is the partial pressure of oxygen.

At equilibrium with the alloy, $\Delta G_{AO} = \Delta G_{BO} = 0$ and p_{O_2} is the same for both oxides. Assuming that the activity of the oxides are equal to 1 and the activity of A and B in the alloy are equal to their molar fraction, the values of N_A and N_B (Raoultian behaviour) can be calculated by combining Equations 72 and 73 so that:

$$\frac{N_B^{2v}}{N_A^{2u}} = \frac{\exp\left(\frac{\Delta G_{BO}^{\circ}}{RT}\right)}{\exp\left(\frac{\Delta G_{AO}^{\circ}}{RT}\right)} \quad (74)$$

In the case where the standard free energy of formation of AO is many times more negative than that of BO, the molar fraction of B, N_B , is very small compared to the molar fraction of A, N_A , leading to:

At 1000°C, the standard free energy of formation of NiO, Cr_2O_3 and Al_2O_3

$$N_B \approx \exp\left(\frac{\Delta G_{BO}^{\circ} - \Delta G_{AO}^{\circ}}{2 v RT}\right) \quad (75)$$

are [62]:

$$\Delta G_{NiO}^{\circ} = -250 \text{ kJ/mole of O}_2$$

$$\Delta G_{Cr_2O_3}^{\circ} = -520 \text{ kJ/mole of O}_2$$

$$\Delta G_{Al_2O_3}^{\circ} = -845 \text{ kJ/mole of O}_2$$

In the Ni-Cr and Ni-Al systems, where Ni corresponds to A and Cr or Al corresponds to B, the values of u and v are respectively 1 and 2/3 and the values of the molar fractions at equilibrium, N_{Cr}^{∞} and N_{Al}^{∞} , can now be estimated with Equation 75:

$$N_{Cr}^{\infty} = 5 \times 10^{-9}$$

$$N_{Al}^{\infty} = 5 \times 10^{-19}$$

N_B^{∞} is then very small, almost 0 which means that the BO oxide is practically always more stable than the AO oxide at the surface of the alloy A-B.

The kinetic conditions for external oxidation of the more active element B of the alloy A-B requires that the flux of B coming from the alloy must be equal to the flux of B required for the growth of a continuous and protective oxide scale of BO at the alloy surface. In terms of equations, the flux $J_{B(m)}$ given by Equation 61 equals to the flux $J_{B(ox)}$ given by Equation 62 at the alloy-oxide interface:

$$J_{B(m)}|_{y=0} = -\frac{D_B}{V_m} \frac{dN_B}{dy} = \frac{1}{V_{ox}} \frac{k_p'(BO)}{x} \quad (76)$$

As the oxide scale thickness, x, increases, the flux of B and the concentration gradient of B at the alloy surface decreases until the flux becomes very small for large oxide scale thicknesses. For this condition, the concentration profile in the deplete zone, described by the solution of Equation 59 or 60, reaches a quasi-steady state when the molar fraction of B at the interface, N_B' , stabilizes. This phenomenon is illustrated for

Ni-Cr alloys with different initial content of Cr, N_{Cr}^0 , in Subsection 5.4 where the surface concentration N_{Cr}' is computed using the finite difference method.

In order to obtain an external BO oxide scale at the surface of the alloy, the thermodynamic and the kinetic conditions can be combined in one formulation. The stabilized value of the molar fraction of B at the interface, N_B' must be superior to the molar fraction of B at equilibrium, N_B^{eq} ; that is, $N_B' > 0$. Thus, the transition from external to internal oxidation of B occurs when N_B' reaches 0 before the steady state. The value of N_B' during quasi-steady state is a function of the parabolic rate of oxidation of B, $k_p'_{(BO)}$, the diffusion coefficient of B in the alloy, D_B , and of the initial content of B in the alloy, N_B^0 . The critical composition of B, N_B^c , as defined for the transition from internal to external oxidation, is determined in Subsection 5.4, where the time-history of N_{Cr}' is computed for different nominal compositions, using the finite difference method.

For values of $k_p'_{(BO)}$, D_B and N_B^0 that would predict external oxidation of B, additional factors can lead to internal oxidation. For instance, a sudden breakdown of the oxide scale causes the flux of B to drastically increase as the scale thickness, x , becomes very small (Equation 76). After repeated oxide scale spallings, the mole fraction of B at the alloy-oxide interface eventually reaches 0 before its stabilization and internal oxidation can take place. The principal cause of scale breakdown is discussed in the following subsection.

2.3.6 Cyclic Oxidation

During thermal cycling, the variation of the substrate temperature affects the oxidation kinetics at two levels: first, it changes the oxidation rate constants, k' , and

second, it causes thermal stresses in the oxide scale and eventually results in scale failure. Such conditions are called cyclic oxidation.

In order to predict the variation of the oxidation rate during thermal cycling, let us first consider the effect of temperature on the oxidation rate constant k_p' and the evaporation rate k_e' . Since k_p' and k_e' represent thermally activated processes (diffusion, evaporation), these values vary with temperature according to the general Arrhenius expression, as defined by Equation 47 in Subsection 2.3.2:

$$k = k_0 \exp\left(\frac{-Q}{RT}\right) = k_0 \exp\left(\frac{-Q_0 + V_m \sigma_H}{RT}\right) \quad (77)$$

Contrary to Equation 47, the activation energy, Q , in Equation 77 is a function of the hydrostatic stress, σ_H , ($\sigma_H = \frac{1}{3}\sigma_{\max}$, under uniaxial loading conditions), where Q_0 is the activation energy without stress and V_m is the molar volume of the alloy or the oxide scale depending on which of the diffusion of species controls the oxidation kinetics.

As T varies during thermal cycling, it is convenient to use an equivalent k^* that represent the mean value of k' during one typical cycle of period Δt :

$$k^* = \frac{\int_0^{\Delta t} k dt}{\Delta t} = \frac{\int_0^{\Delta t} k_0 \exp\left(\frac{-Q_0 + V_m \sigma_H(t)}{RT(t)}\right) dt}{\Delta t} \quad (78)$$

The use of an equivalent oxidation rate constant assumes that the scale is adherent and compact. In reality, cracking, buckling and scalloping of the oxide scale often occurs during thermal cycling and this drastically enhances the metal consumption. This is caused by thermal stresses that build up in the oxide scale during cooling because of the difference in thermal expansion of the metal and oxide. The stress level, σ_{ox} , can be expressed as [62]:

$$\sigma_{ox} = \frac{E_{ox} \Delta T (\alpha_{ox} - \alpha_m)}{1 + 2 \left(\frac{E_{ox}}{E_m} \frac{t_{ox}}{t_m} \right)} \quad (79)$$

where: E is the elastic modulus;
 α is the coefficient of thermal expansion;
t is the thickness;
 ΔT is the temperature variation;
and the subscript ox and m refer to the oxide and the metal, respectively.

For a superalloy, the protective oxide layers Cr_2O_3 and Al_2O_3 formed at its surface have coefficients of thermal expansion two times smaller than that of the substrate causing compressive stresses in the oxide scale during cooling and eventually scale buckling and scalloping. More precisely, spalling occurs when the compressive deformation of the oxide scale reaches a critical value, ϵ_c^p , as defined by Schütze [71]:

$$\epsilon_c^p = \sqrt{\frac{2 \gamma_0}{x E_{ox} (1 - \nu_{ox})}} \quad (80)$$

where: γ_0 is the fracture surface energy of the metal-oxide interface;
x is the scale thickness;
 E_{ox} is the elastic modulus;
 ν_{ox} is the Poisson's ratio of the oxide.

Some values of oxide properties are presented in Table 2.5 [71-73].

Table 2.5 Mechanical properties of principal Ni, Cr, Al oxides.

Oxide	γ_0 (J/m ²)	E_{ox} (GPa)	ν_{ox}	α_{ox} (10 ⁻⁶ m/m/°C)
NiO	3.6	200	0.32	13.5
Cr ₂ O ₃	5.8	280	0.29	9.6
Al ₂ O ₃	7.7	370	0.24	8.1

During cyclic oxidation involving oxide scale scalloping, the evolution of the cumulative scale thickness x_t , which has grown and spalled off, can be represented by the following parabolic expression [74]:

$$x_t = (k'_1 t)^{1/2} + k'_2 t \quad (81)$$

where k'_1 is related to the oxide growth constant and k'_2 is a spalling constant. The thickness of metal loss is given by:

$$y = (k_1 t)^{1/2} + k_2 t \quad (82)$$

where:

$$k_1 = \left(\frac{\bar{V}_m}{\bar{V}_{ox}} \right)^2 k'_1 \quad (83)$$

$$k_2 = \frac{\bar{V}_m}{\bar{V}_{ox}} k'_2 \quad (84)$$

Note that this expression for the metal loss only applies to pure metals and not to alloys as the oxide scale growth and spalling usually implies the consumption of one species (i.e. alloy depletion).

These empirical equations are still an oversimplification of the spalling process but the parameters that fit experimental cyclic oxidation tests are easy to obtain. A more realistic model based on isothermal oxidation parameters and on the definition of a critical scale thickness x_c can be proposed.

The growth of oxide scale follows the parabolic Equation 46 or the parilinear Equations 49 and 51 (depending of the alloy-oxide system) until the thickness reaches a critical value x_c . In this case, the oxide scale ruptures at the scale-substrate interface, because bonds at the interface are usually weaker than bonds within the substrate or in the oxide, resulting in spalling of the scale. The bare surface of the substrate re-oxidizes according to the oxide growth kinetics expressed by Equations 46 or 51 with the initial condition $(x,t) = (0,0)$. This sequence repeats itself during all the cyclic oxidation process.

The critical scale thickness x_c can be derived from Equation 80, assuming that the mechanical compressive deformation of the oxide scale, ϵ_{ox}^P , is constant from one thermal cycle to another:

$$x_c = \frac{2 \gamma_0}{E_{ox} (1 - \nu_{ox}) (\epsilon^P)^2} \quad (85)$$

Here ϵ_{ox}^P developed during cooling of the substrate is determined from:

$$\epsilon_{ox}^P = -(\Delta \epsilon_m^{net} - \alpha_{ox} \Delta T) \quad (86)$$

where, $\Delta \epsilon_m^{net}$ is the net deformation of the metallic substrate and $\alpha_{ox} \Delta T$ is the thermal contraction of the oxide. Note that if ϵ_{ox}^P is negative, the Equation 86 does not apply. In such a case, this would mean that the oxide scale is in tension which can cause transversal oxide cracking but not spalling.

In the derivation of the last two equations, it was assumed that the scale always fails at the metal-oxide interface and that the interface is defect-free and perfectly smooth. In reality, all oxide-substrate interfaces will present wavy structure and defects which will increase the interfacial stresses and subsequently, decrease the critical scale thickness, x_c . Modelling of the cyclic oxidation behaviour of an alloy is quite complex [75, 76] as demonstrated above. Even if numerous simplifying assumptions are made, many factors were considered in the model presented above.

3. EXPERIMENTAL PROGRAM

This Section describes the experimental aspects of the fatigue testing program in the burner rig which aims principally to simulate the thermal fatigue damage occurring in real turbine airfoils and which is used to determine the life to crack initiation as measured in-situ using an alternating current - potential drop (ACPD) technique. It is divided into three subsections. The first subsection describes the experimental details pertaining to thermal fatigue testing itself. The second subsection explains the techniques used to measure the specimen temperatures in-situ during thermal cycling. And the third subsection presents the techniques employed to assess thermal fatigue damage in specimens on-line during testing as well as after testing.

3.1 Thermal Fatigue Testing in the Burner Rig

In this subsection, the experimental aspects of thermal fatigue tests in the burner rig, which include the material and the geometry of the specimens, the burner rig description and instrumentation, the testing conditions and procedure, are fully described.

3.1.1 Material and Specimen Geometry

The material investigated was DS René 80_{cu}, (also designated as DSR80), a nickel-base superalloy used for blades or vanes in many turbines, including the General Electric F404 aero engines. The specimens were procured in the form of double edge-wedge (DEW) investment castings produced by directional solidification. The dimensions of the DEW specimen are shown in Figure 3.1. The DEW geometry was chosen to simulate the leading and trailing edge radii of blades and vanes. This geometry was also used by NASA several years ago for thermal fatigue studies [77]. Its relative simplicity and section symmetry is chosen in order to simplify the thermal and stress-strain finite element analyses.

Prior to testing, the specimens were heat-treated in accordance with G.E. specification (C50TF28, Class A, see Ref. [78]) and inspected for surface and internal defects. Some specimens were coated with Codep B-1, a high aluminium activity aluminide coating applied by pack cementation process by a certified vendor [79]. The aluminium content must range between 35-40 wt% (55-60 at%). Details of bare and

*: Nominal alloy composition:

In wt%:	14.0 Cr, 9.5 Co, 4.8 Ti, 4.0 Mo, 4.0 W, 3.0 Al, 0.75 Hf, 0.08 C, 0.02 Zr, 0.015 B, Bal. Ni;
In at%:	15.50 Cr, 9.28 Co, 5.77 Ti, 2.40 Mo, 1.25 W, 6.40 Al, 0.242 Hf, 0.383 C, 0.013 Zr, 0.080 B, Bal. Ni.

coated microstructure are presented in Subsection 4.1.1.

3.1.2 Burner Rig Description and Instrumentation

3.1.2.1 Burner Rig Installation

The high velocity-low pressure burner rig used in this project was a Becon Model LCS-4B laboratory combustor. Details of the rig nozzle area are shown in Figure 3.2 whereas Figure 3.3 shows a schematic cutaway view [80] of the burner itself. This rig is based on a dynamic combustor similar to that used in modern aero engines [81]. It runs on J-P4 aviation fuel, at fuel to air ratios that can be adjusted to produce typical turbine inlet hot gas temperature, velocity and chemistry (up to 1500°C at up to Mach 0.8). Air flow is adjusted manually while the fuel flow is controlled by a microprocessor as shown in the hardware configuration schematic of Figure 3.4. The fuel is introduced into the primary zone of the combustor chamber by a pressure atomizing fuel nozzle. The combustion is stabilized through the development of a strong swirl recirculation zone. The expanding gases are subsequently cooled by dilution from secondary air jets located downstream of the primary zone.

By independently adjusting the primary and secondary air flows and the exit nozzle geometry, the velocity and temperature of the combustion gases can be controlled independently. The temperature of the gas was controlled using a calibrated bare junction type-S thermocouple mounted 1 cm downstream of the exhaust nozzle, in the middle of the hot gas jet (Item b, Figure 3.2). The wires of the control thermocouple were looped to minimize conduction-heat losses along the wires and their protective sheath, following the recommended practices given in AGARD Report No.245, [82]. More details on the thermocouple design is given in Subsection 5.1.2.3.1.

The exit nozzle geometry for these experiments was circular with an internal diameter of 50.8 mm (2 inches)(Item a, Figure 3.2). The specimen leading edge was located 85 mm downstream of the nozzle flange. With this configuration, only a portion of the airfoil specimen was directly exposed to the combustion gases (about 40 mm over the full length of 100 mm). Cooling of the specimen was done in a cold air stream produced from a pipe with 40.0 mm (1.57 inch) of internal diameter, mounted next to the hot gas nozzle (Item e, Figure 3.2). Translation of the specimen from one gas jet to the other was done by a sliding carrier driven by a pneumatic device (Item d, Figure 3.2). The pneumatic system is controlled by a microprocessor as shown in Figure 3.4. The DEW specimen is fixed to the carrier with a holder equipped with thermally and electrically insulating grips (Figure 3.5). The insulation of the specimen from the rest of the system is important to ensure a more symmetric temperature distribution along the specimen, in order to simplify the thermal analysis. A 1.6 mm (1/16 in.) thickness plate in stainless steel is added to the top of the holder to prevent interactions between the hot and cold gas streams and stabilize the gas flow and the heat fluxes around the specimen, near the holder.

The specimen temperature can be measured during thermal fatigue testing with an IRCON optical pyrometer (Item g, Figure 3.2) or before the fatigue testing program with thin-wire thermocouples embedded inside the specimen. The latter technique cannot be used during the fatigue testing because it requires the machining of some holes in the specimen geometry which can certainly affect the fatigue behaviour of these components. These two temperature measurement techniques will be described in Subsection 3.2.

3.1.2.2 Data Acquisition System

All the important parameters (specimen and gas temperatures, potential drop in the specimen, ...) of a thermal fatigue test in this facility can be monitored by a "Sciometric Instruments" data acquisition and control unit connected to a SIDUS-386 PC (refer to Figure 3.4). The controlling software is written in quick basic. The "Sciometric Instruments" data acquisition system can read up to 32 channels and is equipped with a high speed A/D converter module that can perform 500 readings/sec./channel. The model 236 has a 12 bit analog to digital converter. This 12 bit converter permits the assignment of a value from 0 to 4095 to the measured signals, fixing the resolution of the full analog scale range to 0.024%. Four voltage ranges can be set through software instructions, individually for each channel. The potential drop readings from the crack growth monitor is ± 0.5 V with a corresponding resolution of ± 0.122 mV, corresponding to the potentiometer resolution of the crack growth monitor which will be described in Subsection 3.3.2.

For each thermal cycle, values of the test parameters are stored in a file identified by the sample code and the cycle number. The synchronization between the software increment of the cycle number of the file name and the actual thermal cycle is achieved through the MICRISTAR unit by activating a trigger in the Sciometric Instruments control unit. The test parameters are read at the beginning of each cycle and stored under static variable names. The data are recorded at the rate of up to 500 reading/s (1 reading/s in the present experiments) during each thermal cycle, and stored under dynamic variable names. Data files are written in ASCII code which can be exported for analysis or display. The evolution of each variable can also be followed cycle per cycle during a test on the monitor of the SIDUS-386 PC.

3.1.3 Experimental Conditions

In the present experiment, the fuel flow was set at 30 L/hr (8 U.S. gal/hr) to obtain gas temperature of 1300°C, as measured by the thermocouple in the middle of the hot gas jet, with primary and secondary air flows adjusted for a gas velocity of Mach 0.4. With the special configuration of the thermocouple and after corrections for radiation heat losses from the thermocouple bead to its surrounding, the actual gas temperature was established to be $1323 \pm 15^\circ\text{C}$, with a test-to-test reproducibility of $\pm 2^\circ\text{C}$ (see Subsection 5.1.2.3.1).

During one thermal cycle, the DEW specimens were heated in the hot gas stream for 150 seconds, after which they were moved laterally into the cooling gas jet (20°C) for 90 seconds.

Nine thermal fatigue tests were carried out in the burner rig at 1323°C . In the case of the first six tests (called SRN, SRA, SRB, SRC, SRD and SRE, respectively), the tested specimens were uncoated whereas during the last three tests (called SRF, SRG and SRH, respectively), specimens were coated. All specimens were exposed 150 seconds per cycle to the hot gas stream except for the SRD test where the specimen was exposed for 390 seconds per cycle. This was done to assess the influence of oxidation and erosion on fatigue life. Tests were performed for periods up to about 2500 thermal cycles excepted for SRN, SRE, SRG, SRH tests, that were interrupted after less than 800 cycles, in order to evaluate early damage accumulation.

The ACPD CGM5 monitor was adjusted with the current and the gain respectively set at 0.5 A and 50 dB for SRA and SRB tests. During other tests, an attempt was made to improve sensitivity by increasing the current and the gain level to 1.0 A and 60 dB. The frequency was set at 30 kHz for all tests. Table 3.1 summarizes

the thermal fatigue tests carried out in the burner rig as well as the corresponding CGM5 monitor settings.

Table 3.1 List of the Thermal Fatigue Tests Carried Out on DS René 80 (DEW) Specimens in the Burner Rig

SPECIMEN NUMBER	TEST NAME	COATING	N_{final}	OBJECTIVE & REMARKS
1	SRN	No	200	effect of thermal cycling on microstructure
8	SRA	No	2587	TF:I+G, ACPD setting A
9	SRB	No	2500	TF:I+G, ACPD setting A
10	SRC	No	3000	TF:I+G, ACPD setting B
11	SRD	No	2140	TF:I+G, ACPD setting B, effect of hold time at HT
12	SRE	No	800	TF:I, ACPD setting B
13	SRF	Yes	2500	TF:I+G, ACPD setting B
14	SRG	Yes	780	TF:I, ACPD setting B
15	SRH	Yes	435	TF:I, ACPD setting B

Thermal fatigue test (TF):

I: Determination of the crack initiation

G: Determination of the crack growth

N_{final} : Number of thermal cycles carried out at the end of a test

ACPD CGM5 settings:

A: $f = 30 \text{ kHz}$, $i = 0.500 \text{ A}$, $G = 50 \text{ dB}$

B: $f = 30 \text{ kHz}$, $i = 1.000 \text{ A}$, $G = 60 \text{ dB}$

3.1.4 Testing Procedure

The detailed thermal fatigue testing procedure in the burner rig is fully described in Appendixes A, B, C. The procedure first presents the preliminary testing preparation which includes the instrumentation of the specimens, the ACPD crack growth monitor set-up and the programming of the microprocessor that controls the hot gas stream temperature. The testing procedure itself, which involves the start-up and the shut-down of the burner rig and the data acquisition set-up and operation, is then provided.

3.2 Specimen Temperature Measurement Techniques

To determine specimen temperatures, two techniques were adopted. Firstly, thin-wire sheathed thermocouples (sheath diameter = 0.5 mm) were used to measure the internal temperatures of a thin wall (thickness = 2 mm) shell-like specimen of the same external shape and dimensions as those of the DEW specimen.

Secondly, optical pyrometry was used to measure surface temperatures of the solid DEW specimen, at other than leading edge locations, in greater detail than was possible with thin-wire thermocouples in the shell-like specimen.

3.2.1 Thin-wire Thermocouple

The shell-like specimen for instrumentation with thin-wire thermocouples was produced by electro discharge machining (EDM) from a solid DEW specimen. Eleven thermocouples were spot-welded to the bottoms of small holes, also machined by EDM into the walls of the specimen, so that the thermocouple beads were located about 0.5 mm from the specimen external surface. The locations are identified in Figure 3.6 as positions 1 to 11, with positions 3, 7 and 10 in the mid-section of the specimen corresponding to the axis of the gas stream. Another two thermocouples were spot-welded to the inside surface of the shell-like specimen, as close as possible to positions 3 and 7.

A polished section through a leading edge thermocouple (position 7), with its sheathed bead located about 0.5 mm from the leading edge, is shown in Figure 3.7. Once all thermocouples had been spot-welded in place, the cavity within the shell specimen was filled with plaster of Paris to ensure that the thermocouples would not become dislodged during testing.

3.2.2 Optical Pyrometry

The optical pyrometer (IRCON Model 7-13C10-0-1-0-60-0-100) was located 25 cm above the specimen as shown in Figure 3.2. The instrument was focused on the flat portions of the specimen, using a long range focusing lens (Model T3 - 25 to 30 cm range) while ensuring that its viewing axis was kept perpendicular to the surfaces on which the measurements were made. With the present setup, the temperature measurements were representative of a circular area 2.5 mm in diameter. All measurements were carried out under steady state conditions, at times between 120 and 150 seconds into the thermal cycle when the specimen temperatures were found to be constant as measured by the thermocouples.

Optical pyrometry requires that the emissivity setting of the pyrometer be adjusted to correspond to that of the material under evaluation. This setting was established experimentally by calibration against the temperature readings of reference thermocouples at, and immediately below, the surface of a flat calibration specimen of the test material heated isothermally in still air by induction. After 16 minutes of heating, the specimen was fully oxidized and the emissivity was found to remain constant. All optical pyrometry measurements were made in the burner rig after the test specimen had been oxidized for at least 16 minutes and using the emissivity IRCON setting of 0.85 obtained by calibration. The optical pyrometry readings were estimated to be accurate to within $\pm 5^{\circ}\text{C}$, with a relative error from reading to reading of less than 1°C.

3.3 Damage Assessment Techniques

This subsection presents the metallographic technique used for thermal fatigue and oxidation damages assessment and the ACPD technique developed for on-line crack initiation and crack growth assessment in the burner rig.

3.3.1 Metallography Damage Assessment

Before any metallography work was carried out, the tested specimens were first thoroughly examined by naked eye and with a low magnitude optical microscope. The observations on the specimen geometry, the oxide scale characteristics, the macrocracks location and morphology were recorded and full scale photographs and macrographs were taken.

Subsequently, one or more sections from the tested specimens were prepared for detailed metallographic analysis involving the following steps. The specimens are cut with a diamond saw at different locations identified with numbers in Figure 3.8 which will be referred in Section 4. The sections were then washed in an ultrasonic bath of tetrachloroethylene for five minutes. To protect the brittle oxide scale during the mechanical polishing, an electroless nickel plating was applied by following the practice recommended by Edgemet® (see Appendix D). The plated coupons were then washed with ethyl alcohol, mounted in epoxy resin (Hysol) and polished with emery paper (# 240, 320, 400 and 600) and diamond paste (9, 3, 1 μm). The coupons were washed again for observation with an optical microscope or with a scanning electron microscope (SEM). For optical observation, two etchants were used to reveal the microstructure (Kalling 2 and Marble reagents), whereas no etchant was necessary with the SEM when the backscattered electrons imaging mode (BEI) was used. The metallographic analysis of some non exposed specimens was used as a reference to the damage assessment of

the exposed samples.

3.3.2 On-line Crack Growth Assessment

Thermal fatigue crack initiation and crack growth rate were monitored in-situ during thermal cycling, using an advanced ACPD (Alternating Current/Potential Drop) technique. In this technique, an alternating current of a constant amplitude and frequency is imposed across the specimen, and the change in potential drop associated with the change of impedance of the specimen arising from the formation of cracks is measured during testing. Surface cracks increase the current path length and consequently, the impedance of the near-surface volume of the specimen. To observe a maximum change in potential drop (PD) for a given crack length, the current direction should be perpendicular to the crack plane. In real engine hardware, cracks that form at the leading and trailing edges of airfoils are normally oriented perpendicular to the airfoil edges [83]. Current leads and potential wires were laser welded to the specimen at the strategic locations shown in Figure 3.9. The current leads were attached to both ends of the airfoil so that the current flowed along its longitudinal axis. Two pairs of PD probes were attached along the leading and trailing edges of the airfoil. Two other pairs of PD probes, used as references, were attached along the transition edges between the wedges and the flat face of the specimen, where the PD should not be affected by crack growth at the leading and trailing edges.

The ACPD technique was used in preference to the more commonly used DCPD technique based on direct current, because of its many advantages. The main advantage is that an AC current produces a higher current density near the surface where cracks usually initiate. Therefore, crack initiation can be detected at an earlier stage than is possible with the DCPD technique [84, 85]. The ACPD is also more sensitive to crack growth than is the DCPD technique, because the potential drop per mm of crack length

is much greater than that achieved with the DCPD technique [84, 85]. In addition, noise rejection and signal amplification are more readily achieved with an alternating current, which is important when dealing with very low signal levels in good conductors [84, 85]. With an AC current of 1 A and distance of 65 mm between PD probes along the leading edge, Figure 3.9, the PD signal in René 80 DEW specimen was found to be in the range of 0.5 mV with a potential drop per mm of crack length of about 50 μ V.

The high current density generated near the surface by an AC is described as the skin effect and is characterized by the depth of penetration or skin depth. The skin depth represents the distance under the surface of the conductor for which the current density is 1/e times ($\approx 0.3679\times$) the current density immediately below the surface [86]. For a cylindrical conductor, the skin depth δ is given by [86]:

$$\delta = \left[\frac{\rho}{4\pi^2 \times 10^{-7} \cdot \mu_r \cdot f} \right]^{1/2} \quad (87)$$

where ρ is the electrical resistivity (in Ohm-m), μ_r is the relative permeability (≈ 1 for most nickel-base superalloys), and f is the AC frequency (in Hz). For example, at 100 kHz, the skin depth in a nickel-base alloy such as René 80 is of the order of 2 mm, which is close to the physical definition of a short crack, recognized to be around 1 mm [85]. The higher the frequency, the greater the crack detection sensitivity. Unfortunately, working with frequencies that are too high causes the PD to be unstable because the PD is too sensitive to fracture surfaces roughness and crack faces separation associated to capacitance effects [87].

In this investigation, the crack growth monitor consisted of a multiple-frequency AC potential drop system manufactured by Matelect Ltd. under the CGM5 model name. This system is capable of providing an alternating current of constant amplitude (0 to 2 Amp RMS) at frequencies ranging from 0.3 to 100 kHz, with a stability greater than

$\pm 0.02\%$ over months of testing. It has facility for selecting the frequency and setting the constant amplitude of the current as required. The AC potential drop across the test specimen is amplified and then demodulated using an automatic phase detection system. The resultant DC output voltage is displayed digitally. The exact configuration of the CGM5 monitor is given in Appendix B.

Some modifications had to be made to the crack growth monitor system to meet the specific environmental conditions of a burner rig. Because of the extreme temperature changes in the rig room, the CGM5 unit was placed in the separate control room (Figure 3.4). A 10 metre long cable was employed to detect the PD signals from the specimen to the crack growth monitor. Considering the high impedance of such a cable versus the very low level of signals generated, a preamplifier unit was used, which was positioned next to the specimen at a distance of 20 cm (see Figure 3.4 and 3.9). The CGM5 described here is a two channel version in which a module (called β) was added to the main instrument (called α module). The α module handles the amplified ACPD signal from channel A of the preamplifier. The β module processes the amplified ACPD signal from channel B of the preamplifier. As illustrated in Figure 3.9, the active probes attached to critical zones on the TF specimen (areas where cracks are expected i.e. LE, TE) are connected to channel A. The reference probes are connected to channel B.

The modules of the CGM5 unit operate in parallel but can only process two PD signals simultaneously. A switching unit, using high integrity-low noise relays (Pickering Electronics Ltd, type 101-2-A-5/1.0) reads the PD at the LE probes (A1) and reference probes (B3) during even cycle numbers while the PD at the TE probes (A4) and reference probes (B2) is read during odd cycle numbers (refer to Figure 3.9). For both the leading and the trailing edges, the farthest pair of reference probes were chosen for reference. With this procedure, the CGM5 can track changes in the PD at the LE

and at the TE during testing, with maximum data acquisition efficiency.

To minimize noise pick up and interference, every unit of the crack monitoring system was enclosed in an aluminium box, and every cable was shielded separately. The specimen was also electrically insulated from the shielding and from its holder using special ceramic grips (Figure 3.5). Despite these precautions, a significant PD signal instability was observed when the PD probes or the current leads were moved. Due to the alternating current, the leads act as a transmitting antenna while the potential drop probes act as a reception antenna. The voltage induced in the PD probes is proportional to the current frequency (particularly important at 100 kHz) and is a strong function of the configuration of the probes and leads. To reduce this effect, the wires of each pair of PD probes were twisted to minimize the wire spacing and to keep the spacing constant. Also, the AC leads were separated from the PD leads as much as was physically possible. The probes were also fixed to the specimen holder by screwed plates (Figure 3.5) in order to avoid any change of configuration or vibrations during specimen translation. After all these precautions were taken, the noise level was reduced to less than 0.02% of the measured PD signal which corresponds to an absolute error of ± 0.05 mV, and which is lower than the potentiometer resolution of the CGM5 monitor (i.e. ~ 0.1 mV).

4. EXPERIMENTAL RESULTS

This section presents the thermal fatigue and oxidation damage assessment resulting from the metallographic analysis and the ACPD technique. Whereas the metallographic analysis gives an accurate evaluation of the damage level after testing and can possibly identifies the damage mechanisms, the ACPD technique provides an estimation of the life to crack initiation and of the crack growth rate during testing. The integration of both techniques result in information which is essential for the development and the validation of thermal fatigue and oxidation damages models which will be discussed in Section 5.

4.1 Damage Assessment from Metallographic Analysis

In order to assess the bulk microstructural changes during thermal cycling, the oxidation and the microcracking, a detailed macroscopic and metallographic analysis of the uncoated and coated DEW specimens was carried out after thermal fatigue testing in the burner rig, according to the technique explained in Subsection 3.3.1. The results of this analysis provide the dendrite spacing and their orientation, the size, morphology, and distribution of carbides and γ' precipitates, as well as the relation between the cracks, the oxide scale and the DSR80 substrate microstructure. These observations are used to explain most probable damage mechanisms that are encountered.

4.1.1 Evolution of the Microstructure

In order to study the influence of the imposed thermal cycling on the microstructure, a metallographic analysis of various sections (Figure 3.8) was carried out on uncoated specimens exposed for 200, 800, 2500 and 3000 thermal cycles and on coated specimens exposed for 435, 780 and 2500 cycles. As a reference for this study, an analysis was first carried out in detail on virgin uncoated and coated specimens.

4.1.1.1 Virgin Specimens

Figure 4.1 shows a longitudinal section (cut #1, Figure 3.8) of the virgin uncoated specimen. The orientation of columnar grains and dendrites in the bulk of the specimen is parallel to the LE direction while dendrites near the surface of the specimen deviate by up to 8° from the longitudinal direction (Figures 4.1 a and b). The directionally solidified structure near the surface is not exactly perpendicular to the chill

placed at the bottom of the mould because the inner mould wall also extracts heat during solidification and influences the heat flux orientation. The primary and secondary dendrite arms spacing are 365 and 115 μm , respectively. The primary dendrite arms spacing is comparable to the leading and trailing edge radii which are 1000 and 700 μm , respectively.

Chinese script MC carbides, composed of an agglomeration of needles, are mainly concentrated between the dendrites (Figure 4.1 c). The average length of these needles is approximately 75 μm with a standard deviation of 25 μm .

The cubic gamma prime (γ') precipitates are exposed by using a Marble's etchant, as shown in Figure 4.1 c. The γ' precipitates average size is $0.40 \pm 0.17 \mu\text{m}$. A TEM study on René 80 [36] showed that the coarse γ' phase precipitates of same dimension were surrounded by fine γ' precipitates ($\leq 0.08 \mu\text{m}$) contrary to what was observed by SEM. This could indicate that the heat treatment was different or that TEM analysis is required for the characterisation of the fine precipitates.

The micrographs of longitudinal sections (cut #1, Figure 3.8) coated with Codep B-1 (an high aluminium activity aluminide $\{\beta\text{-NiAl}\}$ processed by standard pack cementation) was compared to that of uncoated specimens (Figures 4.1 and 4.2). It demonstrated that the heat treatment associated with the coating process did not change the microstructural characteristics of the substrate, except at the surface. The application of an Al rich coating is associated with the formation of an interdiffusion zone. The nickel diffuses from the substrate into the coating and the aluminium of the coating diffuses into the substrate. The microstructure is characterized by a columnar zone

between the coating and the substrate (Figure 4.2b), composed of β -NiAl^(*), a topologically close-packed (TCP) σ phase, Al carbides and the γ' -Ni₃Al^(*). The σ phase appears as lamellae or a needle like structure and is also found in the substrate next to the interdiffusion zone. The additive coating layer is formed of a denuded β zone covered with an outer layer of β phase which includes carbides and α -Cr precipitates. [90, 91]

As illustrated in Figure 4.3, the coating thickness varies from 27 to 40 μm around the specimen cross-section while the interdiffusion zone thickness of $16 \pm 1 \mu\text{m}$ is more constant. This coating thickness to interdiffusion thickness ratio meet the GE specifications for a Codep B-1 coating.

4.1.1.2 Tested Specimens

Table 4.1 gives the dendrite arm spacing, the size of the MC carbide and of the gamma prime precipitates of the uncoated specimens exposed to different number of thermal cycles in the burner rig. These average values were measured from micrographs of the sections at the leading edge submitted to the highest temperatures.

The data of Table 4.1 demonstrate that the thermal and the stress cycling affect neither the primary and secondary dendrite arms spacing, nor the MC carbides size. The scatter of the data is associated with the variation of microstructure from one specimen to another before testing. The MC carbides size is stable because of the relative large size of the metallic atoms M (W, Mo, Ti, Cr) with respect to Ni, and which have low

*: more precisely, EDX quantitative chemical analyses in SEM reveal that the β phase is composed of (Ni,Co)(Al,Cr,Ti) and that the γ' phase is composed of (Ni,Co)₃(Al,Cr,Ti).

diffusivity in the alloy. On the other hand, the gamma prime precipitates (γ') seem to have grown after 2500 thermal cycles, especially near the tip of the leading edge which is exposed to the highest temperature and stresses (refer to Subsection 5.2), when compared to the bulk and LE tip γ' sizes in the SRA specimen. Also, some precipitates are formed in aligned arrangements while others agglomerated into elongated shapes, near the leading edge or at the crack tip (see Figure 4.4). In both cases, the longitudinal orientation of the γ' precipitates is perpendicular to the tensile stress developed along the leading edge, as determined from the finite element analysis presented in Subsection 5.2. This phenomenon called rafting is observed in many γ - γ' alloys subjected to creep or high strain, or to low rate fatigue at high temperature (e.g. [36, 92-94]). Some TEM studies [36, 92] have shown a high density of dislocations near the γ' precipitates oriented perpendicular to the tensile stress. This type of dislocation structure can certainly result in fast diffusion paths for the precipitate elements as compared to lattice diffusion even during tensile elastic deformation. In a study where a DS nickel-base superalloy was subjected to tensile stress at high temperature [94], the γ' thickness to length ratio was correlated to the stress and the temperature. In Figure 4.4, this ratio is about 0.2 which corresponds to what was reported in the study [94] for specimens subjected to stresses less than 100 MPa and temperatures over 950°C for 100 hours. It is interesting to note that the region of the leading edge shown in Figure 4.4 experienced similar temperature and stress levels as computed with a finite element method which will be presented in Section 5.

The thickness of the coating of SRG, SRH and SRF specimens was measured to be 45, 43 and 40 μm , respectively, at the leading edge tip near the free end exposed to low temperature where the oxidation is negligible. The average thickness of the coating of tested specimens is higher than for the uncoated specimens studied earlier. This result shows the importance of measuring the coating thickness of all tested specimens.

The micrographs of tested specimens also show the presence of columnar grains in the coating composed of $\gamma'-(\text{Ni},\text{Co})_3(\text{Al},\text{Cr},\text{Ti})$, as determined by EDX quantitative chemical analyses which correspond to the phase diagrams [1]. The grains precipitated with an equally distanced distribution in the degenerated coating (Figure 4.5). The precipitation of nickel-rich phase such as γ' is expected in coatings exposed to high temperatures while the coating is depleted in aluminium due to the Al_2O_3 oxide scale formation and the nickel diffuse from the substrate to the coating.

Table 4.1 Evolution of the Metallurgical Parameters of DS René 80 during TF Testing.

Specimen Label	N_{final} (cycles)	l_{d^*} (μm)	l_{d^*} (μm)	l_{MC} (μm)	d_{γ} (μm)
VIRGIN	0	365	115 \pm 20	75 \pm 25	0.40 \pm 0.17
SRE	800	266	118	—	—
SRD _(*)	2140	515	130	—	0.60 \pm 0.30
SRA	2500	410	105	60 \pm 25	0.46 \pm 0.22 _a 0.78 \pm 0.64 _b 0.77 \pm 0.37 _c
SRB	2500	470	130	—	—
SRC	3000	340	110	—	—

Where:

N_{final} is the total number of thermal cycles carried out during TF testing;

l_{d^*} is the average arm spacing of the primary dendrites;

l_{d^*} is the average arm spacing of the secondary dendrites;

l_{MC} is the average length of needles that compose the MC carbides;

d_{γ} is the average size of the gamma prime precipitates.

* the hold time in the hot gas stream for this specimen was 2.6 times longer then for the other specimens.

a measured in the bulk part of the specimen.

b measured near the leading edge tip.

c measured near a crack tip.

4.1.2 Thermal Fatigue Cracking Damage

4.1.2.1 Crack Initiation

In order to identify the crack initiation mode, some thermal fatigue tests were interrupted few hundred thermal cycles after that crack initiation was detected by the ACPD technique (see Subsection 4.2). This corresponded to 200 and 800 cycles respectively for the SRN and SRE uncoated specimens, and to 435 and 780 cycles for the SRH and SRG coated specimens.

No evidence of subsurface or surface oxide-free cracks were found in both the coated and uncoated specimens. Some oxide spikes however were observed along the leading edge in the region which were exposed to the highest temperatures and stresses. Oxide spikes also initiated near major cracks in specimens exposed for up to 2500 thermal cycles.

In uncoated specimens, oxide spikes formed at the interdendritic zones (Figure 4.6a), or at the carbides surfaces were found to open at the surface or very close to it (Figure 4.6b), as found by Reger and Rémy [4]. Cauliflower-like oxide spikes were occasionally formed at microstructural heterogeneities similar to eutectic pools (Figure 4.6c). Table 4.2 summarizes the length, the position along the leading edge and the type of oxide spikes for all specimens.

In the particular case of the SRE specimen, the major oxide spike which seems to have growth from an interdendritic zone is rounded at the tip (see Figure 4.7). This spike could have been sharp at first which became blunted by lateral oxidation. In the SRN specimen, two sharp oxide spikes or oxidized small cracks (Figure 4.8) initiated

at the two corners of a machined notch of 0.3 mm deep and 0.5 mm wide. These spikes do not seem to be related to a specific microstructural element of the alloy.

Oxide spikes can be the result of preferential oxidation along fast diffusion paths such as interdendritic zones, or at carbide-matrix interfaces, as a result of thermally and stress activated processes. It could also have formed from microcracks initiated in the alloy as observed at the notch of the SRN specimen. If oxide spikes were the result of preferential oxidation, one could find spikes at about every of these microstructural heterogeneities. The micrographs show very few oxide spikes (see Table 4.2) relative to the number of interdendritic zones (9 zones/mm, see Table 4.1) and carbides along the leading edge surface. Based on this argument, the presence of oxide spikes result from the oxidation of microcracks initiated in fatigue rather than from the preferential oxidation of particular microstructural element of the alloy.

In the cases of the SRG and SRH specimens, the coating showed the presence of numerous finger-like oxide protuberances along the leading edge over the 25 mm wide area directly exposed to the hot gas stream (Figure 4.9). These oxide fingers did not completely penetrate the coating thickness and the morphology of the tips are not as sharp as those of some spikes observed in the uncoated specimen. Also, in two moderately hot but highly stressed zones symmetrically positioned about the axis of the hot gas stream (as indicated in Figure 5.21), the oxide fingers are close to one another and equally distributed with a spacing of about 40 μm . This spacing corresponds to that of the columnar grains, composed of γ' - Ni_3Al , which precipitated in the coating (Figure 4.5). This suggest that oxide fingers formation is the result of preferential oxidation of these sites. However, no oxide protuberances were found between the two highly stressed zones (Figure 4.5), where the temperature reaches a maximum. These observations clearly demonstrates that the oxide protrusions must result from the oxidation of the surfaces of fatigue microcracks initiated at the columnar grains of the

coating, where the stress is the highest.

In the SRF coated specimen, some cracks initiated in locally eroded zones or at crevasses (pitting), near the leading edge (Figure 4.10). This effect is similar to that observed for the case of the prenotched SRN specimen after 200 thermal cycles (Figure 4.8) and supports the conclusion that oxide spikes result from oxidation within the microcracks. The embrittling effect of oxygen diffusion into the matrix contributes to the facility of crack propagation.

These notch-like zones in the coated specimen come from local oxidation accelerated by spalling and erosion, resulting in a nonuniform erosion of the leading edge as opposed to the erosion observed in uncoated leading edges. Pitting of the substrate is the result of spalling of closely grouped oxide spikes in the coating, resulting in local elimination of the protective coating.

4.1.2.2 Crack Propagation

Major cracks (up to 2 mm) were found to form at the leading edge of the specimens exposed for up to 2500 thermal cycles. The micrographs shown in Figures 4.11 to 4.13 illustrate typical long cracks that can be observed in the uncoated and coated specimens. In all cases, transgranular cracks progressed through the primary dendrites and between the secondary arms of the dendrites, where brittle Chinese script type carbides are concentrated. This result is expected where the primary dendrites follow the edge direction and the secondary dendrites are normal to the surface. The highest thermal stresses are also found along the longitudinal axis of the specimens (refer to Subsection 5.2).

It should be noted that for the SRD specimen, the hold time in the hot gas stream was 6.5 minutes/cycle instead of 2.5 minutes/cycles for the other specimens, in order to determine the effect of time on the thermal fatigue response of the material. Contrary to the other cases, the crack progression in the SRD specimen seems to be less dependant on the microstructure which could indicate that the creep damage started to have an effect on the cracking mechanisms, due to the longer hold time in the hot gas.

Two mechanisms of crack propagation are proposed here. It can be noticed that all the crack tips are heavily oxidized because of the easy access of oxygen along the crack path. This is well illustrated in Figures 4.11b to 4.13b, where typical crack tips are shown. The presence of oxide products at the tips could suggest that the crack growth mechanism involves successive oxidation of the material and/or carbides ahead of the tip and cracking of the oxide scale. The crack tips could also progress because of the embrittling effect of the dissolution of oxygen and diffusion into the metal. Detailed observation of tips of secondary cracks in the SRA specimen and of tips of the principal cracks in the SRF specimen showed that the carbide-alloy interfaces are sometimes oxidized even if they apparently do not communicate with the crack tip, as illustrated in Figure 4.13b. This can be caused by the continuity of the carbides with the crack tip under the polished surface. This observation would indicate that preferential oxidation of interdendritic zones and of carbide-matrix interfaces is the first stage of the crack growth process. This is most likely because the solubility of oxygen in the alloy is increased with Titanium content (4.8wt%) which therefore increases the penetration of internal oxidation [62]. Assuming that the initiation of a short crack involves the same mechanisms as for the propagation of a long crack, the most plausible propagation mechanism consists of fatigue cracking of the crack tip zone embrittled by oxygen dissolution.

4.1.2.3 Length and Position of Cracks and Oxide Spikes

Tables 4.2 and 4.3 summarize the length and the position (z) of the oxide spikes and of the cracks along the leading edge. The lengths were measured from the micrographs obtained with an optical microscope or with an SEM, whereas the z positions were measured (± 0.01 mm) from polished sections of the specimen leading edge (cut #3, Figure 3.8) using a travelling microscope.

Table 4.2 Length and Position of Oxide Spikes in TF Specimens.

SPECIMEN LABEL	SPIKE NUMBER	SPIKE TYPE	z (± 0.01 mm)	a _s (μ m)
SRA	x	---	---	---
SRB	1	A	24.00	33
	2	A	25.39	28
	3	C	25.8	20
	4	B	53.6	27
	5	C	55.9	18
	6	C	58.05	18
	7	C	58.14	20
	8	C	58.24	25
SRC	1	A	33.46	80
	2	C	35.13	120
	3	C	37.00	120
	4	A	45.80	28
	5	B	48.46	105
SRD	1	B	29.7	88
	2	B	31.6	225
	3	B	32	240
SRE	1	A	40.4	15
	2	C	41.05	25
	3	A	53.25	60
SRF	*	---	---	---
SRG	n	D	24.43-57.73	≤ 45
SRH	n	D	31.50-57.45	≤ 30
SRN	*	---	---	---

In Table 4.2:

- a_s: is the oxide spike length (refer to Figure 2.15);
- z: is the spike position along the leading edge (refer to Figure 3.8);
- x: in these specimens, the complete number of oxide spikes is unknown

- because the micrograph is limited to a small area of the leading edge;
- *: the oxide spikes observed in these specimens are obviously the result of the oxidation of cracks initiated in notches at the leading edge (reported in table 4.3);
 - n: the spikes are too numerous to be reported in this table, only the range of their positions and their maximum length are indicated;
 - A: oxide spike, usually sharp, formed in an interdendritic zone (e.g., see Figure 4.6a);
 - B: oxide spike formed in a carbide (e.g., see Figure 4.6b);
 - C: cauliflower-like oxide spike formed in a microstructural heterogeneity like eutectic pools (e.g., see Figure 4.6c);
 - D: oxide fingers formed at the columnar grain in the coating (e.g., see Figure 4.9).

Table 4.3 Length and Position of Cracks in TF Specimens.

SPECIMEN LABEL	CRACK NUMBER	z (± 0.01 mm)	a (± 5 μ m)
SRA	1	34	635
	2	48.5	2270
SRB	1	56.78	1415
SRC	1	31.33	320
	2	32.32	1385
	3	34.08	505
	4	35.60	265
	5	52.10	295
	6	52.92	640
	7	56.31	855
	8	57.63	615
SRD	1	29	2080
	2	31	455
	3	33	1175
SRE	*	---	---
SRF	1	28.84	110
	2	29.08	400
	3	32.12	1310
	4	36.07	190
	5	36.45	240
	6	40.27	320
	7	42.22	1920
	8	49.02	1065
	9	50.35	700
	10	52.68	240
	11	54.04	130
	12	55.08	55
	13	55.22	65
SRG	*	---	---
SRH	*	---	---
SRN	1	50.33	210
	2	50.58	190

In Table 4.3:

- a: is the crack length;
- z: is the crack position along the leading edge (refer to Figure 3.8);
- *: no major crack was observed in these specimens, only oxide spikes (reported in table 4.2).

4.1.3 Oxidation Damage

4.1.3.1 Uncoated Specimens

The morphology and the nature of the oxides formed at the surface vary with the temperature, stress and strain of the substrate along the leading edge. Three types of zones are identified from the photographs of bare specimens (Figure 4.14): (i) the protective oxidation zones observed on the areas of the specimen not exposed to the hot gases (labelled A), where the temperature and the strain of the substrate are relatively low, (ii) the spalled oxide zone directly exposed to the hot gases (labelled C), where the temperature and the strain are relatively high, and (iii) the transition zones or non-protective oxidation zones (labelled B) where the temperature and the strain are intermediate. A more detailed metallographic analysis of the different zones along the leading edge of specimens is given below.

In the protective oxidation zones (Figure 4.15), the continuous external oxide scale, normally composed of an external layer of Cr_2O_3 and a sub-layer of Al_2O_3 is compact, continuous and adherent to the substrate. These results are in agreement with a study on the oxidation of DSR80 [66, 95, 96] as well as with EDX quantitative chemical analyses on DEW specimens. The absence of microcracks or decohesion combined with the low vacancy concentration^(*) in the Al and Cr rich oxide scale prevent oxygen or cation diffusion. As a result, the oxidation rate of the alloy is very slow as reflected by the thin oxide scale, even after long exposure time to the gas

* One important mechanism of diffusion in oxide scales involves oxygen and cations vacancies. In strongly stoichiometric oxides such as for Al_2O_3 or Cr_2O_3 , the vacancy concentration and the diffusivity of species are very low.

combustion products (10 μm , after 2500 thermal cycles equivalent to 100 hrs at high temperature).

The substrate near the oxide-alloy interface is depleted in Cr and Al due to the formation of the Cr_2O_3 - Al_2O_3 oxide scale. When cracking or spalling of the protective scale occurs, the nickel-rich substrate surface will oxidize at a drastic rate because the new nickel-rich oxide layer formed is usually porous and contains a high vacancy concentration, both of which promote fast diffusion of oxygen and cations. The nickel-rich oxide layer is thus non-protective compared to the Cr_2O_3 - Al_2O_3 oxide scale.

This non-protective nickel-rich oxide layer composed of a mixture of NiO , NiCr_2O_4 and NiAl_2O_4 [97] is formed in the transition zones (Figure 4.16) where the thermal expansion and contraction of the substrate caused cracking and spalling of the brittle Cr_2O_3 - Al_2O_3 protective oxide scale initially formed during the first thermal cycles. The Ni oxide layer beneath the cracked internal oxide scale has a non uniform thickness and is sometimes discontinuous. It becomes continuous and uniform where the protective oxide scale completely spalled off. The Ni oxide scale reaches a maximum thickness of 50 μm after 2500 thermal cycles (equivalent to 100 hrs at high temperature).

In the central zone directly exposed to the hot gas stream (Figure 4.17), both the temperature and the deformation of the substrate at the leading edge are high. The Ni oxide scale frequently spalls off due to the repetitive compressive stress in the scale caused by the contraction of the substrate during cooling [75]. The alloy in this zone is drastically but uniformly consumed, as illustrated in Figure 4.14. A 1.7 mm loss of material at the leading edge of the double-edge wedge SRA and SRB specimens was observed after exposure to an average of 2500 short thermal cycles. This was particularly true in the case of the SRC and SRD specimens, exposed to the hot gas stream for a longer time, which respectively lost 2.1 and 2.3 mm of width instead of

1.7 mm for the other specimens. The SRC specimen was tested during 3000 short cycles and the SRD specimen was subjected to 2140 long cycles. Figure 4.18 gives the material loss profile at the leading edge of SRC and SRD specimens, as measured with a travelling microscope ($\pm 0.5 \mu\text{m}$). The profiles have quite similar shapes and only differ by 0.2 mm at the centre.

4.1.3.2 Coated Specimens

Photographs of the SRF coated specimen exposed for 2500 thermal cycles in the burner rig are shown in Figure 4.19. The coating at the leading and trailing edges was completely destroyed by cyclic oxidation in the zone directly exposed to the hot gas stream, leading to the substrate pitting and an irregular erosion of the edges, contrary to the edge erosion of bare specimens. Elsewhere, the coating integrity did not result in severe deterioration from the cyclic oxidation. Suggested mechanisms of coating degradation and subsequent substrate pitting are presented on the basis of the metallographic analysis of different zones along the leading edge.

In Codep B-1 coated specimens, the hyperstoichiometric $\beta\text{-NiAl}$ (high Al activity) coating promotes the formation of a protective Al_2O_3 oxide scale [91]. A TEM study on isothermal oxidation of a Al-rich aluminide coating on René 80 revealed that the oxide scale may also contain NiAl_2O_4 and NiCr_2O_4 spinels and NiO oxide at some locations which can enhance the oxidation kinetics [98]. However, after up to 780 thermal cycles, the coating in the regions of the specimen not directly exposed to the hot gas stream showed a good resistance to oxidation. This means that the oxide scale is composed mainly of Al_2O_3 , as confirmed by EDX quantitative chemical analyses of the DEW specimens. In the region exposed to the hot gas stream where the temperature and the stress are high, the oxide scale was not protective. In two particular zones

symmetrically positioned about the axis of the hot region, the coating was completely perforated by finger-like oxide protuberances as shown in Figure 4.9, while in the middle of the region, the coating was partially consumed (Figure 4.5). The oxide fingers are believed to be the result of preferential oxidation of the cracked nickel-rich columnar phase γ' -Ni₃Al precipitated in the coating during thermal cycling, whereas the irregular oxidation of the coating seems to be caused by successive growth and spalling of the Al₂O₃ oxide scale. It is expected that, after many cycles of Al₂O₃ scale growth and spalling, the coating is depleted of its Al content. The subsequent oxide composition will most likely be composed of a mixture of NiO, NiCr₂O₄, NiAl₂O₄ oxides and islands of Al₂O₃ oxide, as predicted by Barrett and Lowell [97].

4.1.4 Comparison of the Results to Airfoil Damage Occuring in Other Burner Rigs and in Real Engines

Thermal fatigue and cyclic oxidation damages obtained in the burner rig (BR) as described in the two last subsections are very similar to results obtained in other BR studies and in real engines. Glennly [99], for instance, reported the transverse thermal fatigue cracks of few millimetres at the leading edge of blades of J47 and J33 engines, similar to the bare specimens tested in the BR. The irregular nature of the leading edge of coated specimens tested in the BR was also observed in real coated CF6-50 blades tested in a BR by Mom and Boogers [100]. Patnaik et al. [83] also show the same type of thermal fatigue damage for bare and coated DSR80 blades exposed to real service conditions as well as significant material losses at the LE resulting from severe cyclic oxidation as for specimens tested in the BR.

This clearly demonstrates that the BR system closely simulates service conditions, and can be a convenient laboratory tool for studying thermal fatigue and cyclic oxidation behaviour of blades and vanes in aeroengines.

4.1.5 Conclusions

The microstructure of virgin specimens has been characterized by metallographic analysis and shows that:

- 1° The primary and secondary dendrite arms spacing are 365 and 115 μm respectively.
- 2° The Chinese script MC carbides are concentrated mainly between the primary dendrites, and are composed of agglomeration of needles with an average size of $75 \pm 25 \mu\text{m}$.
- 3° The gamma prime precipitates (γ') have a cuboid shape with an average size of $0.40 \pm 0.17 \mu\text{m}$.
- 4° The Codep B-1 coating thickness varies from 27 to 40 μm while the interdiffusion zone between the substrate and the coating is $16 \pm 1 \mu\text{m}$ thick.

A metallographic study was also conducted on uncoated and coated specimens after testing in the burner rig. The results are summarized as follows:

- 1° No change in microstructure attributed to thermal cycling was noted except for the γ' precipitates which coarsened. This was especially notable in specimen regions where the temperature and the stresses are very high. In some particular regions, the γ' also elongated (γ' rafting) due to the effect of the principal stress in the longitudinal direction of the

specimen.

- 2° Oxide spikes are observed along the leading edge of uncoated specimens after 800 thermal cycles while in coated specimens, some finger-like oxide protuberances penetrated the coating after 780 cycles. A higher density of oxide spikes and fingers are present where the temperature is high and where the stresses are the highest. Oxide spikes result from oxidation of fatigue microcracks which are preferentially initiated in interdendritic regions and at carbide-matrix interfaces. Oxide fingers also formed from fatigue microcracks initiated in nickel-rich aluminide phases precipitated in the coating.
- 3° Major cracks formed at the leading edges of uncoated and coated specimens exposed up to 2500 thermal cycles, where the temperature is high and where the principal stress is the highest. The cracks progressed transgranularly through the primary dendrites and between the secondary dendrites where brittle Chinese script type carbides are segregated. Crack growth mechanism is not well understood, but is believed to progress by successive embrittlement of the matrix, due to oxygen diffusion in the interdendritic regions, and at carbide-matrix interfaces, resulting in cracking of the embrittled zone.
- 4° Important oxidation damage also occurred along the leading edge of tested specimens. In the case of uncoated specimens, the nature and the morphology of the oxides varied according to the temperature, the stress and strain levels. In the areas of the specimen not exposed to the hot combustion gases, where the working temperature and the thermal expansion are relatively low, a protective $\text{Cr}_2\text{O}_3\text{-Al}_2\text{O}_3$ oxide scale is

formed. In areas where the temperature and the thermal expansion are intermediate, the protective oxide scale was found to crack or to spall off. A nickel-rich non-protective oxide scale was then formed, leading to an accelerated substrate consumption. In the area exposed directly to the hot gases, where the temperature and the thermal expansion are high, the oxide layers spall off, resulting in a drastic consumption rate of the substrate. After 2500-3000 thermal cycles, 1.7 to 2.3 millimetres of material are lost at the leading edge.

- 5° In the case of coated specimens, compact and adherent Al_2O_3 oxide scale formed at the surface providing a good resistance to substrate consumption except where the coating was penetrated by oxide fingers at grain boundaries and/or by cyclic oxidation. These locations are usually highly stressed when exposed to extreme temperatures. The formation of oxide fingers and the repeated oxide scale spalling resulted in local destruction of the coating over few millimetres and pitting of the substrate. These pits act as stress concentrators and can initiate small cracks at their roots as observed in a prenotched bare specimen exposed to only 200 cycles.
- 6° Thermal fatigue and cyclic oxidation damage at the leading edge of bare and coated specimens in the burner rig were found to be very similar to that observed at the LE of airfoils in real aeroengines. The burner rig was successfully operated to closely simulate service conditions.

4.2 On-line Crack Growth Assessment

During thermal fatigue testing in the burner rig, crack initiation and growth was monitored in-situ by measuring the change in potential drop (PD) associated with the increase of current path length arising from the formation of these cracks. The complete description of the ACPD technique as well as the crack growth monitor set-up employed for each thermal fatigue test were presented in Subsection 3.1.3. This subsection presents the PD evolution obtained during testing and discusses how the life to crack initiation and the crack growth rates can be determined from these measurements.

4.2.1 Potential Drop Evolution

Figure 4.20 shows the evolution of the potential drop during one thermal cycle, superimposed on the specimen temperature evolution. During heating, the potential drop reaches a maximum, decreases and stabilizes to a constant value as the temperature of the specimen reaches the steady state. After heating, the specimen is cooled and the potential drop rapidly rises to a maximum and then slowly decreases. This behaviour can be explained in terms of the relation between the impedance of the specimen and its temperature. The impedance is a function of the geometry, which can be affected by the thermal expansion of the specimen, and of the electrical resistivity of the material which varies significantly over the range of temperature covered during a thermal cycle (from 25 to 1100°C). Figure 4.21 shows how this property changes with temperature for a typical nickel-based superalloy (Udimet 700, [78]). It should be noted that the resistivity reaches a maximum at approximately 845°C for this alloy. The potential drop during heating and cooling of the specimen was simulated using the change in specimen temperature as the input variable. These simulated PD changes were compared to measured changes (shown in Figure 4.20) during the heating and cooling portions of the

thermal cycle. The similarity between calculated and measured quantities indicates that the electrical resistivity variations are responsible for the change in potential drop during thermal cycling. In particular, the presence of PD maxima during heating and cooling was predicted only by considering the electrical resistivity. Meanwhile, the thermal expansion of the specimen does not induce significant changes in the resistance of the specimen and can not explain the observed PD maxima. During the steady stage of the PD evolution, small variations can still be noticed that correspond to temperature deviations in the hot gas stream, relative to its average value. A positive temperature deviation is associated with a negative potential deviation and vice-versa which is consistent with the temperature dependence of the electrical resistivity at constant RMS current.

The nearly constant plateau value in the potential drop curve provides the best indication of the changes in ACPD signal, cycle after cycle, as demonstrated in Reference [101]. The average values of the PD plateau were taken from the measured data, for each thermal cycle, using a program written in Basic (the listing of this program is given in Appendix E). Figures 4.22-4.26 show the plateau values for the leading edge probes plotted against the number of applied thermal cycles. The PD-N plot of Figure 4.22 gives a typical PD evolution during TF testing. During the first 100 cycles, the PD decreases and then stabilizes. This is associated with the stabilization of the shape of the specimen and of its electrical properties. After about 700-800 cycles, a sudden change in the slope of the PD curves was observed which corresponds to crack initiation. The gradual increase in potential drop beyond crack initiation is associated with crack growth. For the SRA and SRD specimens, (Figures 4.22 and 4.23), the slopes associated with crack growth rates were positive from the initiation to the end of the test. For the other specimens (SRB, SRC and SRF tests, Figures 4.24-4.26), the PD increased suddenly after about 700 cycles and stabilizes for the remainder of the test. The PD plateaus after crack initiation are indicative of the slow-down of the crack

growth or crack arrest. Crack arrest is a consequence of stress release associated with crack propagation and/or crack tip blunting due to oxidation and erosion.

Some periodic discontinuities were noted for all PD-N curves, especially during the SRC, SRD and SRF tests, for which the CGM5 set-up was more sensitive. These discontinuities correspond exactly to the daily starting and stopping of a thermal fatigue test procedure. Between the discontinuities, the PD generally decreased at the beginning of the day to eventually stabilize before the end of the day. This could be explained by the stabilization of the specimen temperature and its associated electrical resistivity and/or by the stabilization of the electronics of the CGM5 system (i.e. amplifier temperature changes, relays reliability). Further investigations are undertaken to explain this phenomenon.

However, due to the periodic discontinuities, the PD signal can be considered to occur as a band instead of a line which reduces the accuracy of the determination of life to crack initiation and crack growth rate. A linear regression technique was employed to determine the PD-intercept, b , the slope, m , and the standard deviation, STD, of each linear segment of the PD-N curves. The parallel straight lines in Figures 4.22-4.26 represent the positive and negative standard deviations from the linear regression of the segments of the PD-N plot. The different slopes are also indicated by m_i , with $i = 0$ for the quasi-plateau PD evolution, and $i = 1$ and 2 for the first and the second slopes of the PD-N curve associated with different crack growth rates.

4.2.2 Crack Initiation

The life to initiation (or number of cycles to initiation, N_i) can be estimated for each specimen by finding the intersection of the plateau and the first sudden important change in the slope of the curves (e.g. the straight lines 0 and 1 in Figures 4.22–4.26). Because of scatter in the PD signal, N_i is given by the projection of the intersection of two bands as illustrated in Figures 4.22–4.26. N_i is given in terms of b , m and STD values for the straight lines 0 and 1 obtained by linear regression:

$$N_i = \frac{b_0 - b_1}{m_1 - m_0} \pm \left| \frac{STD_0 + STD_1}{m_1 - m_0} \right| \quad (88)$$

The measured N_i are given in Table 4.4 for all the tests. The uncertainty can be as low as ± 4 cycles when the sudden crack growth rate sharply contrasts with the stable PD plateau before cracking. N_i presents an average value of 760 ± 20 cycles for the uncoated specimens exposed to the hot gas stream for 2.5 minutes/cycle, a result which does not differ significantly from the SRD specimen exposed for a longer time to the hot gas jet. Only one test has been performed with longer hold time at high temperature but it seems at first that this parameter does not significantly affect N_i , for the hold time range experienced in this study. This result could suggest that extra oxidation and/or creep damages do not strongly influence the crack initiation process for the range of hold time experienced during this test.

Compared to uncoated specimens, life to crack initiation of coated specimens was reduced to 300 ± 100 cycles. This lower life is associated to oxide fingers which formed earlier at the coating grain boundaries rather than the oxide spikes, in the interdendritic regions of bare material. Since the oxide protuberances (spikes or fingers) can be considered as oxidized microcracks (refer to Subsection 4.1.2.1), it is concluded

that the coating induces premature cracking. However, the crack growth evolution in uncoated and coated specimens have to be compared before the coating can be judged to be detrimental to the fatigue behaviour of the material.

4.2.3 Crack Growth Rate

The crack growth rate can be determined from the PD-N curves (Figures 4.22-4.26), by assuming a correlation between crack length and PD. Attempts to calibrate the PD against crack length were made using an artificially induced crack in the leading edge of the test specimen and measuring the PD across the leading edge for increasing length of the crack. The crack was produced by EDM or by using an ultra fine diamond saw. The measurements were made between increments of crack extension, in a furnace set at the test temperature. Difficulties were encountered because of the need to reconnect the ACPD probes to the specimen for crack extension and because of the large scatter in PD output arising from probe manipulation. It was found that simply moving the probes would give rise to changes in PD signal that were larger than the quantities being measured, indicative of the high sensitivity of the technique. Since it was not possible to calibrate the PD against crack length outside of the burner rig test environment, an alternative approach was taken. The ACPD technique provides the number of cycles to crack initiation and a qualitative idea of the crack growth evolution in the burner rig and the metallographic analysis provides the final crack length (Subsection 4.1.2). This information can be used to estimate the crack growth rate.

The relation between the PD response and the crack growth should first be examined in detail. This is particularly important when dealing with a multi-cracking situation as was observed in the SRA, SRC, SRD and SRF specimens. It is recognized that the ΔPD associated with several adjacent cracks depends on the spacing between

cracks relative to the skin depth [85]. When the crack spacing is larger than the skin depth, the ΔPD is proportional to the linear summation of each crack length Δa_k , as given by:

$$\Delta PD \approx \sum_k c_k \cdot \Delta a_k \quad (89)$$

where, c_k is the proportionality constant, characteristic of the crack growth sensitivities of the ACPD system. When crack spacing is less than the skin depth, the ΔPD is proportional to the length of the largest crack, Δa_{\max} , of each group "g" of adjacent cracks and the ΔPD is given by:

$$\Delta PD \approx \sum_g c_g \cdot \Delta a_{\max g} \quad (90)$$

Here, c_g is another proportionality constant. Each crack has its constant as the sensitivity of the technique varies with the crack position along the leading edge. For a non-magnetic material and for the frequency used in the present study, the skin depth is of the order of a millimetre (see Subsection 3.3.2). In the SRA and SRD specimens, two cracks formed with a spacing of 4 and 15 mm respectively, and where the second crack should be picked up by the PD signal. In both cases, the PD-N plots (Figures 4.22 and 4.23) show two different slopes after initiation, which intersect at $N = 1300 \pm 200$ cycles. The first slope is believed to be associated with the crack growth rate of the major crack while the second slope is believed to be the summation of the crack growth rate of the two cracks. The constant c_1 given by Equation 89 or the $\Delta PD_1/\Delta a_1$ ratio for the major crack is estimated to be $5.4 \pm 0.2 \mu V/\mu m$, for the SRA test, and $28 \pm 3 \mu V/\mu m$, for the SRD test. The sensitivity of the CGM5 system is about 5 times greater in the latter case because the gain was tripled and the current doubled. The constant c_2 associated to the second crack is estimated to be $7 \pm 4 \mu V/\mu m$ and $30 \pm 7 \mu V/\mu m$ for the SRA and SRD tests, respectively. It is interesting to note that in

both cases, c_1 and c_2 have similar values while the two cracks are not at the same position along the leading edge. The position range of the cracks seems to have no effect on the sensitivity of the technique.

The growth of each crack was found to vary linearly from the time of crack initiation for the SRA and the SRD tests, as measured with the ACPD technique (Figures 4.22 and 4.23). The crack growth rate $(da/dN)_m$ can therefore be approximated by:

$$\left(\frac{da}{dN}\right)_m \approx \frac{\Delta a}{\Delta N} = \frac{(a_{final} - a_i)}{(N_{final} - N_i)} \quad (91)$$

where a_i and a_{final} are the initial and the final crack lengths and N_i and N_{final} are the number of cycles at the time of crack initiation and at the end of the test. Assuming the crack length a_i to be negligible compared to a_{final} , the value of the final crack length (a_{final}) and the life to initiation can be used to determine the crack growth rates. The rates were estimated to be $1.25 \pm 0.05 \mu\text{m/cycle}$ for the major crack and $0.5 \pm 0.1 \mu\text{m/cycle}$ for the second crack in the SRA specimen, and $1.4 \pm 0.2 \mu\text{m/cycle}$ and $1.4 \pm 0.4 \mu\text{m/cycle}$, respectively for the cracks in the SRD specimen. In these specimens, the crack initiation and growth rates for both cracks are very similar.

For the SRB, SRC and SRF tests, the results are more difficult to interpret. The crack suddenly propagated after initiation and then stopped for the duration of the test (see PD plateaus in Figures 4.24 and 4.25). The initial crack growth rate can not be accurately estimated in this case, because the crack length just before crack arrest is not known. It cannot be approximated by the crack length at the end of the test (a_{final}) because erosion of the leading edge during crack arrest causes a reduction in crack length. This erosion effect is demonstrated in Figure 4.24 (SRB test) where the PD can be seen to decrease after it has stabilized. The sudden crack growth rate can be

estimated by converting the slopes in PD-N plots in term of $\mu\text{m}/\text{cycle}$, using the constant of proportionality c_1 . The constant c_1 determined from the SRA test can be used in the rate calculations for the SRB test and the constant determined from the SRD test can be used in the rate calculations for the SRC and SRF tests because the gain and the current settings and their associated ACPD sensitivities to crack growth are respectively the same. Even if the crack position along the leading edge between specimens does not correspond perfectly, the sensitivity to crack growth is assumed similar, as demonstrated for the cracks growth in the cases of the SRA and SRD specimens.

In the SRB specimen (Figure 4.24), the PD measured from crack initiation to crack arrest showed two slopes intercepting at $N = 1090 \pm 40$ cycles. It is not clear if this discontinuity corresponds to the initiation of another crack or simply to a change in the crack growth rate of the major crack. After testing, only one crack was found but it does not prove that a second one did not initiate during testing because the erosion could remove all evidence of a small crack. However, assuming that the ΔPD is the result of the major crack only and using the constant c_1 determined from the SRA test, the crack growth rate is evaluated to be $1.75 \pm 0.07 \mu\text{m}/\text{cycle}$ from around the 760th to the 1090th cycle and $4.9 \pm 0.2 \mu\text{m}/\text{cycle}$ from the 1090th to the 1240th cycle, when crack propagation came to rest.

In the SRC specimen, the crack growth rate is more difficult to determine due to the presence of eight cracks, arranged into two groups at the leading edge (Figure 4.14). The spacing between the cracks within each group was approximately 1 mm, corresponding to the size of the skin depth. In this situation, the ΔPD falls between the value given by Equation 89 considering the additive effect of the eight cracks, and the value resulting from the combined effect of the largest crack of each group of cracks, as expressed by Equation 90. Using these equations, the measured crack lengths, the constant c_1 determined from the SRD test, and assuming that all the

cracks initiated at the same time, the crack growth rate can be expected to be in the range from 30 to 60 $\mu\text{m}/\text{cycle}$. If it is assumed that the sharp change in PD shown in Figure 4.25, is the result of the propagation of the major crack only (most probable case), the crack growth rate in this case is about 100 $\mu\text{m}/\text{cycle}$. Considering the numerous possibilities, the growth rate can not be reasonably evaluated in this case.

For the coated SRF specimen, the establishment of the crack growth rate is even more difficult than in the preceding case because of the presence of thirteen cracks along the leading edge that include three major cracks of 1 to 2 mm (Table 4.3). However, the initial crack growth rate associated to the first PD increment after the PD plateau, see Figure 4.26, possibly vary from 0.6 to 2.5 $\mu\text{m}/\text{cycle}$, using both Equations 89 and 90. The PD-N plot of Figure 4.26 also indicates a sudden crack growth, after about 740 cycles, followed by crack arrest, as during the SRC test. This very high growth rate is estimated to be between 60 and 200 $\mu\text{m}/\text{cycle}$, using again the same two equations.

Table 4.4 summarizes the initial crack growth rate as measured by the ACPD technique for major cracks in all specimens. These measured rates, $(da/dN)_m$, correspond to the combined effect of crack tip advance caused by thermal fatigue, $(da/dN)_{tf}$, and crack shortening as a result of leading edge erosion, $(da/dN)_e$, and are given by:

$$\left(\frac{da}{dN}\right)_m = \left(\frac{da}{dN}\right)_{tf} - \left(\frac{da}{dN}\right)_e \quad (92)$$

The crack tip advance rate, $(da/dN)_{tf}$, can be deduced if the erosion rate is determined and the crack growth rate is measured. The average erosion rate near major cracks was estimated to be $0.5 \pm 0.1 \mu\text{m}/\text{cycle}$ in the SRA, SRB and SRC specimens, and $0.9 \pm 0.1 \mu\text{m}/\text{cycle}$ in the SRD specimen. The erosion rate was assumed constant from the beginning to the end of thermal fatigue tests, as confirmed by the alloy surface recession at the leading edge of the DEW specimens, presented in Subsection 5.4.

The initial crack growth rates associated with thermal fatigue are presented in Table 4.4. This rate varies from 1.8 to 2.3 $\mu\text{m}/\text{cycle}$ in the SRA, SRB, and SRD specimens, but it can be as high as 30 to 100 $\mu\text{m}/\text{cycles}$ in the SRC specimen. Such a fast crack propagation was observed after a very slow initial rate varying from 1 to 3 in the coated SRF specimen. Even if crack initiation started earlier in the coated specimens, the SRF test seems to demonstrate that rapid crack propagation is not enhanced by applying a coating. Nevertheless, much more thermal fatigue tests are required to confirm this observation.

Except for the SRC case, the dispersion of the initial crack growth rates is very small. However, this can be explained by the fact that the crack did not initiate at the same location along the leading edge from one specimen to another because of the uneven carbide distribution and their difference in shape, for instance. Consequently, the cracks were not subjected to the same thermal and stress-strain history. Further work is required to improve the ACPD technique and understanding of the results, especially for multi-sites cracking. A numerical simulation of the PD signal and the crack growth rate, using FEM, would contribute to the understanding of this phenomenon.

4.2.4 Resolution of the Technique

The spatial resolution, a_i , of the ACPD technique can be defined as the length of the smallest crack that can be detected. Crack detection occurs with the change of slope when the PD deviates from the stable PD plateau. The PD scatter during the initial plateau limit the spatial resolution. A crack which initiates near the lowest values of the signal is detected only when PD measurement reaches the upper values of the signal. In such case, a conservative estimation of a_i can be calculated with the following equation:

$$a_i = \frac{2 \text{STD}_0}{c_k} \quad (93)$$

where STD_0 is the standard deviation of the PD signal during the initial stage from a linear evolution, and c_k is a constant of proportionality between the PD and the crack length as defined in Equation 89. Using Equation 93 with the values of the constant c_k determined previously and with STD_0 obtained from the linear regression of the PD-N data, the spatial resolution is estimated to be $200 \pm 10 \mu\text{m}$ for the SRA test and $260 \pm 30 \mu\text{m}$ for the SRD test. The CGM5 set-up was more sensitive in the last case but the resolution was worse because the PD signal scatter was larger for the case of the SRD test.

Table 4.4 Thermal Fatigue Results.

UNCOATED SPECIMENS							
TEST NAME	N_i	$\left(\frac{da}{dN}\right)_m$	$\left(\frac{da}{dN}\right)_e$	$\left(\frac{da}{dN}\right)_{tr}$	N_a	N_{final}	a_{final}
SRA	770±80	1.25±0.05	0.5±0.1	1.8±0.2	—	2587	2270
SRB	760±5	1.75±0.07	0.5±0.1	2.3±0.2	1240±2	2500	1415
SRC	762±4	30-100	0.5±0.1	30-100	1200±100	3000	1385
SRD ^(*)	600±200	1.4±0.2	0.9±0.1	2.3±0.3	—	2140	2080
SRE	756±7	—	—	—	—	800	60
COATED SPECIMENS							
TEST NAME	N_i	$\left(\frac{da}{dN}\right)_m$	$\left(\frac{da}{dN}\right)_e$	$\left(\frac{da}{dN}\right)_{tr}$	N_a	N_{final}	a_{final}
SRF	440±70	0.6-2.5	0.3±0.1	1-3	750±2	2500	1920
SRG	160±10	—	—	—	—	780	45
SRH	260±5	—	—	—	—	435	30

Where:

- N_i is the number of cycles to crack initiation;
 $(da/dN)_m$ is the apparent crack growth rate derived from the PD measurements (in $\mu\text{m}/\text{cycle}$);
 $(da/dN)_e$ is the erosion rate at the leading edge (in $\mu\text{m}/\text{cycle}$);
 $(da/dN)_{tr}$ is the crack tip advance rate associated with thermal fatigue (in $\mu\text{m}/\text{cycle}$);
 N_a is the number of cycles to crack arrest;
 N_{final} is the total number of cycles carried out for each thermal fatigue test;
 a_{final} is the crack length in microns measured ($\pm 5 \mu\text{m}$) at the end of a thermal fatigue test.
 * During this test, the hold time in the hot gas jet was 2.6 times longer than during the other tests.

4.2.5 Conclusions

- 1° The initiation and subsequent crack growth were successfully monitored on-line during the thermal fatigue tests carried out in the burner rig, using the CGM5 crack growth monitor with potential drop probes attached to the leading and trailing edges of the DEW specimens. The ACPD technique allowed life to crack initiation (N_i) to be determined with an accuracy of ± 5 cycles in the best cases. N_i presented an average value of 760 ± 20 cycles for uncoated specimens exposed 2.5 minutes/cycles to the hot gas stream. In the case where the hold time in the hot gas jet was 6.5 minutes/cycles, N_i was found to be 600 ± 200 cycles. This result could indicate that crack initiation is not significantly affected by cyclic oxidation, erosion or creep. Compared to uncoated specimens, life to crack initiation of coated specimens was reduced to 300 ± 100 cycles.
- 2° The ACPD technique also allowed to evaluate a mean crack growth rate during TF testings. After correction for metal loss due to erosion, initial crack growth rate was estimated to be about $2 \mu\text{m}/\text{cycle}$ in uncoated and coated specimens, excepted in one uncoated specimen where the rate ranged from 30 to $100 \mu\text{m}/\text{cycle}$ after initiation.
- 3° The scatter of the potential drop values measured during thermal fatigue testing limits the spatial resolution of crack detection to about $200 \mu\text{m}$.

5. THERMO-MECHANICAL ANALYSIS AND DAMAGE MODELING

This Section is concerned with the numerical simulation of the thermal fatigue in turbine airfoils tested in the burner rig, which consists of modeling the fatigue and oxidation damage accumulation and the predicting of the life to crack initiation. This task required the computation of the temperature and the stress-strain evolution of each grid element of the specimen. The thermal and mechanical analyses are first presented, followed by the fatigue and oxidation damage accumulation and life prediction.

5.1 Thermal Analysis

The objective of the thermal analysis is to determine the temperature distribution of the specimen thermally cycled in the burner rig, using measurements and computation techniques. Temperatures were measured with thermocouples and optical pyrometry whenever possible. Unfortunately, it is not possible to measure the temperature at every locations on the surface of the specimen nor within the specimen at any time during thermal cycling. The unknown temperatures have then to be computed using a finite element (FE) code which takes into account the heat fluxes at the surface of the specimen and within the specimen. A special attention is brought to the determination of the parameters of the heat fluxes equations which are, for someones, very difficult to get [102], especially the convective heat transfer coefficients that had to be determined from measurements and from complex thermal analysis. The present subsection presents the measurement results and the computed results, and compares the specimen temperatures obtained from both approaches.

5.1.1 Temperature Measurements

Two techniques were adopted to determine surface temperatures. First, thin-wire sheathed thermocouples (diameter = 0.5 mm) were used to measure the internal temperatures of a thin wall (thickness = 2 mm) shell-like specimen of the same external shape and dimensions as those of the DEW specimen. The surface temperatures at the leading edge were obtained from measurements of temperature gradients within the wall thickness of the shell-like specimen. It was not possible to measure surface temperatures directly by spot-welding thermocouples to the external surface of the specimen because the surface thermocouples would be exposed to the hot-gas stream. Conduction along the thermocouple wires and sheath would result in the measurement of higher values.

Optical pyrometry was also used to measure surface temperatures at other than leading edge locations, and in greater detail than was possible with thin-wire thermocouples in the shell-like specimen. Neither leading edge nor trailing edge temperatures could be measured by optical pyrometry since this required that the pyrometer be located in the axis of the hot gas stream, which was obviously not possible.

For tests involving thin-wire thermocouples measurements, the hot gas stream temperature (T/C) was set over the range from 800°C to 1200°C, whereas for tests involving optical pyrometry, the gas temperature was set at 1300°C. The thermocouples measurements were not done for a gas temperature set at 1300°C because this temperature was not considered in the thermal fatigue program at that time.

5.1.1.1 Thin-wire Thermocouple Measurements (T/C = 800-1200°C)

Details of the instrumentation of a shell-like specimen with thin-wire thermocouples are given in Subsection 3.2.1. Eleven thermocouples were spot-welded to the bottoms of small holes into the walls of the specimen, such that the thermocouple beads were located about 0.5 mm from the specimen external surface. The locations are identified in Figure 3.6 as positions 1 to 11, with positions 3, 7 and 10 in the mid-section of the specimen corresponding to the axis of the gas stream. Another two thermocouples were spot-welded to the inside surface of the shell-like specimen, as close as possible to positions 3 and 7.

A polished section (see Figure 3.7) through the leading edge thermocouple located at position 7 shows that the thermocouple junction is located about 0.5 mm from the leading edge. Once all thermocouples had been spot-welded in place, the cavity

within the shell specimen was filled with plaster of Paris to ensure that the thermocouples would not become dislodged during testing.

Wall temperatures of the shell-like specimen are shown in Table 5.1, as a function of the gas temperature. The highest temperatures recorded are associated with positions 7, 3 and 10, along the axis of the gas stream, and are shown in Figure 5.1. The hottest region of the specimen is located at the leading edge. It takes about 60 seconds for the slower heating portion of the specimen to reach a constant temperature. It should also be noted that the specimen temperatures are from 150 to 250°C below the gas temperature depending on location, for a gas temperature of 1225°C, because of radiation heat losses from the specimen to its surroundings.

The surface temperatures were determined from internally welded thermocouple measurements, by calculating the temperature gradients through the thickness of the wall. This was done by considering heat conduction through the wall of the specimen and into the plaster inside the shell-like specimen. The diagram shown in Figure 5.2 models the positions of thermocouples at locations 7 and 13 in the longitudinal plane of the specimen, at the leading edge.

Table 5.1 Specimen Temperatures Measured by Thermocouples Th_i During Steady-state as a Function of Gas Temperature T/C (see Figure 3.6 for location of thermocouples).

T/C (°C)	Th_1 (°C)	Th_2 (°C)	Th_3 (°C)	Th_4 (°C)	Th_5 (°C)	Th_6 (°C)	Th_7 (°C)	Th_8 (°C)	Th_9 (°C)	Th_{10} (°C)	Th_{11} (°C)	Th_{12} (°C)	Th_{13} (°C)
1200	714	978	992	935	699	1055	1058	1010	964	1002	935	1008	1034
1100	656	908	918	861	631	972	975	922	891	929	854	934	959
1000	594	835	848	789	572	887	891	836	815	853	781	860	882
900	531	759	773	717	520	802	809	755	736	778	710	785	807
800	474	684	703	651	465	721	731	684	662	705	644	714	734

Because of the symmetric nature of the hot gas stream at positions 7 and 13 and the planar symmetry of the DEW specimen, the heat flux by conduction in and out of the plane of the Figure 5.2, as well as in the longitudinal direction parallel to the leading edge, may be neglected, relative to that across the wall of the specimen. For this unidirectional heat flow condition, the heat flux through the metal must be the same as that through the plaster, and under steady state conditions, is constant. Since the difference in steady state temperatures measured at positions 7 and 13 is small, the thermal conductivity of both the metal and plaster may be assumed to remain constant over the range of distances considered in Figure 5.2. It follows that the gradients within both the metal and the ceramic can be assumed to be linear, as shown in the Figure. Assuming further that the readings from thermocouples at positions 7 and 13 in Figure 5.2 (Th_7 and Th_{13} in the Figure) give the *average metal* and *average plaster* temperatures at the centroids of the thermocouple beads respectively, the following

equation may be derived:

$$Q_k = -k_m \frac{(T_{m-p} - Th_7)}{\Delta x_m} = -k_p \frac{(Th_{13} - T_{m-p})}{\Delta x_p} = -k_m G_7 \quad (94)$$

where k_m and k_p are the thermal conductivities of the metal and plaster, respectively, T_{m-p} is the metal-plaster interface temperature, Δx_m and Δx_p are dimensions defined in Figure 5.2, and G_7 is the temperature gradient through the wall of the specimen at location 7.

The gradient, G_7 is obtained by eliminating T_{m-p} from Equation 94 while the surface temperature T_{s_7} is obtained by linear extrapolation from Th_7 . In order to calculate G_7 and T_{s_7} , the distances Δx_m , Δx_p and δ_7 (in Figure 5.2) were measured on the polished section through the thermocouple, with a measuring grid superimposed onto the micrograph, Figure 3.7. The thermal conductivities for the metal (René 80) and the plaster were taken from the literature [78, 103]. The results of the calculations, for the five gas temperatures investigated, showed the gradient to be very small and negligible in all cases, except at the leading edge, where it was about $\sim 3^\circ\text{C}/\text{mm}$. This is not surprising due to the high conductivity of the metal and position of the measuring thermocouples from the surface.

In order to establish the surface temperatures at other locations, the gradient was assumed to be the same for all the leading and trailing edge thermocouples (i.e. equal to G_7). Along the face of the specimen, at thermocouple positions 1, 2, 3, 4, 5 in Figure 3.6, the gradient was assumed to be zero. Because of symmetry through the plane transverse to the specimen, the inward gradient at these last 5 locations may be expected to be much smaller than at the leading edge, and could be neglected.

Because of the thinner wall section in the flat face of the specimen, the

thermocouples were much closer together, as compared to the leading edge case. This made it difficult to measure the gradient with any degree of precision. as a result, all surface temperatures were calculated from the expression:

$$TS_i = Th_i + \delta_i G_i \quad (95)$$

where Th_i represents the readings from the embedded thermocouples at positions 1 to 11, δ_i is the distance of each of the thermocouple centroids from the surface and:

$$G_i = G_7 \text{ for positions 6, 7, 8, 9, 10, 11}$$

$$G_i = 0 \text{ for positions 1, 2, 3, 4, 5}$$

The results are presented in Table 5.2.

Table 5.2 Computed Surface Temperatures as a Function of Gas Temperature T/C (see Figure 3.6 for location of thermocouples).

T/C (°C)	T ₁ (°C)	T ₂ (°C)	T ₃ (°C)	T ₄ (°C)	T ₅ (°C)	T ₆ (°C)	T ₇ (°C)	T ₈ (°C)	T ₉ (°C)	T ₁₀ (°C)	T ₁₁ (°C)	G ₇ (°)
1200	714	978	992	935	699	1057.4	1060.3	1013.6	969.4	1007.0	940.6	-2.880
1100	656	908	918	861	631	973.7	976.6	924.5	894.8	932.5	857.9	-2.000
1000	594	835	848	789	572	887.9	891.8	837.3	817.0	854.8	783.0	-1.000
900	531	759	773	717	520	802.2	809.2	755.4	736.5	778.5	710.5	-0.294
800	474	684	703	651	465	721	731	684	662	705	644	-0

*: G_7 is the thermal gradient (in °C/mm) estimated near the specimen surface at the leading edge (location of the thermocouple 7, see Figure 3.6).

5.1.1.2 Optical Pyrometry Measurements (T/C = 1300°C)

The optical pyrometer (IRCON Model 7-13C10-0-1-0-60-0-100) was located 25 cm above the specimen as shown in Figure 3.2. The instrument was focused on the flat portions of the specimen, using a long range focusing lens (Model T3 - 25 to 30 cm range) while ensuring that its viewing axis was kept perpendicular to the surfaces on which the measurements were made. With the present setup, temperature measurements were made over a 2.5 mm diameter circle. All measurements were taken at steady state conditions, normally between 120 and 150 seconds into the thermal cycles after which the specimen temperatures were constant (as also indicated by the thermocouple measurements, see Figure 5.1).

Optical pyrometry requires that the emissivity setting of the pyrometer be adjusted to correspond to that of the material under evaluation. This setting was established experimentally by calibration against the temperature readings of reference thermocouples at, and immediately below, the surface of a flat calibration specimen of the test material heated isothermally in still air by induction. After 16 minutes of heating, the specimen was fully oxidized and the emissivity was found to remain constant. All optical pyrometry measurements were made in the burner rig after the test specimen had been oxidized for at least 16 minutes and using the emissivity IRCON setting of 0.85 obtained by calibration. This value is consistent with experimental data published for this type of material [78]. The optical pyrometry readings were estimated to be accurate to within $\pm 5^{\circ}\text{C}$, with a relative error from reading to reading of less than 1°C.

The distribution of surface temperatures measured by optical pyrometry for a solid specimen around its transverse mid-section corresponding to the axis of the hot gas stream at 1323°C is shown in Figure 5.3.

5.1.2 Temperature Computation

Specimen temperatures were computed using the ABAQUS FE-code which takes into consideration the conductive heat flux within the specimen, the radiation heat losses from the specimen to the surroundings and the convective heat flux from the hot and cold gas stream to the specimen.

5.1.2.1 Conductive Heat Transfer

The uniaxial conductive heat flux in a solid material is proportional to the thermal gradient, $\partial T/\partial x$, and to the thermal conductivity of the material, k , as expressed by the Fourier's law:

$$q_x = -k \frac{\partial T}{\partial x} \quad (96)$$

For steady state conditions, the three dimensions thermal conductivity Equation is given as:

$$\frac{\partial}{\partial x} \left(k \frac{\partial T}{\partial x} \right) + \frac{\partial}{\partial y} \left(k \frac{\partial T}{\partial y} \right) + \frac{\partial}{\partial z} \left(k \frac{\partial T}{\partial z} \right) = 0 \quad (97)$$

For unsteady state conditions, the temperature of the element changes with time. In terms of its internal energy, this can be expressed by:

$$\frac{dE}{dt} = \rho C_p \frac{\partial T}{\partial t} \quad (98)$$

where ρ and C_p are the density and specific heat of the material, respectively.

The transient energy equation is therefore:

$$\frac{\partial}{\partial x} \left(k \frac{\partial T}{\partial x} \right) + \frac{\partial}{\partial y} \left(k \frac{\partial T}{\partial y} \right) + \frac{\partial}{\partial z} \left(k \frac{\partial T}{\partial z} \right) = \rho C_p \frac{\partial T}{\partial t} \quad (99)$$

This equation describes the thermal heat conduction within the specimen thermally cycled in the burner rig.

The thermal conductivity and the specific heat of René-80 are both functions of temperature [78] where k can be represented by:

$$k = 0.0146 T + 5.3 \quad (100)$$

expressed in W/m·K and T is the material temperature in Kelvin, as shown in Figure 5.4.

The specific heat variation with temperature was found too complex to be fitted with a simple equation, and was therefore entered in a tabulated form after digitizing the curve obtained from the literature [78].

5.1.2.2 Radiation Heat Transfer

When the specimen is heated by the gas stream, its hot surface irradiates electromagnetic energy to the colder elements of its surrounding. Radiation heat flux

from the surface of the specimen to its environment is given by:

$$q_r = \epsilon \sigma \sum_j F_{s-j} (T_s^4 - T_j^4) \quad (101)$$

The emissivity of the oxidized material, ϵ , which represents the fraction of the radiation absorbed by the material and emitted to the surrounding (the rest of the radiation being reflected by the material surface), was experimentally measured to be equal to 0.85, as described in Subsection 5.1.1.2. The radiation shape factors, $F_{s,j}$ in Equation 101, represent the fraction of the energy radiated by the specimen to the element j of the surroundings, with $j = w$ for the room walls, $j = n$ for the burner rig nozzle and $j = c$ for the hot core of the combustor. The radiation shape factors were established with respect to the theory of radiation [69]. For the surrounding walls, $j = w$:

$$F_{s-w} = 0.880 \text{ at the leading edge}$$

$$F_{s-w} = 1.000 \text{ elsewhere}$$

$$T_w = 25^\circ\text{C}$$

For the burner rig nozzle, $j = n$:

$$F_{s-n} = 0.072 \text{ at the leading edge}$$

$$F_{s-n} = 0.000 \text{ elsewhere}$$

$$T_n = 529 \text{ to } 735 \text{ depending on gas temperature, as applicable.}$$

For the hot core of the combustor, $j = c$:

$$F_{s-c} = 0.048 \text{ at the leading edge}$$

$$F_{s-c} = 0.000 \text{ elsewhere}$$

$$T_c \approx T_g, \text{ the applicable corrected gas temperature (see Table 5.3 in the next Subsection).}$$

The procedure employed to find the parameters used in the expression of the radiation heat flux are described in more detail in Appendix F.

5.1.2.3 Convective Heat Transfer

Convective heat transfer (q_h) is proportional to the temperature difference between the gas and the specimen surface ($T_g - T_s$), and to the heat transfer coefficient, h , as given by:

$$Q_h = h (T_g - T_s) \quad (102)$$

The heat transfer is a complex function of specimen section geometry, gas velocity and gas physical properties. To fully establish the convective heat transfer, the temperature and velocity of the gas as well as the heat transfer coefficients must be experimentally determined, as explained in the two following subsections.

5.1.2.3.1 Gas Stream Temperature and Velocity

When the fuel is introduced at the front end of the combustor by a pressure atomizing fuel nozzle, the combustion gases from the forward sections of the combustor are cooled by dilution from two air jets which are located at the back of the system (Figures 3.2 and 3.3). By independently adjusting the primary and secondary air flow and the exit nozzle geometry, the velocity and temperature variations of combustion gases can be controlled independently. The primary and secondary mass flow rates of air are controlled by sonic nozzles (venturi tubes) with a neck diameter of 1.27 cm (0.5 inch). The flows are thus accurately known and are directly function of the upstream pressure of the nozzle, for a constant air supply temperature ($\sim 25^\circ\text{C}$). By selecting the proper liners and changing the mass flows of air and fuel, the gas velocities can be varied from Mach 0.2 to Mach 0.8 and the gas temperature from 500 to 1600°C. The mass flow for the cooling air stream, parallel to the hot gas stream, is also controlled by a by a sonic nozzle with a similar neck diameter (1.283 cm or 0.505 inch).

The temperature of the gas was measured using a bare junction type-S thermocouple (T/C) mounted 1 cm downstream of the nozzle. The thermocouple wires were looped to minimize conduction-heat losses along the wires and their sheath. With this design, and after corrections for radiation heat losses from the thermocouple bead to its surrounding, the gas temperature was established to be within $\pm 15^\circ\text{C}$ of its mean value with a test-to-test reproducibility of $\pm 2^\circ\text{C}$ (refer to Appendix G for details). The basic characteristics (average velocity and temperatures) of the hot-gas stream over the range of test temperatures used in this project are summarized in Table 5.3. These values were calculated with the help of the program TFC-P.BAS which is listed in Appendix H.

Mean gas velocities (U_g) were calculated from the mass flow of air supplied to the burner rig (\dot{m}) and the hot gas density (ρ), taken to a first approximation to be that of air at the same temperature, using the relationship:

$$U_g = \frac{\dot{m}}{\rho A_N} = \frac{T_g (P_1 + P_2)}{137.03 \sqrt{T_0}} \quad (103)$$

where \dot{m} is the mass flow given from basic fluid mechanics principles for sonic nozzles [104] and from the pressures P_1 and P_2 (in kPa) upstream of the nozzles (refer to Section 3), A_N is the area of the exhaust nozzle, T_g is the corrected control temperature (in K), measured at the exhaust nozzle, T_0 is the temperature (in K) of the compressed air supplied to the rig for combustion ($\sim 25^\circ\text{C}$) measured upstream of the sonic nozzles, and 137.03 is a constant combining the gas constant of air, fluid mechanics constants and unit conversion factors. The error in the determination of U_g is estimated to be less than 5%.

The temperature profile within the hot gas stream was established by incrementally positioning a type-S thermocouple of the same design as was used for

control of the gas temperature, across a transverse section. The displacement was carried out in steps of $2.54 \text{ mm} \pm 1\%$ ($0.1 \text{ inch} \pm 1\%$) using an optical bench equipped with a X-Y-Z positioning table. The temperature of the thermocouple has stabilized after 2 minutes at each position and 500 measurements were registered at a rate of 10 readings/second. The average value of these measurements was corrected for radiation heat losses using the program TFC-PRO.BAS presented in Appendix H.

The velocity profile within the hot gas was established by assuming that the Lau and Morris Formula [105] for the velocity profile within a cold gas jet is applicable to the hot gas stream. This neglects the temperature effects on viscosity which controls the width and radial position of the layer where the hot gas mixes with room air. However, it may be shown that the experimental data of Knott and Mossey [106], who measured the radial velocity profile of a free gas jet at high temperatures (up to 1000°C) with a laser velocimeter, are reasonably well fitted by Lau and Morris Equation. This equation was therefore used in the present study, for lack of a better model [107] and supporting experimental evidence. According to Lau and Morris' Formula [105], the radial distribution of velocity in a cold gas jet can be described as a function of distance from the nozzle by the relation:

$$\frac{U}{U_g} = 0.5 [1 - \text{erf}(\sigma \eta)] \quad (104)$$

where:

U is the velocity at any point in space;

U_g is the average gas velocity (from Equation 103);

$$\sigma = \frac{10.7}{(1 - 0.273 M_g^2)} \quad (105)$$

M_g is the Mach number of the jet velocity;

$$\eta^* = \frac{(r - r_{0.5})}{X} \quad (106)$$

$$\operatorname{erf}(y) = \frac{2}{\sqrt{\pi}} \int_0^y e^{-t^2} dt \quad (107)$$

r is the radial position considered;

$r_{0.5}$ is the radial position where the velocity U is equal to $0.5 U_j$;

X is the distance from the nozzle flange.

For the experiment carried out with a cold gas at Mach 0.28 and at $X = 0.100$ m, the radius, $r_{0.5}$ normalized to the internal radius of the nozzle exit, r_o ($r_o = 0.0254$ m) is measured to be $r_{0.5}/r_o = 1.12$ and $r_o = 0.0293$ m, [105]. The velocity profiles were computed with the program URADIAL.BAS using these relations and values of parameters (refer to Appendix H).

The temperature and velocity profiles are shown in Figure 5.5 for a position 85 mm downstream of the exhaust nozzle corresponding to the leading edge of the specimen and for a test temperature of 1323°C. The similarity in width and radial position of the transition regions between the two profiles suggest that assumptions made in using Lau and Morris Formula are reasonable.

Table 5.3 Characteristics of the Hot Gas Stream.

T/C	T_g	U_g	M_g	\dot{m}	ρ	ν	k	Pr
1300	1323	313	0.39	0.138	0.221	254	0.0998	0.705
1200	1225	298	0.38	0.140	0.236	229	0.0945	0.705
1100	1119	276	0.37	0.140	0.254	204	0.0887	0.705
1000	1014	255	0.35	0.140	0.274	179	0.0830	0.705
900	910	235	0.34	0.140	0.298	156	0.0774	0.706
800	806	214	0.33	0.140	0.327	134	0.0720	0.704

T/C: Gas temperature measured by the control thermocouple ($^{\circ}\text{C}$).

T_g : Corrected gas temperature ($^{\circ}\text{C}$), see text for details.

U_g : Mean gas velocity (m/s).

M_g : Corresponding Mach number (of U_g).

\dot{m} : Mass flow in the burner (kg/s).

ρ : Gas (air) density at T_g (kg/m^3).

ν : Kinematic viscosity of the gas (air) (m^2/s).

k : Thermal conductivity of the gas (air) ($\times 10^{-6} \text{ W/m}\cdot\text{K}$).

Pr: Prandlt number for air at T_g .

5.1.2.3.2 Convective Heat Transfer Coefficients

Local heat transfer coefficients were experimentally determined along the chordwise section of the specimen (in the axis of the gas stream) from gas and surface temperature measurements and from a local energy balance.

Three heat-transfer fluxes are considered at the surface of the specimen: convection from the hot gas to the specimen, q_h , radiation from the specimen to the surrounding, q_r , and conduction into the specimen, q_k . In steady state, the energy balance for a small volume element at the surface of the specimen of size $dx \cdot dy \cdot dz$ (Figure 5.6) translates into:

$$q_h = q_r + q_{k_x \cdot dx} + \frac{\partial q_k}{\partial y} dy + \frac{\partial q_k}{\partial z} dz$$

$$h(T_g - T_s) = \epsilon \sigma \left[\sum_j F_{s-j} (T_s^4 - T_j^4) \right] - k_m \left(\frac{\partial T}{\partial x} + \frac{\partial^2 T}{\partial y^2} dy + \frac{\partial^2 T}{\partial z^2} dz \right)$$

(108)

where:

- T_g : temperature of the hot gas stream (K);
- T_s : local temperature at the surface of the specimen (K);
- T_j : temperature of the element "j" of the surroundings (K);
- h : local heat-transfer coefficient ($W/m^2 \cdot K$);
- k_m : thermal conductivity of the specimen material ($W/m \cdot K$);
- ϵ : emissivity of the specimen material;
- σ : Stefan-Boltzmann constant ($5.669E-8 W/m^2 \cdot K^4$);
- F_{s-j} : radiation shape factors;

and where the partial derivative terms are used to describe conduction heat fluxes in and out of the elemental volume, in accordance with the reference coordinate indicated in Figure 5.6. With this coordinate system, at any point along the surface of the specimen, the x axis is normal to the surface, the y axis follows the periphery of the transverse mid-section and the z axis is parallel to the leading edge of the specimen.

The emissivity of the material, ϵ , was measured to be 0.85. The radiation shape factors, $F_{s,j}$ in Equation 108, represent the fraction of the energy radiated by the specimen to its surroundings with $j = w$ for the room walls, $j = n$ for the burner rig nozzle and $j = c$ for the hot core of the combustor. The radiation shape factors have the same values as those established in Appendix F and listed in Subsection 5.1.2.2

Equation 108 was used to calculate the convective heat transfer along the perimeter of the specimen's mid-section, corresponding to the axis of the hot gas stream. Because of the symmetry at the mid-section, the second derivative in the z direction in Equation 108 may be neglected. Furthermore, since the temperature varies approximately linearly within each of the flat and wedged portion of the section, Figure 5.3, the second derivative in the y direction (i.e. in the plane of the surface, Figure 5.6) can also be neglected.

The most important temperature gradient in the mid-section of the specimen, is from the leading edge to the trailing edge. At the leading edge, this corresponds to the x direction normal to the surface (c.f. Figure 5.6) and therefore the first derivative term in Equation 108 cannot be neglected for this location. However, the second derivative in y and z can be neglected due to the gas symmetry and specimen geometry. Hence, for

the leading edge, in the mid-section of the specimen, Equation 108 reduces to:

$$h (T_g - T_s) \approx \epsilon \sigma \left[\sum_j F_{s-j} (T_s^4 - T_j^4) \right] - k_m \frac{\partial T}{\partial x} \quad (109)$$

where the temperature gradient $\partial T/\partial x$ is given by G_7 as calculated from Equation 94.

Elsewhere along the perimeter of the mid-section, the thermal gradient in the x direction is small owing to hot gas stream and specimen symmetry. In this case, all the conduction fluxes can be neglected and Equation 108 reduces to:

$$h (T_g - T_s) \approx \epsilon \sigma \left[\sum_j F_{s-j} (T_s^4 - T_j^4) \right] \quad (110)$$

For other than mid-section locations on the specimen, the gradients in the z direction are unknown and not negligible a priori. To determine the heat transfer coefficients at these other locations the concept of geometric factor (GF) is first introduced. The GF is defined as the ratio of the local value, h , to a mean value, h_o :

$$GF = \frac{h(x, y, z)}{h_o(Re(z), Pr)} \quad (111)$$

where h_o is obtained from an empirical formulation proposed by Churchill and Bernstein [108] for a straight cylinder with a characteristic dimension (diameter, $d = 6.4$ mm) equivalent to the maximum thickness of the airfoil. According to Churchill and Bernstein, the Nusselt Number Nu_d for a cylinder in a high velocity gas stream can be expressed as a function of the characteristic dimension, the gas velocity and the physical

properties of the gas by the relation:

$$Nu_d = \frac{h_o d}{k_f} = 0.3 + \frac{0.62 Re^{1/2} Pr^{1/3}}{\left[1 + \left(\frac{0.4}{Pr}\right)^{2/3}\right]^{3/4}} \left[1 + \left(\frac{Re}{282000}\right)^{5/8}\right]^{4/5} \quad (112)$$

where Re and Pr are the Reynolds and Prandlt Numbers. This relation is valid for cases where $10^2 < Re < 10^7$ and $Re \cdot Pr > 0.2$. Errors in the Nusselt number, and therefore in h_o , introduced by neglecting turbulence intensity within the hot gas stream can be shown from the work of Bayley and Priddy [109] to be negligible in the core of the stream, and to be less than 10% in the layer where hot gas mixes with room air. This finding is consistent with the work of Lowery and Vachon [110] who have measured the effect of turbulence intensity on the Nusselt number for cylinders in cross flow.

The geometric factors (GF) from which the h 's are obtained from Equation 111, can be established in the long axis of the mid-section (x' direction, Figures 3.6) from experimental measurements of surface temperatures. First, the local coefficients are obtained from Equation 109 for the leading edge and from Equation 110 for other locations using the experimental data for the mid-section. The GF's are then calculated from Equation 111 using Reynolds and Prandlt Numbers and thermal conductivity data for h_o taken from the literature [69]. The thermal properties of the gas are evaluated at the film temperature, taken as the mean between the local surface temperature and the gas temperature.

The GF chordwise profile is further assumed to be constant in the z direction i.e. independent of the Reynolds Number. This assumption is based on data for non-circular cylindrical shapes approximating the DEW specimen's geometry, which show little change in the chordwise distribution of Nusselt Number (i.e. in h_o , c.f. Equation 112) for the range of Reynolds numbers pertaining to the present experiments ($Re \approx 10\,000$) [69].

The variation of the coefficients estimated along the z axis using GF values obtained from mid-section temperature measurements, and h_o values obtained from Equation 112 at the corresponding radial velocities and temperatures of the gas are given in Figure 5.5. Two programs (HCB-EXP.BAS and HCB-EMP.BAS) were developed in order to calculate the local h , the mean h_o and the GF values, as documented in Appendix H.

Heat Transfer Coefficients Based on Thin-wire Thermocouple Measurements:

Equation 109 was used to calculate the h at the leading edge in the mid-section (position 7, Figure 3.6) since all the parameters were known for that position, including the surface temperature gradient, G_7 (Equation 94). Calculations were also carried out by neglecting the contribution from conduction, i.e. by setting G_7 equal to zero, and/or by using a view factor of 1.0 instead of 0.88. The results are shown in Table 5.4.

Setting G_7 to zero decreased the h value by as much as 36% at the highest test temperature for which the gradient was the highest (c.f. Table 5.2). Changing the view factor also introduced a 10% error in the h values. From these observations, it may be concluded that a small error in G will cause a large error in h and that correctly choosing the view factor for radiation is also important. Finally, a realistic evaluation of h at the leading edge requires that the thermal conduction heat flux normal to the surface (in the x direction) be taken into consideration.

Elsewhere along the chordwise perimeter of the mid-section (positions 3 and 10, c.f. Figure 3.6), the h values were determined using Equation 110. Table 5.4 summarises these results for the range of gas temperature evaluated.

The h values at other airfoil locations (positions 1, 2, 4, 5, 6, 8, 9 and 11) were obtained following the methodology detailed in the last Subsection and are listed in Table 5.4. The GF's were first calculated for the mid-section at the leading edge (LE, position 7), at the flat portion of the section's face (FS, position 3) and at the trailing edge (TE, position 10). The GF's are shown in Table 5.5. Then the local coefficients were obtained from Equation 111 using h_o values obtained from Equation 112 at corresponding local temperatures and velocities of the gas and assuming that the GF profile is constant along the z direction.

Table 5.4 Experimental Heat-transfer Coefficients for Gas Stream Temperature Varying from 800 to 1200°C.

T/C (°C)	LE					FS					TE		
	h_6	h_7	h'_7	h''_7	h_8	h_1	h_2	h_3	h_4	h_5	h_9	h_{10}	h_{11}
1200	1434	924	1435	1020	1434	452	574	575	574	446	622	623	622
1100	1122	764	1122	845	1122	390	494	495	494	386	544	545	544
1000	835	648	836	716	835	359	455	456	455	356	477	479	477
900	657	595	658	657	657	332	420	422	420	330	445	446	445
800	630	631	631	695	630	350	442	443	442	347	455	456	455

NB.: h_i is the local "h" (in W/m²·K) at positions "i" (see Figure 3.6).

h_7 is computed from Equation 109 setting $\partial T/\partial x = 0$, and $F_{s-a} = 0.88$;

h'_7 is computed from Equation 109 setting $\partial T/\partial x = G_7$, and $F_{s-a} = 0.88$;

h''_7 is computed from Equation 109 setting $\partial T/\partial x = 0$, and $F_{s-a} = 1.0$.

For $i = 3$ (Flat Section) and 10 (Trailing Edge), "h" is computed from Equation 110 and setting $F_{s-a} = 1.0$.

Elsewhere, h was computed using the appropriate GF's (see Table 5.5), as detailed in Subsection 5.1.2.3.2.

Table 5.5 Geometric Factors (GF) for Gas Stream Temperature Varying from 800 to 1200°C.

T/C (°C)	T_g (°C)	GF _{LE}	GF _{FS}	GF _{TE}
1200	1225	2.602	1.042	1.128
1100	1119	2.117	0.933	1.026
1000	1014	1.637	0.892	0.936
900	910	1.339	0.856	0.906
800	806	1.341	0.940	0.968

Heat Transfer Coefficients Based on Optical Pyrometry Measurements:

The GF's at 1300°C and the corresponding h's for the mid-section of the specimen are presented in Figure 5.7 as a function of distance from the leading edge along the surface (DP), normalized by the half perimeter of the section (DP_0). Since no optical pyrometry measurements could be made at the tips of the leading and trailing edges, the profile was extrapolated to both locations. Linear extrapolation can be justified by experimental evidence for cylindrical shapes [69, 110] and airfoils [109, 111-113].

The overall profile is generally consistent with measurements for turbine airfoils as reported in the literature [111], including the two discontinuities associated with separation of the flow from the surface at the transition between the flat and sloped portions of the specimen. The profile is also consistent with the oxidation pattern observed on the test specimen after one cycle i.e. after a 2.5 minutes exposure in the hot gas stream, Figure 5.8. The pattern confirms the assumption of constancy in the GF value along the z direction over approximately 2 to 3 cm of the airfoil on both side of the mid-section. Beyond these distances, flow separation disappears as the Reynolds number (gas velocity) drops. For these locations, the discontinuities in the GF profile may be expected to be less sharp than those presumed from Figure 5.7. Nevertheless, the overall profile should remain the same.

The variation in h values along the leading edge (Figure 5.9) is the result of the radial velocity gradient in the gas stream and closely follows the velocity profile shown in Figure 5.5. A profile in h values for the cooling portion of the thermal cycle is also presented in Figure 5.9 for completeness. The profile assumes the same GF's, and the lower coefficients result from the lower velocity of the cooling air stream (Mach 0.24 vs Mach 0.4).

The local coefficients at 198 positions across the airfoil were calculated with GF values obtained from mid-section temperature measurements (c.f. Figure 5.7) assuming the profile to remain constant along the z axis. The results are shown in Table 5.6. The leading edge values are also plotted in Figure 5.9. The Figure identifies the $x'z$ coordinates of the 198 positions.

Table 5.6 Experimental Heat-transfer Coefficients for Gas Stream at 1300°C.

z (mm)	$T_g(z)$ (°C)	$U_g(z)$ (m/s)	$h_o(z)$	$h(x',z)$										
				GF0 2.500	GF1 2.194	GF2 1.864	GF3 1.463	GF4 1.207	GF5 1.332	GF6 1.374	GF7 1.121	GF8 1.272	GF9 1.340	GF10 1.370
0	41	1	34	85	75	63	50	41	45	47	38	43	46	47
5	103	9	97	243	213	181	142	117	129	133	109	123	130	133
10	250	42	211	528	463	393	309	255	281	290	237	268	283	289
15	468	118	353	883	775	658	516	426	470	485	396	449	473	484
20	720	214	472	1180	1036	880	691	570	629	649	529	600	633	647
25	1006	281	536	1340	1176	999	784	647	714	737	601	682	718	734
30	1220	307	560	1400	1229	1044	819	676	746	769	628	712	750	767
35	1275	312	565	1413	1240	1053	827	682	753	776	633	719	757	774
40	1286	313	566	1415	1242	1055	828	683	754	778	635	720	758	775
45	1287	313	566	1415	1242	1055	828	683	754	778	634	720	758	775
50	1271	313	566	1415	1242	1055	828	683	754	778	635	720	758	775
55	1263	312	565	1413	1240	1053	827	682	753	776	633	719	757	774
60	1206	307	560	1400	1229	1044	819	676	746	769	628	712	750	767
65	972	281	538	1345	1180	1003	787	649	717	739	603	684	721	737
70	696	214	474	1185	1040	884	694	572	631	651	531	603	635	649
75	460	118	354	885	777	660	518	427	472	486	397	450	474	485
80	256	42	210	525	461	391	307	254	280	289	235	267	281	288
85	175	9	96	240	211	179	140	116	128	132	108	122	129	132

Where: z is the longitudinal position along the specimen (see Figure 5.9);
 $T_g(z)$ is the corrected temperature of the gas stream at position z ;
 $U_g(z)$ is the gas velocity at position z ;
 $h_o(z)$ is the mean h of the specimen at position z (in $W/m^2 \cdot K$);
 $h(x',z)$ is the local h (in $W/m^2 \cdot K$) at position (x',z) on the specimen
(see Figure 5.0);
 GF_i is the geometric factor at position i along the x' axis (refer to
Figure 5.7).

Comparison of Results Obtained from Both Techniques of Temperature Measurements:

Table 5.7 shows the h and GF values obtained from using the two techniques of temperature measurements, for the mid-section of the specimen at a gas temperature of 1323°C . Since, there was no thermocouple based data at 1323°C , data for gas temperatures in the range from 806 to 1225°C were extrapolated. The h and GF values differ by 20% at the leading edge and are within 11% at the trailing edge. These differences are to be expected, since the experimental errors in determining coefficients by both techniques are of the order of $\pm 20\%$ for the leading edge and $\pm 10\%$ elsewhere, once all possible sources of error are taken into consideration. This level of accuracy is reasonably good, considering the high temperatures at which the measurements were made, and is comparable to the accuracies reported other studies of convective heat flux [69, 112].

Table 5.7 Comparison of GF and h Values Obtained by Thermocouple and Pyrometry Measurements at $T_g = 1323^{\circ}\text{C}$.

LOCATION	$GF_{th} (*)$	GF_{IR}	$h_{th} (*)$ ($\text{W}/\text{m}^2 \cdot \text{K}$)	h_{IR} ($\text{W}/\text{m}^2 \cdot \text{K}$)	Difference (%)
LE	3.00	2.50 (**)	1725	1415 (**)	20
FS	1.16	1.33	657	754	14
TE	1.23	1.37 (**)	696	775 (**)	11

NB.: LE: Leading edge at the mid-section of the specimen;

FS: Flat section at the mid-section of the specimen;

- TE: Trailing edge at the mid-section of the specimen.
- *: extrapolated to 1323°C from thermocouple measurements over 806 to 1225°C range.
- **: extrapolated to LE and TE from surface profile shown in Figure 5.7.

5.1.2.4 Computation of Transient Temperatures During Cycling

The temperature evolution during thermal cycling of the DEW specimen exposed to a gas stream at 1323°C was computed using the ABAQUS FE-code. The mesh and the axes system shown in Figure 5.10.

For the analysis, the local h , displayed in Table 5.6 (Subsection 5.1.2.3.2) for 198 positions across the airfoil, were implemented in the FE-code, as well as the corrected gas temperature profile determined in Subsection 5.1.2.3.1 from measurements across the gas stream at the position of the specimen leading edge. The thermo-physical properties of the René 80 presented in Figure 5.4 were tabulated. The emissivity of the oxidized material and the other radiation parameters considered in this analysis are summarized in Subsection 5.1.2.2.

The rise and fall in temperatures computed at the leading edge tip of the test specimen are shown in Figure 5.11 for different positions along the longitudinal axis z (Figure 5.10). At the position of the specimen directly exposed to the hot gas stream, it takes about 9 seconds for the metal to reach 80% of the steady state temperature at 1164°C. It should also be noted that the maximum leading edge tip temperature reached during cycling is 160°C below the gas temperature. This difference is principally due to radiation heat losses from the specimen to its surroundings which were carefully considered in the thermal analysis. After the heating cycle, the temperature at the free

end of the specimen outside of the hot gas stream ($z = 0$ mm) rises instead of falling immediately, as at the other locations. This temperature rise is attributed to the heat coming by conduction from the hot section of the specimen directly exposed to the hot gas jet.

Figure 5.12 shows the temperature distribution of the leading edge along the longitudinal axis after four incremental exposure times during the thermal cycle. At the end of the heating cycle, a flat temperature distribution is observed over 17 mm on both sides about the axis of the hot gas stream ($z = 45$ mm). This profile is a normal consequence of the distribution of the convection heat-transfer coefficients and of the hot gas temperature, shown in Figures 5.9 and 5.5, respectively. In the determination of the convection heat transfer coefficients from a heat balance on elements along the mid-section of the specimen ($z = 45$ mm), the conduction heat-transfer along the longitudinal axis of the specimen was neglected (refer to Subsection 5.1.2.3.2). According to the flat temperature profile in this region of the specimen, this simplification in the heat balance was justified.

At the end of the cooling cycle, the temperature of the leading edge tip at the longitudinal position corresponding to the cooling air jet ($z = 50$ mm) falls to 39°C which is almost the starting temperature of the specimen (25°C), whereas the temperature at both extremities is still relatively high (267°C at the free end and 336°C at the end in the holder). This means that the temperature of the specimen did not reach their steady state and a good establishment of a representative thermal history along subsequent cycles should require an extended computation. In the present analysis, this aspect was neglected in a first approximation.

Figure 5.13 illustrates the computed isotherms in the DEW specimen in the plane y - z , at the end of the heating and cooling thermal cycles. The Figure also shows

typical spalled oxide patterns observed in specimens after 2500 thermal cycles. It is interesting to note that these oxide patterns match the shape and location of the isotherms very well for the portion of the specimen directly exposed to the hot and cold gas streams. This result is representative of the spalling of the oxide scale build up at high temperature, due to the thermal contraction of the metallic substrate during cooling which is highest in the central region. This result indirectly validates the thermal analysis in terms of its spatial distribution.

In Figure 5.14, the computed steady state isotherms are plotted for the mid-section of the specimen. This result reinforces the assumptions made in Subsection 5.1.2.3.2 regarding the temperature gradients within the specimen. It is interesting to note that the most important gradient is at the leading edge ($\sim 5^\circ\text{C}/\text{mm}$) and that the isotherms are approximately perpendicular to the chordwise direction within the section.

The computed surface temperature profile along the chordwise mid-section of the DEW specimen at the end of the heating cycle is compared to measured temperatures obtained by optical pyrometry in Figure 5.15. While the computed temperature at the leading edge only differs by 15°C from the linear extrapolation of measurements, the computed profile appears as a smooth temperature variation due to the high conductivity of the material whereas the measured profile shows abrupt variations. The difference between the measured and computed temperature profiles is approximately 35°C and the discontinuities are attributed to the abrupt change in the convection heat transfer coefficients as a result of separation of the gas flow from the surface at the transition between the flat and sloped portion of the DEW specimen, as discussed in Subsection 5.1.2.3.2. It can be concluded from this important difference between the two profiles that the optical pyrometer measured the oxide scale surface temperature which results from convection and radiation heat transfer and is not influenced by the

metal temperature under the oxide layer due to its lower thermal conductivity. This oxide property allowed to evaluate more accurate heat-transfer coefficients while the thermal conduction was neglected in their determinations from optical pyrometry measurements (Subsection 5.1.2.3.2). The presence of the oxide scale could also explain the difference of 35°C between the experimental and numerical temperatures.

5.1.3 Conclusions

This section demonstrates that a double-edge wedge specimen simulating airfoil geometry exposed to a high-velocity burner rig simulating the operating environment can be used to calculate heat transfer coefficient profiles across the airfoil akin to values obtained by others for actual airfoils [111-113]. This indicates that thermal history can be properly simulated in the laboratory for thermal fatigue testing of blade and vane materials under realistic conditions.

The thermal analysis of the DEW specimen is complex and requires that all the thermal parameters be accurately known. The determination of the convective heat-transfer coefficients from thermocouples and optical pyrometry temperature measurements along the surface of the DEW specimen was particularly difficult but important. Computed and measured temperatures differs by only 15°C at the leading edge and 35°C, in average, elsewhere along the chordwise mid-section. This result is very good considering the experimental and numerical difficulties met in this analysis and that the thermal parameters were not adjusted after a first run.

The values of the experimental heat transfer coefficients obtained from both techniques of temperature measurements were found to be within 20% of each other. Optical pyrometry based data including values obtained by extrapolation for the leading edge can be therefore used for thermal analysis of the specimen. The thermal analysis indicates that assumptions made regarding the determination of the heat-transfer coefficients from heat balance over small elements of the mid-section of the specimen are valid.

5.2 Mechanical Analysis

The aim of the mechanical analysis was to compute the stress-strain variation of each element of the specimen thermally cycled in the burner rig, using a finite element (FE) code and taking into consideration the temperature variation within the specimen, as determined in the last Subsection. The present Subsection explains the computation methodology, presents the results and compares the location of maxima in the temperature and stress distributions to that of the cracks in the tested specimens.

5.2.1 Computation Methodology

The stress-strain variation of the test specimens was computed using two separate analyses: (i) a thermo-elastoplastic analysis using the subroutine of the ABAQUS FE-code, and (ii) a thermo-elasto-viscoplastic analysis using the subroutine of Walker implemented in the ABAQUS FE-code. The stress and the strain are expressed by tensors, σ and ϵ , of 6 components each, as $\sigma_{ij} = \sigma_{ji}$ and $\epsilon_{ij} = \epsilon_{ji}$. The strain tensor, ϵ , also called the total strain tensor, ϵ^{tot} , or the net strain tensor, ϵ^{net} , is decomposed in an elastic, a plastic and a thermal term, ϵ^e , ϵ^p , ϵ^th , respectively. To determine the value of the 30 components, the following 30 equations (Equations 113 to 122) must be solved for each element of volume $\Delta x \cdot \Delta y \cdot \Delta z$ in the specimen and for each increment of time during each thermal cycle:

3 Differential Equations of Equilibrium:

$$\frac{\partial \sigma_{xx}}{\partial x} + \frac{\partial \sigma_{xy}}{\partial y} + \frac{\partial \sigma_{xz}}{\partial z} = 0 \quad (113)$$

$$\frac{\partial \sigma_{yx}}{\partial x} + \frac{\partial \sigma_{yy}}{\partial y} + \frac{\partial \sigma_{yz}}{\partial z} = 0 \quad (114)$$

$$\frac{\partial \sigma_{zx}}{\partial x} + \frac{\partial \sigma_{zy}}{\partial y} + \frac{\partial \sigma_{zz}}{\partial z} = 0 \quad (115)$$

3 Compatibility Equations:

$$\frac{\partial^2 e_{xx}}{\partial y^2} + \frac{\partial^2 e_{yy}}{\partial x^2} = \frac{\partial^2 e_{xy}}{\partial x \partial y} \quad (116)$$

$$\frac{\partial^2 e_{yy}}{\partial z^2} + \frac{\partial^2 e_{zz}}{\partial y^2} = \frac{\partial^2 e_{yz}}{\partial y \partial z} \quad (117)$$

$$\frac{\partial^2 e_{xx}}{\partial z^2} + \frac{\partial^2 e_{zz}}{\partial x^2} = \frac{\partial^2 e_{xz}}{\partial x \partial z} \quad (118)$$

6 Equations Defining the 6 Components of the Strain Tensor, e :

$$e_{ij} = e_{ij}^e + e_{ij}^p + e_{ij}^{th} \quad (119)$$

6 Equations Defining the 6 Components of the Thermal Strain Tensor, e^{th} :

$$e_{ij}^{th} = \alpha (T - T_0) \delta_{ij} \quad (120)$$

where α is the linear thermal expansion coefficient, T_0 is the initial temperature, T is the local temperature at any time during cycling, and δ_{ij} is the Kronecker delta ($\delta_{ij} = 1$ when $i=j$ and $\delta_{ij} = 0$ when $i \neq j$);

6 Equations Defining the 6 Components of the Elastic Strain Tensor, e^e :

$$e^e = S : \sigma \quad (121)$$

where S is the compliance matrix (6×6);

6 Equations Defining the 6 Components of the Plastic Strain Tensor, e^p of the General Form:

$$e_{ij}^p = \lambda g_{ij} \quad (122)$$

where λ is the plastic multiplier or proportionality factor between the plastic strain and the stress as measured during uniaxial tests, and g is a function of the tridimensional stress state. In the models which use a yield criterion, g_{ij} is equal to the partial derivative $\partial f / \partial \sigma_{ij}$ where the function f describes the yield surface in the space of stress.

The mesh and the coordinate system employed in the mechanical analyses are the same as was used for the thermal analysis (refer to Figure 5.16 and Figure 5.10). The mesh definition, the thermal variation of the DEW geometry as well as the mechanical properties and model constants were defined in input files for both thermo-mechanical analyses. Because of the large volume of these files, they are not listed in this thesis but they can be provided upon request.

5.2.1.1 Thermo-elastoplastic Analysis

In this analysis, the ABAQUS FE-code is used to solve the Equations described above assuming that the material behaviour is purely thermo-elastoplastic. Creep or viscous flow, stress relaxation, cyclic hardening or softening and ratchetting plastic strain are neglected. It is assumed that the thermal expansion is isotropic, that the elastic properties of the material are orthotropic, and that the plastic flow is described by a linear hardening model.

The thermal strain tensor is expressed by Equation 120 that can be rewritten as:

$$\begin{Bmatrix} \varepsilon_{11}^{th} \\ \varepsilon_{22}^{th} \\ \varepsilon_{33}^{th} \\ \varepsilon_{12}^{th} \\ \varepsilon_{23}^{th} \\ \varepsilon_{13}^{th} \end{Bmatrix} = \begin{Bmatrix} \alpha (T - T_0) \\ \alpha (T - T_0) \\ \alpha (T - T_0) \\ 0 \\ 0 \\ 0 \end{Bmatrix} \quad (123)$$

The linear thermal expansion coefficients of René 80 were taken from [78, 114] and are tabulated in Table 5.8. These values were implemented in the FE-code through the *EXPANSION option.

The elastic strain tensor is given by the matrix product of the compliance matrix S with the stress tensor, σ , as expressed in Equation 121. As indicated previously in Subsection 3.1.1, the DS René 80 specimens are produced by directional solidification,

with the crystallographic orientation $\langle 0,0,1 \rangle$ parallel to the solidification direction. The material is composed of independent columnar grains parallel to the longitudinal direction of the specimen (axis z or 3). On a macroscopic scale, the mechanical properties in the longitudinal direction correspond to those of a monocrystal in the $\langle 0,0,1 \rangle$ orientation and the properties can be considered isotropic in the transversal plane of the specimens (defined by the axes x-y or 1-2) and similar to those of a polycrystalline material of the same chemical composition obtained by conventional casting (CC). In this case, the elastic strain components for a transversal isotropic material is given by:

$$\begin{Bmatrix} \epsilon_{11}^e \\ \epsilon_{22}^e \\ \epsilon_{33}^e \\ \epsilon_{12}^e \\ \epsilon_{23}^e \\ \epsilon_{13}^e \end{Bmatrix} = \begin{bmatrix} \frac{1}{E_1} & -\frac{\nu_{12}}{E_1} & -\frac{\nu_{13}}{E_1} & 0 & 0 & 0 \\ -\frac{\nu_{12}}{E_1} & \frac{1}{E_1} & -\frac{\nu_{13}}{E_1} & 0 & 0 & 0 \\ -\frac{\nu_{13}}{E_1} & -\frac{\nu_{13}}{E_1} & \frac{1}{E_3} & 0 & 0 & 0 \\ 0 & 0 & 0 & \frac{1+\nu_{12}}{E_1} & 0 & 0 \\ 0 & 0 & 0 & 0 & \frac{1}{2G_{13}} & 0 \\ 0 & 0 & 0 & 0 & 0 & \frac{1}{2G_{13}} \end{bmatrix} \begin{Bmatrix} \sigma_{11} \\ \sigma_{22} \\ \sigma_{33} \\ \sigma_{12} \\ \sigma_{23} \\ \sigma_{13} \end{Bmatrix} \quad (124)$$

where:

E_i is the Young's modulus in direction "i";

ν_{ij} is the Poisson's ratio associated to the contraction in direction "i" when tension is applied in the direction "j";

G_{ij} is the shear modulus in the plane defined by directions "i" and "j".

The elastic properties of the DS René 80 were not found in the literature. However, the transverse elastic properties can be assumed to be the same as those of the

polycrystalline CC René 80 (CCR80), which are available at many temperatures in [78, 114]. The longitudinal elastic properties can be approximated by combining the properties of CCR80 with the ratio of the longitudinal to transversal properties of DS MAR-M 200 (DSMM200) [115], a nickel-based superalloy obtained by directional solidification as DSR80. More precisely, the following approximations were used to establish the elastic properties of DS René 80 which are summarized in Table 5.8:

$$E_1 = E_2 \approx E_{CCR80}$$

$$E_3 \approx (E_3/E_1)_{DSMM200} E_{CCR80}$$

$$\nu_{13} = \nu_{23} \approx \nu_{CCR80}$$

$$\nu_{12} \approx (\nu_{12}/\nu_{13})_{DSMM200} \nu_{CCR80}$$

$$G_{12} \approx G_{CCR80} = (E/2(1 + \nu))_{CCR80}$$

$$G_{13} = G_{23} \approx (G_{13}/G_{12})_{DSMM200} G_{CCR80}$$

The values of Table 5.8 were implemented in the FE-code through the *ELASTIC option.

Table 5.8 Elastic properties established for DS René 80.

T (°C)	α ($10^{-6}/K$)	E_1 (GPa)	E_3 (GPa)	ν_{13}	ν_{12}	G_{12} (GPa)	G_{13} (GPa)
25	11.30	207	160	.313	.114	79	129
204	11.70	200	152	.316	.118	76	122
316	12.15	196	146	.319	.121	74	119
427	12.60	190	141	.322	.126	72	115
538	13.23	183	135	.326	.132	69	110
649	13.77	176	129	.329	.140	66	106
704	14.04	171	124	.331	.145	64	103
760	14.40	166	119	.334	.151	62	100
816	14.85	162	114	.337	.158	61	96
871	15.30	157	109	.341	.164	59	92
927	15.75	152	104	.345	.172	56	88
982	16.20	144	98	.348	.179	53	83
1093	17.28	110	70	.356	.195	40	60
1149	18.00	93	56	.360	.203	34	49
1204	19.17	69	40	.375	.218	25	35

The plastic behaviour of DSR80 was modelled using the `"*PLASTIC, HARDENING=KINEMATIC"` option of ABAQUS which is based on a linear kinematic hardening model. This model assumes that the plasticity is driven by the effective stress (given by the total stress minus an internal stress) instead of the total stress. The hardening observed in stress-strain curves is not associated to the increase of the yield surface radius defined by the function, f , in Equation 122 but rather to the translation of the yield surface in the space of the stress which corresponds to the hardening of the internal stress assumed to evolve linearly with the plastic strain. If the yield function, f , is described by the von Mises yield criterion, the component "ij" of the plastic strain tensor are given by Equation 122 which becomes:

$$e_{ij}^p = \frac{3}{2} \lambda \left[\frac{S_{ij} - X_{ij}}{|S_{ij} - X_{ij}|} \right] \quad (125)$$

where:

S is the deviatoric of the total stress;

X is the deviatoric of the internal stress;

λ the plastic multiplier.

In order to compute the plastic multiplier, the values of the yield stress and the limit of plasticity (approximated by the maximum stress) obtained from stabilized cyclic stress-strain curves at different temperatures had to be implemented in the FE code, through the `"*PLASTIC"` option. These values were extracted from cyclic stress-strain curves for CCR80 at temperatures ranging from 20° to 1040°C [114], as illustrated for one curve in Figure 5.17. The values are given in Table 5.9.

Table 5.9 Yield stress and maximum stress obtained from cyclic stress-strain curves for CCR80 [114].

T (°C)	ϵ^p	$\sigma_{y, cyc}$ (MPa)	ϵ^p	$\sigma_{max, cyc}$ (MPa)
20	0.0000	720	0.0075	1550
650	0.0000	675	0.0046	1290
870	0.0000	480	0.0055	1025
930	0.0000	315	0.0061	895
980	0.0000	220	0.0043	540
1040	0.0000	80	0.0021	260

Where:

ϵ^p is the plastic strain;

$\sigma_{y, cyc}$ is the yield stress;

$\sigma_{max, cyc}$ is the maximum stress.

5.2.1.2 Thermo-elasto-viscoplastic Analysis

A more sophisticated stress-strain analysis using a visco-plastic model was also attempted. In this analysis, the same thermo-elastic properties given in Table 5.8 were considered. Contrary to the previous analysis, the creep or viscous flow, the stress relaxation, the cyclic hardening or softening and the ratchetting plastic strain were modelled using a subroutine written in FORTRAN by Walker and implemented in the ABAQUS FE-code. The subroutine, originally written for isotropic materials was modified to take into consideration the elastic orthotropy of DSR80 studied in this thesis. A description of the modifications as well as the listing of the modified subroutine are give in Appendix I. The subroutine employs the exponential formulation of the viscoplastic model of Walker. This formulation was chosen because it is better than the formulations based on a power law and a hyperbolic sine function to model the stress-strain behaviour of materials at high temperature [116]. In this model, the creep strain and the plastic strain are represented by the same tensor ϵ^p (also called inelastic stain tensor, ϵ^l). The original model of Walker [117] has been simplified in the form of the following constitutive Equations by eliminating the terms where the material constants are practically zero for the particular alloy considered in this thesis [118]. The terms involving rate of temperature change were also neglected as the stress-strain variation is computed for small temperature steps.

flow rule:

$$\dot{\epsilon}_{ij}^p = \varphi \frac{3}{2} \left(\frac{\Sigma_{ij}}{\Sigma_{eq}} \right) = \varphi \frac{3}{2} \left(\frac{S_{ij} - \omega_{ij}}{\Sigma_{eq}} \right) \quad (126)$$

where:

$$\varphi = \frac{\exp\left(\frac{\Sigma_{eq}}{K}\right) - 1}{\beta} \quad (127)$$

$$\Sigma_{eq} = \sqrt{\frac{3}{2} \sum_{i=1}^3 \sum_{j=1}^3 \Sigma_{ij} \Sigma_{ji}} \quad (128)$$

$$\Sigma_{ij} = S_{ij} - \omega_{ij} \quad (129)$$

$$S_{ij} = \sigma_{ij} - \frac{1}{3} \delta_{ij} \sum_{k=1}^3 \sigma_{kk} \quad (130)$$

$$\omega_{ij} = \frac{2}{3} \Omega_{ij} \quad (131)$$

The fully developed expression of Equation 126 is:

$$\dot{\epsilon}_{ij}^p = \frac{3}{2} \left\{ \frac{\exp\left(\frac{\Sigma_{eq}}{K}\right) - 1}{\beta} \right\} \left(\frac{S_{ij} - \frac{2}{3} \Omega_{ij}}{\Sigma_{eq}} \right) \quad (132)$$

N.B.: δ_{ij} is the Kronecker delta which has the following property:

$\delta_{ij} = 1$ when $i=j$ and $\delta_{ij} = 0$ when $i \neq j$.

evolutionary rules:

$$\dot{K} = 0 \Rightarrow K = K_1 \quad (133)$$

$$\Omega_{ij} = \Omega_{ij1} + \Omega_{ij2} \quad (134)$$

$$\dot{\Omega}_{ij1} = n_2 \dot{\epsilon}_{ij}^p - \Omega_{ij1} (n_3 \dot{\epsilon}_{eq}^p + n_6) \quad (135)$$

$$\dot{\Omega}_{ij2} = n_{11} \dot{\epsilon}_{ij}^p - \Omega_{ij2} (n_9 \dot{\epsilon}_{eq}^p + n_{10}) \quad (136)$$

with:

$$\dot{\epsilon}_{eq}^p = \sqrt{\frac{2}{3} \sum_{i=1}^3 \sum_{j=1}^3 \dot{\epsilon}_{ij}^p \dot{\epsilon}_{ji}^p} \quad (137)$$

According to the flow rule (Equation 126) the plastic strain rate is proportional to the effective stress, Σ , through the plastic rate multiplier, ϕ . The effective stress (Equation 129) is defined to be the difference between the deviatoric stress, S , and the deviatoric back stress, ω , obtained from the stress, σ , and the back stress, Ω , with Equation 130-131, respectively. The deviatoric components of the stress tensors are used in the flow rule as the hydrostatic components of the stress tensor do not contribute to plasticity. Plasticity only processes by shearing and this implies no volume change during plastic deformation or plastic incompressibility: $\sum_k \epsilon_{kk}^p = 0$.

The back stress used to define the effective stress, also called internal stress, corresponds to the residual elastic stress field which develops during deformation and is associated to mechanical mismatch between randomly oriented anisotropic crystallites in polycrystalline materials and to dislocation pile-ups in the crystallites, especially near obstacles such as precipitates, carbides and grain boundaries. The evolution of the back

stress (Equation 134) is described by two evolutionary laws (Equation 135-136), one associated to a dislocation structure stable at low stress level and the other associated to a dislocation structure stable at higher stress level. Each evolutionary law is composed of two opposite terms simulating the effect of two competing mechanisms as proposed by the Bailey-Orowan theory [119]. The first term represents the kinematic hardening of the back stress occurring during plastic deformation and the second term represents the dynamic recovery (associated to recrystallization and precipitates rafting and coarsening) and the thermal recovery (associated to dislocations redistribution and cancelling during material annealing) of the back stress. The use of the effective stress in the flow rule implies that the applied stress has to follow the hardening evolution of the back stress during deformation in order to maintain a constant plastic flow. Note also that the back stress hardening is directional (the back stress is a tensor) and is proportional to the plastic strain. This implies that after plastic deformation in one direction at a given level of plastic flow, the magnitude of applied stress required to produce the same plastic flow in the reverse direction is less important, as the applied stress is now "assisted" by the back stress in that direction (phenomenon well known as the Bauschinger effect) [120, 121]. Reverse flow observed after that the applied stress is brought to zero (thus $\Sigma_{ij} = -\Omega_{ij}$) is another example of the directional manifestation of the back stress.

The plastic rate multiplier, ϕ , in the flow rule is defined by an exponential expression (Equation 127) of the equivalent effective stress to drag stress ratio, Σ_{eq}/K , where the equivalent effective stress is the scalar associated to the effective stress tensor as defined by the von Mises expression, Equation 128. The physical justification for the choice of this formulation is that the plastic flow is controlled by the mobility of dislocations, a process activated by energy which is represented by the effective stress, in this particular case [119, 121]. In this formulation, the plastic flow is inversely proportional to the viscous drag stress (K) or the friction stress which represents the

resistance to dislocation glide, generated by the obstacles such as precipitates, carbides, grain boundaries and dislocation frame-work. In this model, the drag stress is a scalar that means the obstacles are supposed uniformly distributed and the material viscosity to be isotropic. Another assumption made is that the drag stress do not evolve during deformation, in other words, the drag stress is a constant ($K = K_1$, see Equation 133).

In the flow rule and in the evolutionary laws, defined by Equations 126-137, β , K_1 , n_2 , n_3 , n_6 , n_9 , n_{10} , n_{11} are material constants which vary with temperature. The values employed for the computation of the viscoplastic behaviour of the DSR80 tested in the burner rig are those of B1900+Hf (CC) obtained from [118] (see Table 5.10), as the constants of DSR80 were not available. B1900+Hf, obtained from standard casting and heat-treating practices, is a nickel-base superalloy of similar chemical composition to that of DSR80 with a volume fraction of γ' precipitates of 60% and a γ' size of $0.9 \mu\text{m}$, whereas DSR80 has a volume fraction of γ' of 56% and a γ' size of $0.4 \pm 0.2 \mu\text{m}$ (see Subsection 4.1.1.1). As the proportions and the sizes of γ' in the two alloys are approximately equivalent, it is believed that their viscoplastic properties are similar, as the precipitates characteristics mainly controls the viscoplastic behaviour of these alloys.

Table 5.10 Constants of the exponential form of the Walker model for B1900+Hf, [118].

T (°C)	β (MPa)	K_1 (MPa)	n_2 (MPa)	n_3	n_6	n_9	n_{10}	n_{11} (MPa)
21	1.73E11	12.4	2.41E6	4794	0	11.87	0	4.70E3
427	1.73E11	12.4	2.41E6	4794	0	11.87	0	4.70E3
538	1.73E11	12.4	2.41E6	4794	0	11.87	0	4.70E3
649	3.86E10	12.4	8.27E5	1714	0	16.64	0	4.70E3
760	2.55E10	13.8	8.27E5	1880	0	19.83	2.44E-3	4.70E3
871	5.50E12	16.6	2.36E6	621.2	8.73E-4	59.33	2.44E-3	9.65E2
982	4.20E10	13.8	9.65E4	400.0	4.29E-4	136.0	2.44E-3	0
1093	5.57E9	9.0	2.36E4	278.7	4.83E-2	136.0	2.44E-3	0

5.2.2 Results of the Computation

Both the thermo-elastoplastic and the thermo-elasto-viscoplastic analyses, of the DEW specimen subjected to the thermal loading in the burner rig, were carried out using the ABAQUS FE-code on a Crimson computer (Processor of 100MHz, 112Mb of RAM, HD of 3Gb).

5.2.2.1 Thermo-elastoplastic Behaviour

The metallographic analysis of DEW specimens showed that cracks only initiated at the leading edge, along the longitudinal z (or 3) axis (Figure 5.16) and propagated in the transverse direction, y (or 2) axis. This observation leads to a consideration of the variation and the distribution of the principal stress, σ_{33} , and the temperature along the leading edge. The principal stresses in the other directions, σ_{11} and σ_{22} , are not presented in the following analysis, as they represent 5 to 15% of σ_{33} during the thermal cycle.

Figure 5.18 gives the temperature and stress variation during thermal cycling at specific positions: a position corresponding to the axis of the hot gas stream ($z = 46.75$ mm), and two positions symmetrically distributed 17 mm on each side of the stream axis ($z = 29.75$ and 63.75 mm). During the early stage of the heating cycle, the stress at these locations quickly goes in compression (peak H1), rises up and stabilizes to a tensile value at the end of the heating cycle (plateau H2). During cooling, the stress variation is reversed showing a tensile peak (C1) and a compressive plateau (C2). The stress variations in the portion of the leading edge directly exposed to the heating and cooling gasses are associated with the variations of the temperature gradients and thermal expansion gradients in the specimen. Figures 5.19 and 5.20 illustrate the temperature, the schematic loads and real von Mises stress distributions in the plane y - z

(or plane 2-3) of the DEW specimen, at different times during thermal cycling. During the early stage of heating, Figure 5.19a, the leading edge exposed to the hot gas is rapidly heated and expands but the bulk of the specimen still relatively cold. This restrains the full thermal expansion of the leading edge, subjecting this part of the specimen to a compressive stress. While the temperature of the bulk of the specimen increases, the compressive stress is reduced in the leading edge. Near the end of the heating cycle, Figure 5.19b, the central part of the specimen reaches a high and uniform temperature whereas the two ends of the specimen stays relatively cold. The thermal expansion of the central part in the transverse direction (y or 2) is constrained by the cold ends at the interface between the hot and cold parts. This causes the corners of the hot area to be pulled in and their leading and trailing edges to be pushed out in the middle. The edges are then in bending which explains why they are subjected to tensile stress in the longitudinal direction (axis z or 3) near their surfaces. During cooling, the tensile peak (C1) and the compressive plateau (C2) can be explained in an analogous manner (see Figures 5.20a and b).

Figure 5.21 shows the principal stress (σ_{33}) and the temperature distributions at the end of the heating cycle (corresponding to the situation "b" in Figure 5.19) and few seconds after the start of the cooling cycle (corresponding to the situation "a" in Figure 5.20). At the end of the heating cycle, the stresses are highest in the portion of the leading edge directly exposed to the hot gas stream, with two maxima symmetrically distributed 17 mm about the axis of the hot gas stream. The principal stress maxima are of the order of 130 MPa and 110 MPa, respectively, and the metal temperature corresponding to these locations is about 1090°C. Between these maxima, the principal stress level is lower with an average value of 70 MPa and a minimum value of 20 MPa at the location corresponding to the axis of the hot gas stream but the temperature reaches values up to 1160°C in this region. Four seconds after the beginning of the cooling, the principal stress is positive over a larger portion of the leading edge which

represents 31 mm about the axis of the gas stream and reaches a maximum value of 400 MPa (tension) in the middle of the portion. This maximum is about four times that of the values obtained at the end of the heating cycle. However, the temperature reached only 790°C which is few hundreds of degrees lower.

In Figure 5.21, the longitudinal position of the oxide spikes and of the cracks along the leading edge reported in Tables 4.2 and 4.3 of Subsection 4.1 is compared to the distribution of the principal stress and temperature profiles. The location of the cracks generally corresponds to the location of the two maxima obtained during heating although some cracks also appeared between the maxima. No cracks appeared outside the portion of the leading edge in tension during heating even if significant tensile stresses occur over a larger portion during cooling. The present results demonstrate that the thermal and stress-strain analyses are valid in terms of their spacial distributions and that there is a coupling effect between the stress and the temperature on the cracking process. This coupling effect will be quantified at this location of the specimen by using the fatigue life prediction models in the Subsection 5.3.

The coupling effect between the stress and temperature on crack damage is also illustrated for the case of the tip end of the specimens. In Figure 5.19, it can be seen that two high stress regions are generated from thermal distortion that prevails at the tip end of the specimen. This occurs along the geometric discontinuities, between the flat and the wedged portions of the specimen. Such thermal distortion often results in tip cracking of unshrouded DS commercial blades [83]. In the present specimens, no tip cracking was observed because the tip temperature was only about 325°C, which is considerably below the value experienced by blade tips under real service conditions in engines.

Figure 5.22 gives the variation of the thermal strain (ϵ_{33}^{th}), the elastic strain

(ϵ_{33}^e), the plastic strain (ϵ_{33}^p), the mechanical strain ($\epsilon_{33}^{mech} = \epsilon_{33}^e + \epsilon_{33}^p$) and the total or net strain ($\epsilon_{33}^{net} = \epsilon_{33}^{th} + \epsilon_{33}^e + \epsilon_{33}^p$) at the most stressed location along the leading edge ($z = 29.75$ mm) during heating. The thermal strain is dominant during the heating portion of the thermal cycle compared to the mechanical strains. As expected, the elastic and plastic strain histories present compressive and tensile peaks which correspond to that of the principal stress σ_{33} . The mechanical strain is mostly elastic as the plastic strain is negligible even during cooling, according to the thermo-elastoplastic analysis. In this case, a simple thermo-elastic analysis may give reasonably realistic strain values but was not used since the stresses can be overestimated. In the next subsection, the thermo-elasto-viscoplastic analysis will provide more realistic results, especially for the plastic strain.

Figures 5.23 to 5.25 show the stress variations as a function of the different types of strains ϵ_{33}^{th} , ϵ_{33}^e , and ϵ_{33}^p , for the same location ($z = 29.75$ mm). It appears from Figure 5.23 that the stress-thermal strain loop is a typical case of Counterclockwise Diamond, as found in thermal fatigue cycling of turbine airfoils [25]. In this case, the phasing between the mechanical and the thermal strains is just between the In-Phase and Out-of-Phase cases. With temperature, the stress-elastic strain and stress-plastic strain loops shown in Figures 5.24 and 5.25 are the only data required for life prediction from isothermal fatigue-oxidation models. The stress-elastic strain loop indicates that the mean stress is close to zero and that the stress is in tension when the component temperature reaches its maximum value. The stress-plastic strain curve is quite square and does not form a loop because the linear kinematics hardening was used to compute the plastic strain variation over one cycle only. The implications of these results on thermal fatigue are discussed in the next Subsection 5.3.

5.2.2.2 Thermo-elasto-viscoplastic Behaviour

Because of the limited space memory and the speed of the computer, the thermo-elasto-viscoplastic analysis was not successfully executed for all the elements of the mesh. Therefore, the thermo-elasto-viscoplastic analysis was limited to the elements exposed to the most severe thermo-mechanical conditions along the leading edge, located at $z = 38.25$ mm. The temperature variation and the principal mechanical strain ($\epsilon_{33}^{mech} = \epsilon_{33}^e + \epsilon_{33}^p = \epsilon_{33}^{net} - \epsilon_{33}^{th}$), as found from the thermo-elastoplastic analysis was used as an input for the thermo-elasto-viscoplastic analysis, in first approximation. The objective of this analysis using the Walker Subroutine is to obtain a more accurate estimation of the principal viscoplastic strain (ϵ_{33}^p) and of the thermal fatigue life from models based on plastic deformation.

Before carrying out this analysis, the capability of the Walker model to simulate the mechanical behaviour of René 80 using the parameters of B1900+Hf was first tested. In Figure 5.26, the calculated monotonic stress-strain curve at 980°C and at constant strain rate $3.33 \times 10^{-5} \text{ s}^{-1}$ (0.2%/min.) is compared to the experimental data taken from Chan et al. [118]. The shape of the curves are in much better agreement than was achieved with the linear kinematic hardening model used in the previous thermo-elasto-plastic analysis but the stress levels differ by 30% over a strain range of 1%. However, this is the best that can be done as the determination of the parameters from the right data requires the use of complex iteration schemes, a task which was over the time resources of the project.

Figure 5.27 shows the stress-plastic strain hysteresis loops representing the first thermal cycle in the burner rig resulting from the analysis at $z = 38.25$ mm along the leading edge. It can be noted that the plastic strain ranges from -0.016% to 0.49% which is 10 times larger than the computed value using the linear kinematic hardening

model. The stress range is quite different but the maximum stress at the end of the heating portion of the thermal cycle is similar indicating a stress of 110 MPa.

5.2.3 Conclusions

The stress-strain variation of each element of the DEW specimen was computed from the temperature variation, using a thermo-elastoplastic subroutine of the ABAQUS FE-code based on a linear kinematic hardening model. The principal stress, σ_{33} , as well as the temperature, was found to be highest in the portion of the leading edge directly exposed to the hot gas stream. Cracking occurs where both the temperatures and stresses are high along the leading edge during thermal cycling. This result confirms the validity of the thermal and the stress-strain analysis in terms of their spatial distributions and demonstrates that there is a coupling effect of the stress and the temperature on the cracking process.

The variation of the principal stress, at the location exposed to the most severe loading conditions along the leading edge, shows a compressive peak at the beginning of the heating cycle and a tensile peak at the beginning of the cooling cycle. The stress stabilizes to a moderate tensile value during heating. The coupling between the stress and the temperature is complex as demonstrated by the stress-thermal strain loop which corresponds to the Counterclockwise Diamond phasing case between the mechanical and the thermal strains.

According to this thermo-elastoplastic analysis, the comparison between the variation of the different natures of the strain (thermal, elastic, plastic) shows that the thermal strain is dominant and that the mechanical deformation mostly occurs in the elastic regime. The stress-elastic strain loop reveals that the mean stress is close to zero and the tensile regime occurs at high temperature during thermal cycling.

A thermo-elasto-viscoplastic analysis using the Walker model, modified to take into consideration the orthotropy of the elastic properties of the tested DS material was

also undertaken to obtain a more accurate estimation of the inelastic strain and of the stress relaxation. This analysis was limited to one location at the leading edge which was exposed to the most severe thermo-mechanical conditions, and to only 10 thermal cycles, because of the lack of computer capacity. The plastic strain range was found to be 10 times larger than the computed value obtained with the thermo-elastoplastic model. The maximum tensile stress developed during heating cycle was 110 MPa.

5.3 Thermal Fatigue Damage Modelling

This Subsection proposes an approach for thermal fatigue life prediction from four isothermal fatigue-oxidation models presented in Subsection 2.2.2. The fatigue life of the elements along the leading edge of DEW specimens tested in the burner rig are then evaluated with this approach and compared to experimental measurements given in Section 4. Life prediction is also computed from a thermo-mechanical creep-fatigue-oxidation model which is compared to the results obtained from the isothermal fatigue-oxidation models. Before embarking into life prediction of the DEW specimens, the theoretical and experimental validities of the models are discussed.

5.3.1 Theoretical and Experimental Validities of the Models

In order to compare the validities of the different fatigue-oxidation models presented in Subsection 2.2.2, their theoretical hypotheses and their application to experimental results are discussed in this subsection. A description of the different models is summarized in Table 5.11. The fatigue-oxidation mechanism, the mathematical expression of the life to failure, N_f , the variables and the constants employed, as well as the type of tests used to determine the constants are given in the table for each of the models described.

5.3.1.1 Theoretical Validity

The Coffin and Ostergren empirical models are not based on a specific mechanism but take into consideration the time-dependant oxidation damage on life to failure in terms of the effective cyclic frequency, $\nu_{\text{eff}} = 1/(\Delta t + t_h)$, where Δt is the cyclic period and t_h is the hold time during tension and/or during compression ($t_h = t_{hT} + t_{hC}$). The driving force for crack propagation in Coffin's models is the elastic or plastic strain range whereas in the Ostergren model, it is the hysteretic tensile energy given by the product of the maximum stress and the plastic strain range. Both models are relatively simple and require the determination of three constants by multiple regression analysis of data obtained from strain-controlled isothermal fatigue tests conducted with different strain ranges and effective cyclic frequencies.

The other four models, Antolovich et al., Romanoski et al., Reuchet-Rémy and Neu-Sehitoglu are based on postulated or identified mechanisms of environmentally assisted oxide spike or crack growth to a critical length which leads to rapid crack propagation (controlled by mechanical loading) and eventual failure. The two possible

mechanisms (named A and B and described in Subsection 2.2.1) are well identified and are considered in the development of the models of Romanoski et al. and Neu-Sehitoglu, contrary to the models of Antolovich et al. and Reuchet-Rémy which apply for both cases.

The models of Antolovich et al. and Romanoski et al. define the critical oxide spike length, x_f or a_f , in terms of a fracture mechanics failure criterion whereas these quantities are determined experimentally in the Reuchet-Rémy and Neu-Sehitoglu Models. The general form of the failure criterion is given by $\sigma_{\max} \cdot a_f^p = K_c$ where the left term of the same formulation as the basic definition of the stress intensity factor and the right term related to the material fracture toughness. The reader could be surprised to note that a concept issue of the LEFM theory is used at high temperature (up to 1000°C) where plastic and creep deformations are obviously not confined only to the crack tip. Actually, in the LEFM theory [46], the fracture is assumed to be of brittle nature with very limited plasticity and the stress distribution around a defect or a crack and within the body of a component is determined by assuming an elastic stress field. Two factors can be used to justify the validity of the LEFM concept under such conditions. First, the dominant fracture characteristic at the crack tip is its brittleness due to the effect of oxygen dissolution into the material at the crack tip. Also, the stress distribution under the uniaxial fatigue test conditions is uniform in the specimen under both elastic or plastic conditions.

Table 5.11 Summary of oxidation-fatigue models studied in this Subsection.

Model	Mechanism ₍₁₎	Equation ₍₂₎	Variables	Constants	Tests _(3,4)
Coffin [5, 7, 8]	---	$N_f = \left(\frac{A'}{\Delta \sigma} \right)^{1/\beta'} \frac{k_1' \beta'}{v_{eff}} ; \quad (\Delta \sigma = E \Delta \epsilon_e) ; \quad f o r N > N_c$	$\Delta \sigma$ (or $\Delta \epsilon_e$), v_{eff}	$A', \beta', k_1', (E)$	IF
		$N_f = \left(\frac{C_2}{\Delta \epsilon_p} \right)^{1/\beta} \frac{1}{v_{eff}^{(1-k)}} ; \quad N < N_c$	$\Delta \epsilon_p, v_{eff}$	C_2, β, k	IF
Ostergren [9]	---	$N_f = \left(\frac{C}{\sigma_{max} \Delta \epsilon_p} \right)^{1/\beta} \frac{1}{v_{eff}^{(1-k)}}$	$\sigma_{max}, \Delta \epsilon_p, v_{eff}$	C, β, k	IF
Antolovich et al. [1]-[4, 16, 18, 19]	A, B	$N_f = \left(\frac{K}{\sigma_{max}} \right)^{n/p} \frac{1}{v_{eff}}$ <p>With:</p> $K = K_0 \left[\frac{\exp \left(\frac{Q_0 - V_m \sigma_{max}}{RT} \right)}{n k'_{s0}} \right]^{p/n}$	σ_{max}, v_{eff}, T	$K_0, n, p, k'_{s0}, Q_0, V_m (n/p = 8)$	IF (OX)
Romanoski et al. [3]	A	$N_f = \left[\frac{K_f}{\sigma_{max} (\sigma_{max} - \sigma_{th})^{m/2}} \right]^2$	σ_{max}	$K_f, \sigma_{th}, m (m=2)$	IF

Model	Mechanism ₍₁₎	Equation ₍₁₎	Variables	Constants	Tests _(1,2)
Reuchet-Rémy [24]	A, B, Carbide Oxidation	$N_f = \frac{1}{B} \ln \left[\frac{B a_f}{\left(\frac{da}{dN} \right)_{ox}} + 1 \right]$ $B = \alpha \Delta \epsilon_p \left[\frac{1}{\cos \left(\frac{\pi}{2} \frac{\sigma_{max}}{\sigma_f} \right)} - 1 \right]$ $\left(\frac{da}{dN} \right)_{ox} = \left(\frac{da}{dN} \right)_{ox, M} (1 - f_c^*) + \left(\frac{da}{dN} \right)_{ox, c} f_c^*$ $\left(\frac{da}{dN} \right)_{ox, M} = n k_M^{\frac{1}{n}} \left[1 + k_{cyc0} \frac{\Delta \epsilon_p}{2} \right] v_{eff}^{-1/n}$ $\left(\frac{da}{dN} \right)_{ox, c} = 4 k_{c0}^{\frac{1}{4}} \exp \left(\frac{V_m \sigma_{max}}{12 R T} \right) v_{eff}^{-1/4}$	$\Delta \epsilon_p, \sigma_{max},$ v_{eff}, T	$a_f, \sigma_f, \alpha,$ $n, k_M,$ $k_{cyc0}, k_{c0},$ f_c^*, V_m	IF OX

With:

Model	Mechanism _(*)	Equation _(**)	Variables	Constants	Tests _(***)
Neu-Sehitoglu [26-30]	B	$\frac{1}{N_f} = \frac{1}{N_f^{fat}} + \frac{1}{N_f^{ox}}$ <p>With:</p> <p>N_f^{fat} defined from the relation of Manson-Hirshberg [54]</p> $N_f^{ox} = \left[\frac{X_f \delta_0}{B \Phi^{ox} k_p^*} \right]^{1/\beta} \frac{\dot{\epsilon}^{1 - (a/\beta)}}{2 (\Delta \epsilon_{mech})^{(2/\beta) + 1}}$ $\Phi^{ox} = \frac{1}{\Delta t + t_h} \int_0^{\Delta t + t_h} \exp \left[-\frac{1}{2} \left(\frac{(\dot{\epsilon}_{th}/\dot{\epsilon}_{mech}) + 1}{\xi^{ox}} \right)^2 \right] dt$ $k_p^* = \frac{1}{\Delta t + t_h} \int_0^{\Delta t + t_h} k_{po} \exp \left(\frac{-Q}{RT} \right) dt$	$\Delta \epsilon_{mech}, \dot{\epsilon}_{th},$ $\dot{\epsilon}_{mech}, T$ $v_{eff} =$ $1/(\Delta t + t_h)$	$x_f, \delta_0, B,$ $\beta, a, \xi^{ox},$ k_{po}, Q	IF (at low and high T) TMF (OP IP) OX

*: A and B refer to mechanisms described in Subsection 2.2.1.

** : For all the models, the effective frequency, v_{eff} , have been used instead of the continuous frequency, v . In the Equation of Ostergren, σ_T have been substituted by σ_{max} . All other symbols keep their usual meaning as described in Subsection 2.2.2.

***: OX, IF, TMF refer to oxidation, isothermal fatigue and thermo-mechanical fatigue tests, respectively.

The solutions predicted by the LEFM should apply to uniaxially loaded specimens subjected to high temperatures and for inelastic deformations. In more complex geometries where stress gradients are inevitable, a local stress approach has to be used and consists in computing the stress distribution within the specific geometry using the elasto-viscoplastic flow equations and using the local stress next to the crack in the fracture criterion.

Most of the models use the maximum stress (alone or with another factor) as the driving force for crack or oxide spike growth. Even in the elastic strain range model of Coffin, the maximum stress is considered via the stress range which applies for lives as short as hundreds of cycles in nickel-base superalloys, their transition lives, N_t , being demonstrated to be lower than one hundred cycles [7]. The use of the maximum stress is believed to be more justified than the use of $\Delta\epsilon_p$ for many reasons. First, the fracture enhanced by oxidation is brittle and consequently controlled by the tensile stress in contrast to a ductile fracture which is controlled by plastic deformation [46]. This does not preclude the role of plastic deformation in the fracture process, which promotes oxygen diffusion, as well as fatigue damage by increasing the dislocation density and its distribution. Plastic deformation is, in fact, a variable used in some models (as in the modified Coffin-Manson Law). The second reason for using the maximum stress instead of converting it to the plastic strain range or using the total strain range, is that stress relaxation (during hold time) and cyclic hardening or softening phenomena occur during strain-controlled fatigue. Such evolution of the maximum stress influences the crack growth rate and the critical crack length to failure. These effects can not be partially or totally represented by the use of $\Delta\epsilon_p$ and especially $\Delta\epsilon$. A third advantage offered by the use of the maximum stress is its capacity to rationalise the effect of the elastic anisotropy on the fatigue life of DS materials, as discussed in Subsection 2.2.1.2.

On the other hand, The models of Reuchet-Rémy and Neu-Sehitoglu use explicit

linear fatigue-oxidation interaction rules and complex equations for predicting the life controlled by cyclic oxidation whereas in the other models, the fatigue-oxidation interaction is implicitly determined by the experimental determination of the constants.

5.3.1.2 Experimental Validity

The theoretical considerations of the models, empirical or mechanistically based, need to be experimentally verified for each of the models in order to determine fatigue-oxidation life with any degree of accuracy. The respective authors have shown their life predictions to be in reasonably "good agreement" with the experimental data. A statistical analysis has been carried out and the standard relative deviation or average relative error of predicted vs experimental life is compared. Also, the correlation factor, R , between graphical representations of calculated and experimental data is presented.

In order to compare the prediction capacities of the models, the same sets of data and the same statistical criterion must be used. The data obtained from strain-controlled IF tests on CC René 80 conducted at 871°C and 982°C with different continuous cyclic frequencies (0.034-56.7 cpm) and hold times in compression and in tension (0-30 min) were collected from various studies [5, 6, 14] for comparison. The data cover a wide range of testing conditions and explicitly includes the values of the maximum stress, the plastic range and the corresponding life to failure. The data are reproduced in Tables J.1 to J.6 of Appendix J. The average relative error (RE) of the predicted life is used in this comparison:

$$RE(\%) = \frac{100\%}{n} \sum_{i=1}^n \frac{|(N_{f \text{ cal}})_i - (N_{f \text{ exp}})_i|}{(N_{f \text{ exp}})_i} \quad (138)$$

where $N_{f \text{ cal}}$ and $N_{f \text{ exp}}$ are respectively predicted and experimental fatigue life for n

measurements.

The values of the constants of each model which minimize the RE are determined by multiple regression using programs written in Basic, presented in Appendix J. A specific program is used to enter the values (v , t_{HT} , t_{HC} , $\Delta\epsilon_p$, $\Delta\sigma$, σ_{max} , N_f) of each set of data in different files, while other programs are used to calculate the values of the constants and the corresponding RE, according to two methods.

Since the models of Reuchet-Rémy and Neu-Sehitoglu require the measurement of some parameters which are not provided by the studies [5, 6, 14] and since the determination of the other parameters by regression is very difficult due to the relative complexity of these models, they were not submitted to this analysis. On the other hand, Romanoski et al.'s Model does not explicitly express the effect of the effective cycle frequency on life. In order to include this model in the analysis, the constant K_f which is directly related to the grain boundary cohesive strength, can be replaced with a function of v_{eff} as:

$$K_f(v_{eff}) = K_{f0}(v_{eff})^{1/2n} \quad (139)$$

where K_{f0} is the new constant and $1/2n$ is a positive exponent. This relation can be obtained from the substitution of the proportionality $R \propto v_{eff}^{1/n}$ (defined in the footnote of Subsection 2.2.2.4) in the derivation of the constant, K_f , of the model of Romanoski et al.

Table 5.12 gives the RE for the four models and six data sets given by Tables in Appendix J. Ostergren's Model globally has the lowest RE with an average value of $16\% \pm 6\%$ at 871°C , closely followed by Coffin's Models, whereas the model of Antolovich et al. is associated with the highest error. For some of the models, this RE is doubled at 982°C relative to the RE at 871°C and can be as large as 1255% in the

case of Antolovich et al.'s Model. The models of Ostergren and Coffin are judged the best based on the relative error.

The capability of the models to predict the effect of hold time during compression was also evaluated. The usual definition of the effective frequency and the modified effective frequency, as proposed by Coffin and Ostergren, defined by Equations 5 and 40, were employed to predict the life given by the C1 data set. Effective frequency considers tensile and compressive hold time to be equally damaging, whereas the modified effective frequency considers the damaging effect of unreversed tensile creep to be greater than the compressive creep. The RE resulting from both frequency definitions are presented in the columns C1 and C1' of Table 5.12. The use of the modified effective frequency definition reduced the error by a factor of two, except in the case of the Ostergren model which handles the compressive strain hold time effect (RE = 10% in each case) equally well.

Table 5.12 Life prediction relative error, RE, for different models and data sets obtained for IF tests on CC René 80 [5, 6, 14].

Model	RE(%) on $N_{f,cal}$ at 871°C						982°C	
	Continuous Cycling			Hold Time			\overline{RE} (%)	Cont. Cyc.
	A1 [14]	C3 [5]	C4 [5]	A2 [14]	C1 [6]	C1' [6]		A3 [14]
Coffin ($\Delta\epsilon_p$)	28.8	37.9	16.0	29.2	38.6	15.8	28±9	47.2
Coffin ($\Delta\epsilon_p$)	19.3	19.6	32.9	4.0	32.7	17.2	21±10	25.2
Ostergren	17.1	20.7	28.0	11.0	10.4	10.7	16±6	30.5
Antolovich et al.	70.6	155.7	82.3	57.6	105.5	76.1	91±32	1255.2
Romanoski et al.	69.6	38.0	14.2	49.1	50.3	14.8	39±21	209.3

Where:

RE is the error of predicted life relatively to experimental life;

\overline{RE} is the average RE for data sets obtained from fatigue tests conducted at 871°C;

For the A1, C3, C4, A2, C1 and A3 data sets, the life was calculated with the usual definition of the effective frequency (Equation 5) whereas for C1', the modified effective frequency was used (Equation 9).

The applicability of the models in terms of their RE can be evaluated on the distribution of the scatter in $N_{f,cal}$ vs $N_{f,exp}$ plots, as illustrated in Figures 5.28-5.36. Continuous cycling data set (C4) and hold time in tension and in compression data set (C1) are employed for this evaluation. In continuous cycling conditions, Figures 5.28-5.31, the scatter obtained from all the models is small and uniformly distributed except for the Antolovich et al. model which gives a large scatter, underestimating the short fatigue life and overestimating the long life.

Under compressive strain hold time conditions shown in Figures 5.32-5.36, Coffin models exhibit a constant predicted life when the usual effective frequency

definition is employed and it overestimated the life when the modified definition of the effective frequency for short lives is used. The models of Ostergren and Romanoski et al. give the lowest scatter. In particular, the Ostergren model results in the lowest scatter for both short and long life and is independent of the effective frequency definition used. Antolovich's Model shows the poorest prediction lives.

From these observations, it can be concluded that a proper relation between the effective frequency and the life is required and that the effect of hold time on the maximum stress, σ_{\max} , also has to be incorporated into the models, as specified by the models of Ostergren and Romanoski et al. The use of a modified effective frequency, which postulates a beneficial effect of the hold time during compression on life, reduces the relative error, except in the case of Ostergren's Model which predicted a life within 10% independently of the effective frequency formulation employed. Thus, it cannot be clearly concluded that the compressive strain hold time is beneficial to fatigue-oxidation life for the particular case of CC René 80.

In addition to the evaluation of predictive capabilities of the models, the stability of the constants found for different data sets obtained at the same temperature should be considered since this variable was not included in all models. Table 5.13 presents the average value and the relative standard deviation STD (in %) of the various constants and exponents found for data sets obtained from IF tests at 871°C on CC René 80. The constants varied from $\pm 25\%$ to $\pm 85\%$ whereas the exponents varied from $\pm 10\%$ to $\pm 55\%$ (except for k_1' of the Coffin Model with a STD of $\pm 155\%$). Considering the strong influence of exponents on the calculated life, the models which have low variance of their constants and especially very low variance of their exponents are the best. On this basis, the models can be listed into the following decreasing order of performance: Coffin ($\Delta \epsilon_p$), Ostergren, Antolovich et al., Romanoski et al. and Coffin ($\Delta \epsilon_c$).

The constants and exponents were also determined from one data set at 982°C (A3 from [14]). Theoretically, the exponents' value (β' , k' , β , k , p , n) should not change with temperature if the mechanism(s) of deformation, oxygen diffusion, or oxidation do not change significantly. In practice, these exponents can vary just because of the experimental scatter, as shown in Table 5.13. The values of the constants (A' , C_2 , C , K , K_0) are related to mechanisms mentioned above which are thermally activated. Their variation should follow an Arrhenius type of expression of the form of:

$$cte = cte_0 \exp\left(\frac{A}{RT}\right) \quad (140)$$

where A is a pseudo activation term or a term associated to the activation energy, Q , involved in the oxide spike or crack growth. This type of expression has been explicitly used by the models of Antolovich et al., Reuchet-Rémy, and Neu-Sehitoglu. Table 5.13 gives the values of A associated with the constant of the various models. However, in computational damage modelling, it may be more accurate to use the proper set of constants and coefficients interpolated at the temperature of interest than using an Arrhenius expression for the evaluation of the constants at the temperature of interest with a specific value for each exponent.

Table 5.13 Values of the model constants and exponents determined from data sets obtained for isothermal fatigue tests carried out at 871°C and at 982°C on CC René 80 (after A1, A2, A3, C1, C3 and C4 data sets [5, 6, 14]).

Model	Constants	871°C	STD (%)	982°C	A/R
Coffin ($\Delta\epsilon_e$)	E (MPa)	153795	0.6	140000	1215
	A' (MPa)	5281	53.6	2078	12070
	β'	0.241	37.6	0.218	---
	k_1'	0.124	154.2	0.091	---
	$N_t(\bar{v}_{eff})$	140	41.4	130	---
Coffin ($\Delta\epsilon_p$)	C_2	0.550	56.2	0.250	10200
	β	0.845	13.2	0.776	---
	k	1.051	10.1	1.026	---
Ostergren	C	421.5	75.3	63.84	24410
	β	0.922	19.7	0.784	---
	k	0.923	19.5	1.003	---
Antolovich et al.	K (MPa)	2036	84.8	1018	8965
	n/p	6.170	39.5	4.055	---
Romanoski et al.	K_{10} (MPa ²)	4.32×10^6	26.2	2.04×10^6	9705
	S_{th} (MPa)	97.6	83.4	0.0	---
	n	2.102	53.7	7.299	---

Where:

STD is the standard deviation of the values of the constants and exponents determined from different data sets obtained from IF tests at 871°C;

A is a pseudo thermal activation term as defined in Equation 140;

and all the other symbols of the Equations of Table 5.11 have been defined in Subsection 2.2.2.

5.3.2 Prediction of Thermal Fatigue Life from Burner Rig Conditions

The fatigue life models, that were previously presented and evaluated in this Subsection, are now considered for prediction of the thermal fatigue (TF) life for burner rig (BR) testing conditions. The models include the isothermal fatigue-oxidation (IF) models of Coffin, of Ostergren, of Antolovich et al., of Romanoski et al., and the thermo-mechanical fatigue (TMF) model of Neu-Sehitoglu. The model of Reuchet and Rémy is not considered because the determination of its parameters requires more information than provided in the literature.

In order to predict the fatigue life in the BR, the isothermal fatigue-oxidation damage models must incorporate the temperature cycling effects on the TF behaviour. Only the Neu-Sehitoglu model is applicable in the predicting of the life under TMF and TF conditions present in the BR. In theory, only models with constants determined from TMF tests should be applied to thermal fatigue cases [26].

However, in practice, the method which consists of applying isothermal fatigue-oxidation damage models with the constants determined at the highest temperature in the BR (or in aero-engines during service), was shown to reasonably estimate the TMF life. For instance, Cook et al. [10] successfully applied this method along with Ostergren model to predict the fatigue life of CC René 80 tested in-phase, out-of-phase and diamond strain-temperature cyclic conditions (between 760°C and 982°C). The success of this method seems to be attributed to the fact that damage mostly accumulates at maximum temperature, especially when a hold time is imposed at high temperature. In the BR case, the periods between low and high temperature are quite fast (< 10 seconds) compared to the hold time at high temperature (≥ 140 seconds) and can be regarded as equivalent to a quench. The oxidation damage and the creep deformation occur mostly during the hold period at high temperature and the temperature cycling can be

considered to cause thermal strains and stresses only. This method certainly simplifies the testing and numerical procedures for obtaining the constants and will have to be validated by comparing the predicted life with the experimental life.

The overall methodology used to determine the constants for the high temperature LCF life prediction models of Coffin, Ostergren, Antolovich et al. and Romanoski et al. is presented in the following subsection. Subsequently, the fatigue life of the DEW specimens tested in the BR is computed. The results obtained from this simplified method are compared to those obtained with the more complex model of Neu-Sehitoglu. The creep damage life is also evaluated with the latter model in order to check if this factor can really be neglected.

5.3.2.1 Methodology for the Determination of the Constants for IF Life Prediction Models

Subsection 5.3.1.2 showed the method for determining the parameters used for the models of Coffin, of Ostergren, of Antolovich et al. and of Romanoski et al. by fitting the results of isothermal fatigue tests conducted on polycrystalline René 80 at high temperature in air [5, 6, 14].

The variables employed in the four isothermal fatigue models are the temperature, the maximum stress, the stress and plastic strain ranges, the continuous cycling frequency and the hold time. These values for every element of the leading edge are determined by the thermal and the mechanical analysis based on a elasto-plastic model, as presented in Subsections 5.1 and 5.2. The elasto-viscoplastic model of Walker was only used for one element of the LE. Figure 5.37 shows the variation of the temperature and the principal stress (σ_1) during one thermal cycle. The stress as well as the

temperature change rapidly at the beginning of the heating and the cooling cycles and stabilize during heating and cooling. This complex variation could not be accounted by the models. The problems to be solved are the temperature at which the parameters of the models must be evaluated, the maximum stress or stress range that must be used, and the effective cycling frequency that should be determined.

As suggested by Cook et al. [10], the parameters have to be evaluated at the highest temperature encountered during thermal cycling, because damage accumulation is more important at high temperature. This method implies that the maximum stress is evaluated at the end of the heating cycle, that the effective frequency is equal to the inverse of the total period of the thermal cycle, and that the tensile peak at the beginning of the cooling cycle is negligible at lower temperature. A better approach is proposed here. Lets consider separately the temperature-stress unsteady states (USH during heating and USC during cooling) and the temperature-stress steady states (SSH during heating and SSC during cooling) in the thermal cycle (refer to Figure 5.37) and assume linear damage accumulation. The fatigue life or life to failure (N_f) is then given by:

$$\frac{1}{N_f} = \frac{1}{N_{f, US}} + \frac{1}{N_{f, SS}} \quad (141)$$

where $N_{f, US}$ and $N_{f, SS}$ are the fatigue life of the unsteady (transient) and steady state temperature-stress correlation. In the determination of $N_{f, US}$, the maximum stress ($\sigma_{max, US}$) corresponds to the value of the tensile peak during cooling. The effective frequency ($\nu_{eff, US}$) is given by the inverse of the sum of the unsteady state periods for heating and cooling ($\Delta t_{USH} + \Delta t_{USC}$) and the model parameters are evaluated at the temperature (T_{US}) corresponding to the tensile peak. In the determination of $N_{f, SS}$, the maximum stress ($\sigma_{max, SS}$) corresponds to the value of the tensile plateau during heating, the effective frequency ($\nu_{eff, SS}$) is given by the inverse of the sum of the steady state periods ($\Delta t_{SSH} + \Delta t_{SSC}$) and the parameters of the models are evaluated at the maximum

temperature (T_{ss}) during cycling. According to Figure 5.37, the values for Δt_{USH} , Δt_{USC} , Δt_{SSH} and Δt_{SSC} are 15, 25, 135 and 65 seconds, respectively, which sets the value of $v_{eff, US}$ at 0.025 Hz (1.5 cpm) and the value of $v_{eff, SS}$ at 0.005 Hz (0.3 cpm). A program written in Basic to facilitate the computation of the fatigue life is given in the Appendix K including the values of the parameters and the variables used.

5.3.2.2 Life Prediction Results

5.3.2.2.1 Predicted Life from Isothermal Fatigue-Oxidation Damage Models

Life to failure (N_f) along the leading edge was estimated with the four high-temperature LCF life prediction models, following the methodology explained in the previous Subsection. Table 5.14 gives the shortest fatigue life ($N_{f, US, min}$, $N_{f, SS, min}$, $N_{f, min}$) obtained for the region exposed to the most severe thermo-mechanical loading conditions along the leading edge which is located at $z = 38.25$ mm. The Table gives the life computed from the elasto-plastic analysis and from the elasto-viscoplastic analysis in order to show the influence of the plastic deformation and stress relaxation which is underestimated in the first analysis.

The life for the case of damage accumulation occurring during the unsteady state cycles, $N_{f, US, min}$, are many orders of magnitude larger than for the case of damage accumulation occurring during the steady state cycles, $N_{f, SS, min}$, so that the values of $N_{f, SS, min}$ are equivalent to the life associated with the total damage accumulation during cycling, $N_{f, min}$ (obtained from the combination of $N_{f, US, min}$ and $N_{f, SS, min}$ using Equation 141). This indicates that the damage accumulation occurring during the unsteady state temperature-stress cycle has a negligible effect on fatigue life in the specimens tested in the burner rig under the conditions experienced during the thermal fatigue program reported in Subsection 3.1.3.

Only the values of the life computed with the Coffin ($\Delta\epsilon_p$) and Ostergren models were affected by the nature of the mechanical analysis because they explicitly depend on the plastic deformation. The minimal life computed from the results of the more realistic elasto-viscoplastic analysis were found to vary from 1 to 74 cycles, except with for the model of Romanoski et al. which gave a life of 3600.

The life was also determined along the leading edge using the same methodology as previously presented. The life was found to be many orders of magnitude higher, where the temperatures and the stresses computed from the elasto-plastic analysis were considerably lower. Figures 5.38 to 5.41 show the distribution of the probability to get a crack during the first $N_{f, \min}$ (approximated by the ratio $N_{f, \min}/N_f$, where $N_{f, \min}$ is given in Table 5.14) found from each model and compare this probability distribution to the cracks distribution observed in all specimens. It can be noted that the cracks are more frequently found in the regions corresponding to the location of the two stress and cracking probability maxima. On both sides of the portion of the specimens where these maxima are located, the probability to get a crack during the first $N_{f, \min}$ cycles drops sharply and no crack were observed in these portions of the specimens.

Table 5.14 Minimal fatigue life at the leading edge of the DEW specimen as computed from different fatigue-oxidation models and from the results of two mechanical analyses.

Fatigue-Oxidation Model	Elasto-plastic Analysis			Elasto-viscoplastic Analysis		
	$N_{f, \text{US, min}}$	$N_{f, \text{SS, min}}$	$N_{f, \text{min}}$	$N_{f, \text{US, min}}$	$N_{f, \text{SS, min}}$	$N_{f, \text{min}}$
Coffin ($\Delta\sigma$)	1000000	5	5	5400000	1	1
Coffin ($\Delta\epsilon_p$)	11000	310	300	1590	45	44
Ostergren	170000	140	140	7810	21	21
Antolovich et al.	65000	74	73	2600000	74	74
Romanoski et al.	7900	3600	2500	310000	3600	3600

where:

$N_{f, \text{US, min}}$ is the minimal fatigue life associated with damage accumulation occurring during unsteady state temperature-stress cycling;

$N_{f, \text{SS, min}}$ is the minimal fatigue life associated with damage accumulation occurring during steady state temperature-stress cycling;

$N_{f, \text{min}}$ is the minimal fatigue life associated with the total damage accumulation occurring during thermal cycling.

5.3.2.2.2 Predicted Life from a TMF Fatigue-Oxidation-Creep Damage Model

The model of Neu-Sehitoglu was also used to compute the life for pure fatigue (N_f^{fat}), oxidation-fatigue (N_f^{ox}), creep-fatigue (N_f^{creep}) and overall failure life (N_f), using the linear damage interaction rule (Equation 35 of Subsection 2.2.2.6). Values were obtained for the location where the fatigue life determined with the IF models above was found to be minimal (see details of this computation in Appendix K). The constants of the model were evaluated by Sehitoglu and Boismier [28] from TMF tests on CC Mar-M247, a nickel-base superalloy similar to René 80. It is determined that the failure life (N_f) is 17 cycles, with $N_f^{\text{fat}} = 210$ cycles, $N_f^{\text{ox}} = 16$ cycles and $N_f^{\text{creep}} = 55000$ cycles. It is clear from this result that the oxidation-fatigue damage interactions are dominant, leading to a very short predicted life, and that pure fatigue and creep damage modes have a negligible effect for the hold time conditions experienced in the BR, as assumed in this Subsection. Compared to values in Table 5.14, the life found from the Neu-Sehitoglu model is of the same order of magnitude than that obtained from the first three high-temperature LCF life prediction models previously used, which suggest that the methodology using the later class of models can be valid a priori.

5.3.2.3 Comparison of Predicted and Experimental Life

Before comparing the predicted life obtained in the last Subsection from the different models with the experimental lives obtained from the thermal fatigue tests in the burner rig, two factors have to be considered:

- 1- The life to failure values for IF and TMF tests were obtained with the stress drop technique (SD) whereas the life to crack initiation for TF tests in the BR was assessed with the ACPD technique. Both techniques do not have the same sensitivity.
- 2- The specimens tested for the determination of the model parameters were obtained by conventional casting (CC) of René 80 resulting in a polycrystalline microstructure, whereas the specimens tested in the BR of the same alloy composition were directionally solidified (DS) resulting in columnar grains oriented in the load direction. Under high temperature fatigue conditions in air, polycrystalline alloys show a shorter life than the DS alloys [33, 43], because many grain boundaries are perpendicular to the load direction for the conventionally cast alloys.

In the next Subsections, two correcting factors, defined as life ratios, are proposed and applied to the predicted life in order to rationalize these differences and which allow a valid comparison between predicted and experimental life.

5.3.2.3.1 Comparison of SD and ACPD Techniques

The fatigue life determined by these two techniques are conceptually equivalent in that the current flow and the stress flow in a body near its surface are analogous and have to bypass the geometrical discontinuities (cracks) at the surface. First, the sensitivity of each technique and its effect on the fatigue life must be compared. The spatial resolution which is defined as the length of the smallest detectable crack, must be first established. The resolution of the ACPD technique, a_{ACPD} , for the BR testing conditions was estimated to be of 200 μm . The resolution of the SD technique used in the determination of the parameters of IF models (Coffin, Ostergren, Antolovich et al., Romanoski et al.), is limited by the testing conditions and specimen geometry employed, giving values of a_{SD} of the order of 1000 μm [5, 6, 14]. For the determination of the parameters of TMF model of Neu-Sehitoglu, a_{SD} is of the order of 500 μm [28].

From the knowledge of these resolutions, the relation between the life obtained from both techniques can be estimated from the life ratio $R_{ACPD/SD}$ generally defined as:

$$R_{ACPD/SD} = \frac{N_f(a_{ACPD})}{N_f(a_{SD})} \quad (142)$$

where $N_f(a)$ is the fatigue life function of the crack length. The form of the function depends of the damage accumulation assumed by each of the models presented. For the case of the Coffin and of Ostergren models, the function is not defined. As for the Romanoski et al. model, where the crack growth rate da/dN is assumed constant until failure, the relation between the fatigue life and the crack length can be assumed to be

linear for these models. The ratio $R_{ACPD/SD}$ is then given by:

$$R_{ACPD/SD} = \frac{a_{ACPD}}{a_{SD}} \quad (143)$$

and thus $R_{ACPD/SD} = 200/1000 = 0.2$. In the case of the Antolovich et al. model, the crack growth rate is assumed to follow a parabolic oxidation kinetics law, which means that the crack length varies with the square root of the life. The ratio $R_{ACPD/SD}$ is then given by:

$$R_{ACPD/SD} = \left(\frac{a_{ACPD}}{a_{SD}} \right)^2 \quad (144)$$

and thus $R_{ACPD/SD} = (200/1000)^2 = 0.04$. In the case of the Neu-Sehitiglu model, the crack growth rate is assumed to follow a power law (with the power equal to $3/2$ for a nickel base superalloy [26]), which means that the crack length varies with the life to the power $2/3$. The ratio $R_{ACPD/SD}$ is then given by:

$$R_{ACPD/SD} = \left(\frac{a_{ACPD}}{a_{SD}} \right)^{2/3} \quad (145)$$

and thus $R_{ACPD/SD} = (200/450)^{2/3} = 0.54$.

5.3.2.3.2 Comparison of CC and DS Alloys

As in the previous problem, the effect of the alloy microstructure obtained from the two different casting processes, CC and DS, on fatigue life can be rationalized through a life ratio $R_{DS/CC}$ simply expressed by:

$$R_{DS/CC} = \frac{N_f(DS)}{N_f(CC)} \quad (146)$$

This ratio can be approximated from the IF tests results on René 120, illustrated in Figure 2.2 [33]. The Figure shows that the DS alloy with the columnar grain structure oriented parallel to the load direction has roughly a life 1.7 order of magnitude longer than that of the CC alloy with equiaxed grain structure, at 982°C and for stresses less than 200 MPa. In other words, the ratio $R_{DS/CC} \approx 50$.

5.3.2.3.3 Correction of Predicted Life

By using the ratios $R_{ACPD/SD}$ and $R_{DS/CC}$, the predicted life obtained in Subsection 5.3.2.2, can be corrected to consider both the life assessment technique and the grain structure factors. The predicted life, $N_f(ACPD,DS)$, can be given as:

$$N_f(ACPD, DS) = R_{ACPD/SD} \cdot R_{DS/CC} \cdot N_f(SD, CC) \quad (147)$$

which approximates the experimental life of uncoated René 80 (DS) tested in the BR. For the coated substrates, because the coating has an equiaxed structure as for CC alloys, the $R_{DS/CC}$ ratio is not necessary and the corrected predicted life $N_f(ACPD,CC)$ can be represented as:

$$N_f(ACPD, CC) = R_{ACPD/SD} \cdot N_f(SD, CC) \quad (148)$$

The life prediction corrections are compared with experimental values in Table 5.15. The life to crack initiation of a crack of less than 200 μm in uncoated DEW specimens were determined to be 760 ± 20 cycles from measurements with the ACPD technique (see Subsection 4.2). All values of the predicted life are within an order of magnitude of the experimental values, with the best prediction provided by the model of Ostergren. The life of coated DEW specimens was found to be 300 ± 100 cycles from the ACPD measurements (Subsection 4.2). In this case, the predicted life is generally lower than the experimental value with up to 2.5 order of magnitude of difference. This may be attributed to the fact that the coating has a thickness of less than 50 μm at the LE (see Subsection 4.1.1.1) which is 4 times smaller than the resolution of the ACPD technique. Consequently, it maybe possible that the crack grows rapidly in the polycrystalline coating but it has to pass through about 150 μm of the DS substrate at a rate 50 times slower (according to $R_{DS/CC}$) before the crack is detected with the ACPD technique. In such a case, the life to failure of the coating is not 300 cycles

but about 150 times less, that is 2 cycles, a result in much better agreement with predictions.

It is not possible to select one model over another on the basis of the results of thermal fatigue tests on both uncoated and coated specimens, because the fatigue life ratios $R_{ACPD/SD}$ and $R_{DS/CC}$ used for the correction of predicted fatigue life are too approximative and because the number of different operating conditions of the testing program is limited. Nevertheless in general, the models were able to predict life within one order of magnitude.

Table 5.15 Corrected life predictions, $N_f(\text{ACPD,DS})$, computed from different models versus experimental life for initiation of a short crack, $N_{i,\text{exp}}$, obtained in the BR.

UNCOATED SUBSTRATE			
$N_{i,\text{exp}}$	Model	$N_f(\text{ACPD,DS})$	$\text{Log}\left(\frac{N_f(\text{ACPD,DS})}{N_{f,\text{exp}}}\right)$
760 ± 20	Coffin ($\Delta\sigma$)	10	-1.9
	Coffin ($\Delta\epsilon_p$)	440	-0.2
	Ostergren	210	-0.6
	Antolovich et al.	150	-0.7
	Romanoski et al.	36000	1.7
	Neu-Sehitoglu	460	-0.2
COATED SUBSTRATE			
$N_{i,\text{exp}}$	Model	$N_f(\text{ACPD,CC})$	$\text{Log}\left(\frac{N_f(\text{ACPD,CC})}{N_{f,\text{exp}}}\right)$
300 ± 100	Coffin ($\Delta\sigma$)	1	-2.5
	Coffin ($\Delta\epsilon_p$)	9	-1.5
	Ostergren	5	-1.8
	Antolovich et al.	3	-2.0
	Romanoski et al.	720	0.4
	Neu-Sehitoglu	5	-1.8

5.3.3 Conclusions

Six fatigue-oxidation damage models have been studied and compared in order to establish their applicability to the prediction of the fatigue life of turbine airfoils. The result of this evaluation can be summarised as following.

From theoretical considerations, the mechanistically-based models developed by Antolovich et al. and Romanoski et al. could be expected to be more accurate method of life prediction as compared to the empirical models of Coffin and of Ostergren. However, it was found that the empirical models were able to predict the results of experimental IF data obtained on CC René 80 tested at 871°C under various cycling frequency and hold times within $\pm 20\%$, whereas the models of Antolovich et al. and of Romanoski et al. gave predictions with a relative error (RE) of $\pm 90\%$ and 40% respectively. At 982°C, their predictions were even worse with values of RE of $\pm 210\%$ and higher compared to ± 25 to 50% for the empirical models. While the correlation between the maximum stress and the oxide spike length at initiation is experimentally correct, the lack of accuracy of the Antolovich et al. model can be attributed to the difference in the oxide spike growth kinetics for constant load (or stress-free) and cyclic loading conditions. The resultant model assumes that the fatigue life is directly proportional to the frequency whereas, for the empirical models, the life is proportional to the frequency raised to the power of an exponent which can be different of 1. Therefore, the success of the empirical models could be attributed to their mathematical flexibility.

In general, the Ostergren model gives the best predictions with an average RE of $\pm 16\%$ at 871°C and can accommodate the effect of strain hold time with RE = $\pm 11\%$. In addition to correctly relating the fatigue life to the frequency, the justification of this model stems from the use of the maximum stress. In the case of brittle fracture during

fatigue-oxidation at high temperature, the driving force for crack initiation and growth is the maximum stress. Under strain controlled conditions, the effect of cyclic hardening or softening and the effect of stress relaxation during the strain hold period are well represented by the maximum stress. The use of this variable can very well account for the effect of elastic anisotropy of DS or SC materials on fatigue life. Even if the Antolovich et al. and of Romanoski et. models use this variable, the improper frequency exponent in the first model and the specific postulated relation between the life and the stress, perhaps explain their poorer life prediction capabilities.

The Reuchet-Rémy model, which consider the role of carbides in the fatigue oxidation damage evolution under IF conditions, and the Neu-Sehitoglu model, which can apply to TMF conditions as found in actual turbine airfoils in aeroengines, were not included in the present evaluation because the metallurgical information required for analysis was not available and because the parameters of these mathematically complex models could not easily be computed from the experimental data.

Only the model of Neu-Sehitoglu with parameters determined from TMF tests on bare or coated DS René 80 is entirely adequate for accurately predicting life of the specimens tested in the burner rig. In spite of this, the LCF fatigue-oxidation models were used to establish the experimental results obtained in the burner rig. The parameters of these models were determined from IF tests on polycrystalline René 80 obtained by conventional casting (CC), with the life determined from a stress drop technique. In order to take into account the variation of the temperature and the principal stress during cycling, the fatigue life of the steady state temperature-stress region was computed independantly from the value of the unsteady state temperature-stress region. The total life was obtained from these two values assuming linear damage accumulation. It was found that the total life is equal or very close to the value of the steady state region. The minimum life was found to range from 1 to 74 cycles except

for the case of the model of Romanoski et al. which gave 3600 cycles.

The Neu-Sehitoglu model was also used to determine the pure fatigue life, the oxidation-fatigue life, the creep-fatigue life and the total failure life at the location along the leading edge where maximum damage occurs. The oxidation-fatigue life was determined to be the shortest with 17 cycles compared to 210 for the pure fatigue life and 55000 cycles for the creep-fatigue life. As assumed in this Subsection, the effect of oxidation or environment is clearly dominant and the creep effect is negligible for the period of the holding time at high temperature experienced in the burner rig. The order of magnitude of the total life is comparable to that obtained with the IF models, which suggests that the methodology used for life prediction with IF models is valid.

These results are one to two orders of magnitude lower than the values measured with the ACPD technique during BR thermal fatigue tests of DS René 80, with columnar grains oriented in the direction of the principal stress. This difference between predicted and experimental life was expected since the parameters of the models were established from fatigue tests on a CC Ni-base superalloy instead of a DS superalloy. Polycrystalline CC materials are known to result in a shorter life than the DS materials, under similar thermal fatigue conditions. The difference in sensitivity between the stress drop (SD) and the ACPD techniques can also explain these results. Life ratios were determined in order to include the effect of these two factors in life prediction. With these corrections, the predicted life was found to be in better agreement with the experimental results, the difference being less than one order of magnitude. Nevertheless, it was not possible to determine which of models or approaches were the best. The corrected predictions are still too approximate due to the lack of consistent IF and TMF data on René 80 (DS) and due to the lack of variable experimental conditions with the BR.

The life along the leading edge of DEW specimens was also computed with the IF fatigue-oxidation models. The profile of the probability to crack initiation, obtained from the inverse of the life distribution, corresponds well to the cracks and oxide spikes distributions observed in all the DEW specimens. Cracks are more frequently found where the stress and the probability are maximal. Even though the adopted methodology for life prediction is approximate, the present results demonstrate that the thermal and stress-strain analyses are valid in terms of their spatial distributions along the leading edge.

5.4 Oxidation Damage Modelling

This subsection develops a model or algorithm for the computation of the equivalent thickness of the base metal consumed according to the equations and the parameters which best describe the principal mechanisms of degradation during oxidation under burner rig and real engine conditions. The validity of the model is then verified by comparing the computed and the experimental thickness of metal losses along the leading edge of the specimens tested in the burner rig.

5.4.1 Algorithm for Modelling Alloy Depletion Profile and Alloy Surface Recession

Based on theoretical considerations presented in Subsection 2.3, an algorithm and four programs have been developed for modelling changes in the alloy depletion profile and alloy surface recession, during cyclic oxidation. The algorithm is presented schematically in Figure 5.42 and the programs are listed in Appendix L. The first two programs, called DEPLETIO.BAS and DEP-COAT.BAS, only compute alloy depletion profiles, respectively in uncoated and coated substrates, whereas the last two programs, called YA-REC.BAS and YAR-COAT.BAS, compute the depletion profiles and the alloy surface recession for uncoated and coated substrates, respectively. In the algorithm and in the programs, the nickel-base superalloy DSR80 is considered as a binary alloy A-B where A represents the noble elements (principally nickel) and B represents the active elements (principally the chromium and the aluminium). The Codep B-1 coating is assumed to be an aluminium-rich Ni-Al alloy represented by C or CO. In the following description of the algorithm, the name of the principal variables are given in brackets. The other variables and constants are defined in Appendix L.

The algorithm starts with the input of the values of variables describing the initial conditions, with the initialization of the constants and the parameters of the equations describing the kinetics of oxidation and the oxide scale spalling conditions. The variables are the position number along the leading edge (ZNO), the substrate temperatures after heating and cooling (TC1 and TC2), the substrate net or total strain after heating and cooling (ENETM1 and ENETM2), the total number of thermal cycles (NTOT), the length of the heating period (PERIOD), the correction factor of the parabolic rate constant (CFKP), and the thickness of the coating (YCO) when applicable. The correction factor is employed in the programs for converting the parabolic oxidation rate constants, k_p' , computed for the case of the maximum temperature, T_{max} , reached during the heating periods of the thermal cycles, to their equivalent expressions (k_p''), as

given by Equation 78) in order to take into consideration the temperature variation during heating. The correction factor is defined by:

$$CF_{k_p'} = \frac{k_p' (T)}{k_p' (T_{\max})} \quad (149)$$

and the correction is simply achieved by multiplying the constants determined at T_{\max} with this $CF_{k_p'}$ factor.

In a second stage, the alloy depletion profile (NB) and the alloy surface recession (YA) are computed for each thermal cycle (CYCLE), for two possible cases:

Case 1:

An external protective oxide scale of BO grows at the surface of the alloy according to parabolic oxidation kinetics (Equation 46, Subsection 2.3.2) where the equivalent oxidation rate constant for BO is applied. If the scale thickness (XBO) reaches the critical value for spalling (XCBO), defined as a function of the mechanical properties and straining range of BO with Equations 85 and 89 (Subsection 2.3.6), the time of growth (TIMEBO) is reset to 0. TIMEAO is also reset to 0 because the BO oxide usually forms between the AO oxide scale and the substrate so that the spalling of this sublayer also causes the spalling of the AO scale. The alloy near the interface is depleted in B due to the BO scale growth. The resulting alloy depletion profile (NB(I)) is computed by solving Fick's second law (Equation 59) using the finite difference method presented in Subsection 2.3.4. The oxidation of B is considered external and protective until the alloy interface content in B (NBP(0)) reaches 0.

Case 2:

In this case, where the alloy interface is completely depleted ($N_B' = 0$; $NBP(0) = 0$), the oxide AO is stable since N_B' is inferior to the molar fraction

of equilibrium between the oxide AO and BO (N_B^{eq} given by Equation 75). The oxidation of B is internal and an external scale of AO grows according to the parabolic oxidation kinetics (Equation 46) of AO. If the scale thickness (XAO) reaches the critical value for spalling (XCAO) determined from the mechanical properties and straining range of AO with Equations 85 and 86, the time of growth of this oxide (TIMEAO) is reset to 0. The oxidation and the consumption of the depleted zone, composed of mostly A, leads to the alloy surface recession over a distance, y_A (or Y_A), expressed by Equation 55. As the alloy is consumed, the depletion profile is translated of a quantity y_A , assuming that the oxidation kinetics of the depleted zone is faster than the counter-diffusion of B. The recession stops only when the alloy interface content in B reaches the transition value from internal to external oxidation of B, N_B^u (NBTR), which was determined to be 0.12 in Subsection 2.3.5.

At the end of each cycle, the variation of alloy depletion profile and alloy surface recession are entered in separated files and are displayed on the screen.

5.4.2 Prediction of the Alloy Depletion profiles and Alloy Surface Recession Under Burner Rig Conditions

The programs DEPLETIO.BAS, DEP-COAT.BAS, YA-REC.BAS and YAR-COAT.BAS were used for computing the alloy depletion profiles and the alloy surface recession along the leading edge tip of the DEW specimens exposed to at least 2500 thermal cycles in the burner rig. The values of the variables describing the operating conditions were entered for each nodal position along the leading edge, 4.25 mm apart. They are: the position number along the leading edge, the substrate temperatures reached after heating and cooling, the substrate net strain reached after heating and cooling, the total number of thermal cycles, the heating period, the correction factor of the parabolic rate constant, and the thickness of the coating. These values are generated by the thermal and stress-strain analyses presented in Subsections 5.1 and 5.2. The unit system L-t-T-E (Length-time-Temperature-Energy) employed is based on $\mu\text{m-s-K-J}$.

The nominal alloy content, N_B^0 , and the content defining the transition from internal to external oxidation, N_B^u (where $N_B = N_{Cr} + N_{Al}$), are respectively set to 0.22 and 0.12, for DSR80. The content of B in the coating is set to 0.6. The values of the parameters of the kinetic equations and the oxide scale failure criteria are determined from the data given in Table 2.2 to 2.5. In the case of external oxidation of Cr and Al, where the alloy interface content in Cr and Al is superior to 0 ($N_B' > 0$), the oxidation kinetics parameters of DSR80 and the mechanical properties of Cr_2O_3 were taken for uncoated substrates whereas, for coated substrates, the oxidation kinetics parameters of Al-rich Ni-Al alloys and the mechanical properties of Al_2O_3 are used up to the time when the coating is completely consumed. In the case of internal oxidation of Cr and Al, where the alloy near the surface is completely depleted of Cr and Al ($N_B' = 0$), the oxidation kinetics parameters of Ni-Cr alloys with traces of Cr and the mechanical properties of NiO are considered for the case of uncoated and coated substrates. In all

cases, the parameters of the Arrhenius expression for the diffusion of Cr and Al in René 80 are assumed to be the same as the diffusion of Cr in a Ni-Cr-Ti alloy of a similar composition. These parameters are also assumed to be independent of the changes in the alloy composition occurring during the diffusion process.

The average value of the correction factor of the parabolic oxidation rate constant, at the leading edge portion directly exposed to the hot gas stream, is determined to be 0.75 from Equations 78 and 149 for thermal cycles with short heating periods of 150 s, and 0.91 for thermal cycles with long heating periods of 390 s.

5.4.2.1 Alloy Depletion Profiles

The depletion profiles in Ni-Cr alloys, with nominal Cr contents (N_{Cr}^0) varying from 5 to 20 at%, were computed at 1150 °C, with the program DEPLETIO.BAS, in order to test the finite difference equations used in the algorithm. As the temperature is constant, oxide scale spalling does not occur and the mechanical strain of the scale is set to a very small value. Figure 5.43 shows the decrease of Cr content at the alloy interface for the various alloy compositions. For alloys with a Cr content higher or equal to 12 at%, the Cr content at the interface drops until it reaches a quasi-steady value. This quasi-steady state is obtained when the flux of Cr required at the alloy-oxide interface to form the oxide scale becomes small since the scale growth rate vary asymptotically with the oxide scale thickness and thus stabilizes (the rate is inversely proportional to the oxide scale thickness, as described in the parabolic oxidation law, Equation 45). For alloys with a Cr content lower than 12 at%, the Cr content at the interface drops to 0 before it reaches a quasi-steady value. It is interesting to note that the value of 12 at% Cr corresponds to the experimental values of the transition composition between external to internal oxidation of Cr for these alloys (see

Subsection 2.3.2). This result supports the transition criteria based on thermodynamic and kinetics arguments, as defined in Subsection 2.3.5.

The depletion profiles at the leading edge of uncoated and coated DEW specimens exposed to cyclic conditions in the burner rig were also computed using the programs DEPLETIO.BAS and DEP-COAT.BAS.

Figures 5.44-5.46 show the computed Cr depletion profiles at different times for the Ni-22at%Cr alloy, the uncoated and coated DSR80 substrates at the location of highest temperature along the leading edge ($z = 46.75$ mm). After 4.04 cycles (Figure 5.44), the Ni-Cr alloy surface was completely depleted and the depletion zone reaches $80\text{ }\mu\text{m}$ whereas for the uncoated DSR80 alloy, it takes only 1.7 cycles (Figure 5.45) for complete depletion of its surface and the depleted zone is only $10\text{ }\mu\text{m}$ thick. For the coated DSR80 substrates, the complete surface depletion was observed after 25 cycles (Figure 5.46) and the depletion zone was only $20\text{ }\mu\text{m}$ thick. Since the diffusion coefficient of B in the alloys is assumed the same in these computations, the different results can only be attributed to the difference in the parabolic oxidation rate constants, k_p' . The alloy DSR80, which has the largest number of components with a susceptible doping effect on oxidation kinetics, has the highest constant, k_p' compared to the Ni-Cr alloy and the coating is constituted principally of Al and Ni. The growth rate of the oxide scale on this alloy is the highest causing the most rapid depletion in B. The high aluminium content in the coating forms a very compact and protective layer of alumina that grows very slowly. Thus the depletion of B in the coating is very slow, as confirmed by the results of the computations. Figure 5.46 shows that the depletion of B in the coating also occurs at the coating-substrate interface, due to the diffusion of B into the substrate. Oxidation, thermal fatigue and the interdiffusion of species between the coating and the substrate represent the three principal degradation mechanisms for aluminide coatings. All of these factors are considered in the algorithm

developed for computing alloy depletion profiles and alloy surface recession.

Figures 5.47-5.49 illustrate the variation of the oxidized solute content ($N_B = N_{Cr} + N_{Al}$) at different depths from the surface of the Ni-Cr, the uncoated and coated DSR80 alloys, subjected to conditions corresponding to that of three locations along the leading edge. The composition at the alloy-oxide interface (N_B') shows discontinuities at the end of some cycles. These abrupt depletions correspond to the spalling of oxide scale which causes an immediate increase of the flux of the the solute at the interface, associated to the growth of the new oxide scale. At the position exposed to the most severe temperatures and deformations ($z = 38.25$ and 46.75 mm), the oxide scale rupture occurs at every cycles for the uncoated and coated DSR80 alloys and after every two cycles for the Ni-Cr alloy where the oxide scale thickness reaches the critical spalling value more slowly. At position $z = 25.50$ mm which is exposed to less severe conditions, scale spalling takes place only after every 8 cycles.

The repeated scale spalling causes the rapid alloy depletion of the solute which results in internal oxidation of the alloys and in surface recession. The effect of the consumption of the depleted zone on the solute content profiles was simply modelled by translating the depletion profile for a distance corresponding to the surface recession. Figures 5.50 and 5.51 illustrates the variation of the solute content at the surface of Ni-22at%Cr and DSR80 alloys respectively. Initially, the surface is completely depleted in B. Then, the solute content increases as the depleted zone is consumed until it reaches the transition value N_B^* which defines the return to external oxidation of the solute and the arrest of surface recession. The depletion starts again. Some results of the computation of the alloy surface recession rate are presented in the next Subsection.

5.4.2.2 Alloy Surface Recession

The surface recession of the leading edge of uncoated and coated DEW specimens during thermal cycling in the burner rig was computed using the YAREC.BAS and YAR-COAT.BAS programs. Figure 5.52 shows the variation of the surface recession at the position exposed to the most severe conditions ($z = 46.75$ mm) and at a position exposed to moderately severe conditions ($z = 25.50$ mm). In the case of the uncoated substrates, the progression of the surface consumption is linear from the beginning to the end of testing. At $z = 46.75$ mm where the maximum temperature of 1164°C is obtained, the coated substrates show a lower recession rate until the coating is completely consumed (over a depth corresponding to the coating thickness of $50\text{ }\mu\text{m}$), after which the recession rate corresponds to that of the bare substrate. The total recession after 2500 thermal cycles is $1665\text{ }\mu\text{m}$ at this location for the bare substrate, versus $1585\text{ }\mu\text{m}$ for the coated case. The presence of the coating results in a difference of less than twice its original thickness. At $z = 25.50$ mm where the temperature reaches 936°C , the total surface recession after 2500 thermal cycles is very low: $56.3\text{ }\mu\text{m}$ for the uncoated substrates, and $0.0\text{ }\mu\text{m}$ for the coated substrates. These results indicate that the alloy DSR80 is quite resistant to oxidation under 1000°C and that the Codep B-1 provides complete protection below this temperature. This is in good agreement with the recommended standard engine practices for these alloys.

Figure 5.53 gives the computed surface recession profiles of the leading edge of uncoated DEW specimens after short (150 s) and long (390 s) periods of exposure to the hot gas stream in the burner rig. In both cases, the alloy consumption is negligible for positions below $z = 25$ mm and above $z = 70$ mm. The zone between these two limits, directly exposed to the hot gas stream, is severely attacked leading to material losses of $1330\text{ }\mu\text{m}$ for short periods and of $2430\text{ }\mu\text{m}$ for long periods, after 2000 thermal cycles. The effect of the period of exposure to the hot gases is quite significant as

experimentally observed in Subsection 4.1.3. In Figure 5.54, the measured surface recession profiles of the SRC specimen (exposed to 3000 short thermal cycles) and SRD (exposed to 2140 long thermal cycles) obtained in Subsection 4.1.3 are compared to computed profiles. While the magnitude and the position of the maxima correspond very well, the shape of the measured and the computed profiles differ somewhat. At $z = 46.75$ mm, the prediction underestimates the real values obtained for the SRC specimen whereas in the regions symmetrically distributed about this position, the profile is overestimated for both SRC and SRD specimens. The overestimation can be attributed to the cracking of the substrate, more frequent in these regions, which reduces the compressive stresses in the oxide scale and which is not considered in the algorithm for computations of the surface recession.

Table 5.16 compares the measured maximal surface recession at the leading edge of the specimens which were tested over a number of thermal cycles and for heating periods to the predicted values. A non negligible lateral swelling of the SRN specimen in the portion directly exposed to the hot gas stream was observed after 200 thermal cycles. This permanent swelling of the leading edge is due to the plastic deformation that occurs during the first hundred cycles and was measured to have a maximum value of $95\text{ }\mu\text{m}$ relative to the original leading edge geometry. As the surface recession was measured relative to the portions of the specimens not exposed to the hot gas stream, the swelling quantity was added to the measured recession values before comparison with the computed values. The relative error of the predictions ranges from 3 to 8% for the different total numbers of cycles which vary from 800 to 3000 cycles. This result certainly validates the algorithm developed in this Subsection as well as the Equations and parameters used for describing the kinetics and oxide spalling processes.

Despite the numerous simplifications assumed and the lack of more accurate values for the parameters of the equations describing the kinetics and failure, the

predicted profiles are in good agreement with experimental profiles, within less than 10% at the locations exposed to the most severe conditions.

Table 5.16 Measured Maximal Surface Recession along the Leading Edge of DEW Specimens after Testing in the Burner Rig Compared to Predicted Values.

TEST NAME	N_{final} (cycles)	Δt_{H} (s)	$y_{\text{A,exp}}$ (μm)	$y_{\text{A,corr}}$ (μm)	$y_{\text{A,cal}}$ (μm)	RE (%)
SRE	800	150	405	500	530	6
SRB	2500	150	1715	1810	1665	8
SRC	3000	150	2065	2160	2000	7
SRD	2140	390	2435	2530	2605	3

where:

N_{final} is the total number of thermal cycles;

Δt_{H} is the heating period;

$y_{\text{A,exp}}$ is the maximum surface recession, y_{A} , measured along the leading edge of DEW specimens after testing;

$y_{\text{A,corr}}$ is the measured value of $y_{\text{A,exp}}$ corrected to take into consideration the permanent swelling of the specimen width during thermal cycling;

$y_{\text{A,cal}}$ is the calculated or predicted value of y_{A} ;

RE is the relative error or deviation of $y_{\text{A,cal}}$ from $y_{\text{A,corr}}$

5.4.3 Conclusions

An algorithm was developed for modeling Ni-base superalloy surface recession at the leading edge of a nickel-base airfoil during cyclic oxidation in a burner rig. The algorithm takes into consideration the succession of complex mechanisms, identified as the growth of the internal protective oxide scale, the alloy depletion of the most active elements, the transition from external to internal oxidation, the consumption of the completely depleted zone, and the transition from internal to external oxidation. The effect of repeated spalling of the oxide scales associated with the cooling of the airfoils is considered in terms of depletion kinetics and recession.

Many simplifications were made to formulate the equations, including the parameters and the algorithm which describe the mechanisms involved during cyclic oxidation. First of all, the DSR80 alloy was considered to be a Ni-Cr-Al system. In particular, the substrate was assumed to be a Ni-22at%Cr alloy forming a Cr_2O_3 protective oxide scale at its surface. The coded B-1 coating was seen as a Ni-60at%Al alloy (covered with an Al_2O_3 protective oxide scale) and the depleted zone was considered to be a Ni rich alloy with traces of Cr, which is consumed to form a NiO oxide layer. The oxide scale growth rates follow a parabolic law with the parameters established from experimental studies on DSR80, Ni-Cr and Ni-Al alloys. The depletion profile resulting from the diffusion of the active elements from the alloy to the growing oxide scale was computed using a finite difference method. The coefficient of diffusion of Cr determined from a study on superalloys similar to DSR80 was taken for all cases of alloy diffusion. The transition from external to internal oxidation was assumed to take place when the alloy surface is completely depleted in Cr or Al. The depleted zone is then consumed until the Cr or Al content at the surface reaches the composition of transition from internal to external oxidation. This value is set to 0.12 according to studies on oxidation of Ni-Cr and Ni-Al alloys. Oxide scale failure was assumed to be

caused by the built up of compressive stages during cooling and to occur at the alloy-oxide interface when the scale thickness reaches a critical value as given by the simplest equation developed by Schütze. The effect of porosities, micro-cracks and interface roughness were neglected in this analysis. The effect of curvature of the leading edge on oxide kinetics, scale failure, diffusion and surface recession was not considered.

Despite all these assumptions and the lack of accurate parameters for the oxide oxidation kinetics and the oxide fracture modeling, good results were obtained using the algorithm and the programs developed in this Subsection. Variation of the depletion profiles of Cr were established with respect to the parabolic rate constants and abrupt variation of oxidation rate associated with oxide scale spallings. Based on kinetics criteria implemented in the algorithm, the nominal composition defining the transition between internal and external oxidation was successfully predicted for Ni-Cr and Ni-Al alloys. It was shown that the algorithm could be used to compute the Al depletion in the coating as a result of oxidation and diffusion into the substrate.

The recession of the leading edge surface for both uncoated and coated airfoils were successfully predicted. Computed and experimental recession profiles of the leading edge portion exposed directly to the hot gas stream were shown to be within less than 10% and the consumption rate of uncoated substrates was found to be linear. The metal losses are significant (few millimetres) in the portion exposed to the most severe thermal and deformation conditions as observed in the experimental results and supported by predictions. The coating offers protection for a period up to 200 cycles in the portions of the leading edge where temperature exceeds 1000 °C. Elsewhere the coating was not affected by oxidation as confirmed by experimental results.

6. GENERAL CONCLUSIONS

The main goals of the project described in this thesis were to develop and validate a methodology for thermal fatigue life prediction and oxidation damage modeling of aircraft engine turbine blades and vanes. The project was divided into an experimental phase, which consisted in reproducing and assessing damage accumulation in airfoil-like specimens tested under well simulated service conditions, and to a numerical or modelling phase which consisted in establishing the thermal fatigue life and the oxidation damage from the knowledge of the thermal and mechanical histories of the critical elements in the specimens.

Experiments were carried out for eight thermal fatigue tests conducted on double-edge wedge (DEW) specimens of DS René 80 (coated and uncoated) in a burner rig. The DEW specimens were alternately exposed to a hot gas stream (at 1323°C and Mach 0.4) and a cold air jet (at ambient temperature), up to 3000 times. A metallographic analysis of the tested specimens resulted in the following conclusions.

No change in microstructure attributed to thermal cycling was noted except for the γ' precipitates which coarsened. This was especially notable in specimen regions where the temperature and the stresses are very high. In some particular regions, the γ' also elongated (γ' rafting) due to the effect of the principal stress in the longitudinal direction of the specimen.

Oxide spikes are observed along the leading edge of uncoated specimens after 800 thermal cycles while in coated specimens, some finger-like oxide protuberances penetrated the coating after 780 cycles. Oxide spikes and fingers are more prevalent

where the temperature is high and where the stresses are the highest. Oxide spikes are attributed to oxidation of fatigue microcracks which preferentially initiated in interdendritic regions and at carbide-matrix interfaces. Oxide fingers also formed from fatigue microcracks initiated in nickel-rich aluminide phases which precipitated in the coating.

Major cracks are formed at the leading edge of uncoated and coated specimens exposed up to 2500 thermal cycles, where the temperature is high and where the principal stress is the highest. Cracks progressed transgranularly through the primary dendrites and between the secondary dendrites where brittle Chinese script type carbides are segregated. The crack growth mechanism is not well identified, but is believed to progress by successive embrittlement of the matrix, due to oxygen diffusion in interdendritic regions, and at carbide-matrix interfaces, resulting in cracking of the embrittled zone.

Significant oxidation damage also occurred along the leading edge of tested specimens. In the case of uncoated specimens, the nature and the morphology of the oxides varied according to the temperature, the stress and strain levels. In the portions of the specimen not exposed to the hot combustion gases, where the temperature and the thermal exposition are relatively low, a protective $\text{Cr}_2\text{O}_3\text{-Al}_2\text{O}_3$ oxide scale formed. In portions of the specimen where the temperature and the thermal expansion are intermediate, the protective oxide scale breaks and/or spalls off, and a nickel-rich non-protective oxide scale grew, leading to an accelerated substrate consumption. In the portion of the specimen exposed directly to the hot gases, where the temperature and the thermal expansion are high, the oxide layers had spalled off, leading to drastic consumption rates of the substrate and causing 1.7 to 2.3 millimetres of material lost at the leading edge, after 2500-3000 thermal cycles.

In the case of coated specimens, compact and adherent Al_2O_3 oxide scale formed at the surface providing a good protection against drastic substrate consumption except where the coating had been penetrated by oxide fingers at grain boundaries and/or by cyclic oxidation. At these locations, which are highly stressed and exposed to extreme temperatures, the oxide fingers and the repeated oxide scale spalling destroyed the coating resulted in pitting of the substrate to a depth of few millimeters. These pits act as stress concentrators and some small cracks were found to be initiated at their roots as it was observed in a prenotched uncoated specimen exposed to 200 cycles only.

Thermal fatigue and oxidation damages encountered by turbine blades and vanes are well reproduced in tested specimens using a high velocity burner rig. The burner rig can closely reproduce real service conditions such as temperature, velocity and chemistry of combustion gases produced in aero engines.

The initiation and growth of leading edge cracks in the DEW specimens were measured on-line using an advanced alternating current - potential drop (ACPD) technique. The conclusions found from this damage assessment study are summarised here.

The initiation and subsequent crack growth were successfully monitored on-line using the CGM5 crack growth monitor with current and potential drop probes attached to the specimen. The ACPD technique allowed life to crack initiation (N_i) to be determined with an accuracy of ± 5 cycles in the best cases. N_i presented an average value of 760 ± 20 cycles for uncoated specimens exposed 2.5 minutes/cycles to the hot gas stream. In the case where the hold time in the hot gas jet was 6.5 minutes/cycles, N_i was found to be 600 ± 200 cycles. This result could indicate that crack initiation is not significantly affected by cyclic oxidation, erosion or creep. Compared to uncoated specimens, life to crack initiation of coated specimens was reduced to 300 ± 100 cycles.

The ACPD technique also allowed the crack growth rate to be evaluated during TF testings. After correction for metal loss due to erosion, the initial crack growth rate was estimated to be about $2\text{ }\mu\text{m/cycle}$ in uncoated and coated specimens, except in one uncoated specimen, where the rate ranged from 30 to $100\text{ }\mu\text{m/cycle}$ after initiation. Such fast crack propagation was also observed in one coated specimen, after a very slow initial rate. Even if coatings seem to have a detrimental effect on fatigue life, drastic crack propagation did not occur earlier in the coated specimen. More thermal fatigue tests are needed to validate these conclusions.

A numerical analysis of the thermo-mechanical behaviour of the specimens tested in the burner rig was carried out in the second phase of this project. Thermal fatigue and oxidation damages in these airfoils were predicted from the knowledge of the thermo-mechanical histories and from models and methods developed during this project. The results of these analyses and simulations result in the following conclusions.

The thermal analysis of the DEW specimen was found to be complex and requires that all the thermal parameters be accurately known. The specimen temperature distribution was computed with the ABAQUS-FE code from experimentally determined values of convective heat transfer coefficients and the emissivity of the oxidised material. The determination of the convective heat-transfer coefficients from thermocouple and optical pyrometry temperature measurements along the surface of the DEW specimen was particularly difficult to evaluate. Computed and measured temperatures were found to differ by only 15°C at the leading edge and by about 35°C elsewhere along the chordwise mid-section. This result is reasonably good considering the experimental and numerical difficulties of this analysis.

The magnitudes of the experimental heat transfer coefficients obtained by both techniques of temperature measurements were found to be generally consistent with each

other. Therefore, optical pyrometry based data including values obtained by extrapolation for the leading edge can be used for thermal analysis of the specimen. The thermal analysis indicates that assumptions made in the determination of the heat-transfer coefficients from heat balance over small elements of the mid-section of the specimen are valid.

This thermal analysis demonstrates that using a high-velocity laboratory combustor to simulate turbine airfoil operating environment and a double-edge wedge specimen to simulate airfoil geometry, it is possible to achieve heat transfer coefficient profiles across the airfoil that are similar to profiles obtained for actual airfoils. This indicates that thermal history can be properly simulated in the laboratory for thermal fatigue testing of blade and vane materials under realistic conditions.

The stress-strain variation of each element of the DEW specimen was computed from the temperature history, using a thermo-elastoplastic subroutine of the ABAQUS FE-code. The principal stress, σ_{33} , as well as the temperature, was found to be high in the portion of the leading edge directly exposed to the hot gas stream. Cracking occurs where both the computed temperatures and stresses are high along the leading edge during thermal cycling. This result indirectly validates the thermal and the stress-strain analysis in terms of their spatial distributions and demonstrates that there is a coupling effect of the stress and the temperature on the cracking process.

The variation of the principal stress, at the location exposed to the most severe loading conditions along the leading edge, shows a compressive peak at the beginning of the heating cycle and a tensile peak at the beginning of the cooling cycle. The stress stabilizes to a moderate tensile value during heating. The coupling between the stress and the temperature is complex as demonstrated by the stress-thermal strain loop which corresponds to the Counterclockwise Diamond phasing case between the mechanical and

the thermal strains.

According to this thermo-elastoplastic analysis, the comparison between the variation of the different natures of the strain (thermal, elastic, plastic) shows that the thermal strain is dominant and that the mechanical deformation mostly occurs in the elastic regime. Stress-elastic strain loop shows that the mean stress is close to zero and the tensile regime takes place at high temperature during thermal cycling.

A thermo-elasto-viscoplastic analysis using the model of Walker, modified to take into consideration the orthogonality of the elastic properties of the tested DS material was also undertaken to get a more realistic estimation of the inelastic strain and of the stress relaxation. The analysis was limited to one location of the leading edge, exposed to the most severe thermo-mechanical conditions, and to 10 thermal cycles, because of the lack of computer capacity. The plastic strain range was found to be 10 times larger than that computed with the thermo-elastoplastic model. The maximum tensile stress developed during heating was of 110 MPa at the end of heating during the thermal cycle.

Thermal fatigue life was predicted using four isothermal fatigue-oxidation damage models and one thermo-mechanical fatigue-oxidation-creep model. The parameters of the isothermal models were determined from isothermal fatigue (IF) tests on polycrystalline René 80 obtained by conventional casting (CC), with fatigue life determined from a stress drop technique. In order to take into account the variation of the temperature and the principal stress during cycling, the fatigue life associated with the steady state temperature-stress portions of the cycles was computed separately from the unsteady state temperature-stress portions. The total life was obtained from these two values assuming linear damage accumulation. It was found that the total life is equal or very close to that associated to the steady state portions of the cycles. A

minimal fatigue life was found to range between 1 and 74 cycles except for one model which resulted in 3600 cycles.

The thermo-mechanical fatigue (TMF) model of Neu-Sehitoglu was also used to determine the pure fatigue life, the oxidation-fatigue life, the creep-fatigue life and the total failure life at the location along the leading edge where maximum damage occurs. The oxidation-fatigue life was determined to be the shortest with 17 cycles compared to 210 for the pure fatigue life and 55000 cycles for the creep-fatigue life. As assumed in this thesis, the effect of oxidation or environment is clearly dominant and the creep effect is negligible for the period of holding time at high temperature experienced in the burner rig. The order of magnitude of the total life is comparable to that obtained with the IF models, which suggests that the methodology used for life prediction with IF models is valid.

These results are one to two orders of magnitude lower than the values measured with the ACPD technique during thermal fatigue tests of DS René 80, with columnar grains oriented in the direction of the principal stress. This difference between predicted and experimental life was expected since the parameters of the models were established from fatigue tests on a CC Ni-base superalloy. Polycrystalline CC materials are known to result in a shorter life than the DS materials, under similar thermal fatigue conditions. The difference in sensitivity between the stress drop (SD) and the ACPD techniques can also explain these results. Life ratios were determined in order to include the effect of these two factors in life prediction. With these corrections, the predicted life was found to be in better agreement with the experimental results, the difference being less than one order of magnitude. Nevertheless, it was not possible to determine which of models or approaches were the best. The corrected predictions are still too approximate due to the lack of consistent IF and TMF data on René 80 (DS) and due to the lack of variable experimental conditions with the BR.

The life along the leading edge of DEW specimens was also computed with these isothermal fatigue-oxidation models. The profile of the probability to crack initiation, obtained from the inverse of the life distribution, corresponds well to the cracks and oxide spikes distributions observed in all the DEW specimens. Cracks are more frequently found where the stress and the probability are maximal. Even though the adopted methodology for life prediction is approximate, the present results demonstrate that the thermal and stress-strain analyses are valid in terms of their spatial distributions along the leading edge.

Concerning oxidation damage modelling, an algorithm have been developed for modelling Ni-base superalloy surface recession at the leading edge of a nickel-base airfoil during cyclic oxidation in a burner rig. The algorithm takes into consideration the succession of complex mechanisms, identified as the growth of the internal protective oxide scale, the alloy depletion of the most active elements, the transition from external to internal oxidation, the consumption of the completely depleted zone, and the transition from internal to external oxidation. The effect of repeated spalling of the oxide scales associated with the cooling of the airfoils was considered in terms of depletion kinetics and recession.

Many simplifications were made to formulate the equations, including the parameters and the algorithm which describe the mechanisms involved during cyclic oxidation. First of all, the DSR80 alloy was considered to be a Ni-Cr-Al system. In particular, the substrate was assumed to be a Ni-22at%Cr alloy forming a Cr_2O_3 protective oxide scale at its surface. The coded B-1 coating was seen as a Ni-60at%Al alloy (covered with an Al_2O_3 protective oxide scale) and the depleted zone was considered to be a Ni rich alloy with traces of Cr, which is consumed to form a NiO oxide layer. The oxide scale growth rates follow a parabolic law with the parameters established from experimental studies on DSR80, Ni-Cr and Ni-Al alloys. The depletion

profile resulting from the diffusion of the active elements from the alloy to the growing oxide scale was computed using a finite difference method. The coefficient of diffusion of Cr determined from a study on superalloys similar to DSR80 was taken for all cases of alloy diffusion. The transition from external to internal oxidation was assumed to take place when the alloy surface is completely depleted in Cr or Al. The depleted zone is then consumed until the Cr or Al content at the surface reaches the composition of transition from internal to external oxidation. This value is set to be 0.12 according to studies on oxidation of Ni-Cr and Ni-Al alloys. Oxide scale failure was assumed to be caused by the built up of compressive stresses during cooling and to occur at the alloy-oxide interface when the scale thickness reaches a critical value as given by the simplest equation developed by Schütze. The effect of porosities, micro-cracks and interface roughness were neglected in this analysis. The effect of curvature of the leading edge on oxide kinetics, scale failure, diffusion and surface recession was not considered.

Despite all these assumptions and the lack of accurate parameters for the oxide oxidation kinetics and the oxide fracture modeling, good results were obtained using the algorithm and the programs developed in this thesis. Variation of the depletion profiles of Cr were established with respect to the parabolic rate constants and abrupt variation of oxidation rate associated with oxide scale spallings. Based on kinetics criteria implemented in the algorithm, the nominal composition defining the transition between internal and external composition was successfully predicted for Ni-Cr and Ni-Al alloys. It was shown that the algorithm could be used to compute the Al depletion in the coating as a result of oxidation and diffusion into the substrate.

The recession of the leading edge surface for both uncoated and coated airfoils were successfully predicted. Computed and experimental recession profiles of the leading edge portion exposed directly to the hot gas stream were shown to be within less than 10% and the consumption rate of uncoated substrates was found to be linear. The

metal losses are significant (few millimetres) in the portion exposed to the most severe thermal and deformation conditions as observed in the experimental results and supported by predictions. The coating offers protection for a period up to 200 cycles in the portions of the leading edge where temperature exceeds 1000 °C. Elsewhere the coating was not affected by oxidation as confirmed by experimental results.

7. RECOMMENDATIONS

According to the general conclusions of this thesis, the validation of the methodology developed for thermal fatigue life prediction and oxidation damage modelling suffers from the lack of experimental data used to determine the parameters of the prediction models which apply to the specific chemistry and microstructure of the uncoated and coated nickel-base superalloy tested in the burner rig and, from the lack of thermal fatigue tests in the burner rig. The main recommendation consists in elaborating a more exhaustive experimental study where the validation of the models is achieved on many superalloy and coating systems in order to capture the effect of the chemistry and the microstructure on fatigue and oxidation behaviours. The experimental program should include:

- creep tests at various temperatures and applied loads
- isothermal fatigue tests at various temperatures, strain rates and hold times;
- thermo-mechanical fatigue tests at various temperature ranges, strain rates and phasing between the thermal and the mechanical strains;
- thermal fatigue tests in the burner rig at various gas temperatures and velocities.

The Alternating Current - Potential Drop (ACPD) technique, which has been successfully used to determine life to crack initiation for thermal fatigue tests carried out in the burner rig, should be integrated to the tests suggested above. An improved version of the crack growth monitor like the CGM6 or CGM7 as provided by Matelect Ltd., after careful calibration over the range of testing conditions and specimen geometries, should provide an excellent crack detection resolution and a fair comparison

between lives measured for different thermo-mechanical conditions. The interpretation of the measurements obtained for different specimen and probe configurations could be assisted with a finite element code able to solve the equations of Maxwell in order to predict the potential drop occurring from surface oxidation and cracking.

Ultimately, the predictions obtained from the refined lifing methodology could be extended to the case of airfoils exposed to real engine conditions with more complex temperature variations and more aggressive gas environment. This would require a detailed thermo-mechanical analysis of the real case based on temperature measurements, where the viscoplastic strain and the creep damage accumulation occurring in airfoils are carefully simulated.

REFERENCES

- [1] *Superalloys II*, Eds. C. T. Sims, N. S. Stoloff and W. C. Hagel, Wiley, New York, pp. 359-384, 1987.
- [2] SPERA, D.A., What is Thermal Fatigue, *Thermal Fatigue of Materials and Components*, ASTM STP 612, ASTM, pp. 3-9, 1976.
- [3] ROMANOSKI, G.R., ANTOLOVICH, S.D. and PELLOUX, R.M., A Model for Life Prediction of Nickel-Base Superalloys in High-Temperature Low Cycle Fatigue, in *Low Cycle Fatigue*, ASTM STP 942, ASTM, Philadelphia, pp. 456-469, 1988.
- [4] REGER, M. and RÉMY, L., Fatigue Oxidation Interaction in IN 100 Superalloy, *Met. Trans. A*, Vol. 19A, pp. 2259-2268, 1988.
- [5] COFFIN Jr., L.F., The Effect of Frequency on the Cyclic Strain and Fatigue Behavior of Cast René 80 at 1600°F, *Met. Trans.*, Vol. 5, pp. 1053-1060, 1974.
- [6] LORD, D.C. and COFFIN Jr., L.F., Low Cycle Fatigue Hold Time Behavior of Cast René 80, *Met. Trans.*, Vol. 4, pp. 1647-1654, 1973.
- [7] COFFIN Jr., L.F., Fatigue at High Temperature, *Fatigue at Elevated Temperatures*, ASTM STP 520, ASTM, Philadelphia, pp. 5-34, 1973.
- [8] COFFIN Jr., L.F., The Prediction of Wove Shape Effects in Time-Dependent Fatigue, *Proceedings of the Second International Conference on Mechanical Behavior of Materials*, Boston, Massachusetts, 16-20 August 1976, pp. 866-875, 1976.
- [9] OSTERGREN, W.J., A Damage Function and Associated Failure Equations for Predicting Hold Time and Frequency Effects in Elevated Temperature, Low Cycle Fatigue, *J. of Testing and Evaluation*, Vol. 4, No. 5, pp. 327-339, 1976.
- [10] COOK, T.S., KIM, K.S. and MCKNIGHT, R.C., Thermal Mechanical Fatigue of Cast René 80, *Low Cycle Fatigue*, ASTM STP 942, ASTM, Philadelphia, pp. 692-708, 1988.

- [11] ANTOLOVICH, S.D., Aspects Métallurgiques de la Fatigue à Haute Température, Chap. 15 of *La Fatigue des Matériaux et des Structures*, Ed. by C. Bathias and J.-P. Baille, Maloine S.A. Éditeurs, Paris, pp. 466-496, 1980.
- [12] RITCHIE, R.O., GERBERICH, W.W. and ANTOLOVICH, S.D., Fundamentals of Fracture and Fatigue: A Basis for Alloy Design, *Mechanical Properties and Phase Transformations in Engineering Materials*, New Orleans, Louisiana, U.S.A., 2-6 March 1986, pp. 59-98, 1986.
- [13] ANTOLOVICH, S.D., BAUR, R. and LIU, S., A Mechanistically Based Model for High Temperature LCF of Ni Base Superalloys, *Superalloys 1980*, Ed. by J.K. Tien et al., ASM, Metals Park, OH, pp. 605-613, 1980.
- [14] ANTOLOVICH, S.D., LIU, S. and BAUR, R., Low Cycle Fatigue Behavior of René 80 at Elevated Temperature, *Met. Trans. A*, Vol. 12A, pp. 473-481, 1981.
- [15] ANTOLOVICH, S.D., DOMAS, P.A. and STRUDEL, J.L., Low Cycle Fatigue of René 80 as Affected by Prior Exposure, *Met. Trans. A*, Vol. 10A, pp. 1859-1868, 1979.
- [16] DOMAS, P.A. and ANTOLOVICH, S.D., A Mechanistically Based Model for High Temperature Notched LCF of René 80, *Eng. Fract. Mech.*, Vol. 21, No. 1, pp. 203-214, 1985.
- [17] RAGUET, M., ANTOLOVICH, S.D. and KELLY PAYNE, R., Fatigue and Deformation Behavior of Directionally Solidified René 80, *Superalloys 84*, Ed. by M. Gell et al., ASM, Warrendale, PA, pp. 231-241, 1984.
- [18] ANTOLOVICH, S.D. and JAYARAMAN, N., Effects of Environment and Structural Stability on The Low Cycle Fatigue Behaviour of Nickel-Base Superalloys, *High Temp. Technol.*, Vol. 2, No. 1, pp. 3-13, 1984.
- [19] ANTOLOVICH, S.D. and JAYARAMAN, N., The Effects of Microstructure on the Fatigue Behavior of Ni Base Superalloys, in *Fatigue, Environment and Temperature Effects*, Ed. by Burke et al., Boston, N.Y., pp. 119-144, 1980.
- [20] ANTOLOVICH, S.D., Elevated Temperature Low Cycle Fatigue of Nickel Base

- Superalloys in the Conventionally Cast, Directionally Solidified and Single Cristal Forms, **Report AFOSR-TR-83-0827**, Project 2306, Task A1, Grant AFOSR-80-0065, 61 p., August 1983.
- [21] ANTOLOVICH, S.D., Microstructural Effects and Fatigue Life Predictions of Notched and Un-notched Ni Base Superalloys at Elevated Temperatures, **Report AFOSR-TR-80-0341**, Project 2306, Task A1, Grant AFOSR-76-2952, 54 p., April 1980.
 - [22] ANTOLOVICH, S.D., ROSA, E. and PINEAU, A., Low Cycle Fatigue of René 77 at Elevated Temperatures, *Mater. Sci. Eng.*, Vol. 47, pp. 47-57, 1981.
 - [23] ROMANOSKI, G.R., Mechanisms of Deformation and Fracture in High-Temperature Low-Cycle Fatigue of René 80 and IN100, *M.S. Thesis*, University of Cincinnati, also **NASA Contractor Report 165498**, 1981.
 - [24] REUCHET, J. and RÉMY, L., Fatigue Oxidation Interaction in a Superalloy - Application to Life Prediction in High Temperature Low Cycle Fatigue, *Met. Trans. A*, Vol. 14A, pp. 141-149, 1983.
 - [25] RÉMY, L., High Temperature Fatigue of Superalloys, *Proc. Fatigue 93*, 3-7 May, Montréal, Canada, Ed. by J.-P. Bailon and J.I. Dickson, Pub. EMAS, pp. 825-835, 1993.
 - [26] SEHITOGLU, H., Thermo-Mechanical Fatigue Life Prediction Methods, *Advances in Fatigue Lifetime Predictive Techniques*, ASTM STP 1122, Ed. by M.R. Mitchell and R.W. Landgraf, ASTM, Philadelphia, pp. 47-76, 1992.
 - [27] BOISMIER, D.A. and SEHITOGLU, H., Thermo-Mechanical Fatigue of MAR-M247: Part 1 - Experiments, *J. Eng. Mat. Tech.*, Trans. ASME, Vol. 112, pp. 68-79, 1990.
 - [28] SEHITOGLU, H. and BOISMIER, D.A., Thermo-Mechanical Fatigue of MAR-M247: Part 2 - Life Prediction, *J. Eng. Mat. Tech.*, Trans. ASME, Vol. 112, pp. 80-89, 1990.
 - [29] NEU, R.W. and SEHITOGLU, H., Thermomechanical Fatigue, Oxidation, and

- Creep: Part I - Damage Mechanisms, *Met. Trans. A*, Vol. 20A, pp. 1755-1767, 1989.
- [30] NEU, R.W. and SEHITOGLU, H., Thermomechanical Fatigue, Oxidation, and Creep: Part II - Life Prediction, *Met. Trans. A*, Vol. 20A, pp. 1769-1783, 1989.
- [31] CHALLENGER, K.D., MILLER, A.K. and BRINKMAN, C.R., An Explanation for the Effects of Hold Periods on the Elevated Temperature Fatigue Behavior of 2¼ Cr - 1 Mo Steel, *J. Eng. Mat. Tech.*, Vol. 103, pp. 7-14, 1981.
- [32] LIU, H.W. and OSHIDA, Y., Grain Boundary Oxidation and its Effects on High Temperature Fatigue Life, *NASA Grant NAG3-348*, pp. 407-414, 1985.
- [33] WRIGHT, P.K. and ANDERSON, A.F., The Influence of Orientation on the Fatigue of Directionally Solidified Superalloys, *Superalloys 80*, Ed. by J.K. Tien et al., ASM, Metals Park, OH, pp. 689-698, 1980.
- [34] WRIGHT, P.K., Oxidation-Fatigue Interactions in a Single-Crystal Superalloy, *Low Cycle Fatigue*, ASTM STP 942, ASTM, Philadelphia, pp. 558-575, 1988.
- [35] COFFIN, L.F., *Fracture 1977 (ICF4)*, Ed. by D.M.R. Taplin, University of Waterloo Press, Vol. 1, p. 263, 1977.
- [36] ANTOLOVICH, S.D. and JAYARAMAN, N., Metallurgical Instabilities During the High Temperature Low Cycle Fatigue of Nickel-Base Superalloys, *Mater. Sci. Eng.*, Vol. 57, pp. L9-L12, 1982.
- [37] BRICKNELL, R.H. and WOODFORD, D.A., The Embrittlement of Nickel Following High Temperature Air Exposure, *Met. Trans. A*, Vol. 12A, pp. 425-433, 1981.
- [38] WOODFORD, D.A., Environmental Damage of a Cast Nickel Base Superalloy, *Met. Trans. A*, Vol. 12A, pp. 299-308, 1981.
- [39] WOODFORD, D.A. and BRICKNELL, R.H., Air Embrittlement of a Cobalt-Base Superalloy, *Met. Trans. A*, Vol. 12A, pp. 1945-1949, 1981.
- [40] WOODFORD, D.A. and BRICKNELL, R.H., The Effect of High Temperature Air Exposure on the Stress Rupture Life of Nickel and Cobalt Base Superalloys,

- Superalloys 80*, Ed. by J.K. Tien et al., ASM, Metals Park, OH, pp. 633-641, 1980.
- [41] HANSEN, M., *Constitution of Binary Alloys*, McGraw-Hill Book Compagny, New-York, Toronto, London, pp. 1068-1072, 1958.
 - [42] PORTEVIN, A. and LE CHÂTELIER, F., *Compt. Rend. Acad. Sci. Paris*, Vol. 176, p. 507, 1923.
 - [43] BIZON, P.T. and SPERA, D.A., *Thermal Fatigue of Materials and Components*, ASTM STP 612, ASTM, pp. 106-122, 1976.
 - [44] WOODFORD, D.A. and MOWBRAY, D.F., *Mater. Sci. Eng.*, Vol. 16, pp. 5-43, 1974.
 - [45] GEMMA, A.E., LANGER, B.S. and LEVERANT, G.R., *Thermal Fatigue of Materials and Components*, ASTM STP 612, pp. 199-213, 1976.
 - [46] MEYERS, M.A. and CHAWLA, K.K., *Mechanical Metallurgy, Principles and Applications*, Prentice-Hall Inc., Englewood Cliffs, New Jersey, 761 p., 1984.
 - [47] INGLIS, C.E., *Proc. Inst. Naval Arch.*, Vol. 55, p. 163, 1913.
 - [48] NEWMAN Jr., J.C., A Crack Closure Model for Predicting Fatigue Crack Growth under Aircraft Spectrum Loading, in *Methods and Models for Predicting Fatigue Crack Growth under Random Loading*, ASTM STP 748, ASTM, pp. 53-84, 1981.
 - [49] PARIS, P.C. and ERDOGAN, F., *J. Basic Eng.*, Trans. ASME, Vol. 85, p. 528, 1963.
 - [50] PARIS, P.C. et al., *Extensive Study of the Low Cycle Fatigue Crack Growth Rates in A533 and A508 Steels*, ASTM STP 513, ASTM, Philadelphia, p. 141, 1972.
 - [51] COFFIN, L.F., *A Study of the Effects of Cyclic Thermal Stresses on a Ductile Metal*, Transactions of the ASME, Vol. 76, pp. 931-950, 1954.
 - [52] BASQUIN, O.H., *Proc. ASTM*, Vol. 10, p. 25, 1910.
 - [53] MORROW, J.D., *Internal Friction, Damping and Cyclic Plasticity*,

- ASTM STP 378, ASTM, Philadelphia, p. 72, 1965.
- [54] MANSON, S.S. and HIRSCHBERG, M.H., *Fatigue - An Interdisciplinary Approach*, Proc. 10th Sagamore Conf., Syracuse Univ. Press, Syracuse, N.Y., p. 133, 1964.
 - [55] LANDGRAF, R.W., ASTM STP 467, ASTM, Philadelphia, p. 3, 1970.
 - [56] FISHER, J.C., Calculation of Diffusion Penetration Curves for Surface and Grain Boundary Diffusion, *J. of Applied Physics*, Vol. 22, No. 1, 1951.
 - [57] MARTIN, G. and PERRAILLON, B., *Grain Boundaries Structure and Kinetics*, ASM, pp. 239-295, 1980.
 - [58] CHABOCHE, J.L., *Revue Française de Mécanique*, No. 50-51, pp. 71-82, 1974.
 - [59] TOMKINS, B., *Philosophical Magazine*, Vol. 18, pp. 1041-66, 1968.
 - [60] LEMAITRE, J. and CHABOCHE, J.L., *Mécanique des matériaux solides*, Pub. Dunod, Paris, 532 p., 1985.
 - [61] SMIALEK, J.L. and MEIER, G.H., High-Temperature Oxidation, in *Superalloys II*, Eds. C.T. Sims et al., New York, pp. 293-326, 1987.
 - [62] BIRKS, N. and MEIER, G.H., *Introduction to High Temperature Oxidation of Metals*, Pub. Edward Arnold, London, 198 p., 1983.
 - [63] GIGGINS, C.S. and PETIT, F.S., Oxidation of Ni-Cr Alloys Between 800° and 1200°C, *Trans. TMS-AIME*, Vol. 245, pp. 2495-2507, 1969.
 - [64] PETIT, F.S., *Trans. TMS-AIME*, Vol. 239, p. 1296, 1967.
 - [65] THIBAUT, S., Détermination des paramètres cinétiques d'oxydation du MAR-M247 à haute température, *Final Year Project*, École Polytechnique de Montréal, Août 1989.
 - [66] DALPÉ, É., Détermination des paramètres cinétiques d'oxydation du René 80 DS à haute température, *Final Year Project*, École Polytechnique de Montréal, Avril 1993.
 - [67] KIRKALDY, J.S. and YOUNG, D.J., *Diffusion in Condensed State*, Pub. The Institute of Metals, Carlton House Terrace, London, UK, 1987.

- [68] LITZ, J., RAHMEL, A. and SCHORR, M., Selective Carbide Oxidation and Internal Nitridation of Ni-Base Superalloys IN 738 LC and IN 939 LC, *Oxidation of Metals*, Vol. 30, Nos. 1/2, pp. 95-105, 1988.
- [69] HOLMAN, J.P., *Heat Transfer*, 5th Edition, pub. by Mc Graw Mill Company, 1982.
- [70] ASKILL, J., Tracer Diffusion Data for Metals, Alloys, and Simple Oxides, IFI/Plenum, New York, p. 68, 1970.
- [71] SCHÜTZE, M., Assessment of the Limits to the Protective Effect of Oxide Scales in High Temperature Technology, Set by Deformation of the Substrate Material, *Int. J. Pres. Ves. & Piping*, Vol. 47, pp. 293-315, 1991.
- [72] SAMSONOV, G.V., *The Oxide Handbook*, IFI/Plenum, New York, 2nd Ed., 1982.
- [73] ROBERTSON, J. and MANNING, M.I., Limits to Adherence of Oxide Scales, *Mater. Sci. Techn.*, Vol. 6, pp. 81-91, 1990.
- [74] MEVREL, R., Cyclic Oxidation of High-Temperature Alloys, *Materials Science and Technology*, Vol. 3, 1987.
- [75] SCHÜTZE, M., Failure of Oxide Scales on Advanced Materials Due to the Presence of Stresses, *Proc. on High Temperature Corrosion of Advanced Materials and Protective Coatings*, 5-7 December 1990, Tokyo, Japan, Eds. Y. Saito et al., Pub. Elsevier Science, pp. 39-49, 1992.
- [76] LOWELL, C.E., SMIALEK, J.L. and BARRETT, C.A., in *High Temperature Corrosion*, Ed. R.A. Rapp, Houston, Texas, National Association of Corrosion Engineers, pp. 219-226, 1983.
- [77] SPERA, D.A. and GRSAFFE, S.J., Life Prediction of Turbine Components: On-Going Studies at the NASA Lewis Research Center, *Technical Memorandum X-2664*, NASA, 1973.
- [78] *Aerospace Structural Metals Handbook*, Belfour Stulen Inc., Department of Defence, Vol. 5, 1991.

- [79] Vac Aero International, St-Laurent, Québec, Canada.
- [80] GUPTA, A.K., TERADA, T., PATNAIK, P.C. and IMMARIGEON, J.P., Evaluation of High Temperature Protective Coatings for Gas Turbine Engines under Simulated Service, *AGARD Conference Proc. No. 461*, High Temperature Surface Interactions, Specialists Meeting Held in Ottawa, Canada, April 24-26th 1989, pp. 14.1-14.31.
- [81] DILS, R.R. and FALLANSBEE, F.S., Dynamic Oxidation and Corrosion in Power Generating Units, *Corrosion, NACE*, ed., Vol. 33, pp. 385-395, 1977.
- [82] Recommended Practices for Measurement of Gas Path Pressures and Temperatures for Performance Assessment of Aircraft turbine Engines and Components, H.I.H. Saravanamuttoo Editor, *AGARD Advisory Report No 245*, pp.77-102, 1990.
- [83] PATNAIK, P.C., ELDER, J.E. and THAMBURAJ, R., Degradation of Aluminide Coated Directionally Solidified Superalloy Turbine Blades in an Aero Gas Turbine Engine, *Superalloys 88*, S. Reichman et al., ed., The Metallurgical Society, Pennsylvania, pp. 815-824, 1988.
- [84] VENKATASUBRAMANIAN, T.V. and UNVALA, B.A., An AC Potential Drop System for Monitoring Crack Length, *J. Phys. E: Sci. Instrum.*, Vol. 17, pp. 765-771, 1984.
- [85] HWANG, I.S. and BALLINGER, R.G., A Multi-Frequency AC Potential Drop Technique for the Detection of Small Cracks, *Meas. Sci. Technol.*, Vol. 3, pp. 62-74, 1992.
- [86] VERPOEST, I., AERNOUDT, E., DERUYTTERE, A. and NEYRINCK, D.M., An Improved AC Potential Drop Method for Detecting Surface Microcracks During Fatigue Tests of Unnotched Specimens, *Fatigue of Engineering Materials and Structures*, Vol. 3, pp. 203-217, 1981.
- [87] CARLSSON, J., Experimental Studies of Brittle Fracture Propagation, *Trans. R. Inst. Technol.*, Stockholm, No. 189, pp. 1-55, 1962.

- [88] Matelect Ltd., *Crack Growth Monitor CGM5 - Operation and Applications Manual*, London, U.K., 1986.
- [89] RESEARCH INC., *Micristar's User Manual, model 828D*, U.S.A., 1984.
- [90] SHEN, P., GAN, D. and LIN, C.C., Microstructures and Cristallographic Relationships in Aluminized Coatings on René 80, *Materials Science and Engineering*, Vol. 78, pp. 171-178, 1986.
- [91] WOOD, J.H. and GOLDMAN, E.H., Protective Coatings in *Superalloys II*, Eds. C. T. Sims, N. S. Stoloff and W. C. Hagel, Wiley, New York, pp. 359-384, 1987.
- [92] MACKAY, R.A. and EBERT, L.J., Factors Which Influence Directional Coarsening of γ' During Creep in Nickel-Base Superalloy Single Crystals in *Superalloys 84*, pp. 135-144.
- [93] NATHAL, M.V. and EBERT, L.J., Influence of Composition on the Microstructure and Mechanical Properties of a Nickel-Base Superalloy Single Crystal in *Superalloys 84*, pp. 125-133.
- [94] OHE, J. and WAKITA, S., Practical Method of Thermal History Analysis by γ' Morphology Changes in Nickel-Base Superalloys in *Superalloy 84*, pp. 93-102.
- [95] GIGGINS, C.S. and PETTIT, F.S., *J. Electrochem. Soc.*, Vol. 118, p. 1782, 1971.
- [96] WALLWORK, G.R. and HED, A.Z., *Oxid. Met.*, Vol.3, p. 171, 1971.
- [97] BARRETT, C.A. and LOWELL, C.E., *Oxid. Met.*, Vol. 11, p. 199, 1977.
- [98] TSAI, M.J. and SHEN, P., Oxidation of Aluminized Coatings on René 80, A Transmission Electron Microscopy Study, *Materials Science and Engineering*, Vol. 83, pp. 135-144, 1986.
- [99] GLENNY, R.J.E., Thermal Fatigue, *High-Temperature Materials in Gas Turbines*, Eds. P.R. Sahm and M.O. Speidel, Pub. Elsevier Science, p. 258, 1974.
- [100] MOM, A.J.A. and BOOGERS, J.A.M., Simulated Service Test Behaviour of Various Internal and External Coating Applied on CF6-50 First Stage Turbine Blades, Eds. W. Betz et al., D. Reidel Pub. Compagny, pp. 1245-1264, 1986.

- [101] MARCHAND, N.J., DORNER, W. and ILSCHNER, B., A Novel Procedure to Study Crack Initiation and Growth in Thermal Fatigue Testing, Surface-Crack Growth: Models, Experiments, and Structures, *ASTM STP 1060*, pp. 237-259, 1990.
- [102] THOMAS, F.O., Private Communication (see [107]).
- [103] *Handbook of Chemistry and Physics*, 67th Edition, CRC Press, page F.98, 1987.
- [104] ROBERSON, J.A. and CROWE, C.T., *Engineering Fluid Mechanics*, Houghton Mifflin Compagny, Boston, MA, pp. 383-388, 1975.
- [105] LAU, J.C. and MORRIS, P.J., Measurements in Subsonic and supersonic Free Jets Using a Laser Velocimeter, *J. Fluid Mech.*, Vol. 93, part 1, pp. 1-27, 1979.
- [106] KNOTT, P. and MOSSEY, P., Supersonic Jet Exhaust Noise Investigation, *Air Force Aero Propulsion Lab.*, TR-76-68, Vol. II, pp. 390-416, 1975.
- [107] THOMAS, F.O., Structure of Mixing Layers and Jets, *Applied Mechanics Review*, Vol. 44, no. 3, pp.119-153, 1991.
- [108] CHURCHILL, S.W. and BERNSTEIN, M., *J.Heat Transfer*, Vol.99, pp. 300-306, 1977.
- [109] BAYLEY, F.J. and PRIDDY, W.J., Effects of Free-Stream Turbulence Intensity and Frequency on Heat Transfer to Turbine Blading, *ASME Gas Turbine Conference*, paper No. 80-GT-79, 1980.
- [110] LOWERY, G.W. and VACHON, R.I., The effect of turbulence on Heat Transfer from Heated Cylinders, *Journal of Heat and Mass Transfer*, Vol. 18, pp. 1229-1242, 1975.
- [111] GLADDEN, H.J. and SIMONEAU, R.J., Review and Assessment of the Database and Numerical Modelling for Turbine Heat Transfer, *Toward Improved Durability in Advanced Aircraft Engine Hot Sections*, IGTI-Vol. 2, Ed. by D.E. Sokolowski, ASME, New York, NY, pp.39-55, 1988.
- [112] NEALY, D.A., MIHELIC, M.S., HYLTON, L.D. and GLADDEN, H.J., Measurements of Heat Transfer Distribution Over the Surfaces of Highly Loaded

- Turbine Nozzle Guide Vanes, *J. of Eng. for Gas Turbines and Power*, Vol. 106, pp.149-158, 1984.
- [113] SATO, T., TAKEISHI, K., and SAKON, T., Thermal Fatigue Life Prediction of Air-Cooled Gas Turbine Vanes, *J. of Eng. for Gas Turbines and Power*, Vol. 108, pp. 414-420, 1986.
- [114] MCKNIGHT, R.L., LAFLEN, J.H. and SPAMER, G.T., Turbine Blade Tip Durability Analysis, *NASA Contract Report NASA CR-165268*, 112 p., 1981.
- [115] Directionally Solidified Materials for High Temperature Service, Ed. by M. McLean, The Metal Society, pp.151-205, 1983.
- [116] WALKER, K.P. and WILSON, D.A., Creep Crack Growth Predictions in INCO 718 Using a Continuum Damage Model, in *Proc. 2nd Symp. Nonlinear Constitutive Relations for High Temperature Application - 1984*, Cleveland, Ohio, USA, NASA CP-2369, pp. 349-372, 1985.
- [117] WALKER, K.P., Research and Development Programs for Nonlinear Structural Modelling with Advanced Time-Temperature Dependant Constitutive Relationships, *NASA Contract Report NASA CR 165533*, 1981.
- [118] CHAN, K.S., LINDHOLM, U.S., BODNER, S.R. and WALKER, K.P., High Temperature Inelastic Deformation Under Uniaxial Loading: Theory and Experiment, *J. of Eng. Mater. and Technol.*, Vol. 111, pp. 345-353, 1989.
- [119] POIRIER, J.-P., Plasticité à haute température des solides cristallins, *Eyrolles Press*, Paris, France, 1976.
- [120] RICE, J.R., Continuum Mechanics and Thermodynamics of Plasticity in Relation to Microscale Deformation Mechanisms, in *Constitutive Equations in Plasticity*, Ed. A.S. Argon, MIT Press, pp. 23-79, 1975.
- [121] KOCKS, U.F., Constitutive Relations for Slip, in *Constitutive Equations in Plasticity*, Ed. A.S. Argon, MIT Press, pp. 81-115, 1975.

FIGURES

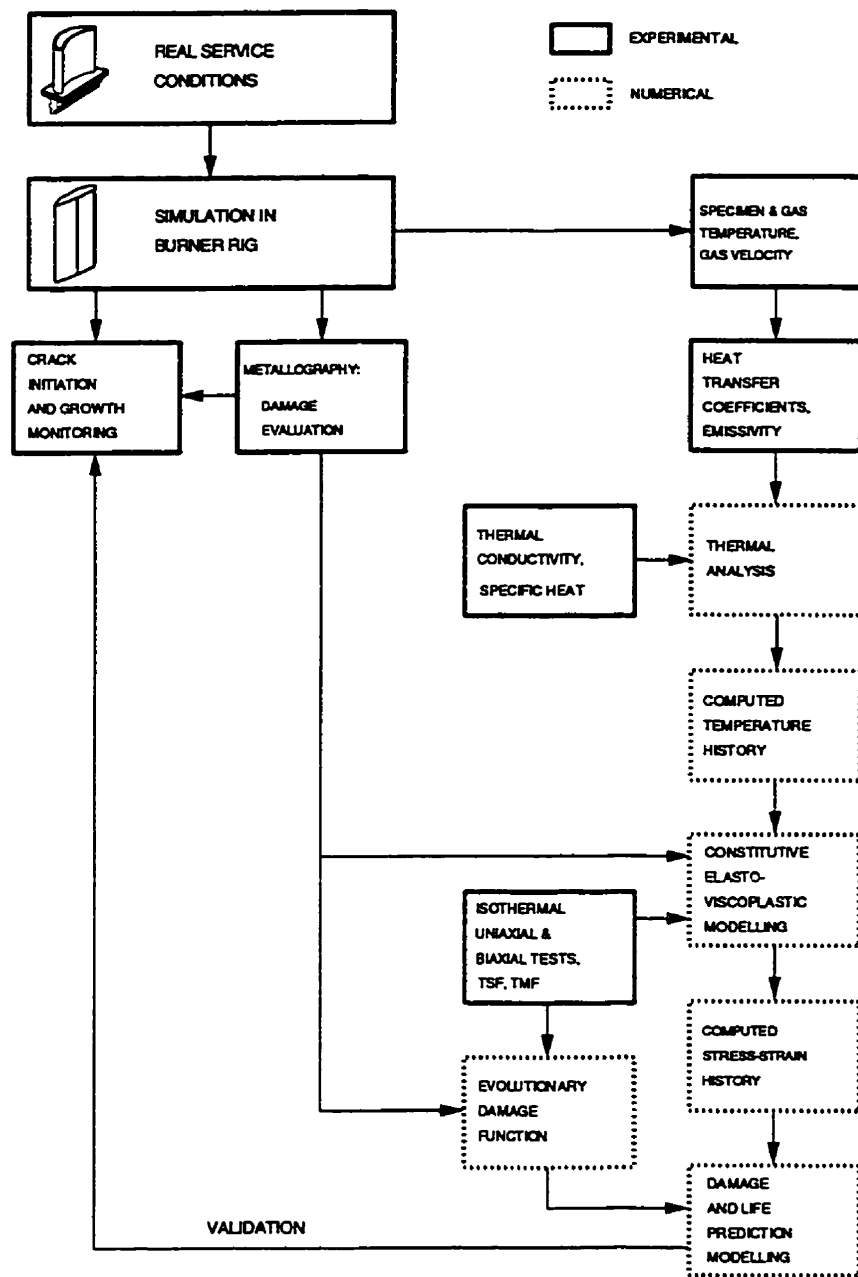
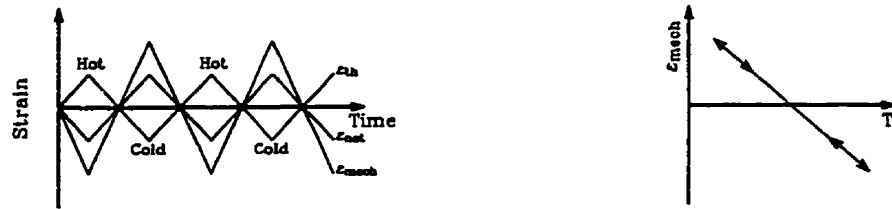
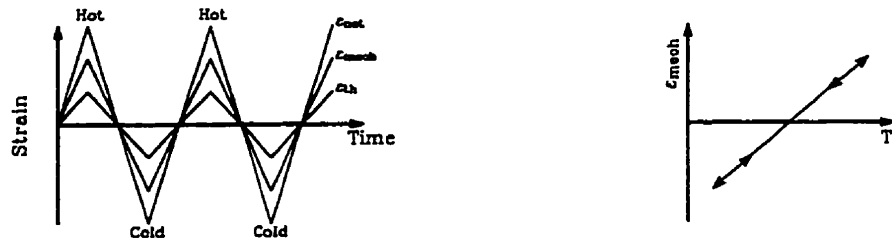


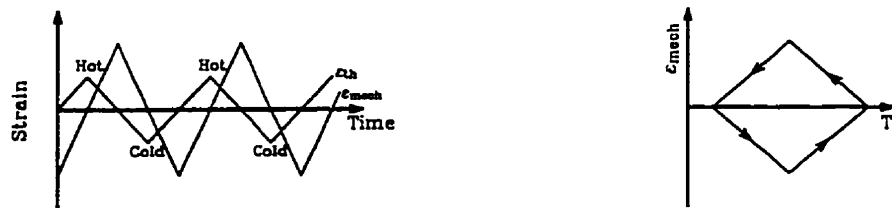
Figure 1.1 Flow chart process of thermal fatigue modelling damage accumulation in turbine blades and vanes.



a) Out-of Phase (OP)



b) In-Phase (IP)



c) Counterclockwise Diamond (CCWD)

Figure 2.1 Strain versus time and temperature under OP, IP and CCWD TMF testing conditions.

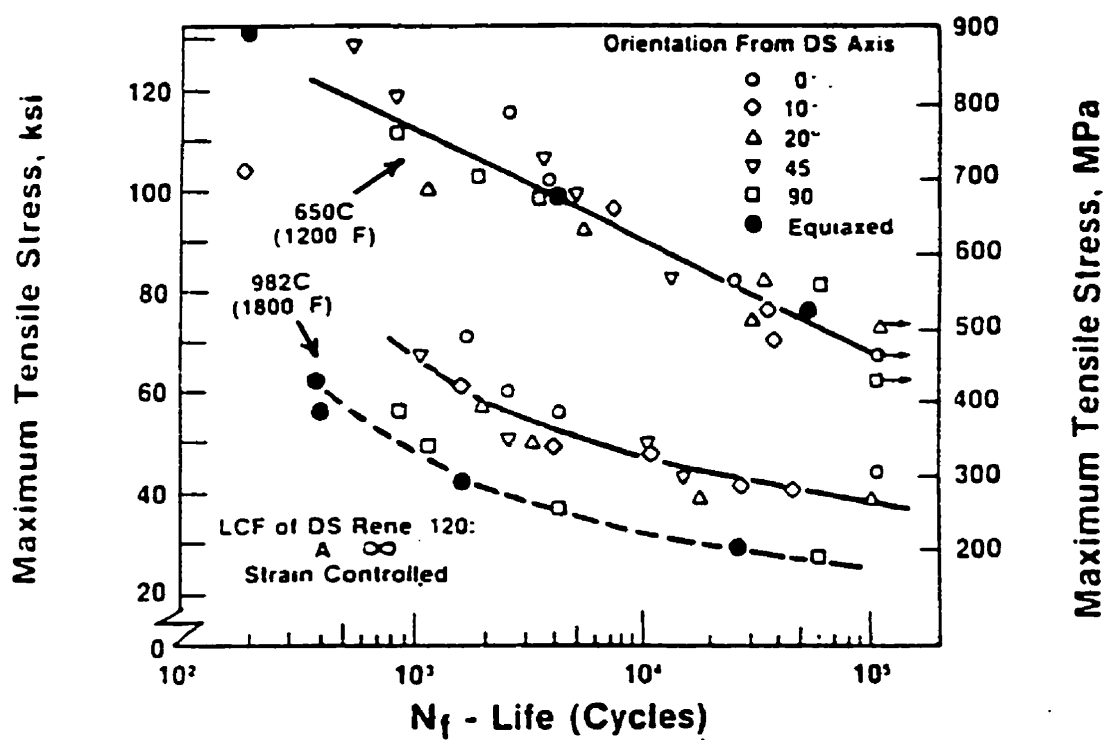


Figure 2.2 Dependence of strain-controlled LCF life on maximum cyclic tensile stress for various orientation in DS René 120. (After [33])



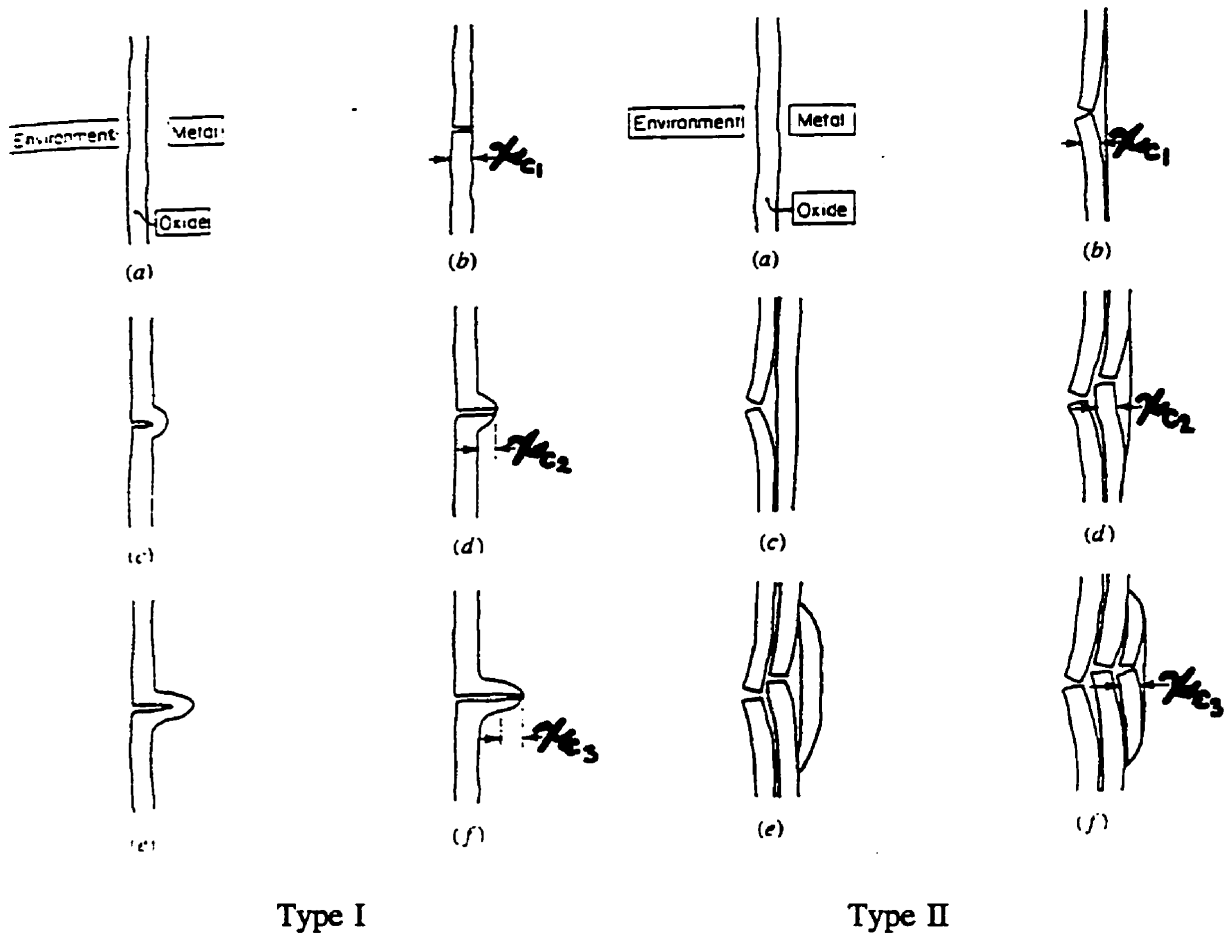


Figure 2.4 Fatigue-oxidation crack growth mechanism B which processes by oxide intrusion of Type I and Type II. Oxide intrusion processes by the following steps: a) Initially an oxide layer forms on the surface; b) When this oxide layer reaches a critical thickness, x_{c1} , the oxide ruptures and crack nucleation occurs; c) then a fresh metallic surface is exposed to the environment which rapidly oxidizes; d) When the thickness of this nearly formed oxide reaches x_{c2} , the oxide again ruptures. The process continues, as illustrated in e) and f). (After [26, 30])

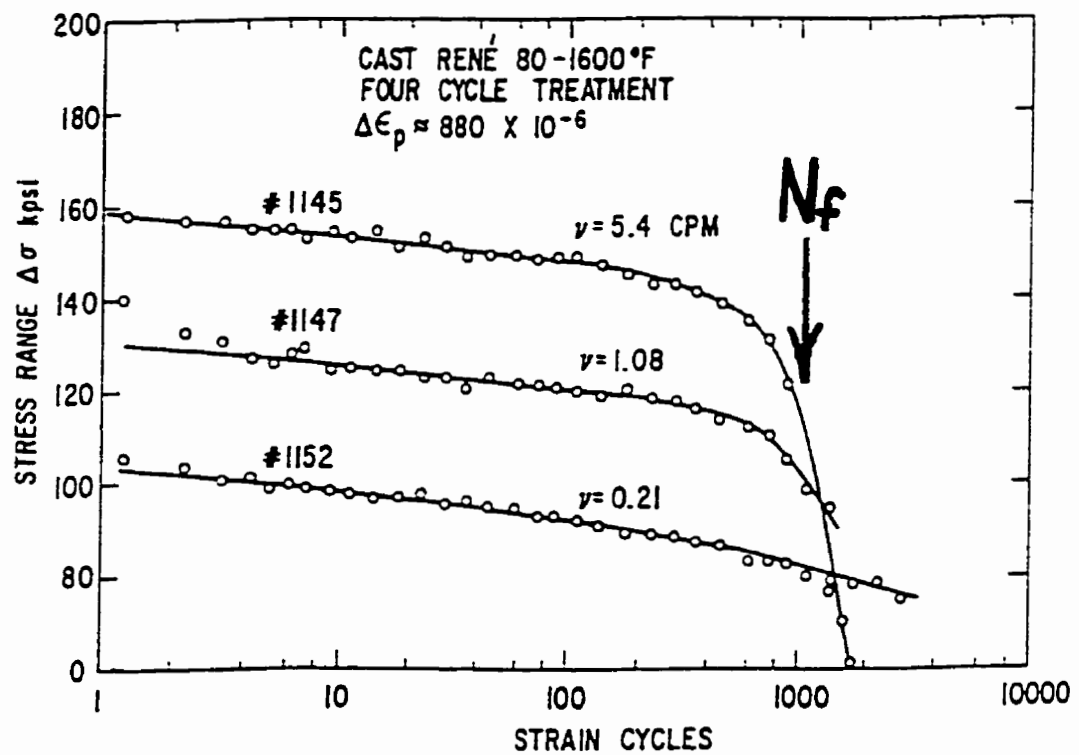


Figure 2.5 Cyclic strain softening behaviour at different frequencies. (After [5])

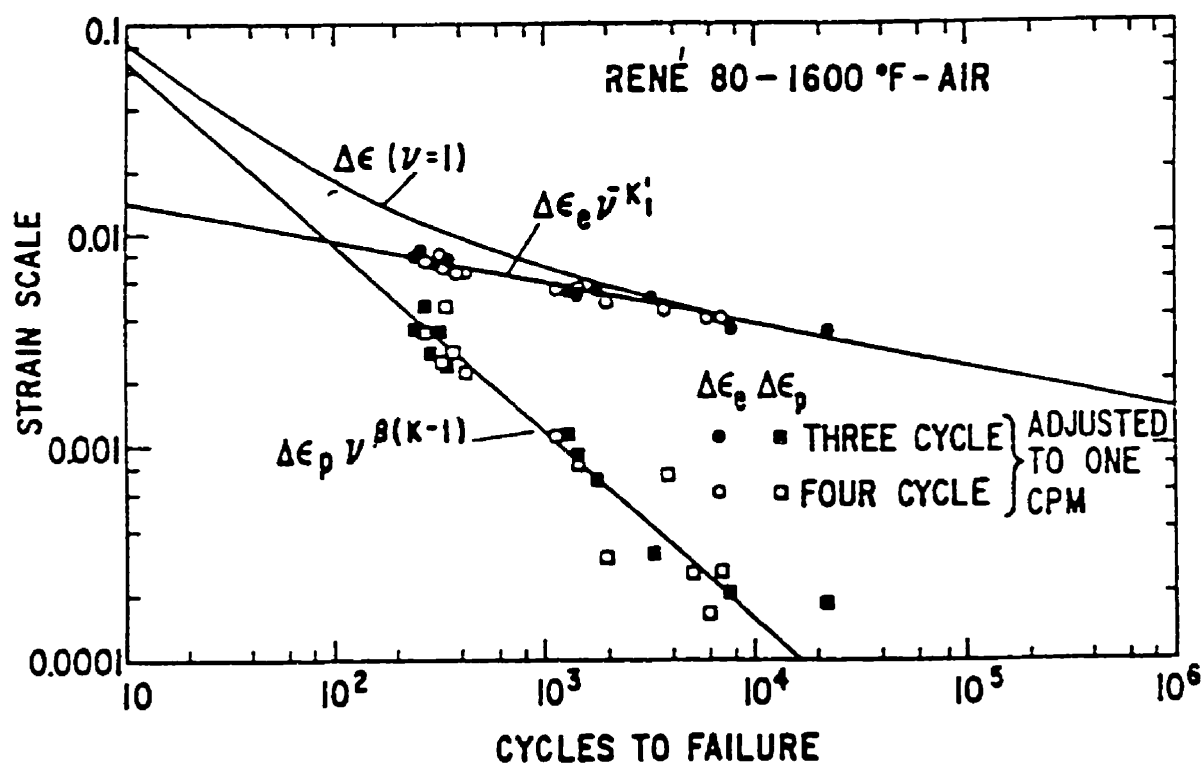


Figure 2.6 Comparison of frequency-modified elastic and plastic strain range vs cycles to failure with test results. (After [5])

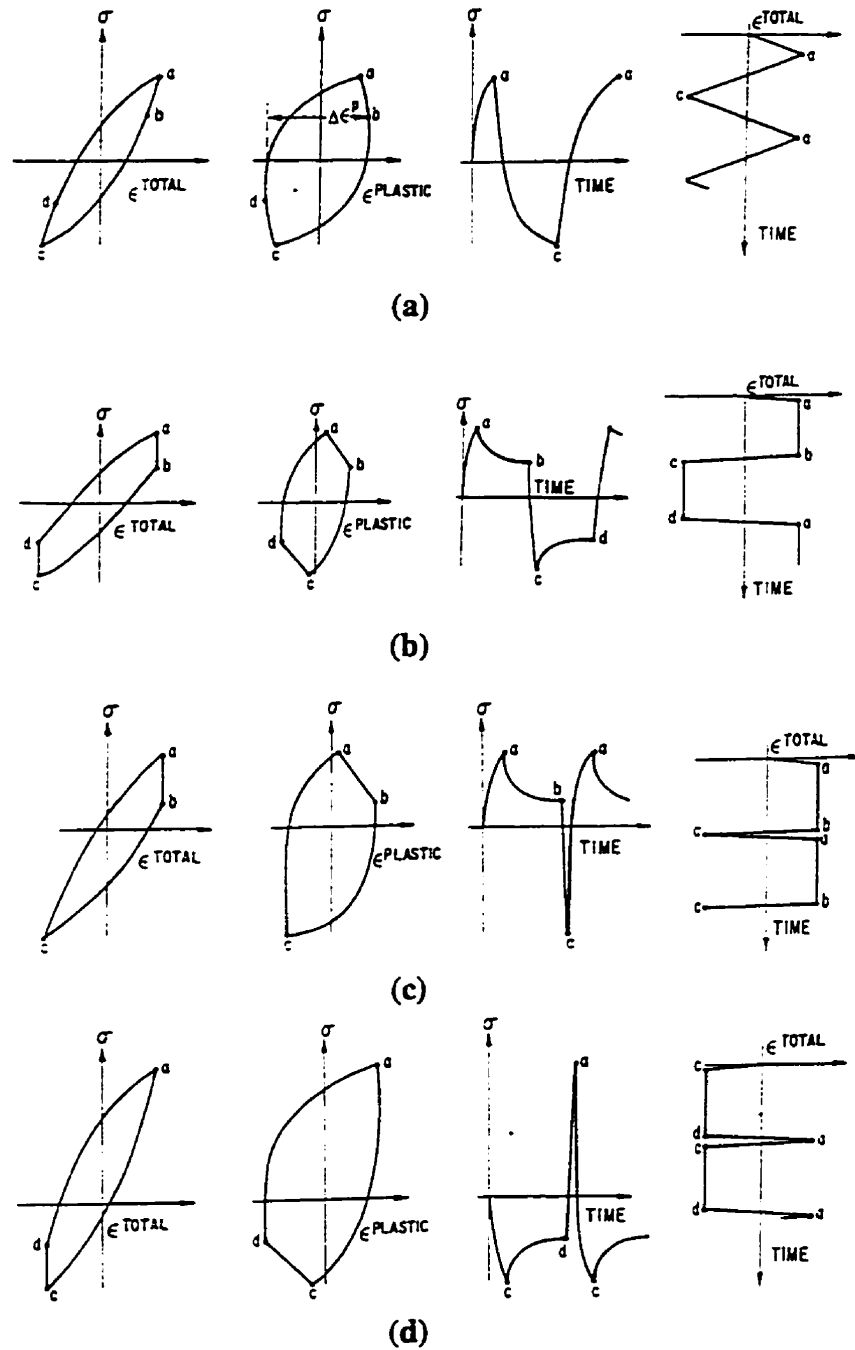


Figure 2.7 Schematic hysteresis loops, stress and strain vs time records for: a) continuous cycling; b) equal hold times in tension and in compression; c) tensile strain hold periods; and d) compressive strain hold periods. (After [6])

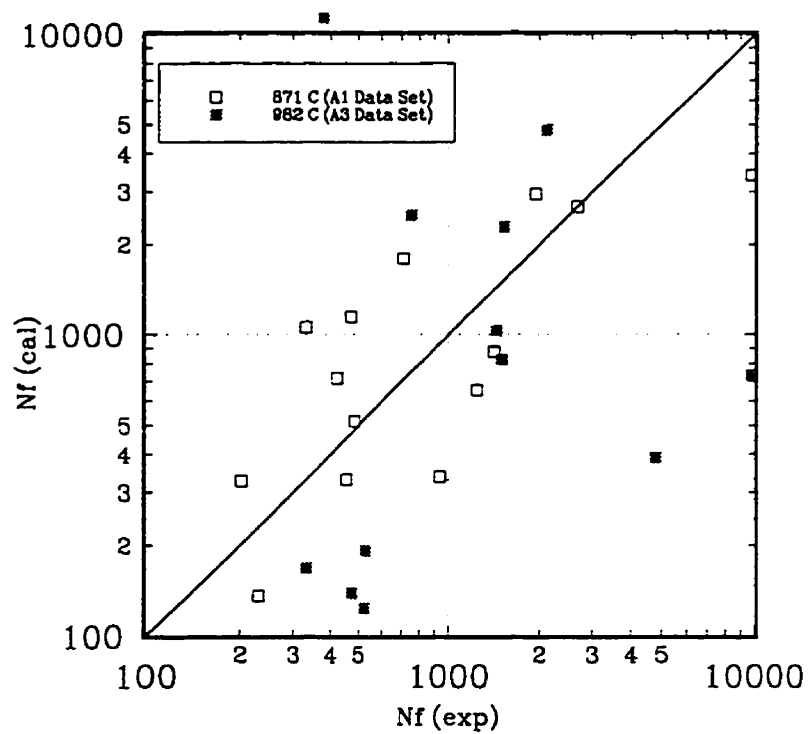


Figure 2.8 Experimental fatigue lives ($N_{f,exp}$) obtained from IF tests on CC René 80 compared with lives ($N_{f,cal}$) calculated with Equation 15.

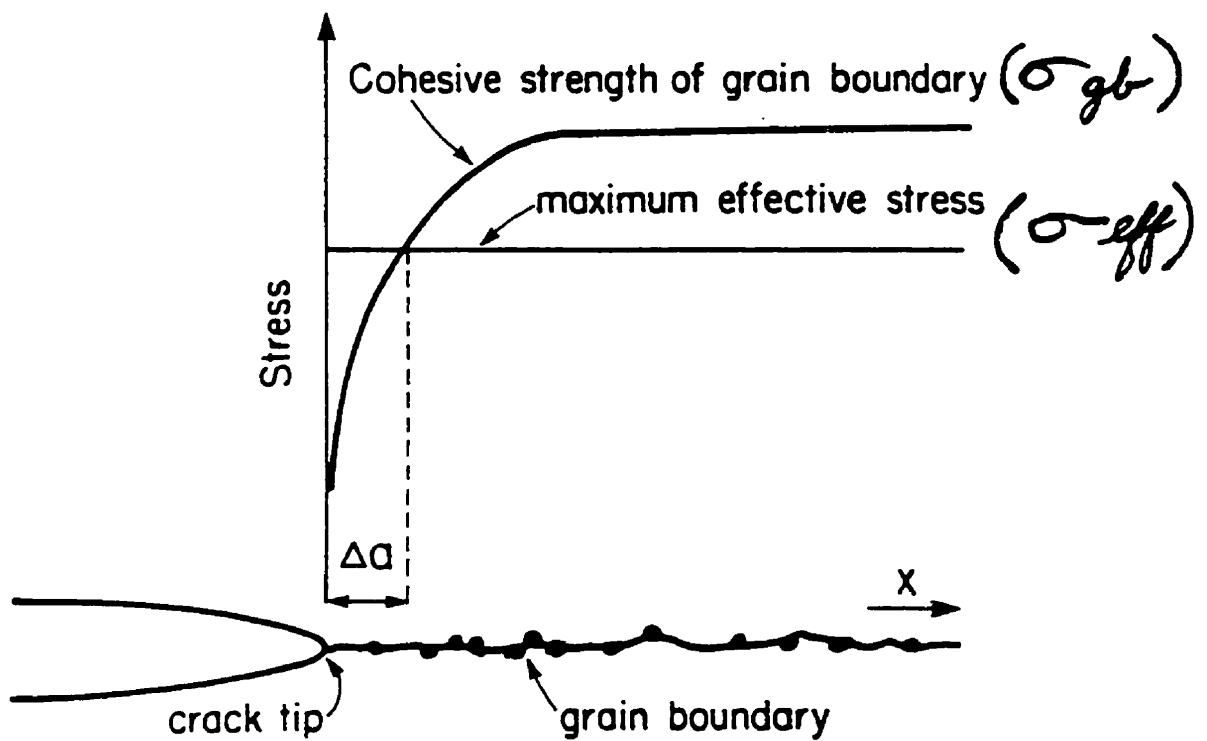


Figure 2.9 Schematic illustration of the mechanism of incremental decohesion along a grain boundary. The cohesive strength of the grain boundary is shown to be reduced in the near crack tip region due to the diffusion of oxygen. (After [3])

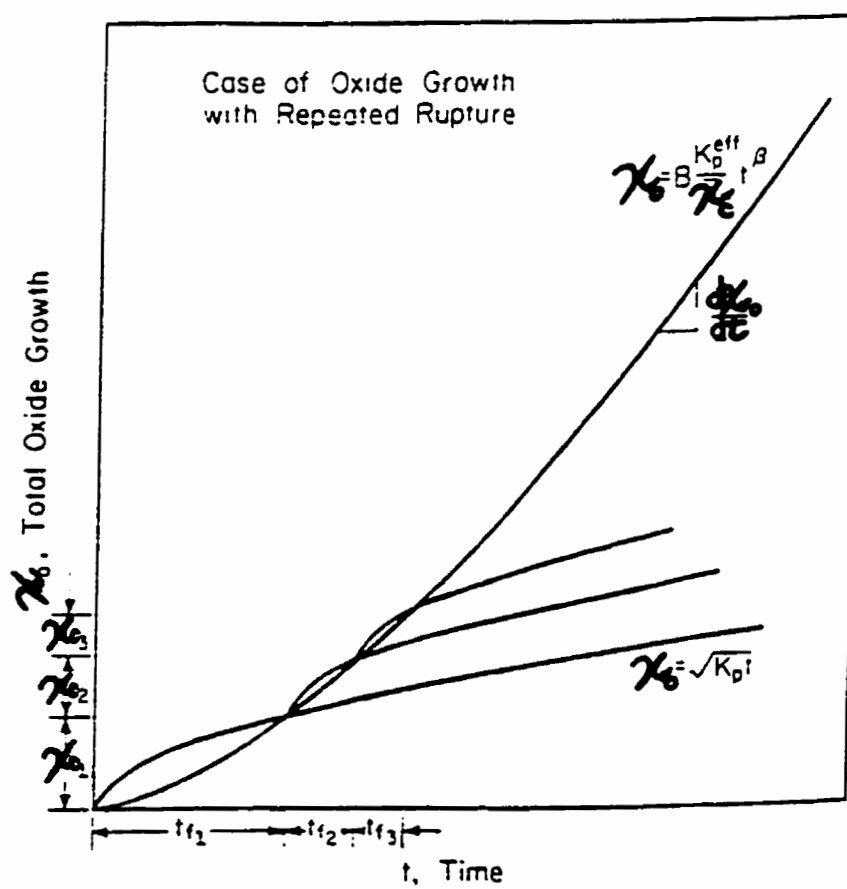
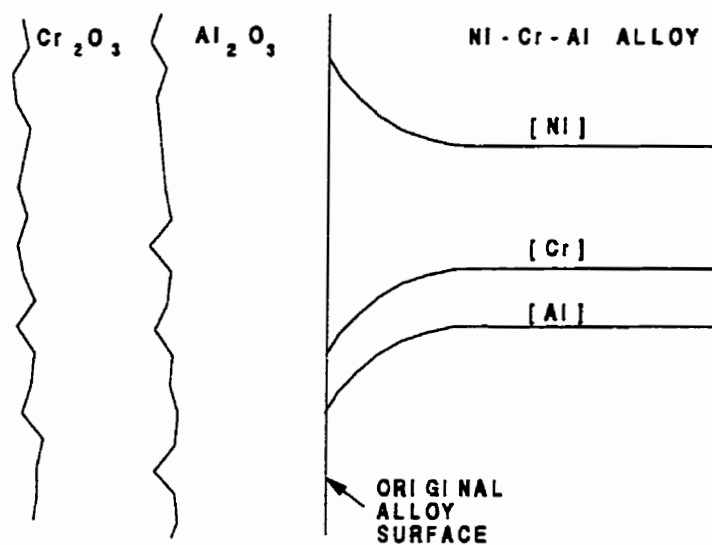
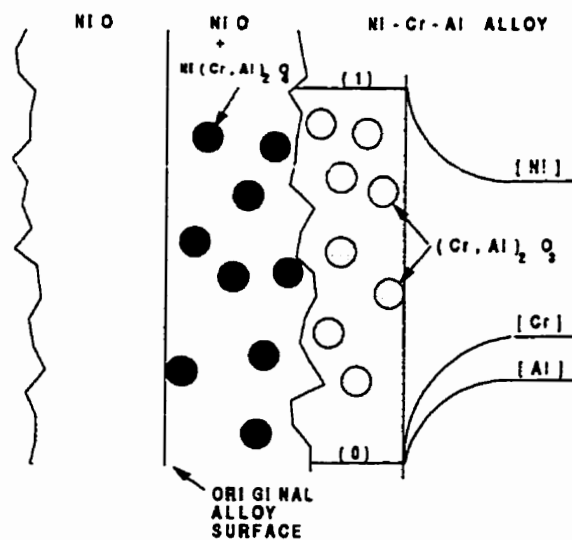


Figure 2.10 Schematic diagram of oxide growth with repeated rupture. (After [30])



(a)



(b)

Figure 2.11 Schematic diagram of the oxide composition and morphology formed at the surface of Cr-Al rich (a) and dilute (b) Ni-Cr-Al alloys [62].

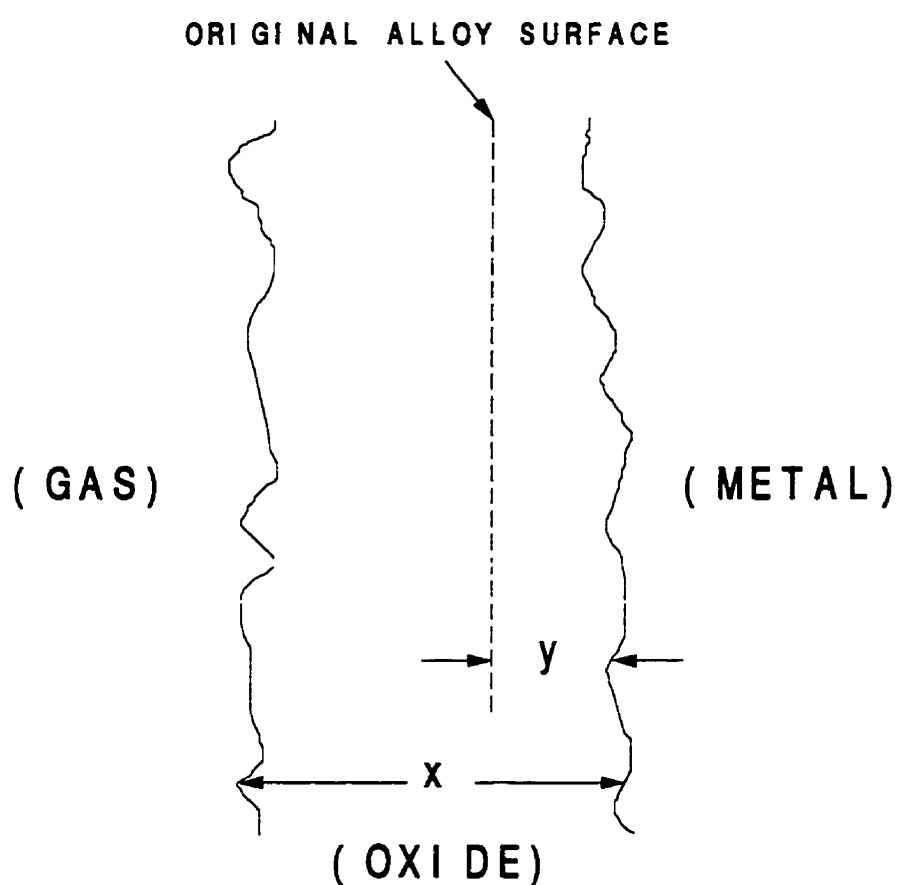
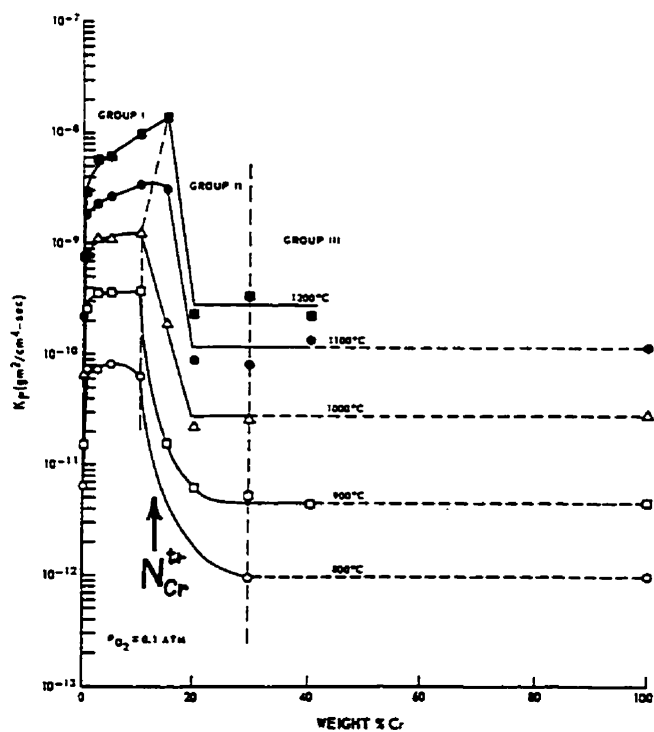
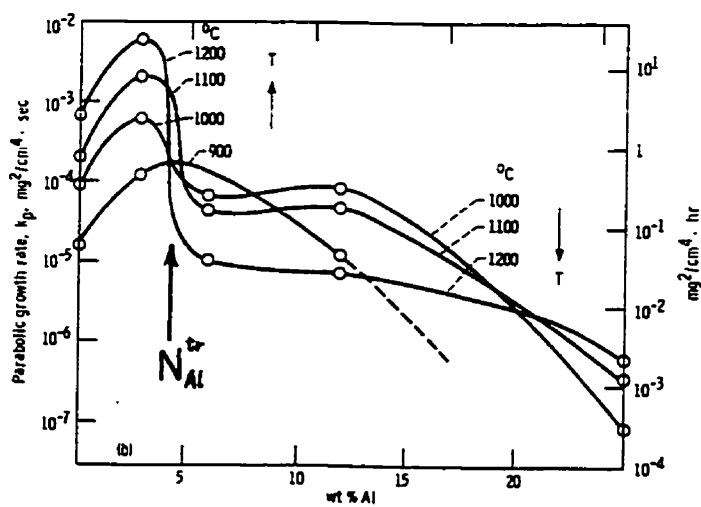


Figure 2.12 Schematic of an oxide scale formed at the surface of a metallic substrate. The variable x represents the oxide scale thickness while the variable y represents the thickness of the substrate layer uniformly consumed through oxidation.



(a)



(b)

Figure 2.13 Solute content effect on the parabolic rate constant k_p' for (a) the Ni-Cr and (b) Ni-Al alloys at different temperatures [63, 64].

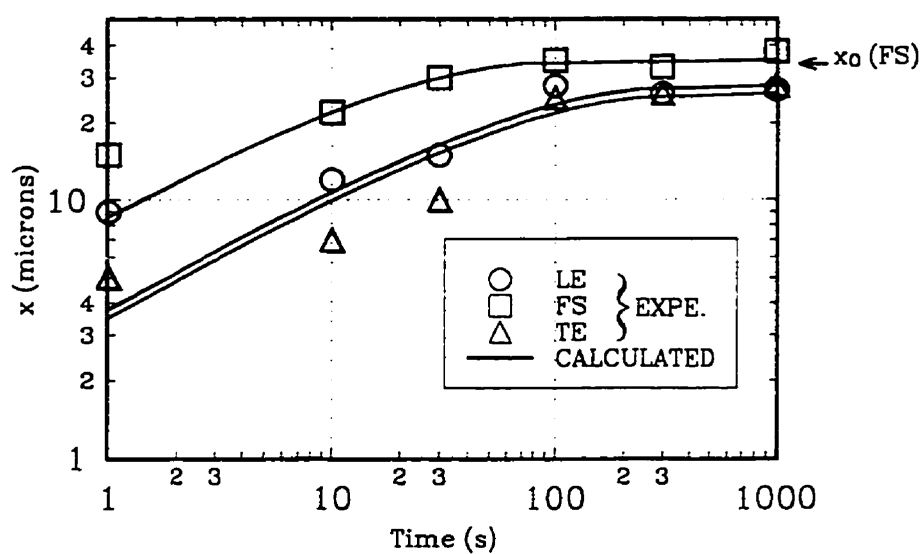


Figure 2.14 Kinetics of oxidation of DS René 80 at 1050 °C for the leading edge (LE), the flat surface (FS) and the trailing edge of a DEW specimen. The experimental data [66] are compared to computed values obtained from Equation 51. The limiting scale thickness x_0 for the FS is indicated by an arrow.

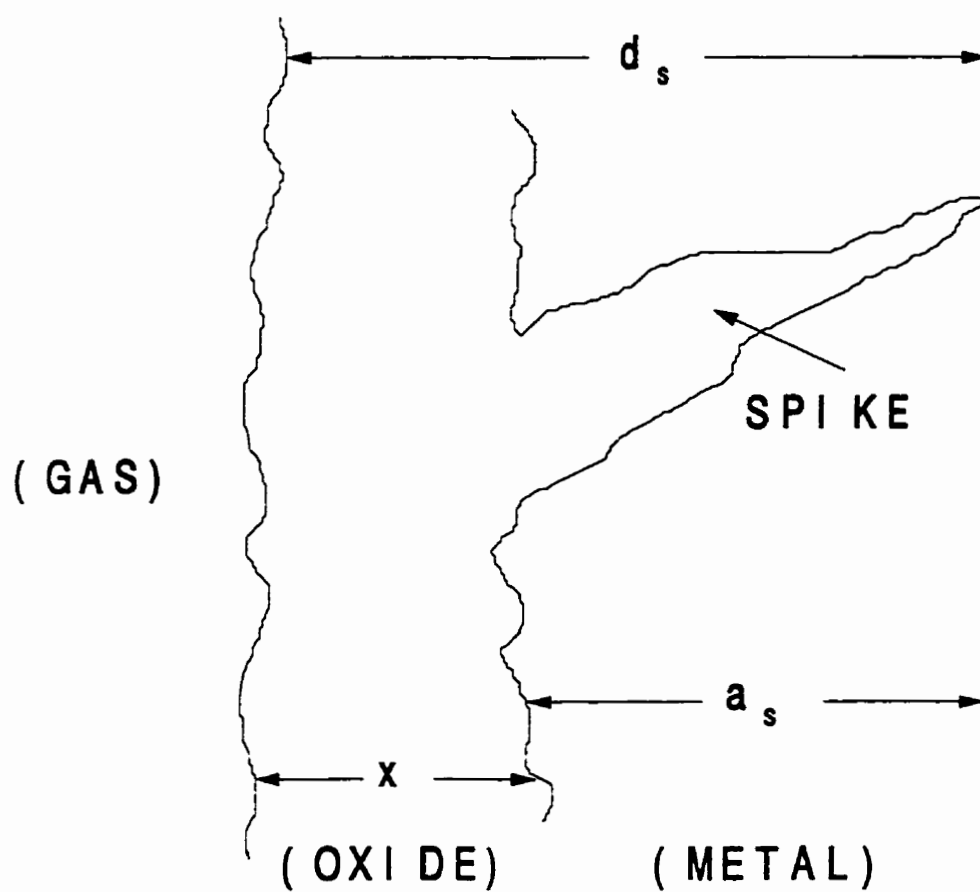


Figure 2.15 Penetrating oxide spike associated with the preferential oxidation of a carbide, a grain boundary or an interdendritic zone next to the surface of the substrate.

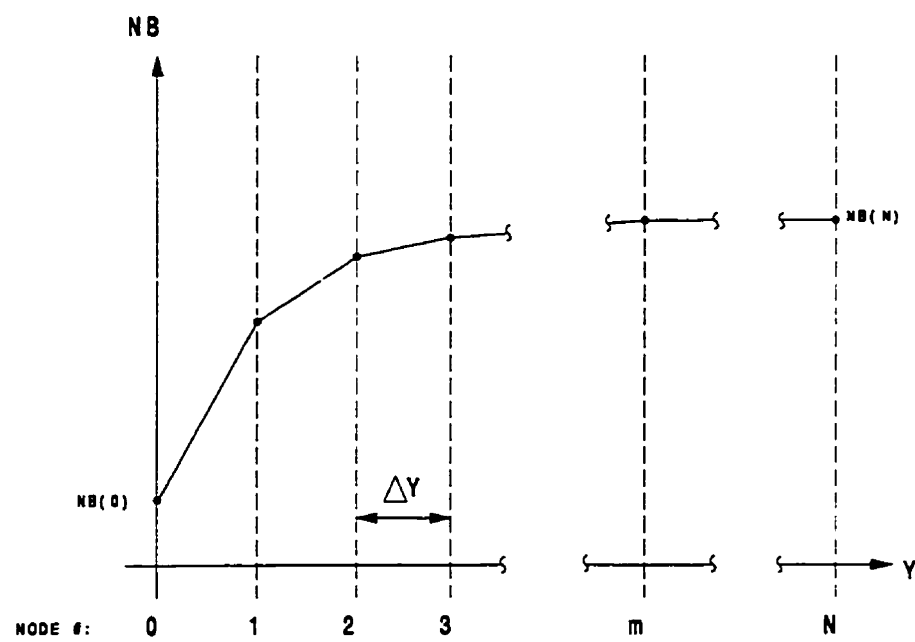
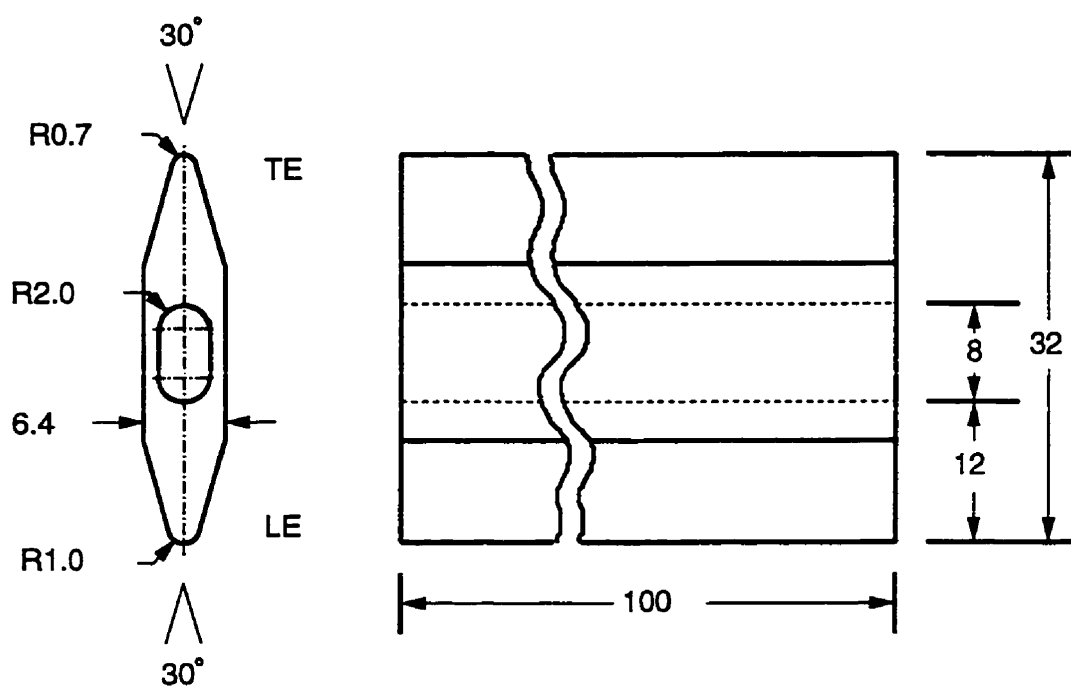


Figure 2.16 Definition of nodal points used in the finite difference method for solving the alloy depletion profile during oxidation.



*all dimensions in mm

Figure 3.1 Double edge-wedge (DEW) specimen geometry meant to reproduce leading edge and trailing edge radii of real airfoils.

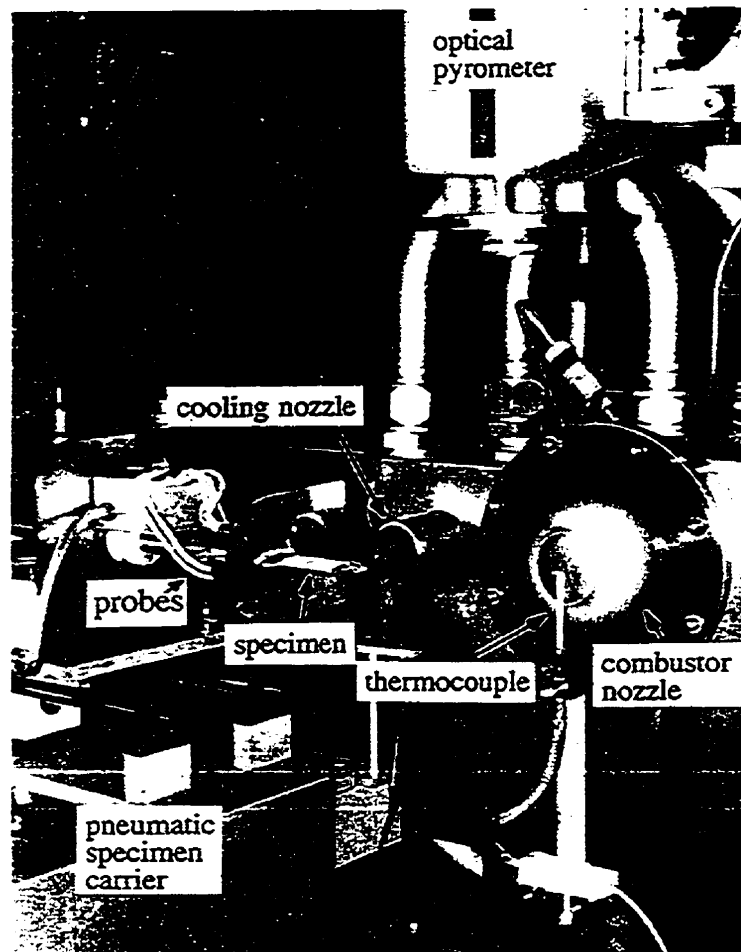


Figure 3.2 IAR burner rig test facility instrumented for thermal fatigue test showing: a) the combustor nozzle, b) the thermocouple used to control hot gas temperature, c) the double-edge wedge airfoil-like specimen in the cooling air stream, d) the pneumatic specimen carrier used to translate the specimen between the hot gas stream and the cooling air stream, e) the cooling nozzle, f) ACPD probes attached to the specimen, g) the optical pyrometer for specimen temperature measurements.

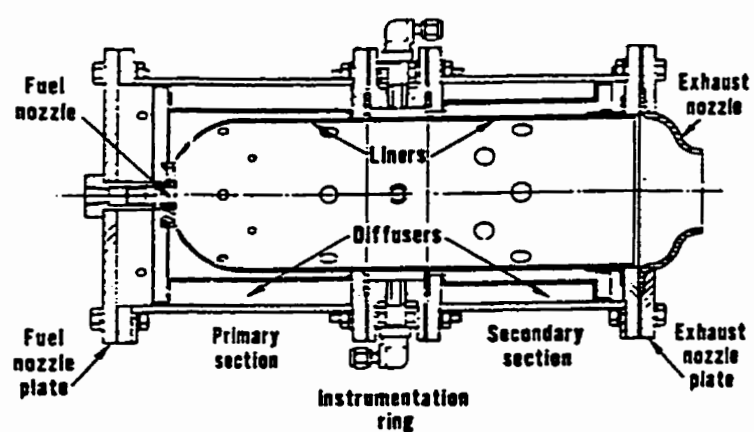


Figure 3.3 Schematic cutaway view of the combustor of the IAR burner rig (after [80]).

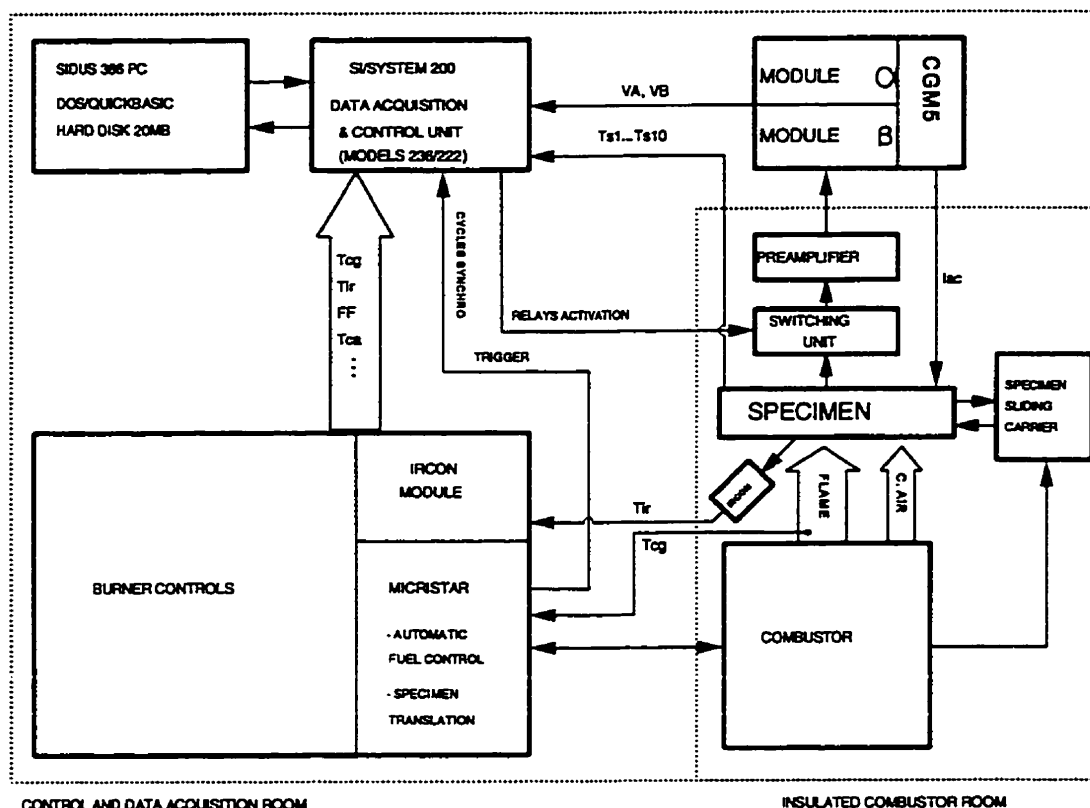


Figure 3.4 Hardware configuration of the burner rig controls and data acquisition system. On this Figure, VA and VB are potential drop in the specimen after amplification by Modules α and β of the CGM5 crack growth monitor, Ts1 to Ts10 are temperatures measured from ten thermocouples attached to the specimen, Tcg is the temperature of control of the hot gas stream, Tir is the temperature of the specimen measured by the optical pyrometer IRCON, FF is the fuel flow, Tca is the temperature of the cooling air jet, Iac is the alternating current applied to the specimen by the CGM5 unit.

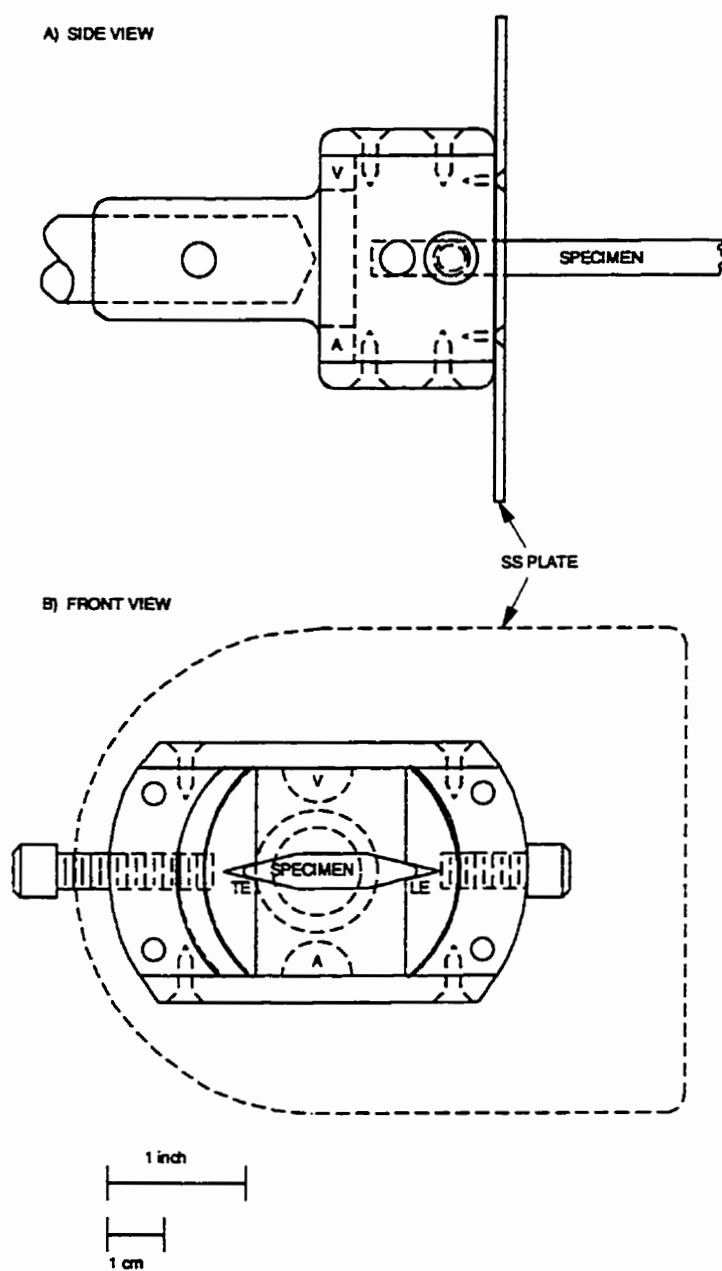


Figure 3.5 Design of the specimen holder which is fixed to the pneumatic carrier in the burner rig (V = hole for the passage of the PD probes; A = hole for the passage of the AC probes).

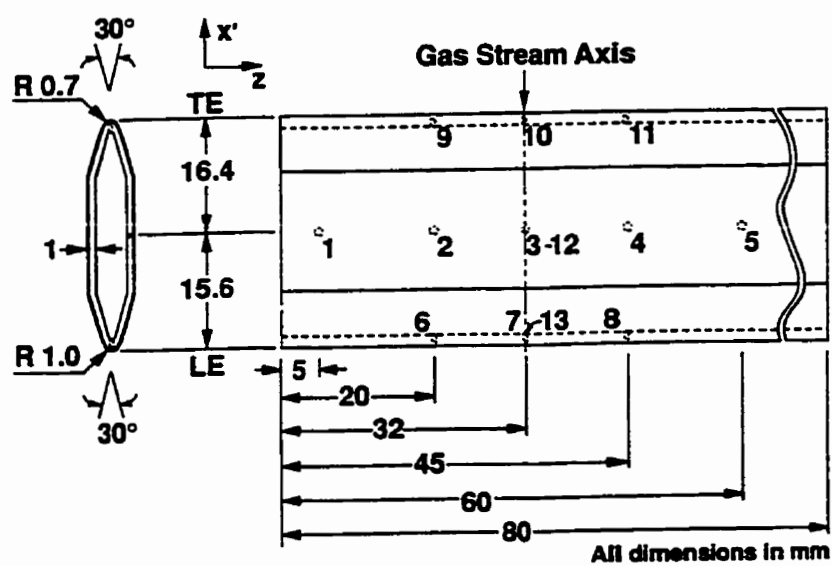


Figure 3.6 Schematic of the instrumented shell-like specimen showing the 13 locations where thin-wire thermocouples were spot-welded inside the specimen.

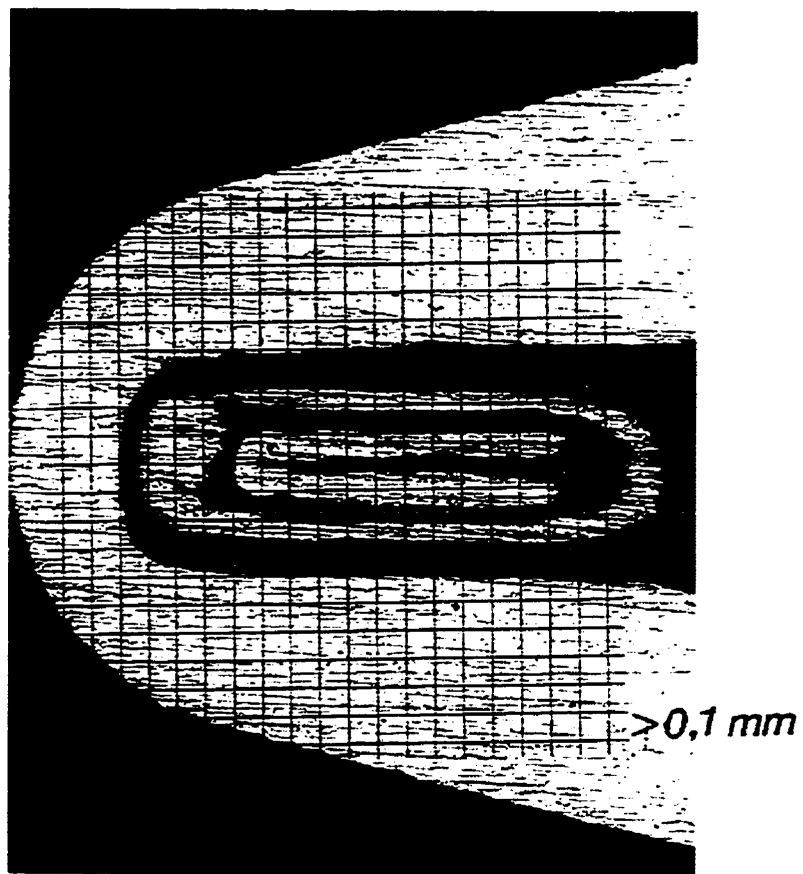


Figure 3.7 Polished leading edge section through the DEW specimen showing the embedded thermocouple inside its metal (310 SS) sheath.

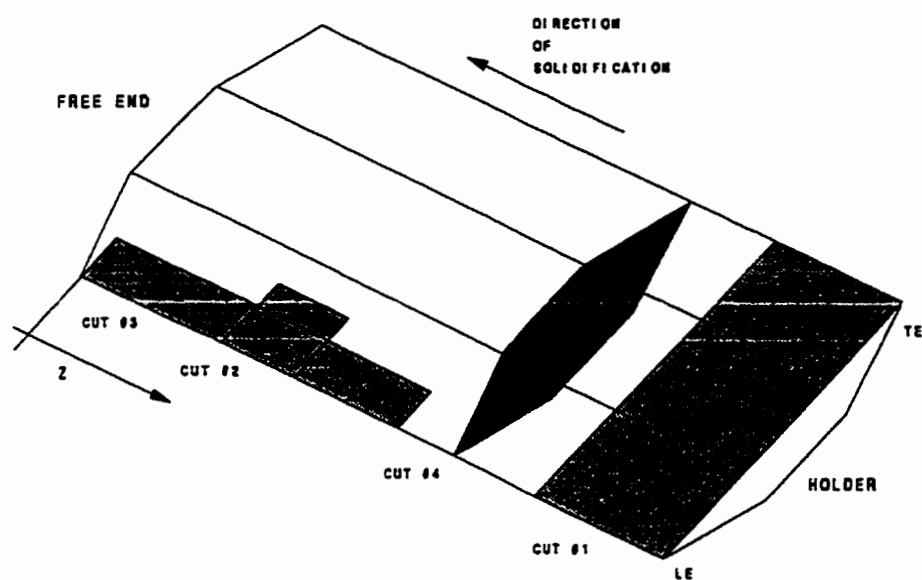


Figure 3.8 Drawing of the different sections cut off the specimens for the metallography. Note that the longitudinal axis z , used to define the metallographic sections along the leading edge (LE, Cuts #2 and #3), is parallel to the direction of solidification.

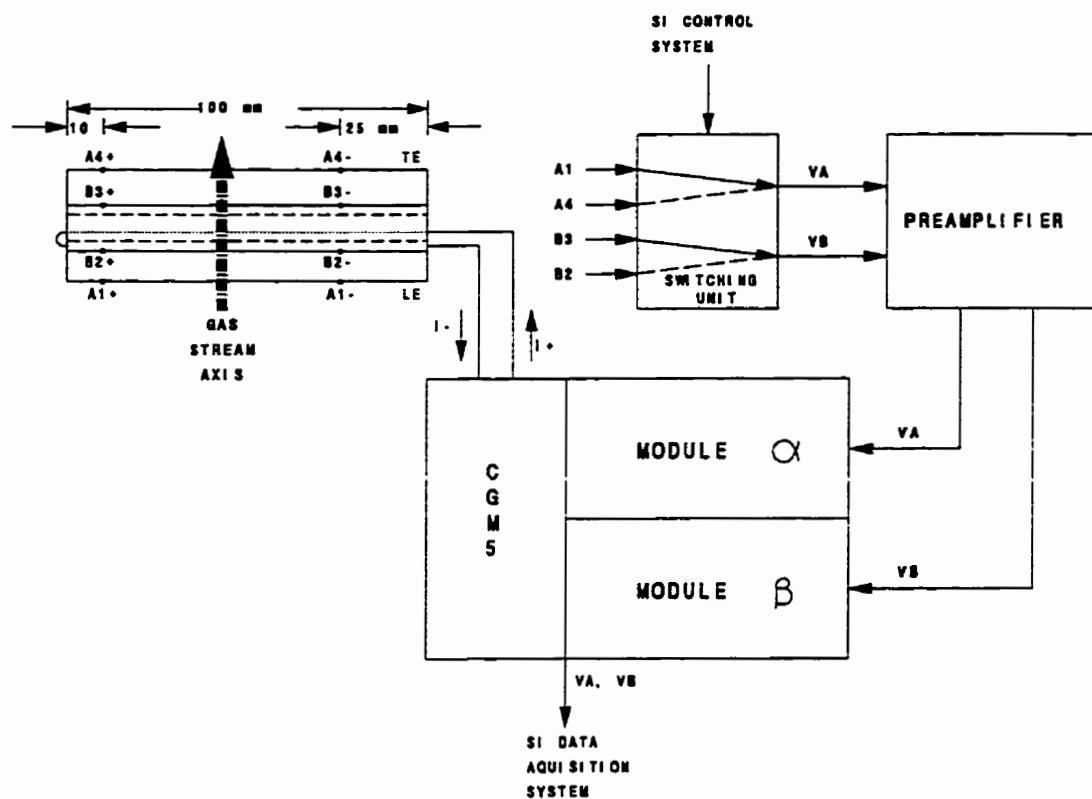


Figure 3.9 Drawing of the double edge-wedge cast specimen with the indication of the current probes location (i) and, the potential probes locations (A1, A4, B2, B3). The ACPD hardware configuration is also illustrated (refer also to Figure 3.4 and see text for details).

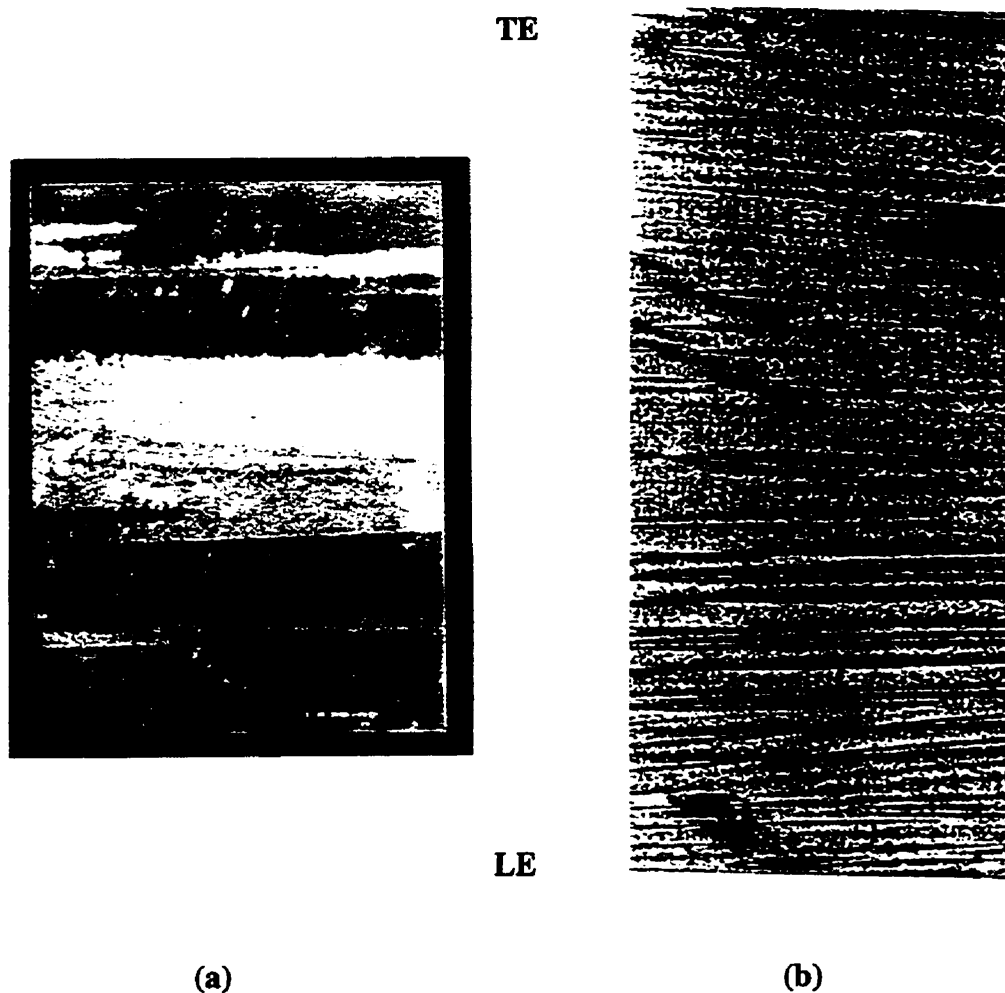
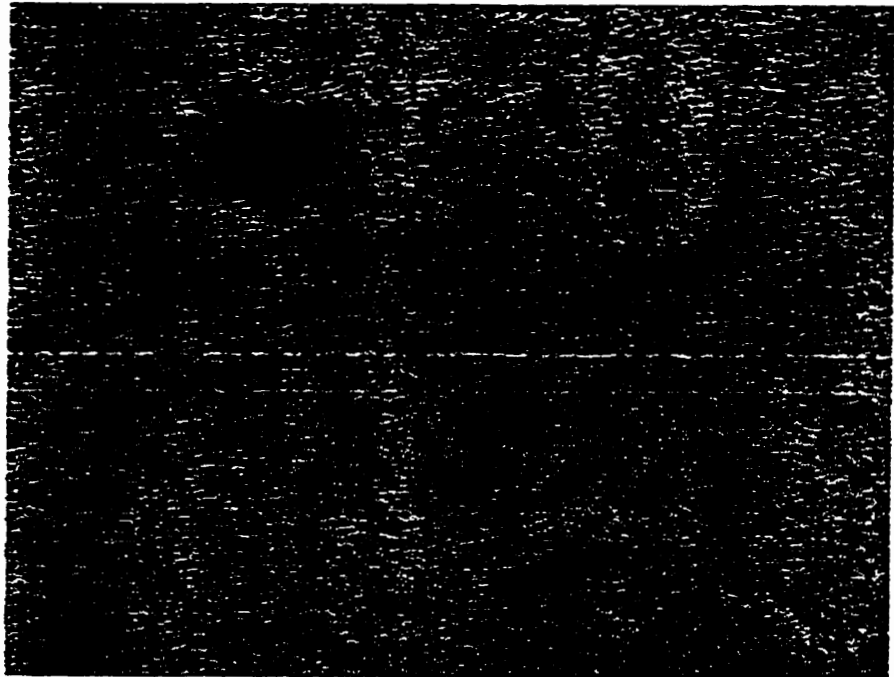
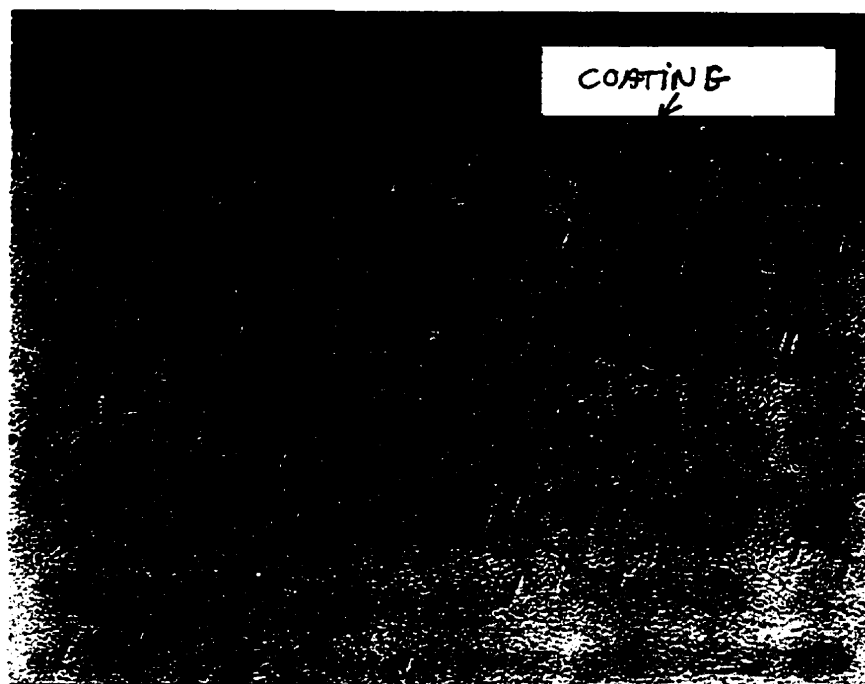


Figure 4.1 Metallographic aspect of the virgin material of an uncoated DEW specimen (Cut #1 on Figure 3.8): (a) columnar grains structure oriented in the direction of solidification (5mL HNO₃, 200mL HCl, 65g FeCl₃, 10 s, 7.5X); (b) dendrites microstructure (Kalling's reagent, 10 s, 6X); and (c) close-up of Chinese script carbides and of cubic γ' precipitates (Marble's reagent, 10 s, 1000X).

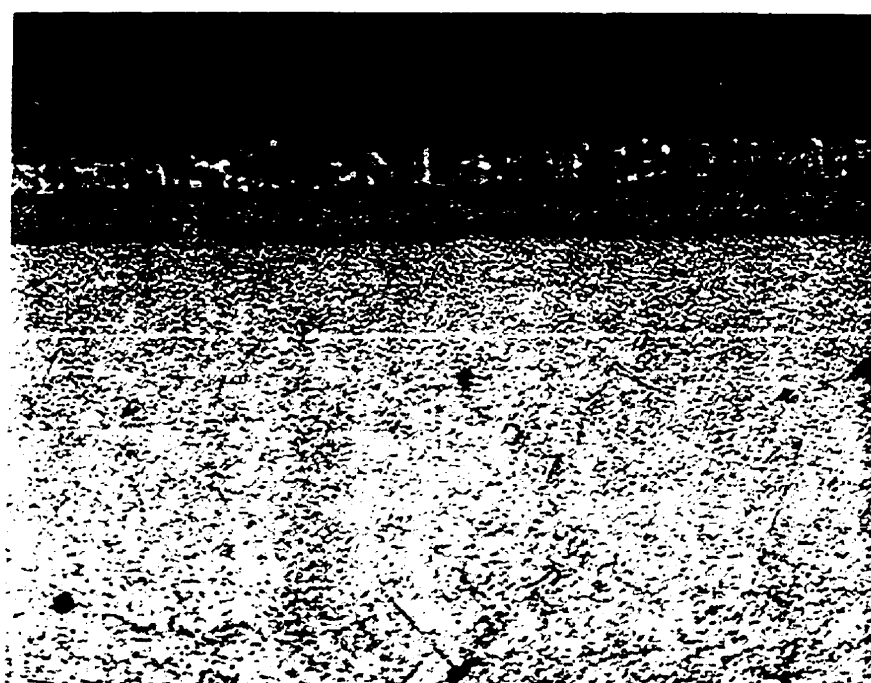


(c)

Figure 4.1 Cont'd.



(a)



Coating

Interdiffusion
Zone

Substrate

(b)

Figure 4.2 Micrographs of the virgin material from a longitudinal section through a coated DEW specimen (Cut #1 on Figure 3.8): (a) dendrites microstructure (37.5X), (b) close-up of the coating and of the interdiffusion zone (5mL HNO_3 , 200mL HCl , 65g FeCl_3 , 10 s, 300X).

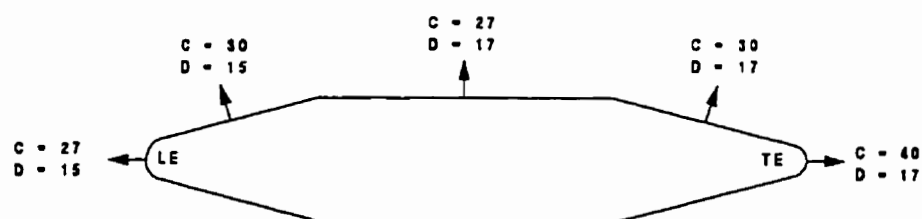


Figure 4.3 Thickness (in μm) of the coating (C) and of the interdiffusion zone (D) around the specimen cross-section.

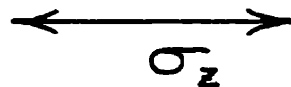


Figure 4.4 γ' precipitates aligned and elongated perpendicularly to the principal stress near a crack tip. (micrograph crack #8 in SRF specimen, along Cut #3 on Figure 3.8, 2500X)

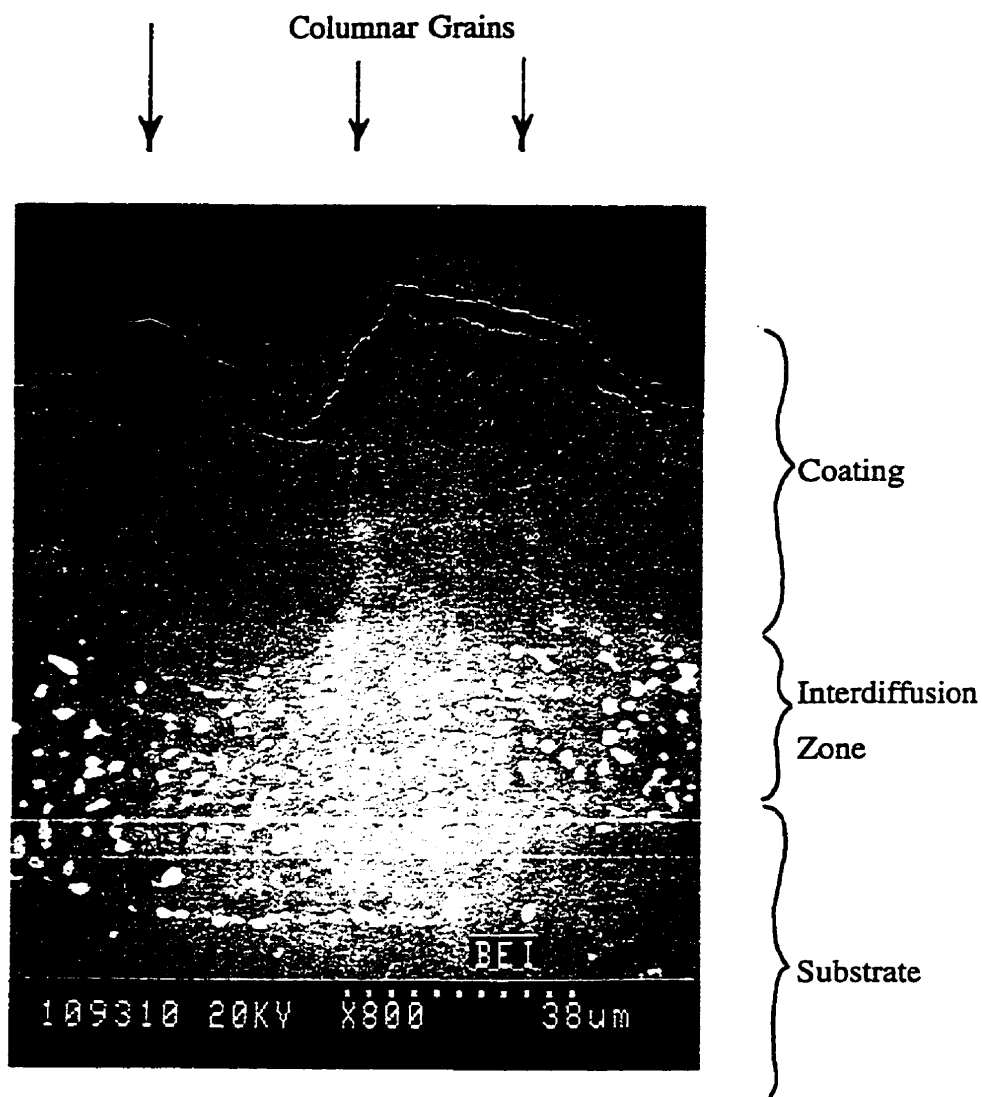
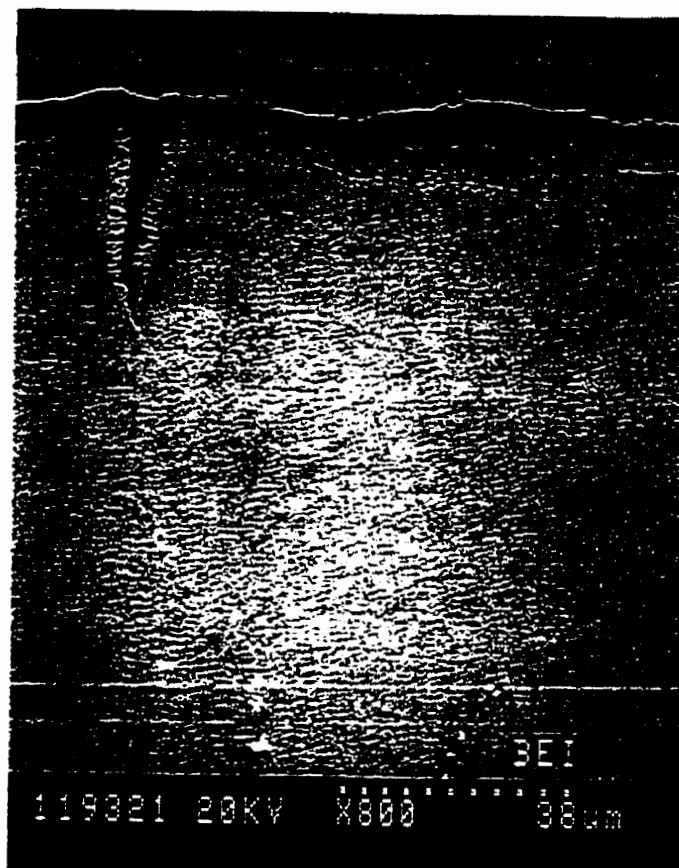


Figure 4.5 Columnar grains of γ -Ni₃Al precipitated at grain boundaries in the coating exposed to 780 thermal cycles. (SRG specimen, along Cut #3 on Figure 3.8, 800X)

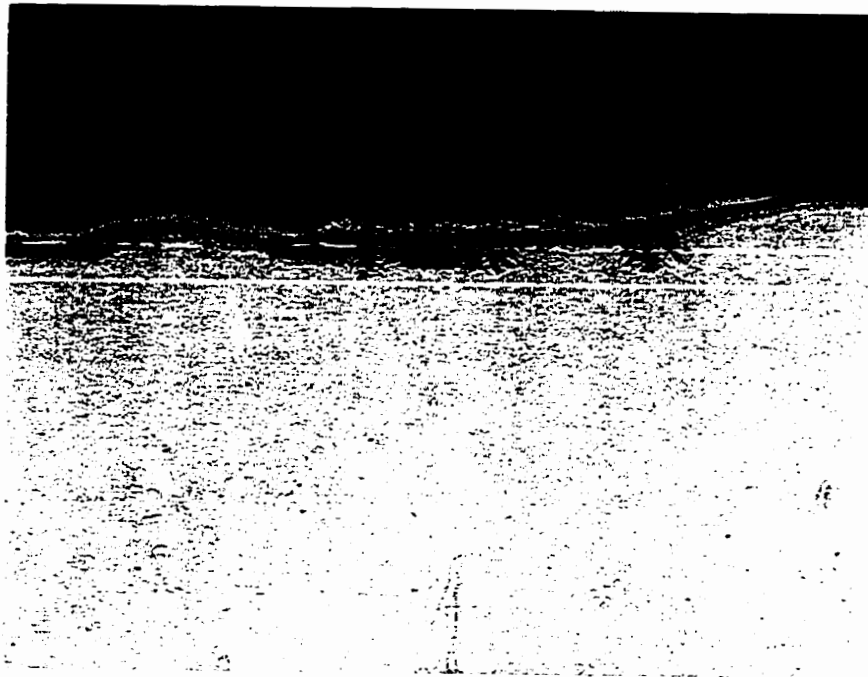


(a)

Figure 4.6 Oxide spikes: (a) formed at the interdendritic regions (SRB specimen, 800X), (b) formed at a carbide (SRC specimen, 300X); (c) formed at microstructural heterogeneities (SRB specimen, 200X). (Cut #3 on Figure 3.8)



(b)



(c)

Figure 4.6 (Continued)



Figure 4.7 Oxide spikes blunted by lateral oxidation. (SRE specimen, along Cut #3 on Figure 3.8, 500X)

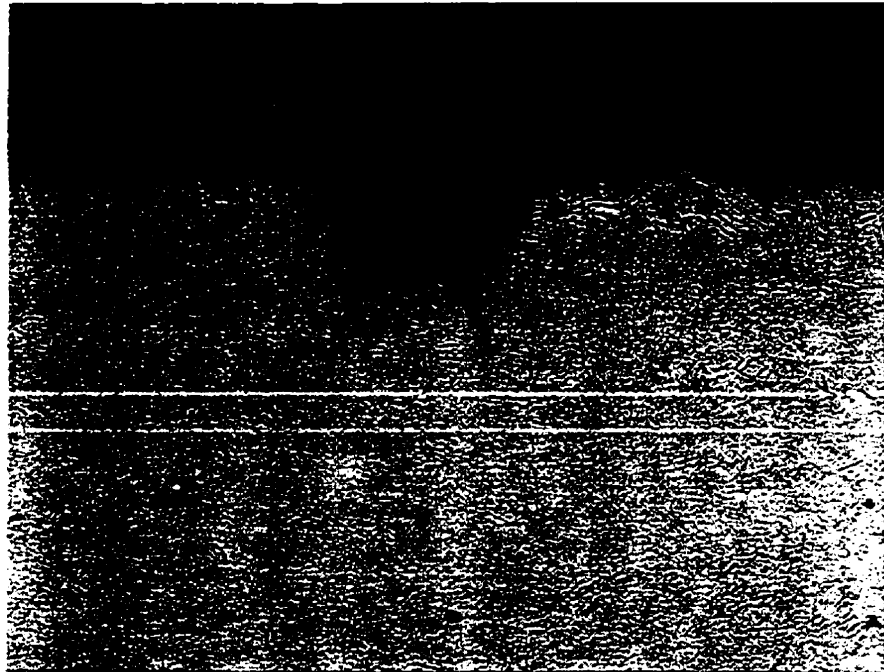


Figure 4.8 Two sharp oxide spikes at the root of a notch, machined 0.3 mm deep and 0.5 mm wide at the leading edge, before testing. (SRN specimen, along Cut #3 on Figure 3.8, 50X).

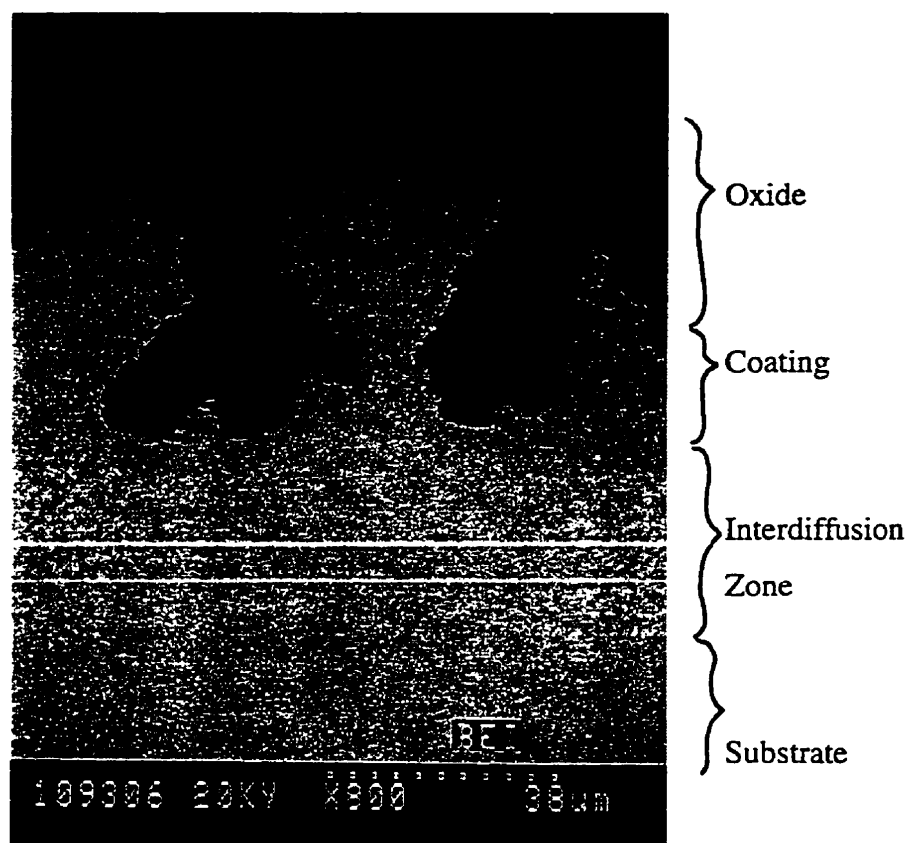


Figure 4.9 Oxide fingers formed into the columnar grains in the coating (refer to Figure 4.5). (SRG specimen, along Cut #3 on Figure 3.8, 800X)

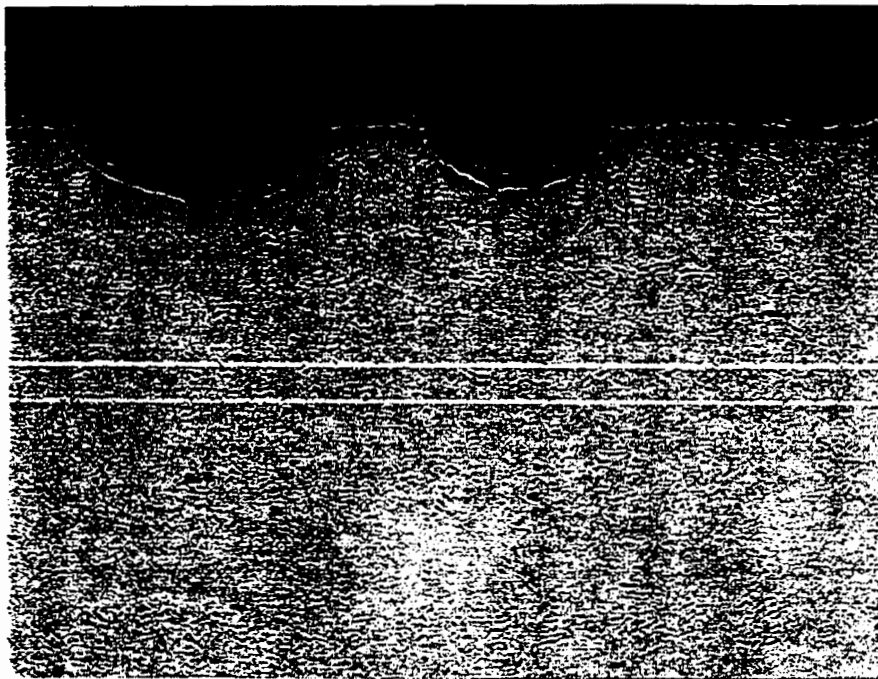
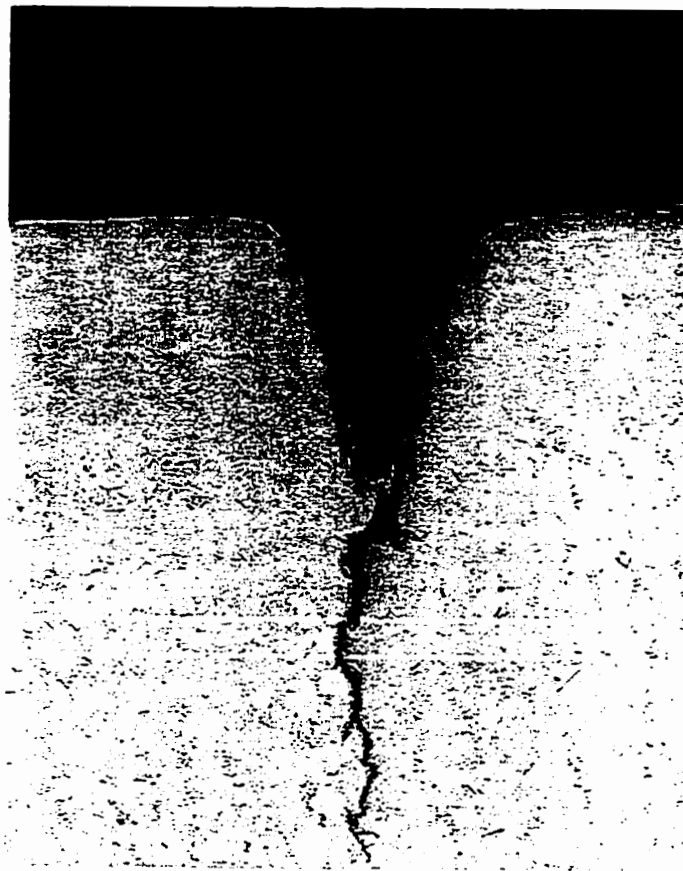


Figure 4.10 Small cracks initiated at the root of crevices (pits) in the substrate of a coated specimen. (SRF specimen, along Cut #3 on Figure 3.8, 37.5X)



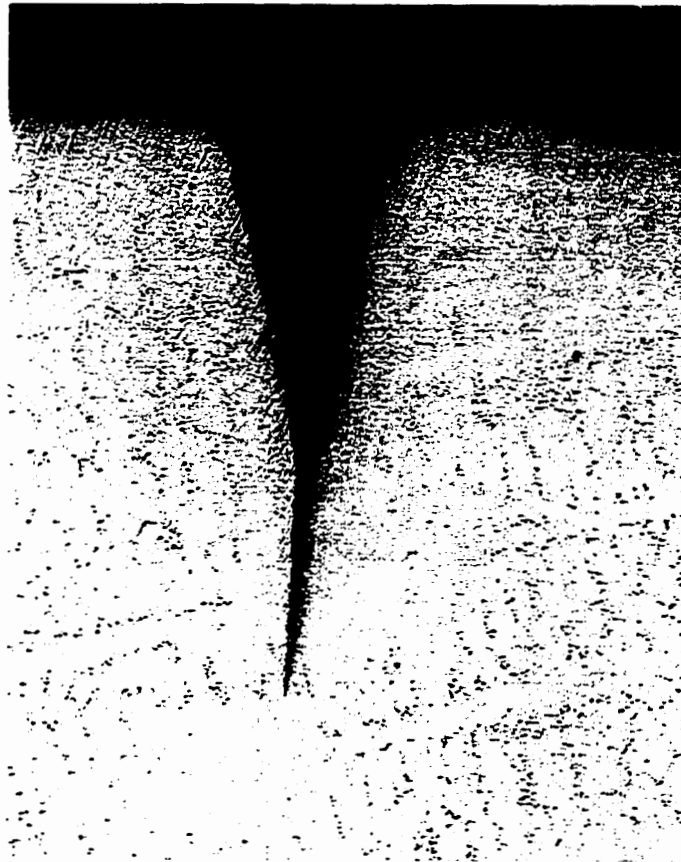
(a)

Figure 4.11 Crack propagated at the leading edge of a specimen exposed to 2500 short thermal cycles (2.5 minutes/cycle in the hot gas stream): (a) general view (37.5X), (b) crack tip close-up (Marble's reagent, 10 s, 500X). (crack #2 in SRA specimen, along Cut #2 on Figure 3.8)



(b)

Figure 4.11 Cont'd.



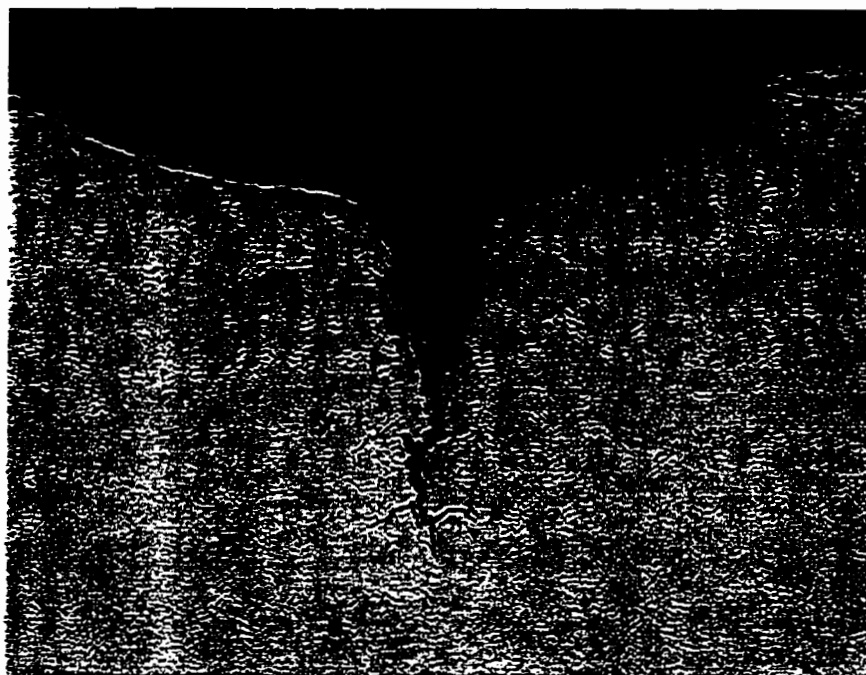
(a)

Figure 4.12 Crack propagated at the leading edge of a specimen exposed to 2140 long thermal cycles (6.5 minutes/cycle in the hot gas stream): (a) general view (37.5X), (b) crack tip close-up (1500X). (crack #1 in SRD specimen, along Cut #2 on Figure 3.8)

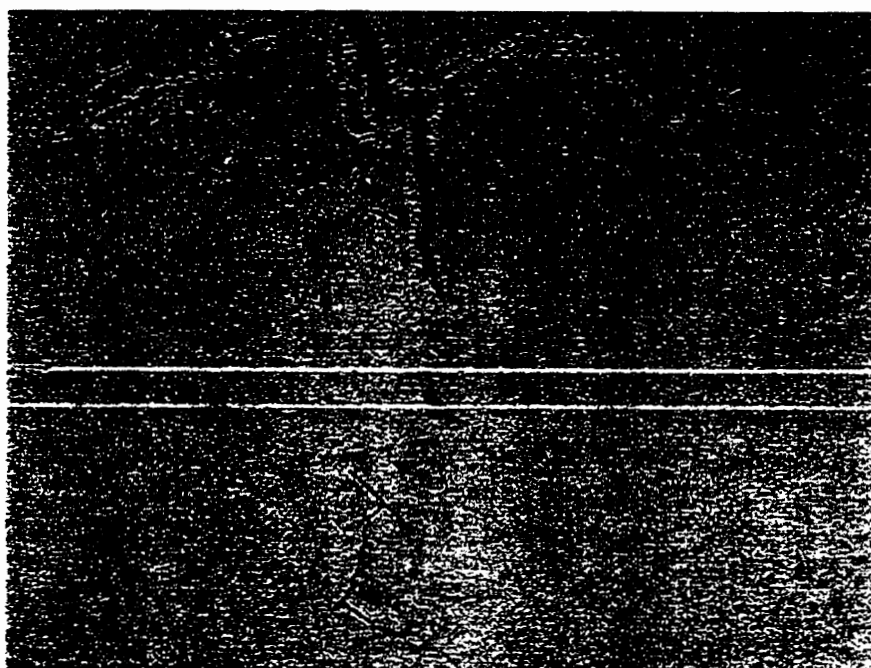


(b)

Figure 4.12 Cont'd.



(a)



(b)

Figure 4.13 Crack propagated at the root of a large crevice at the leading edge of a coated specimen exposed to 2500 short thermal cycles (2.5 minutes/cycle in the hot gas stream): (a) general view (37.5X), (b) crack tip close-up (200X). (crack #3 in SRF specimen, along Cut #3 on Figure 3.8.

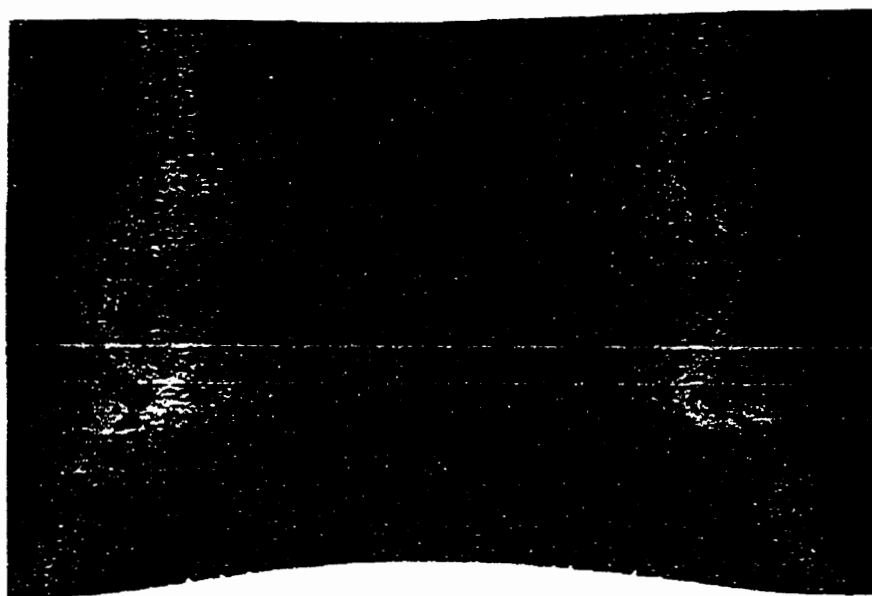
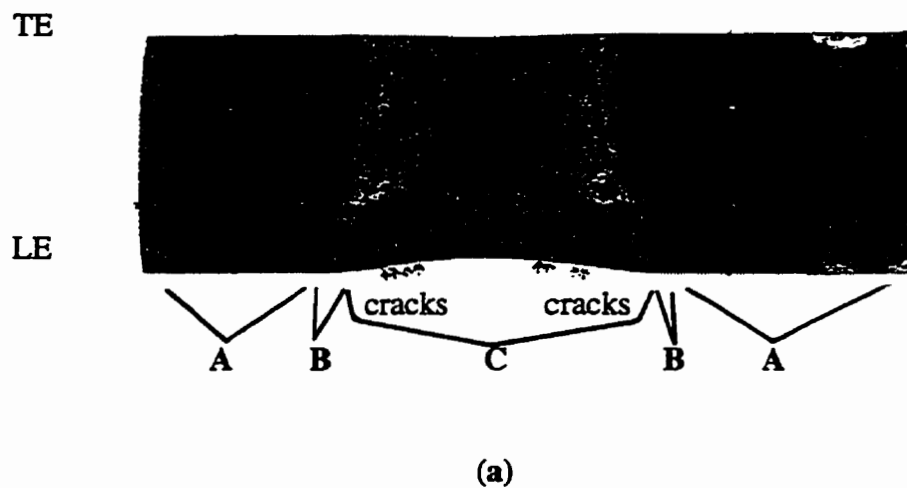


Figure 4.14 Full scale photograph (in a) and macrography (in b) of the SRC bare specimen exposed to 3000 thermal cycles in the burner rig, showing eight cracks and important material losses at the leading edge, labelled C. The protective oxidation zones are labelled A while the transition zones between A and C are labelled B.

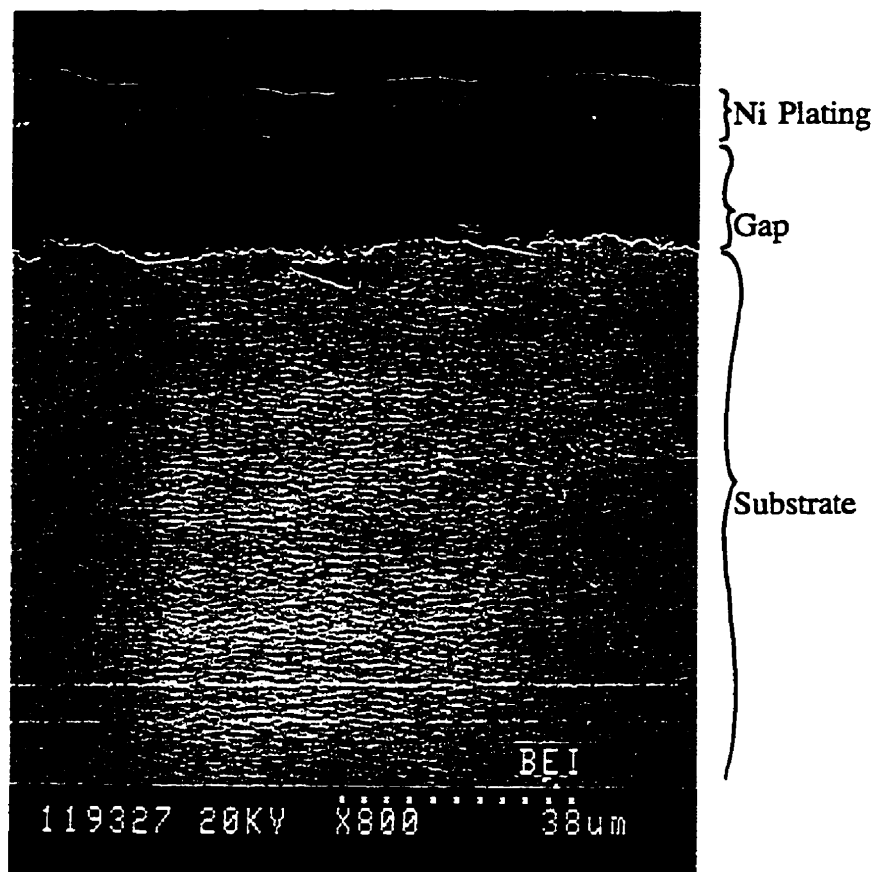


Figure 4.15 In the protective oxidation zones (labelled A in Figure 4.14) a continuous external oxide scale, normally composed of a Cr_2O_3 external layer and of an Al_2O_3 sub-layer formed. The oxide scale spalled off during polishing because of its brittle nature, leaving a gap between the electroless nickel and the substrate. (metallography of SRC specimen, along Cut #3 on Figure 3.8, 800X)

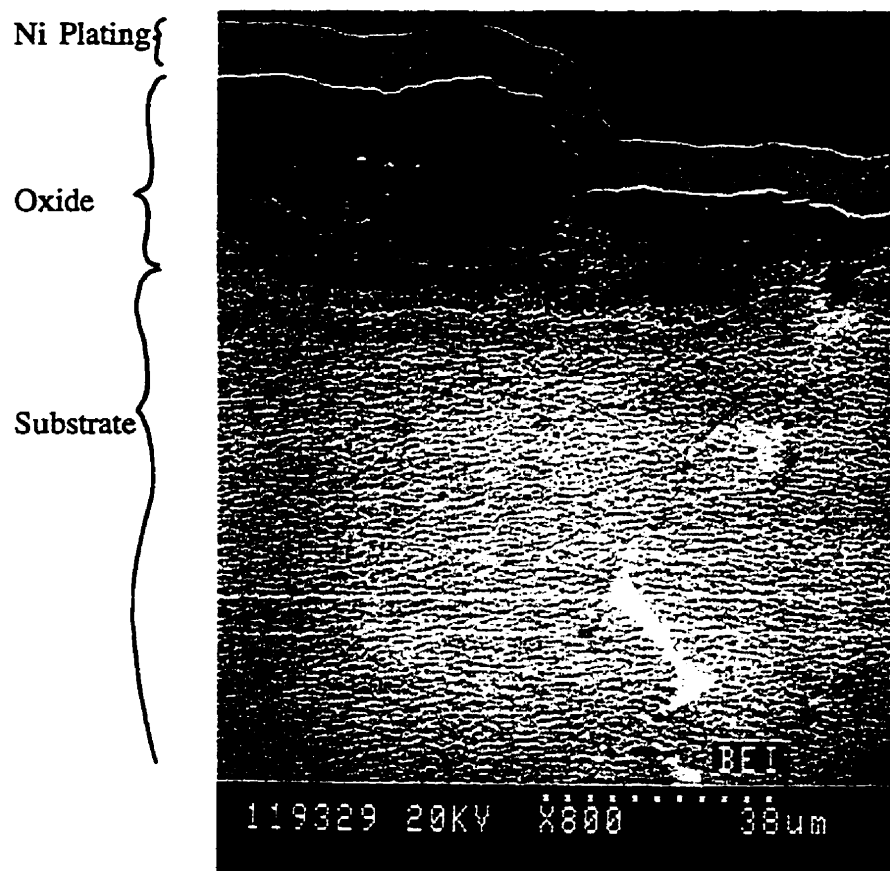


Figure 4.16 In the transition zones (labelled B in Figure 4.14), the protective oxide scale of Figure 4.15 spalls off which leads to the formation of a porous non-protective nickel-rich oxide scale. On the micrograph, the Ni oxide scale (at the left) reaches a critical thickness (in the middle) that cause its spalling (at the right) due to compressive stresses. (SRC specimen, along Cut #3 on Figure 3.8, 800X)

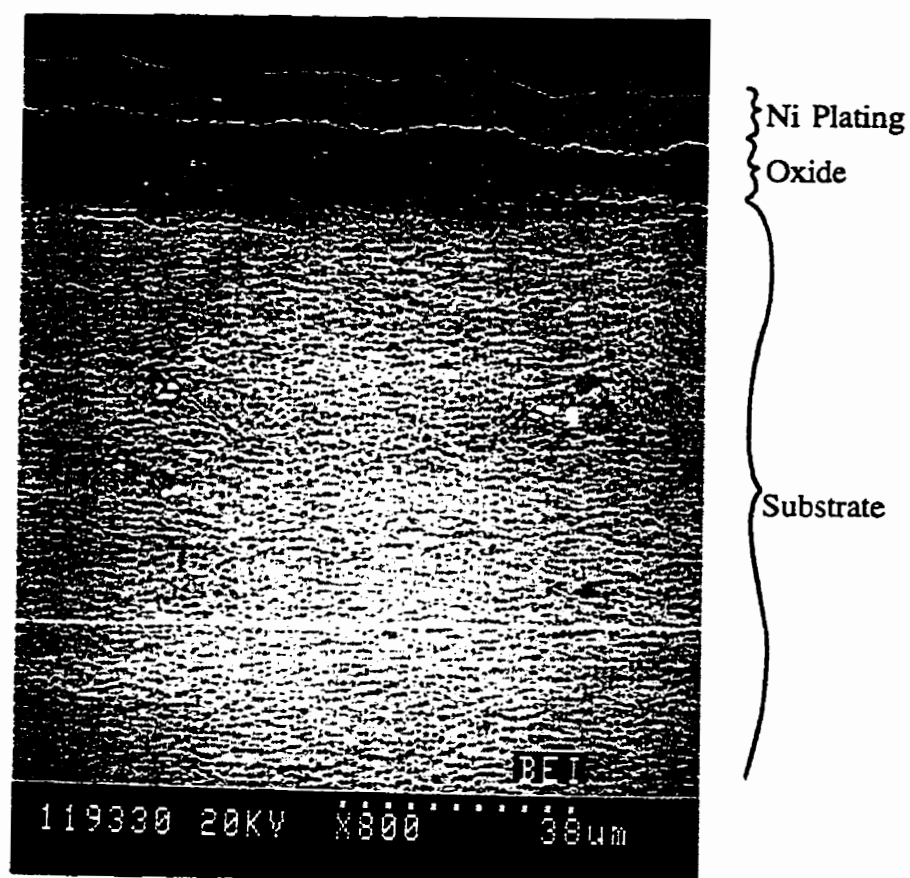


Figure 4.17 In the spalled oxide zone (labelled C in Figure 4.14, the substrate is drastically consumed. (SRC specimen, along Cut #3 on Figure 3.8, 800X)

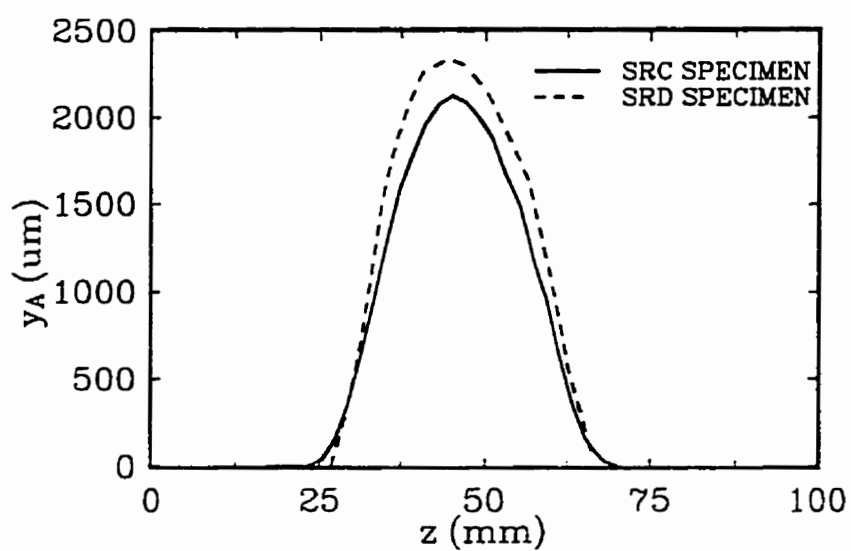


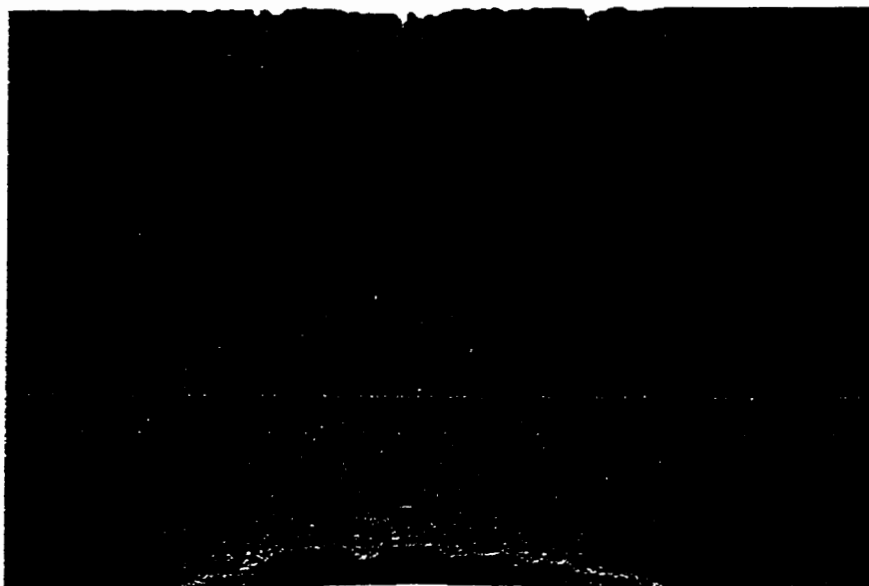
Figure 4.18 Material loss (y_A) along the leading edge of SRC and SRD specimens after testing in the burner rig. The SRC specimen was exposed to short heating periods (150 s) during thermal cycling whereas the SRD specimen was exposed to long heating periods (390 s).

LE

TE



(a)



(b)

Figure 4.19 Full scale photograph (in a) and macrography (in b) of the SRF coated specimen exposed to 2500 thermal cycles in the burner rig, showing numerous cracks and an irregular leading edge, caused by local destruction of the coating and subsequent pitting of the substrate.

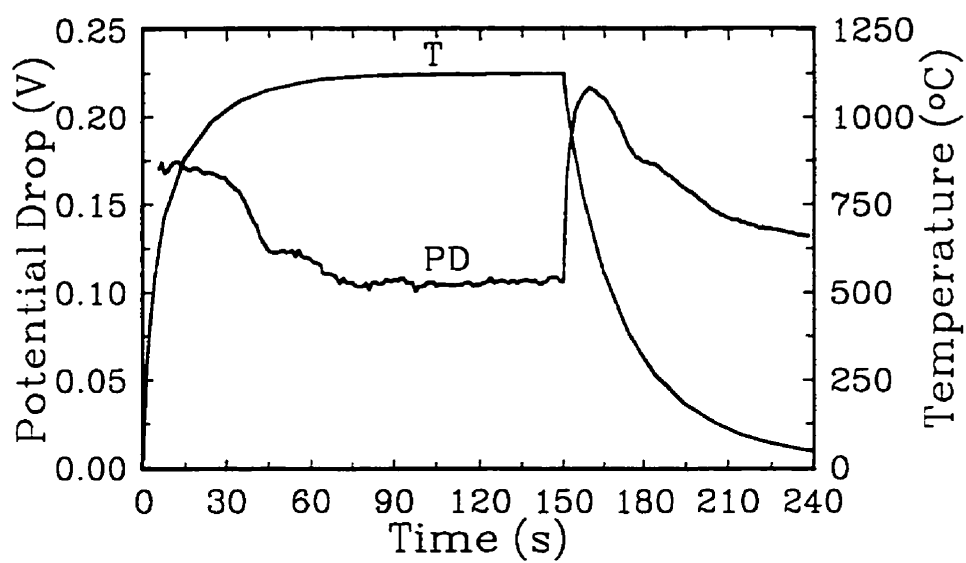


Figure 4.20 Measured evolution of the potential drop during a typical thermal cycle (SRC test).

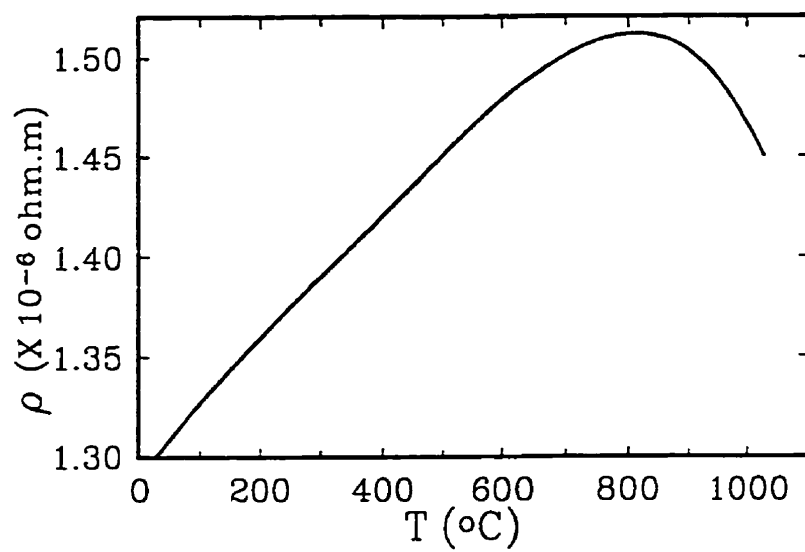


Figure 4.21 Variation of the electrical resistivity of a typical nickel-based superalloy (Udimet 700) with temperature [78].

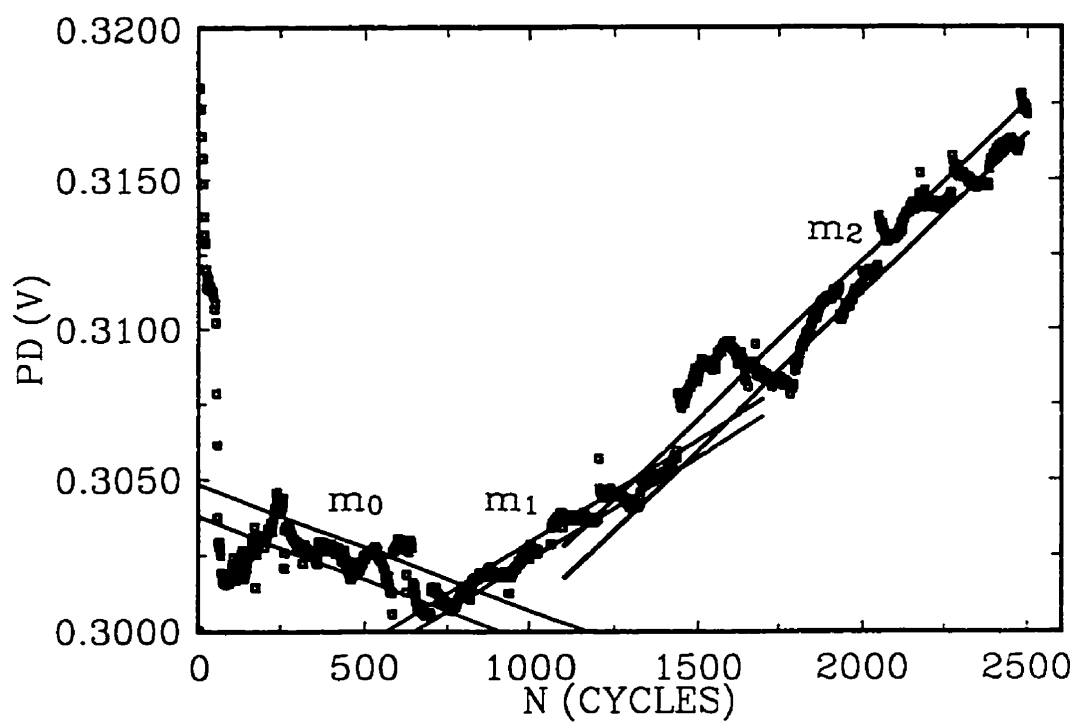


Figure 4.22 Evolution of the potential drop (measured during the steady state portion of thermal cycles) during TF testing SRA.

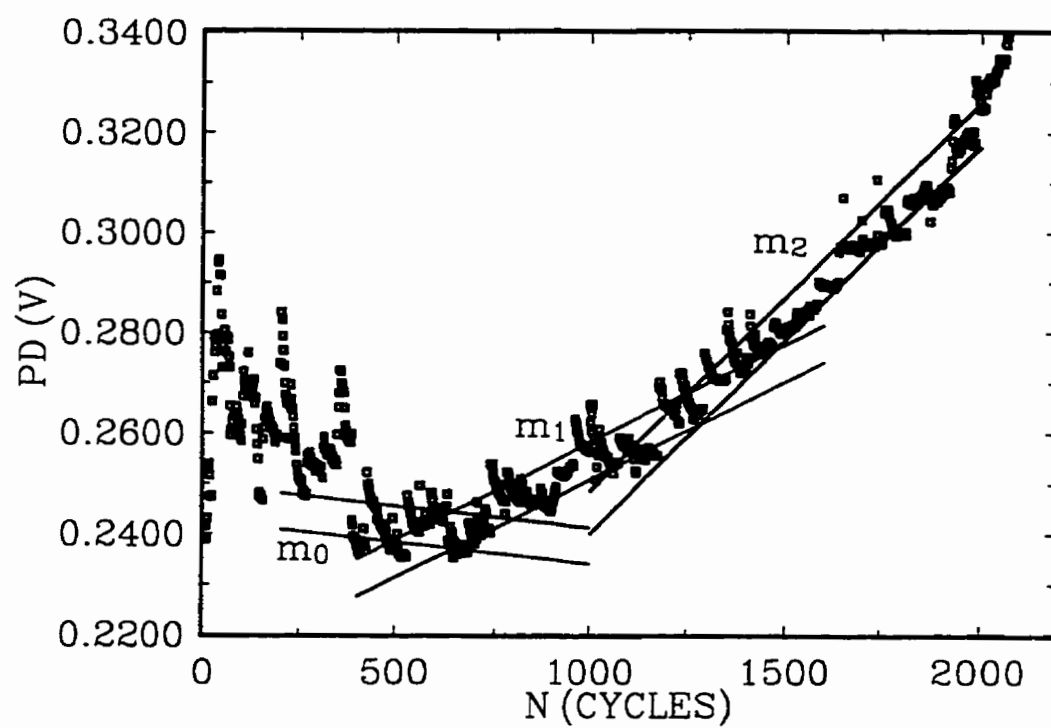


Figure 4.23 Evolution of the potential drop (measured during the steady state portion of thermal cycles) during TF testing SRD.

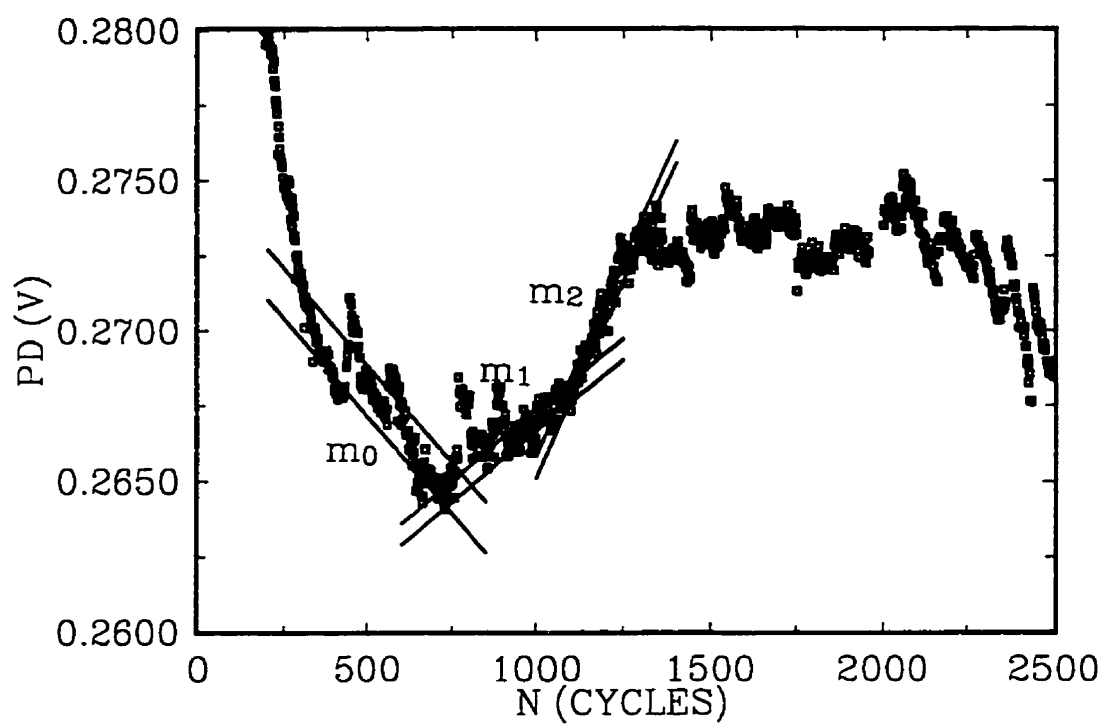


Figure 4.24 Evolution of the potential drop (measured during the steady state portion of thermal cycles) during TF testing SRB.

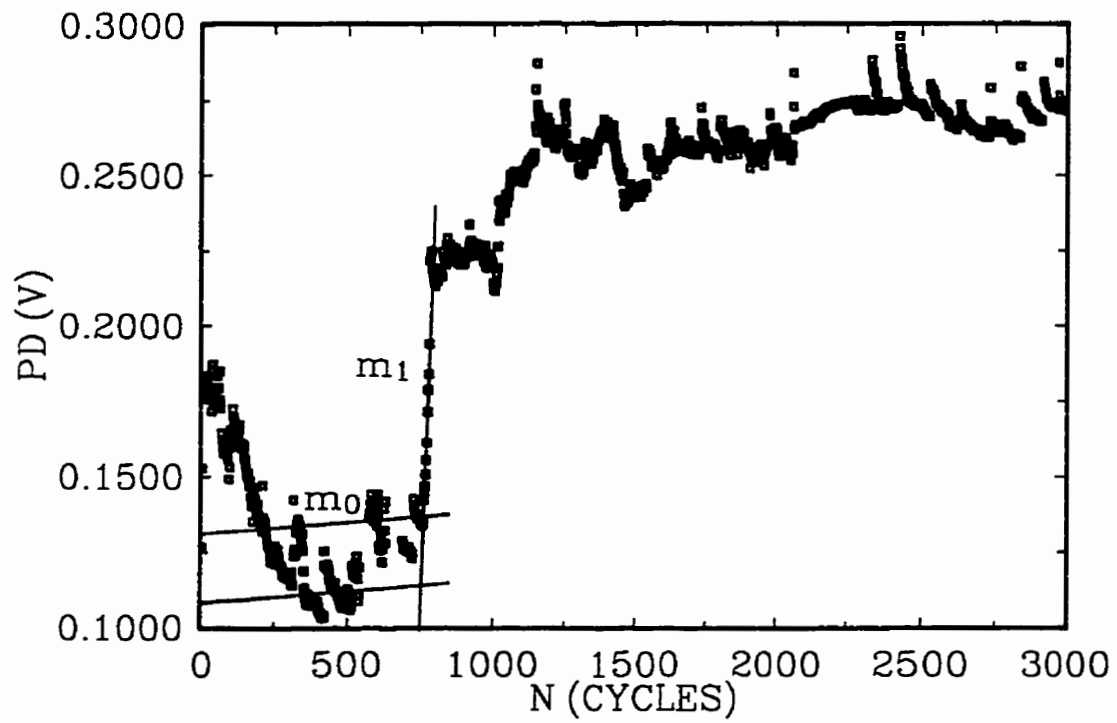


Figure 4.25 Evolution of the potential drop (measured during the steady state portion of thermal cycles) during TF testing SRC.

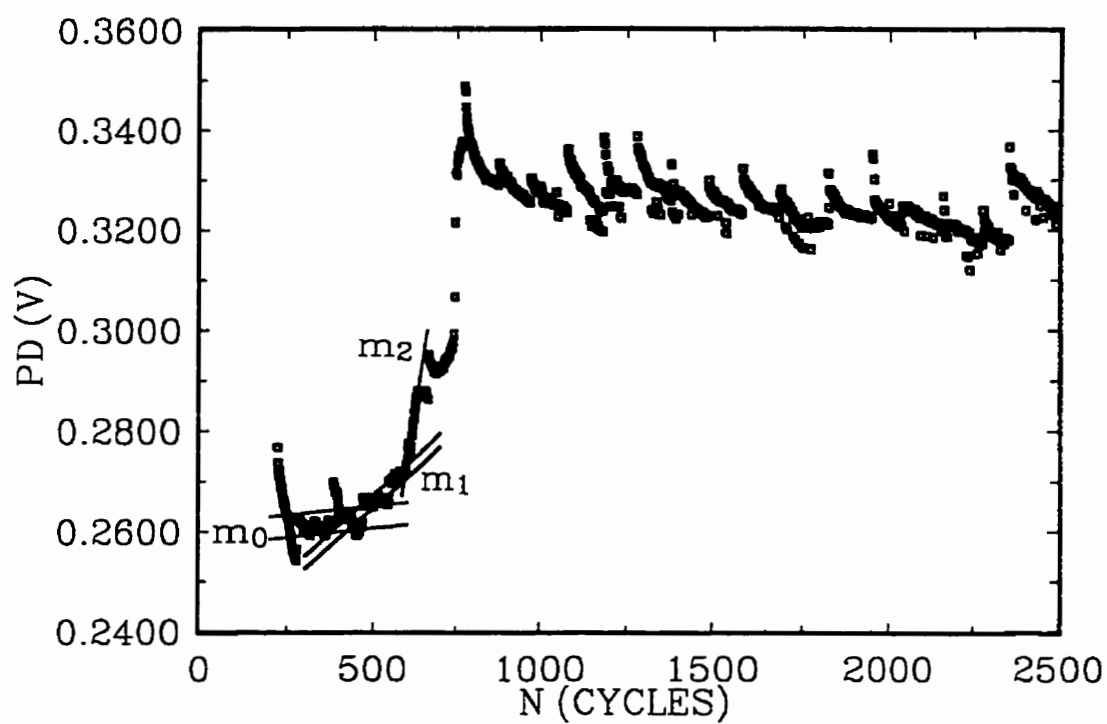


Figure 4.26 Evolution of the potential drop (measured during the steady state portion of thermal cycles) during TF testing SRF.

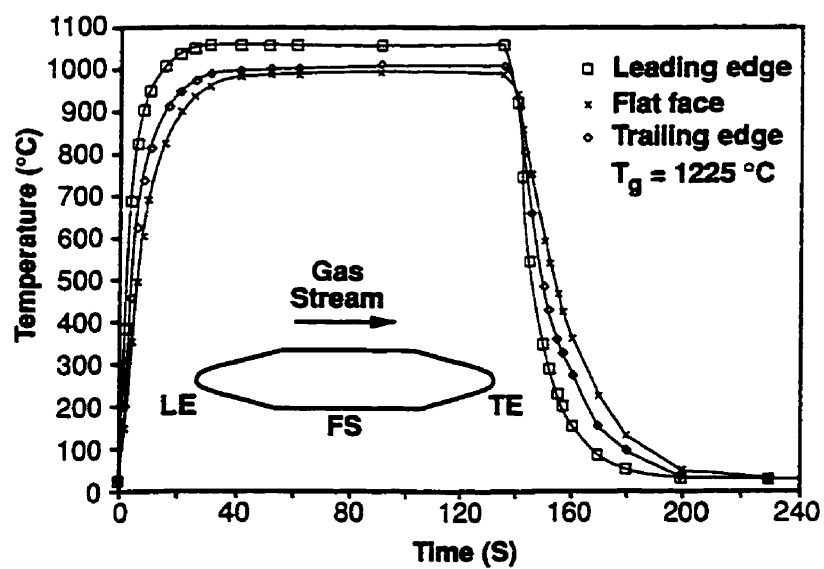


Figure 5.1 Representative temperature profile during thermal cycling in rig as established by thermocouples embedded within the body of the DEW specimen.

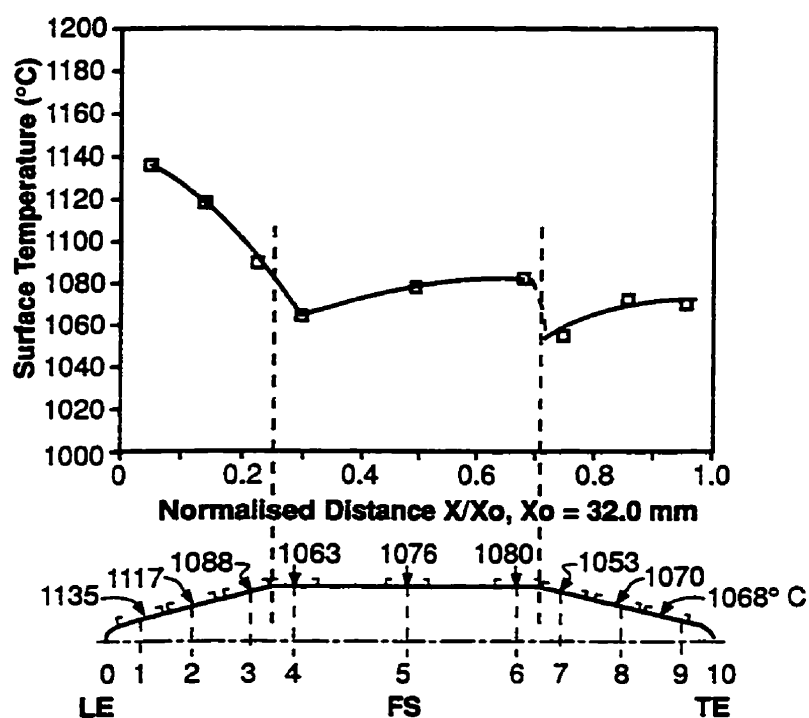


Figure 5.3 Distribution of surface temperature along the mid-section of the DEW specimen corresponding to the axis of the hot gas stream ($T_g = 1323^\circ\text{C}$), as measured with an optical pyrometer.

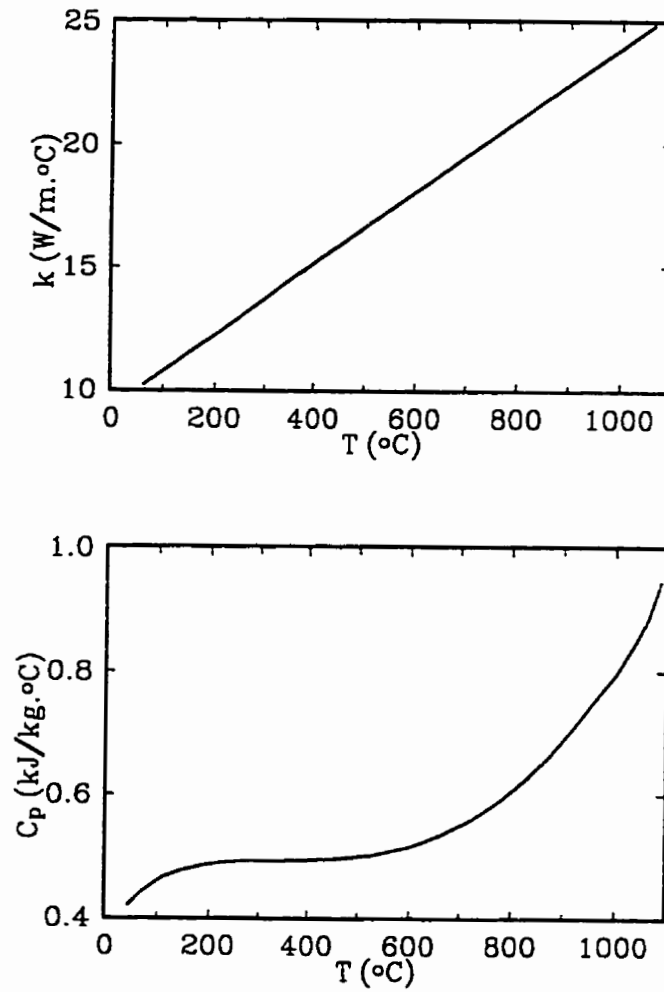


Figure 5.4 Thermal conductivity (k) and specific heat (C_p) of René 80 as a function of temperature [78].

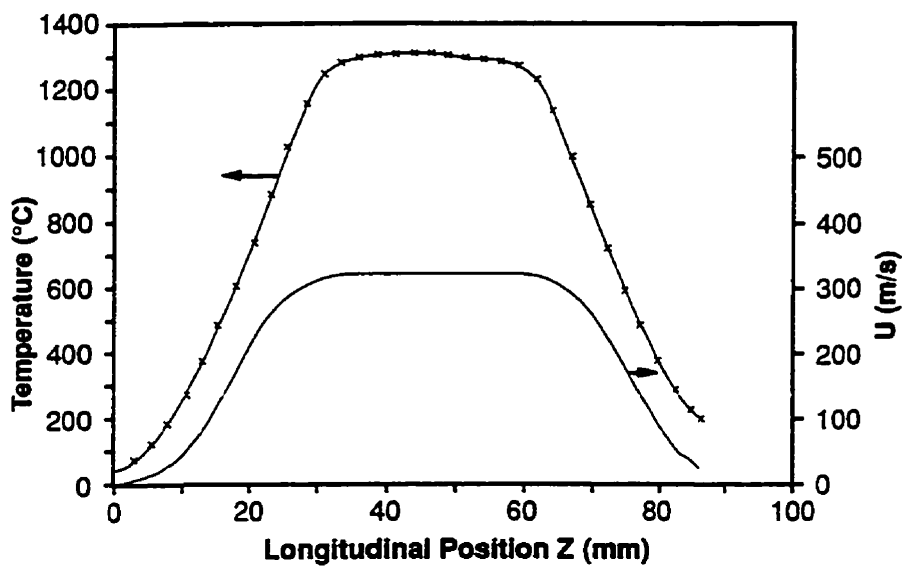


Figure 5.5 Measured temperatures (corrected for radiation) and computed velocity profiles within the hot gas stream ($T_g = 1323^\circ\text{C}$) produced by the rig. Each temperature data point is the time average of 500 measurements made at a rate of 10 readings/sec. The standard deviation of temperature is less than 10°C . The velocity profile is computed from Equation 104.

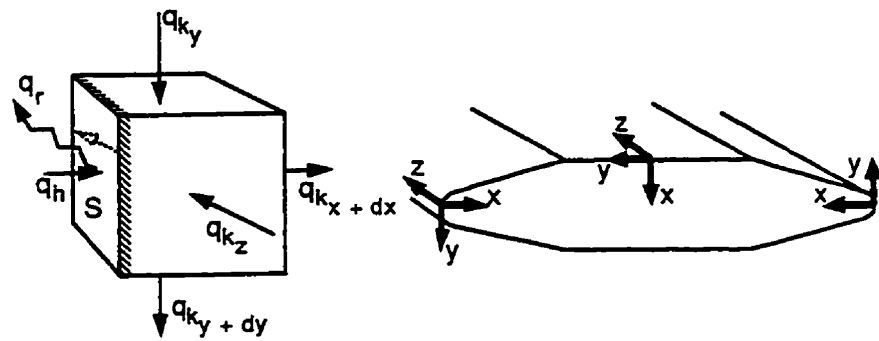


Figure 5.6 Surface elemental volume of size $dx.dy.dz$ over which the energy balance is derived from different locations over the surface of the DEW specimen in accordance with the coordinate system shown.

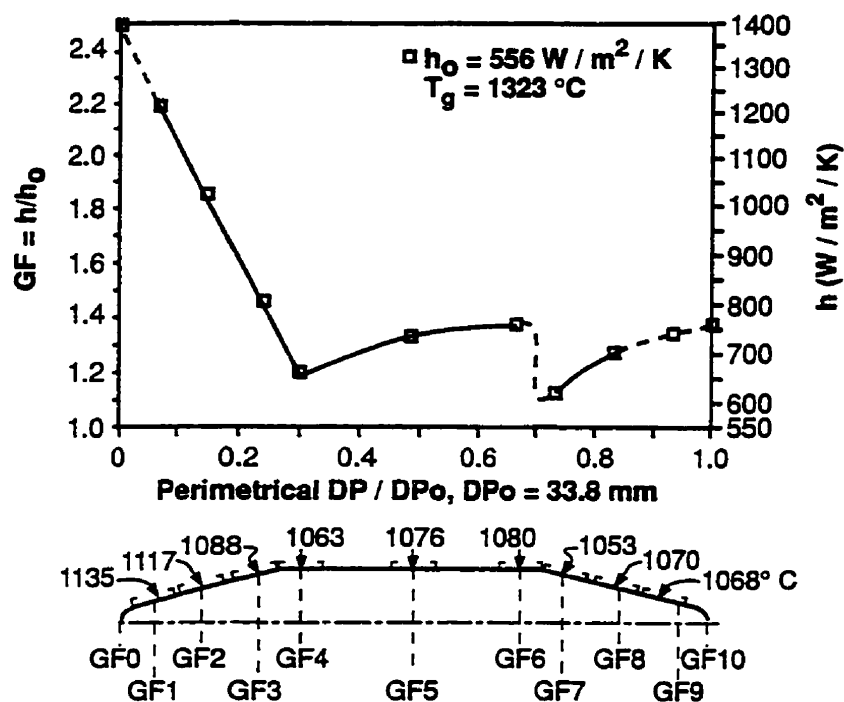


Figure 5.7 Profile of experimental geometric factors (GF) and their corresponding heat-transfer coefficients along chordwise section (axis x') of specimen in the axis of the hot gas stream (mid-section in text). The temperature measurements from which the GF's are derived are shown with the specimen sections.



Figure 5.8 Photograph of DEW specimen after one thermal cycle in the test rig showing oxidation pattern characteristic of flow separation at the transition between the flat and wedged portion of the specimen (see text for details).

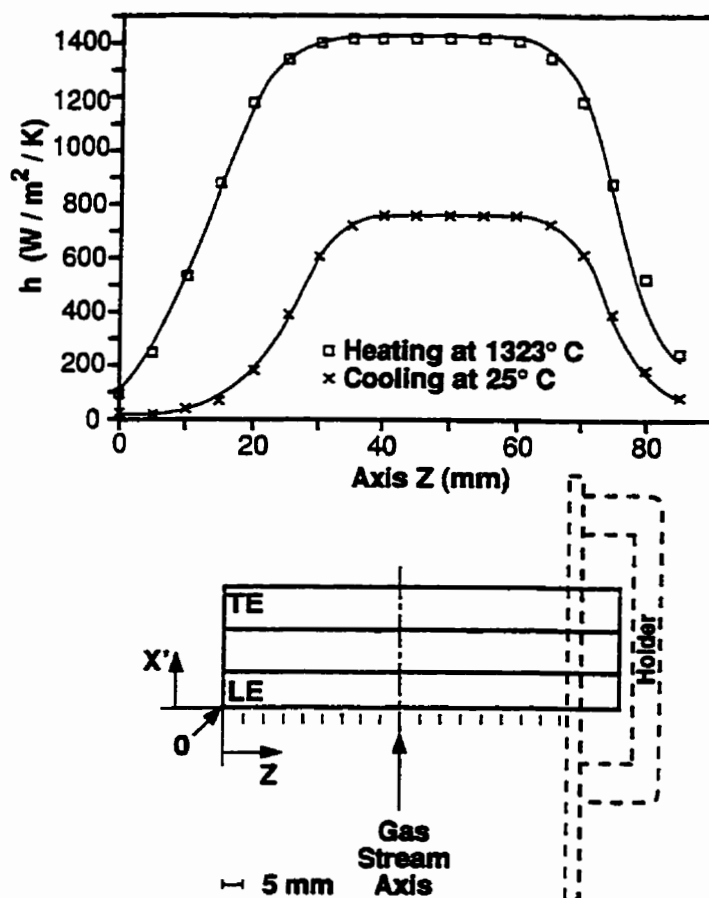


Figure 5.9 Heat-transfer coefficient profile at the leading edge along the longitudinal axis z during the heating ($T_g = 1323^\circ\text{C}$) and cooling ($T_{\text{air}} = 25^\circ\text{C}$). The reference coordinates are indicated in the schematic top view of the specimen.

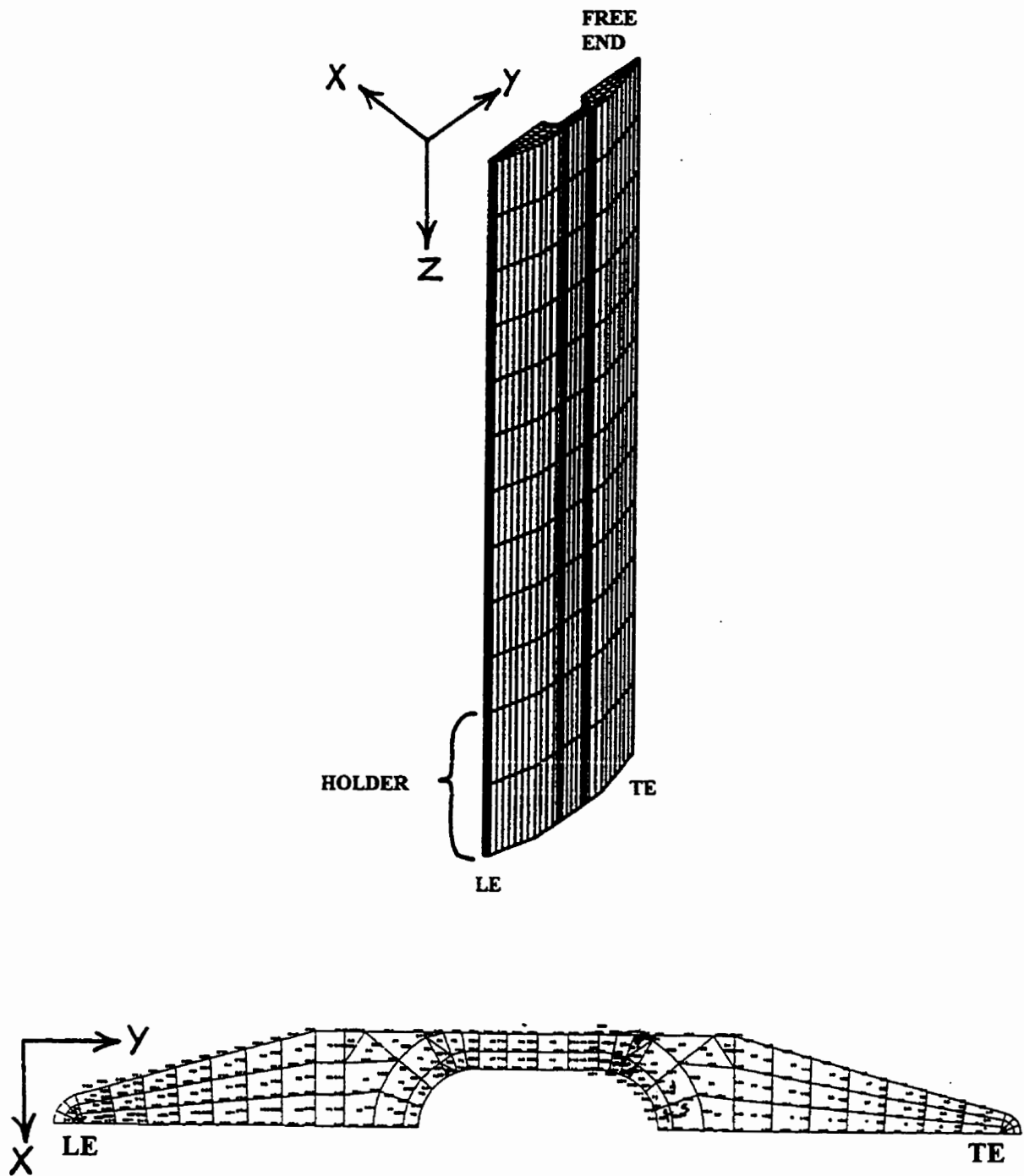


Figure 5.10 Mesh and axes system used in the thermal FE-analysis.

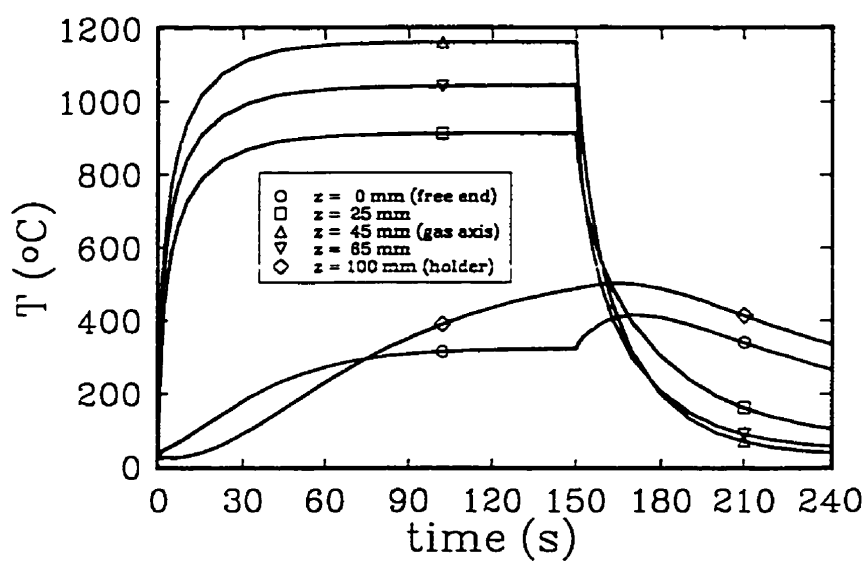


Figure 5.11 Computed temperature history at different locations of the leading edge tip of the DEW specimen during thermal cycling in the burner rig (150 s is the transition time between the heating and the cooling portions of the cycle).

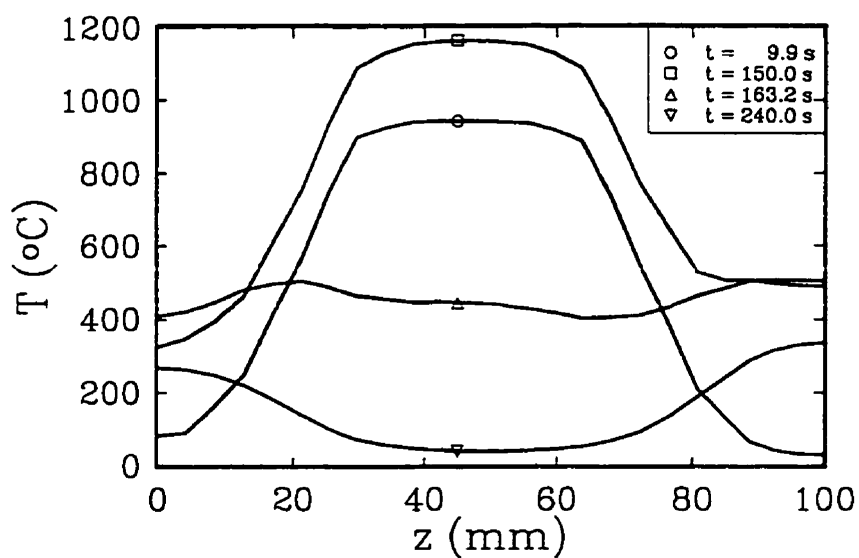
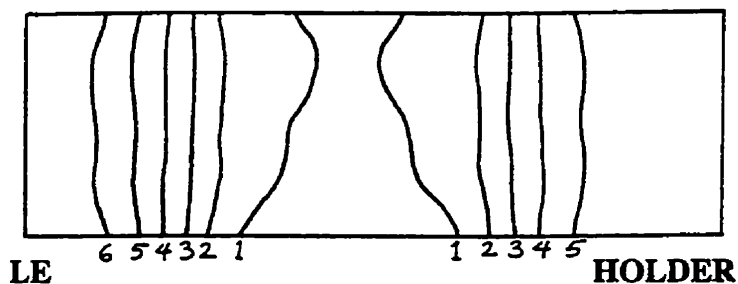


Figure 5.12 Computed temperature profile along the leading edge tip of the DEW specimen (axis z in Figure 5.10) at different times during thermal cycling (150 s is the transition time between the heating and the cooling portions of the cycle).

HEATING:

6 = 454
 5 = 538
 4 = 712
 3 = 841
 2 = 970
 1 = 1099°C

TE**COOLING:**

6 = 61
 5 = 108
 4 = 154
 3 = 201
 2 = 248
 1 = 294°C

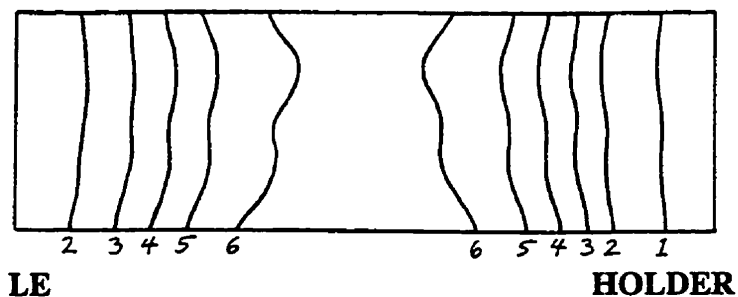
TE

Figure 5.13 Computed isotherms in the DEW specimen (in the plane y-z, see Figure 5.10), at the end of the heating and cooling thermal cycling, compared to typical spalled off oxide patterns observed in specimens after 2500 thermal cycles.

12 = 1104
 11 = 1109
 10 = 1114
 9 = 1119
 8 = 1124
 7 = 1129
 6 = 1134
 5 = 1139
 4 = 1144
 3 = 1149
 2 = 1154
 1 = 1159°C

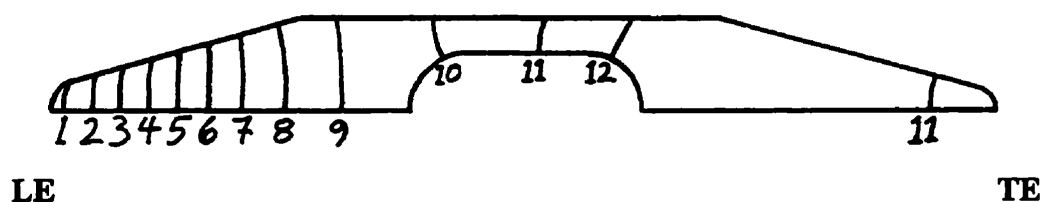


Figure 5.14 Computed isotherms in the mid-section of the DEW specimen (in the plane x-y, see Figure 5.10) at the end of the heating cycle.

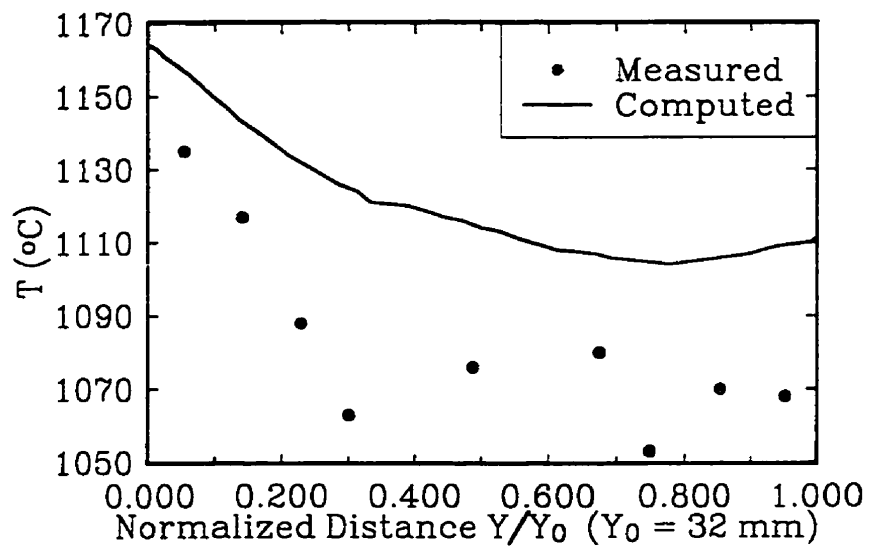


Figure 5.15 Computed surface temperature profile along the chordwise mid-section of the DEW specimen at the end of the heating cycle, compared to measured temperatures obtained by optical pyrometry.

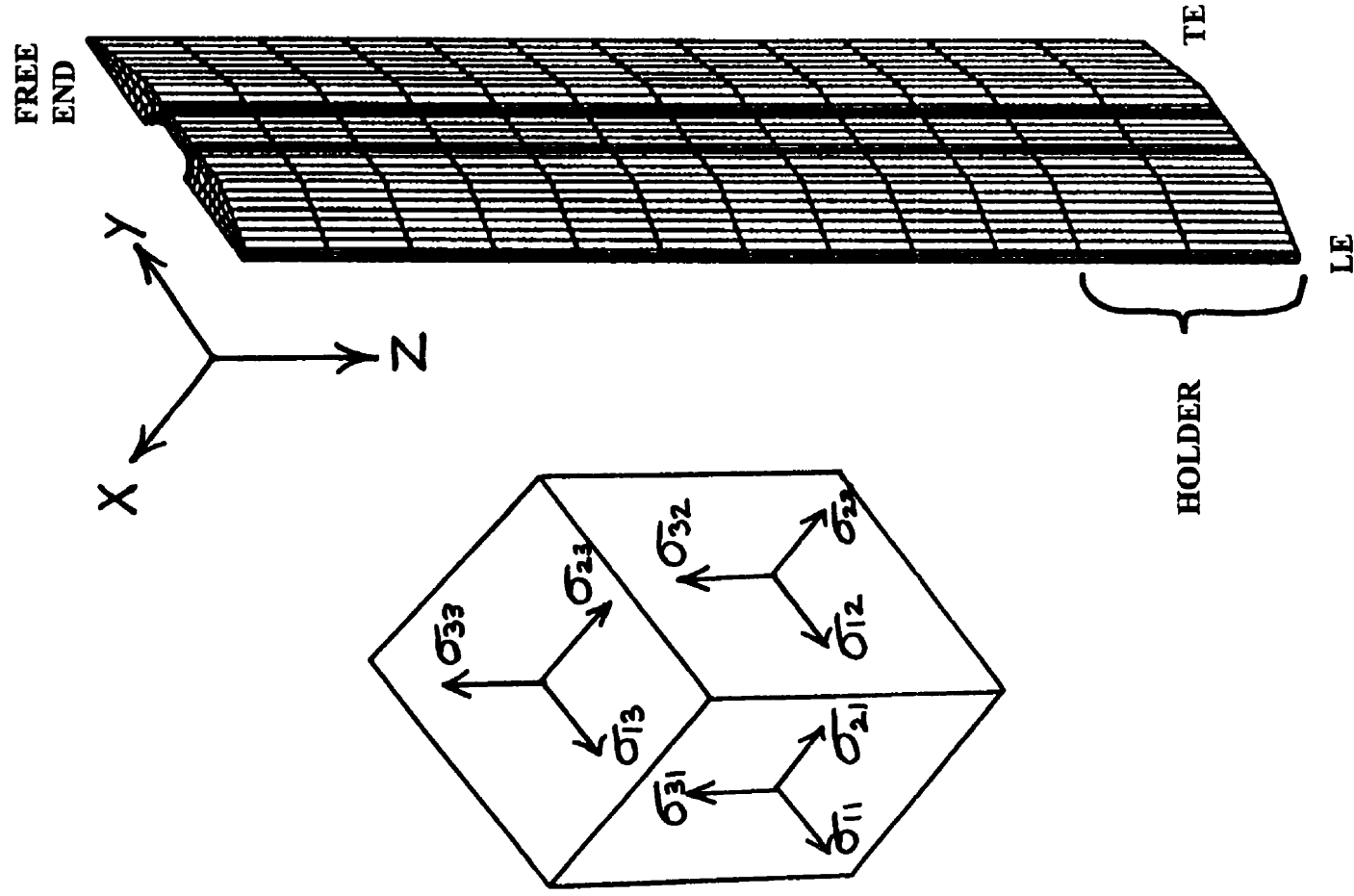


Figure 5.16 Mesh and axes system used in the mechanical FE-analysis.

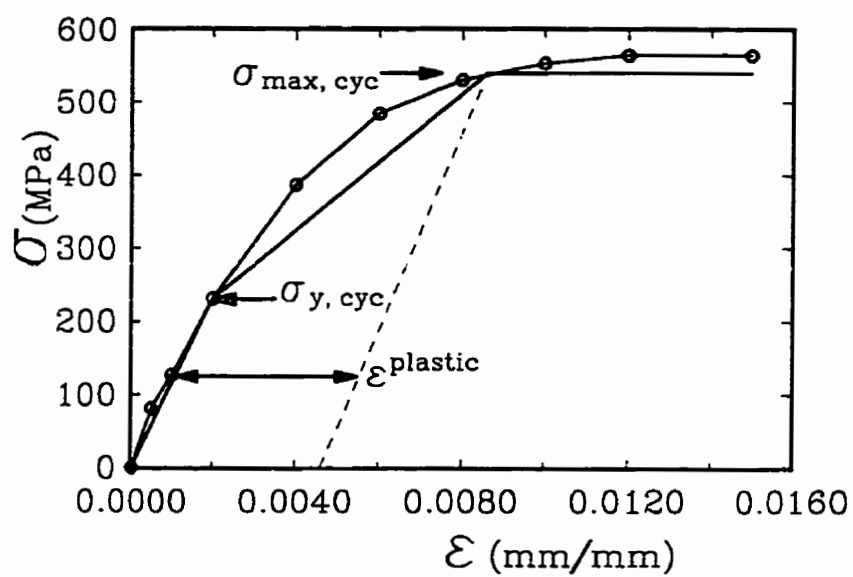


Figure 5.17 Cyclic stress-strain (σ - ϵ) curve for CCR80 at 980°C (data taken from [114]).

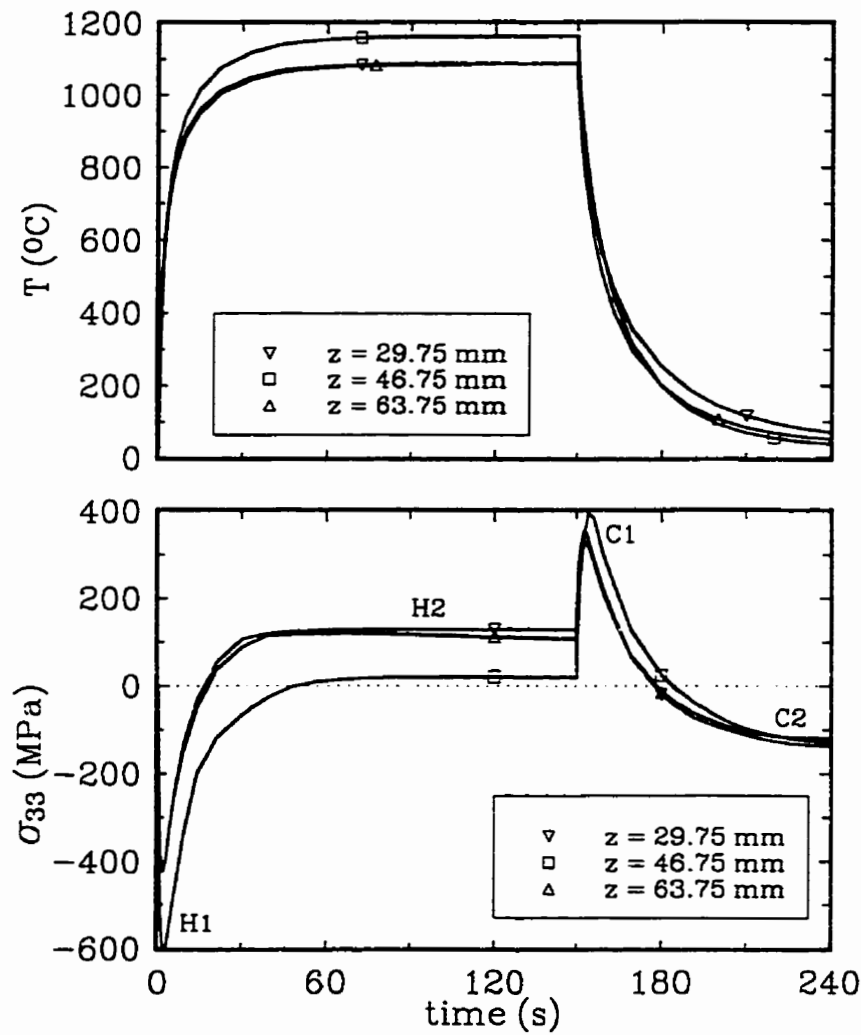
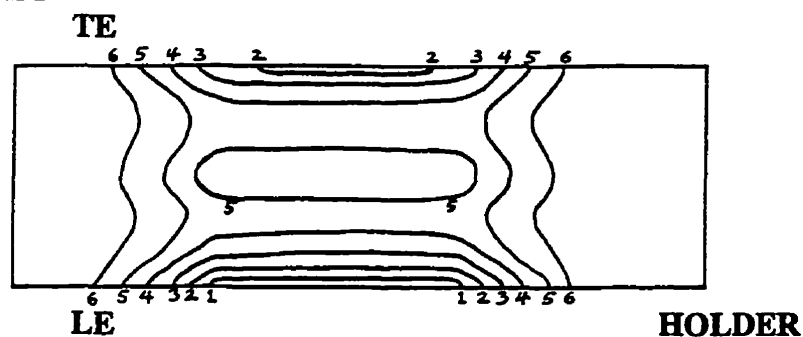
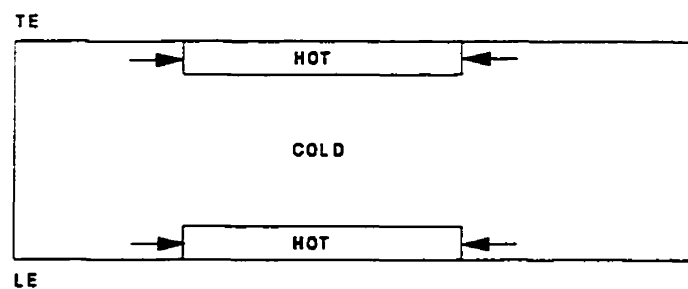


Figure 5.18 Computed temperature (T) and principal stress (σ_{33} or σ_2) histories at three highly stressed locations along the leading edge tip of the DEW specimen (axis z in Figure 5.16) during thermal cycling in the burner rig (150 s is the transition time between the heating and the cooling portions of the cycle).

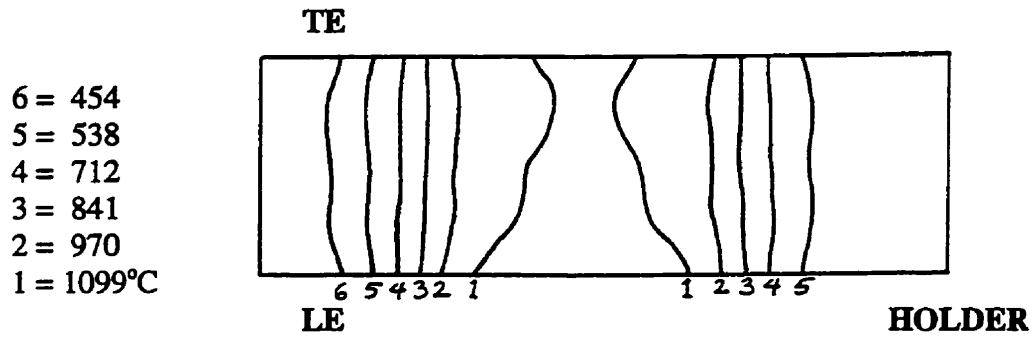
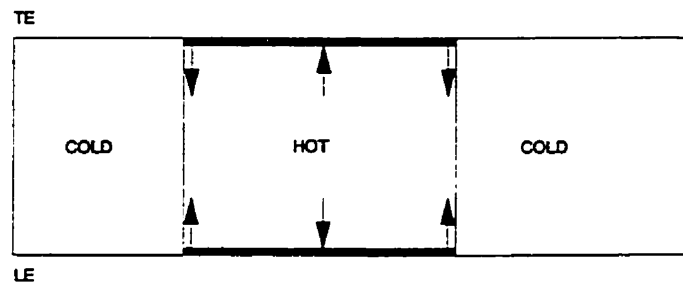
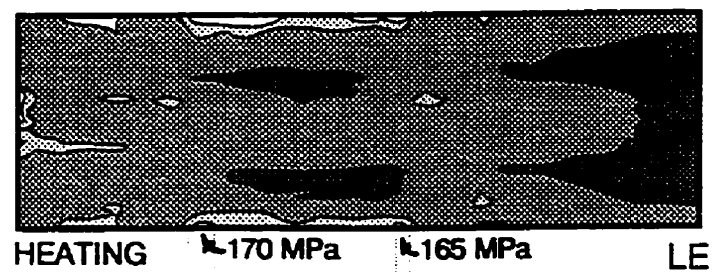
TEMPERATURES

6 = 116
 5 = 207
 4 = 299
 3 = 390
 2 = 481
 1 = 572°C

**LOADS**

(a) after 1.85 seconds of heating (point H1 in Figure 5.18)

Figure 5.19 Isotherms, schematic loads and real von Mises stress distributions (plane 2-3) in the DEW specimen during heating.

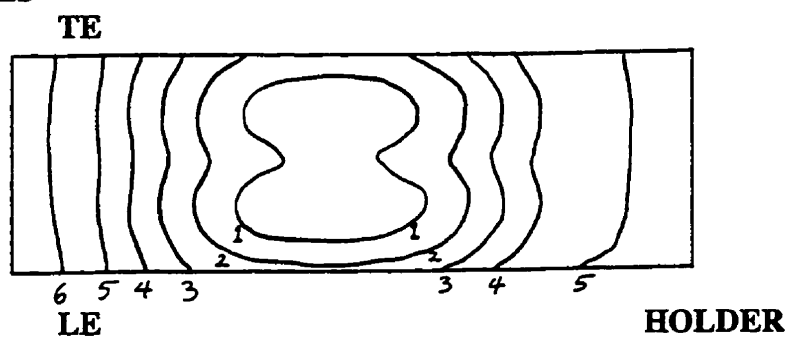
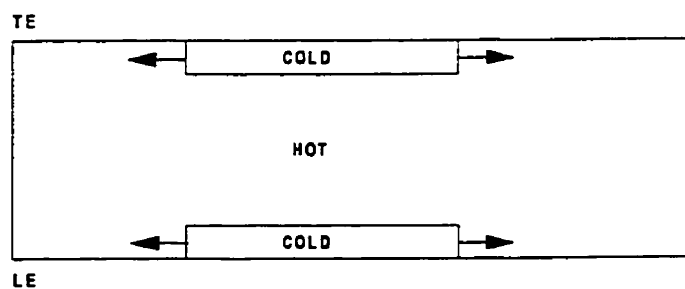
TEMPERATURES**LOADS****VON MISES STRESSES**

(b) after 150 seconds of heating (point H2 in Figure 5.18)

Figure 5.19 Cont'd.

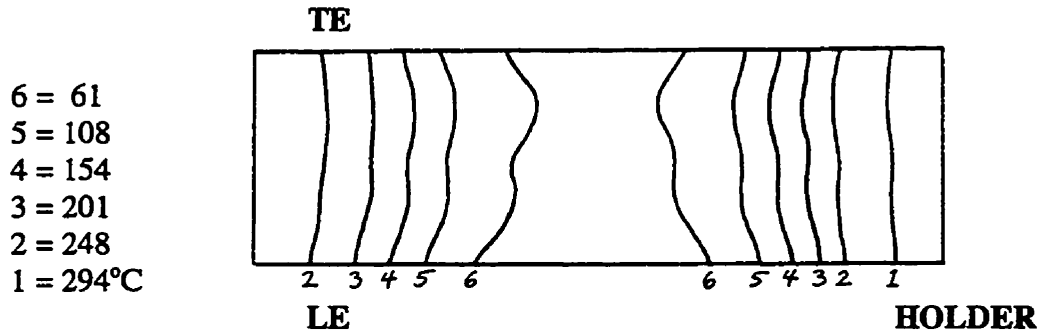
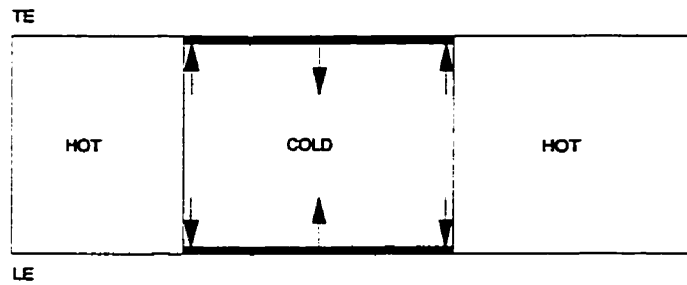
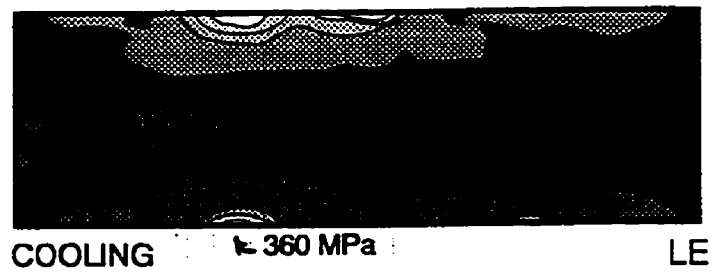
TEMPERATURES

6 = 414
 5 = 513
 4 = 611
 3 = 709
 2 = 807
 1 = 905°C

**LOADS**

(a) after 4 seconds of cooling (point C1 in Figure 5.18)

Figure 5.20 Isotherms, schematic loads and real von Mises stress distributions (plane 2-3) in the DEW specimen during cooling.

TEMPERATURES**LOADS****VON MISES STRESSES**

(b) after 90 seconds of cooling (point C2 in Figure 5.18)

Figure 5.20 Cont'd.

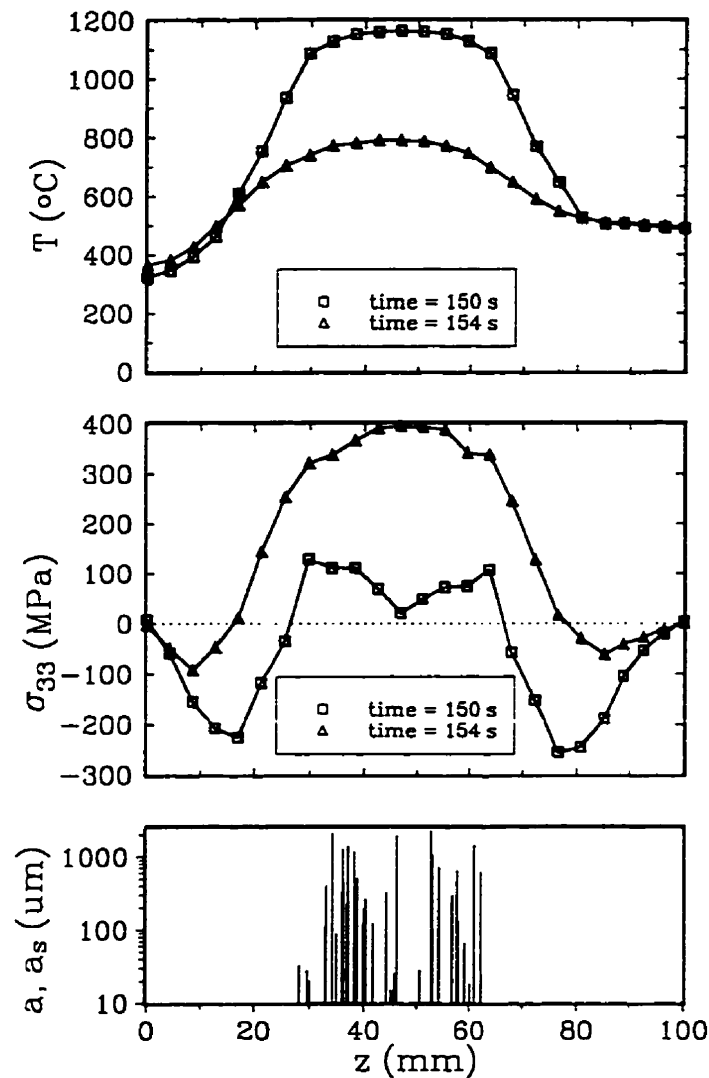


Figure 5.21 Computed temperature (T) and principal stress (σ_{33} or σ_z) distributions along the leading edge tip (axis z in Figure 5.16) at the end of the heating cycle (time = 150 s) and 4 seconds after the beginning of the cooling cycle (time = 154 s). Oxide spikes (a_s) and crack (a) locations along the leading edge are concentrated in the central region where the maximal temperatures and stresses were observed.

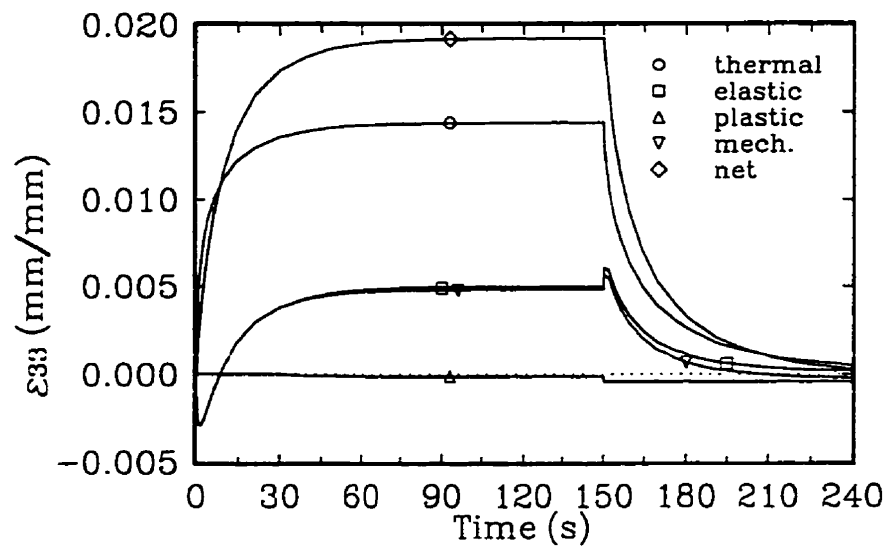


Figure 5.22 Computed variation of the different strains during one thermal cycle at the most stressed location of the leading edge of the DEW specimen ($z = 29.75$ mm). The principal strains in direction 3, represented by ϵ_{33}^{th} , ϵ_{33}^e , ϵ_{33}^p , ϵ_{33}^{mech} and ϵ_{33}^{net} , are respectively the thermal strain, the elastic strain, the plastic strain, the mechanical strain and the net or total strain.

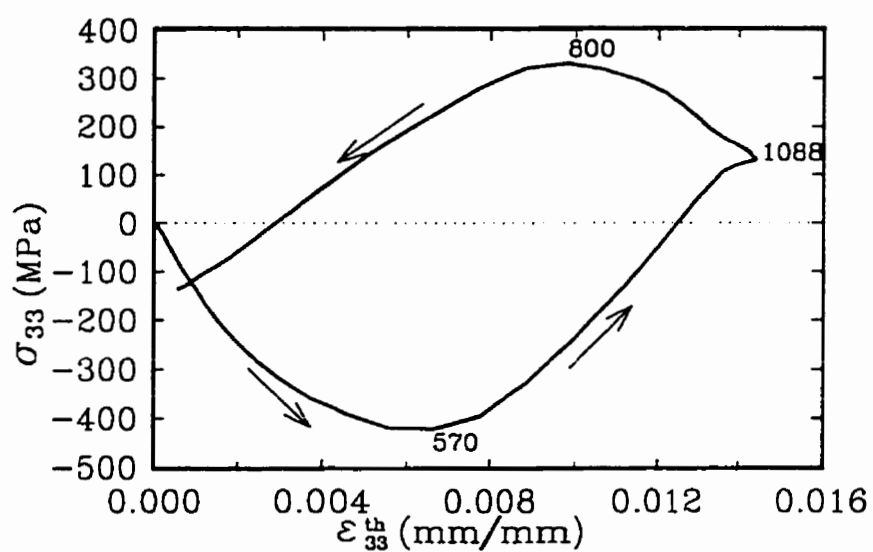


Figure 5.23 Computed stress-strain variation during one thermal cycle in the burner rig at the most stressed location of the leading edge of the DEW specimen ($z = 29.75$ mm). The stress and the strain are expressed as the principal stress (σ_{33} or σ_z) and the principal thermal strain (ϵ_{33}^{th}), respectively. The numbers along the curve indicate the temperature (in $^{\circ}\text{C}$) reached during cycling.

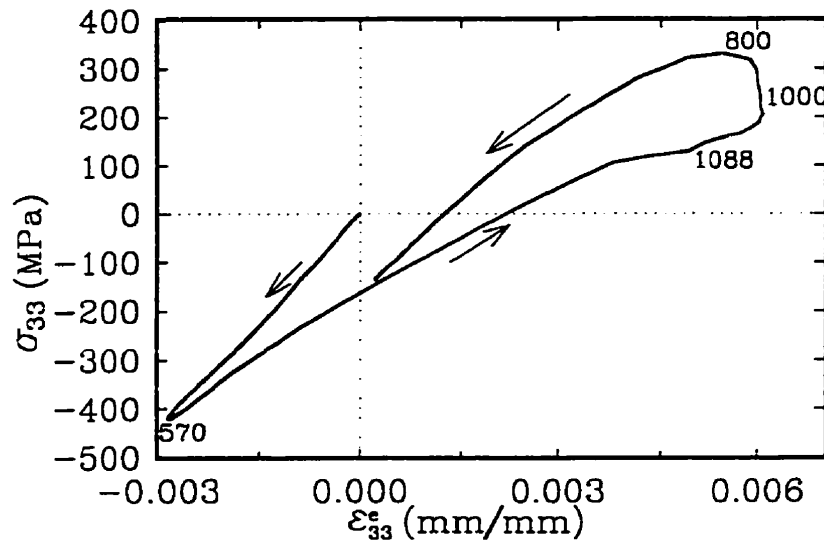


Figure 5.24 Computed stress-strain variation during one thermal cycle in the burner rig at the most stressed location of the leading edge of the DEW specimen ($z = 29.75$ mm). The stress and the strain are expressed as the principal stress (σ_{33} or σ_z) and the elastic strain (ϵ_{33}^e), respectively. The numbers along the curve indicate the temperature (in $^{\circ}\text{C}$) reached during cycling.

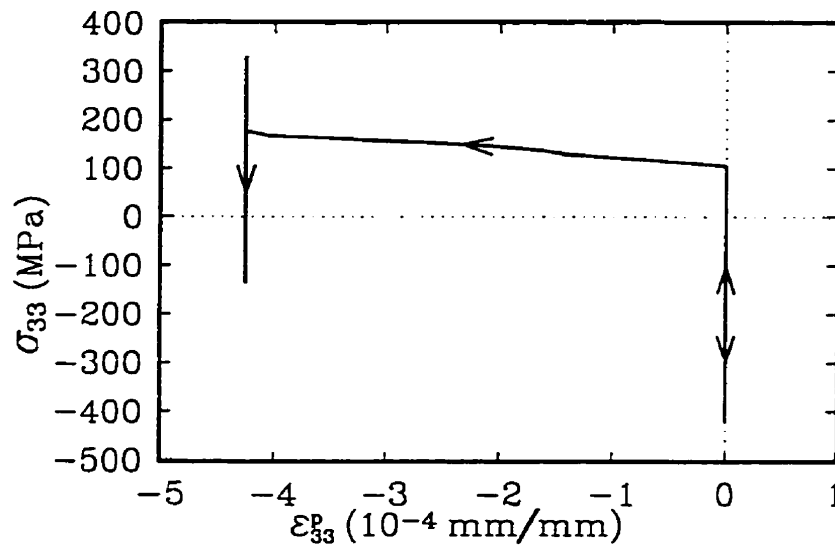


Figure 5.25 Computed stress-strain variation during one thermal cycle in the burner rig at the most stressed location of the leading edge of the DEW specimen ($z = 29.75$ mm). The stress and the strain are expressed as the principal stress (σ_{33} or σ_z) and the plastic strain (ϵ_{33}^p), respectively.

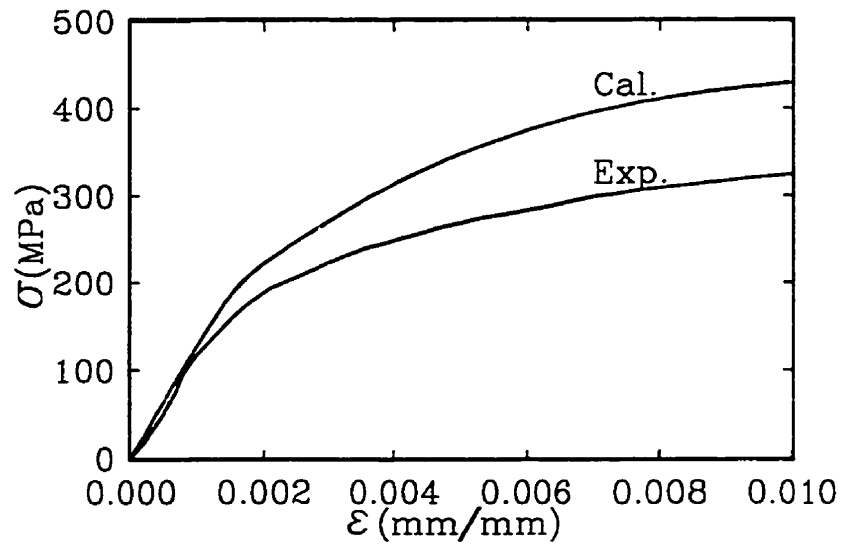


Figure 5.26 Experimental monotonic stress-strain curve of CCR80 tested at 980°C and at constant strain rate $3.33 \times 10^{-5} \text{s}^{-1}$ (data taken from Chan et al.[118]) compared to computed curve from the modified elasto-viscoplastic model of Walker using the constitutive parameters of B1900+Hf (parameters taken from Chan et al.[118]).

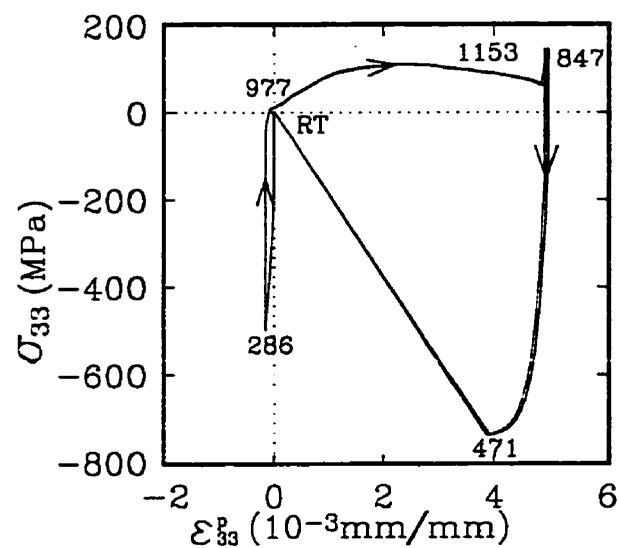


Figure 5.27 Stress-strain loops (10 thermal cycles in the burner rig) computed with the thermo-elasto-viscoplastic model of Walker, at the location exposed to the most severe thermo-mechanical condition along the leading edge of the DEW specimen ($z = 38.25$ mm). The stress and the strain are expressed as the principal stress (σ_{33} or σ_z) and the plastic strain (ϵ_{33}^p), respectively. The numbers along the curve indicate the temperature (in °C) reached during cycling.

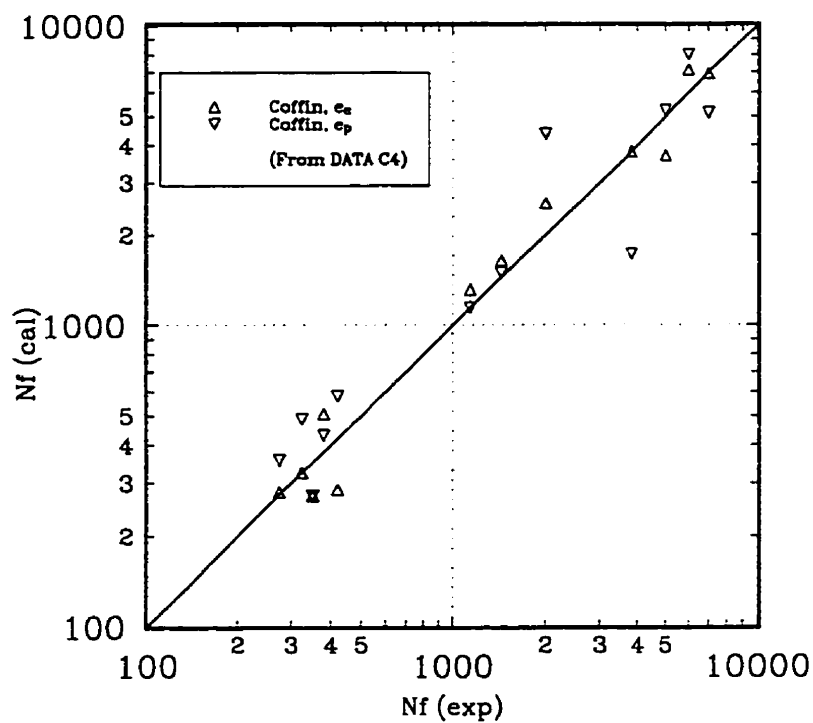


Figure 5.28 Comparison of life predicted with the Coffin's Models ($\Delta\epsilon_e$ and $\Delta\epsilon_p$) with experimental life obtained for isothermal fatigue tests carried out under continuous cycling at 871°C on CC René 80. (After C4 data set [4])

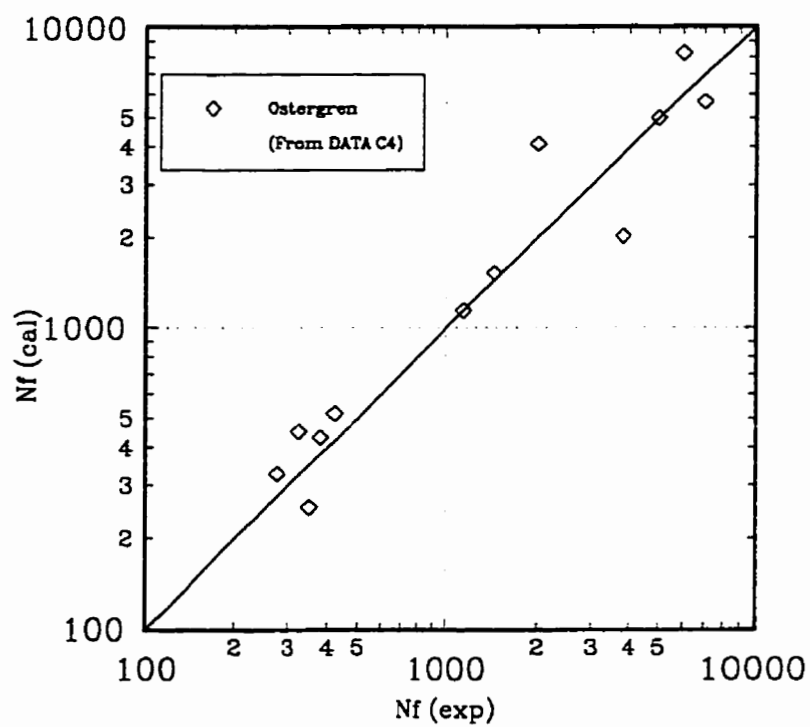


Figure 5.29 Comparison of life predicted with the Ostergren's Model with experimental life obtained for isothermal fatigue tests carried out under continuous cycling at 871°C on CC René 80. (After C4 data set [4])

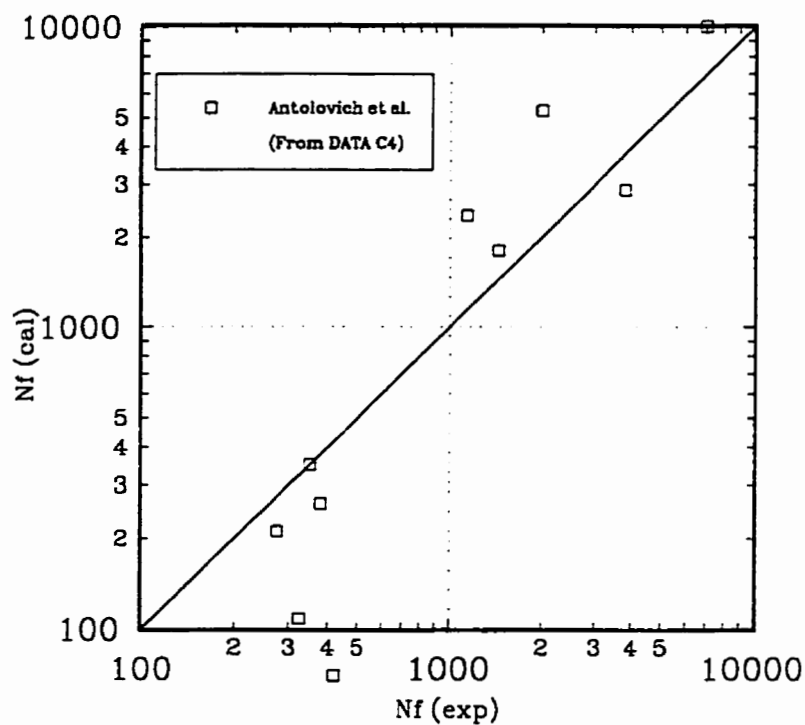


Figure 5.30 Comparison of life predicted with the Antolovich et al.'s Model with experimental life obtained for isothermal fatigue tests carried out under continuous cycling at 871°C on CC René 80. (After C4 data set [4])

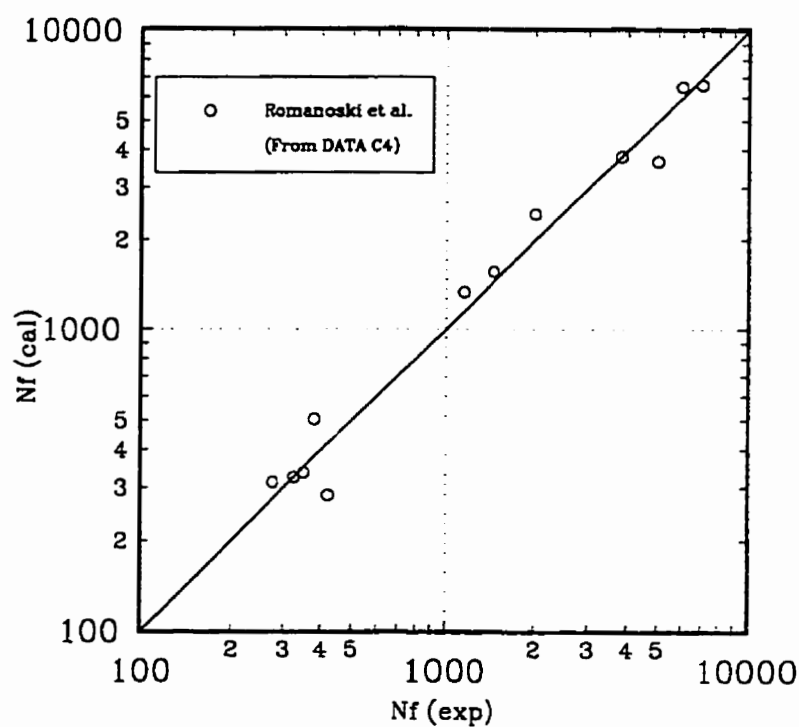


Figure 5.31 Comparison of life predicted with the Romanoski et al.'s Model with experimental life obtained for isothermal fatigue tests carried out under continuous cycling at 871°C on CC René 80. (After C4 data set [4])

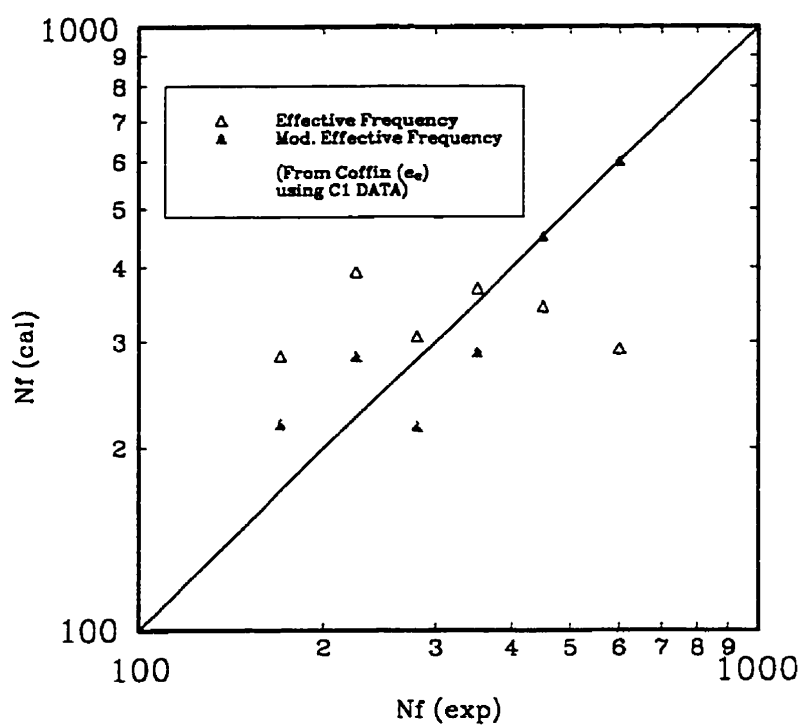


Figure 5.32 Comparison of life predicted with the Coffin's Model ($\Delta\epsilon_e$) with experimental life obtained for isothermal fatigue tests carried out under tensile and/or compressive strain hold time at 871°C on CC René 80. (After C1 data set [5])

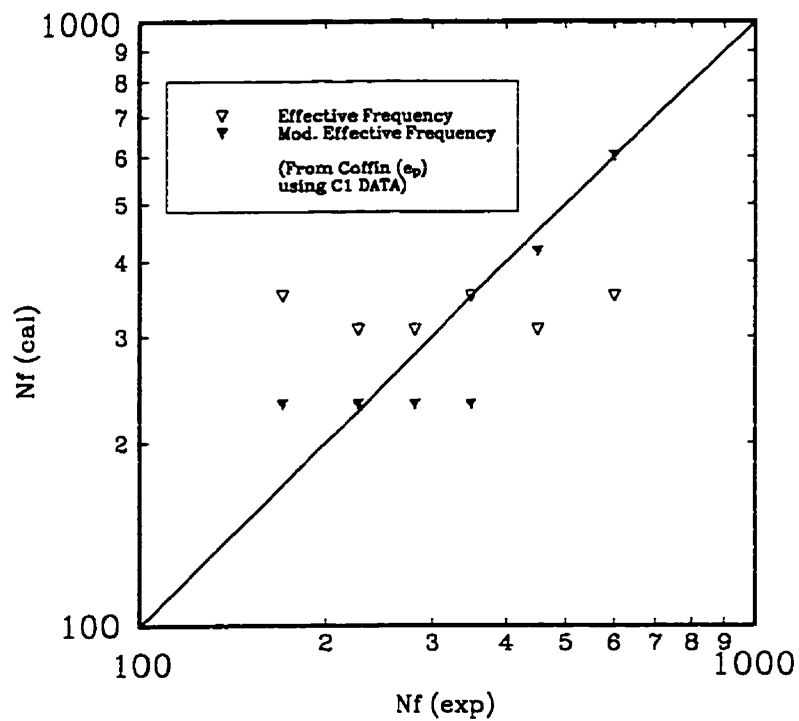


Figure 5.33 Comparison of life predicted with the Coffin's Models ($\Delta\epsilon_p$) with experimental life obtained for isothermal fatigue tests carried out under tensile and/or compressive strain hold time at 871°C on CC René 80. (After C1 data set [5])

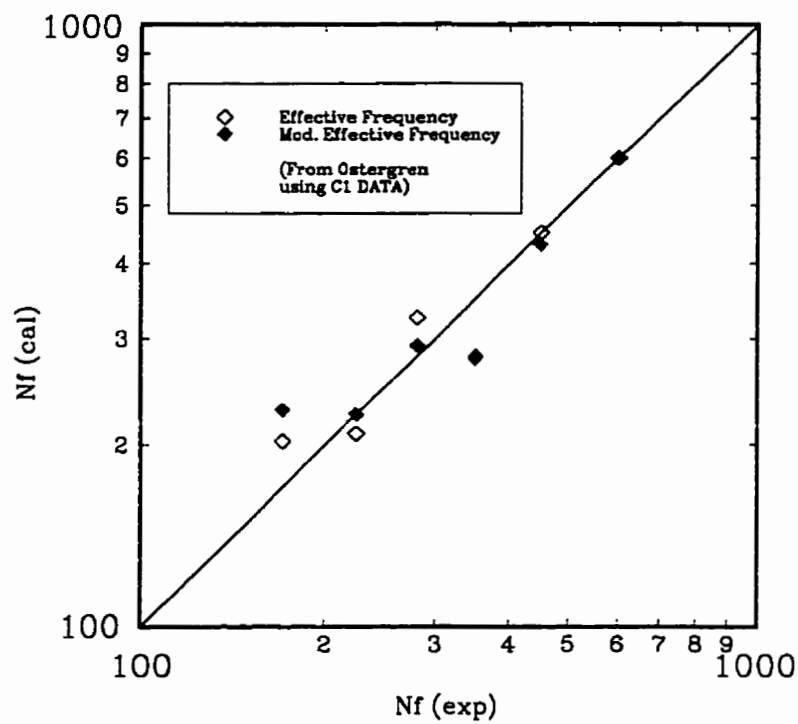


Figure 5.34 Comparison of life predicted with the Ostergren's Model with experimental life obtained for isothermal fatigue tests carried out under tensile and/or compressive strain hold time at 871°C on CC René 80. (After C1 data set [5])

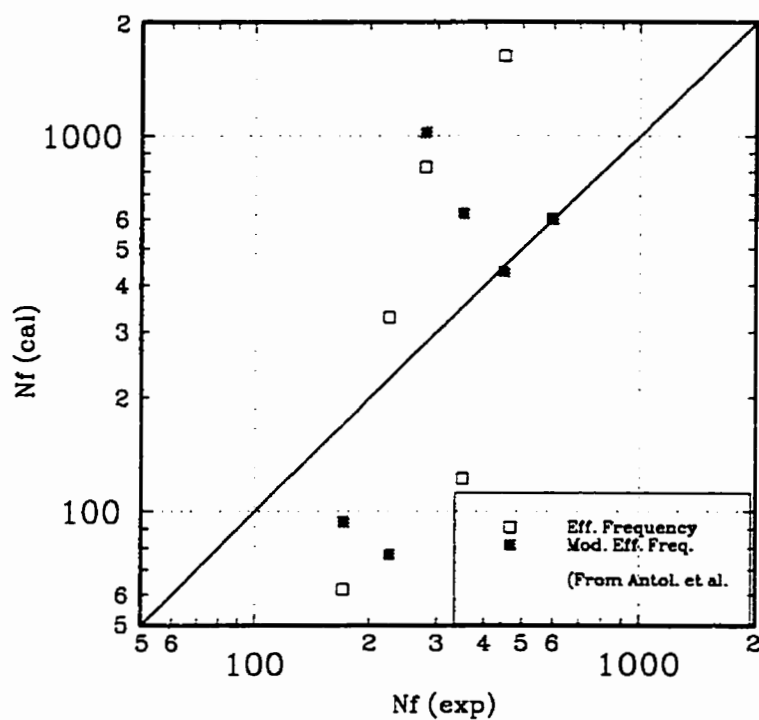


Figure 5.35 Comparison of life predicted with the Antolovich et al.'s Model with experimental life obtained for isothermal fatigue tests carried out under tensile and/or compressive strain hold time at 871°C on CC René 80. (After C1 data set [5])

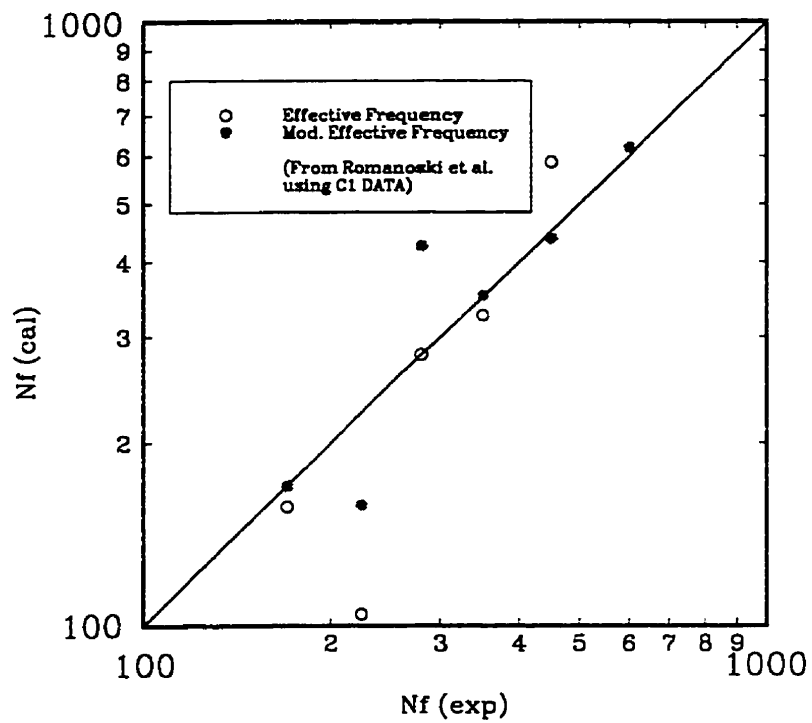


Figure 5.36 Comparison of life predicted with the Romanoski et al.'s Model with experimental life obtained for isothermal fatigue tests carried out under tensile and/or compressive strain hold time at 871°C on CC René 80. (After C1 data set [5])

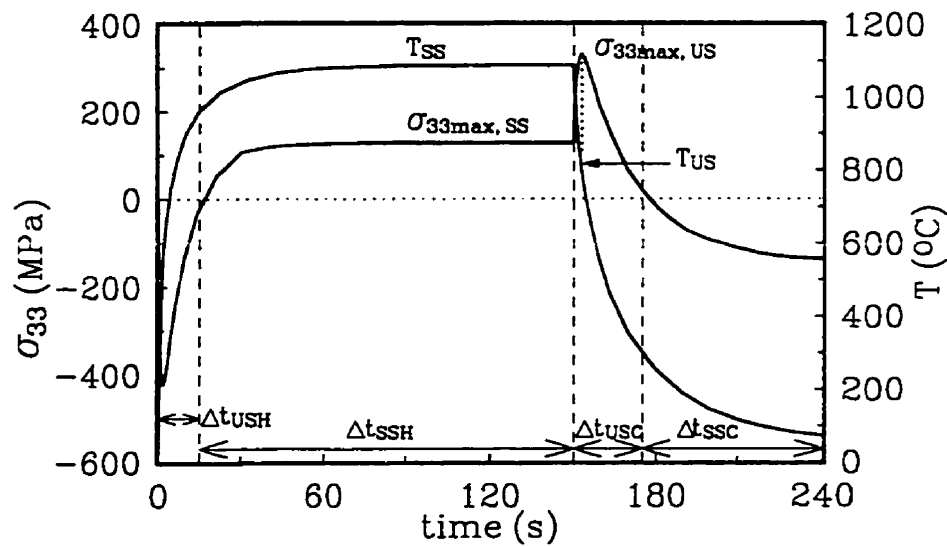


Figure 5.37 Computed temperature (T) and principal stress (σ_{33} or σ_z) variation at position $z = 29.75$ mm along the leading edge of the DEW specimen (axis z in Figure 5.16) (150 s is the transition time between the heating and the cooling portions of the cycle).

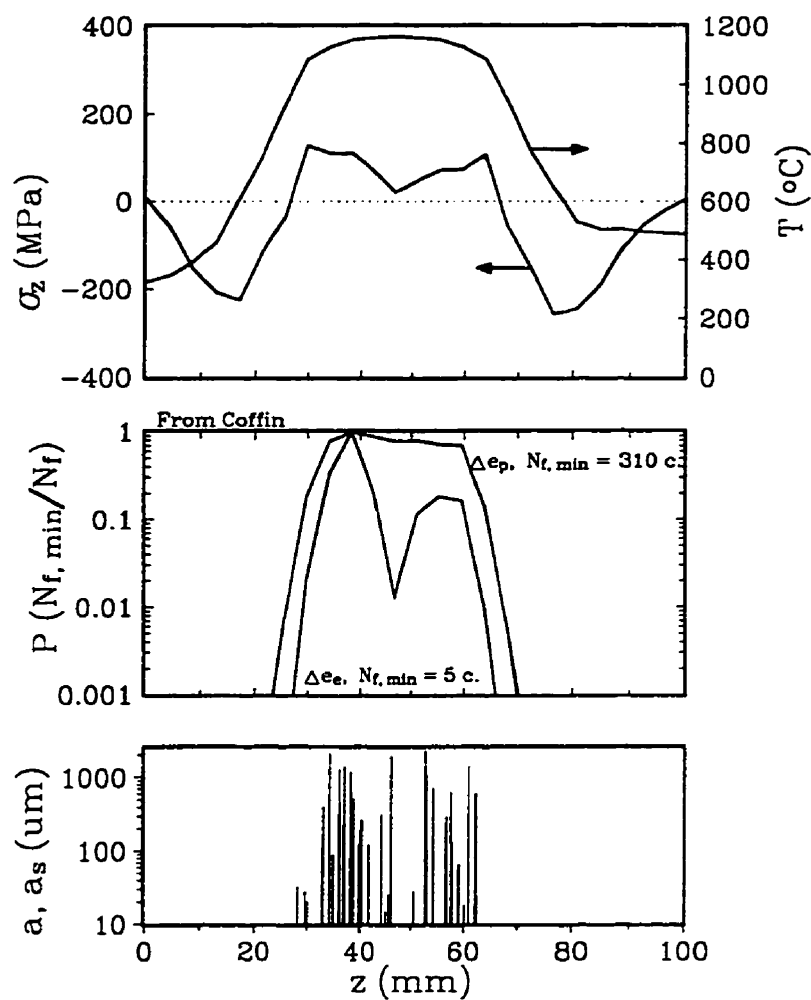


Figure 5.38 Distribution of the principal stress (σ_z), the temperature (T) and the probability (P) of crack initiation after $N_{f, \min}$ cycles (computed from the models of Coffin) compared to oxide spikes (a_s) and cracks (a) along the leading edge (axis z).

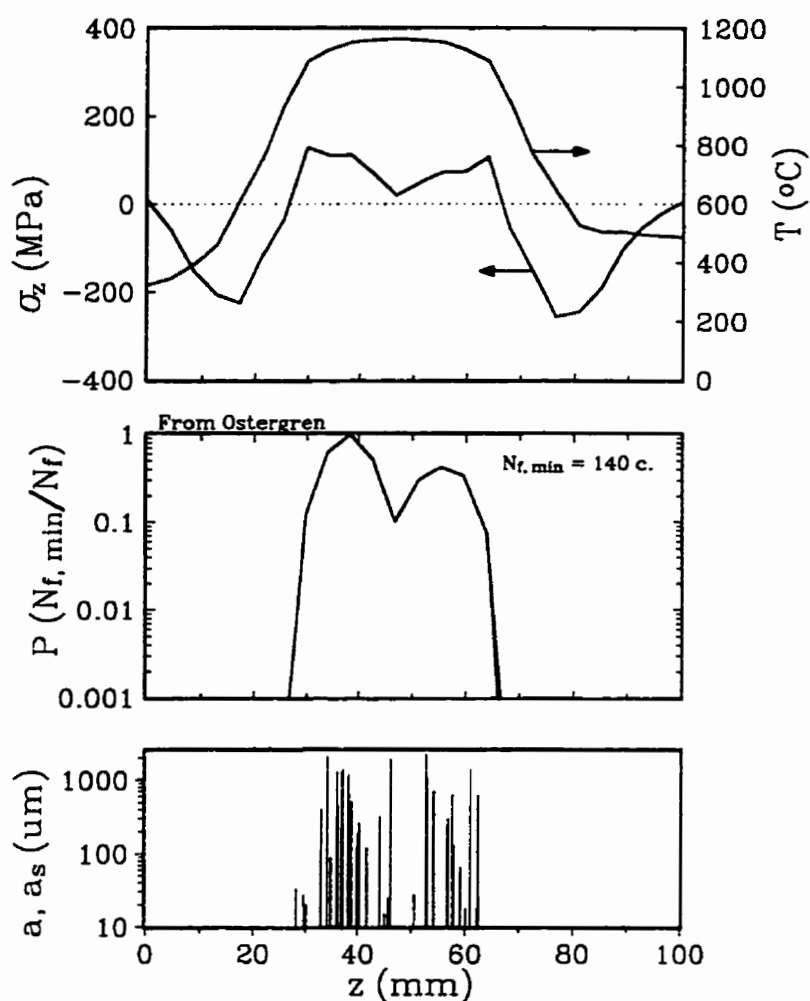


Figure 5.39 Distribution of the principal stress (σ_z), the temperature (T) and the probability (P) of crack initiation after $N_{f, \min}$ cycles (computed from the model of Ostergren) compared to oxide spikes (a_s) and cracks (a) along the leading edge (axis z).

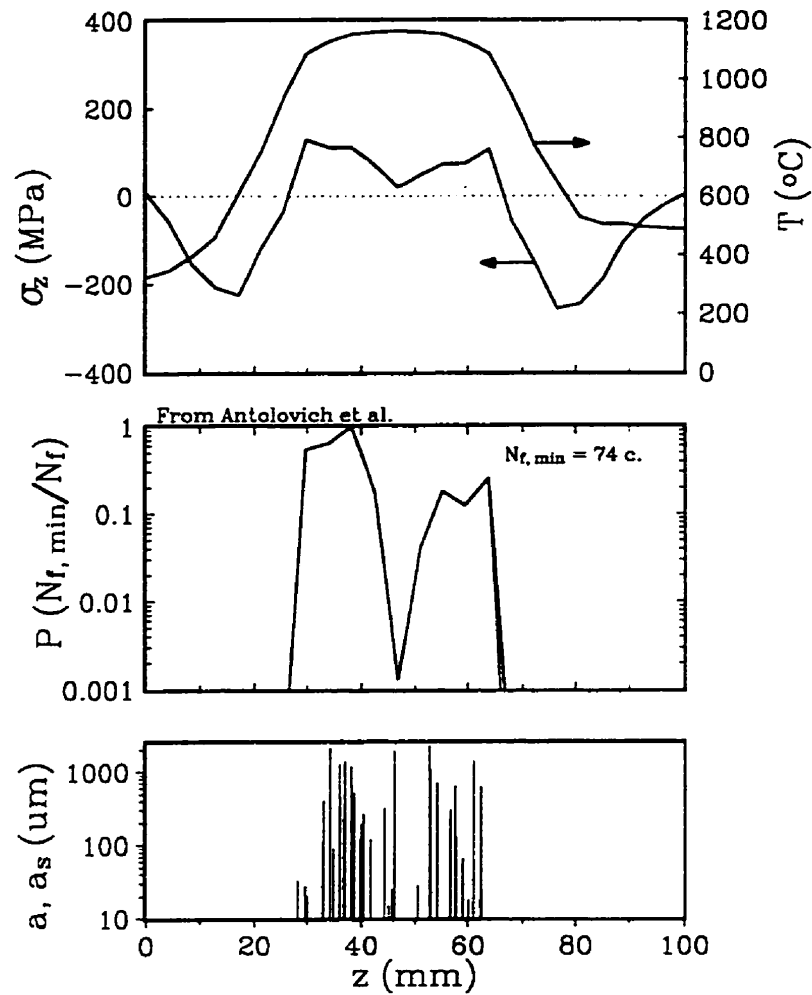


Figure 5.40 Distribution of the principal stress (σ_z), the temperature (T) and the probability (P) of crack initiation after $N_{f, \min}$ cycles (computed from the model of Antolovich et al.) compared to oxide spikes (a_s) and cracks (a) along the leading edge (axis z).

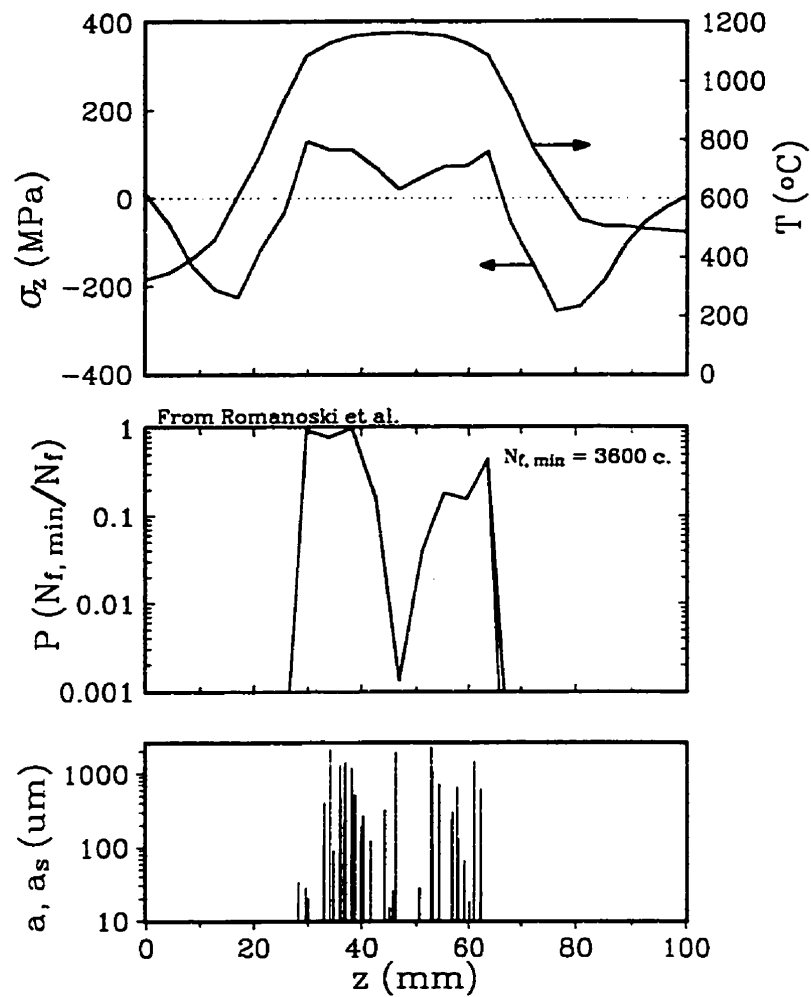


Figure 5.41 Distribution of the principal stress (σ_z), the temperature (T) and the probability (P) of crack initiation after $N_{f, \min}$ cycles (computed from the model of Romanoski et al.) compared to oxide spikes (a_s) and cracks (a) along the leading edge (axis z).

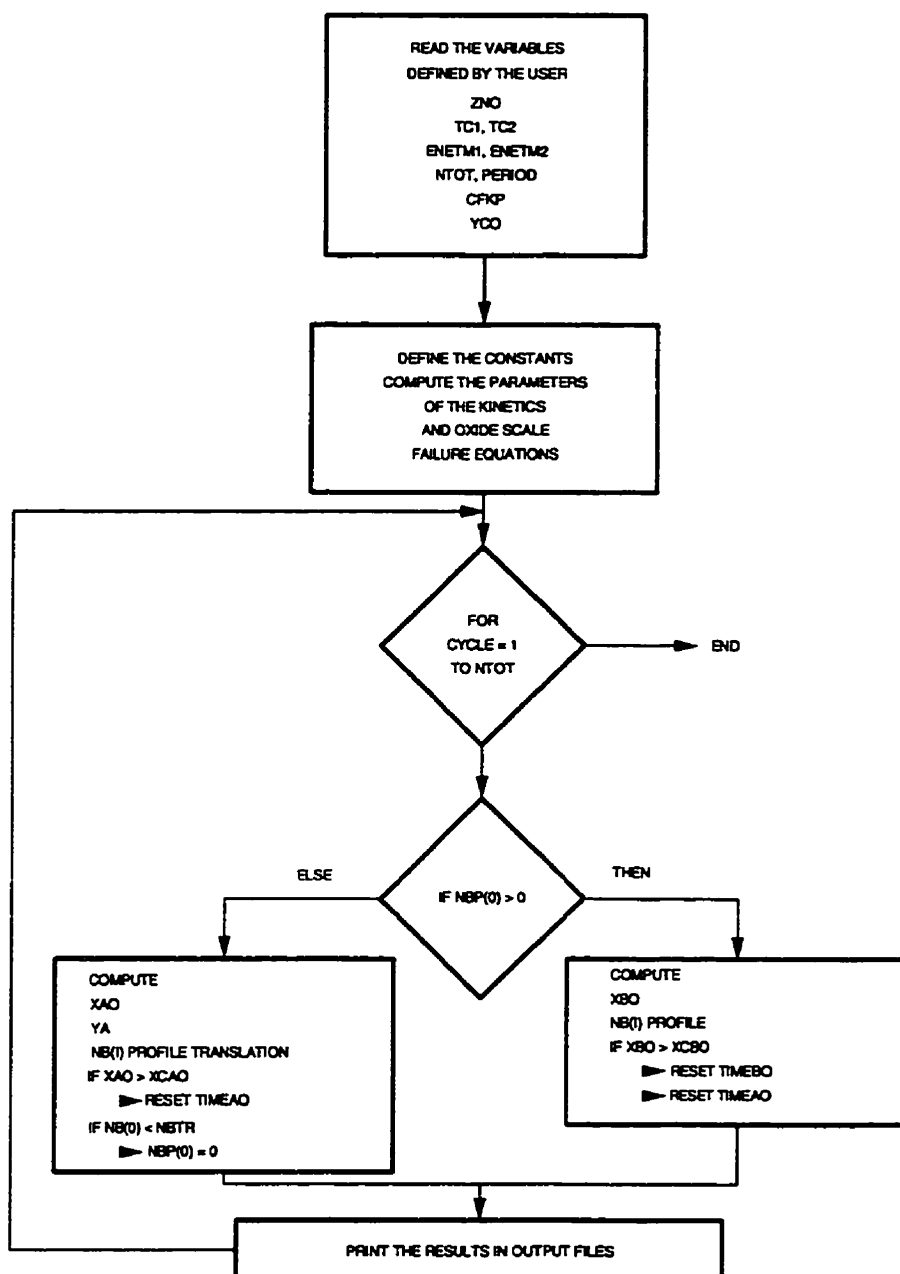


Figure 5.42 Algorithm for Modelling Alloy Depletion Profile and Alloy Surface Recession. Refer to Subsection 5.4.1 and to Appendix L for the definition of the variables.

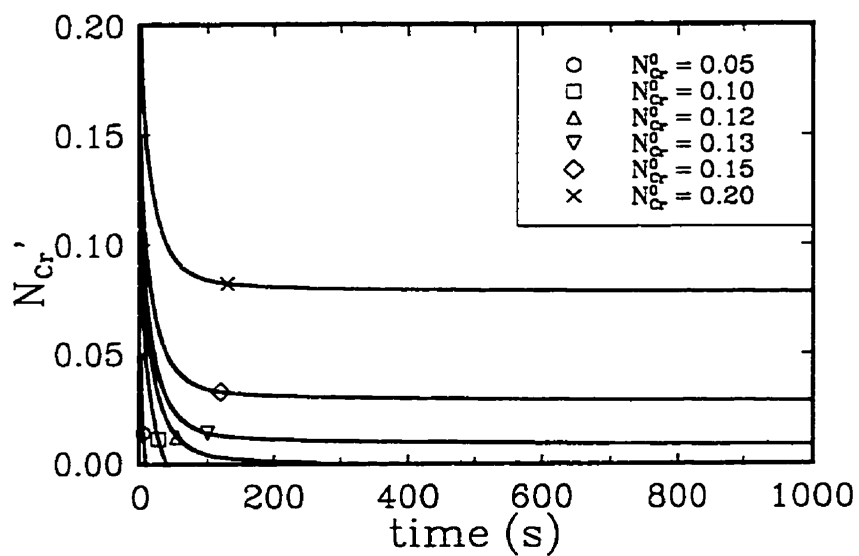


Figure 5.43 Computed variation the Cr content (N_{Cr}') at the metallic surface of Ni-Cr alloys with various nominal Cr contents (expressed in molar fraction of Cr in the alloy), during isothermal oxidation at 1164°C.

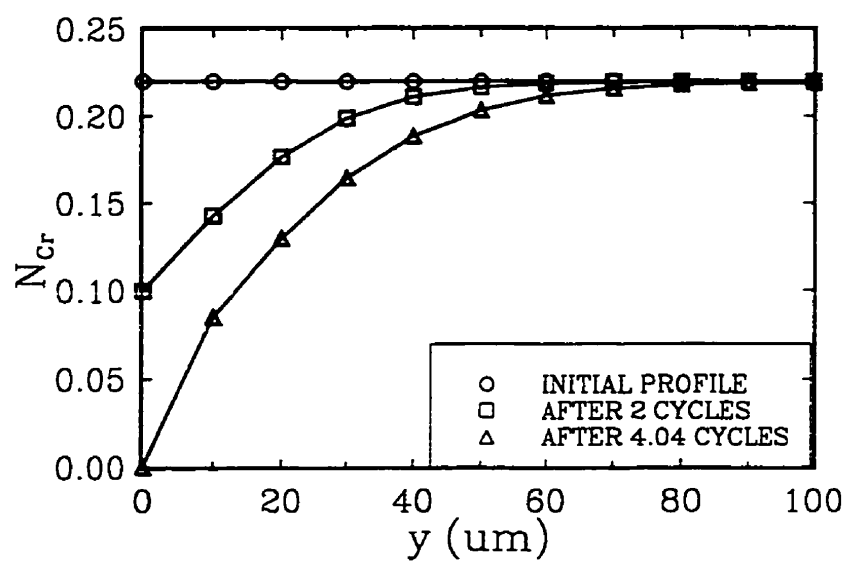


Figure 5.44 Computed Cr content (N_{Cr}) profile in the depleted zone of a Ni-22at%Cr alloy exposed to different number of typical thermal cycles in the burner rig with a maximum alloy temperature of 1164°C ($z = 46.25$ mm).

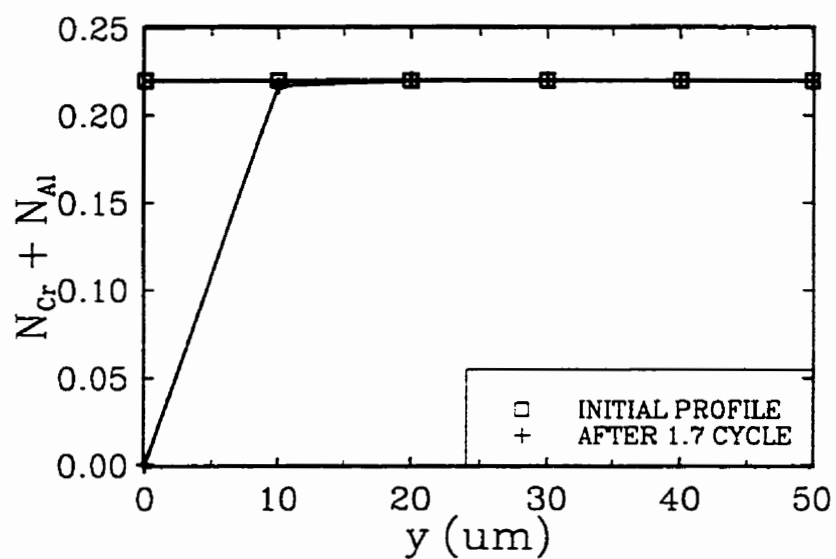


Figure 5.45 Computed Cr and Al content profile ($N_{Cr} + N_{Al}$) in the depleted zone of an uncoated DSR80 alloy exposed to 1.7 thermal cycles in the burner rig with a maximum alloy temperature of 1164°C ($z = 46.75$ mm).

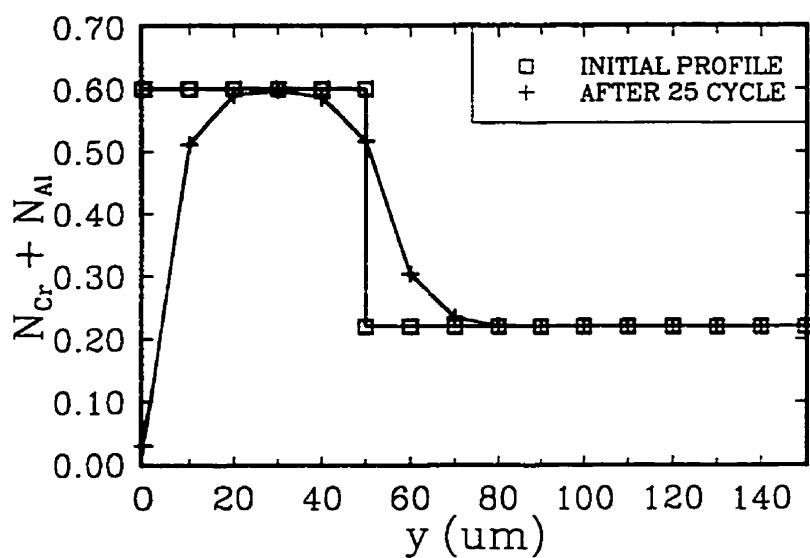


Figure 5.46 Computed Cr and Al content profile ($N_{Cr} + N_{Al}$) in the depleted zone of a coated DSR80 alloy exposed to 25 thermal cycles in the burner rig with a maximum alloy temperature of 1164°C ($z = 46.75$ mm).

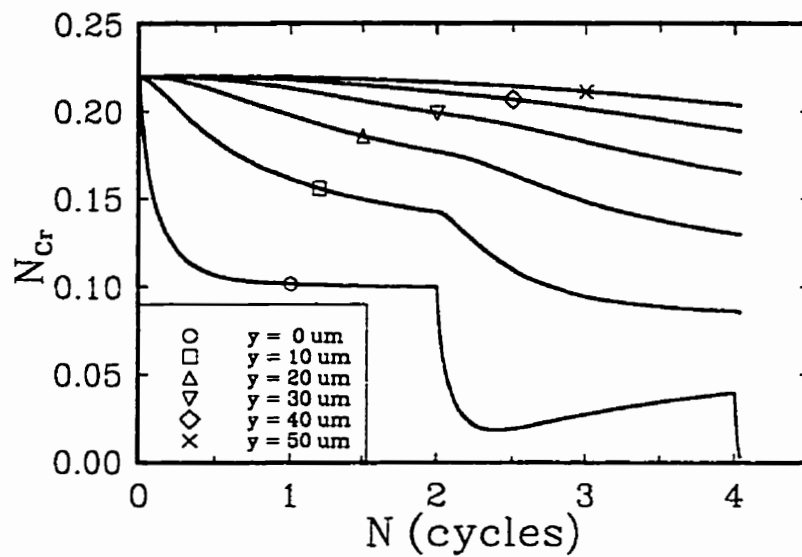


Figure 5.47 Computed variation of the Cr content (N_{Cr}) at different depths in the depleted zone of a Ni-22at%Cr alloy during thermal cycling in a burner rig with a maximum alloy temperature of 1164°C ($z = 46.75 \text{ mm}$).

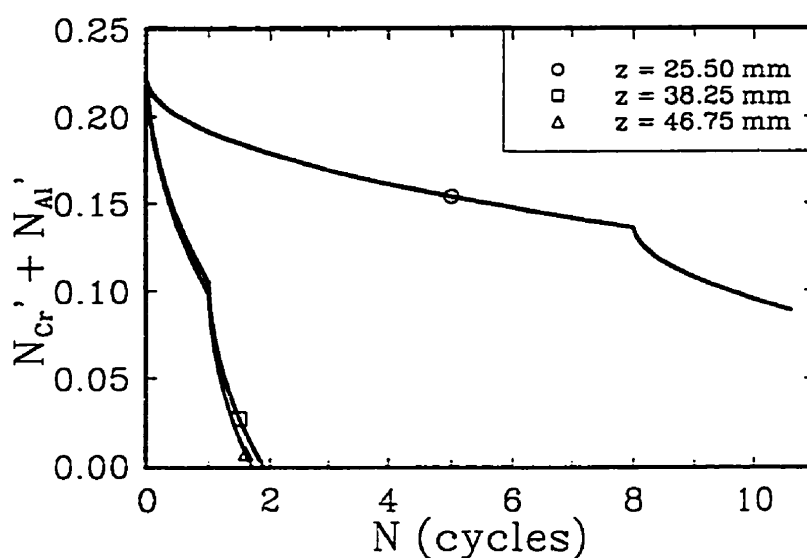
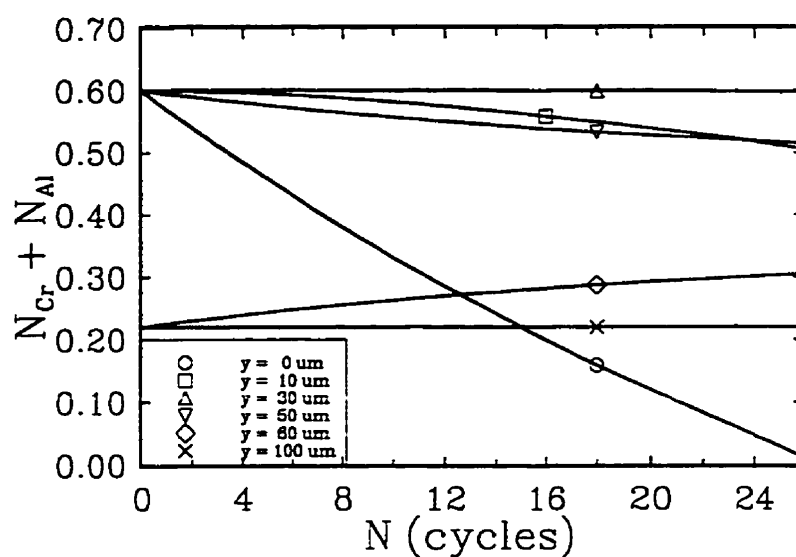
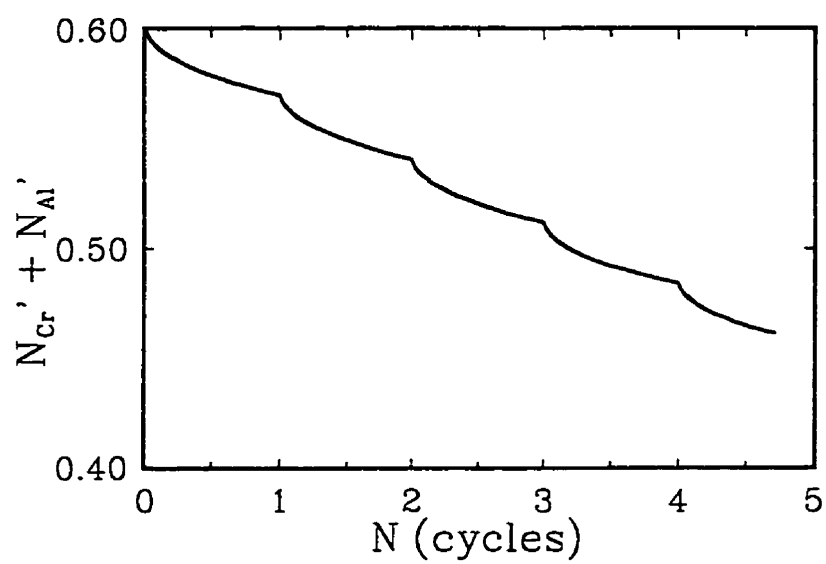


Figure 5.48 Computed variation of the Cr and Al content ($N_{Cr} + N_{Al}$) at the metallic surface of the uncoated DSR80 alloy at different longitudinal positions along the leading edge of DEW specimens during thermal cycling in a burner rig at: $z = 46.75$ mm with a maximum alloy temperature of 1164°C , $z = 38.25$ mm with a maximum alloy temperature of 1153°C and, $z = 25.50$ mm with a maximum alloy temperature of 936°C .



(a)

Figure 5.49 (a) Computed variation of the Cr and Al content ($N_{Cr} + N_{Al}$) at different depths in the depleted zone of the coated DSR80 alloy at the longitudinal position $z = 46.75$ mm along the leading edge of DEW specimens during thermal cycling in a burner rig (the maximum alloy temperature reaches 1164°C at this position). (b) detailed variation of the Cr and Al content ($N_{Cr}' + N_{Al}'$) at the metallic surface of the coating.



(b)

Figure 5.49 Cont'd.

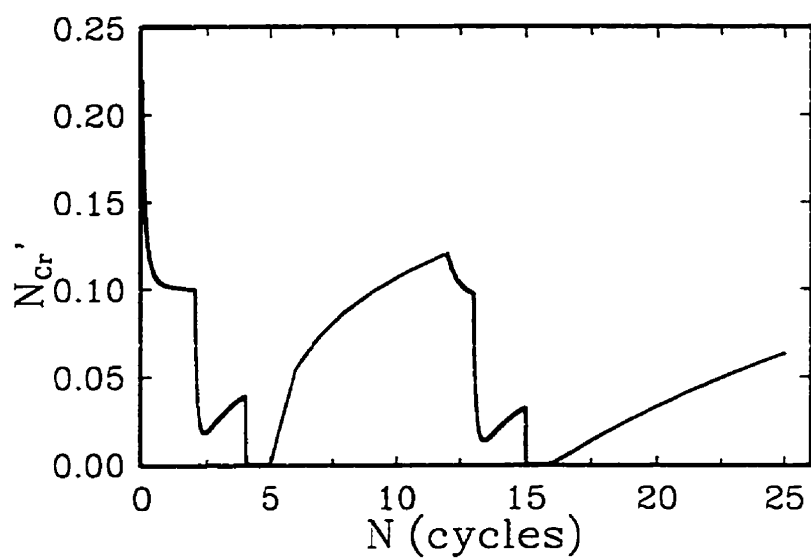


Figure 5.50 Effect of alloy surface recession on the computed variation of the Cr content (N_{Cr}') at the surface of a Ni-22at%Cr alloy during thermal cycling in a burner rig with a maximum alloy temperature of 1164°C ($z = 46.75$ mm).

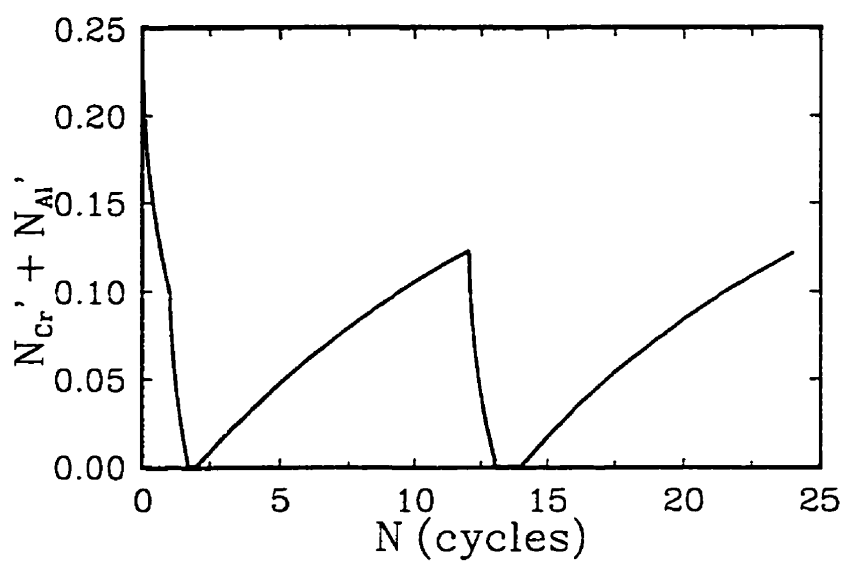
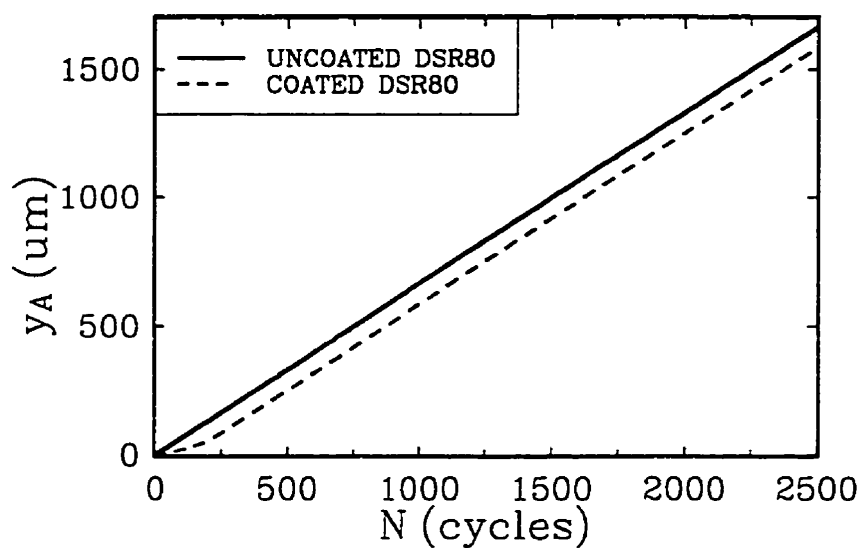
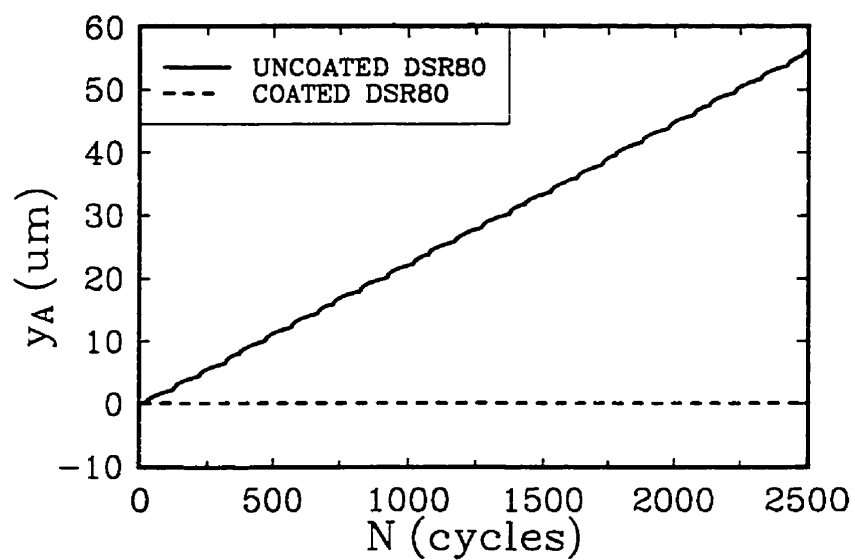


Figure 5.51 Effect of alloy surface recession on computed of the Cr and Al content ($N_{Cr} + N_{Al}$) at the surface of the uncoated DSR80 alloy at the longitudinal position $z = 46.75$ mm at 1164°C .



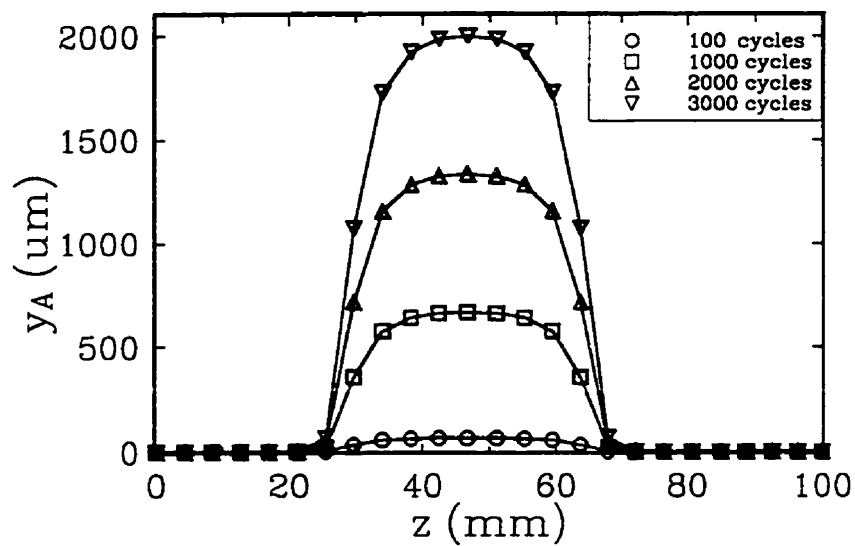
(a)

Figure 5.52 Computed alloy surface recession (y_A) of an uncoated and a coated DSR80 alloy at two positions along the leading edge of DEW specimens during thermal cycling in a burner rig: (a) $z = 46.75$ mm with a maximum alloy temperature of 1164°C ; and (b) $z = 25.50$ mm with a maximum alloy temperature of 936°C .



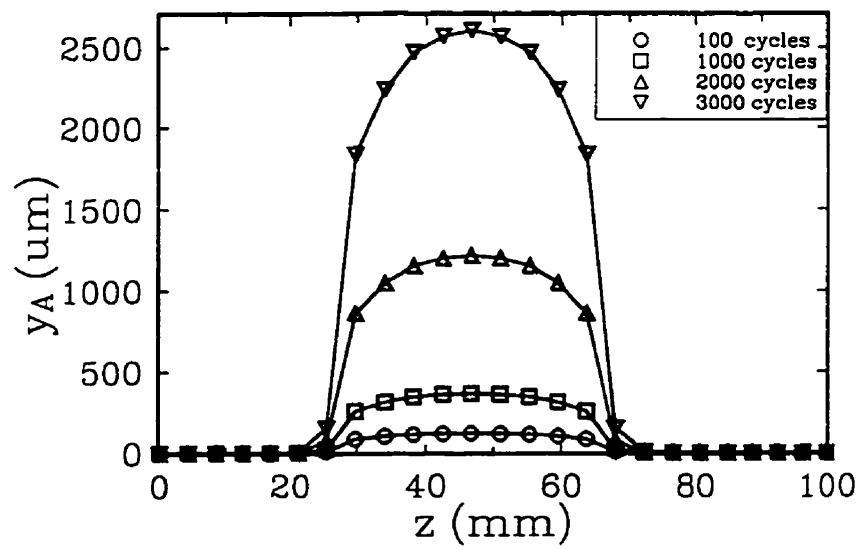
(b)

Figure 5.52 Cont'd.



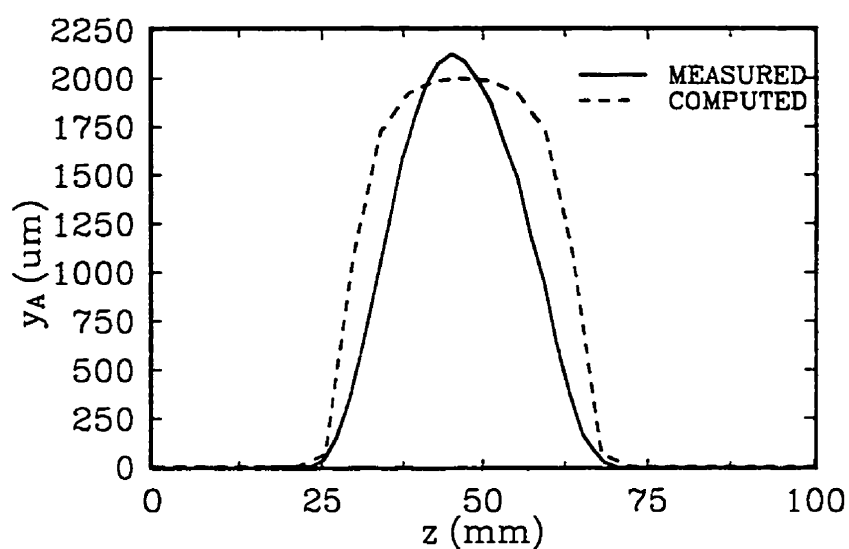
(a)

Figure 5.53 Computed alloy surface recession (y_A) along the leading edge (axis z) of uncoated DEW specimens in DRS80 during thermal cycling in a burner rig with (a) short periods of 150 s in the hot gas stream (case of tests SRA, SRB, SRC, SRF, refer to Subsection 3.1), and with (b) long periods of 390 s in the hot stream (case of the test SRD).



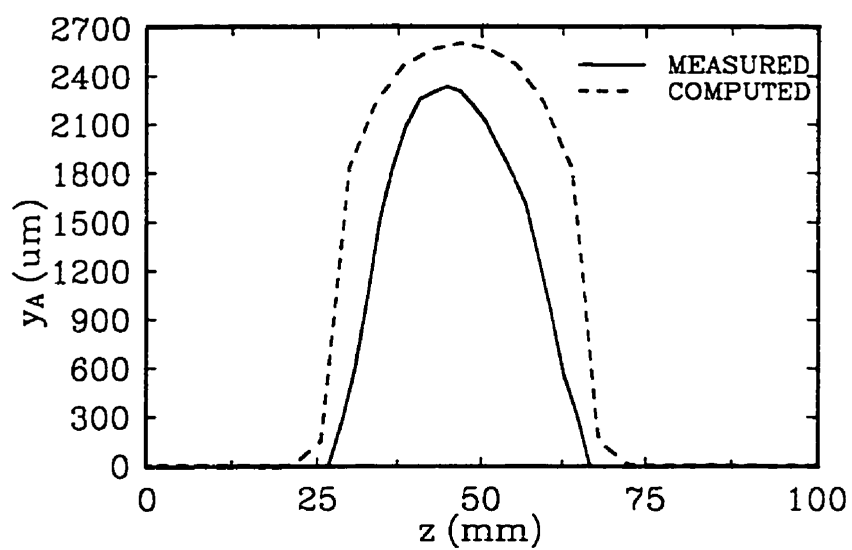
(b)

Figure 5.53 Cont'd.



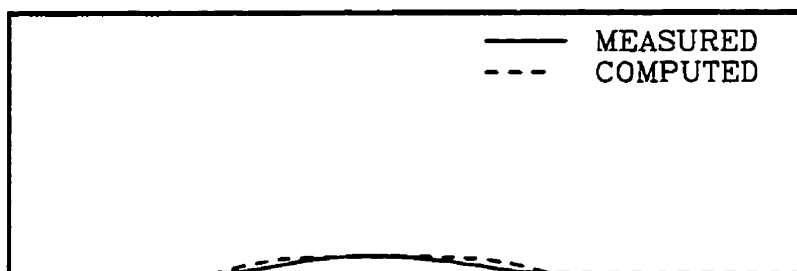
(a)

Figure 5.54 Measured vs computed alloy surface recession (y_A) along the leading edge (axis z) of uncoated DEW specimens of DRS80 after testing in a burner rig with (a and c) short periods of 150 s in the hot gas stream (test SRC, refer to Subsection 3.1), and with (b and d) long periods of 390 s in the hot stream (test SRD).

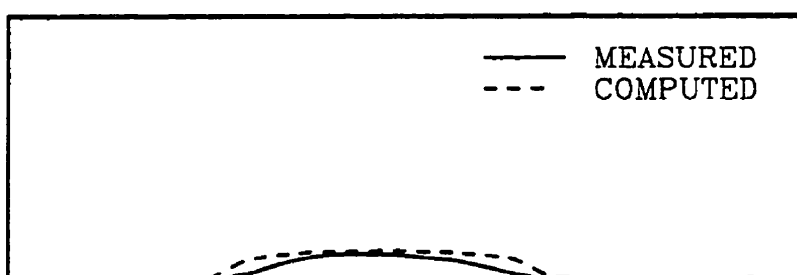


(b)

Figure 5.54 Cont'd.



(c) Full Scale representation of specimen SRC



(d) Full Scale representation of specimen SRD

Figure 5.54 Cont'd.

APPENDIXES

APPENDIX A

DETAILED THERMAL FATIGUE TESTING PROCEDURE IN BURNER RIG

This Appendix describes in details the procedure applied for each thermal fatigue test carried out in the burner rig. The procedure, which follows, is divided in three tasks: the preliminary testing preparation, the burner rig operation and the data acquisition system operation.

A.1 Preliminary Testing Preparation

- 1.0 **INSTRUMENTATION OF THE SPECIMEN** (refer to Figures 3.1 and 3.5 concerning the entire sub-section)
- 1.1 A longitudinal hole is practised through the specimen by Electro Discharge Machining (EDM). This hole allows the passage of the AC-DP probes that have to be fixed to the free end of the specimen (opposite to the one gripped to the holder). Tiny holes are machined by EDM on the specimen, at the locations of the AC-PD probes to facilitate their attachment.
- 1.2 The specimen is washed with water and soap then with methylic alcohol in an ultrasonic bath.
- 1.3 The platinum and nickel AC-PD probes are laser-welded at the surface of the specimen, using the tiny holes machined by EDM. Before welding, the probes passing through the specimen hole are insulated at this level with alumina ceramic tubes.
- 1.4 Each probe is individually insulated from the specimen to the terminal block with a 1/16 and 1/8 I.E. ceramic fibre sleeving (NEXTEL trademark). The sleeving is a very good thermal and electrical insulator that can be exposed to high temperatures (up to 1000°C) during many hours.
- 1.5 The specimen is then gripped between the jaws of the holder. The specimen should be exposed 89 mm outside of the holder. The AC-PD

probes wiring are positioned in the slot of the holder, previously covered with ceramic fabric. The top and bottom plates of the holder are screwed with their asbestos gaskets. The front SS plate is screwed to the holder with its asbestos gasket. A high-temperature lubricant is applied on all screws used here.

- 1.6 The holder (with the instrumented specimen) is fixed to its shaft, mounted on the specimen carrier.
- 1.7 The AC-PD probes are carefully connected to terminal blocks according to their respective polarity and location at the specimen surface.
- 1.8 The specimen is finally washed with methylic alcohol. The specimen and especially the probes should not be touched during the testing operation.

2.0 **SET-UP OF THE AC-PD MONITOR (CGM5)** (Refer to Figures B.1 and B.2 in Appendix B, for this sub-section)

- 2.1 To allow the electronic stabilization of the instrument, the power switch has to be positioned at "ON" at least two (2) hours before testing.
- 2.2 The frequency of the alternating current is set through the frequency selector (6) (frequency range: 0.3 to 100 kHz).
- 2.3 In order to set the current, the current monitor switch (8) is positioned at "UP" and the current value can be adjusted by turning the current set potentiometer (10) clockwise until the expected reading is displayed on the panel meter (1) (suggested values: 0.5 to 1.0A).
- 2.4 The phase switch (15) should be positioned at "LOW". At this position, the phasing between the signal of the modulus α and β is automatically optimized.
- 2.5 The filter switch (18) should be positioned at "OFF" for this particular application.
- 2.6 The gain is set to obtain the desired sensitivity signal level, using the gain

selectors (4) and (29) for modules α and β , respectively (suggested range: 50 to 70 db).

- 2.7 For the module α , the initial signal output can be offset by up to 200 mV if the offset switch (12) is positioned at "UP" (fine) or by up to 2 volts if it is positioned at "LOW". The offset can be adjusted to a precise value by using the potentiometer (13) for module α and, the potentiometer (30) for module β . These facilities make it possible to optimize the sensitivity of the signal by allowing a higher gain lever, for a given fixed current. Note that the fixed offset switch (17) has to be positioned at "MIDDLE" (OFF), if the variable offset potentiometer (13) is used like it is suggested here.

- 3.0 **MICRISTAR PROGRAMMING** (The complete description of the programming steps of Micristar Unit is given in Appendix C)

A.2 Burner Rig Operational Procedures for Thermal Fatigue Testing

Every time the test is started or restarted, the next procedure has to be followed:

1.0 BURNER RIG START-UP PROCEDURES

- 1.1 Inspect liners of the burner, the controlling thermocouple (T/C), the specimen and AC-PD probes. Change the T/C if needed. Read the time displayed on the **EAGLE SIGNAL TIMER** mounted on the control console panel and record it in the **BURNER LOG-BOOK** along with your name, the date, the starting cycle number of the fatigue test to be carried on, and your observations about the rig inspection.
- 1.2 Turn-OFF the Micristar Alarms switch installed on the left of the RED

EMERGENCY STOP button.

- 1.3 Push-ON the EXHAUST button and wait for one (1) minute.
- 1.4 Push-ON the POWER button.
- 1.5 Push the RESET button once.
- 1.6 Push the ACKNOWLEDGE button once.
- 1.7 Push-ON the AIR button to supply power to main air solenoids.
- 1.8 Push-ON the AUTO CONTROLLER button to supply power to the Micristar.
- 1.9 Turn-ON the Micristar Alarms button (only if %OUTPUT do not exceed 95%, (refer to Appendix C).
- 1.10 Turn-ON the SI data acquisition system and the computer to run the program NRC.EXE on NRC sub-directory of disk drive C. See next section for detailed procedure, steps 1.0 to 1.23.
- 1.11 Phone the **HEATING PLANT** at 993-2412 for supply of compressed air directly to M-14.)
- 1.12 Check the Micristar operating parameters (refer to Appendix C). Normally the following parameters need to be re-set after every successful run:
 - a. Ensure that the Micristar controller is in **HOLD** mode. If not, press the **HOLD** key to set the Micristar controller to **HOLD** mode.
 - b. Press the **MANUAL/AUTO** key to set the Micristar on **MANUAL** mode.
 - c. Open operator panel.
 - d. Set % **OUTPUT** to value = 10.0
 - e. Check the values for all parameters.
 - f. Close the operating panel.
 - g. The Micristar controller should still be on **HOLD** and **MANUAL**

modes.

- h. Press the **RUN** key (Led red light should flash).
 - i. Use **INC/DEC** key to select **SEGMENT No. 1**.
- 1.13 Adjust Micristar PV-HI alarm trigger level to maximum:
- a. Select **FULL ACCESS**.
 - b. On **HOLD** and **MANUAL**, depress **CONTROLLER** and scroll to **PV-HI**.
 - c. Press **ENTER**.
 - d. Set **PV-HI** value to 100.
 - e. Touch **ENTER** to complete the process.
- 1.14 **Push-In** the **MANUAL** button on the **BURNER** control console for **MANUAL** mode.
- 1.15 Wait for air to arrive.
- 1.16 Turn-**OFF** the air supply for the control thermocouple (i.e., close the gauge inside the rig chamber.)
- 1.17 Push-**IN** the **EXHAUST CONTROL THERMOCOUPLE PROBE** button on the console to insert the probe into the testing position.
- 1.18 Slowly turn-**ON** the air supply for the control thermocouple (i.e., open the gauge inside the rig chamber). Check **T/C** position.
- 1.19 Check test fixture position (i.e. keep the test section at 85 mm distance from nozzle flange).
- 1.20 Turn-**ON** the **EXHAUST FAN** - set at low speed.
- 1.21 Run the program **NRC.EXE** to get the data acquisition ready.
- 1.22 Set the **PRIMARY** pressure to 15 psia (for 0.5" DIA FUEL NOZZLE IS USED)
- 1.23 Set the **SECONDARY** pressure to 17 psia
- 1.24 Set the **COOLING AIR** pressure to 35 psia
- 1.25 Make sure that the **HONEYWELL** recorder is controlled by the

EXHAUST TEMPERATURE (Push-IN the **EXHAUST** button on the **HONEYWELL** control panel.)

- 1.26 Make sure that the Micristar is controlled by the **EXHAUST TEMPERATURE** (Push-IN the **T/C-EXHAUST** button on the Micristar control panel.)
- 1.27 Turn-**ON** outside **FUEL PUMP** to activate **FUEL SUPPLY** pressure gage.
- 1.28 Push-**ON** the **FUEL** button.
- 1.29 Set the **FUEL PILOT SIGNAL (BYPASS)** valve to 1/4 (23% on scale).
- 1.30 Push the **START** button once to ignite.
- 1.31 Once ignited, quickly increase **PRIMARY** pressure faster than the **SECONDARY** pressure to bring down the exhaust temperature.
- 1.32 Turn-down the **FUEL PILOT SIGNAL** to lower the exhaust temperature to 800°C.
- 1.33 Adjust the **PRIMARY** pressure to 40.0 psia
- 1.34 Adjust the **SECONDARY** pressure to 27.5 psia
- 1.35 Adjust the **COOLING AIR** pressure to 60.0 psia
- 1.36 Lower the **FUEL PILOT SIGNAL** to idle exhaust temperature.
- 1.37 The burner is now ready to switch from **MANUAL** to **AUTOMATIC FUEL** control.
- 1.38 To switch from **MANUAL** to **AUTOMATIC FUEL** control, do the following:
 - a. Make sure that the Micristar Controller is on **MANUAL** mode.
 - b. Make sure that the Micristar Controller is on **HOLD** mode with run light flashing.
 - c. Make sure that the **%OUTPUT** is set at 10.0
 - d. Make sure, with the run light flashing, that the **SEGMENT DISPLAYED IS No. 1.**
 - e. Make sure that the **BURNER** is at **IDLE** condition and

MANUAL mode.

- f. Almost instantly, press:
 - i. The **MANUAL/Auto** key on the Micristar controller once;
 - ii. The **Run** key on the Micristar controller once;
 - iii. The **ENTER** key on the Micristar Controller once; and
 - iv. The **AUTO** key on the **BURNER CONTROL CONSOLE** once.
 - g. Observe the **SEGMENT** display and when **SEGMENT No.3** appears, watch the data acquisition starting on the screen of computer.
 - h. Observe the temperature increase after the transfer, an over-shoot in temperature of up to 1300°C is acceptable.
- 1.39 With Honeywell recorder OFF, adjust Honeywell alarm to 1500°C. At approximately 1 minute into the test, turn on the Honeywell recorder. Adjust the alarm setting to 1400°C only after the flame has stabilized.

2.0 BURNER RIG SHUT DOWN PROCEDURES

- 2.1 Check that the programmed number of cycles had been run, on the screen of the computer.
- 2.2 A successful RUN (i.e., Automatically controlled) will shut the FUEL off and put the burner to FLAME-OUT and the Micristar on HOLD mode (i.e., SEGMENT No.5)
- 2.3 Press the **RESET** button once.
- 2.4 Press the **ACKNOWLEDGE** button once.
- 2.5 Press the **FUEL** button **OFF**.
- 2.6 Press/**PUSH-IN** the outside FUEL PUMP button to stop fuel supply.
- 2.7 Press/**PUSH-IN** the Manual button on console for **MANUAL** operation.
- 2.8 Keep Pressure settings for two (2) minutes.

- 2.9 Turn-**OFF** the DATA LOGGER.
- 2.10 Turn-**OFF** the HONEYWELL recorder.
- 2.11 Call the **HEATING PLANT** at 993-2412 to shut-off the compressor.
- 2.12 Let release the excess air in the pipes until Main Pressure and cooling air are 14.6 for all gauges on the console.
- 2.13 Turn-**OFF** the EXHAUST FAN.
- 2.14 Push-**OFF** the air button.
- 2.15 Push-**OFF** the EXHAUST button.
- 2.16 Push-**OFF** the AUTO CONTROLLER button.
- 2.17 If POWER is not OFF, Push-**OFF** the POWER button.
- 2.18 Set the Micristar Alarms button to **OFF** mode.
- 2.19 Record the TIME displayed and the last cycle number run, on the EAGLE TIMER in the burner LOG-BOOK.
- 2.20 Copy the data files SRYx-xxx.PRN from the hard disk to floppy disk, and delete the files on the hard disk. Here, Y represents a capital letter used for specimen identification and xxxx designates the cycle number. See more detailed procedure in next section, steps 2.0 to 3.12.

3.0 BURNER RIG EMERGENCY SHUT DOWN PROCEDURES

- 3.1 Press **HOLD** key on the Micristar controller.
- 3.2 Press/**Push-IN** FUEL button **OFF**.
- 3.3 Press/**Push-IN** FUEL PUMP button to stop fuel supply.
- 3.4 Press/**Push-IN** RESET button once.
- 3.5 Press/**Push-IN** ACKNOWLEDGE button once.
- 3.6 Press **MANUAL** Key on the Micristar controller.
- 3.7 Press/**Push-IN** MANUAL button on control console.
- 3.8 If air supply shut down is requested, call the HEATING PLANT (993-2412).

- 3.9 Turn-OFF recorders (i.e., DATA LOGGER and HONEYWELL).
- 3.10 Turn-OFF the EXHAUST FAN.
- 3.11 Call for a Technician (i.e., Mr. Tak Terada at 993-0204 or 993-6179) or your supervisor.

A.3 Data Acquisition System Operational Procedures for Thermal Fatigue Testing

1.0 DATA ACQUISITION SYSTEM START-UP PROCEDURES

(Can be done before burner rig start-up)

- 1.1 Turn on computer ⇒ will go to C directory
- 1.2 Type CD NRC [ENTER] ⇒ C:\NRC
- 1.3 Type NRC [ENTER] ⇒ Main Menu shows up
- 1.4 GOTO CONFIGURATION FILE LOAD/SAVE [ENTER]
- 1.5 GOTO LOAD CONFIGURATION FILE [ENTER]
- 1.6 Should be in SRY (default). If not type SRY [ENTER]
(here, Y is a capital letter that identifies the tested specimen)
- 1.7 [ESC]
- 1.8 GOTO SENSOR CONFIGURATION [ENTER]
- 1.9 Check to make sure that the values in the slope column correspond to values reported in Appendix C. If not, the next steps should be followed:
 - 1.9.1 GOTO CONFIGURATION FILE LOAD/SAVE [ENTER]
 - 1.9.2 GOTO First level i.e. LOAD CONFIGURATION FILE [ENTER]
 - 1.9.3 TYPE SRX [ENTER]
 - 1.9.4 GOTO Second Level i.e. SAVE CONFIGURATION FILE [ENTER]

1.9.5 Type SRY [ENTER]

1.9.6 GOTO First level i.e. LOAD CONFIGURATION

1.9.7 TYPE SRY [ENTER]

1.9.8 Check CONFIGURATION PARAMETERS.

1.9.9 GOTO CONFIGURATION FILE LOAD/SAVE [ENTER]

1.9.10 GOTO Second Level i.e. SAVE CONFIGURATION
FILE [ENTER]

1.10 GOTO CONFIGURATION PARAMETERS [ENTER] ⇒ Check values
for starting cycle and ending cycle.

* TEST LABEL: SRY0 for first 999 cycles;
SRY1 for 1000-1999 cycles;
SRY2 for 2000-2999 cycles.

TRIGGER CHANNEL: 7

LIMIT SENSOR REF: Fpress

STAGE I	60	1	0	NONE
STAGE II	330	1	0	NONE
STAGE III	90	1	0	NONE

1.11 GOTO DIAGNOSTIC TEST MENU [ENTER]

1.12 GOTO Second Level i.e. MODEL 222 A/D Unit [ENTER]

1.13 SELECT option #2 i.e. 8 input states ⇒ should see 0 in all columns.

1.14 PRESS keypad #1 and #3 to activate relays

1.15 PRESS Q to quit

1.16 PRESS option #4 to exit

1.17 [ESC]

1.18 GOTO CONFIGURATION FILE LOAD/SAVE [ENTER]

1.19 GOTO Second level i.e. SAVE... [ENTER]

1.20 [ENTER]

1.21 [ESC]

1.22 GOTO BEGIN SCANNING/SAVE/GRAPHICS [ENTER]

1.23 START TEST IN AUTOMATIC MODE

2.0 DATA ACQUISITION SYSTEM SHUTDOWN PROCEDURES

(Shutdown burner rig test only when MICRISTAR programme controller is in segment #4 ⇒ cooling period. PRESS [HOLD])

2.1 Press [ESC]

2.2 [ESC] ⇒ Main Menu

2.3 Quit Menu

3.0 STORAGE PROCEDURE OF TF DATA INTO NETWORK

3.1 GOTO NRC DIRECTORY ⇒ C:\NRC>

3.2 Type CD\ [ENTER]

3.3 Type NET [ENTER]

3.4 Type LOGIN NAME ⇒ GENDRON

3.5 Type PASSWORD ⇒ LUCIE User menu appears

3.6 [ESC]

3.7 Answer "YES" ⇒ Now, you should be in D:\>

3.8 Type C: [ENTER]

3.9 Type CD NRC [ENTER]

3.10 Type COPY SRY*.* b d: [ENTER] ⇒ Files transferring

3.11 After copying ⇒ type DEL SRY*.* [ENTER]

3.12 LOGOUT [ENTER]

APPENDIX B

DESCRIPTION OF THE CGMS CRACK GROWTH MONITOR

(After MATELECT LTD, [88])

The Crack Growth Monitor CGM5 is a multiple-frequency, A.C. potential drop system, designed for accurate measurement of crack growth utilising the skin effect. It contains a current source capable of delivering an alternating current of constant amplitude and frequency into the specimen. It has facilities for selecting the frequency and setting the constant amplitude of the current as required. The A.C. potential drop across the crack in the test specimen is amplified and then demodulated using an automatic phase detection system. The resultant D.C. output voltage is displayed digitally. For the purpose of recording, both analog and digital outputs are available. A number of facilities are provided for research applications. The system is contained in a precision-engineered, portable, instrument case. The CGM5 described here is a new version in which a module (called β) is added to the main instrument (called module α). The module α takes the amplified ACPD signal from channel A of the preamplifier. The module β processes the amplified ACPD signal from channel B of the preamplifier. As described in Subsection 1.2.2, the active probes attached to critical zones on the TF specimen (areas where cracks are expected i.e. LE, TE) are connected to channel A. The reference probes are connected to channel B. The module β that controls the gain and offset of channel B, also provides output signals representing the difference between processed ACPD signals from channels A and B (A-B), and the output signals representing (A-B)/B.

The next sub-sections will describe the two modules of the CGM5 instrument. Refer to Figures B.1 and B.2 at the end of this Appendix.

B.1 MODULE α **Front Panel Description:**

- 1) **PANEL METER**

4½ digit liquid crystal panel meter displays output voltage automatically changing range when the output exceeds 2 volts. The meter is also used to display the RMS value of the specimen current. A battery low indication is given at the top left hand corner of the display for battery powered instruments.
- 2) **CHARGE INDICATOR**

This LED is only on battery powered instruments and indicates the rate at which the batteries are charging. It operates only when the 220 V mains are connected to the instrument. When RED it indicates a high rate of charge (or instrument in main operation). When GREEN it indicates a low rate of charge, the batteries being float charged.
- 3) **POWER SWITCH**

Press ON/OFF

4) GAIN SELECTOR

The gain select switch sets the gain of the input signal amplifier in 10 dB steps from 50 to 90 dB.

$$50 \text{ dB} = \times 316.2$$

$$60 \text{ dB} = \times 1000$$

$$70 \text{ dB} = \times 3162$$

$$80 \text{ dB} = \times 10000$$

$$90 \text{ dB} = \times 31620$$

5) SIGNAL INPUT

The input is transformer decoupled to give high common mode rejection and low 'noise'. Care should be taken to ensure the source impedance is low. (PLUG TO FIT type LEMO FG2B302CN070).

6) FREQUENCY SELECTOR

The frequency of the alternating current can be selected from one of six preset values of 0.3, 1, 3, 10, 30 and 100 kHz.

7) CURRENT / LIMIT INDICATOR

The LED turns RED when panel meter is displaying the specimen current. If at any time the load resistance is too high for the set current the LED flashes RED. The LED turns GREEN when the amplified input signal exceeds the set value.

N.B. The LED will display combinations of RED and GREEN.

- 8) **CURRENT MONITOR SWITCH**
- It has three positions. In the UP (Set Current) position the panel meter reads the RMS value of the alternating current running through the specimen as set by the potentiometer (9). In the MIDDLE position the panel meter displays the value of the amplified voltage signal. In the LOW (Set Relay) position the panel meter displays the set value of the output signal at which a relay operates (to switch external equipment OFF or ON).
- 9) **SET RELAY ADJUSTMENT**
- The potentiometer, which can be adjusted using a screw driver, sets the value of the output signal voltage at which the relay mentioned above is required to operate.
- 10) **SET CURRENT ADJUSTMENT**
- The alternating current through the specimen is continuously variable up to 2 Amperes RMS by means of this 10 turn lockable potentiometer.
- 11) **OFFSET INDICATOR**
- LED lights when the offset is in use. LED flashes when signal gain is excessive i.e. there is clipping of the signal waveform. This is remedied by lowering the signal gain frequency.

- 12) **OFFSET SWITCH** This enables the initial signal output to be offset by up to 200 mV in the UP (Fine) position and up to 2 Volts in the LOW (Coarse) position. This makes it possible to use more gain (4) so that small variations in the initial signal can be recorded.
- 13) **OFFSET ADJUSTMENT** The offset voltage is continuously variable and is set by means of a 10 turn potentiometer.
- 14) **PHASE INDICATOR** The LED lights intermittently when the phase is not adjusted correctly. In the UP (Manual) position of switch (15) it will remain lit or ON steadily when correct phase adjustment has been made using the potentiometer (16). In the LOW (Automatic) position of switch (15) it will go out (or OFF) when the correct phase adjustment is attained after a certain time.
- 15) **PHASE SWITCH** In the UP (Manual) position the phase is adjusted manually by using the potentiometer (16). In the LOW (Automatic) position the phase is adjusted automatically.

16) PHASE ADJUSTMENT

This 10 turn lockable potentiometer adjusts the phase and is operational only in the UP (Manual) position of switch (15). It should be set to give the maximum value of the output signal on the panel meter.

17) FIXED OFFSET SWITCH

In the UP (500 mV) position of this switch it introduces a fixed offset of 500 mV to the output signal. In the LOW (50 mV) position it introduces a fixed offset of 50 mV. In the MIDDLE (Off) position the switch has no effect.

18) FILTER SWITCH

In the MAX. position of the switch a filter is used to reduce 'noise' to a minimum for use during slow strain rate tests. The MIN. position is used mainly for fatigue tests where a special filter allows the fatigue frequency to come through but blocks the higher frequencies and reduces 'noise'. In the OUT position the filter is taken out in order to enable dynamic tests at higher speeds to be monitored.

19) HOLD SWITCH

This can be used to 'Hold' or freeze the reading on the panel meter when required. When in 'Hold' state the reading flashes.

Back Panel Description:

20) CURRENT OUTPUT

3 pin lockable socket.

PIN CONFIGURATION

Pin 1 +ve Output

Pin 2 (-)

Pin 3 GND

21) I/O SIGNAL SOCKET

Optional facilities for comparison/division technique. In cases where very high stability and accuracy are required, it is possible to overcome the effect of temperature variations in the specimen by using a similar specimen placed near the specimen under test, as a reference. The reference specimen will be subject to the same ambient conditions, but not the same stress.

Pre-cracking of a specimen is often carried out by fatiguing it over a period of time. The CGM5 has facilities for a relay to stop the testing machine or initiate an alarm when the crack formed reaches a certain preset value. The contacts of the relay used for fatigue pre-cracking of the specimen are provided on this socket.

22) DIGITAL INTERFACE
RS-232

Provides a serial digital output from the panel meter which may be used to interface to a computer or digital data logging system.

23) RECORDER OUTPUT

3 pin lockable socket.

PIN CONFIGURATION

Pin 1 Output

Pin 2 GND

Pin 3 NC

24) GND 1

Common for circuit.

25) GND 2

Case of instrument.

26) MAINS SOCKET

200V AC, contains two fuses.

B.2 MODULE β Front Panel Description:

- 27) PANEL METER 4½ digit liquid crystal panel meter displays output offset B, B and (A-B)/B.
- 28) OUTPUT SWITCH 3 positions toggle switch.
Select the output offset B, B, and (A-B)/B to be displayed. The corresponding LED is lit to clearly show the position of this switch. Also if any of the outputs exceed approximately 3.8 volts, or if they are negative, the corresponding LED will flash RED.
- 29) GAIN SELECTOR The gain select switch sets the gain of the input signal of channel B in 10 dB steps from 50 to 90 dB.
- 50 dB = x 316.2
60 dB = x 1000
70 dB = x 3162
80 dB = x 10000
90 dB = x 31620

30) OFFSET ADJUSTMENT

The offset voltage of channel B is continuously variable and is set by means of a 10 turn potentiometer (range of ± 1 volt).

Back Panel Description:

31-33) R E C O R D E R
OUTPUTS

3 pin lockable sockets.

Pin 1 Output

Pin 2 GND

Pin 3 NC

The processed outputs of signals B, offset of B and $(A-B)/B$ are provided via these corresponding sockets.

34) PA INPUT SOCKET

The amplified ACPD signals from channel A and B of the preamplifier are supplied to the CGM5 with a 10 m cable connected to the PA INPUT SOCKET.

35) POLARITY SWITCH

This switch is provided to correct the phase of the B signal in cases where the two voltage probe wires from the specimen have been connected in opposition to those emerging from the preamplifier unit.

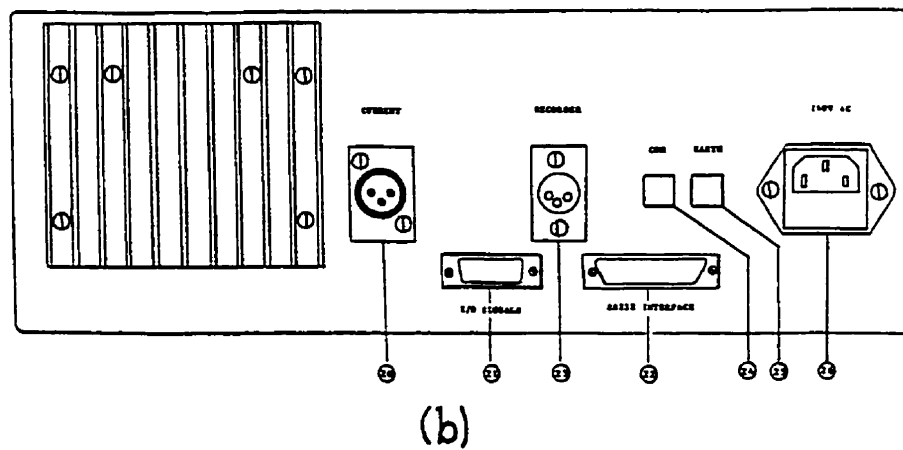
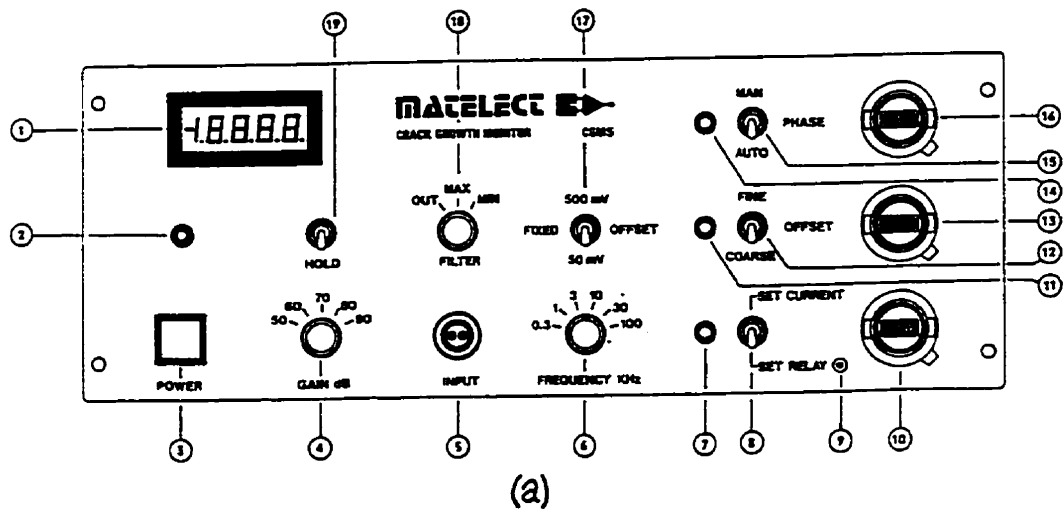
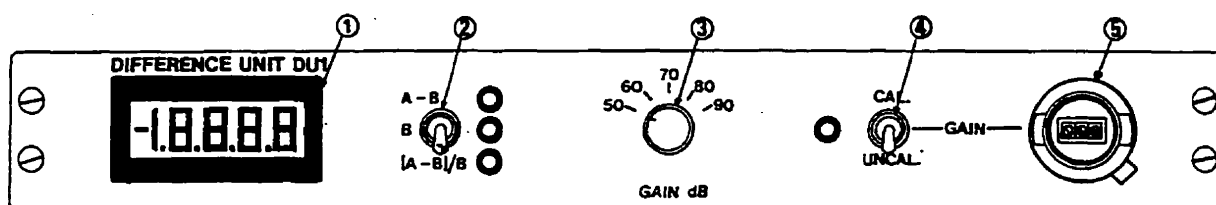
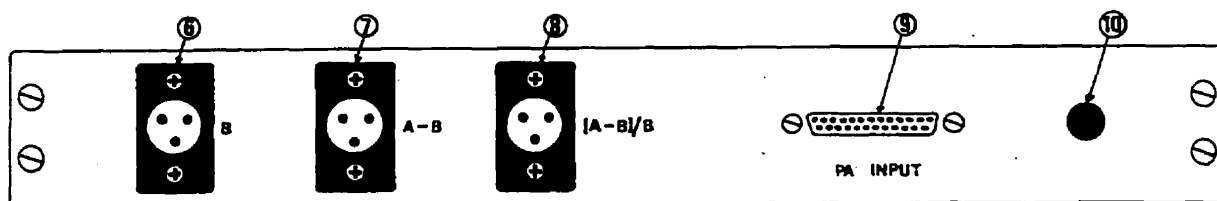


Figure B.1 Crack Growth Monitor CGM5 [88]: a) front panel; b) back panel.



(a)



(b)

Figure B.2 Difference Unit DUD1 [88]: a) front panel; b) back panel.

APPENDIX C

PROGRAMMING OF THE MICRISTAR

The Micristar unit has three (3) functions:

- (1) Control (automatically) the flame temperature during the duration of the tests;
- (2) control the carrier which soaks the specimen in and out the hot flame and the stream of cold air;
- (3) Synchronize the SI/data acquisition system with the cycling sequence of the carrier.

Steps 1.0 to 1.19 shows how to set the operating parameters of the Micristar which control the flame temperature during the thermal fatigue tests. The principal parameter that sets the gas temperature level as measured by a thermocouple of control (T/C) is called %OUTPUT and express the fuel flow capacity of the burner rig (in %) for a set-up. The relation between this parameter and the gas temperature is given in Figure C.1.

Steps 2.0 to 2.11 explains how to set the operating parameters programmed to control the thermal cycle and the Sciometric Instruments data acquisition and control units as described in detail in Figure C.2 and Table C.1.

The Micristar's controller and programmer operating parameters must be entered before the Micristar begins normal operations. These parameters can be entered through the primary panel lower display in **FULL ACCESS**. Use these steps to place the primary panel to **FULL ACCESS**:

- a. open operator panel (refer to Figures C.3 and C.4)
- b. press the RI LOGO (hidden key)
- c. press a hidden key located to the left of the upper display scroll key.

Before beginning this section, the user should already have a working knowledge of how to operate each of the programmer displays. A detailed description of each Programmer (PGMR) TABLES display may be found in the Micristar's User Manual, model 828D, [89].

1.0 **CONTROLLER OPERATING PARAMETERS FOR THERMAL FATIGUE TESTING**

- 1.1 Put the Micristar on **AUTOMATIC** mode. (If the unit is on **MANUAL**, press the **MANUAL/AUTO** key once.)
- 1.2 Select **DEV** deviation in the upper display. (Press the upper display scroll key until the deviation display appears for the appropriate channel.)
- 1.3 Put the Micristar in **FULL ACCESS**. (Open Contact Input 5 + Press RI Logo + Press Hidden key between the upper display and the upper display scroll keys.)
- 1.4 Press the controller Key to activate the **CONTROLLER** function to select the appropriate channel.
- 1.5 Access the **SETPOINT** display and set to value = 76.9
- 1.6 Access the **DEVIATION (DEV)** display and document value.
- 1.7 Access the **%OUTPUT** display and set to value = 10.0
- 1.8 Access the **DEV-HI** alarm trigger and set to value = 100

- 1.9 Access the **DEV-LO** alarm trigger and set to value = 100
- 1.10 Access the **PV-HI** alarm trigger and set to value = 100
- 1.11 Access the **PV-LO** alarm trigger and set to value = -2.5
- 1.12 Press the lower display scroll key until the **GAIN** display is selected.
- 1.13 Press the **ENTER** key and press the **FAST INC** key to select a value = 0.1
- 1.14 Press the lower display scroll key until the **RESET** display is selected.
- 1.15 Press the **ENTER** key and press the **FAST INC** key to select a value = r 5.00
- 1.16 Press the lower display scroll key until **RATE** display is selected.
- 1.17 Press the **ENTER** key and press the **FAST INC** key to select a value = r 0.00
- 1.18 Close operator panel.
- 1.19 Activate the Micristar PV-HI alarm for automatic shutdown:
 - a. Select Full Access.
 - b. Select Configuration Access (Press RI Logo + Press the **HIDDEN** key below the controller key.)
 - c. Set CF-42 to 2 and close the operator panel.

2.0 **PROGRAMMER OPERATING PARAMETERS FOR THERMAL FATIGUE TESTING**

- 2.1 Put the Micristar in **FULL ACCESS**. (Open Contact Input 5 + Press RI Logo + Press Hidden key between the upper display Led and the upper display scroll).
- 2.2 Put the programmer on **HOLD** mode. (If the RUN LED is lit, press HOLD key once.)
- 2.3 Press the **MANUAL/AUTO** key to put the controller on Manual mode. (Led lights to indicate **MANUAL** operation.)
- 2.4 Press **PROGRAMMER** (PGMR) **TABLES** key to select Programmer Tables function.
- 2.5 Use the **Scroll** key to select the display type. (Scroll down to **SEGMENT**.)
- 2.6 Press the **ENTER** key to enable the INC/DEC and the FAST INC/DEC keys as

applicable.

- 2.7 Use **INC/DEC** and **FAST INC/DEC** keys to change displayed values as applicable. Access **SEGMENT No. 1** and enter parameters as per the attached BRT Process Profile Chart (see Table C.1).

NOTE: The Micristar's **ADVANCE** key can save time and effort when entering parameters. For the Programmer Tables, use the **ADVANCE** key to increment the currently-addressed segment by 1 as follows:

- a. scroll to the **SEGMENT** display
- b. press **ADVANCE** key
- c. press **ENTER** key

- 2.8 Check all entered values.

- 2.9 Press **RUN** key to prepare the controller on RUN mode (RUN Led light should blink.)

- 2.10 Use **INC/DEC** key to select proper SEGMENT (select SEGMENT No.1.)

- 2.11 Close operator panel.

NOTE: The controller is now ready for transfer from **MANUAL** to **AUTOMATIC FUEL CONTROL** operation (starting with SEGMENT No.1.)

Table C.1 Micristar programmer table process profile chart for thermal fatigue testing
(refer to Figure C.2)

SEGMENT	1	2	3	4	5
SETPOINT Channel 1	99.8	99.8	99.8	99.8	10.0
SETPOINT Channel 2					
SPECIMEN EVENT #1 1 = OUT	1	1	--	1	1
EVENT #2					
FLAME EVENT #3 3 = OFF	--	--	--	--	3
TRIGGER EVENT #4 4 = Hi	--	--	4	--	--
EVENT #5					
EVENT #6					
EVENT #7					
EVENT #8					
SEG TIME	0':10"	5':00"	2':30"	1':33"	0'.05"
RECYCLES				N	
NEXT SEG	2	3	4	3	5

N.B.: $N + 1$ = total number of thermal cycles desired.

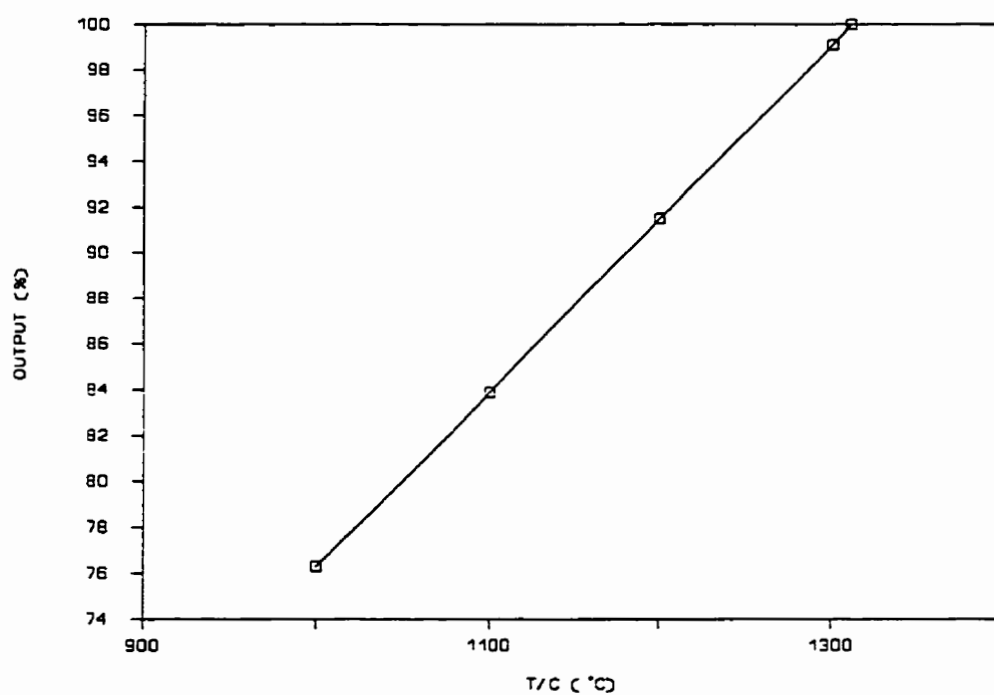


Figure C.1 Percentage of the set fuel flow capacity of the burner rig (% OUTPUT) as a function of the temperature (T/C) of the gas stream at the exit of the nozzle.

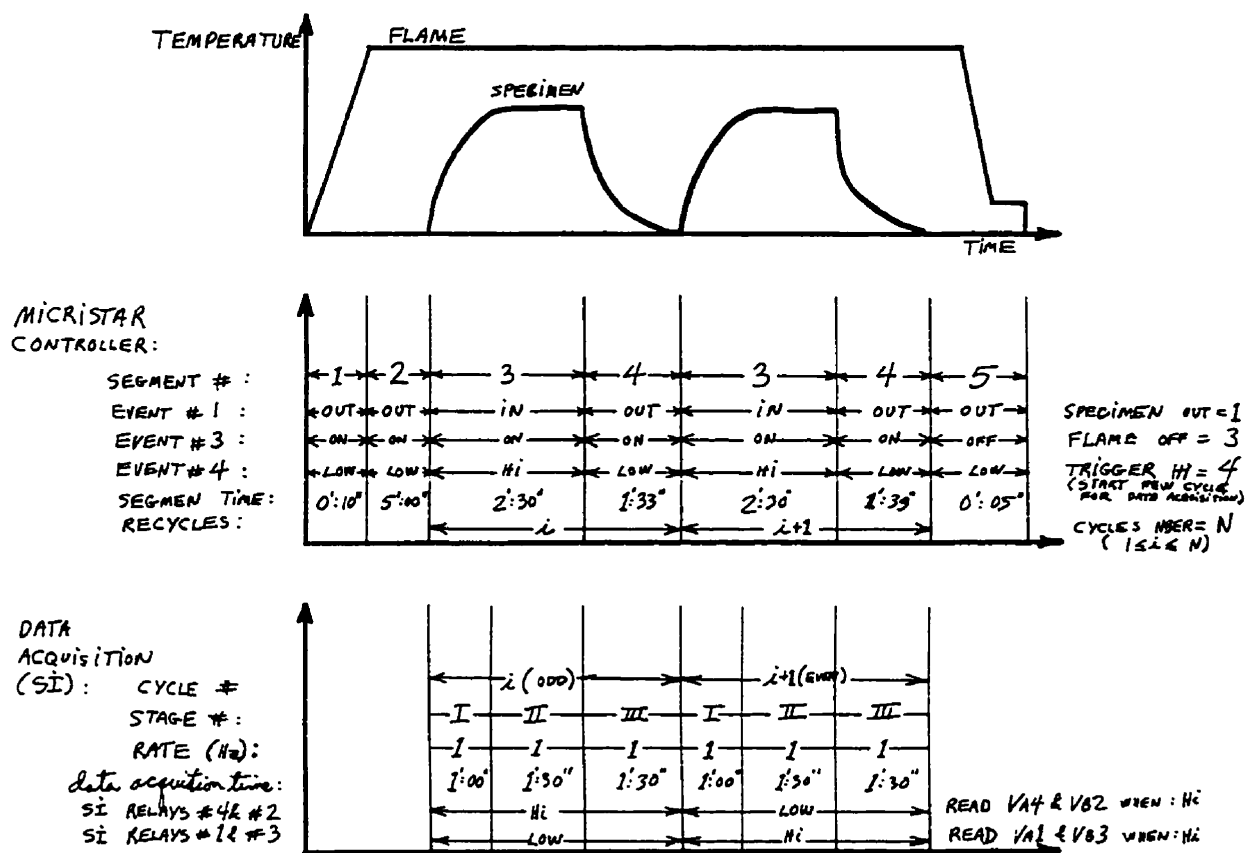


Figure C.2 Evolution of the parameters of the Micristar controller and the SI data acquisition system programmed to insure full automation of the test.

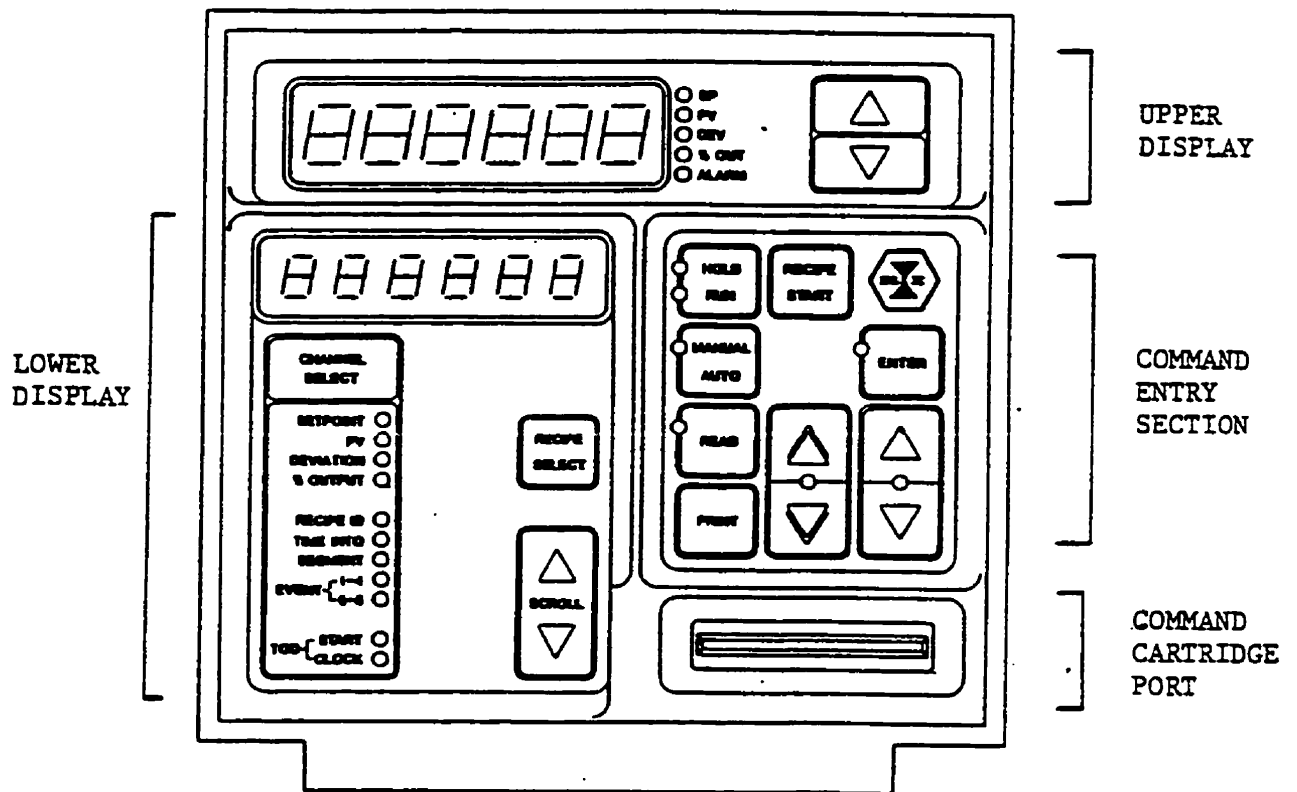


Figure C.3 Operator panel of the MICRISTAR controller unit.

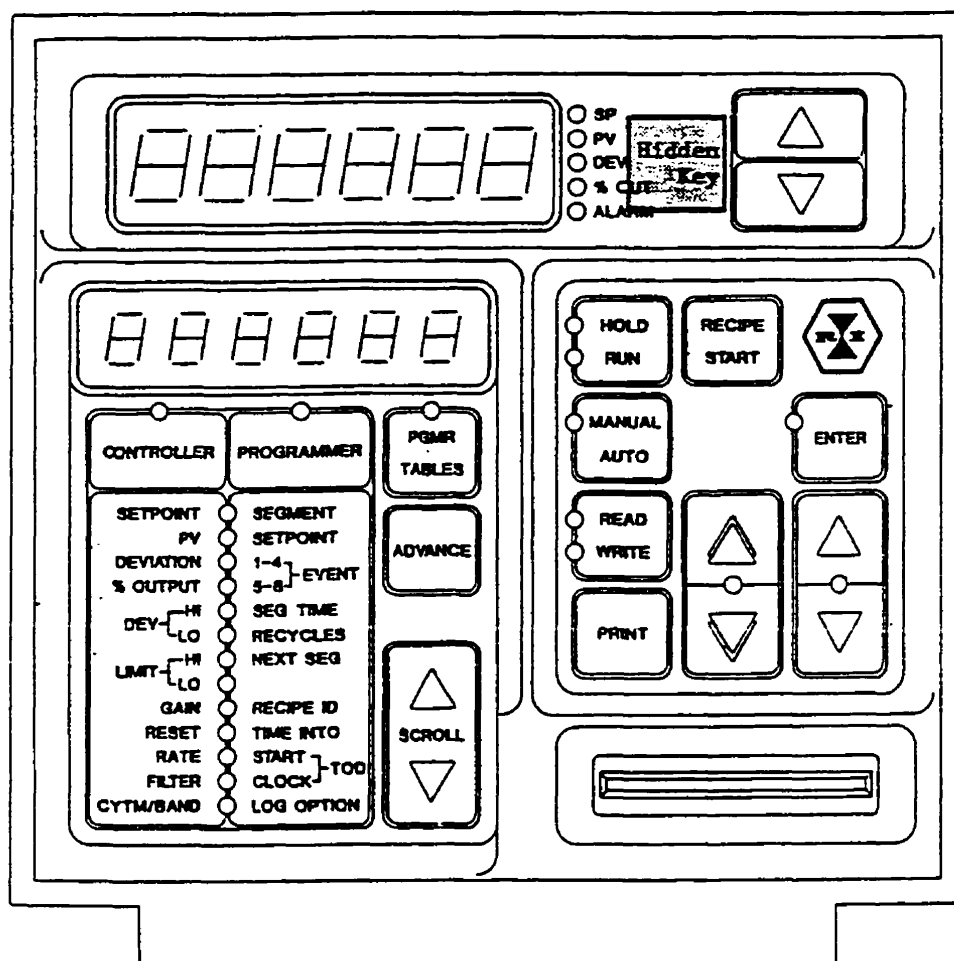


Figure C.4 Primary panel of the MICRISTAR controller unit.

APPENDIX D

AUTONICKEL PLATING PROCEDURE

During the preparation of the metallography of sections of the specimens tested in the burner rig, an electroless nickel plating process is practiced in order to protect the friable oxide scales during the mechanical polishing of the sections. The procedure and chemical composition of the bath recommended by Edgemet® are given as following:

1. wash the sections to be coated in an ultrasonic bath of tetrachloroethylene (or acetone) during 5 minutes;
2. apply by plasma a thin gold film as in sample preparation for scanning electron microscopy (SEM);
3. mix equal parts (200 mL each) of solutions "A" and "B" in a 500 mL beaker and heat the bath to operating temperature of 80-85°C with a heating plate (IMPORTANT NOTE: the solution should never be allowed to boil);
4. during the time that the solution temperature reaches the desired level, wash the sections with the "Pre-Clean" solution during 5-30 sec. and rinse them with warm water;
5. put the sections in the bath and cover the beaker with watch glass when the bath is at temperature (N.B.: make sure that the bath temperature do not exceeds 90°C during the plating process);
6. remove the sections from the bath after 5-7 hours (a 20 µm thick nickel coating should be obtained);
7. rinse the sections with hot water and carefully dry under a hot air stream.

The composition of the pre-clean solution and of the solutions "A" and "B" used for the electroless nickel plating is given in the next page.

Pre-Clean Solution

Hydrochloric Acid	10 mL/L
Stannous Chloride	2 g/L
Distilled Water	Balance

Solution "A"

Nickel Chloride	45 g/L
Sodium Acetate	50 g/L
Sodium Citrate	100 g/L
Distilled Water	Balance

Solution "B"

Sodium Hypophosphite	26.4 g/L
Distilled Water	Balance

APPENDIX E

PLOTTING OF THE POTENTIAL DROP VS NUMBER OF CYCLES FROM MEASURED PD DURING THERMAL FATIGUE TESTS

As discussed in Subsection 4.2.1, the average value of the PD measured during the steady state portion of each thermal cycle is the most convenient value for following the evolution of the PD during fatigue tests. This Appendix explains how this average value of the potential drop (V) is plotted against the number of cycle (N) to obtain the V-N graphs corresponding to each thermal fatigue test.

For each cycle carried out during TF testing, the data acquisition system stores on files the test name, the cycle number and the evolution of dynamic variables as the PD in the specimen and the hot gas stream temperature. The general name of these data file is "SRYx-xxx.PRN" where SRY is the test name (Y is the specimen code) and x-xxx is the cycle number. More details on the data acquisition system are given in Subsection 3.1.2.2.

To perform the calculation of the average value of the PD, a program named AVGSTD-V.BAS was written in Basic and is listed at the end of this Appendix.

The program contains three parts. The first one (lines 80 to 120) gives to the user the opportunity to enter the name of the test (i.e. SRY), the type of cycle performed (long or short). A short cycle implies that the average value of the PD will be performed in the time range of 95.5 - 126.8 seconds whereas for a long cycle, the average value is determined for the time range of 246.8 - 351.2 seconds.

The second part of the program (lines 140 to 230) defines the dimension of some array variables, opens the SRY-EVEN.N and SRY-ODD.N files in which average values will be stored separately for even and odd cycle numbers. This process is required since the PD from the probes at the leading edge (VA1) and its reference probes (VB3) are registered during even cycles. In the meantime, the PD from the probes at the trailing edge (VA4) and its reference probes (VB2) are registered during odd cycles.

The third part of the program (lines 250 to 340), the user can choose a specific range of cycle data file. Each file is called and relevant data are read. This is executed in the first subroutine (1000-1230) of this part, which includes an error subroutine that handles bugs associated with bad file names or wrong data in files. A second subroutine (2000-2120) computes the average value of the potential drop, VA and VB and the average gas stream temperature T, for each cycle data file. The third subroutine (3000-3120) is then called to calculate the standard deviation for these parameters (VA, VB and T). The average and standard deviation of these parameters are finally stored with their corresponding cycle number in output data files SRY-EVEN.N or SRY-ODD.N, during the execution of the 4th subroutine (4000-4050).

Following the treatment of all data files, the user is asked if other data files of the same test name will be treated.

Files SRY-EVEN.N and SRY-ODD.N can then be imported to graphic software such as SYMPHONY, LOTUS or AXUM to generate V-N graphs. At this stage, it is easy to plot the PD at the leading edge or at the trailing edge or both PD versus the cycle number N.

Listing of the AVGSTD-V.BAS Program

```

10 ***** PROGRAM AVGSTD-V.BAS *****
20 *****
30 *** COMPUTE THE AVERAGE VALUE AND THE STANDARD DEVIATION ***
40 *** OF THE PD IN DEW SPECIMEN DURING THE THERMAL FATIGUE TESTINGS ***
50 *****
60 ***** FOR S. GENDRON TF PROGRAM JHP00 *****
70 '
80 'ENTER THE TEST NAME AND THE TYPE OF CYCLE
90 CLS
100 INPUT "ENTER THE TEST NAME (3 CAPITAL LETTERS) AND PRESS ENTER: ", TESTS
110 INPUT "SHORT CYCLE (S) OR LONG CYCLE (L) "; DUREES
120 IF DUREES = "S" THEN K = 126: M = 31 ELSE K = 271: M = 101
130 '
140 'DEFINE DIMENSION OF ARRAY VARIABLES
150 'AND OPEN OUTPUT DATAFILES
160 DIM DATUM$(K)
170 DIM TIME(M)
180 DIM VA(M)
190 DIM VB(M)
200 DIM T(M)
210 OPEN "O", #1, TESTS + "-EVEN.N"
220 OPEN "O", #2, TESTS + "-ODD.N"
230 SUFS = ".PRN"
240 '
250 'CALL EACH CYCLE FILE AS REQUESTED, AND TREAT ITS CORRESPONDING DATA:
260 INPUT "ENTER THE INITIAL CYCLE NUMBER, AND PRESS ENTER: ", NI%
270 INPUT "ENTER THE LAST CYCLE NUMBER, AND PRESS ENTER: ", NF%
280 CLS
290 FOR N% = NI% TO NF%
300 GOSUB 1000 'CALL AND READ THE DATA FILES
310 GOSUB 2000 'COMPUTE THE AVERAGE VALUES (AVG) OF VA, VB AND T
320 GOSUB 3000 'COMPUTE THE STANDARD DEVIATION (STD) OF VA, VB AND T
330 GOSUB 4000 'STORE THE AVG AND THE STD OF VA, VB AND T
340 NEXT N%
350 '
360 INPUT "HAVE YOU FINISHED TO TREAT DATA (Y OR N) "; RESPS
370 IF RESPS = "Y" GOTO 380 ELSE GOTO 260
380 CLOSE #1, #2
390 END
400 '
410 '
1000 'SUBROUTINE 1000; CALL AND READ THE DATA FILE
1010 ' COMPOSE THE NAME OF THE DATA FILE
1020 JJ! = (N%+.1)/10000 + 1!
1030 THOUSANDS$ = MID$(STR$(JJ!),4,1)
1040 UNITS$ = MID$(STR$(JJ!),5,3)
1050 FILENAME$ = TESTS + THOUSANDS$ + "-" + UNITS$ + SUFS
1060 ' OPEN AND READ THE DATA FILE
1070 ON ERROR GOTO 1190
1080 OPEN "I", #3, FILENAME$
1090 FOR II% = 1 TO K
1100 INPUT#3, DATUM$(II%)
1110 NEXT II%
1120 IF VAL(DATUM$(6)) <> VAL(UNITS$) GOTO 1190
1130 FOR J = 1 TO M
1140 INPUT#3, TIME(J), VA(J), VB(J), T(J)
1150 NEXT J
1160 RETURN 310
1170 '
1180 'FILE NOT FOUND OR FILE READING ERRORS SUBROUTINE
1190 VA=-1!: VB=-1!: T=0!: STDVA=0!: STDVB=0!: STDT=0!
1200 IF (ERR=53) THEN PRINT FILENAME$; " DOES NOT EXIST!": RESUME 1230
1210 IF (ERR=62) THEN RESUME 1220
1220 PRINT FILENAME$; " IS WRONG!"
1230 RETURN 330
1240 '
1250 '

```

```

2000 'SUBROUTINE 2000; COMPUTE THE AVERAGE VALUE OF VA, VB, AND T
2010     SUMVA = 0!
2020     SUMVB = 0!
2030     SUMT = 0!
2040     FOR J = 1 TO M
2050         SUMVA = VA(J) + SUMVA
2060         SUMVB = VB(J) + SUMVB
2070         SUMT = T(J) + SUMT
2080     NEXT J
2090     VA = SUMVA/M
2100     VB = SUMVB/M
2110     T = SUMT/M
2120 RETURN 320
2130 '
2140 '
3000 'SUBROUTINE 3000; COMPUTE THE STANDARD DEVIATION OF VA, VB, AND T
3010     SUMSTDVA = 0!
3020     SUMSTDVB = 0!
3030     SUMSTDT = 0!
3040     FOR J = 1 TO M
3050         SUMSTDVA = ABS(VA(J)-VA) + SUMSTDVA
3060         SUMSTDVB = ABS(VB(J)-VB) + SUMSTDVB
3070         SUMSTDT = ABS(T(J)-T) + SUMSTDT
3080     NEXT J
3090     STDVA = SUMSTDVA/M
3100     STDVB = SUMSTDVB/M
3110     STDT = SUMSTDT/M
3120 RETURN 330
3130 '
3140 '
4000 'SUBROUTINE 4000; STORE THE AVG AND THE STD OF VA, VB AND T
4010     NB = N%/2 -INT(N%/2)
4020     IF NB < .1 THEN PRINT #1, N%, VA, STDVA, VB, STDVB, T, STDT
4030     IF NB > .1 THEN PRINT #2, N%, VA, STDVA, VB, STDVB, T, STDT
4040     CLOSE #3
4050 RETURN 340

```

APPENDIX F

DETERMINATION OF THE RADIATION HEAT TRANSFER PARAMETERS

The radiation heat transfer from the specimen to the surroundings (the burner rig room) was covered in Subsection 5.1.2.1. Roughly, it was mentioned that the radiative heat flux is expressed by:

$$q_r = \epsilon \sigma \sum_j F_{s-j} [T_s^4 - T_j^4]$$

where:

ϵ is the emissivity of the specimen;

σ is the Stefan-Boltzmann constant which has the value $5.669\text{E-}8 \text{ W/m}^2\cdot\text{K}^4$;

$F_{s,j}$ is the radiation shape factor or fraction of the energy radiated from the specimen surface to the element "j" of the surroundings;

T_s is the surface temperature of the specimen (in K);

and T_j is the temperature of the element "j" of the surroundings.

The radiation shape factors, $F_{s,j}$ in this Equation, more precisely represent the fraction of the energy radiated by the specimen to its surrounding elements and T_j is the temperature of the elements, with $j = w$ for the room walls, $j = n$ for the burner rig nozzle and $j = c$ for the hot core of the combustor. While the temperature of the room is easy to get and can be neglected in the Equation, the estimation of the values of the other parameters is an important and more difficult task.

This Appendix explains how the radiation shape factors, the temperature of the nozzle and of the internal core of the combustion chamber was determined.

F.1 Radiation Shape Factors

At the Leading Edge:

At the leading edge, the surface emits radiations to the room walls, to the nozzle and to the internal core of the combustion chamber of the gas burner. In the determination of the fractions of the heat radiated from the leading edge to the room wall, to the nozzle and to the combustor, defined by their respective shape factors F_{s-w} , F_{s-n} and F_{s-c} , let's assume that the leading edge is a disk of 1 mm radius, the nozzle is a disk with an internal and external diameter of 50 mm and 108 mm, respectively, and the internal core of the combustor is a 50 mm diameter disk, as shown in Figure F.1. Moreover, all these pseudo-disks are assumed parallel and concentric, and the leading edge disk distanced from the others by 85 mm, as in the burner rig set-up described in Subsection 3.1.2.1. In Figure F.2, the radiation shape factor F_{1-2} for radiation between two parallel concentric disks of radius r_1 and r_2 and distanced by a length L is given by the chart. Hence, if the leading edge is 1 and the internal core is 2, $r_1 = 1$ mm, $r_2 = 25$ mm and $L = 85$ mm, then the factor $F_{s-c} = F_{1-2} = 0.065$. As the core and the nozzle represent a disk of radius $r_2 = 54$ mm, the factor associated with the radiation of the leading edge to these two elements together is $F_{s-(c,n)} = F_{s-c} + F_{s-n} = F_{1-2} = 0.259$. Thus, the factor for the radiation of the leading edge to the nozzle is given by $F_{s-n} = 0.259 - 0.065 = 0.194$. As the sum of the fraction of the energy radiated from the leading edge to the elements of its environment is equal to 1, the factor for radiation between the leading edge and the walls of the room is given by $F_{s-w} = 1 - (F_{s-c} + F_{s-n}) = 1 - 0.259 = 0.741$. In summary: $F_{s-c} = 0.065$, $F_{s-n} = 0.194$ and $F_{s-w} = 0.741$.

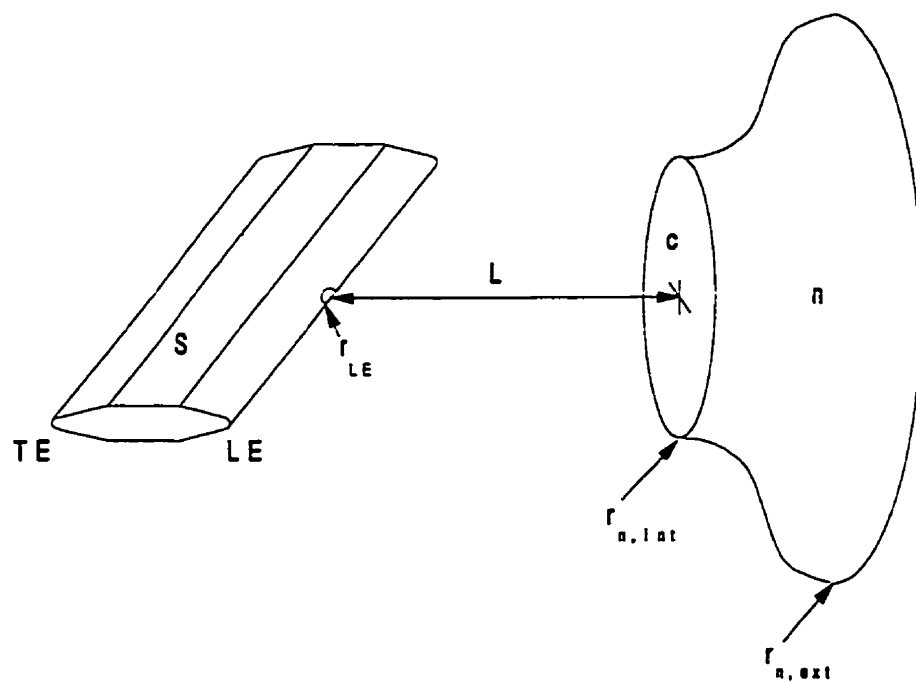


Figure F.1 Configuration of the DEW specimen (s), the nozzle (n) and the internal core (c) of the combustor in the burner rig.

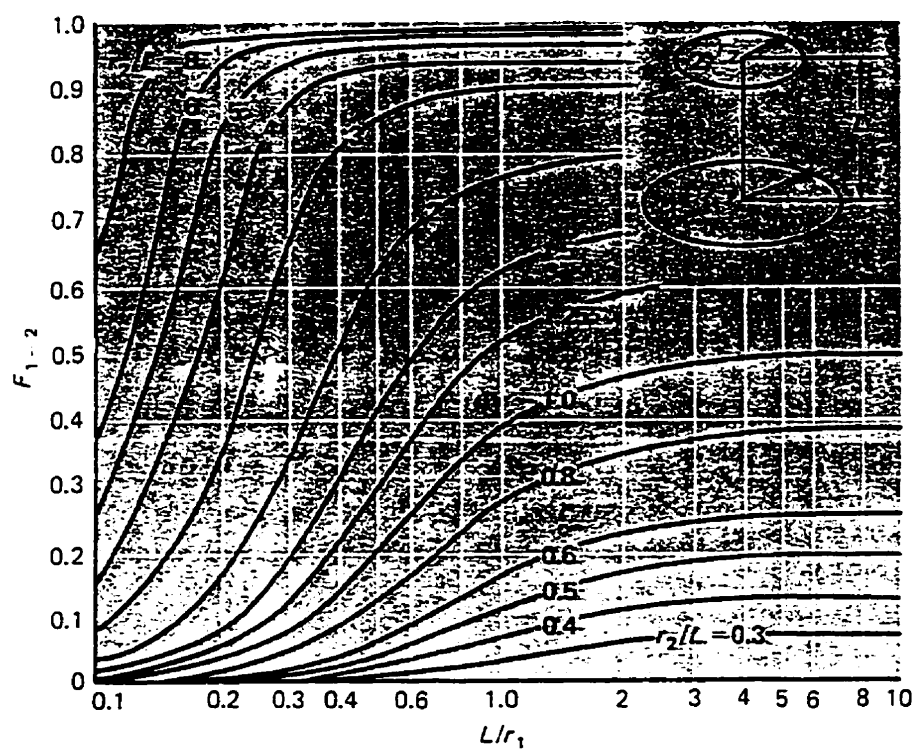


Figure F.2 Chart giving the radiation shape factor for radiation between two parallel concentric disks [69].

In the previous analysis, the surfaces of the nozzle and the leading edge were assumed flat and parallel which is obviously not the case. Figure F.3 shows the incident radiation from the leading edge to the nozzle. The angles ϕ , θ define the deviation of surfaces' normal (leading edge and nozzle) to the radiation directions. The shape factor is then given by [69]:

$$F(\phi, \theta) = F_o \cos \phi \cos \theta$$

$$\phi = 60^\circ \text{ at the nozzle}$$

where F_o is the shape factor for two parallel surfaces, as supposed earlier. For the infinitesimal elements at the tip of the leading edge, θ varies from 0° to 75° where θ_i is also the angular position of the element i . The mean angle ϕ for the nozzle is around 60° while ϕ for the combustor is 0° so the new shape factors are:

$$F_{s-n, i} = F_{s-n, o} \cos 60^\circ \cos \theta_i = 0.194 \cos \theta_i$$

$$F_{s-c, i} = F_{s-c, o} \cos 0^\circ \cos \theta_i = 0.065 \cos \theta_i$$

$$F_{s-w, i} = 1 - F_{s-n, i} - F_{s-c, i}$$

Now, if we consider all the elements of the leading edge where θ_i varies from -75° to 75° , the corresponding shape factors can be defined as:

$$F_{s-n} = 0.194 \frac{\int_{-75^\circ}^{75^\circ} \cos \theta \, d\theta}{\int_{-75^\circ}^{75^\circ} d\theta} = 0.072$$

$$F_{s-c} = 0.065 \frac{\int_{-75^\circ}^{75^\circ} \cos \theta \, d\theta}{\int_{-75^\circ}^{75^\circ} d\theta} = 0.048$$

$$F_{s-w} = 1 - 0.072 - 0.048 = 0.88$$

Elsewhere on the specimen:

Elsewhere on the specimen (refer to Figure F.3), as these surfaces do not "see" directly the nozzle and the core of the combustor, they only irradiate the walls of the room and shape factors can take the following values:

$$F_{s-w} = 1.0$$

$$F_{s-n} = 0.0$$

$$F_{s-c} = 0.0$$

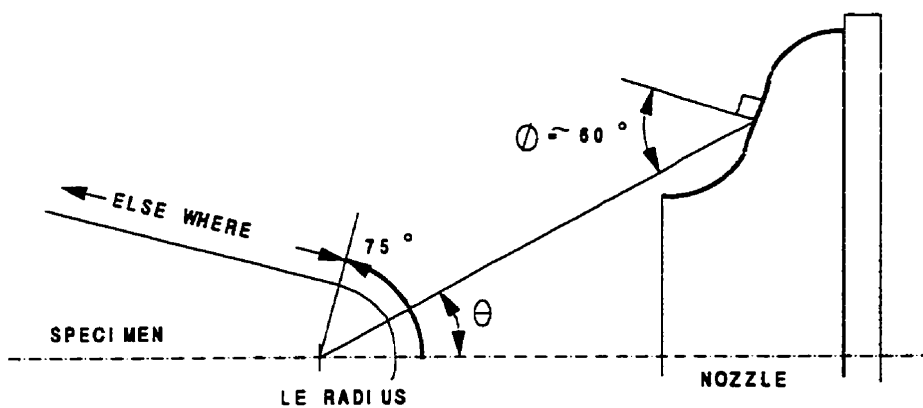


Figure F.3 Sketch showing elements of the specimen and the nozzle used in deriving radiation shape factor which consider the curvature and the non-parallelism of the surfaces.

F.2 Nozzle and Combustor Temperatures

The nozzle temperature was measured with the optical pyrometer IRCON that was also used for specimen temperature measurements during the thermal fatigue tests. Since the nozzle material is an oxidized nickel-base alloy, the emissivity of the IRCON was set at 0.85 as for the tested DEW specimens made of René 80. The temperature of the nozzle was also computed based on a heat balance on the nozzle wall that is heated by convection from the hot gas stream and cooled at its internal surface by radiation. Experimental measurements and computed values are in good agreement and differ by only 1%.

Since the inside wall of the combustor is insulated from the surroundings, the temperature of the internal core of the combustor (T_c) was assumed equal to the hot gas stream temperature (T_g). Gas temperature was obtained by measurements from the thermocouple of control positioned 1 cm downstream of the nozzle flange. The measured values (T/C) were corrected to take into consideration the radiation heat losses from the thermocouple bead (heat transfer effects described in Appendix G), by using the program TFC-P.BAS presented in Appendix H.

Table F.1 gives the values of the nozzle and the combustion core as a function of measured gas temperature (T/C) ranging from 800 to 1300°C.

Table F.1 Combustor (T_c) and nozzle (T_n) temperatures for different measured gas temperatures (T/C)

T/C (°C)	T_c (°C)	T_n (°C)	T_n (°C)	T_n (°C)
1300	1323	1600	735	1008
1200	1225	1498	705	978
1100	1119	1392	658	931
1000	1014	1287	616	889
900	910	1183	573	846
800	806	1079	529	802

APPENDIX G**EVALUATION OF THE EFFECT OF CONDUCTION AND RADIATION
HEAT LOSSES FROM JUNCTION OF A THERMOCOUPLE
ON GAS TEMPERATURE MEASUREMENT**

G.1 Effect of Conduction

As mentioned in Subsection 3.1.2.1, a vertical thermocouple is used to measure and control the hot gas stream temperature. In this situation, the thermocouple is exposed to a temperature gradient along its longitudinal axis. It was measured that the end of alumina sleeve of the thermocouple was around 100°C under the hot junction. The wires of the junction are exposed to heat loss by conduction and then the junction will be at lower temperature than the hot gas stream.

To compute this effect, a heat balance can be done on each cylindrical element of the wire of length dx , from the alumina sleeve to the end of the junction, assuming that the wires of the loop junction are straight (refer to Figure G.1).

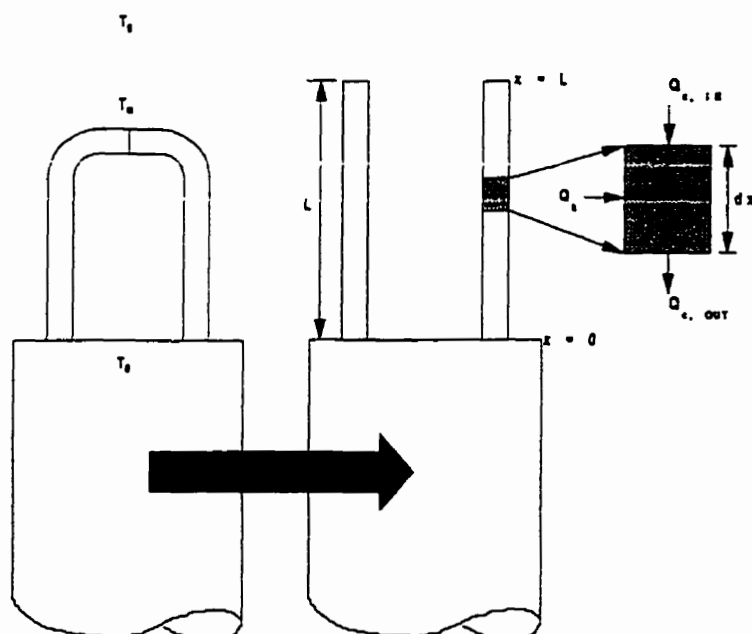


Figure G.1 Heat balance on wires of the hot junction of the controlling thermocouple in the hot gas stream.

Considering the conduction heat transfer within one element dx of the wire of length L , and the convection heat transfer at its surface exposed to the gas, the heat balance can be written as:

$$Q_{c \text{ IN}} - Q_{c \text{ OUT}} + Q_h = 0$$

where:

$$Q_{c \text{ IN}} = -kA \left. \frac{dT}{dx} \right|_x$$

$$Q_{c \text{ OUT}} = -kA \left. \frac{dT}{dx} \right|_{x+dx} = -kA \left(\frac{dT}{dx} + \frac{d^2T}{dx^2} dx \right)$$

$$Q_h = hP(T - T_g) dx$$

and

k	=	thermal conductivity of the wire
A	=	area of the section of the wire
P	=	perimeter of the wire
T	=	temperature of the wire at position x
h	=	mean heat-transfer coefficient
$Q_{c \text{ IN}}$	=	energy IN by conduction
$Q_{c \text{ OUT}}$	=	energy OUT by conduction
Q_h	=	energy transferred from the hot gas stream to the wire by convection
T_g	=	temperature of the hot gas stream

The combination of the three terms of the heat-balance Equation gives:

$$\frac{d^2 T}{dx^2} + \frac{hP}{kA} (T - T_g) = 0$$

Using the variable $\Theta = T - T_g$, and $m^2 = hP/kA$, the differential equation can be written as following:

$$\frac{d^2 \Theta}{dx^2} + m^2 \Theta = 0$$

The boundary conditions are:

$$1^\circ \quad \Theta = \Theta_0 = T_0 - T_g, \text{ at } x = 0$$

$$2^\circ \quad \frac{d\Theta}{dx} = \frac{d\Theta}{dx} = 0, \text{ at } x = L \quad (\text{due to the symmetry})$$

The final solution to this problem is:

$$\frac{\Theta}{\Theta_0} = \frac{e^{m(L-x)} + e^{m(x-L)}}{e^{-mL} + e^{mL}}$$

or

$$\frac{\Theta}{\Theta_0} = \frac{\cosh(m(L-x))}{\cosh(mL)}$$

The temperature T_m at the junction corresponds to the measured value given by the thermocouple. So, Θ as to be evaluated at $x = L$:

$$\frac{\Theta_m}{\Theta_0} = \frac{2}{e^{-mL} + e^{mL}} = \frac{1}{\cosh(mL)}$$

$$\text{Where:} \quad \Theta_m = T_m - T_g$$

$$\Theta_0 = T_0 - T_g$$

This function is plotted in graph of Figure G.2 for typical values of "m" which require that the convective heat transfer coefficient, h, for a wire in a gas stream

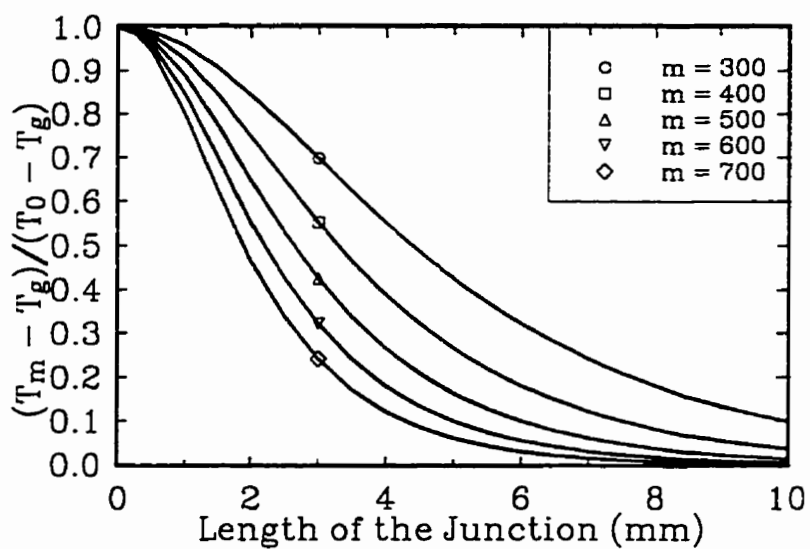


Figure G.2 Effect of conduction heat loss due to the colder thermocouple sleeve (at T_0) on the thermocouple measurement (T_m) of the hot gas stream temperature (T_g), as a function of the length of the junction directly exposed to the hot gas stream.

must be calculated. This can be achieved with the following empirical relation [69]:

$$\frac{hd}{k_f} = 0.683 \left(\frac{\bar{V}d}{\nu_f} \right)^{0.466} Pr^{1/3}$$

where:

d = diameter of the wire = 5×10^{-4} m

Pr = Prandtl number = 0.705

ν_f = kinematic viscosity of the gas estimated at the film temperature T_f

k_f = thermal conductivity of the gas estimated at the film temperature T_f

T_f = temperature of the film of the gas formed at the surface of the thermocouple = $(T_m + T_g)/2$

T_m = temperature of the junction of the thermocouple

T_g = temperature of the gas or the hot gas stream

\bar{V} = mean velocity of the gas

The way to determine the mean velocity of the gas is given in Subsection 5.1.2.3.1 and the gas properties can be found in [69]. For a gas temperature set at 1300°C and a gas velocity of 340 m/s, h is of the order of 2500 W/m²/°C and m has a value of 500. In this case, the length of each segment of the loop junction of the thermocouple has to be superior to 7.5 mm in order to get a difference between the junction and the gas temperatures of less than 5°C, according to the graph in Figure G.2. In the design of the thermocouples junction used for gas measurements in the present project, the length of the segments was of 8 mm and over.

G.2 Effect of radiation

From the first part of this Appendix, it was found that in the case of a thermocouple with looped junction, the conduction effect on the hot gas stream temperature measurement is at least equal to the incertitude of the reading, estimated to $\pm 5^\circ\text{C}$. Next factor to consider is the heat lost by the radiation of the platinum junction to the surrounding. Lets consider the case where the hot gas stream temperature is set to 1300°C as measured by the thermocouple of control (T/C). The heat balance on the junction, neglecting the heat transfer by conduction is:

$$Q_{convection} = Q_{radiation}$$

$$P dx h (T_g - T_m) = P dx \epsilon \sigma (T_m^4 - T_\infty^4)$$

Where:

- P = perimeter of the platinum wire
- dx = length of the junction considered
- h = mean heat-transfer coefficient equals to $2515 \text{ W/m}^2\cdot^\circ\text{C}$ (see the details of computation in the last Subsection)
- ϵ = emissivity of the platinum, equals to 0.17 for the range of temperature considered [69]
- σ = Stefan-Boltzmann constant which the value is $5.669 \times 10^{-8} \text{ W/m}^2\cdot\text{K}^4$
- T_g = temperature of the hot gas stream in K
- T_m = temperature measured by the junction of T/C in K, equals to 1577 K
- T_∞ = temperature of the surrounding, about 293 K

The difference between the hot gas stream temperature and the thermocouple reading can

be expressed, as following:

$$T_g - T_m = \frac{\epsilon \sigma}{h} (T_m^4 - T_{\infty}^4) \approx \frac{\epsilon \sigma}{h} T_m^4$$

The difference is a function of the fourth power of the junction temperature. In the present case, for a thermocouple reading of 1300°C, the hot gas stream temperature is 1323°C. The controlling thermocouple underestimates the hot gas stream temperature of 23°C that is more than five times the error due to the conduction effect.

Lets now determine the incertitude on the knowledge of the gas temperature. First, the incertitude of the thermocouple reading associated with the thermocouple physical imperfection, the data aquisition system and the conduction heat losses in the sleeve is $\pm 10^\circ\text{C}$. This incertitude also induces an incertitude of less than $\pm 1^\circ\text{C}$ on the computation of $T_g - T_m$. The incertitude on the value of h is $\pm 15\%$ [69] and it induces an incertitude of $\pm 4^\circ\text{C}$ in the determination of the value of $T_g - T_m$. Thus, the measured gas stream temperature is:

$$T_m = 1300 \pm 10^\circ\text{C},$$

the difference between the real gas temperature and the measurement is:

$$T_g - T_m = 23 \pm 5^\circ\text{C},$$

and the corrected hot gas stream temperature is about:

$$T_g = 1323 \pm 15^\circ\text{C}.$$

APPENDIX H

**PROGRAMS FOR ASSISTANCE IN THERMAL ANALYSIS
APPLIED TO THE DEW SPECIMEN IN THE BURNER RIG**

Thermal analysis of the double-edge wedge specimen used in the high velocity burner rig was complex and long. Especially, the correction of the gas temperature measurements and the determination of local heat-transfer coefficients from heat balances, required complex expressions, iterative calculations, and numerous interpolations of the thermal properties of the hot gas and of the alloy tabulated as a function of temperature. In order to assist and minimize the errors during these calculations, five software programs based on improved procedures, formula and data base presented in Subsection 5.1 were developed. The five programs written in BASIC are named TFC-P.BAS, URADIAL.BAS, TFC-PRO.BAS, HCB-EXP.BAS, and HCB-EMP.BAS. The program TFC-P.BAS computes the corrected maximum temperatures and velocities according to the measurement of the control thermocouple and with the air flow measurement supplied to the combustor. Based on these outputs, URADIAL.BAS and TFC-PRO.BAS give respectively the velocity and the corrected radial profiles of temperature of the hot gas at the exit of the nozzle where the specimen is positioned for actual thermal tests. The program HCB-EXP.BAS was developed to derive the heat-transfer coefficients from the temperature measured along the chordwise of the mid-section of the specimen. The resulting coefficients profile is extrapolated, using the program HCB-EMP.BAS, to the overall specimen length using the empirical expression of Churchill & Bernstein and the data provided by URADIAL.BAS and TFC-PRO.BAS (the velocity and the temperature profiles of the hot gas).

All the programs are listed at the end of this Appendix with an example of output that they provide. The algorithm of the programs TFC-P.BAS and HCB-EXP.BAS is also illustrated.

H.1 Corrected Gas Temperature and Velocity

The corrected gas temperature measured by the controlling thermocouple and the mean velocity of the gas at the exit of the nozzle are the first parameters to be determined, for the thermal analysis. Since the correction of the measurements of the gas temperature is a function of the gas velocity and that this parameter is also a function of the temperature of the gas, those parameters must be determined simultaneously in an iterative scheme.

A software program TFC-P.BAS has been developed to solve this problem. The algorithm is presented at the end of this Appendix. The description of the main variables used in this program is presented hereafter:

TGC:	Temperature of the hot gas at the exit of the combustor, in °C.
TSC:	Temperature of the surface junction of the control thermocouple used to measure the temperature of the hot gas, located 1 cm from the flange of the nozzle, expressed in °C.
TFC:	Temperature of the stagnant film of the gas around the thermocouple junction that is estimated as the average between the hot gas temperature and the temperature of the thermocouple junction (in °C).
TAC:	Temperature (in °C) of the air supplied in the burner for the combustion of the fuel.
TGK, TSK,	
TFK, TAK:	Expression in K of the temperatures TGC, TSC, TFC, and TAC, respectively.
TG:	Variable used to record the last gas temperature (in K) computed during the iterative process.

T:	Temperature of the gas film (TFK) used to interpolate the thermal properties of the gas.
P1, P2:	Air pressures (psia) in the pipes connected to the primary and the secondary stages of the burner, respectively.
U:	Local centerline velocity of the hot gas at the nozzle exit (m/s).
R:	Ratio of the local velocity to the mean velocity of the gas, at the centerline.
D:	Diameter of the junction wires of the control thermocouple (in mm).
V or NUAIR:	Kinematic viscosity of the gas estimated at the gas film temperature (TFK), in m^2/s .
K or KUAIR:	Thermal conductivity of the gas estimated at the gas film temperature (TFK), in $\text{W}/\text{m}\cdot\text{K}$.
PR or PRAIR:	Prandtl number of the gas estimated at the gas film temperature (TFK).
PA(50):	Array variable that contains the thermal properties of the air from 0 to 2500 K and used to interpolate these values at the gas film temperature.
NT:	Total number of data in the files VAIR, KAIR, PRAIR.
NI:	Ordinal number (in the file) of the gas property value at the closest inferior temperature to the gas film temperature.
DT:	Interval of temperature between two following values in the gas property files (here 100 K).
T0:	Starting temperature of the first value stored in the gas property file.
RE:	Reynolds number of the gas defined by $U \cdot D / V$.
PE:	Peclet number of the gas defined as to be $RE \cdot PR$.
H:	Heat-transfer coefficient around the wires of the junction of the

	control thermocouple.
NUD:	Nusselt number around the junction wire of the thermocouple defined as to be $H \cdot D / K$.
C, N:	Constants in the empirical expression used to compute NUD.
SIGMA:	Stefan-Boltzmann constant ($5.669 \times 10^{-8} \text{ W/m}^2 \cdot \text{K}^4$) used in the expression to describe the radiation of the thermocouple wires in Pt and Pt-10%Rh.
EPT:	Emissivity of the platinum at the temperature of the thermocouple junction.
I, JJ:	Counters used during loop executions.

The corresponding algorithm is divided in three parts: (1) the input of the experimental values, (2) the computation of the corrected temperature and velocity, and (3) the display and printing of the results.

The first part of the program TFC-P.BAS is an interactive routine that ask the user via the CRT, to enter the values of TSC, D, P1, P2, TAC, and R.

The second part compute the mean velocity of the gas and its corresponding corrected temperature. The central velocity of the gas is a function of the hot gas temperature (TGK) and is given by the following formula:

$$U = \frac{R \cdot \text{TGK} \cdot (P1 + P2)}{19.874 \cdot (\text{TAK})^{0.5}}$$

As demonstrated in the previous Appendix G, the thermocouple junction induces an underestimation of the real gas temperature due to radiation. However, this temperature can be estimated through an heat balance. The heat loss by radiation is

equal to the heat transferred by convection from the hot gas. In turn, the heat-transfer coefficient (H) is required as well as the thermal properties of the gas V , K , PR and its velocity. The thermal properties of the flame are to be estimated by interpolation at the gas film temperature, i.e. the average temperature between the known thermocouple reading and the unknown actual (real) temperature of the hot gas. But as mentioned before, the velocity of the hot gas is a function of the unknown real temperature.

The computation of the real temperature can be only done through an iterative process assuming at first that the temperature of the gas is the same as the thermocouple reading. The variable TGK is used to stock the corrected gas temperature after an iteration and the variable TG records the value of the corrected temperature computed during the previous iteration. The stabilization of the value of TGK is assumed to be achieved when $(TGK - TG)$ is less than 0.05 K. At this final stage, the velocity of the gas as well as the thermal properties of the gas and the heat-transfer coefficient around the thermocouple junction are determined at that temperature which is believed to be reasonably close to the real gas temperature at the exit of the burner. The third part of this program prints the input and computed results.

H.2 Gas Velocity Profile

The burner rig produces a high velocity and high temperature gas that flows in the cool and stagnant surrounding air. Very close to the exit of the nozzle, the gas flow distribution follows a square function and the velocity on the plateau is close to the mean gas velocity determined by iteration using the program TFC-P.BAS. As the distance from the nozzle increases, the gas velocity profile becomes flarer. The modelling of this profile is very complex and difficult as demonstrated by Thomas [107]. Fortunately, Lau and Morris [105] have measured the gas flow distribution under various conditions as a function of the distance from the nozzle. They collapsed the experimental data with a Görtler error function profile, i.e.:

$$\frac{U}{U_j} = 0.5 [1 - \operatorname{erf}(\sigma \eta^*)]$$

where σ and η^* are nondimensional numbers, U and U_j are the radial velocity and the centerline velocity respectively. The error function $\operatorname{erf}(y)$ takes its usual definition, i.e.:

$$\operatorname{erf}(y) = \frac{2}{\sqrt{\pi}} \int_0^y e^{-t^2} dt$$

These relations are described in Subsection 5.1.2.3.1.

The software program URADIAL.BAS has been developed to compute the radial flow profile using the relation mentioned above. The error function is estimated using the trapezoidal rule. The following variables involved in the program are:

D: Internal diameter of the nozzle (0.0508 m).

R0: internal radius of the nozzle (D/2).

R5: Radial position where the local velocity is 0.5 times the maximum

- velocity of the gas stream (centerline).
- R: Radial position where the local velocity is computed (m).
- UJ: Centerline velocity of the gas stream (m/s).
- MJ: MACH number expression of UJ.
- X: Distance from the nozzle flange (m).
- T: Product of the two adimensional numbers σ and η^* .
- N: Number of elements used to approximate the integration of the function by the trapezoidal rule.
- I: I^{th} element of the N elements considered.
- TI: Value of the variable T for the I^{th} element.
- DT: Step or interval of integration ($DT = 0.001$).
- YI: Product of the value of the exponential of $(-TI^2)$ by DT.
- ERFT: Value of the integral of the exponential function.
- UUJ: Ratio of the radial velocity on the centerline velocity (U/UJ).
- PI: Value of π approximated by 3.1415927.

The user inputs the radial position which is considered, the centerline velocity UJ (in m/s) and the corresponding MACH number (MJ), and the distance from the flange nozzle normalized to the internal diameter (X/D). Note that the centerline velocity (in m/s and the MACH number) is provided by the TFC-P.BAS program (using the flame temperature and air pressures set for the tests in the burner rig). The distance between the specimen and the nozzle flange varies from 85 to 117 mm so the mean X/D value is 2.0. This important output will be used to correct the gas temperature profile measured by the thermocouples and to estimate the variation of the convective heat-transfer coefficients (h) along the longitudinal axis (Z) of the specimen. The parameter h is effectively a strong function of the Reynolds number and then of the specific velocity at the considered Z position.

H.3 Correction of the Gas Temperature Profile

The gas temperature has been measured at various radial positions with a thermocouple type-S. As mentioned before in the previous Appendix G, the thermocouple reading underestimates the gas temperature due to the heat loss by radiation at the hot junction. The heat transfer from the hot gas to the thermocouple junction is due to convection and is proportional to the gas velocity around the junction. The same software TFC-P.BAS, with some little modifications was then used to compute the correction needed to the thermocouples readings. Hence:

- The velocity is now known from the URADIAL.BAS program at the position being considered and is entered as an input of the program. Only the film temperature is determined by iteration to estimate the thermal properties of the gas.
- All the thermocouple readings of all the thermocouples can be corrected in one execution.
- The results are written in the file TFCxxxx (xxxx is the considered operating gas temperature) that can be imported by SYMPHONY software to allow statistical calculus, the display of tables, and graphs.

The modified program is saved under the name of TFC-PRO.BAS. The variables used are the same as those for TFC-P.BAS. Only the next variables have been added:

M: The number of temperature readings to be corrected.

NO(I): The number of the corresponding thermocouple I.

U(I): The velocity around the thermocouple junction being considered.

The corrected temperature profile of the gas is an important data for the evaluation of the gas properties needed to compute the local heat-transfer coefficients along the specimen. It is also an important input for the computation of the thermal history of the specimen in the burner rig, using the ABAQUS finite element code.

H.4 Experimental Heat-transfer Coefficient along the Specimen Surface

The experimental method to determine the heat-transfer coefficient along the specimen profile (from leading to trailing edge) has been fully described in Subsection 5.1.2.3.2. A short recall should even though summarize the procedure.

There are three heat-transfer fluxes that occur in an infinitesimal element at the surface of the specimen: convection from the hot gas to the specimen; radiation from the specimen to the surrounding; and conduction in the metal. After simplification, the energy balance that derives from these heat-transfer fluxes can be written as follows:

$$Q_{CONVECTION} = Q_{CONDUCTION} + Q_{RADIATION}$$

$$h (T_g - T_s) = k_m \left(\frac{T_s - T_i}{\delta_m} \right) + \epsilon \sigma \left[\sum_j F_{s-j} (T_s^4 - T_j^4) \right]$$

where:

- T_g : temperature of the gas stream in the burner (K);
- T_s : local temperature of the specimen surface (K);
- T_i : corresponding internal temperature of the specimen (K);
- T_j : temperature of the j^{th} element of the surroundings (i.e. combustion chamber, nozzle, room walls) (K);
- h : local heat-transfer coefficient ($\text{W}/\text{m}^2 \cdot \text{K}$);
- k_m : thermal conductivity of the specimen material ($\text{W}/\text{m} \cdot \text{K}$);
- δ_m : depth location of the internal temperature T_i (m);
- ϵ : emissivity of the specimen material;
- σ : Stefan-Boltzmann constant ($5.669\text{E-}8 \text{ W}/\text{m}^2 \cdot \text{K}^4$);
- F_{s-j} : radiation shape factors or view factors.

The local heat-transfer coefficient can then be estimated if all the other parameters are known. The temperature on the specimen surface was specially measured along the hottest chordwise section of the specimen corresponding to the axis of the hot gas stream. The local gas temperature has been measured and corrected using the program TFC-PRO.BAS whereas the origin of the other parameters is given in Subsection 5.1.

The program HCB-EXP.BAS has been developed to estimate the local h where the specimen temperature has been measured along the chordwise section of the specimen. It also computes the geometrical factor, GF (also called FC in the program), defined to be the ratio of the local h to the mean empirical h for the specimen, as estimated by the Churchill-Bernstein expression for cylinders across a gas stream, which is used to extrapolate the h values along the specimen where the specimen temperature was not measured. The list of variables employed in this program is given below:

LS:	The specimen location number that corresponds to a position considered along the profile.
POSITION:	Position number considered along the longitudinal axis of the specimen.
D:	Characteristic diameter of the specimen (6.4mm).
U:	Local gas velocity at the considered position (m/s).
TGC:	Local gas temperature at the considered position along the specimen ($^{\circ}\text{C}$).
TSC:	Local specimen temperature ($^{\circ}\text{C}$).
TFC:	Temperature ($^{\circ}\text{C}$) of the stagnant film of gas at the specimen surface that is approximated by $(\text{TGC} + \text{TSC})/2$.
TIC:	Internal temperature of the specimen measured at DX meter from the surface (same location as TSC).

TGK, TSK,	
TFK, TIK:	TGC, TSC, TFC, TIC (in K).
QR:	Heat loss from the specimen surface by radiation (W/m^2).
SIGMA:	Stefan-Boltzmann constant ($5.669 \times 10^{-8} \text{ W/m}^2 \cdot \text{K}^4$).
ES:	Emissivity of the oxidized specimen René 80 ($\text{ES} = 0.85$).
FSA:	Fraction of the energy leaving the surface to the surroundings (at the leading edge $\text{FSA} = 0.88$, elsewhere $\text{FSA} = 1.0$).
TAK:	Temperature of the surroundings, in the burner rig room ($\text{TAK} = 290 \text{ K}$).
FSN:	Fraction of the energy leaving the surface to the nozzle (at the leading edge $\text{FSN} = 0.072$, elsewhere $\text{FSN} = 0.0$).
TNK:	Temperature of the nozzle (K).
FSC:	Fraction of the energy leaving the surface to the combustor (at the leading edge $\text{FSC} = 0.048$, elsewhere $\text{FSC} = 0.0$).
TCK:	Inner temperature of the combustor (K).
QK:	Heat flux at the specimen surface by conduction.
KS:	Thermal conductivity of the material at the temperature TSK.
KS0:	Thermal conductivity at 0 K.
DK:	Rate of change of KS by Kelvin.
GRADT:	Thermal gradient measured at the specimen surface.
QH:	Convection heat flux at the specimen surface.
HTH:	Characteristic mean heat-transfer coefficient computed from the empirical expression of Churchill-Bernstein with the local thermal properties of gas.
NUD:	Corresponding Nusselt number of HTH.
F:	"Local HTH"/"mean HTH" ratio suggested by the user.
HEXP:	Heat-transfer coefficient computed from the experimental data.
FC:	Ratio of the experimental HEXP on the empirical mean HTH

computed for the thermal properties of gas (called GF in the text).

The other variables PA(T), V, NUAIR, K, KAIR, PR, PRAIR, RE, PE, NT, NI, DT, TO, I, JJ have the same definition as described in the Subsection H.1.

The value of LS, POSITION, F, D, TSC, TIC, DX, TGC, and U are entered by the user during the execution of the READ sub-routine.

The mean empirical heat-transfer coefficient HTH is then computed using the expression of Churchill & Bernstein and the thermal properties are interpolated for the gas film temperature TFK (see sub-routines 10000 to 50000).

The radiation and conduction heat fluxes (QR, QK) are computed from their respective expression. After, the convective heat flux (QH) is estimated as the sum of the QR and QK, according to the energy balance at the specimen surface. As QH is defined by:

$$QH = HEXP * (TGK - TSK)$$

the experimental HEXP is easily deducted. The FC ratios of HEXP to HTH are computed afterwards. The results are then printed. The main results printed in the starframe are HTH, HTH*F, HEXP and FC.

HL5 Empirical Heat-transfer Coefficients

As explained in Subection 5.1.2.3, the heat-transfer coefficient "h" can be computed at any location on the surface of the specimen using the experimental "h", HEXP, obtained along the mid-section of the specimen profile, normalized by the empirical "h", HTH, obtained from the expression of Churchill-Bernstein and the thermal properties of the gas at the considered location. The GF or FC ratio:

$$FC = \frac{HEXP(mid-section chordwise)}{HTH(Re(U_g), air-properties(T_g))}$$

computed along the mid-section of the specimen using the HCB-EXP.BAS program, is assumed to be constant along the longitudinal axis of the specimen. Then, the local heat-transfer profile can be determined as a product of FC and of the local HTH (for the specific velocity and thermal properties of the gas) i.e. $H(location) = FC * HTH$.

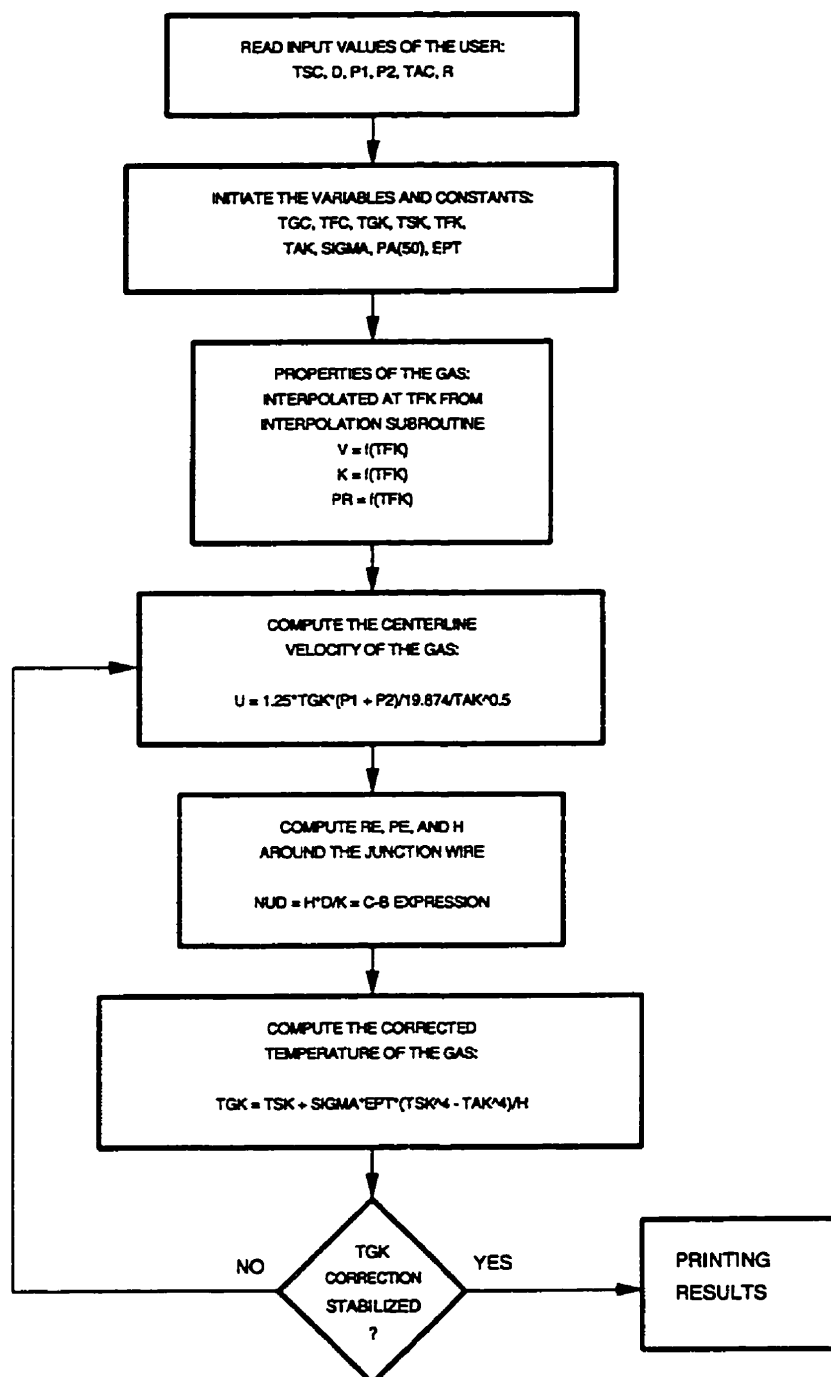
The program HCB-EMP.BAS computed the HTH's using the gas temperature and velocity according to the specific inputs and according to the considered location. Its structure is a simplification of the previous program (only HEXP is not computed) and corresponds to the part where HTH is calculated.

ALGORITHM, LISTING, AND OUTPUT OF THE PROGRAMS:

TFC-P.BAS
URADIAL.BAS
TFC-PRO.BAS
HCB-EXP.BAS
HCB-EMP.BAS

PROGRAM TFC-P.BAS

ALGORITHM OF TFC-P.BAS



```

10 /
20 /
30 /
40 /
50 /
60 ***** PROGRAM TFC-P.BAS *****
70 /
80 /
90 /
100 /      *      CORRECTION OF THE FLAME TEMPERATURE MEASURED      *
110 /      *      BY THE CONTROLLING THERMOCOUPLE:                  *
120 /      *      COMPUTATION OF THE EFFECT OF THE RADIATION        *
130 /      *      OF THE HOT JUNCTION ON THIS MEASUREMENT          *
140 /      *      *
150 /      *      REFER TO THE APPENDIX-III                          *
160 /      *      OF THE 7th INTERIM REPORT                          *
170 /      *      *
180 /      *
190 / *** NB.: PROPERTIES OF THE GAS ARE EVALUATED AT GAS FILM TEMPERATURE ***
200 /
210 /
220 /
230 /
240 /
300 ***** PRINCIPAL PROGRAM *****
310 /
320 /
330 ***** READ SOME INPUT VALUES LIKE THE FLAME TEMPERATURE MEASURED *****
340 GOSUB 1000
350 /
360 ***** COMPUTE THE REAL FLAME TEMPERATURE *****
370 GOSUB 2000
380 /
390 ***** PRINT THE RESULTS *****
400 GOSUB 3000
410 /
420 END
500 /
510 /
520 /
530 ***** SUBROUTINES *****
540 /
550 /
1000 ***** SUBROUTINE FOR READING THE DATA FROM THE USER:
1010 CLS
1020 PRINT "ENTER THE FLAME TEMPERATURE MEASURED IN CELCIUS"
1030 PRINT "BY THE CONTROLLING THERMOCOUPLE AND PRESS ENTER:": INPUT TSC
1040 PRINT "ENTER THE DIAMETER (IN MM) OF THE JUNCTION WIRES"
1050 PRINT "OF THE THERMOCOUPLE AND PRESS ENTER:"
1060 INPUT D: D = D*.001
1070 PRINT "ENTER PRIMARY PRESSURE IN COMBUSTOR (IN PSIA) AND PRESS ENTER:"
1080 INPUT P1
1090 PRINT "ENTER SECONDARY PRESSURE IN COMBUSTOR (IN PSIA) AND PRESS ENTER:"
1100 INPUT P2
1110 PRINT "ENTER THE TEMPERATURE OF THE INLET AIR IN CELCIUS"
1120 PRINT "AND PRESS ENTER:": INPUT TAC
1130 PRINT "ENTER THE LOCAL VELOCITY ON THE MEAN VELOCITY RATIO, R"
1140 PRINT "AND PRESS ENTER:": INPUT R
1150 PRINT "PLEASE WAIT!"
1160 RETURN
1170 /
1180 /
2000 ***** SUBROUTINE FOR COMPUTATION OF THE REAL FLAME TEMPERATURE:
2010 /
2020 / CONSTANT DATA:
2030 TGC = TSC
2040 TFC = (TGC + TSC)/2
2050 TKG = TGC + 273
2060 TSK = TSC + 273
2070 TFK = TFC + 273
2080 TAK = TAC + 273
2090 SIGMA = 5.669E-08

```

```

2100 DIM PA(50)
2110 ' INTERPOLATION OF EPT AT JUNCTION TEMPERATURE:
2120 GOSUB 40000
2130 '
2140 * COMPUTATION OF THE FLAME TEMPERATURE:
2150 JJ = 0
2160 TG = 0!
2170 WHILE ABS(TGK-TG) > .05
2180     TG = TGK
2190     GOSUB 10000: V = NUAIR
2200     GOSUB 20000: K = KAIR
2210     GOSUB 30000: PR = PRAIR
2215     U = R*TGK*(P1+P2)/19.874/TAK^.5
2220     RE = U*D/V
2230     PE = RE*PR
2240     ' COMPUTE H:
2250     C = .683
2260     N = .466
2270     NUD = C*RE^N*PR^.3333
2280     H = NUD*K/D
2290     ' COMPUTE TGK:
2300     TGK = TSK + SIGMA*EPT/H*(TSK^4 - TAK^4)
2310     TFK = (TSK+TGK)/2
2320     JJ = JJ + 1
2330 WEND
2340 RETURN
2350 '
2360 '
3000 '*** SUBROUTINE FOR PRINTING THE RESULTS:
3010 '
3020 LPRINT ***** PROGRAM TFC-P.BAS *****
3030 LPRINT *****
3040 LPRINT ***** COMPUTATION OF THE CORRECTED FLAME TEMPERATURE *****
3050 LPRINT ***** USING COMPUTED GAS VELOCITY BY ITERATION *****
3060 LPRINT *****
3070 LPRINT *****
3080 LPRINT ""
3090 LPRINT ""
3100 LPRINT "FLAME TEMPERATURE MEASURED BY THE CONTROLLING ";
3110 LPRINT USING "THERMOCOUPLE = #### C"; TSC;
3120 LPRINT USING " OR #### K"; TSC + 273
3130 LPRINT USING "GAS FILM TEMPERATURE = #### C"; TFK - 273;
3140 LPRINT USING " OR #### K"; TFK
3145 LPRINT USING "INLET AIR TEMPERATURE = #### C"; TAK - 273;
3146 LPRINT USING " OR #### K"; TAK
3150 LPRINT USING "PRIMARY PRESSURE IN COMBUSTOR, P1 = ##.# PSIA"; P1
3160 LPRINT USING "SECONDARY PRESSURE IN COMBUSTOR, P2 = ##.# PSIA"; P2
3170 LPRINT USING "MEAN VELOCITY OF THE GAS = ### M/S"; U/R;
3180 LPRINT USING " (MACH #.##)"; U/R/(1.4*287*TGK)^.5
3190 LPRINT USING "LOCAL VELOCITY OF THE GAS USED FOR RE NUMBER = ### M/S"; U;
3200 LPRINT USING " (MACH #.##)"; U/(1.4*287*TGK)^.5
3210 LPRINT "RATIO OF LOCAL VELOCITY ON THE MEAN VELOCITY OF THE GAS, R = ";
3220 LPRINT USING "###"; R
3230 LPRINT USING "DIAMETER OF THE JUNCTION WIRES = ### MM"; D*1000
3240 LPRINT USING "KINEMATIC VISCOSITY OF THE GAS = ###.###^ M^2/S"; V
3250 LPRINT USING "THERMAL CONDUCTIVITY OF THE GAS = ###.###^ W/M/K"; K
3260 LPRINT USING "REYNOLDS NUMBER, RE = #####"; RE
3270 LPRINT USING "PRANDTL NUMBER, PR = ###.###"; PR
3280 LPRINT USING "PECLET NUMBER, PE = RE*PR = #####"; PE
3290 IF PE < .2 OR RE > 1E+07 OR RE < 100! , THEN LPRINT "RE OR PE OUT OF RANGE"
3300 LPRINT USING "NUSELT NUMBER, NUD = ##.##"; NUD
3310 LPRINT USING "HEAT-TRANSFER COEFFICIENT, H = ##### W/M^2/K"; H
3320 LPRINT USING "EMISSIVITY OF THE PLATINUM WIRES = .#####"; EPT;
3330 LPRINT USING " (FOR A JUNCTION TEMPERATURE OF #### C)"; TSC
3340 LPRINT ""
3350 LPRINT *****
3360 LPRINT *****
3370 LPRINT *****
3380 LPRINT USING "_*_*_ REAL FLAME TEMPERATURE = #### C ";TGK-273;
3390 LPRINT USING "OR #### K _*_*_";TGK
3400 LPRINT "**** FLAME TEMPERATURE WAS UNDERESTIMATED BY";
3410 LPRINT USING " ### C _*_*_"; TGK - TSK

```



```

3420 LPRINT "****"
3430 LPRINT "*****"
3440 LPRINT "*****"
3450 LPRINT CHR$(12)
3460 RETURN
3470 '
3480 '
10000 '*** SUBROUTINE NUAIR:
10100 ' EVALUATION OF THE EXACT VALUE OF NUAIR:
10200 OPEN"I",#1,"NUAIR"
10300 INPUT#1, NT, DT, TO
10400 FOR I=1 TO NT: INPUT#1, PA(I): NEXT I
10500 CLOSE#1
10600 T = TFK
10700 ' GET THE INTERPOLATED VALUE OF NUAIR:
10800 GOSUB 50000
10900 NUAIR = PA
11000 RETURN
11100 '
20000 '*** SUBROUTINE KAIR:
20100 ' EVALUATION OF THE EXACT VALUE OF KAIR:
20200 OPEN"I",#2,"KAIR"
20300 INPUT#2, NT, DT, TO
20400 FOR I=1 TO NT: INPUT#2, PA(I): NEXT I
20500 CLOSE#2
20600 T = TFK
20700 ' GET THE INTERPOLATED VALUE OF KAIR:
20800 GOSUB 50000
20900 KAIR = PA
21000 RETURN
21100 '
30000 '*** SUBROUTINE PRAIR:
30100 ' EVALUATION OF THE EXACT VALUE OF PRAIR:
30200 OPEN"I",#3,"PRAIR"
30300 INPUT#3, NT, DT, TO
30400 FOR I=1 TO NT: INPUT#3, PA(I): NEXT I
30500 CLOSE#3
30600 T = TFK
30700 ' GET THE INTERPOLATED VALUE OF PRAIR:
30800 GOSUB 50000
30900 PRAIR = PA
31000 RETURN
31100 '
40000 '***SUBROUTINE EPT:
40100 ' EVALUATION OF THE EMISSIVITY OF THE JUNCTION WIRES, EPT:
40200 OPEN"I",#4,"EPT"
40300 INPUT#4, NT, DT, TO
40400 FOR I=1 TO NT: INPUT#4, PA(I): NEXT I
40500 CLOSE#4
40600 T = TSK
40700 ' GET THE INTERPOLATED VALUE OF EPT:
40800 GOSUB 50000
40900 EPT = PA
41000 RETURN
41100 '
50000 '*** INTERPOLATION SUBROUTINE:
50100 ' INTERPOLATE TO FIND THE EXACT VALUE OF THE PROPERTY, "PA",
50200 ' FOR THE TEMPERATURE, T, CONSIDERED:
50300 NI = INT((T - T0)/DT) + 1
50400 IF T < T0 THEN PA = PA(1):PRINT "EXTRAPOLATION UNDER ", T0," K":GOTO 50900
50500 IF T >= (NT-1)*DT+T0 THEN PA = PA(NT): GOTO 50700
50600 PA = PA(NI) + (PA(NI+1) - PA(NI))*(T - (NI-1)*DT - T0)/DT: GOTO 50900
50700 IF T > (NT-1)*DT+T0 THEN PRINT "EXTRAPOLATION OVER ", (NT-1)*DT+T0," K"
50800 GOTO 50900
50900 RETURN

```

```

***** PROGRAM TFC-P.BAS *****
*****
***** COMPUTATION OF THE CORRECTED FLAME TEMPERATURE *****
***** USING COMPUTED GAS VELOCITY BY ITERATION *****
*****

```

```

FLAME TEMPERATURE MEASURED BY THE CONTROLLING THERMOCOUPLE = 1300 C OR 1573 K
GAS FILM TEMPERATURE = 1311 C OR 1584 K
INLET AIR TEMPERATURE = 25 C OR 298 K
PRIMARY PRESSURE IN COMBUSTOR, P1 = 45.0 PSIA
SECONDARY PRESSURE IN COMBUSTOR, P2 = 22.5 PSIA
MEAN VELOCITY OF THE GAS = 314 M/S (MACH 0.39)
LOCAL VELOCITY OF THE GAS USED FOR RE NUMBER = 392 M/S (MACH 0.49)
RATIO OF LOCAL VELOCITY ON THE MEAN VELOCITY OF THE GAS, R = 1.25
DIAMETER OF THE JUNCTION WIRES = 0.50 MM
KINEMATIC VISCOSITY OF THE GAS = 2.51E-04 M^2/S
THERMAL CONDUCTIVITY OF THE GAS = 9.92E-02 W/M/K
REYNOLDS NUMBER, RE = 783
PRANDTL NUMBER, PR = 0.705
PECLET NUMBER, PE = RE*PR = 552
NUSSELT NUMBER, NUD = 13.6
HEAT-TRANSFER COEFFICIENT, H = 2690 W/M^2/K
EMISSIONIVITY OF THE PLATINUM WIRES = 0.175 (FOR A JUNCTION TEMPERATURE OF 1300 C)

```

```

*****
*****
***                                     ***
*** REAL FLAME TEMPERATURE = 1323 C OR 1596 K ***
*** FLAME TEMPERATURE WAS UNDERESTIMATED BY 23 C ***
***                                     ***
*****
*****

```

PROGRAM URADIAL.BAS

```

10 ***** URADIAL.BAS *****
20 'COMPUTATION OF THE RADIAL VELOCITY OF THE GAS IN THE BURNER RIG:
30 '
40 D = .0508
50 R0 = D/2
60 R5 = 1.12*R0
70 PRINT "ENTER R (IN M) AND PRESS ENTER:": INPUT R:
80 PRINT "ENTER Uj (IN M/S) AND PRESS ENTER:": INPUT UJ:
90 PRINT "ENTER Mj AND PRESS ENTER:": INPUT MJ:
100 PRINT "ENTER X/D AND PRESS ENTER:": INPUT X: X = X*D
110 T = 10.7*(R-R5)/(1-.273*MJ^2)/X
120 DT = .001
130 N = ABS(INT(T/DT))
140 ERFT = 0!
150 PI = 3.1415927#
160 FOR I = 1 TO N
170     TI = (I-.5)*DT
180     YI = EXP(-(TI)^2)*DT
190     ERFT = ERFT + YI
200 NEXT I
210 IF R<R5 THEN ERFT = -ERFT
220 UJ = .5*(1 - ERFT^2/PI^.5)
225 LPRINT ""
226 LPRINT ""
227 LPRINT ""
228 LPRINT ***** PRINT OUT OF THE RESULT *****
229 LPRINT ""
230 LPRINT **** RADIAL VELOCITY OF THE GAS, U, AT THE POSITION R ****
240 LPRINT ""
250 LPRINT USING "R = ###.### m"; R
260 LPRINT USING "X/D = ###.###"; X/D
270 LPRINT USING "SIGMA*ETA = ###.###"; T
280 LPRINT USING "Mj = ###.###"; MJ
290 LPRINT USING "Uj = ###.### m/s"; UJ
300 LPRINT USING "U/Uj = ###.###"; UJ
310 LPRINT USING "U = ###.### m/s"; UJ*UJ
320 LPRINT ""
330 LPRINT ""
340 END

```

PROGRAM TFC-PRO.BAS

```

10 '
20 '
30 '
40 '
50 '
60 ***** PROGRAM TFC-PRO.BAS *****
70 '
80 '
90 '
100 '      *      CORRECTION OF THE FLAME TEMPERATURE PROFILE      *
110 '      *      MEASURED BY THERMOCOUPLES TYPE-S                *
120 '      *      COMPUTATION OF THE EFFECT OF THE RADIATION      *
130 '      *      OF THE HOT JUNCTION ON THIS MEASUREMENT        *
140 '      *
150 '      *      REFER TO THE APPENDIX-III                        *
160 '      *      OF THE 7th INTERIM REPORT                       *
170 '      *
180 '      *****
190 ' *** NB.: PROPERTIES OF THE GAS ARE EVALUATED AT GAS FILM TEMPERATURE ***
200 '
210 '
220 '
230 '
240 '
300 ***** PRINCIPAL PROGRAM *****
310 '
320 '
330 ***** READ SOME INPUT VALUES LIKE THE FLAME TEMPERATURE MEASURED *****
340 GOSUB 1000
350 '
360 ***** COMPUTE THE REAL FLAME TEMPERATURE PROFILE *****
370 GOSUB 2000
380 '
390 ***** PRINT THE RESULTS *****
400 GOSUB 3000
410 '
420 ***** WRITE THE RESULTS IN THE FILE "TFC*PRO" *****
430 GOSUB 4000
440 '
450 END
500 '
510 '
520 '
530 ***** SUBROUTINES *****
540 '
550 '
1000 ***** SUBROUTINE FOR READING THE DATA FROM THE USER:
1001 PRINT "ENTER THE NUMBER OF DATA TO CONSIDER AND PRESS ENTER:": INPUT M
1002 DIM NO(M), U(M), TSC(M), TGC(M)
1005 CLS
1010 FOR I = 1 TO M
1020 PRINT "ENTER THE FLAME TEMPERATURE MEASURED IN CELCIUS"
1030 PRINT "BY THE THERMOCOUPLE AND PRESS ENTER:": INPUT TSC(I)
1040 PRINT "ENTER THE CORRESPONDING NUMBER OF THE THERMOCOUPLE"
1050 PRINT "AND PRESS ENTER:"
1060 INPUT NO(I)
1070 PRINT "ENTER VELOCITY IN M/S AND PRESS ENTER:"
1080 INPUT U(I)
1085 NEXT I
1090 PRINT "PLEASE WAIT!"
1100 RETURN
1110 '
1120 '
2000 ***** SUBROUTINE FOR COMPUTATION OF THE REAL FLAME TEMPERATURE:
2010 DIM PA(50), OVER(M)
2020 FOR J = 1 TO M
2030 ' CONSTANT DATA:
2040 TGC = TSC(J)
2050 TFC = (TGC + TSC(J))/2
2060 TKG = TGC + 273
2070 TSK = TSC(J) + 273
2080 TFK = TFC + 273

```

```

2090 TA = 290
2100 SIGMA = 5.669E-08
2110 ' INTERPOLATION OF EPT AT JUNCTION TEMPERATURE:
2120 GOSUB 40000
2130 '
2140 ' COMPUTATION OF THE FLAME TEMPERATURE:
2150 JJ = 0
2160 TG = 0!: D = .0005: PRINT "DIAMETER OF THE JUNCTION WIRES IS ", D,"m ?"
2170 WHILE ABS(TGK-TG) > .05
2180     TG = TGK
2190     GOSUB 10000: V = NUAIR
2200     GOSUB 20000: K = KAIR
2210     GOSUB 30000: PR = PRAIR
2220     RE = U(J)*D/V
2230     PE = RE*PR
2240     ' COMPUTE H:
2250     C = .683
2260     N = .466
2270     NUD = C*RE*N*PR^.3333
2280     H = NUD*K/D
2290     ' COMPUTE TGK:
2300     TGK = TSK + SIGMA*EPT/H*(TSK^4 - TA^4)
2310     TFK = (TSK+TGK)/2
2320     JJ = JJ + 1
2330 WEND
2335 IF PE < .2 OR RE > 1E+07 OR RE < 100! , THEN OVER(J) = 1
2340 TGK(J) = TGK
2350 NEXT J
2360 RETURN
2370 '
2380 '
3000 '*** SUBROUTINE FOR PRINTING THE RESULTS:
3010 '
3020 LPRINT "***** PROGRAM TFC-PRO.BAS *****"
3030 LPRINT "*****"
3040 LPRINT "***** COMPUTATION OF THE CORRECTED FLAME TEMPERATURE *****"
3050 LPRINT "***** PROFILE USING SUGGESTED GAS VELOCITY *****"
3060 LPRINT "*****"
3070 LPRINT "*****"
3080 LPRINT ""
3100 LPRINT ""
3110 LPRINT "NO      U-GAS      TFM      TFC      TFM      TFC      TFC-TFM"
3120 LPRINT "      (M/S)      (C)      (C)      (K)      (K)      (C OR K)"
3130 LPRINT ""
3140 FOR I = 1 TO M
3150 LPRINT USING "###"; NO(I);
3160 LPRINT USING "    ###.##"; U(I);
3170 LPRINT USING "    ###.##"; TSC(I);
3180 LPRINT USING "    ###.##"; TGK(I)-273;
3190 LPRINT USING "    ###.##"; TSC(I)+273;
3200 LPRINT USING "    ###.##"; TGK(I);
3210 LPRINT USING "    ###.##";TGK(I)-TSC(I)-273;
3220 IF OVER(I) = 1 THEN LPRINT " (*)" ELSE LPRINT ""
3230 OV = OV + OVER(I)
3240 NEXT I
3250 LPRINT ""
3260 LPRINT ""
3270 LPRINT "WHERE:"
3280 LPRINT ""
3290 LPRINT "NO IS THE THERMOCOUPLE NUMBER,"
3300 LPRINT "U-GAS IS THE PROPOSED VELOCITY OF THE GAS AT THIS LOCATION,"
3310 LPRINT "TFM IS THE FLAME TEMPERATURE MEASURED AT THIS LOCATION,"
3320 LPRINT "TFC IS THE CORRESPONDING CORRECTED FLAME TEMPERATURE,"
3330 LPRINT "TFC-TFM IS THE DIFFERENCE BETWEEN TFC AND TFM."
3340 LPRINT ""
3350 LPRINT ""
3360 IF OV >=1 THEN LPRINT **: RE OR PE WAS OUT OF RANGE FOR COMPUTATION OF TFC"
3370 LPRINT CHR$(12)
3380 RETURN
3390 '
3400 '
4000 '*** SUBROUTINE FOR PRINTING THE RESULTS IN THE FILE TFC*PRO:

```

```

4010 OPEN "O",#5, "TFC0000"
4020 PRINT #5, "***** PROGRAM TFC-PRO.BAS *****"
4030 PRINT #5, "*****"
4040 PRINT #5, "***** COMPUTATION OF THE CORRECTED FLAME TEMPERATURE *****"
4050 PRINT #5, "***** PROFILE USING SUGGESTED GAS VELOCITY *****"
4060 PRINT #5, "*****"
4070 PRINT #5, "*****"
4080 PRINT #5, ""
4100 PRINT #5, ""
4110 PRINT #5, " NO ";
4111 PRINT #5, " U-GAS ";
4112 PRINT #5, " TFM ";
4113 PRINT #5, " TFC ";
4114 PRINT #5, " TFM ";
4115 PRINT #5, " TFC ";
4116 PRINT #5, " TFC-TFM ";
4120 PRINT #5, " ";
4121 PRINT #5, " (M/S) ";
4122 PRINT #5, " (C) ";
4123 PRINT #5, " (C) ";
4124 PRINT #5, " (K) ";
4125 PRINT #5, " (K) ";
4126 PRINT #5, " (C OR K) "
4130 PRINT #5, ""
4140 FOR I = 1 TO M
4150 PRINT #5, USING " ###; NO(I);
4160 PRINT #5, USING " ###.##; U(I);
4170 PRINT #5, USING " ####.##; TSC(I);
4180 PRINT #5, USING " ####.##; TGK(I)-273;
4190 PRINT #5, USING " ####.##; TSC(I)+273;
4200 PRINT #5, USING " ####.##; TGK(I);
4210 PRINT #5, USING " ###.##;TGK(I)-TSC(I)-273;
4220 IF OVER(I) = 1 THEN PRINT #5, " (*) " ELSE PRINT #5, ""
4230 NEXT I
4240 '
4250 PRINT #5, ""
4260 PRINT #5, ""
4270 PRINT #5, "WHERE:"
4280 PRINT #5, ""
4290 PRINT #5, "NO IS THE THERMOCOUPLE NUMBER,"
4300 PRINT #5, "U-GAS IS THE PROPOSED VELOCITY OF THE GAS AT THIS LOCATION,"
4310 PRINT #5, "TFM IS THE FLAME TEMPERATURE MEASURED AT THIS LOCATION,"
4320 PRINT #5, "TFC IS THE CORRESPONDING CORRECTED FLAME TEMPERATURE,"
4330 PRINT #5, "TFC-TFM IS THE DIFFERENCE BETWEEN TFC AND TFM."
4340 PRINT #5, ""
4350 PRINT #5, ""
4360 IF OV >= 1 THEN PRINT #5, "": RE OR PE WAS OUT OF RANGE ";
4370 IF OV >= 1 THEN PRINT #5, "FOR COMPUTATION OF TFC."
4380 CLOSE #5
4390 RETURN
4400 '
4410 '
10000 '*** SUBROUTINE NUAIR:
10100 ' EVALUATION OF THE EXACT VALUE OF NUAIR:
10200 OPEN "I",#1, "NUAIR"
10300 INPUT#1, NT, DT, TO
10400 FOR I=1 TO NT: INPUT#1, PA(I): NEXT I
10500 CLOSE#1
10600 T = TFK
10700 ' GET THE INTERPOLATED VALUE OF NUAIR:
10800 GOSUB 50000
10900 NUAIR = PA
11000 RETURN
11100 '
20000 '*** SUBROUTINE KAIR:
20100 ' EVALUATION OF THE EXACT VALUE OF KAIR:
20200 OPEN "I",#2, "KAIR"
20300 INPUT#2, NT, DT, TO
20400 FOR I=1 TO NT: INPUT#2, PA(I): NEXT I
20500 CLOSE#2
20600 T = TFK
20700 ' GET THE INTERPOLATED VALUE OF KAIR:

```



```

20800 GOSUB 50000
20900 KAIR = PA
21000 RETURN
21100 '
30000 '*** SUBROUTINE PRAIR:
30100 ' EVALUATION OF THE EXACT VALUE OF PRAIR:
30200 OPEN"I",#3, "PRAIR"
30300 INPUT#3, NT, DT, T0
30400 FOR I=1 TO NT: INPUT#3, PA(I): NEXT I
30500 CLOSE#3
30600 T = TFK
30700 ' GET THE INTERPOLATED VALUE OF PRAIR:
30800 GOSUB 50000
30900 PRAIR = PA
31000 RETURN
31100 '
40000 '***SUBROUTINE EPT:
40100 ' EVALUATION OF THE EMISSIVITY OF THE JUNCTION WIRES, EPT:
40200 OPEN"I",#4, "EPT"
40300 INPUT#4, NT, DT, T0
40400 FOR I=1 TO NT: INPUT#4, PA(I): NEXT I
40500 CLOSE#4
40600 T = TSK
40700 ' GET THE INTERPOLATED VALUE OF EPT:
40800 GOSUB 50000
40900 EPT = PA
41000 RETURN
41100 '
50000 '*** INTERPOLATION SUBROUTINE:
50100 ' INTERPOLATE TO FIND THE EXACT VALUE OF THE PROPERTY, "PA",
50200 ' FOR THE TEMPERATURE, T, CONSIDERED:
50300 NI = INT((T - T0)/DT) + 1
50400 IF T < T0 THEN PA = PA(1):PRINT "EXTRAPOLATION UNDER ", T0," K":GOTO 50900
50500 IF T >= (NT-1)*DT+T0 THEN PA = PA(NT): GOTO 50700
50600 PA = PA(NI) + (PA(NI+1) - PA(NI))*(T - (NI-1)*DT - T0)/DT: GOTO 50900
50700 IF T > (NT-1)*DT+T0 THEN PRINT "EXTRAPOLATION OVER ", (NT-1)*DT+T0," K"
50800 GOTO 50900
50900 RETURN

```

```

***** PROGRAM TFC-PRO.BAS *****
*****
***** COMPUTATION OF THE CORRECTED FLAME TEMPERATURE *****
***** PROFILE USING SUGGESTED GAS VELOCITY *****
*****
*****

```

NO	U-GAS (M/S)	TFM (C)	TFC (C)	TFM (K)	TFC (K)	TFC-TFM (C OR K)
0	9.1	174.9	175.1	447.9	448.1	0.2
1	20.9	205.1	205.3	478.1	478.3	0.2
2	42.2	265.2	265.5	538.2	538.5	0.3
3	74.8	354.8	355.3	627.8	628.3	0.5
4	117.8	459.3	460.3	732.3	733.3	1.0
5	166.4	569.7	571.4	842.7	844.4	1.7
6	213.5	692.9	695.8	965.9	968.8	2.9
7	252.7	827.3	832.4	1100.3	1105.4	5.1
8	280.7	963.0	971.7	1236.0	1244.7	8.7
9	297.8	1099.0	1112.8	1372.0	1385.8	13.8
10	306.7	1188.2	1206.3	1461.2	1479.3	18.1
11	310.8	1228.6	1249.0	1501.6	1522.0	20.4
12	312.3	1241.6	1262.7	1514.6	1535.7	21.1
13	312.8	1245.0	1266.3	1518.0	1539.3	21.3
14	313.0	1249.2	1270.8	1522.2	1543.8	21.6
15	313.0	1257.2	1279.3	1530.2	1552.3	22.1
16	313.0	1264.5	1287.1	1537.5	1560.1	22.6
17	313.0	1267.0	1289.8	1540.0	1562.8	22.8
18	313.0	1263.5	1286.1	1536.5	1559.1	22.6
19	312.8	1258.6	1280.8	1531.6	1553.8	22.2
20	312.3	1252.8	1274.7	1525.8	1547.7	21.9
21	310.8	1241.5	1262.7	1514.5	1535.7	21.2
22	306.7	1200.9	1219.7	1473.9	1492.7	18.8
23	297.8	1121.1	1135.9	1394.1	1408.9	14.8
24	280.7	996.0	1005.9	1269.0	1278.9	9.9
25	252.7	856.4	862.3	1129.4	1135.3	5.9
26	213.5	716.3	719.6	989.3	992.6	3.3
27	166.4	588.3	590.2	861.3	863.2	1.9
28	117.8	466.9	467.9	739.9	740.9	1.0
29	74.8	356.9	357.5	629.9	630.5	0.6
30	42.2	249.9	250.2	522.9	523.2	0.3
31	20.9	166.7	166.8	439.7	439.8	0.1
32	9.1	102.9	103.0	375.9	376.0	0.1
33	3.5	60.2	60.2	333.2	333.2	0.0 (*)
34	1.1	40.6	40.6	313.6	313.6	0.0 (*)
35	0.3	34.5	34.5	307.5	307.5	0.0 (*)
36	0.1	31.6	31.7	304.6	304.7	0.1 (*)
37	0.0	31.1	31.2	304.1	304.2	0.1 (*)
38	0.0	31.2	31.5	304.2	304.5	0.3 (*)
39	0.0	31.0	31.6	304.0	304.6	0.6 (*)
40	0.0	30.9	31.5	303.9	304.5	0.6 (*)
41	0.0	30.8	31.4	303.8	304.4	0.6 (*)

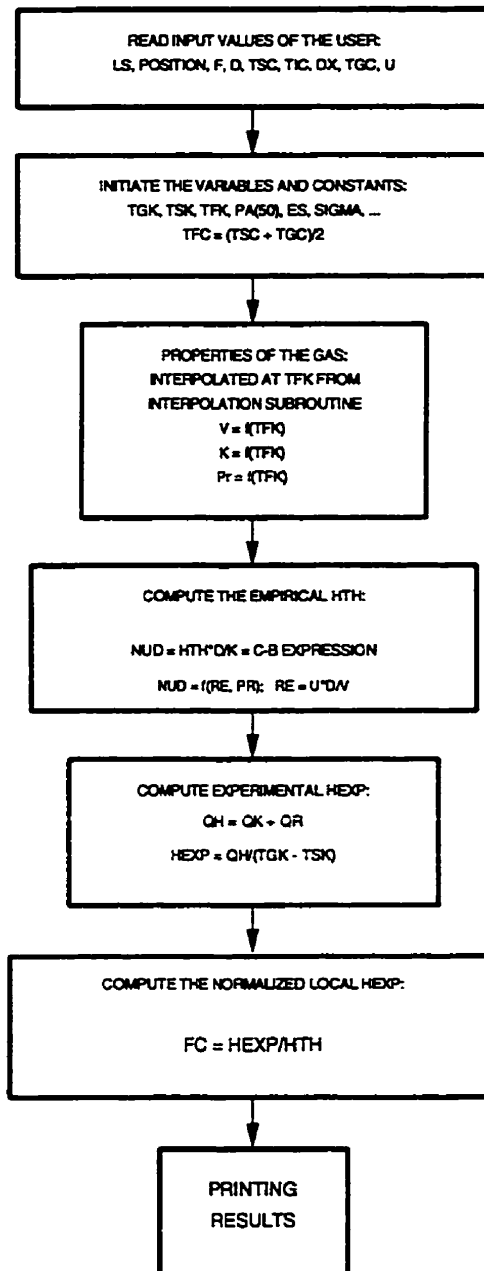
WHERE:

NO IS THE THERMOCOUPLE NUMBER,
 U-GAS IS THE PROPOSED VELOCITY OF THE GAS AT THIS LOCATION,
 TFM IS THE FLAME TEMPERATURE MEASURED AT THIS LOCATION,
 TFC IS THE CORRESPONDING CORRECTED FLAME TEMPERATURE,
 TFC-TFM IS THE DIFFERENCE BETWEEN THE CORRECTED AND THE MEASURED TEMPERATURE.

*: RE OR PE WAS OUT OF RANGE FOR COMPUTATION OF TFC

PROGRAM HCB-EXP.BAS

ALGORITHM OF HCB-EXP.BAS



```

10 '
20 '
30 '
40 '
50 '
60 '***** PROGRAM HCB-EXP.BAS *****'
70 '
80 '
90 '
100 '
110 '      *      HEAT-TRANSFER COEFFICIENTS      *
120 '      *      AROUND DEW SPECIMEN IN A      *
130 '      *      HIGH VELOCITY GAS STREAM      *
140 '      *
150 '      *      THEORETICAL H COMPUTED FROM      *
160 '      *      MODEL OF CHURCHILL & BERNSTEIN  *
170 '      *      (1977)                          *
180 '      *
190 '
200 ' *** NB.: PROPERTIES OF THE GAS ARE EVALUATED AT GAS FILM TEMPERATURE ***
210 '
220 '
230 '
240 '
250 '
300 '***** PRINCIPAL PROGRAM *****'
310 '
320 '
330 '***** READ SOME INPUT VALUES LIKE THE FLAME TEMPERATURE MEASURED *****
340 GOSUB 1000
350 '
360 '*** COMPUTE THE THEORETICAL AND EXPERIMENTAL HEAT-TRANSFER COEFFICIENTS ***
370 GOSUB 2000
380 '
390 '***** PRINT THE RESULTS *****
400 GOSUB 3000
410 '
420 END
500 '
510 '
520 '
530 '***** SUBROUTINES *****'
540 '
550 '
1000 '*** SUBROUTINE FOR READING THE DATA FROM THE USER:
1010 CLS
1020 PRINT "ENTER THE NO. OF THE CONSIDERED LOCATION ON THE SPECIMEN (0 TO 10) "
1030 PRINT "AND PRESS ENTER": INPUT LS: IF LS<0 OR LS>10 GOTO 1020
1035 PRINT "ENTER THE NO. OF THE CONSIDERED POSITION ON THE SPECIMEN"
1036 PRINT "AND PRESS ENTER": INPUT POSITION
1040 PRINT "ENTER THE SUGGESTED LOCAL HEAT-TRANSFER COEFFICIENT FACTOR"
1050 PRINT "AND PRESS ENTER": INPUT F: IF F<0 OR F>10 GOTO 1040
1060 PRINT "ENTER THE CHARACTERISTIC DIAMETER D (IN MM) OF THE SPECIMEN"
1070 PRINT "AND PRESS ENTER": INPUT D: IF D<0 GOTO 1060 ELSE D = D*.001
1080 PRINT "ENTER THE LOCAL SURFACE TEMPERATURE OF THE SPECIMEN (IN DEGREE C)"
1090 PRINT "AND PRESS ENTER": INPUT TSC: IF TSC<-273 OR TSC>2000 GOTO 1080
1100 PRINT "ENTER THE LOCAL INTERNAL TEMPERATURE OF THE SPECIMEN (IN DEGREE C)"
1110 PRINT "AND PRESS ENTER": INPUT TIC: IF TIC<-273 OR TIC>2000 GOTO 1100
1120 PRINT "ENTER THE DEPTH OF THE INTERNAL TEMPERATURE MEASUREMENT (IN MM)"
1130 PRINT "AND PRESS ENTER": INPUT DX: IF DX<0 GOTO 1120 ELSE DX = DX*.001
1140 PRINT "ENTER THE FLAME TEMPERATURE (IN DEGREE C)"
1150 PRINT "AND PRESS ENTER": INPUT TGC: IF TGC<-273 OR TGC>2000 GOTO 1140
1160 PRINT "ENTER VELOCITY IN M/S AND PRESS ENTER:"
1170 INPUT U: IF U<0 GOTO 1160
1180 PRINT "PLEASE WAIT!"
1190 RETURN
1200 '
1210 '
2000 '*** SUBROUTINE FOR COMPUTATION OF THE HEAT-TRANSFER COEFFICIENTS:
2010 '
2020 ' DATA FOR HTH EXPRESSION:
2030 TFC = (TGC + TSC)/2

```

```

2040 TGC = TGC + 273
2050 TSK = TSC + 273
2060 TFC = TFC + 273
2070 DIM PA(50)
2080 GOSUB 10000: V = NUAIR
2090 GOSUB 20000: K = KAIR
2100 GOSUB 30000: PR = PRAIR
2110 RE = U*D/V
2120 PE = RE*PR
2130 ' COMPUTATION OF MEAN HTH, USING THE EXPRESSION OF CHURCHILL & BERNSTEIN:
2140 C = .683
2150 N = .466
2160 NUD=.3+.62*RE^.5*PR^.33333*(1+(RE/282000!)^.625)^.8/(1+ (.4/PR)^.66667)^.75
2170 HTH = NUD*K/D
2180 '
2190 '
2200 'COMPUTATION OF HEXP:
2210 IF LS = 0 THEN GOSUB 2800 ELSE
2220 IF LS >= 1 AND LS <= 3 THEN GOSUB 2900 ELSE
2230 IF LS >= 4 AND LS <= 6 THEN GOSUB 2900 ELSE
2240 IF LS >= 7 AND LS <= 9 THEN GOSUB 2900 ELSE
2250 IF LS = 10 THEN GOSUB 2900
2260 ' ENERGY LOST BY RADIATION FROM THE SPECIMEN LOCATION, QR:
2270 SIGMA = 5.669E-08
2280 ES = .85
2290 QR = SIGMA*ES*(FSA*(TSK^4-TAK^4) + FSN*(TSK^4-TNK^4) + FSC*(TSK^4-TCK^4))
2300 ' ENERGY LOST BY CONDUCTION IN THE SPECIMEN LOCATION, QK:
2310 KS0 = 5.3
2320 DK = .01458
2330 KS = DK*TSK + KS0
2340 GRADT = (TIC - TSC)/DX
2350 QK = -KS*GRADT
2360 ' ENERGY PROVIDED BY CONVECTION BY THE FLAME TO THE SPECIMEN, QH:
2370 QH = QR + QK
2380 '
2390 '
2400 ' DEDUCTION OF THE VALUE OF HEXP:
2410 ' QH = HEXP*(TGC-TSK)
2420 HEXP = QH/(TGC-TSK)
2430 ' COMPUTE THE EXPERIMENTAL LOCAL HEAT-TRANSFER COEFFICIENT FACTOR, FC:
2440 FC = HEXP/HTH
2500 RETURN
2510 '
2800 '*** DEFINE THE RADIATION SHAPE FACTORS FOR THE LEADING EDGE:
2810 ' FRACTION OF ENERGY LEAVING THE SURFACE TO THE SURROUNDINGS (AT TAK):
2820 FSA = .88: TAK = 290 'K
2830 ' FRACTION OF ENERGY LEAVING THE SURFACE TO THE NOZZLE (AT TNK):
2840 FSN = .072: TNK = 1020 'K
2850 ' FRACTION OF ENERGY LEAVING THE SURFACE TO THE COMBUSTOR (AT TCK):
2860 FSC = .048: TCK = TGC 'K
2870 GOTO 2260
2880 RETURN
2890 '
2900 '*** DEFINE THE RADIATION SHAPE FACTORS ELSEWHERE:
2910 ' FRACTION OF ENERGY LEAVING THE SURFACE TO THE SURROUNDINGS (AT TAK):
2920 FSA = 1!: TAK = 290 'K
2930 ' FRACTION OF ENERGY LEAVING THE SURFACE TO THE NOZZLE (AT TNK):
2940 FSN = 0!: TNK = 1020 'K
2950 ' FRACTION OF ENERGY LEAVING THE SURFACE TO THE COMBUSTOR (AT TCK):
2960 FSC = 0!: TCK = TGC 'K
2970 GOTO 2260
2980 RETURN
2990 '
3000 '*** SUBROUTINE FOR PRINTING THE RESULTS:
3010 LPRINT ***** PROGRAM HCB-EXP.BAS *****
3020 LPRINT *****
3030 LPRINT ***** EXPERIMENTAL HEAT-TRANSFER COEFFICIENT COMPUTATION *****
3040 LPRINT ***** FOR SPECIMEN LOCATION NO. ";
3050 LPRINT USING "##, "; LS;
3055 LPRINT USING "AND POSITION NO. ## _*_*_*_"; POSITION
3060 LPRINT *****
3070 LPRINT *****

```

```

3080 LPRINT ""
3090 LPRINT "      GENERAL DATA:"
3100 LPRINT ""
3110 LPRINT USING "FLAME TEMPERATURE = #### C"; TGC;
3120 LPRINT USING "  OR #### K"; TKG
3130 LPRINT USING "VELOCITY OF THE GAS = ###.# M/S"; U
3140 LPRINT USING "LOCAL SURFACE TEMPERATURE OF THE SPECIMEN = ####.# C"; TSC;
3150 LPRINT USING "  OR ####.# K"; TSK
3160 LPRINT USING "LOCAL INTERNAL TEMPERATURE OF THE SPECIMEN = ####.# C"; TIC;
3170 LPRINT USING "  OR ####.# K"; TIC + 273
3180 LPRINT USING "MEASURED AT ##.# MM FROM THE SURFACE"; DX*1000
3190 LPRINT USING "CHARACTERISTIC DIAMETER OF THE SPECIMEN = #.# MM"; D*1000
3200 LPRINT USING "GAS FILM TEMPERATURE = #### C"; TFC;
3210 LPRINT USING "  OR #### K"; TFK
3220 LPRINT ""
3230 LPRINT "      DATA AND INTERMEDIATE RESULTS USED TO EVALUATE"
3240 LPRINT "      THE THEORETICAL HEAT-TRANSFER COEFFICIENT:"
3250 LPRINT "      (CHURCHILL & BERNSTEIN'S EXPRESSION IS USED)"
3260 LPRINT ""
3270 LPRINT USING "KINEMATIC VISCOSITY OF THE GAS = ##.###^ M^2/S"; V
3280 LPRINT USING "THERMAL CONDUCTIVITY OF THE GAS = ##.###^ W/M/K"; K
3290 LPRINT USING "REYNOLDS NUMBER, RE = #####"; RE
3300 LPRINT USING "PRANDTL NUMBER, PR = #.###"; PR
3310 LPRINT USING "PECLET NUMBER, PE = RE*PR = #####"; PE
3320 IF PE < .2 OR RE > 1E+07 OR RE < 100! , THEN LPRINT "RE OR PE OUT OF RANGE"
3330 LPRINT USING "NUSETT NUMBER, NUD = ##.##"; NUD
3340 LPRINT ""
3350 LPRINT "      DATA AND INTERMEDIATE RESULTS USED TO EVALUATE"
3360 LPRINT "      THE EXPERIMENTAL HEAT-TRANSFER COEFFICIENT:"
3370 LPRINT ""
3380 LPRINT USING "STEFAN-BOLTZMANN CONSTANT = ##.###^ W/M^2/T^4"; SIGMA
3390 LPRINT USING "EMISSIVITY OF THE SPECIMEN AFTER OXIDATION = #.###"; ES
3400 LPRINT "RADIATION SHAPE FACTOR BETWEEN THE LOCATION AND THE SURROUNDINGS,";
3410 LPRINT USING " FSA = #.###"; FSA
3420 LPRINT USING "TEMPERATURE OF THE SURROUNDINGS = #### C"; TAK-273;
3430 LPRINT USING "  OR #### K"; TAK
3440 LPRINT "RADIATION SHAPE FACTOR BETWEEN THE LOCATION AND THE NOZZLE,";
3450 LPRINT USING " FSN = #.###"; FSN
3460 LPRINT USING "TEMPERATURE OF THE NOZZLE = #### C"; TNK-273;
3470 LPRINT USING "  OR #### K"; TNK
3480 LPRINT "RADIATION SHAPE FACTOR BETWEEN THE LOCATION AND THE COMBUSTOR,";
3490 LPRINT USING " FSC = #.###"; FSC
3500 LPRINT USING "TEMPERATURE OF THE COMBUSTOR = #### C"; TCK-273;
3510 LPRINT USING "  OR #### K"; TCK
3520 LPRINT "TEMPERATURE GRADIENT AT THE SPECIMEN SURFACE = ";
3530 LPRINT USING "##.###^ C/M"; GRADT
3540 LPRINT USING "THERMAL CONDUCTIVITY OF RENE-80 = ###.# W/M/K"; KS;
3550 LPRINT USING "  AT #### C"; TSC
3560 LPRINT USING "      RADIATION HEAT FLUX, QR = ##.###^ W/M^2"; QR
3570 LPRINT USING "      CONDUCTION HEAT FLUX, QK = ##.###^ W/M^2"; QK
3580 LPRINT USING "      CONVECTION HEAT FLUX, QH = ##.###^ W/M^2"; QH
3590 LPRINT ""
3600 LPRINT ""
3610 LPRINT "*****";
3620 LPRINT "*****";
3630 LPRINT "*****";
3640 LPRINT "*****";
3650 LPRINT "****";
3660 LPRINT "      ****";
3670 LPRINT "      THEORETICAL MEAN HEAT-TRANSFER COEFFICIENT, HTH = ";
3680 LPRINT USING "##### W/M^2/K      _*_^"; HTH
3690 LPRINT "      SUGGESTED LOCAL HEAT-TRANSFER COEFFICIENT FACTOR, F = ";
3700 LPRINT USING "###      _*_^"; F
3710 LPRINT "      LOCAL HEAT-TRANSFER COEFFICIENT, HTH*F = ";
3720 LPRINT USING "##### W/M^2/K      _*_^"; HTH*F
3730 LPRINT "****";
3740 LPRINT "      ****";
3750 LPRINT "      EXPERIMENTAL HEAT-TRANSFER COEFFICIENT, HEXP = ";
3760 LPRINT USING "##### W/M^2/K      _*_^"; HEXP
3770 LPRINT "      COMPUTED LOCAL HEAT-TRANSFER COEFFICIENT FACTOR, FC = ";
3780 LPRINT USING "###      _*_^"; FC
3790 LPRINT "****";

```

```

3800 LPRINT "      ****"
3810 LPRINT "*****";
3820 LPRINT "*****"
3830 LPRINT "*****";
3840 LPRINT "*****"
3850 LPRINT CHR$(12)
3860 RETURN
3870 '
3880 '
10000 '*** SUBROUTINE NUAIR:
10100 ' EVALUATION OF THE EXACT VALUE OF NUAIR:
10200 OPEN"I",#1,"NUAIR"
10300 INPUT#1, NT, DT, TO
10400 FOR I=1 TO NT: INPUT#1, PA(I): NEXT I
10500 CLOSE#1
10600 T = TFK
10700 ' GET THE INTERPOLATED VALUE OF NUAIR:
10800 GOSUB 50000
10900 NUAIR = PA
11000 RETURN
11100 '
20000 '*** SUBROUTINE KAIR:
20100 ' EVALUATION OF THE EXACT VALUE OF KAIR:
20200 OPEN"I",#2,"KAIR"
20300 INPUT#2, NT, DT, TO
20400 FOR I=1 TO NT: INPUT#2, PA(I): NEXT I
20500 CLOSE#2
20600 T = TFK
20700 ' GET THE INTERPOLATED VALUE OF KAIR:
20800 GOSUB 50000
20900 KAIR = PA
21000 RETURN
21100 '
30000 '*** SUBROUTINE PRAIR:
30100 ' EVALUATION OF THE EXACT VALUE OF PRAIR:
30200 OPEN"I",#3,"PRAIR"
30300 INPUT#3, NT, DT, TO
30400 FOR I=1 TO NT: INPUT#3, PA(I): NEXT I
30500 CLOSE#3
30600 T = TFK
30700 ' GET THE INTERPOLATED VALUE OF PRAIR:
30800 GOSUB 50000
30900 PRAIR = PA
31000 RETURN
31100 '
50000 '*** INTERPOLATION SUBROUTINE:
50100 ' INTERPOLATE TO FIND THE EXACT VALUE OF THE PROPERTY, "PA",
50200 ' FOR THE TEMPERATURE, T, CONSIDERED:
50300 NI = INT((T - TO)/DT) + 1
50400 IF T < TO THEN PA = PA(1):PRINT "EXTRAPOLATION UNDER ", TO," K":GOTO 50900
50500 IF T >= (NT-1)*DT+TO THEN PA = PA(NT): GOTO 50700
50600 PA = PA(NI) + (PA(NI+1) - PA(NI))*(T - (NI-1)*DT - TO)/DT: GOTO 50900
50700 IF T > (NT-1)*DT+TO THEN PRINT "EXTRAPOLATION OVER ", (NT-1)*DT+TO," K"
50800 GOTO 50900
50900 RETURN

```



```

***** PROGRAM HCB-EXP.BAS *****
***** EXPERIMENTAL HEAT-TRANSFER COEFFICIENT COMPUTATION *****
***** FOR SPECIMEN LOCATION NO. 0, AND POSITION NO. 9 *****
*****

```

GENERAL DATA:

```

FLAME TEMPERATURE = 1287 C OR 1560 K
VELOCITY OF THE GAS = 313.0 M/S
LOCAL SURFACE TEMPERATURE OF THE SPECIMEN = 1157.0 C OR 1430.0 K
LOCAL INTERNAL TEMPERATURE OF THE SPECIMEN = 1157.0 C OR 1430.0 K
MEASURED AT 1.0 MM FROM THE SURFACE
CHARACTERISTIC DIAMETER OF THE SPECIMEN = 6.40 MM
GAS FILM TEMPERATURE = 1222 C OR 1495 K

```

DATA AND INTERMEDIATE RESULTS USED TO EVALUATE
THE THEORETICAL HEAT-TRANSFER COEFFICIENT:
(CHURCHILL & BERNSTEIN'S EXPRESSION IS USED)

```

KINEMATIC VISCOSITY OF THE GAS = 2.28E-04 M^2/S
THERMAL CONDUCTIVITY OF THE GAS = 9.43E-02 W/M/K
REYNOLDS NUMBER, RE = 8789
PRANDTL NUMBER, PR = 0.705
PECLET NUMBER, PE = RE*PR = 6196
NUSSELT NUMBER, NUD = 38.4

```

DATA AND INTERMEDIATE RESULTS USED TO EVALUATE
THE EXPERIMENTAL HEAT-TRANSFER COEFFICIENT:

```

STEFAN-BOLTZMANN CONSTANT = 5.669E-08 W/M^2/T^4
EMISSION OF THE SPECIMEN AFTER OXIDATION = 0.85
RADIATION SHAPE FACTOR BETWEEN THE LOCATION AND THE SURROUNDINGS, FSA = 0.880
TEMPERATURE OF THE SURROUNDINGS = 17 C OR 290 K
RADIATION SHAPE FACTOR BETWEEN THE LOCATION AND THE NOZZLE, FSN = 0.072
TEMPERATURE OF THE NOZZLE = 747 C OR 1020 K
RADIATION SHAPE FACTOR BETWEEN THE LOCATION AND THE COMBUSTOR, FSC = 0.048
TEMPERATURE OF THE COMBUSTOR = 1287 C OR 1560 K
TEMPERATURE GRADIENT AT THE SPECIMEN SURFACE = 0.00E+00 C/M
THERMAL CONDUCTIVITY OF RENE-80 = 26.1 W/M/K AT 1157 C
RADIATION HEAT FLUX, QR = 1.84E+05 W/M^2
CONDUCTION HEAT FLUX, QK = 0.00E+00 W/M^2
CONVECTION HEAT FLUX, QH = 1.84E+05 W/M^2

```

```

*****
*****
*** THEORETICAL MEAN HEAT-TRANSFER COEFFICIENT, HTH = 567 W/M^2/K ***
*** SUGGESTED LOCAL HEAT-TRANSFER COEFFICIENT FACTOR, F = 2.500 ***
*** LOCAL HEAT-TRANSFER COEFFICIENT, HTH*F = 1416 W/M^2/K ***
***
*** EXPERIMENTAL HEAT-TRANSFER COEFFICIENT, HEXP = 1412 W/M^2/K ***
*** COMPUTED LOCAL HEAT-TRANSFER COEFFICIENT FACTOR, FC = 2.493 ***
***
*****
*****

```

PROGRAM HCB-EMP.BAS

```

10 '
20 '
30 '
40 '
50 '
60 '***** PROGRAM HCB-EMP.BAS *****'
70 '
80 '
90 '
100 '
110 '          *
120 '          * HEAT-TRANSFER COEFFICIENT *
130 '          * AROUND CYLINDERS ACROSS *
140 '          * HIGH VELOCITY GAS STREAM *
150 '          *
160 '          * MODEL OF CHURCHILL & BERNSTEIN *
170 '          * (1977) *
180 '          *
190 ' *** NB.: PROPERTIES OF THE GAS ARE EVALUATED AT GAS FILM TEMPERATURE ***
200 '
210 '
220 '
230 '
240 '
300 '***** PRINCIPAL PROGRAM *****'
310 '
320 '
330 '***** READ SOME INPUT VALUES LIKE THE FLAME TEMPERATURE MEASURED *****'
340 GOSUB 1000
350 '
360 '***** COMPUTE THE REAL FLAME TEMPERATURE *****'
370 GOSUB 2000
380 '
390 '***** PRINT THE RESULTS *****'
400 GOSUB 3000
410 '
420 END
500 '
510 '
520 '
530 '***** SUBROUTINES *****'
540 '
550 '
1000 '*** SUBROUTINE FOR READING THE DATA FROM THE USER:
1010 CLS
1020 PRINT "ENTER THE FLAME TEMPERATURE IN DEGREE CELCIUS";
1030 PRINT " AND PRESS ENTER:": INPUT TGC
1040 PRINT "ENTER THE SURFACE TEMPERATURE OF THE SPECIMEN IN DEGREE CELCIUS"
1050 PRINT "AND PRESS ENTER:": INPUT TSC
1060 PRINT "ENTER THE CORRESPONDING LOCAL HEAT-TRANSFER FACTOR";
1070 PRINT " AND PRESS ENTER:": INPUT F
1080 PRINT "ENTER THE DIAMETER D (IN MM) OF THE LOCAL AREA OF THE OBJECT"
1090 PRINT "AND PRESS ENTER:": INPUT D: D = D*.001
1100 PRINT "ENTER VELOCITY IN M/S AND PRESS ENTER:"
1110 INPUT U: PRINT "PLEASE WAIT!"
1120 RETURN
1130 '
1140 '
2000 '*** SUBROUTINE FOR COMPUTATION OF THE HEAT-TRANSFER COEFFICIENT:
2010 '
2020 ' CONSTANT DATA:
2030 TFC = (TGC + TSC)/2
2040 TGK = TGC + 273
2050 TSK = TSC + 273
2060 TFK = TFC + 273
2070 DIM PA(50)
2080 GOSUB 10000: V = NUAIR
2090 GOSUB 20000: K = KAIR
2100 GOSUB 30000: PR = PRAIR
2110 RE = U*D/V
2120 PE = RE*PR
2130 ' COMPUTATION OF MEAN H:

```

```

2140      C = .683
2150      N = .466
2160      NUD=.3+.62*RE^.5*PR^.33333*(1+(RE/282000!)^.625)^(.8/(1+(.4/PR)^(.66667))^(.75
2170      H = NUD*K/D
2180      RETURN
2190      '
2200      '
3000      '*** SUBROUTINE FOR PRINTING THE RESULTS:
3010      '
3020      LPRINT ***** PROGRAM HCB-EMP.BAS *****
3030      LPRINT *****
3040      LPRINT ***** HEAT-TRANSFER COEFFICIENT COMPUTATION *****
3050      LPRINT ***** USING THE EXPRESSION OF CHURCHILL & BERNSTEIN *****
3060      LPRINT *****
3070      LPRINT *****
3080      LPRINT ""
3090      LPRINT ""
3100      LPRINT USING "FLAME TEMPERATURE = #### C"; TGC;
3110      LPRINT USING " OR #### K"; TGC
3120      LPRINT USING "SPECIMEN TEMPERATURE = #### C"; TSC;
3130      LPRINT USING " OR #### K"; TSC
3140      LPRINT USING "GAS FILM TEMPERATURE = #### C"; TFC;
3150      LPRINT USING " OR #### K"; TFC
3160      LPRINT USING "VELOCITY OF THE GAS = ### M/S"; U
3170      LPRINT USING "CORRESPONDING DIAMETER = #.## MM"; D*1000
3180      LPRINT USING "KINEMATIC VISCOSITY OF THE GAS = ##.##^M^2/S"; V
3190      LPRINT USING "THERMAL CONDUCTIVITY OF THE GAS = ##.##^W/M/K"; K
3200      LPRINT USING "REYNOLDS NUMBER, RE = #####"; RE
3210      LPRINT USING "PRANDTL NUMBER, PR = #.###"; PR
3220      LPRINT USING "PECLET NUMBER, PE = RE*PR = #####"; PE
3230      IF PE < .2 OR RE > 1E+07 OR RE < 100! , THEN LPRINT "RE OR PE OUT OF RANGE"
3240      LPRINT USING "NUSELT NUMBER, NUD = ##.##"; NUD
3250      LPRINT ""
3260      LPRINT ""
3270      LPRINT USING "LOCAL HEAT-TRANSFER COEFFICIENT FACTOR, F = #.##"; F
3280      LPRINT ""
3290      LPRINT *****
3300      LPRINT *****
3310      LPRINT *****
3320      LPRINT ***** MEAN HEAT-TRANSFER COEFFICIENT, H = ";
3330      LPRINT USING "##### W/M^2/K _*_ _"; H
3340      LPRINT ***** LOCAL HEAT-TRANSFER COEFFICIENT, H*F = ";
3350      LPRINT USING "##### W/M^2/K _*_ _"; H*F
3360      LPRINT *****
3370      LPRINT *****
3380      LPRINT *****
3390      LPRINT CHR$(12)
3400      RETURN
3410      '
3420      '
10000     '*** SUBROUTINE NUAIR:
10100     ' EVALUATION OF THE EXACT VALUE OF NUAIR:
10200     OPEN "I",#1, "NUAIR"
10300     INPUT#1, NT, DT, T0
10400     FOR I=1 TO NT: INPUT#1, PA(I): NEXT I
10500     CLOSE#1
10600     T = TFK
10700     ' GET THE INTERPOLATED VALUE OF NUAIR:
10800     GOSUB 50000
10900     NUAIR = PA
11000     RETURN
11100     '
20000     '*** SUBROUTINE KAIR:
20100     ' EVALUATION OF THE EXACT VALUE OF KAIR:
20200     OPEN "I",#2, "KAIR"
20300     INPUT#2, NT, DT, T0
20400     FOR I=1 TO NT: INPUT#2, PA(I): NEXT I
20500     CLOSE#2
20600     T = TFK
20700     ' GET THE INTERPOLATED VALUE OF KAIR:
20800     GOSUB 50000
20900     KAIR = PA

```

```

21000 RETURN
21100 '
30000 '*** SUBROUTINE PRAIR:
30100 ' EVALUATION OF THE EXACT VALUE OF PRAIR:
30200 OPEN"1",#3, "PRAIR"
30300 INPUT#3, NT, DT, T0
30400 FOR I=1 TO NT: INPUT#3, PA(I): NEXT I
30500 CLOSE#3
30600 T = TFK
30700 ' GET THE INTERPOLATED VALUE OF PRAIR:
30800 GOSUB 50000
30900 PRAIR = PA
31000 RETURN
31100 '
50000 '*** INTERPOLATION SUBROUTINE:
50100 ' INTERPOLATE TO FIND THE EXACT VALUE OF THE PROPERTY, "PA",
50200 ' FOR THE TEMPERATURE, T, CONSIDERED:
50300 NI = INT((T - T0)/DT) + 1
50400 IF T < T0 THEN PA = PA(1):PRINT "EXTRAPOLATION UNDER ", T0," K":GOTO 50900
50500 IF T >= (NT-1)*DT+T0 THEN PA = PA(NT): GOTO 50700
50600 PA = PA(NI) + (PA(NI+1) - PA(NI))*(T - (NI-1)*DT - T0)/DT: GOTO 50900
50700 IF T > (NT-1)*DT+T0 THEN PRINT "EXTRAPOLATION OVER ", (NT-1)*DT+T0," K"
50800 GOTO 50900
50900 RETURN

```

```

***** PROGRAM HCB-EMP.BAS *****
*****
***** HEAT-TRANSFER COEFFICIENT COMPUTATION *****
***** USING THE EXPRESSION OF CHURCHILL & BERNSTEIN *****
*****

```

```

FLAME TEMPERATURE = 468 C OR 741 K
SPECIMEN TEMPERATURE = 468 C OR 741 K
GAS FILM TEMPERATURE = 468 C OR 741 K
VELOCITY OF THE GAS = 118 M/S
CORRESPONDING DIAMETER = 6.40 MM
KINEMATIC VISCOSITY OF THE GAS = 7.28E-05 M^2/S
THERMAL CONDUCTIVITY OF THE GAS = 5.46E-02 W/M/K
REYNOLDS NUMBER, RE = 10370
PRANDTL NUMBER, PR = 0.686
PECLET NUMBER, PE = RE*PR = 7114
NUSSELT NUMBER, NUD = 41.5

```

LOCAL HEAT-TRANSFER COEFFICIENT FACTOR, F = 2.50

```

*****
*****
*** MEAN HEAT-TRANSFER COEFFICIENT, H = 354 W/M^2/K ***
*** LOCAL HEAT-TRANSFER COEFFICIENT, H*F = 884 W/M^2/K ***
***
*****
*****

```

APPENDIX I

GENERALISATION OF THE WALKER SUBROUTINE FOR ISOTROPIC MATERIALS TO THE CASE OF ORTHOTROPIC MATERIALS

The original version of the subroutine of Walker introduced in Subsection 5.1.2 is designed to compute the stress, the total strain and the viscoplastic strain for materials showing isotropic elastic properties. It was required for the needs of the thermal fatigue program exposed in the introduction of this thesis that the subroutine of Walker can also run for materials with orthotropic elastic properties. This Appendix briefly explains the modifications that have been brought to the subroutine in this matter and gives a listing of the modified subroutine at the end.

I.1 Change of the Definition of the Iteration Parameter RHO(1)

In the subroutine of Walker, the i^{th} component of the plastic strain increment, DEPLAS(I), is given by:

$$d\epsilon_i^p = \frac{\rho_1}{2\mu} \left(S_i - \frac{2}{3} \Omega_i \right) \quad (\text{I-1})$$

where:

S_i (DEVSIG(I)) is the i^{th} component of the deviatoric stress;

Ω_i (BACK(I)) is the i^{th} component of the back stress;

μ (MU) is one of the constants of Lamé and

ρ_1 (RHO(1)) is an iteration parameter

(N.B.: the names in brackets are the names of the variables as defined by Walker in his subroutine).

In the constitutive viscoplastic model of Walker, the i^{th} component of the plastic strain

rate, $d\epsilon_i^p/dt$, is expressed by the following flow rule:

$$\frac{d\epsilon_i^p}{dt} = \frac{3}{2}\phi \left(s_i - \frac{2}{3}\Omega_i \right) \quad (I-2)$$

where:

ϕ is the plastic multiplier rate and

dt (DSUBTIME) is the time subincrement.

By comparing Equations I-1 and I-2, it can be found that ρ_1 (RHO(1)) is related to the plastic multiplier rate, ϕ , as following:

$$\rho_1 = 3\mu \phi dt \quad (I-3)$$

As mentioned above, RHO(1) is an iteration parameter that Walker used to find the proper value of the plastic multiplier rate at each subincrement of time during the execution of his subroutine. The value of RHO(1) is adjusted according to the iterative method of Newton-Ralphson until convergence. As it can be noted in Equation I-3, RHO(1) is arbitrarily a function of μ (MU), a constant which only applies to isotropic materials. In order to extend the application of the subroutine of Walker to orthotropic materials, a new definition of RHO(1) has to be used where the constant MU is removed, as:

$$\rho_1 = \frac{3}{2} \phi dt \quad (I-4)$$

The introduction of the new definition of RHO(1) in the subroutine only consisted to substitute the old RHO(1) with $RHO(1)/(2*MU)$. The changes involved by this substitution can be noted by the absence of the constant MU in the listing of modified subroutine at the end of this Appendix.

I.2 Implementation of the Stiffness Matrix C for Orthotropic Materials

In the original version of the subroutine of Walker, the elastic properties of isotropic materials, which are the Young's modulus and the poisson ratio, are input through the UMAT_CON_HASTX subroutine as a function of temperature. These two elastic constants are required in the determination of the constants of lamé used in the UMAT_INT_HASTX subroutine which solves the viscoplastic flow rule and the evolutionary rules of the stress and the back stress, all written in the integral formulation of Walker. The stiffness matrix, C, which is employed at different locations of the subroutine of Walker, is builded from the elastic properties in the UMAT_ELASTIC subroutine, assuming again the isotropy.

In order to deal with orthotropic materials, the constants of Lamé have first to be replaced by combinations of the components of the stiffness matrix C in the evolutionary rule of the stress. The differential form of the evolutionary rule of stress expressed in terms of the elastic strain rates and for isotropic materials is:

for i = 1 to 3:

$$\dot{\sigma}_i = \lambda (\dot{\epsilon}_1^{el} + \dot{\epsilon}_2^{el} + \dot{\epsilon}_3^{el}) + 2\mu \dot{\epsilon}_i^{el} \quad (I-5)$$

for i = 4 to 6:

$$\dot{\sigma}_i = 2\mu \dot{\epsilon}_i^{el} \quad (I-6)$$

where:

$\dot{\sigma}_i$ is the i^{th} component of the cauchy stress rate;

$\dot{\epsilon}_i^{el}$ is the i^{th} component of the elastic strain rate.

In the subroutine of Walker, the elastic strain rate in Equations I-5 and I-6 is expressed in term of the total strain rate minus the plastic strain rate ($\dot{\epsilon}_i - \dot{\epsilon}_i^p$). Also, the plastic

strain rate has been substituted by the Equation I-2 with the deviatoric stress (S) expressed in term of the cauchy stress (σ) and the plastic multiplier rate ($\dot{\phi}$) expressed in term of ρ_1 (see the Equation I-3). The resulting expression of the Equations I-5 and I-6 are:

for i = 1:

$$\begin{aligned} \dot{\sigma}_1 + \frac{2}{3} \frac{\rho_1}{dt} \sigma_1 &= \frac{\rho_1}{3dt} (\sigma_2 + \sigma_3) \\ &+ \frac{1}{2\mu} \left[(\lambda + 2\mu) \left(2\mu \dot{\epsilon}_1 + \frac{2}{3} \frac{\rho_1}{dt} \Omega_1 \right) \right. \\ &\quad + \lambda \left(2\mu \dot{\epsilon}_2 + \frac{2}{3} \frac{\rho_1}{dt} \Omega_2 \right) \\ &\quad \left. + \lambda \left(2\mu \dot{\epsilon}_3 + \frac{2}{3} \frac{\rho_1}{dt} \Omega_3 \right) \right] \end{aligned} \quad (I-7)$$

for i = 2:

$$\begin{aligned} \dot{\sigma}_2 + \frac{2}{3} \frac{\rho_1}{dt} \sigma_2 &= \frac{\rho_1}{3dt} (\sigma_1 + \sigma_3) \\ &+ \frac{1}{2\mu} \left[(\lambda + 2\mu) \left(2\mu \dot{\epsilon}_2 + \frac{2}{3} \frac{\rho_1}{dt} \Omega_2 \right) \right. \\ &\quad + \lambda \left(2\mu \dot{\epsilon}_1 + \frac{2}{3} \frac{\rho_1}{dt} \Omega_1 \right) \\ &\quad \left. + \lambda \left(2\mu \dot{\epsilon}_3 + \frac{2}{3} \frac{\rho_1}{dt} \Omega_3 \right) \right] \end{aligned} \quad (I-8)$$

for i = 3:

$$\begin{aligned} \dot{\sigma}_3 + \frac{2}{3} \frac{\rho_1}{dt} \sigma_3 &= \frac{\rho_1}{3dt} (\sigma_1 + \sigma_2) \\ &+ \frac{1}{2\mu} \left[(\lambda + 2\mu) \left(2\mu \dot{\epsilon}_3 + \frac{2}{3} \frac{\rho_1}{dt} \Omega_3 \right) \right. \\ &\quad + \lambda \left(2\mu \dot{\epsilon}_1 + \frac{2}{3} \frac{\rho_1}{dt} \Omega_1 \right) \\ &\quad \left. + \lambda \left(2\mu \dot{\epsilon}_2 + \frac{2}{3} \frac{\rho_1}{dt} \Omega_2 \right) \right] \end{aligned} \quad (I-9)$$

for i = 4 to 6:

$$\dot{\sigma}_i + \frac{\rho_1}{dt} \sigma_i = 2\mu \dot{\epsilon}_i + \frac{2}{3} \frac{\rho_1}{dt} \Omega_i \quad (\text{I-10})$$

In the case of orthotropic materials, Equations I-5 and I-6 have to be written in terms of the components of the stiffness matrix C instead of the constants of Lamé. As the stress matrix of 6 components is obtained by the product of the stiffness matrix (6X6) with the elastic strain matrix of 6 components, Equations I-5 and I-6 becomes:

for i = 1 to 3

$$\dot{\sigma}_i = \sum_{j=1}^3 C_{ij} \dot{\epsilon}_j \quad (\text{I-11})$$

for i = 4 to 6

$$\dot{\sigma}_i = C_{ii} \dot{\epsilon}_i \quad (\text{I-12})$$

and, as for Equations I-7 to I-10, the following Equations, which have to be implemented in the UMAT_INT_HASTX subroutine, can be derivated:

for i = 1

$$\begin{aligned} \dot{\sigma}_1 + \frac{\rho'_1}{3} (2C_{11} - C_{12} - C_{13}) \sigma_1 = & \frac{\rho'_1}{3} [(C_{11} + C_{13} - 2C_{12}) \sigma_2 + (C_{11} + C_{12} - 2C_{13}) \sigma_3] \\ & + C_{11} (\dot{\epsilon}_1 + \frac{2}{3} \rho'_1 \Omega_1) + C_{12} (\dot{\epsilon}_2 + \frac{2}{3} \rho'_1 \Omega_2) + C_{13} (\dot{\epsilon}_3 + \frac{2}{3} \rho'_1 \Omega_3) \end{aligned}$$

(I-13)

for i = 2

$$\sigma_i + \frac{3}{\rho'_i} (2C_{22} - C_{21} - C_{23}) \sigma_2 = \frac{3}{\rho'_i} [(C_{22} + C_{23} - 2C_{21}) \sigma_1 + (C_{22} + C_{21} - 2C_{23}) \sigma_3] + C_{21} (\epsilon_1 + \frac{3}{2} \rho'_i \sigma_1) + C_{22} (\epsilon_2 + \frac{3}{2} \rho'_i \sigma_2) + C_{23} (\epsilon_3 + \frac{3}{2} \rho'_i \sigma_3)$$

(I-14)

for i = 3

$$\sigma_i + \frac{3}{\rho'_i} (2C_{33} - C_{31} - C_{32}) \sigma_3 = \frac{3}{\rho'_i} [(C_{33} + C_{32} - 2C_{31}) \sigma_1 + (C_{33} + C_{31} - 2C_{32}) \sigma_2] + C_{31} (\epsilon_1 + \frac{3}{2} \rho'_i \sigma_1) + C_{32} (\epsilon_2 + \frac{3}{2} \rho'_i \sigma_2) + C_{33} (\epsilon_3 + \frac{3}{2} \rho'_i \sigma_3)$$

(I-15)

for i = 4 to 6

$$\sigma_i + 2\rho'_i C_{ii} \sigma_i = 2C_{ii} (\epsilon_i + \frac{3}{2} \rho'_i \sigma_i)$$

(I-16)

Note that, in Equations I-13 to I-16, ρ'_i is equal to the new $\text{RHO}(i)$ (ρ'_i defined by Equation I-4) divided by dr .

Obviously, the consideration of orthotropic materials in the subroutine of Walker also implies that the elastic moduli (E_{11} , E_{22} , E_{33}), the poisson ratios (ν_{12} , ν_{13} , ν_{23}) and the shear moduli (G_{12} , G_{23} , G_{13}) are input in the `UMAT_CON_HASTX` subroutine as a function of temperature and that the stiffness matrix, C , is builded from these elastic properties in the `UMAT_ELASTIC` subroutine, as shown in the listing of the modified version of the Walker's subroutine.

I.3 Listing of the Modified Version of the Subroutine of Walker

```

** MODELLING OF THE THERMO-MECHANICAL BEHAVIOUR OF DS RENE 80 (DSR80)
** USING THE MODIFIED SUBROUTINE OF WALKER
**
** File WALK-BR1.INP
**
*HEADING
WALKER'S SUBROUTINE USED TO SIMULATE 10 TMF CYCLES IN BR
** FILE twalker1a,two elements
*NODE
1,0.,0.
2,1.,0.
3,1.,1.
4,0.,1.
5,0.,0.,.5
6,1.,0.,.5
7,1.,1.,.5
8,0.,1.,.5
9,0.,0.,1.
10,1.,0.,1.
11,1.,1.,1.
12,0.,1.,1.
*NSET,NSET=B,GENERATE
1,4,1
*NSET,NSET=L
1,4,5,8,9,12
*NSET,NSET=F
1,2,5,6,9,10
*NSET,NSET=TOP,GENERATE
9,12,1
*NSET,NSET=NALL,GENERATE
1,12,1
*ELEMENT,TYPE=C3D8,ELSET=MODEL
1,1,2,3,4,5,6,7,8
2,5,6,7,8,9,10,11,12
*BOUNDARY
B,3
L,1
F,2
*AMPLITUDE,NAME=LCYCLIC,DEFINITION=TABULAR,VALUE=ABSOLUTE
0.000055,-0.000009,0.000110,-0.000017,0.000192,-0.000030,0.000316,-0.000045
0.000502,-0.000066,0.000780,-0.000091,0.001198,-0.000123,0.001824,-0.000161
0.002764,-0.000205,0.004174,-0.000256,0.006288,-0.000317,0.009460,-0.000390
0.014217,-0.000481,0.021353,-0.000593,0.032057,-0.000732,0.048114,-0.000904
0.072198,-0.001116,0.108324,-0.001373,0.162510,-0.001673,0.243795,-0.002013
0.365730,-0.002383,0.548610,-0.002767,0.822945,-0.003129,1.234440,-0.003410
1.851750,-0.003491,2.777550,-0.003248,4.166400,-0.002551,6.249600,-0.001339
9.374400,0.000189,14.061750,0.001945,21.090000,0.003507,30.090000,0.004609
39.090000,0.005343,48.090000,0.005817,57.090000,0.006116,66.089996,0.006290
75.089996,0.006383,84.089996,0.006449,93.089996,0.006479,102.089996,0.00649
111.089996,0.006504,120.089996,0.006513,129.089996,0.006505,138.089996,0.006504
147.089996,0.006506,150.000000,0.006506,150.000001,0.006524,150.000002,0.006524
150.000003,0.006524,150.000004,0.006524,150.000005,0.006524,150.000006,0.006542
150.000007,0.006560,150.000008,0.006578,150.000009,0.006614,150.000010,0.006632
150.000011,0.006668,150.000012,0.006703,150.000013,0.006754,150.000014,0.006822
150.000015,0.006905,150.040000,0.080000,150.120000,0.007134,150.150000,0.007285
150.179993,0.007476,150.270004,0.007586,150.360001,0.007610,150.539993,0.007658
150.809998,0.007639,151.259995,0.007663,151.889999,0.007569,152.789993,0.007131
154.139999,0.006405,156.210007,0.005266,159.360001,0.003899,164.039993,0.002622
169.440002,0.001676,174.839996,0.001193,180.240005,0.000797,185.639999,0.000564
191.039993,0.000373,196.440002,0.000242,201.839996,0.000132,207.240005,0.000058
212.639999,0.000011,218.039993,-0.000014,223.440002,-0.000025,228.84,-0.000032
234.240005,-0.000030,239.639999,-0.000028,240.000000,-0.000028
*AMPLITUDE,NAME=TCYCLIC,DEFINITION=TABULAR,VALUE=ABSOLUTE
0.000055,298.800000,0.000110,299.500000,0.000192,300.620000,0.000316,302.010000
0.000502,303.850000,0.000780,306.070000,0.001198,308.890000,0.001824,312.320000
0.002764,316.290000,0.004174,320.870000,0.006288,326.380000,0.009460,333.030000
0.014217,341.350000,0.021353,351.820000,0.032057,365.010000,0.048114,381.700000

```

```

0.072198,402.930000,0.108324,429.800000,0.162510,463.150000,0.243795,504.050000
0.365730,553.820000,0.548610,613.660000,0.822945,684.020000,1.234440,763.990000
1.851750,850.910000,2.777550,941.100000,4.166400,1031.290000,6.249600,1117.9000
9.374400,1200.510000,14.061750,1273.230000,21.090000,1333.160000,30.090,1372.69
39.090000,1395.430000,48.090000,1408.46,57.090000,1415.440000,66.089996,1419.55
75.089996,1422.290000,84.089996,1423.19,93.089996,1424.09000,102.089996,1424.99
111.089996,1425.000000,120.089996,1425.00,129.089996,1425.69,138.089996,1426.00
147.089996,1426.000000,150.000000,1426.00,150.000001,1425.00,150.000002,1425.00
150.000003,1425.000000,150.000004,1425.00,150.000005,1425.00,150.000006,1424.00
150.000007,1423.000000,150.000008,1422.00,150.000009,1420.00,150.000010,1419.00
150.000011,1417.000000,150.000012,1415.00,150.000013,1412.00,150.000014,1408.00
150.000015,1403.000000,150.010000,1396.00,150.040000,1388.00,150.089996,1377.00
150.179993,1362.000000,150.270004,1348.70,150.360001,1335.80,150.539993,1314.87
150.809998,1286.970000,151.259995,1240.88,151.889999,1182.49,152.789993,1120.45
154.139999,1041.500000,156.210007,945.13,159.360001,828.31,164.039993,702.80000
169.440002,600.610000,174.839996,537.95,180.240006,480.97,185.639999,445.280000
191.039993,413.310000,196.440002,391.60,201.839996,373.26,207.240006,359.650000
212.639999,348.740000,218.039993,339.94,223.440002,333.29,228.839996,327.510000
234.240006,323.36000,240.000000,319.200000
*INITIAL CONDITIONS,TYPE=TEMPERATURE
NALL,298.
*SOLID SECTION,ELSET=MODEL,MATERIAL=DSR80
*MATERIAL,NAME=DSR80
*USER MATERIAL,CONSTANTS=1
1.
*DEPVAR
29
*RESTART, WRITE, FREQUENCY = 1
**
** 10 THERMO-MECHANICAL CYCLES:
*STEP,INC=1000,CYCLIC=10
*STATIC
0.00006,240.,0.000001,1.
*BOUNDARY,AMPLITUDE=LCYCLIC
TOP,3,,0.050
*TEMPERATURE,AMPLITUDE=TCYCLIC
NALL
*EL PRINT,FREQUENCY=5
E
S
*NODE PRINT,FREQUENCY=5
U
*EL FILE
E,S,SDV
*NODE FILE, NSET=NALL,FREQUENCY=5
U,RF
*END STEP
**
** Walker's Subroutine
*USER SUBROUTINE

      SUBROUTINE UMAT(STRESS,STATE,DDSDDE,SSE,SPD,SCD,
&                    RPL,DDSDDT,DRPLDE,DRPLDT,
&                    STRAIN,DSTRAIN,TIME,DTIME,TEMP,DTEMP,
&                    PREDEF,DPRD,CMNAME,NDI,NSHEAR,NTENS,NSTATV,
&                    PROPS,NPROPS,COORDS,DROT)
      IMPLICIT REAL*8 (A-H,O-Z)
      PARAMETER (MAXPARAM = 1)
      PARAMETER (TINY = 1.0E-15)

C *** SUBROUTINE ARGUMENT PARAMETERS ***

C      STRESS : PASSED IN AS STRESS AT BEGINNING OF INCREMENT,
C               PASSED OUT AS STRESS AT END OF INCREMENT
C      STATE  : PASSED IN AS STATE VARIABLES AT BEGINNING OF INCREMENT,
C               PASSED OUT AS STATE VARIABLES AT END OF INCREMENT
C      DDSDDE : STRESS-STRAIN JACOBIAN EVALUATED AT END OF INCREMENT
C      SSE    : ELASTIC STRAIN ENERGY AT END OF INCREMENT
C      SPD    : TOTAL PLASTIC DISSIPATION AT END OF INCREMENT
C      SCD    : TOTAL CREEP DISSIPATION AT END OF INCREMENT
C      RPL    : NOT CURRENTLY USED
C      DDSDDT : STRESS-TEMPERATURE JACOBIAN AT END OF INCREMENT,

```

```

C          CURRENTLY SET TO ZERO
C      DRPLDE : NOT CURRENTLY USED
C      DRPLDT : NOT CURRENTLY USED
C      STRAIN : STRAIN AT BEGINNING OF INCREMENT
C      DSTRAIN : STRAIN INCREMENT
C      TIME : TIME AT BEGINNING OF INCREMENT
C      DTIME : TIME INCREMENT
C      TEMP : TEMPERATURE AT BEGINNING OF INCREMENT
C      DTEMP : TEMPERATURE INCREMENT
C      PREDEF : NOT CURRENTLY USED
C      DPRED : NOT CURRENTLY USED
C      CMNAME : MATERIAL NAME GIVEN ON *MATERIAL OPTION
C      NDI : NUMBER OF DIRECT STRESS COMPONENTS
C      NSHEAR : NUMBER OF ENGINEERING STRESS COMPONENTS (SHEAR)
C      NTENS : NDI+NSHEAR, SIZE OF STRESS-STRAIN COMPONENT ARRAY
C      NSTATV : NUMBER OF STATE VARIABLES DEFINED ON *DEPVAR OPTION,
C              CURRENTLY THIS NUMBER IS 29 FOR RENE 80
C      PROPS : NUMBER OF CONSTANTS SET ON *USER MATERIAL OPTION,
C              NOT CURRENTLY USED
C      NPROPS : NUMBER OF MATERIAL CONSTANTS FOR DIMENSIONING THE
C              VARIABLE PROPS, NOT CURRENTLY USED
C      COORDS : THE ARRAY OF CURRENT COORDINATES OF THE MATERIAL GAUSS
C              POINT, NOT CURRENTLY USED
C      DROT : ROTATION INCREMENT MATRIX, NOT CURRENTLY USED

      DIMENSION STRESS(NTENS), STATE(NSTATV), DDSDDDE(NTENS,NTENS),
+      DDSDDT(NTENS), DRPLDE(NTENS), STRAIN(NTENS), DSTRAIN(NTENS),
+      PREDEF(1), DPRED(1), PROPS(NPROPS), COORDS(3), DROT(3,3)
      CHARACTER*8 CMNAME

C *** LOCAL VARIABLES ***

C      INTEGRATE : FLAG SET AT EITHER 'DIFFERENTIAL' OR 'INTEGRAL' TO
C              : CHOOSE THE INTEGRATION PROCEDURE
C      DSTRESS : STRESS INCREMENT
C      D : STRESS-STRAIN ELASTICITY MATRIX
C      G : NEGATIVE PLASTIC STRESS INCREMENT
C      DSTATE : USER DEFINED STATE VARIABLE INCREMENTS

      CHARACTER*80 INTEGRATE
      DIMENSION DSTRESS(6), D(6,6), G(6), DSTATE(29)

C *** SET INTEGRATION METHOD TO EITHER DIFFERENTIAL
C *** OR ASYMPTOTIC INTEGRAL TYPE

      INTEGRATE = 'INTEGRAL'
C      INTEGRATE = 'DIFFERENTIAL'

C *** ADD TINY INCREMENTS TO INCREMENTAL QUANTITIES ***
C *** THIS AVOIDS OVERFLOW IF THEY OCCUR IN THE THE ***
C *** DENOMINATORS OF EXPRESSIONS, EG. THE JACOBIAN ***
C      WRITE(6,7000) TIME,DTIME,TEMP,DTEMP
7000  FORMAT(1X,'TIME=',E10.3,2X,'DT=',E10.3,'TEMP=',E10.3)
      DTEMP = DTEMP + TINY

C      WRITE(UNIT=88,*) 'UMAT'

      DO I=1,NTENS
          DSTRAIN(I) = DSTRAIN(I) + TINY
      END DO
C      WRITE(6,7001) ( STRAIN(L),L=1,6)
7001  FORMAT(1X,'STRAIN=',6E10.3)
C      WRITE(6,7007) (DSTRAIN(L),L=1,6)
7007  FORMAT(1X,'DSTRAIN=',6E12.3)

C
C *** IF TIME = 0.0, INITIALIZE THE STATE VARIABLES
C
      IF (TIME .GT. 0.0) GO TO 2000
      DO I = 1,NSTATV
          STATE(I) = 0.0
      END DO

```



```

C *** INITIALIZATION OF RHO(1) == STATE(23). SINCE MAXPARAM == 1
C *** THEREFORE, MAXPARAMP == 23
      MAXPARAMP=22+MAXPARAM
      DO I = 23,MAXPARAMP
        STATE(I) = 4.0E-6
        DSTATE(I) = 0.0
      END DO
C   ADDED MAY 1993
      DO I =1,NTENS
        STRESS(I)=0.
        STRAIN(I)=0.
      END DO
      SSE = 0.0
      SPD = 0.0
      SCD = 0.0
2000    CONTINUE
C      WRITE(6,7) (DSTRAIN(L),L=1,6)
7      FORMAT(1X,'DSTRAIN=',6E12.3)

C      WRITE(UNIT=88,*) 'STRESS(3) = ',STRESS(3)
C      WRITE(UNIT=88,*) 'STRAIN(3) = ',STRAIN(3)
C      WRITE(UNIT=88,*) 'DSTRAIN(3)= ',DSTRAIN(3)
C      WRITE(UNIT=88,*) 'TIME      = ',TIME
C      WRITE(UNIT=88,*) 'TEMP      = ',TEMP
C      WRITE(UNIT=88,*) 'DTEMP     = ',DTEMP

      STATE(1) = TEMP
      DSTATE(1) = DTEMP
      STATE(2) = TIME
      DSTATE(2) = DTIME
C      WRITE(6,7) (DSTRAIN(L),L=1,6)
C
C *** INTEGRATE UNIFIED VISCOPLASTIC RELATIONS ***
C
      CALL UMAT_UNICORN (D,G,STRAIN,DSTRAIN,
&                      STRESS,DSTRESS,
&                      STATE,DSTATE,NTENS,CMNAME,NDI,
&                      NSHEAR,TIME,DTIME,INTEGRATE,
&                      DDSDD,DDSDDT,TEMP,DTEMP,
&                      SSE,SPD,SCD)

C
C *** UPDATE STRESS AND STATE VARIABLES ***
C
      DO I = 1,NTENS
        STRESS(I) = STRESS(I) + DSTRESS(I)
C      WRITE(6,7010) I,STRESS(I),DSTRESS(I)
7010    FORMAT(1X,I3,2X,'STRESS=',E10.3,2X,'DS=',E10.3)
      END DO
C      WRITE(6,7013) (STRESS(L),L=1,6)
7013    FORMAT(1X,'STRESS=',6E10.2)
C      WRITE(6,7016) (DSTRESS(L),L=1,6)
7016    FORMAT(1X,'DSTRESS=',6E10.2)
      DO I = 1,NSTATV
        STATE(I) = STATE(I) + DSTATE(I)
C      WRITE(6,7017) I,STATE(I),DSTATE(I)
7017    FORMAT(1X,'STATE,DS',2X,I2,2E12.3)
      END DO
      DO 1000 I=1,NTENS
C      WRITE(6,7025) I,(DDSDD(I,L),L=1,6)
7025    FORMAT(1X,I3,2X,'DDSDD=',6E10.3)
1000    CONTINUE

C      WRITE(UNIT=88,*) 'FIN UMAT'

C      CLOSE(UNIT=88)

      RETURN
      END

```

```

C-----
C

```

```

C PROGRAM NAME: UMAT_DIFF_MATER
C
C PURPOSE: 3D VISCOPLASTIC MATERIAL MODEL (DIFFERENTIAL FORMULATION)
C
C INPUT: STRAIN, TEMPERATURE AND TIME INCREMENTS
C
C OUTPUT: RESPONSE & STATE VARIABLE INCREMENTS, ELASTIC MATERIAL MATRIX
C
C CALLING SUBROUTINE: UMAT_UNICORN
C
C CALLED SUBROUTINES: UMAT_CONSTANT, UMAT_FIRSTINV, UMAT_SECONDINV,
C                     UMAT_SUBSPLIT, UMAT_EFFRAT_MATER
C
      SUBROUTINE UMAT_DIFF_MATER (SUBSIG,DSUBSIG,SUBETOT,
&                                DSUBETOT,
&                                STATE,DSTATE,
&                                NSTRESS,NNORMAL,NSHEAR,
&                                ELEMTYPE,CONTROL,
&                                DDSDE3D,DDSDDT3D,
&                                SSE,SPD,SCD)

C *** USER DEFINED PARAMETERS ***

      PARAMETER (MAXCONST = 9)
      PARAMETER (MAXSTATE = 29)
      PARAMETER (MAXSIG = 6)

C *** SUBROUTINE PARAMETERS ***

C *** SUBSIG      : CURRENT STRESS
C *** DSUBSIG     : STRESS SUBINCREMENT
C *** SUBETOT     : TOTAL STRAIN AT START OF INCREMENT
C *** DSUBETOT    : TOTAL STRAIN SUBINCREMENT
C *** STATE:      : STATE VARIABLES AT START OF INCREMENT
C *** DSTATE      : INCREMENTS OF STATE VARIABLES
C *** NSTRESS     : TOTAL NUMBER OF STRESS COMPONENTS
C *** NNORMAL     : NUMBER OF NORMAL STRESSES
C *** NSHEAR      : NUMBER OF SHEAR STRESSES
C *** ELEMTYPE    : ELEMENT TYPE
C *** CONTROL     : LOAD CONTROL (STRESS OR STRAIN)
C *** DDSDE3D     : FULL 3D STRESS-STRAIN JACOBIAN
C *** DDSDDT3D    : FULL 3D STRESS-TEMPERATURE JACOBIAN
C *** SSE         : ELASTIC STRAIN ENERGY AT END OF INCREMENT
C *** SPD         : PLASTIC DISSIPATION AT END OF INCREMENT
C *** SCD         : CREEP DISSIPATION AT END OF INCREMENT
      IMPLICIT REAL*8(A-H,O-Z)
      DIMENSION SUBSIG(6),DSUBSIG(6),SUBETOT(6),DSUBETOT(6),
& STATE(29),DSTATE(29),DDSDE3D(6,6),DDSDDT3D(6)
      CHARACTER*80 ELEMTYPE
      CHARACTER*80 CONTROL

C *** SUBINCREMENT DATA ***

C *** SUBTIME     : CURRENT SUBINCREMENT TIME
C *** DSUBTIME    : CURRENT TIME SUBINCREMENT (TO BE SCALED IN UMAT_EFFRAT)
C *** SAVE_DSUBTIME : ACTUAL TIME SUBINCREMENT
C *** TEMPC       : CURRENT TEMPERATURE
C *** DTEMPC      : CURRENT TEMPERATURE SUBINCREMENT
C *** SUBINC      : SUBINCREMENT COUNTER
C *** NSUBINC     : NUMBER OF SUBINCREMENTS

      INTEGER SUBINC
      INTEGER NSUBINC

C *** LOCAL STATE VARIABLES ***

C *** DEVSIG      : DEVIATORIC STRESS TENSOR
C *** OVERSIG     : 'OVER STRESS': DIFF BETWEEN DEVIATOR & BACK STRESS T
C *** SIGSCALE    : SCALAR TOTAL STRESS
C *** EPLAS       : PLASTIC STRAIN
C *** DEPLAS      : PLASTIC STRAIN INCREMENT

```

```

C *** DELAS1      : FIRST NORMAL COMPONENT OF ELASTIC STRAIN INCREMENT
C *** DELAS2      : SECOND NORMAL COMPONENT OF ELASTIC STRAIN INCREMENT
C *** EPSSCALE     : SCALAR TOTAL PLASTIC STRAIN
C *** EPSDOTSCALE  : SCALAR TOTAL PLASTIC STRAIN RATE
C *** CONMULT      : MULTIPLIER FOR PLASTIC STRAIN RATE
C *** BACK0        : 0TH BACK STRESS
C *** BACK1        : 1ST BACK STRESS
C *** DBACK1       : 1ST BACK STRESS INCREMENT
C *** BACK1SCALE   : SCALAR TOTAL 1ST BACK STRESS
C *** BACK2        : 2ND BACK STRESS
C *** DBACK2       : 2ND BACK STRESS INCREMENT
C *** BACK2SCALE   : SCALAR TOTAL 2ND BACK STRESS
C *** DRAG         : DRAG STRESS
C *** DDRAG        : DRAG STRESS INCREMENT
C *** DEVIATOR     : MULTIPLIERS FOR DEVIATORIC STRESS
C *** ENGRSTRN     : CONVERT FROM TENSOR TO ENGINEERING STRAIN
C *** FORMULATE    : INELASTIC STRAIN FORMULATION
C *** NUMERATOR1   : NUMERATOR IN STRESS-STRAIN JACOBIAN
C *** NUMERATOR2   : NUMERATOR IN STRESS-STRAIN JACOBIAN
C *** DENOMINATOR  : DENOMINATOR IN STRESS-STRAIN JACOBIAN

      DIMENSION DEVSIG(6),OVERSIG(6),EPLAS(6)
      + ,DEPLAS(6),BACK(6),BACK0(6),BACK1(6),
      + DBACK1(6),BACK2(6),DBACK2(6),
      + DEVIATOR(6),ENGRSTRN(6)
      CHARACTER*80 FORMULATE
      REAL*8 NUMERATOR1(6),NUMERATOR2(6),
      + KRONECKER(6)

C
      DATA DEVIATOR/3*1.0,3*0.0/
      DATA ENGRSTRN/3*1.0,3*2.0/
      DATA KRONECKER/3*1.0,3*0.0/
C
      DATA FORMULATE/'POWER LAW'/
      DATA FORMULATE/'EXPONENTIAL'/

C *** MATERIAL CONSTANTS

C *** NCON         : MATERIAL CONSTANTS
C *** DNCO         : RATE OF CHANGE OF CONSTANTS W.R.T. TEMP
C *** MEXP         : MATERIAL EXPONENTS
C *** DMEX         : RATE OF CHANGE OF EXPONENTS W.R.T. TEMP
C *** EMOD         : ELASTIC TENSILE YOUNG'S MODULUS
C *** POISSON      : POISSON RATIO
C *** CONSTIT      : ELASTIC MATERIAL MATRIX
C *** DEVZERO      : MACHINE ZERO DEVIATORIC 6 VECTOR
      REAL*8 NCON(9)
      DIMENSION DNCON(9),CC(6,6),DEVZERO(6)
      DATA DEVZERO/1.E-10,-0.5E-10,-0.5E-10,3*0.0/
C *** TEMPORARY VARIABLES
C
C *** ARG          : ARGUMENT OF EXPONENTIAL IN FIRST BACK STRESS EQUATION
C *** DYNAMIC1     : VALUE OF DYNAMIC RECOVERY TERM IN BACK1 EQUATION
C *** DYNAMIC2     : VALUE OF DYNAMIC RECOVERY TERM IN BACK2 EQUATION
C
C *** OUTPUT UNIT NUMBER ***

      INTEGER OUNIT
      DATA OUNIT/6/

C
      WRITE(UNIT=88,*) 'UMAT_DIFF_MATER'

C *** INITIALIZE LOCAL VARIABLES ***

      DRAG = 0.0
      DDRAG = 0.0

      DO I = 1,MAXSIG
         DEVSIG(I) = DEVZERO(I)
         OVERSIG(I) = DEVZERO(I)
         EPLAS(I) = DEVZERO(I)
         DEPLAS(I) = DEVZERO(I)
         BACK1(I) = DEVZERO(I)

```

```

        DBACK1(I) = DEVZERO(I)
        BACK2(I) = DEVZERO(I)
        DBACK2(I) = DEVZERO(I)
        DO J = 1,MAXSIG
            CC(I,J) = 0.0
            DDSDE3D(I,J) = 0.0
        END DO
    END DO

C *** INITIALIZE MATERIAL CONSTANTS ***

    DO I = 1,MAXCONST
        NCON(I) = 0.
        DNCON(I) = 0.
    END DO

C *** LOAD STATE VARIABLES ***

    TEMPC = STATE(1)
    DTEMPC = DSTATE(1)
    SUBTIME = STATE(2)
    DSUBTIME = DSTATE(2)
    NSUBINC = STATE(16)

C
C    WRITE(6,6100) TEMPC,DTEMPC,SUBTIME,DSUBTIME,NSUBINC
6100    FORMAT(1X,'INITIALS',4E12.3,I3)
    DO I = 1,MAXSIG
        BACK1(I) = STATE(I+3)
        DBACK1(I) = 0.0
        EPLAS(I) = STATE(I+9)
        DEPLAS(I) = 0.0
        BACK2(I) = STATE(I+16)
        DBACK2(I) = 0.0
    END DO

C
C    WRITE(6,1999) I,BACK1(I),EPLAS(I),BACK2(I)
1999    FORMAT(1X,'*****B1,EPL,B2=',I3,3E12.3)
    END DO

C *** CHECK SUBINCREMENT SIZE ***

    CALL UMAT_SUBSPLIT (DSUBTIME,DTEMPC,DSUBTOT,NSUBINC)
C25    WRITE(6,7025) NSUBINC,(DSUBTOT(L),L=1,6)
    SUBINC = 0
7025    FORMAT(1X,'NS,DSUBT=',I4,6E10.2)

C *** SAVE SUBINCREMENT TIME IN SAVE_DSUBTIME TIME FOR UPDATING.
C *** THE VALUE OF DSUBTIME IS CHANGED IN THE RATE INDEPENDENT
C *** SUBROUTINE UMAT_EFFRAT_MATER, AND THEREFORE NEEDS TO BE
C *** SAVED FOR THE FINAL UPDATE.

    SAVE_DSUBTIME = DSUBTIME

C
C *****
C *** START OF SUBINCREMENTATION LOOP ***
C *****

    DO WHILE (SUBINC .LT. NSUBINC)
        SUBINC = SUBINC + 1
C    DO SUBINC = 1,NSUBINC
C
C        WRITE(6,17) NSUBINC
17        FORMAT(1X,'DO LOOP NSUBINC=',I5)
C *** EVALUATE EFFECTIVE TIME INCREMENT BASED ON TEMPERATURE

        CALL UMAT_EFFRAT_MATER (DSUBTOT,SAVE_DSUBTIME,TEMPC,DSUBTIME)

C
C    WRITE(6,7010) SUBINC,TEMPC,(DSUBTOT(L),L=1,6)
C    WRITE(UNIT=88,*) 'NSUBINC= ',NSUBINC
C    WRITE(UNIT=88,*) 'SUBINC= ',SUBINC
C    WRITE(UNIT=88,*) 'TEMPC= ',TEMPC
C    WRITE(UNIT=88,*) 'DSUBTIME= ',DSUBTIME

```

```

7010     FORMAT(1X,I4,'TEMP,DSUB=',7E10.3)
C *** EVALUATE MATERIAL CONSTANTS AT END OF SUBINCREMENT ***

        CALL UMAT_CON_MATER (TEMPC,DTEMPC,NCON,DNCON)

        DRAG = NCON(1)

C       WRITE(6,7016) TEMPC,EMOD,POISSON
7016     FORMAT(1X,'TEMP,E,NI=',3E12.3)
C *** ELASTIC CONSTITUTIVE MATRIX ***

        CALL UMAT_ELASTIC (TEMPC,DTEMPC,CC)
C       WRITE(UNIT=88,*) 'CC11 = ',CC(1,1)
C       WRITE(UNIT=88,*) 'CC21 = ',CC(2,1)
C       WRITE(UNIT=88,*) 'CC31 = ',CC(3,1)
C
C       DO 6500 I=1,6
C       WRITE(6,6501) I,(CONSTIT(I,K),K=1,6)
C6501     FORMAT(1X,I3,'CONSTIT',6E10.3)
C6500     CONTINUE

C *** INELASTIC STRAIN RATE ***

        CALL UMAT_BZERO(BACK0,EPLAS,KRONECKER,NCON)

C       WRITE(6,3334) (SUBSIG(L),L=1,6)
3334     FORMAT(1X,'SUBSIG=',6E10.3)
        CALL FIRSTINV(3,3,SUBSIG,FINV)
        DO I = 1,MAXSIG
            IBR=I/4
            BR=1.0-DFLOAT(IBR)
            DEVSIG(I)=SUBSIG(I)-BR*FINV/3.

C
C       P1=BR*FINV/3.0
C       WRITE(6,6502) BR,P1,SUBSIG(I),DEVSIG(I)
6502     FORMAT(1X,'BR,P1,SUBS,DEVSIG=',4E12.3)

        BACK(I) = BACK0(I) + BACK1(I) + BACK2(I)
C       WRITE(UNIT=88,*) 'BACK(I)= ',BACK(I)
        OVERSIG(I) = DEVSIG(I) - 2.0*BACK(I)/3.0
        DEPLAS(I) = 0.0
C       WRITE(6,4998) FINV,BACK0(I),BACK1(I),BACK2(I)
4998     FORMAT(1X,'FIN,B0,B1,B2=',4E12.3)
C       WRITE(6,4999) I,SUBSIG(I),DEVSIG(I),BACK(I)
C       + ,OVERSIG(I)
4999     FORMAT(1X,'SUBSIG,DEVS,BACK,OVSIG=',I3,4E12.3)
        END DO
        CALL SECONDINV(3,3,OVERSIG,SINV)
        SIGSCALE = DSQRT(3.0*SINV/2.0)
C       WRITE(6,5007) SIGSCALE
5007     FORMAT(1X,'SIGSCALE=',E12.3)
C
        IF (SIGSCALE .GT. 0.0) THEN

C *** CHECK INELASTIC STRAIN FORMULATION ***

            IF (FORMULATE .EQ. 'POWER LAW') THEN
                CONMULT = 1.5*(SIGSCALE/DRAG)**(1.)
C       WRITE(6,131) SIGSCALE,DRAG,MEXP(1)
1       FORMAT(1X,'SIGSCALE,DRAG=',3E12.3)
            ELSE IF (FORMULATE .EQ. 'EXPONENTIAL') THEN
                CONMULT = 1.5*(DEXP(SIGSCALE/DRAG) - 1.0)/NCON(6)
            ELSE IF (FORMULATE .EQ. 'HYPERBOLIC SINE') THEN
                CONMULT = 1.5*DSINH(SIGSCALE/DRAG)**(1.)
            ENDIF

            DO I=1,MAXSIG

                DEPLAS(I) = CONMULT*OVERSIG(I)/SIGSCALE*DSUBTIME

C
C       WRITE(6,130) I,CONMULT,OVERSIG(I),SIGSCALE,DSUBTIME,
C       + DEPLAS(I)

```

```

130      FORMAT(1X,'CMU,OVERS,SIGS,DSUBT,DEPLS=',I4,5E10.3)
      END DO
    ENDIF

C
C *** CALCULATE SCALAR PLASTIC STRAIN INCREMENT
C *** AND SCALAR PLASTIC STRAIN RATE
C
      CALL SECONDINV(3,3,DEPLAS,SINV)
      EPSSCALE = DSQRT(2.0*SINV/3.0)
      EPSDOTSCALE = EPSSCALE/DSUBTIME

C
C *** DRAG STRESS -- IN THIS MODEL IT IS ONLY A FUNCTION ***
C *** OF TEMPERATURE ***
C
      DDRAG = 0.0

C
C *** 1ST BACK STRESS ***
C
      CALL SECONDINV(3,3,BACK,SINV)
      BACK1SCALE = DSQRT(2.0*SINV/3.0)

      DYNAMIC1 = NCON(3)*EPSDOTSCALE+NCON(4)

      DO I=1,MAXSIG
C
C      WRITE(6,3301) DYNAMIC1,NCON(3),EPSDOTSCALE
3301      FORMAT(1X,'DYNP1,NCON3,EPSPD=',3E12.3)
C      DYNAMIC1 = DYNAMIC1+NCON(4)*BACK1SCALE**(1.0-1.0)
C
C      DBACK1(I)=NCON(2)*DEPLAS(I) - DYNAMIC1*BACK1(I)*DSUBTIME
C
C      PART1=NCON(2)*DEPLAS(I)
C
C      SUM=PART1-PART2
C      WRITE(6,2998) PART1,PART2,SUM
2998      FORMAT(1X,'P1,P2,SUM=',3E12.3)
C      WRITE(6,2999) I,DBACK1(I),NCON(2),DEPLAS(I),
C      + DYNAMIC1,BACK1(I),DSUBTIME
2999      FORMAT(1X,'DB,NC,DEPL,DYN,B1,DSUBTIM=',I3,6E10.3)
      END DO

C
C *** 2ND BACK STRESS ***
C
      CALL SECONDINV(3,3,BACK2,SINV)
      BACK2SCALE = DSQRT(2.0*SINV/3.0)

      DYNAMIC2 = NCON(7)*EPSDOTSCALE+NCON(8)
      DO I=1,MAXSIG
C
C      DBACK2(I) = NCON(9)*DEPLAS(I)-DYNAMIC2*BACK2(I)*DSUBTIME
      END DO

C *** CALCULATE STRESS SUBINCREMENT ***
C
C      WRITE(6,5000) (DSUBETOT(L),L=1,6)
C      WRITE(6,5001) (DEPLAS(L),L=1,6)
5000      FORMAT(1X,'DSUBTOT=',6E10.2)
5001      FORMAT(1X,'DEPLAS=',6E10.2)
      DO I=1,NNORMAL
C
C      DSUBSIG(I) = 0.0
C      DO J=1,MAXSIG
C
C      DSUBSIG(I) = DSUBSIG(I)
&      + CC(I,J)*ENGRSTRN(J)
&      * (DSUBETOT(J)-DEPLAS(J))
C
C      END DO
      END DO

C
C      WRITE(6,5002) (DSUBSIG(L),L=1,3)
5002      FORMAT(1X,'DSUBSIG=',3E12.3)

      DO I=1,NSHEAR
C
C      DSUBSIG(I+3) = 0.0

```

```

      DO J=1,MAXSIG
        DSUBSIG(I+3) = DSUBSIG(I+3)
&          + CC(I+3,J)*ENGRSTRN(J)
&          * (DSUBETOT(J)-DEPLAS(J))
      END DO
    END DO

C *** CALCULATE ELASTIC STRAIN ENERGY AND PLASTIC DISSIPATION ***

    DO I=1,MAXSIG
      SSE = SSE + SUBSIG(I)*DSUBETOT(I)
      SPD = SPD + SUBSIG(I)*DEPLAS(I)
      SCD = SCD + 0.0
    END DO

C *** UPDATE STATE VARIABLES ***

    TEMPC = TEMPC + DTEMPC
    TIME0 = SUBTIME
    TIMEL = SAVE_DSUBTIME/2

C
    SUBTIME = SUBTIME + SAVE_DSUBTIME
    DRAG = DRAG + DDRAG
    DO I = 1,MAXSIG
      SUBSIG(I) = SUBSIG(I) + DSUBSIG(I)
      SUBETOT(I) = SUBETOT(I) + DSUBETOT(I)
      EPLAS(I) = EPLAS(I) + DEPLAS(I)
      BACK1(I) = BACK1(I) + DBACK1(I)
      BACK2(I) = BACK2(I) + DBACK2(I)
C
C      WRITE(6,1331) I,SUBSIG(I),SUBETOT(I),EPLAS(I),
C      + BACK1(I),BACK2(I)
1331    FORMAT(1X,'SSIG,STOT,EPL,B1,B2=',I3,5E12.3)
    END DO
C
C      WRITE(6,4444) SUBINC,SUBSIG(3),SUBETOT(3),EPLAS(3),BACK1(3)
4444    FORMAT(1X,'N,SSIG,STOT,EPL,B1=',I4,4E12.3)
    END DO

C *****
C *** END OF SUBINCREMENTATION LOOP ***
C *****

C *** CALCULATE 3D STRESS-STRAIN JACOBIAN ***

    DENOMINATOR = 0.0
    DO I = 1,MAXSIG
      NUMERATOR1(I) = 0.0
      NUMERATOR2(I) = 0.0
      DO J = 1,MAXSIG
        NUMERATOR1(I) = NUMERATOR1(I)
&          + CC(I,J)*ENGRSTRN(J)
&          * DEPLAS(J)
        NUMERATOR2(I) = NUMERATOR2(I)
&          + CC(I,J)*ENGRSTRN(J)
&          * DSUBETOT(J)
        DENOMINATOR = DENOMINATOR
&          + ENGRSTRN(I)*DSUBETOT(I)
&          * CC(I,J)
&          * ENGRSTRN(J)*DSUBETOT(J)
      END DO
    END DO

    DO 1000 I = 1,MAXSIG
      DDSDDT3D(I) = 0.0
      DO 1000 J = 1,MAXSIG
        DDSDDE3D(I,J) = CC(I,J)
C
C      WRITE(6,6999) TIME0
6999    FORMAT(1X,'TIME0=',E10.3)
C
        IF(TIME0.LT.TIMEL) GO TO 1000
        IF(DABS(DEPLAS(J)).LT.1.E-8) GO TO 1000
        IF(DABS(DSUBETOT(J)).LT.1.E-8) GO TO 1000
        DDSDDE3D(I,J)=DDSDDE3D(I,J)

```

```

      &          - NUMERATOR1(I)*NUMERATOR2(J)
      &          /DENOMINATOR
C      WRITE(6,7003) I,J,CC(I,J),DDSDDE3D(I,J)
7003      FORMAT(1X,'DIF CON DS/DE',2X,2I4,2E12.3)
C      WRITE(6,7004) NUMERATOR1(I),NUMERATOR2(J),DENOMINATOR
7004      FORMAT(1X,'NUMERATORS',3E12.3)
1000      CONTINUE

C *** LOAD STATE AT END OF INCREMENT INTO DSTATE ***

      DSTATE(1) = TEMPC
      DSTATE(2) = SUBTIME
      DSTATE(3) = DRAG
      DSTATE(16) = DFLOAT(NSUBINC)
      STATE(16) = 0.0
      DO I=1,MAXSIG
          DSTATE(I+3) = BACK1(I)
          DSTATE(I+9) = EPLAS(I)
          DSTATE(I+16) = BACK2(I)
      END DO

      RETURN

100      FORMAT(/,' *** DIFFERENTIAL: NNORMAL = ',I5,
&          ' NSHEAR = ',I5,' NOT SUPPORTED *** ',/)
110      FORMAT(/,' *** DIFFERENTIAL: FAILED TO CALCULATE
&          RESPONSE INCREMENT *** ',/)
120      FORMAT(/,' *** DIFFERENTIAL: FAILED TO UPDATE LOAD *** ',/)

      END

C
C
C PROGRAM NAME: UMAT_INT_MATER
C
C AUTHOR: K.P. WALKER
C
C ADDRESS: ESS, INC.
C          315 LOG ROAD
C          SMITHFIELD, R.I. 02917
C
C TELEPHONE: (401) 231-3182
C
C PURPOSE: 3D ASYMPTOTIC VISCOPLASTIC MATERIAL MODEL (INTEGRAL FORMULATION)
C
C INPUT: STRAIN INCREMENTS
C
C OUTPUT: RESPONSE & STATE VARIABLE INCREMENTS, ELASTIC MATERIAL MATRIX
C
C CALLING SUBROUTINE: UMAT_UNICORN
C
C CALLED SUBROUTINES: UMAT_CONSTANT, UMAT_EFFRAT_MATER, UMAT_U11,
C                    UMAT_U12, UMAT_U13, UMAT_V11, UMAT_V12,
C                    UMAT_V13, UMAT_EVAL1, UMAT_BZERO
C
C REFERENCES: (1) K.P. WALKER AND A.D. FREED, "ASYMPTOTIC INTEGRATION
C              ALGORITHMS FOR NONHOMOGENEOUS, NONLINEAR, FIRST ORDER,
C              ORDINARY DIFFERENTIAL EQUATIONS", NASA TM 103793, 1991.
C
C              (2) A. CHULYA AND K.P. WALKER, "A NEW UNIFORMLY VALID
C              ASYMPTOTIC INTEGRATION ALGORITHM FOR ELASTO-PLASTIC
C              CREEP AND UNIFIED VISCOPLASTIC THEORIES INCLUDING
C              CONTINUUM DAMAGE", NASA TM 102344, 1989. ALSO IN:
C              INTERNATIONAL JOURNAL FOR NUMERICAL METHODS IN
C              ENGINEERING, VOL. 32, 385-418, 1991.
C
C              (3) K.P. WALKER, "A UNIFORMLY VALID ASYMPTOTIC INTEGRATION
C              ALGORITHM FOR UNIFIED VISCOPLASTIC CONSTITUTIVE MODELS",
C              ADVANCES IN INELASTIC ANALYSIS, EDS. S. NAKAZAWA, K. WILLAM
C              AND N. REBELO, AMERICAN SOCIETY OF ENGINEERS, AMD-VOL. 88 AND
C              PED-VOL. 28, PP. 13-27, 1987.
C
C

```



```

C          (4) A.D. FREED AND K.P. WALKER, "EXPONENTIAL INTEGRATION
C          ALGORITHMS APPLIED TO VISCOPLASTICITY", NASA TM 104461, 1991.
C
C
C          SUBROUTINE UMAT_INT_MATER (SUBSIG,DSUBSIG,SUBETOT,DSUBETOT,
C          & STATE,DSTATE,
C          & NSTRESS,NNORMAL,NSHEAR,
C          & ELEMTYPE,CONTROL,
C          & DDSDE3D,DDSDDT3D,
C          & SSE,SPD,SCD)
C
C *** USER DEFINED PARAMETERS ***
C
C *** MAXITER      : MAXIMUM NUMBER OF NEWTON-RAPHSON ITERATIONS PERMITTED
C *** MAXCONST     : MAXIMUM NUMBER OF MATERIAL CONSTANTS STORED IN TABLES
C *** MAXSTATE     : MAXIMUM NUMBER OF STATE VARIABLES
C *** MAXSIG       : MAXIMUM NUMBER OF STRESS/STRAIN COMPONENTS
C *** MAXPARAM     : MAXIMUM NUMBER OF NEWTON-RAPHSON ITERATION PARAMETERS
C *** RHOTOL       : MAXIMUM ERROR ALLOWED IN THE PARAMETER C/RHO
C *** PERT         : AMOUNT OF RHO PARAMETER USED AS PERTURBATION
C
C      IMPLICIT REAL*8 (A-H,O-Z)
C      REAL*8 KRONECKER(6)
C      PARAMETER (MAXITER = 50)
C      PARAMETER (MAXCONST = 9)
C      PARAMETER (MAXSTATE = 29)
C      PARAMETER (MAXSIG = 6)
C      PARAMETER (MAXPARAM = 1)
C      PARAMETER (MAXPARAM1=2)
C      PARAMETER (RHOTOL = 0.001)
C      PARAMETER (PERT = 0.01)
C
C *** SUBROUTINE PARAMETERS ***
C
C *** SUBSIG       : CURRENT STRESS
C *** SUBSIGH      : CURRENT HYDROSTATIC STRESS
C *** SUBSIGN      : NEW STRESS AT END OF ITERATION
C *** SUBSIGNH     : NEW HYDROSTATIC STRESS AT END OF ITERATION
C *** SUBSIGF      : FIXED STRESS DURING AN ITERATION (SET TO
C ***              : PREVIOUS NEW VALUE)
C *** SUBSIGFH     : FIXED HYDROSTATIC STRESS DURING AN ITERATION
C ***              : (SET TO PREVIOUS NEW VALUE)
C *** SUBETOT      : TOTAL STRAIN AT START OF INCREMENT
C *** DSUBETOT     : TOTAL STRAIN SUBINCREMENT
C *** DSUBETOTH    : HYDROSTATIC STRAIN INCREMENT
C *** STATE        : STATE VARIABLES AT START OF INCREMENT
C *** DSTATE       : INCREMENTS OF STATE VARIABLES
C *** NSTRESS      : TOTAL NUMBER OF STRESS COMPONENTS
C *** NNORMAL      : NUMBER OF NORMAL STRESSES
C *** NSHEAR       : NUMBER OF SHEAR STRESSES
C *** ELEMTYPE     : ELEMENT TYPE
C *** CONTROL      : LOAD CONTROL (STRESS OR STRAIN)
C *** DDSDE3D      : FULL 3D STRESS-STRAIN JACOBIAN
C *** DDSDDT3D     : FULL 3D STRESS-TEMPERATURE JACOBIAN
C *** SSE          : ELASTIC STRAIN ENERGY AT END OF INCREMENT
C *** SPD          : PLASTIC DISSIPATION AT END OF INCREMENT
C *** SCD          : CREEP DISSIPATION AT END OF INCREMENT
C
C      DIMENSION SUBSIG(6),SUBSIGN(6),SUBSIGF(6),
C      + DSUBSIG(6),SUBETOT(6),DSUBETOT(6),
C      + STATE(29),DSTATE(29),DDSDE3D(6,6),DDSDDT3D(6)
C      CHARACTER*80 ELEMTYPE
C      CHARACTER*80 CONTROL
C
C *** LOCAL STATE VARIABLES ***
C
C *** DEVSIG       : DEVIATORIC STRESS TENSOR
C *** OVERSIG      : 'OVER STRESS': DIFF BETWEEN DEVIATOR & BACK STRESS
C ***              : (BEGINNING OF INCREMENT)
C *** OVERSIGN     : 'OVER STRESS': DIFF BETWEEN DEVIATOR & BACK STRESS
C ***              : (NEW VALUE PREDICTED FOR END OF ITERATION)
C *** OVERSIGF     : 'OVER STRESS': DIFF BETWEEN DEVIATOR & BACK STRESS
C ***              : (FIXED TO PREVIOUS NEW VALUE FOR USE DURING AN ITERATION)

```

```

C *** SIGSCALE : SCALAR OVERSTRESS
C *** SIGSCALEN : SCALAR NEW OVERSTRESS
C *** SIGSCALEF : SCALAR FIXED OVERSTRESS
C *** RATION : RATIO OF SIGSCALEN/DRAIN
C *** ETOT : TOTAL STRAIN AT END OF INCREMENT
C *** EPLAS : PLASTIC STRAIN
C *** DEPLAS : PLASTIC STRAIN SUBINCREMENT
C *** DELAS1 : FIRST COMPONENT OF ELASTIC STRAIN
C *** DELAS2 : SECOND COMPONENT OF ELASTIC STRAIN
C *** EPSSCALE : SCALAR TOTAL PLASTIC STRAIN
C *** BACK : TOTAL BACK STRESS
C *** BACKN : NEW TOTAL BACK STRESS (END OF ITERATION)
C *** BACKF : TOTAL BACK STRESS (FIXED AT PREVIOUS NEW VALUE DURING AN
C *** ITERATION)
C *** BACK0 : 0TH BACK STRESS (BEGINNING OF INCREMENT)
C *** BACK0N : 0TH BACK STRESS (NEW VALUE AT END OF ITERATION)
C *** BACK0F : 0TH BACK STRESS (FIXED AT PREVIOUS NEW VALUE DURING AN
C *** ITERATION)
C *** BACK1 : 1ST BACK STRESS (BEGINNING OF INCREMENT)
C *** BACK1N : 1ST BACK STRESS (NEW VALUE AT END OF ITERATION)
C *** BACK1F : 1ST BACK STRESS (FIXED AT PREVIOUS NEW VALUE DURING AN
C *** ITERATION)
C *** BACK2 : 2ND BACK STRESS (BEGINNING OF INCREMENT)
C *** BACK2N : 2ND BACK STRESS (NEW VALUE AT END OF ITERATION)
C *** BACK2F : 2ND BACK STRESS (FIXED AT PREVIOUS NEW VALUE DURING AN
C *** ITERATION)
C *** BACKSCALE : SCALAR TOTAL BACK STRESS
C *** BACKSCALEN : SCALAR TOTAL BACK STRESS (NEW VALUE AT END OF ITERATION)
C *** BACK1SCALE : SCALAR TOTAL 1ST BACK STRESS
C *** BACK1SCALEN : NEW SCALAR TOTAL 1ST BACK STRESS
C *** BACK2SCALE : SCALAR TOTAL 2ND BACK STRESS
C *** BACK2SCALEN : NEW SCALAR TOTAL 2ND BACK STRESS
C *** DRAG : DRAG STRESS
C *** DRAGN : DRAG STRESS (END OF INCREMENT)
C *** DRAGF : DRAG STRESS (FIXED AT PREVIOUS NEW VALUE DURING AN
C *** ITERATION)
C *** KRONECKER : KRONECKER DELTA MULTIPLIERS FOR DEVIATORIC STRESS
C *** DEVZERO : DEVIATORIC MACHINE ZERO (TO AVOID UNDERFLOWS)
C *** FORMULATE : INELASTIC STRAIN FORMULATION
C *** STATE_END : STATE VARIABLES AT END OF INCREMENT
C *** DSTATE_END : SMALL STATE VARIABLE INCREMENTS AT END OF INCREMENT
C *** STRN_END : STRAIN AT END OF INCREMENT
C *** STRS_END : STRESS AT END OF INCREMENT
C *** DSTRS_PLAS : PLASTIC STRESS INCREMENT AT END OF INCREMENT
C *** DSTRN_END : SMALL STRAIN INCREMENT AT END OF INCREMENT
C
C DIMENSION DEVSIG(6),OVERSIG(6),OVERSIGN(6),
C + OVERSIGF(6),EPLAS(6),EPLASN(6),EPLASF(6),
C + DEPLAS(6),BACK(6),BACKN(6),BACKF(6),
C + BACK0(6),BACK0N(6),BACK0F(6),BACK1(6),
C + BACK1N(6),BACK1F(6),BACK2(6),BACK2N(6),
C + BACK2F(6),DEVZERO(6),
C + STATE_END(29),DSTATE_END(29),STRN_END(6),
C + STRS_END(6),DSTRS_PLAS(6),DSTRN_END(6)
C
C DATA KRONECKER/3*1.0,3*0.0/
C
C DATA DEVZERO/1.0E-10,-0.5E-10,-0.5E-10,3*0.0/
C
C CHARACTER*80 FORMULATE
C
C *** TYPE OF VISCOPLASTIC FORMULATION ***
C
C DATA FORMULATE/'POWER LAW'/
C DATA FORMULATE/'EXPONENTIAL'/
C DATA FORMULATE/'HYPERBOLIC'/
C
C *** LOCAL VARIABLES ***
C
C *** TEMP : TEMPERATURE AT BEGINNING OF INCREMENT
C *** DTEMP : TEMPERATURE CHANGE OVER INCREMENT
C *** SUBTIME : TIME

```

```

C *** DSUBTIME      : TOTAL TIME INCREMENT (TO BE SCALED BY UMAT_EFFRAT)
C *** SAVE_DSUBTIME : TOTAL TIME INCREMENT
C *** U1(1-3)       : COEFFICIENTS IN EQUATIONS  $DX / DT + U1 * X = V1$ 
C ***              :  $IJ \quad I \quad IJ \quad IJ$ 
C ***              : WHERE X CAN BE BACK1, BACK2, OR SUBSIG
C *** V1(1-3,1-6)   : RIGHT HAND SIDE OF ABOVE EQUATION
C ***              : DIMENSION U1(3),V1(3,6),U11(6)
C
C *** MATERIAL CONSTANTS ***
C
C *** NCON          : MATERIAL CONSTANTS
C *** DNCON         : RATE OF CHANGE OF CONSTANTS W.R.T. TEMP
C *** MEXP          : MATERIAL EXPONENTS
C *** DMEXP         : RATE OF CHANGE OF EXPONENTS W.R.T. TEMP
C *** EMOD          : YOUNG'S MODULUS
C *** POISSON       : POISSON'S RATIO
C *** GMOD          : SHEAR MODULUS
C *** CC            : ELASTIC MATERIAL MATRIX
C ***              : REAL*8 NCON(9),JACOBIAN(MAXPARAM
+ ,MAXPARAM)
C ***              : DIMENSION DNCON(9),CC(6,6)
C
C *** ITERATION PARAMETERS ***
C
C *** RHO           : ITERATION PARAMETER  $RHO = U1(1)*DSUBTIME$ 
C *** DRHO          : PERTURBATION OF PARAMETER RHO
C *** RHON          : SUM OF RHO + DRHO
C *** F             : VALUE OF THE ITERATION FUNCTION
C *** JACOBIAN      : JACOBIAN MATRIX
C *** C             : PREDICTED CHANGES TO RHO FOR GIVEN ITERATION
C *** CUTBAC        : AMOUNT PREDICTED CHANGES OF RHO IN AN ITERATION ARE
C ***              : CUT BACK TO ENSURE STABILITY OF METHOD
C *** RHOTOL        : TOLERANCE ON  $C(1)/RHO(1)$  FOR CONVERGENCE
C *** CHANGE        :  $C(1)/RHO(1)$ , I.E. RELATIVE CHANGE IN  $RHO(1)$ 
C *** ITER          : ITERATION NUMBER WITHIN A GIVEN INCREMENT
C ***              : DIMENSION RHO(MAXPARAM),DRHO(MAXPARAM),RHON(MAXPARAM),
+ F(MAXPARAM,MAXPARAM1),C(MAXPARAM)
C ***              : CHARACTER*8 ELASTIC
C
C *** OUTPUT UNIT NUMBER ***
C
C ***              : INTEGER OUNIT
C ***              : DATA OUNIT/6/
C
C *** INITIALIZE LOCAL VARIABLES ***
C
C ***              : DRAG = 0.0
C
C ***              : DO I = 1,MAXSIG
C ***              :   DEVSIG(I) = DEVZERO(I)
C ***              :   OVERSIG(I) = DEVZERO(I)
C ***              :   EPLAS(I) = DEVZERO(I)
C ***              :   DEPLAS(I) = DEVZERO(I)
C ***              :   BACK1(I) = DEVZERO(I)
C ***              :   BACK2(I) = DEVZERO(I)
C ***              :   DO J = 1,MAXSIG
C ***              :     CC(I,J) = 0.0
C ***              :     DDSDE3D(I,J) = 0.0
C ***              :   END DO
C ***              : END DO
C
C *** INITIALIZE MATERIAL CONSTANTS ***
C
C ***              : DO I = 1,MAXCONST
C ***              :   NCON(I) = 0.0
C ***              :   DNCON(I) = 0.0
C ***              : END DO
C
C *** LOAD STATE VARIABLES ***
C
C ***              : TEMPC = STATE(1)
C ***              : DTEMPC = DSTATE(1)

```

```

SUBTIME = STATE(2)
DSUBTIME = DSTATE(2)

DO I = 1,MAXSIG
  BACK1(I) = STATE(I+3)
  EPLAS(I) = STATE(I+9)
  BACK2(I) = STATE(I+16)
END DO

C
C   WRITE(6,2500) (EPLAS(L),L=1,6)
2500 FORMAT(1X,'INIT EPLAS=',6E10.2)
C *** MAXPARAM == 1, SO NEXT LOOP IS NOT USEFUL
DO I = 1,MAXPARAM
  RHO(I) = STATE(I+22)
END DO
C   WRITE(6,2450) RHO(I)
2450 FORMAT(1X,'ro=',E12.3)
C
C *** ONLY NEED TO EVALUATE ELASTIC PROPERTIES ONCE AT THE TEMPERATURE
C *** CORRESPONDING TO THE END OF THE INCREMENT.
C
CALL UMAT_CON_MATER (TEMPC,DTEMPC,NCON,DNCON)
C
C *** GET CONSTANT DRAG VALUE FROM NCON(1) ***
DRAG = NCON(1)
C
C *** CALCULATE ZEROth BACK STRESS ***
C
DO I = 1,MAXSIG
  EPLASN(I) = EPLAS(I) + DEPLAS(I)
END DO
C   WRITE(6,2501) (DEPLAS(L),L=1,6)
2501 FORMAT(1X,' inDEPLAS=',6E10.2)
CALL UMAT_BZERO(BACK0,EPLASN,KRONECKER,NCON)
C
C *** CALCULATE ELASTIC MATERIAL MATRIX
C
CALL UMAT_ELASTIC(TEMPC,DTEMPC,CC)
C   WRITE(UNIT=88,*) 'CC11 = ',CC(1,1)
C   WRITE(UNIT=88,*) 'CC21 = ',CC(2,1)
C   WRITE(UNIT=88,*) 'CC31 = ',CC(3,1)
C
C *** CALCULATION OF DEVIATORIC STRESS AND OVERSTRESS AT
C *** BEGINNING OF INCREMENT.
C
CALL FIRSTINV(3,3,SUBSIG,FINV)
SUBSIGH=FINV

DO I = 1,MAXSIG
  DEVSIG(I) = SUBSIG(I) - KRONECKER(I)*SUBSIGH/3.0
  BACK(I) = BACK0(I) + BACK1(I) + BACK2(I)
  OVERSIG(I) = DEVSIG(I) - 2.0*BACK(I)/3.0
END DO

P1=KRONECKER(3)*SUBSIGH/3.
C   WRITE(6,1800) DEVSIG(3),SUBSIG(3),KRONECKER(3),SUBSIGH,P1
1800 FORMAT(1X,'DEVS,SUBS,KRO,SUBSIG,P1=',5E12.3)
CALL SECONDINV(3,3,OVERSIG,SINV)
SIGSCALE = DSQRT(3.0*SINV/2.0)
&      +1.0E-10

C
C *** SAVE SUBINCREMENT TIME IN SAVE_DSUBTIME FOR UPDATING. THE
C *** VALUE OF DSUBTIME IS CHANGED IN THE RATE INDEPENDENT
C *** SUBROUTINE UMAT_EFFRAT_MATER, AND THEREFORE NEEDS TO BE
C *** SAVED FOR THE FINAL UPDATE.
C
SAVE_DSUBTIME = DSUBTIME
CALL UMAT_EFFRAT_MATER (DSUBTOT,DSUBTIME,TEMPC,DSUBTIME)
C
C *** INITIALIZE BEST GUESS FOR VALUES OF VARIABLES AT TIME
C *** = T + DT. CURRENTLY THE GUESS FOR THE END OF THE INCREMENT

```

```

C *** ARE THE VALUES AT THE END OF THE PREVIOUS INCREMENT.
C
  DRAGN = DRAG
  DO I = 1,MAXSIG
    EPLASN(I) = EPLAS(I)
    SUBSIGN(I) = SUBSIG(I)
    BACKON(I) = BACKO(I)
    BACK1N(I) = BACK1(I)
    BACK2N(I) = BACK2(I)
    BACKN(I) = BACK(I)
  END DO

C
C      *****
C      ***** START OF ITERATION *****
C      *****
C
C *** CONVERGENCE WILL BE BASED ON THE LAST CALCULATED CHANGE
C *** BEING LESS THAN RHOTOL. IF NUMBER OF ITERATIONS EXCEED
C *** MAXITER, GET OUT OF THE ITERATION LOOP. IF WE ARE IN
C *** THE ELASTIC REGION GET OUT OF THE ITERATION LOOP.
C
  ITER = 0
C
C *** SET INITIALLY HIGH CHANGE IN RHO(1) TO GET INTO WHILE LOOP ***
C
  ELASTIC = 'FALSE'
  CHANGE = 1.0
  CUTBAC = 1.0
C
  DO WHILE (CHANGE .GT. RHOTOL .AND.
    & ELASTIC .EQ. 'FALSE' .AND. ITER .LT. MAXITER)
    ITER = ITER + 1
C
C *** SET VALUE OF RHO PERTURBATION ***
C
  DO I = 1,MAXPARAM
    IF(RHO(I) .EQ. 0.0) THEN
      DRHO(I) = 1.E-8
    ELSE
      DRHO(I) = PERT*RHO(I)
    ENDIF
  END DO
C
C *** KEEP PREVIOUS ITERATION SOLUTIONS IN ...F ARRAYS
C *** USE THEM AS EQUATION COEFFICIENTS. ...F ARRAYS WILL
C *** NOT CHANGE DURING THE COURSE OF ONE ITERATION. THEY
C *** ARE, HOWEVER, UPDATED AFTER EVERY ITERATION.
C
  DO I = 1,MAXSIG
    EPLASF(I) = EPLASN(I)
    SUBSIGF(I) = SUBSIGN(I)
    BACKOF(I) = BACKON(I)
    BACK1F(I) = BACK1N(I)
    BACK2F(I) = BACK2N(I)
    BACKF(I) = BACKN(I)
  END DO
  DRAGF = DRAGN
  CALL FIRSTINV(3,3,SUBSIGF,FINV)
  SUBSIGFH=FINV

  DO I = 1,MAXSIG
    DEVSIG(I) = SUBSIGF(I) - KRONECKER(I)*SUBSIGFH/3.0
    OVERSIGF(I) = DEVSIG(I) - 2.0*BACKF(I)/3.0
  END DO
C
  P1=KRONECKER(3)*SUBSIGFH/3.
C
  WRITE(6,1805) DEVSIG(3),SUBSIGF(3),SUBSIGFH,P1
1805 FORMAT(1X,'%%% DEVSIG,SUBSF,SUBSFH,P1=',4E12.3)
  CALL SECONDINV(3,3,OVERSIGF,SINV)
  SIGSCALEF = DSQRT(3.0*SINV/2.0)
  CALL SECONDINV(3,3,BACK1F,SINV)
  BACK1SCALEF = DSQRT(2.0*SINV/3.0)

```

```

      CALL SECONDINV(3,3,BACK2F,SINV)
      BACK2SCALEF = DSQRT(2.0*SINV/3.0)
      CALL SECONDINV(3,3,BACKF,SINV)
      BACKSCALEF = DSQRT(2.0*SINV/3.0)
      TEMPDOT = DTEMPC/SAVE_DSUBTIME

      IF ( ITER .LT. 2 ) THEN
C
C *** IF ITER = 1 ESTIMATE PLASTIC STRAIN RATE AS BEING
C *** EQUAL TO THE TOTAL STRAIN RATE
C
      CALL FIRSTINV(3,3,DSUBETOT,FINV)
      DSUBETOTH=FINV

      DO I = 1,6
        DEPLAS(I) = DSUBETOT(I)-1./3.*KRONECKER(I)
      &      *DSUBETOTH
      END DO

      ELSE
C
C *** AFTER FIRST ITERATION, CALCULATE PLASTIC STRAIN RATE
C *** USING MOST RECENT RHO(1).
C
      DO I = 1,MAXSIG
        DEPLAS(I) = RHO(1)*OVERSIGF(I)
      END DO
      ENDIF
      CALL SECONDINV(3,3,DEPLAS,SINV)
      EPSSCALE=DSQRT(2.0/3.0*SINV)

C
C *** CALCULATE U1(1,2 AND 3)[T + DT] AND V1(1,2, AND 3)[T + DT]
C *** BASED ON BEST GUESSES OR MOST RECENT ITERATION FOR
C *** RHO[T+DT] AND DSUBETOT(1 TO 6)[T+DT]
C
C THE INTEGRATION METHOD IS TAKEN FROM PAPER BY KEVIN WALKER AND
C ALAN FREED ENTITLED "ASYMPTOTIC INTEGRATION ALGORITHMS FOR
C NONHOMOGENEOUS, NON-LINEAR, FIRST ORDER, ORDINARY DIFFERENTIAL
C EQUATIONS", NASA TM 103793. THE NAMES OF THE VARIABLES ARE
C PATTERNED AFTER THE METHOD OUTLINED THERE IN EXAMPLE 4. THE
C EQUATIONS HAVE THE FORM
C
C
C      DX /DT +U1 *X = V1
C      IJ      I IJ      IJ
C
C WHERE I GOES FROM 1 TO 3 IN OUR CASE. I = 1 IS STRESS, I = 2 IS FIRST
C BACK STRESS, I = 3 IS SECOND BACK STRESS. ALL EQUATIONS HAVE SIX COMPONENTS,
C SO THAT J GOES FROM 1 TO 6. U11 IS COEFFICIENT OF STRESS, U12 IS COEFFICIENT
C OF BACK1, U13 IS COEFFICIENT OF BACK2. THE V1'S ARE THE RIGHT SIDE OF THE
C EQUATIONS. SUBROUTINES U11, U12, U13 ARE THE CALCULATION OF LEFT HAND SIDE
C COEFFICIENTS. V11, V12 AND V13 ARE THE CALCULATIONS OF THE RIGHT HAND SIDE.
C
C
      CALL UMAT_BZERO(BACKON,EPLASF,KRONECKER,NCON)
      CALL UMAT_U11(U11,RHO,NCON,CC,DSUBTIME)
      CALL UMAT_U12(U1,RHO,SIGSCALEF,NCON,DSUBTIME)
      CALL UMAT_U13(U1,RHO,SIGSCALEF,NCON,DSUBTIME)

C
C      WRITE(6,666) (DSUBETOT(L),L=1,6)
666      FORMAT(1X,'DSTOT=',6E10.3)
C      WRITE(6,667) (BACKF(L),L=1,6)
667      FORMAT(1X,'BACK=',6E10.3)
C      WRITE(6,668) RHO(1),DSUBTIME
668      FORMAT(1X,'ro,dsibt=',2E12.3)
      CALL UMAT_V11(V1,DSUBETOT,RHO,SUBSIGF,BACKF,NCON,
      &      CC,DSUBTIME)
      CALL UMAT_V12(V1,RHO,SUBSIGF,BACK2F,BACKOF,NCON,DSUBTIME)
      CALL UMAT_V13(V1,RHO,SUBSIGF,BACK1F,BACKOF,NCON,DSUBTIME)
C
C *** THE RECURSION ROUTINES ARE THE CALCULATIONS OF THE NEW STRESS, AND

```

```

C *** TWO BACK STRESSES BY THE IMPLICIT RECURSION METHOD DESCRIBED IN THE
C *** WALKER/FREED PAPER.
C
      CALL UMAT_STRESS_RECURSION (SUBSIGN,SUBSIG,U11,V1,DSUBTIME)
C
      CALL UMAT_BACK1_RECURSION (BACK1N,BACK1,U1,V1,DSUBTIME)
C
      CALL UMAT_BACK2_RECURSION (BACK2N,BACK2,U1,V1,DSUBTIME)
C
      DRAGN = DRAG
C
C *** CALCULATE NEW DEVIATORIC STRESS, BACK STRESS AND OVERSTRESS FOR [T+DT] ***
C
      CALL FIRSTINV(3,3,SUBSIGN,FINV)
      SUBSIGNH=FINV
      DO I = 1,MAXSIG
        DEVSIG(I) = SUBSIGN(I) - KRONECKER(I)*SUBSIGNH/3.0
        BACKN(I) = BACK0N(I) + BACK1N(I) + BACK2N(I)
        OVERSIGN(I) = DEVSIG(I) - 2.0*BACKN(I)/3.0
      END DO
C
      P1=KRONECKER(3)*SUBSIGNH/3.
C
      WRITE(6,1801) DEVSIG(3),SUBSIGN(3),SUBSIGNH,P1
1801  FORMAT(1X,'***DEVS,SUBSN,SUBSIGNH,P1=',4E12.3)
      CALL SECONDINV(3,3,OVERSIGN,SINV)
      SIGSCALEN = DSQRT(3.0*SINV/2.0)
      CALL SECONDINV(3,3,BACKN,SINV)
      BACKSCALEN = DSQRT(2.0*SINV/3.0)
      RATION = SIGSCALEN/DRAGN
C
      WRITE(6,1850) BACKSCALEN,RATION
1850  FORMAT(1X,'BASCA,RATIO=',2E12.3)
C
C *** THE METHOD SOLVES FOR CHANGE OF RHO. SINCE THERE IS ONLY ONE RHO
C *** IN THE CURRENT IMPLEMENTATION, A FUNCTION IS SET UP IN EVAL1 WHICH
C *** IS CLOSE TO ZERO WHEN THE VALUES FOR RHO AND THE NEW STRESSES MATCH
C *** UP. THE VALUE OF THE FUNCTION IS CALCULATED FIRST WITH THE CURRENT
C *** RHO AND NEW STRESSES. LATER A NUMERICAL DERIVATIVE IS PERFORMED USING
C *** A PERTURBED VALUE OF RHO AND THE VALUES OF THE STRESSES CALCULATED WITH
C *** THAT PERTURBED VALUE. THE DERIVATIVE OF THE FUNCTION IN EVAL1 TIMES
C *** THE NECESSARY CHANGE IN RHO(1), I.E. C(1), IS SET EQUAL TO THE
C *** VALUE OF THE FUNCTION IN EVAL1 CALCULATED WITH CURRENT VALUES.
C
C *** EVALUATION OF FUNCTION IN EVAL1 WITH CURRENT END OF INCREMENT VALUES
C *** OF RHO AND STRESSES
C
      CALL UMAT_EVAL1(F(1,2),RHO,OVERSIGN,DRAGN,NCON,
&      FORMULATE,RATION,DSUBTIME)
C
C *** INCREMENT RHO(1) FOR EVALUATION OF NUMERICAL DERIVATIVE ***
C
      RHON(1) = RHO(1) + DRHO(1)
C
      CALL UMAT_BZERO(BACK0N,EPLASF,KRONECKER,NCON)
      CALL UMAT_U11(U11,RHON,NCON,CC,DSUBTIME)
      CALL UMAT_U12(U1,RHON,SIGSCALEF,NCON,DSUBTIME)
      CALL UMAT_U13(U1,RHON,SIGSCALEF,NCON,DSUBTIME)
      CALL UMAT_V11(V1,DSUBTOT,RHON,SUBSIGF,BACKF,
&      NCON,CC,DSUBTIME)
      CALL UMAT_V12(V1,RHON,SUBSIGF,BACK2F,BACK0F,NCON,DSUBTIME)
      CALL UMAT_V13(V1,RHON,SUBSIGF,BACK1F,BACK0F,NCON,DSUBTIME)
C
      CALL UMAT_STRESS_RECURSION (SUBSIGN,SUBSIG,U11,V1,DSUBTIME)
C
      CALL UMAT_BACK1_RECURSION (BACK1N,BACK1,U1,V1,DSUBTIME)
C
      CALL UMAT_BACK2_RECURSION (BACK2N,BACK2,U1,V1,DSUBTIME)
C
      DRAGN = DRAG
C
C
C

```

```

C      WRITE(6,1851) BACK1N(3),BACK1(3),U1(3),V1(1,3),DSUBTIME,RHON(1)
1851  FORMAT(1X,'BACK1N,B,U,V,DST,r=',6E10.2)
      CALL FIRSTINV(3,3,SUBSIGN,FINV)
      SUBSIGNH=FINV

      DO I = 1,MAXSIG
        DEVSIG(I) = SUBSIGN(I) - KRONECKER(I)*SUBSIGNH/3.0
        BACKN(I)  = BACKON(I) + BACK1N(I) + BACK2N(I)
        OVERSIGN(I) = DEVSIG(I) - 2.0*BACKN(I)/3.0
      END DO

C      P1=KRONECKER(3)*SUBSIGNH/3.
C      WRITE(6,1802) DEVSIG(3),SUBSIGN(3),SUBSIGNH,P1
1802  FORMAT(1X,'$$$ DEVSIG,SUBSIGN,SUBSIGNH,P1=',4E12.3)
C
C *** EVALUATION OF FUNCTION IN EVAL1 WITH PERTURBED VALUES OF RHO AND STRESSES
C      CALL UMAT_EVAL1(F(1,1),RHON,OVERSIGN,DRAGN,NCON,
&      FORMULATE,RATION,DSUBTIME)

C
C *** PUT JACOBIAN (I.E., EVALUATION OF NUMERICAL DERIVATIVE OF FUNCTION
C *** IN EVAL1) INTO JACOBIAN(1,1). SINCE THERE IS ONLY ONE RHO WE SOLVE
C ***  $DF/DRHO * C = F$ 
C *** I.E., TRYING TO SOLVE FOR DRHO WHICH MAKES F = 0 IN NEXT ITERATION
C
      JACOBIAN(1,1) = (F(1,1)-F(1,2))/DRHO(1)
      IF (JACOBIAN(1,1) .EQ. 0.0) THEN
        C(1) = 0.5*RHO(1)
      ELSE
        C(1) = -F(1,2)/JACOBIAN(1,1)/(1.0 + CUTBAC)
      ENDIF

C
C *** REDUCE CUTBAC BY A FACTOR OF TWO ON EVERY ITERATION ***
C      CUTBAC = 0.5*CUTBAC

C
C *** GET UPDATED VALUE OF PARAMETER RHO ***
C      DO I = 1,MAXPARAM
        RHO(I) = RHO(I) + C(I)
      END DO

C
C *** EVALUATE RELATIVE CHANGE IN RHO ***
C      CHANGE = DABS(C(1)/RHO(1))

C
C *** DETERMINE IF WE ARE IN THE ELASTIC REGION ***
C      WRITE(6,7) ITER,RHO(1),C(1),JACOBIAN(1,1),F(1,2)
7      FORMAT(1X,'IT,RO,C,JACB,F12=',I4,4E12.3)
      IF (RHO(1) .LT. 1.0E-12 .AND. ITER .GT. 2) THEN
        ELASTIC = 'TRUE'

C      WRITE(6,8)
8      FORMAT(1X,'ELASTIC')
      ELSE
        ELASTIC = 'FALSE'

C      WRITE(6,9)
9      FORMAT(1X,'PLASTIC')
      ENDIF

C
C *** USE NEWLY CALCULATED VALUES OF RHO TO GET END OF ITERATION
C *** VALUES OF SUBSIGN AND BACK1N
C
C *** ** REMPLACER MU PAR CODAGE ADEQUAT
      DO I = 1,MAXSIG
        DEPLAS(I) = RHO(1)*OVERSIGF(I)
      END DO

```



```

      CALL UMAT_BZERO(BACK0N,EPLASF,KRONECKER,NCON)
      CALL UMAT_U11(U11,RHO,NCON,CC,DSUBTIME)
      CALL UMAT_U12(U1,RHO,SIGSCALEF,NCON,DSUBTIME)
      CALL UMAT_U13(U1,RHO,SIGSCALEF,NCON,DSUBTIME)
      CALL UMAT_V11(V1,DSUBTOT,RHO,SUBSIGF,BACKF,
&          NCON,CC,DSUBTIME)
      CALL UMAT_V12(V1,RHO,SUBSIGF,BACK2F,BACK0F,NCON,DSUBTIME)
      CALL UMAT_V13(V1,RHO,SUBSIGF,BACK1F,BACK0F,NCON,DSUBTIME)
      CALL UMAT_STRESS_RECURSION (SUBSIGN,SUBSIG,U11,V1,DSUBTIME)
      CALL UMAT_BACK1_RECURSION (BACK1N,BACK1,U1,V1,DSUBTIME)
      CALL UMAT_BACK2_RECURSION (BACK2N,BACK2,U1,V1,DSUBTIME)
C
      DRAGN=DRAG
C
      CALL FIRSTINV(3,3,SUBSIGN,FINV)
      SUBSIGNH=FINV

      DO I=1,MAXSIG
        DEVSIG(I) = SUBSIGN(I) - KRONECKER(I)*SUBSIGNH/3.0
        BACKN(I) = BACK0N(I) + BACK1N(I) + BACK2N(I)
        OVERSIGN(I) = DEVSIG(I) - 2.0*BACKN(I)/3.0
        EPLASN(I) = EPLAS(I) + DEPLAS(I)
      END DO
C
      P1=KRONECKER(3)*SUBSIGNH/3.
C      WRITE(6,1803) DEVSIG(3),SUBSIGN(3),SUBSIGNH,P1
1803  FORMAT(1X,'&&& DEVSIG,SUBS,SUBSNH,P1=',4E12.3)
C      WRITE(6,1600) DEVSIG(3),BACKN(3),BACK0N(3),BACK1N(3),
C      + BACK2N(3),OVERSIGN(3),EPLASN(3),DEPLAS(3)
1600  FORMAT(1X,'DEVSIG,BAK,B0,B1,B2,OVS,EPL,DEPL=',8E10.2)
C
      END DO
C
C      *****
C      ***** END OF ITERATION *****
C      *****
C *** LOAD STATE AT END OF INCREMENT INTO DSTATE ***
      DSTATE(1) = TEMPC+DTEMPC
      DSTATE(2) = SUBTIME + SAVE_DSUBTIME
      DSTATE(3) = DRAGN
      DSTATE(16) = DFLOAT(ITER)
      STATE(16) = 0.0
      DO I = 1,MAXSIG
        DSTATE(I+3) = BACK1N(I)
        DSTATE(I+9) = EPLAS(I) + DEPLAS(I)
        DSTATE(I+16) = BACK2N(I)
      END DO
      DO I = 1,MAXPARAM
        IP22=I+22
        DSTATE(IP22) = RHO(I)
        IF(DSTATE(IP22).LT.1.E-12) DSTATE(IP22)=1.E-12
      END DO
C
C *** CALCULATE STRESS AT END OF INCREMENT ***
C
      DO I = 1,MAXSIG
        SUBSIG(I) = SUBSIGN(I)
      END DO
C
C      WRITE(6,1601) TEMPC,SUBSIG(3)
1601  FORMAT(1X,'TEMPC,SUBSIG=',2E12.3)
C
C *** CALCULATE ELASTIC STRAIN ENERGY AND PLASTIC DISSIPATION ***
C
      DO I=1,MAXSIG
        SSE = SSE + SUBSIG(I)*DSUBTOT(I)
        SPD = SPD + SUBSIG(I)*DEPLAS(I)
        SCD = SCD + 0.0
      END DO
C

```



```

C BACK          : TOTAL BACK STRESS (BACK0+BACK1+BACK2)
C NCON          : MATERIAL CONSTANTS
C CC            : ELASTIC MATERIAL MATRIX
C DSUBTIME      : SCALED TIME INCREMENT
C
C   IMPLICIT REAL*8 (A-H,O-Z)
C   REAL*8 NCON(9)
C   DIMENSION V1(3,6),RHO(5),DSUBTOT(6),BACK(6),SUBSIG(6)
C   + ,P(3),DEDOT(MAXSIG),CC(6,6)
C
C LOCAL VARIABLES
C
C P            : COMMON GROUPING OF TERMS IN STRESS RATE EQUATION
C DEDOT        : TOTAL STRAIN RATE
C A,A1,A2,A3   : TEMPORARY GROUPING OF VARIABLES
C B,B1,B2,B3   : TEMPORARY GROUPING OF VARIABLES
C
C   DO I = 1,MAXSIG
C     DEDOT(I) = DSUBTOT(I)/DSUBTIME
C   END DO
C   DO I = 1,3
C     P(I) = DEDOT(I)+2.0/3.0*RHO(1)/DSUBTIME*BACK(I)
C   END DO
C
C *** CALCULATE V11 PARAMETER
C
C   A1 = RHO(1)/DSUBTIME/3.0*((CC(1,1)+CC(1,3)-2*CC(1,2))*SUBSIG(2)+
C & (CC(1,1)+CC(1,2)-2*CC(1,3))*SUBSIG(3))
C   B1 = CC(1,1)*P(1)+CC(1,2)*P(2)+CC(1,3)*P(3)
C   V1(1,1) = A1 + B1
C   A2 = RHO(1)/DSUBTIME/3.0*((CC(2,2)+CC(2,3)-2*CC(2,1))*SUBSIG(1)+
C & (CC(2,2)+CC(2,1)-2*CC(2,3))*SUBSIG(3))
C   B2 = CC(2,1)*P(1)+CC(2,2)*P(2)+CC(2,3)*P(3)
C   V1(1,2) = A2 + B2
C   A3 = RHO(1)/DSUBTIME/3.0*((CC(3,3)+CC(3,2)-2*CC(3,1))*SUBSIG(1)+
C & (CC(3,3)+CC(3,1)-2*CC(3,2))*SUBSIG(2))
C   B3 = CC(3,1)*P(1)+CC(3,2)*P(2)+CC(3,3)*P(3)
C   V1(1,3) = A3 + B3
C   DO I = 4,MAXSIG
C     V1(1,I) = 2*CC(I,I)*(DEDOT(I)+2.0/3.0*RHO(1)/DSUBTIME*BACK(I))
C   END DO
C
C   WRITE(6,7) (DEDOT(L),L=1,6)
C   FORMAT(1X,'DEDOT=',6E10.2)
C   WRITE(6,8) (SUBSIG(L),L=1,6)
C   FORMAT(1X,'SUBSIG=',6E10.2)
C   WRITE(6,9) DSUBTIME,RHO(1),LAMBDA,MU
C   FORMAT(1X,'DST,ro,LAM,MU=',4E12.3)
C
C   RETURN
C   END
C
C *****
C
C   SUBROUTINE UMAT_V12(V1,RHO,SUBSIG,BACK2,BACK0,NCON,DSUBTIME)
C
C CALCULATION OF RIGHT HAND SIDE OF 1ST BACK STRESS RATE EQUATION
C
C   PARAMETER (MAXSIG = 6)
C
C   V1(2,6)      : VALUE OF RIGHT SIDE FOR 6 EQUATIONS
C   RHO          : ITERATION PARAMETER
C   SIGSCALE     : OVERSTRESS SCALER
C   BACK1SCALE   : 1ST BACK STRESS SCALER
C   SUBSIG       : STRESS AT END OF INCREMENT
C   BACK2        : 2ND BACK STRESS
C   BACK0        : 0TH BACK STRESS
C   NCON         : MATERIAL CONSTANTS
C   MEXP         : MATERIAL EXPONENTS
C   DSUBTIME     : SCALED TIME INCREMENT
C
C   IMPLICIT REAL*8(A-H,O-Z)

```



```

      B1 = BACK1(I)*DECAY
      B2 = V1(2,I)/U1(2)*(1.0-DECAY)
      BACK1N(I) = B1 + B2
    ELSE
      B1 = BACK1(I)*(1.0-TAU+TAU**2/2.0-TAU**3/6.0
&          +TAU**4/24.0)
      B2 = V1(2,I)*DSUBTIME*(1.0-TAU/2.0+TAU*TAU/6.0
&          -TAU**3/24.0)
      BACK1N(I) = B1 + B2
    ENDIF
  END DO

C
C   WRITE(6,1600) BACK1N(3),BACK1(3),U1(2),V1(2,3),TAU
1600 FORMAT(1X,'B1N,B1,U1,V1(2,3),TAU=',5E12.3)

RETURN
END

CCCCCCCCCCCCCCCCCCCCCCCCCCCCCCCCCCCCCCCCCCCCCCCCCCCCCCCCCCCCCCCCCCCCCCCCCC

SUBROUTINE UMAT_BACK2_RECURSION (BACK2N,BACK2,U1,V1,DSUBTIME)

C
C IMPLICIT RECURSION METHOD USED TO CALCULATE NEW VALUE OF
C 2ND BACK STRESS
C
C
C BACK2N           : NEW VALUE OF BACK2
C BACK2            : OLD VALUE OF BACK2
C U1(3)            : COEFFICIENTS OF BACK2 IN BACK2 RATE EQUATION
C V1(3,1-6)        : RIGHT SIDE OF BACK2 RATE EQUATIONS
C DSUBTIME         : SCALED TIME INCREMENT
C
PARAMETER (MAXSIG = 6)
IMPLICIT REAL*8(A-H,O-Z)
DIMENSION BACK2N(6),BACK2(6),U1(3),V1(3,6)

C
C LOCAL VARIABLES
C
C TAU              : DECAY CONSTANT
C DECAY            : EXP OF -(DECAY CONSTANT)
C B1,B2            : TEMPORARY STORAGE VARIAIBLES
C
DO I = 1,MAXSIG
  TAU = U1(3)*DSUBTIME

C
C MUST CALCULATE 1. - EXP(-TAU), IF EXP(-TAU) IS TOO SMALL
C 1. - EXP(-TAU) WILL BE ZERO BECAUSE OF SINGLE PRECISION
C IF -TAU IS CLOSE TO ZERO IT IS BETTER TO CALCULATE 1.-EXP(-TAU)
C USING A TAYLOR EXPANSION. THIS WILL GIVE A DECENT CALCULATED VALUE
C
  IF (TAU.GT.1.E-4) THEN
    DECAY = DEXP(-TAU)
    B1 = BACK2(I)*DECAY
    B2 = V1(3,I)/U1(3)*(1.0-DECAY)
    BACK2N(I) = B1 + B2
  ELSE
    B1 = BACK2(I)*(1.0-TAU+TAU**2/2.0-TAU**3/6.0
&          +TAU**4/24.0)
    B2 = V1(3,I)*DSUBTIME*(1.0-TAU/2.0+TAU*TAU/6.0
&          -TAU**3/24.0)
    BACK2N(I) = B1 + B2
  ENDIF
END DO

C
RETURN
END

CCCCCCCCCCCCCCCCCCCCCCCCCCCCCCCCCCCCCCCCCCCCCCCCCCCCCCCCCCCCCCCCCCCCCCCCCC

SUBROUTINE UMAT_EVAL1(F,RHO,OVERSIG,DRAW,NCON,
& FORMULATE,RATION,DSUBTIME)

```

```

C
C EVALUATION OF RHO FUNCTIONAL. AT CONVERGENCE THE FUNCTION
C F SHOULD BE ZERO
C
C F : VALUE OF FUNCTIONAL FOR RHO(1), WILL BE ZERO AT CONVERGENCE
C RHO : ITERATION PARAMETER
C OVERSIG : OVERSTRESS
C DRAG : DRAG STRESS
C NCON : MATERIAL CONSTANTS
C MEXP : MATERIAL EXPONENTS
C MU : LAME CONSTANT
C CC : MATERIAL ELASTIC MATRIX
C FORMULATE : TYPE OF PLASTIC STRAIN RATE LAW( THIS IS EXPONENTIAL)
C RATION : RATIO OF SIGSCALE/DRAG -- USED TO DETERMINE WHETHER TO
C EVALUATE FUNCTIONAL OR LN(FUNCTIONAL)
C DSUBTIME : TIME INCREMENT
C IMPLICIT REAL*8(A-H,O-Z)
C REAL*8 NCON(9)
C DIMENSION RHO(5),OVERSIG(6),CC(6,6)
C CHARACTER*(*) FORMULATE
C
C *** LOCAL VARIABLES ***
C
C *** RATIO : CURRENT VALUE OF SIGSCALE/DRAG
C *** SIGSCALE : OVERSTRESS SCALER
C *** FAC : GROUPING OF TERMS FOR CONVENIENCE
C
C CALCULATION OF RHO FUNCTIONAL, F, BASED ON VALUES OF RHO AND
C STRESSES.
C
C CALL SECONDINV(3,3,OVERSIG,SINV)
C SIGSCALE = DSQRT(3.0*SINV/2.0)
C & + 1.0E-10
C
C *** CHECK INELASTIC STRAIN FORMULATION ***
C
C IF (FORMULATE .EQ. 'POWER LAW') THEN
C POWER = 1.0/1.0
C RDOT = (SIGSCALE/DRAG)**POWER
C F = 3.0/2.0*RDOT**(1.0-1.0/POWER)/DRAG*DSUBTIME-RHO(1)
C ELSE IF (FORMULATE .EQ. 'EXPONENTIAL') THEN
C
C FOR LARGE ARGUMENTS, THE FUNCTIONAL MAY GET VERY LARGE. BY TAKING
C THE NATURAL LOG OF THE FUNCTION(SAME FUNCTIONAL BUT SCALED TO SMALLER
C VALUE -- TAKING LN OF BOTH SIDES OF AN EQUATION) ALL ARGUMENTS CAN BE
C HANDLED. IF RATIO IS GE 10 USE LN(FUNCTIONAL), IF LT 10 USE FUNCTIONAL.
C ALSO TO BE CONSISTENT DURING ONE ITERATION, BASE WHICH FUNCTIONAL TO USE
C ON FIRST CALCULATED VALUE OF RATIO WITHIN ONE ITERATION LOOP, (RATION).
C
C RATIO = SIGSCALE/DRAG
C FOLLOWING FUNCTION DONE ACCORDING TO NCON(6)
C IF (RATION .GE. 10.0) THEN
C FAC = 2.*RHO(1)/DSUBTIME*SIGSCALE*NCON(6)/3.0
C IF (FAC .LE. 1.0E-3) THEN
C F = RATIO-(FAC-FAC*FAC/2.0+FAC**3/3.0
C & -FAC**4/4.0)
C ELSE
C F = RATIO - DLOG(FAC + 1.0)
C ENDIF
C ELSE
C F = 3.0/2.0*DSUBTIME/SIGSCALE*(DEXP(RATIO)-1.0)/NCON(6)-RHO(1)
C ENDIF
C
C ELSE IF (FORMULATE .EQ. 'HYPERBOLIC SINE') THEN
C POWER = 1.0/1.0
C F = 3.0/2.0*DSUBTIME/SIGSCALE*DSINH(SIGSCALE/DRAG)**POWER-RHO(1)
C ENDIF
C
C RETURN
C END

```


[illegible]

```

SUBROUTINE UMAT_BZERO(BACKO, EPLAS, KRONECKER, NCON)
C
C CALCULATION OF ZEROth BACK STRESS
C
C     PARAMETER (MAXSIG = 4)
C
C     IMPLICIT REAL*8 (A-H,O-Z)
C     REAL*8 NCON(9), KRONECKER(6)
C     DIMENSION BACKO(6), EPLAS(6), BACKNON(6)
C
C CALCULATE ZEROth BACK STRESS
C
C     CALL SECONDINV(3,3,EPLAS,SINV)
C     W=SINV
C     WRITE(6,13) W
C 13    FORMAT(1X,'W=',E12.3)
C     EPSSCALE = (2.0/3.0)*W + 1.E-10
C
C     WRITE(6,7) (EPLAS(L),L=1,6)
C 7     FORMAT(1X,'EPLAS=',6E10.2)
C 200
C     WRITE(6,8) EPSSCALE
C 8     FORMAT(1X,'EPSSCALE=',E12.3)
C
C     BACKNON(1) = - NCON(5) + 2.0*NCON(5)*(EPLAS(1)*EPLAS(1)
C &      + EPLAS(4)*EPLAS(4) + EPLAS(6)*EPLAS(6)
C &      + 1.E-10)/EPSSCALE
C     BACKNON(2) = - NCON(5) + 2.0*NCON(5)*(EPLAS(4)*EPLAS(4)
C &      + EPLAS(2)*EPLAS(2) + EPLAS(5)*EPLAS(5)
C &      + 1.E-10)/EPSSCALE
C     BACKNON(3) = - NCON(5) + 2.0*NCON(5)*(EPLAS(6)*EPLAS(6)
C &      + EPLAS(5)*EPLAS(5) + EPLAS(3)*EPLAS(3)
C &      + 1.E-10)/EPSSCALE
C     BACKNON(4) = - 2.0*NCON(5)*(EPLAS(1)*EPLAS(4)
C &      + EPLAS(2)*EPLAS(4) + EPLAS(5)*EPLAS(6)
C &      + 1.E-10)/EPSSCALE
C     BACKNON(5) = - 2.0*NCON(5)*(EPLAS(4)*EPLAS(6)
C &      + EPLAS(2)*EPLAS(5) + EPLAS(3)*EPLAS(5)
C &      + 1.E-10)/EPSSCALE
C     BACKNON(6) = - 2.0*NCON(5)*(EPLAS(1)*EPLAS(6)
C &      + EPLAS(4)*EPLAS(5) + EPLAS(3)*EPLAS(6)
C &      + 1.E-10)/EPSSCALE
C
C GET DEVIATORIC PART OF ZEROth BACK STRESS
C
C     CALL FIRSTINV(3,3,BACKNON,FINV)
C     BACKOH=FINV/3.0
C
C     WRITE(6,1600) (NCON(L),L=1,5)
C 1600  FORMAT(1X,'NCON=',5E10.2)
C     WRITE(6,1601) (EPLAS(L),L=1,6)
C 1601  FORMAT(1X,'EPLAS=',6E10.2)
C     WRITE(6,1602) (BACKNON(L),L=1,6)
C 1602  FORMAT(1X,'BONON=',6E10.2)
C     DO I = 1, MAXSIG
C         BACKO(I) = BACKNON(I) - KRONECKER(I)*BACKOH
C         BK=KRONECKER(I)*BACKOH
C         BI=BACKNON(I)-BK
C         WRITE(6,16) BACKO(I),BI,BK,KRONECKER(I),BACKOH,BACKNON(I)
C 16     FORMAT(1X,'BO,BI,BK,KR,BONON=',6E10.3)
C 7000  FORMAT(1X,'SUBR BO,BO,BONON,BOH,KR=',I3,4E12.3)
C         WRITE(6,7001) (BACKNON(L),L=1,6)
C         WRITE(6,7002) (KRONECKER(L),L=1,6)
C 7001  FORMAT(1X,'BONON=',6E12.3)
C 7002  FORMAT(1X,'KRO=',6E12.3)
C     END DO
C
C     WRITE(6,25) BACKO(3)
C 25    FORMAT(1X,'BO=',E12.3)
C     WRITE(6,26) BACKNON(3),BACKOH

```

```

26  FORMAT(1X,'BNON3,BACKoh=',2E12.4)
C
      RETURN
      END

C
C  AUTHOR: K.P. WALKER
C
C  PURPOSE: 3D UNIFIED VISCOPLASTIC MATERIAL MODEL
C
C  INPUT: LOADING INCREMENTS; STRAIN CONTROL
C
C  OUTPUT: RESPONSE & STATE VARIABLE INCREMENTS
C          ELASTIC MATERIAL MATRIX
C
C  CALLING SUBROUTINE: UMAT
C
C  CALLED SUBROUTINES: UMAT_CONSTANT, UMAT_FIRSTINV,
C                      UMAT_SECONDINV, UMAT_THIRDINV,
C                      UMAT_ELASTIC, UMAT_DIFF_MATER,
C                      UMAT_INT_MATER
C
C  REVISIONS:
C
C          1) INCLUSION OF INTEGRAL METHOD FOR EQUATION
C              SOLUTION.
C
C
C          SUBROUTINE UMAT_UNICORN (D,DSIGPLAS,ETOT,DETOT,SIG,
C          &                        DS,STATE,DSTATE,
C          &                        NSTRESS,CMNAME,NNORMAL,NSHEAR,TIME,
C          &                        DTIME,INTEGRATE,DDSDDE,DDSDDT,
C          &                        TEMP,DTEMP,
C          &                        SSE,SPD,SCD)
C
C *** USER DEFINED PARAMETERS ***
      IMPLICIT REAL*8(A-H,O-Z)

      PARAMETER (MAXCONST = 9)
      PARAMETER (MAXSIG   = 6)
      PARAMETER (MAXSTATE = 29)
      PARAMETER (MAXPARAM = 1)

C *** SUBROUTINE PARAMETERS ***

C *** D          : ELASTIC STRESS-STRAIN MATRIX
C *** DSIGPLAS   : PLASTIC STRESS INCREMENT VECTOR
C *** ETOT       : TOTAL STRAIN AT START OF INCREMENT
C *** DETOT      : TOTAL STRAIN INCREMENT
C *** SIG        : STRESS TENSOR AT START OF INCREMENT
C *** DS         : TOTAL STRESS INCREMENT
C *** STATE:     : STATE VARIABLES AT START OF INCREMENT
C *** DSTATE     : INCREMENTS OF STATE VARIABLES
C *** NSTRESS    : TOTAL NUMBER OF STRESS COMPONENTS
C *** CMNAME     : CURRENT MATERIAL ID
C *** NNORMAL    : NUMBER OF NORMAL STRESSES
C *** NSHEAR     : NUMBER OF SHEAR STRESSES
C *** TIME       : TIME AT START OF INCREMENT
C *** DTIME      : TIME INCREMENT
C *** INTEGRATE  : FLAG FOR DIFFERENTIAL OR INTEGRAL FORM
C *** DDSDDE    : STRESS-STRAIN JACOBIAN AT END OF INCREMENT
C *** DDSDDT     : STRESS-TEMPERATURE JACOBIAN
C *** TEMP       : TEMPERATURE AT BEGINNING OF INCREMENT
C *** DTEMP      : TEMPERATURE INCREMENT
C *** SSE        : ELASTIC STRAIN ENERGY
C *** SPD        : PLASTIC DISSIPATION
C *** CPD        : CREEP DISSIPATION

      CHARACTER*8 CMNAME
      CHARACTER*80 INTEGRATE

```

```

      DIMENSION D(6,6),DSIGPLAS(6),ETOT(6),
+ DETOT(6),SIG(6),DS(6),STATE(29),DSTATE(29),
+ DDSdde(6,6),DDSDDT(6)

```

```

C *** LOCAL VARIABLES ***

```

```

C *** CONTROL      : LOAD CONTROL
C *** ELEMTYPE     : ELEMENT TYPE STRING
C *** TEMP         : TEMPERATURE AT BEGINNING OF INCREMENT
C *** DTEMP        : PROJECTED TEMPERATURE CHANGE OVER INCREMENT
C *** SUBSIG       : CURRENT STRESS
C *** DSUBSIG      : STRESS SUBINCREMENT
C *** SUBTOT       : SUBINCREMENTAL TOTAL STRAIN
C *** DSUBTOT      : SUBINCREMENTAL TOTAL STRAIN SUBINCREMENT
C *** DEVIATOR     : MULTIPLIERS FOR DEVIATORIC STRESS
C *** ENGRSTRN     : CONVERT FROM TENSOR TO ENGINEERING STRAIN
C

```

```

      CHARACTER CONTROL*80
      CHARACTER ELEMTYPE*80
      DIMENSION SUBSIG(6),DSUBSIG(6),SUBTOT(6),
+ EPLAS(6),DSUBTOT(6),ENGRSTRN(6),
+ DDSdde3D(6,6),DDSDDT3D(6)

```

```

C
      DATA ENGRSTRN/3*1.0,3*2.0/

```

```

C *** MATERIAL CONSTANTS

```

```

C *** NCON         : MATERIAL CONSTANTS
C *** DNCON        : RATE OF CHANGE OF CONSTANTS W.R.T. TEMP
C *** MEXP         : MATERIAL EXPONENTS
C *** DMEXP        : RATE OF CHANGE OF EXPONENTS W.R.T. TEMP
C *** EMOD         : YOUNG'S MODULUS
C *** POISSON      : POISSON RATIO
C *** GMOD         : SHEAR MODULUS
C *** CC(6,6)      : ELASTIC MATERIAL MATRIX

```

```

      REAL*8 NCON(9)
      DIMENSION DNCON(9),CC(6,6)

```

```

C *** OUTPUT UNIT NUMBER ***

```

```

      INTEGER OUNIT
      DATA OUNIT/6/

```

```

C*****
C
C
C          SUMMARY OF STATE VARIABLES
C
C      STATE(1)  -- TEMPERATURE
C      STATE(2)  -- TIME
C      STATE(3)  -- DRAG STRESS
C      STATE(4)  -- 1ST COMPONENT OF 1ST BACK STRESS
C      STATE(5)  -- 2ND COMPONENT OF 1ST BACK STRESS
C      STATE(6)  -- 3RD COMPONENT OF 1ST BACK STRESS
C      STATE(7)  -- 1ST SHEAR COMPONENT OF 1ST BACK STRESS
C      STATE(8)  -- 2ND SHEAR COMPONENT OF 1ST BACK STRESS
C      STATE(9)  -- 3RD SHEAR COMPONENT OF 1ST BACK STRESS
C      STATE(10) -- 1ST COMPONENT OF PLASTIC STRAIN
C      STATE(11) -- 2ND COMPONENT OF PLASTIC STRAIN
C      STATE(12) -- 3RD COMPONENT OF PLASTIC STRAIN
C      STATE(13) -- 1ST SHEAR COMPONENT OF PLASTIC STRAIN
C      STATE(14) -- 2ND SHEAR COMPONENT OF PLASTIC STRAIN
C      STATE(15) -- 3RD SHEAR COMPONENT OF PLASTIC STRAIN
C      STATE(16) -- NUMBER OF SUBINCREMENTS FOR GIVEN ITERATION
C
C      IN DIFFERENTIAL FORM
C      STATE(17) -- 1ST COMPONENT OF 2ND BACK STRESS
C      STATE(18) -- 2ND COMPONENT OF 2ND BACK STRESS
C      STATE(19) -- 3RD COMPONENT OF 2ND BACK STRESS
C      STATE(20) -- 1ST SHEAR COMPONENT OF 2ND BACK STRESS
C      STATE(21) -- 2ND SHEAR COMPONENT OF 2ND BACK STRESS
C      STATE(22) -- 3RD SHEAR COMPONENT OF 2ND BACK STRESS
C      STATE(23) -- ITERATION PARAMETER FOR INTEGRAL METHOD
C      STATE(24) -- NOT USED

```

```

C      STATE(25)      -- NOT USED
C      STATE(26 - 29) -- NOT USED
C
C*****
C
C      WRITE(6,7000) (DETOT(K),K=1,6)
C7000      FORMAT(1X,'CORN DETOTS=',6E10.3)
C
C      TEMPC = TEMP
C      DTEMP = DTEMP
C
C      CALL UMAT_CON_MATER(TEMP,DTEMP,NCON,DNCON)
C      WRITE(6,7016) EMOD,POISSON
C7016      FORMAT(1X,'E=',E10.3,2X,'NI=',E10.3)
C
C      MUST MAKE SURE STATE(3) IS SET EQUAL TO INITIAL DRAG STRESS
C
C      *** EXP & INT: STATE(3) = DRAG = NCON(5)
C      *** POWER LAW & DIFF: STATE(3) = DRAG = NCON(1)
C      STATE(3) = NCON(1)
C
C
C      WRITE(OUNIT,*) ' THIS ANALYSIS IS USING: MATER  '//
C      &      ' CONSTITUTIVE MODEL '
C      WRITE(OUNIT,*) '                                GENERAL D'//
C      &      ' DESCRIPTION:
C      WRITE(OUNIT,*) ' THIS MODEL IS IN-GENERAL AS DESCRIBED I'//
C      &      ' N PWA REPORT "RESEARCH AND DEVELOPMENT '
C      WRITE(OUNIT,*) ' PROGRAM FOR NONLINEAR STRUCTURAL MODELING'//
C      &      ' WITH ADVANCED TIME-TEMPERATURE CONSTITUTIVE'//
C      &      ' RELATIONSHIPS" BY K.P. WALKER,
C      WRITE(OUNIT,*) ' NASA CR 165533, 1981, EXCEPT THAT THE '//'
C      &      ' MODEL IS RATE INDEPENDENT BELOW 1200F.'
C      WRITE(OUNIT,*) ' DATA USED IN FINDING MATERIAL CONSTANTS'//
C      &      ' : ISOTHERMAL CYCLIC DATA FOR THE
C      WRITE(OUNIT,*) ' FOLLOWING TEMPERATURES: 70, 800, 1000, '//
C      &      ' 1200, 1400, 1600, 1800, 2000 DEGREES
C      WRITE(OUNIT,*) ' FAHRENHEIT. STRAIN RATES USED WERE GENE'//
C      &      ' RALLY BETWEEN 1.0E-6 IN/IN/S AND 0.001
C      WRITE(OUNIT,*) ' IN/IN/S. OVERALL STRAIN RANGES WERE UP'//
C      &      ' TO 0.006 IN/IN. IN ADDITION MONOTONIC
C      WRITE(OUNIT,*) ' DATA , CREEP DATA, AND SOME TMF DATA WA'//
C      &      ' S USED TO AID IN FINDING THE CONSTANTS.'
C      WRITE(OUNIT,*) '
C      WRITE(OUNIT,*) ' APPLICABLE ELEMENTS: '
C      WRITE(OUNIT,*) '
C      WRITE(OUNIT,*) ' 1) PLANE STRESS '
C      WRITE(OUNIT,*) ' 2) PLANE STRAIN '
C      WRITE(OUNIT,*) ' 3) AXISYMMETRIC SOLID '
C      WRITE(OUNIT,*) ' 4) 3-D SOLID '
C      WRITE(OUNIT,*) ' 5) TRUSS ELEMENT '
C      WRITE(OUNIT,*) '
C      WRITE(OUNIT,*) ' NOT APPLICABLE FOR: '
C      WRITE(OUNIT,*) '
C      WRITE(OUNIT,*) ' BEAMS, SHELLS, OR ANY ELEMENT WITH ROTA'//
C      &      ' TIONAL DEGREES OF FREEDOM.'
C      WRITE(OUNIT,*) '
C      WRITE(OUNIT,*) ' CURRENT LIMITATIONS OF MODEL: '
C      WRITE(OUNIT,*) '
C      WRITE(OUNIT,*) ' 1) STRAIN RATE INDEPENDENCE OF STRESS A'//
C      &      ' T LOW TEMPERATURES IS INCLUDED BUT
C      WRITE(OUNIT,*) ' SHOULD BE COMPARED MORE RIGOROUSLY T'//
C      &      ' O DATA.'
C      WRITE(OUNIT,*) ' 2) MEAN STRESS CURRENTLY RELAXES TO ZER'//
C      &      ' O FOR STRAIN CONTROLLED CYCLIC LOADING.'
C      WRITE(OUNIT,*) ' 3) TEMPERATURE RATE TERMS SHOULD BE ADD'//
C      &      ' ED BACK IN MODEL WHEN MEAN STRESS
C      WRITE(OUNIT,*) ' PROBLEM IS ADDRESSED AND ALL CONSTAN'//
C      &      ' TS ARE RE-REGRESSED.'
C      WRITE(OUNIT,*) '

```

```

C
C *** INITIALIZE LOCAL VARIABLES ***
C
      DO I=1,MAXSIG
        SUBSIG(I) = 0.
        DSUBSIG(I) = 0.
        SUBTOT(I) = 0.
        DSUBTOT(I) = 0.
        DO J=1,MAXSIG
          CC(I,J) = 0.
        END DO
      END DO

C *** INITIALIZE MATERIAL CONSTANTS ***

      DO I=1,MAXCONST
        NCON(I) = 0.
        DNCON(I) = 0.
      END DO

C *** LOAD STRESS, STRAIN, & INCREMENTS ***

      DO I = 1,NNORMAL
        SUBSIG(I) = SIG(I)
        SUBTOT(I) = ETOT(I)
        DSUBTOT(I) = DETOT(I)
      END DO
      DO I = 1,NSHEAR
        SUBSIG(I+3) = SIG(I+NNORMAL)
        SUBTOT(I+3) = ETOT(I+NNORMAL)/2.0
        DSUBTOT(I+3) = DETOT(I+NNORMAL)/2.0
      END DO

C
C *** GET PLASTIC STRAINS
C
      DO I = 1,MAXSIG
        EPLAS(I) = STATE(I+9)
      END DO

C
C      WRITE(6,2700) (EPLAS(L),L=1,6)
C      2700   FORMAT(1X,'CORN EPLAS=',6E10.2)
C *** ESTABLISH ELEMENT TYPE ***

      ELEMTYPE = '3D'

C
C *** INTEGRATE STATE EQUATIONS ***
C
C SEVERAL DIFFERENT VISCOPLASTIC MATERIALS CAN BE USED AT ONCE BY
C INCLUDING THEM IN THE "IF" STATEMENT BELOW. DEPENDING ON THE
C VALUE OF CMNAME, THERE WOULD BE A CALL TO A DIFFERENT DIFFERENTIAL
C ROUTINE. THE ROUTINES THAT MUST BE SUPPLIED WOULD BE A DIFF'MAT '
C AN INT'MAT ', AND A CON'MAT '. IF RATE INDEPENDENCE IS INCLUDED
C VIA AN EFF'MAT ' THEN THIS ROUTINE MUST ALSO BE SUPPLIED. THE
C ELASTIC ROUTINE AS WELL AS ALL THE OTHER SUBROUTINES ARE MATERIAL
C INDEPENDENT.

C ***** IF (CMNAME .EQ. 'DSR80') THEN *****
C      IF (INTEGRATE .EQ. 'DIFFERENTIAL') THEN
C
C *** DIFFERENTIAL FORMULATION ***
C
C      CALL UMAT_DIFF_MATER(SUBSIG,DSUBSIG,SUBTOT,
C      &
C      & DSUBTOT,
C      & STATE,DSTATE,
C      & NSTRESS,NNORMAL,NSHEAR,
C      & ELEMTYPE,CONTROL,
C      & DDSDE3D,DDSDDT3D,
C      & SSE,SPD,SCD)
C
C *** INTEGRAL FORMULATION ***
C

```

```

ELSE IF (INTEGRATE .EQ. 'INTEGRAL') THEN
C
C
C      WRITE(6,7777) (SUBSIG(L),L=1,6)
7777  FORMAT(1X,'CORN SUBSIG=',6E10.3)
C      WRITE(6,7778) (SUBETOT(L),L=1,6)
7778  FORMAT(1X,'COR SUTOT=',6E10.3)
C      WRITE(6,7779) (EPLAS(L),L=1,6)
7779  FORMAT(1X,'COR EPLAS=',6E10.3)
      CALL UMAT_INT_MATER(SUBSIG,DSUBSIG,SUBETOT,
&                          DSUBETOT,
&                          STATE,DSTATE,
&                          NSTRESS,NNORMAL,NSHEAR,
&                          ELEMTYPE,CONTROL,
&                          DDSDE3D,DDSDDT3D,
&                          SSE,SPD,SCD)
      ELSE
        WRITE(OUNIT,*) ' INTEGRATION PROCEDURE NOT SUPPORTED '
      ENDIF
C ***** END IF *****
C
C *** LOAD STATE VARIABLE SUBINCREMENTS ***
C
C      ON EXIT FROM DIFF_MATER AND INT_MATER,
C      DSTATE CONTAINS THE STATE AT THE END
C      OF THE UMAT LOAD INCREMENT
C
      DO I=1,MAXSTATE
        DSTATE(I) = DSTATE(I) - STATE(I)
      END DO
C
C *** LOAD ELASTIC CONSTITUTIVE AND JACOBIAN MATRIX ***
C
      CALL UMAT_CON_MATER (TEMP,DTEMP,NCON,DNCON)
      CALL UMAT_ELASTIC (TEMPC,DTEMPC,CC)
C      WRITE(UNIT=88,*) 'CC11 = ',CC(1,1)
C      WRITE(UNIT=88,*) 'CC21 = ',CC(2,1)
C      WRITE(UNIT=88,*) 'CC31 = ',CC(3,1)
C
      DO I=1,NSTRESS
        DDSDDT(I) = DDSDDT3D(I)
        DO J=1,NSTRESS
          D(I,J) = CC(I,J)
          DDSDDE(I,J) = DDSDDE3D(I,J)
C      WRITE(6,7777) I,J,DDSDDE(I,J),D(I,J)
C7777  FORMAT(1X,'CORN,DS/DE,CONSTIT',2I5,E10.3,2X,E10.3)
        END DO
      END DO
C
C *** LOAD STRESS INCREMENT AND INELASTIC STRESS INCREMENT ***
C
      DO I=1,NNORMAL
        DSIGPLAS(I) = SUBSIG(I) - SIG(I)
        DS(I) = SUBSIG(I) - SIG(I)
        DO J=1,NSTRESS
          DSIGPLAS(I) = DSIGPLAS(I) - D(I,J)*DETOT(J)
        END DO
      END DO
      DO I=1,NSHEAR
        DSIGPLAS(I+NNORMAL) = SUBSIG(I+3) - SIG(I+NNORMAL)
        DS(I+NNORMAL) = SUBSIG(I+3) - SIG(I+NNORMAL)
        DO J=1,NSTRESS
          DSIGPLAS(I+NNORMAL) = DSIGPLAS(I+NNORMAL)
&          - D(I+NNORMAL,J)*DETOT(J)
        END DO
      END DO
C
      RETURN
100  FORMAT(/,' *** UMAT: NNORMAL = ',I5,

```

```

&
110 FORMAT(/, ' ***      ' NSHEAR = ',15,' NOT SUPPORTED *** ',/)
&
120 FORMAT(/, ' ***      UMAT: FAILED TO CALCULATE
      RESPONSE INCREMENT *** ',/)
120 FORMAT(/, ' ***      UMAT: FAILED TO UPDATE LOAD *** ',/)

```

```

      END

```

```

C PROGRAM NAME: UMAT_LOCATE
C
C PURPOSE: INTERPOLATION OF TABULAR VALUES
C
C INPUT: TABLE OF X-VALUES, CURRENT X
C
C OUTPUT: RANGE OF CURRENT Y, INTERPOLATION FRACTION
C
C CALLING SUBROUTINE: UMAT_CONSTANT
C
C CALLED ROUTINES: NONE
C
C REFERENCES:
C

```

```

      SUBROUTINE UMAT_LOCATE (XTABLE,NX,X,KMIN,KMAX,FRAC)

```

```

C *** LOCATES X IN PIECEWISE LINEAR TABLE ***

```

```

C *** XTABLE : TABLE OF VALUES
C *** NX      : NUMBER OF VALUES IN XTABLE
C *** X       : CURRENT VALUE OF X
C *** KMIN    : POINTER TO MIN RANGE VALUE
C *** KMAX    : POINTER TO MAX RANGE VALUE
C *** FRAC    : FRACTION LOCATING X IN RANGE

```

```

      IMPLICIT REAL*8 (A-H,O-Z)
      DIMENSION XTABLE(*)

```

```

C *** CASE 1: X BELOW MINIMUM VALUE IN TABLE ***

```

```

      IF (X .LT. XTABLE(1)) THEN
        KMIN = 1
        KMAX = 2

```

```

C *** CASE 2: X ABOVE MAXIMUM VALUE IN TABLE ***

```

```

      ELSE IF (X .GE. XTABLE(NX)) THEN
        KMIN = NX - 1
        KMAX = NX

```

```

C *** CASE 3: X IN TABLE ***

```

```

      ELSE
        DO I=1,NX
          IF ((X .GE. XTABLE(I)) .AND. (X .LT. XTABLE(I+1))) THEN
            KMIN = I
            KMAX = I+1
          ENDIF
        END DO
      ENDIF

```

```

C *** CALCULATE FRACTION AND RETURN ***
C *** FRAC = 1: X = XTABLE(KMAX) ***
C *** FRAC = 0: X = XTABLE(KMIN) ***

```

```

      FRAC = (X-XTABLE(KMIN))/(XTABLE(KMAX)-XTABLE(KMIN))

```

```

      RETURN
      END

```

```

C PROGRAM NAME: UMAT_FIRSTINV, UMAT_SECONDINV, UMAT_THIRDINV
C
C PURPOSE: REAL FUNCTIONS TO CALCULATE INVARIANTS

```

```

C           OF SYMMETRIC 2ND RANK TENSORS
C
C INPUT: SYMMETRIC 2ND RANK TENSOR IN VECTOR FORM
C
C OUTPUT: SCALAR INVARIANTS
C
C CALLING ROUTINES:
C
C CALLED ROUTINES: NONE
C
C REFERENCES: FUNG, Y. C. "FOUNDATIONS OF SOLID MECHANICS"
C
C           REAL FUNCTION UMAT_FIRSTINV (NNORMAL,NSHEAR,S)
C
C *** NNORMAL : NUMBER OF NON-ZERO NORMAL COMPONENTS
C *** NSHEAR  : NUMBER OF NON-ZERO SHEAR COMPONENTS
C
C *** S      : SYMMETRIC 2ND RANK TENSOR IN VECTOR FORM
C *** I      : VECTOR OF INVARIANTS
C
C *** S(1): S(1,1)
C *** S(2): S(2,2)
C *** S(3): S(3,3)
C *** S(4): S(1,2)
C *** S(5): S(2,3)
C *** S(6): S(3,1)
C      IMPLICIT REAL*8 (A-H,O-Z)
C      DIMENSION S(6)
C
C      UMAT_FIRSTINV = 0.0
C      DO J=1,NNORMAL
C        UMAT_FIRSTINV = UMAT_FIRSTINV + S(J)
C      END DO
C      WRITE(6,1600) UMAT_FIRSTINV,(S(L),L=1,6)
C1600  FORMAT(1X,'UFIRST,S=',7E10.3)
C      RETURN
C      END
C
C *** COMPUTE FIRST STRESS INVARIANT
C      SUBROUTINE FIRSTINV(NNORMAL,NSHEAR,S,FINV)
C
C      IMPLICIT REAL*8 (A-H,O-Z)
C      DIMENSION S(6)
C
C      FINV=0.
C      DO J=1,NNORMAL
C        FINV = FINV + S(J)
C      END DO
C
C      RETURN
C      END
C
C *** COMPUTE SECOND STRESS INVARIANT
C      SUBROUTINE SECONDINV(NNORMAL,NSHEAR,S,SINV)
C
C      IMPLICIT REAL*8 (A-H,O-Z)
C      DIMENSION S(6)
C
C      SINV=0.
C      NSTRESS=NNORMAL+NSHEAR
C      DO J=1,NSTRESS
C        IF (J .LT. 4) THEN
C          COEF=1.0
C        ELSE
C          COEF=2.0
C        ENDIF
C        SINV=SINV+S(J)*S(J)*COEF
C      END DO

```



```

C      WRITE(6,8) SINV
8      FORMAT(1X,'SINV=',E12.3)

      RETURN
      END

C PROGRAM NAME: UMAT_SUBSPLIT
C
C PURPOSE: CALCULATE NUMBER OF SUBINCREMENTS FOR
C          DIFFERENTIAL FORMULATION
C
C INPUT:
C
C OUTPUT:
C
C CALLING ROUTINES: UMAT_DIFF_MATER
C
C CALLED ROUTINES: UMAT_SECONDINV
C
C REFERENCES:
C

      SUBROUTINE UMAT_SUBSPLIT (DTIMEC,DTEMPC,DETOT,NSUBINC)

C *** DTIME      : CURRENT TIME INCREMENT
C *** DTEMP      : CURRENT TEMPERATURE INCREMENT
C *** DETOT      : CURRENT STRAIN INCREMENT
C *** NSUBINC    : NUMBER OF SUBINCREMENTS
C          IMPLICIT REAL*8(A-H,O-Z)
C          DIMENSION DETOT(*)

C *** LOCAL VARIABLES ***

C *** MAXDTEMP   : MAX ALLOWABLE TIME STEP
C *** MAXDTEMP   : MAX ALLOWABLE TEMPERATURE STEP
C *** MAXDETOT   : MAX ALLOWABLE STRAIN STEP
C *** MAXSUBINC  : MAX ALLOWABLE SUBINCREMENTS
C *** EPSSCALE   : TOTAL STRAIN SCALAR

      REAL*8 MAXDTEMP,MAXDETOT

      DATA MAXDTEMP/50.0/
      DATA MAXDETOT/1.0E-5/
      DATA MAXDETOT/0.00000999999/
      DATA MAXSUBINC/1024/

C *** MAX TEMP STEP CRITERION ***

      NSUBINC = IDINT(DABS(DTEMP)/MAXDTEMP)+1
C *** MAX STRAIN STEP CRITERION ***
      DEPSMAX = DMAX1(DABS(DETOT(1)),DABS(DETOT(2)),
+      DABS(DETOT(3)),DABS(DETOT(4)),
+      DABS(DETOT(5)),DABS(DETOT(6)))
      NLOC=DEPSMAX/MAXDETOT+1.
      NSUBINC = DMAX1(NSUBINC,NLOC)
C *** MAX ALLOWABLE SUBINCREMENT CRITERION ***

      NSUBINC = DMIN1(NSUBINC,MAXSUBINC)

C *** ADJUST SUBINCREMENT SIZES ***

      DTEMPC = DTEMPC/NSUBINC
      DTIMEC = DTIMEC/NSUBINC
      DO I = 1,6
          DETOT(I) = DETOT(I)/ NSUBINC
      END DO

      RETURN
      END

```

```

C PROGRAM NAME: UMAT_ELASTIC
C
C PURPOSE: EVALUATE ELASTIC CONSTITUTIVE MATRIX FOR MATERIAL MODEL
C
C INPUT: CONSTANTS AT ENDSTEP TEMPERATURE, ELEMENT STATUS, LOAD CONTROL
C
C OUTPUT: ELASTIC STIFFNESS OR COMPLIANCE MATRIX
C
C CALLING ROUTINES:
C
C CALLED ROUTINES: NONE
C
C REFERENCES:
C

```

```

      SUBROUTINE UMAT_ELASTIC (TEMPC,DTEMP,CC)

```

```

C *** EMOD      : YOUNG'S MODULUS
C *** POISSON   : POISSON RATIO
C *** GMOD      : SHEAR MODULUS
C *** NNORMAL   : NUMBER OF NON-ZERO NORMAL STRESSES
C *** NSHEAR    : NUMBER OF NON-ZERO SHEAR STRESSES
C *** ELEMTYPE  : 1D, PLANE STRESS, PLANE STRAIN, OR 3D ELEMENT TYPE
C *** CONTROL   : LOAD CONTROL STATUS
C *** CC        : FULL 3D ELASTIC STIFFNESS MATRIX

```

```

      IMPLICIT REAL*8(A-H,O-Z)
      DIMENSION CC(6,6)
      CHARACTER ELEMTYPE*80
      CHARACTER CONTROL*80
      REAL*8 LAMBDA

```

```

C *** LOCAL VARIABLES ***

```

```

C *** EMOD1     : E11
C *** EMOD2     : E22
C *** EMOD3     : E33
C *** POIS1     : NU12
C *** POIS2     : NU13
C *** POIS3     : NU23
C *** GMOD1     : G12
C *** GMOD2     : G23
C *** GMOD3     : G13

```

```

C *** INITIALIZE ***

```

```

      DO I=1,6
        DO J=1,6
          CC(I,J) = 0.
        END DO
      END DO

```

```

C *** EVALUATE STIFFNESS MATRIX ***

```

```

C *** LOAD MATRIX ENTRIES ***

```

```

C *** POLYNOMES EXPRESSING THE ELASTIC CONSTANTS OF DSR80
C AS A FUNCTION OF TEMPERATURE IN KELVIN (TEMPL)

```

```

      TEMPL = TEMPC + DTEMPC
      FT = TEMPL/2000.0
      EMOD1 = 163691.6 + (675059.51*FT) - 3443603.52*(FT**2) +
& 6450102.05*(FT**3) - (4415268.078*(FT**4))
      EMOD2 = EMOD1
      EMOD3 = 149420.55 + (242091.98*FT) - 1582912.48*(FT**2) +
& 3156630.13*(FT**3) - (2343990.97*(FT**4))
      GMOD1 = 65992.7 + (213873.93*FT) - 1140899.54*(FT**2) +
& 2164206.05*(FT**3) - (1508006.35*(FT**4))
      GMOD2 = 121263.27 + (187547.82*FT) - 1278029.54*(FT**2) +
& 2665333.25*(FT**3) - (2023708.86*(FT**4))
      GMOD3 = GMOD2
      POIS1 = 0.11248 + (0.00666*FT) - 0.01078*(FT**2) +
& 0.31535*(FT**3) - (0.07611*(FT**4))
      POIS2 = 0.32554 - (0.20001*FT) + 1.01790*(FT**2) -

```

```

&      1.76442*(FT**3) + (1.17523*(FT**4))
      POIS3 = POIS2

C *** COMPLIANCE MATRIX ENTRIES
C      WRITE(UNIT=88,*) 'EMOD1 = ', EMOD1
C      WRITE(UNIT=88,*) 'EMOD2 = ', EMOD2
C      WRITE(UNIT=88,*) 'EMOD3 = ', EMOD3
C      WRITE(UNIT=88,*) 'POIS1 = ', POIS1
C      WRITE(UNIT=88,*) 'POIS2 = ', POIS2
C      WRITE(UNIT=88,*) 'POIS3 = ', POIS3
C      WRITE(UNIT=88,*) 'GMOD1 = ', GMOD1
C      WRITE(UNIT=88,*) 'GMOD2 = ', GMOD2
C      WRITE(UNIT=88,*) 'GMOD3 = ', GMOD3

      S11 = 1./EMOD1
C      WRITE(UNIT=88,*) 'S11 = ', S11
      S22 = 1./EMOD2
C      WRITE(UNIT=88,*) 'S22 = ', S22
      S33 = 1./EMOD3
C      WRITE(UNIT=88,*) 'S33 = ', S33
      S12 = -POIS1/EMOD1
C      WRITE(UNIT=88,*) 'S12 = ', S12
      S13 = -POIS2/EMOD1
C      WRITE(UNIT=88,*) 'S13 = ', S13
      S23 = -POIS3/EMOD2
C      WRITE(UNIT=88,*) 'S23 = ', S23

C *** STIFFNES MATRIX

      DETS = S11*(S22*S33-S23**2)+S12*(S13*S23-S33*S12)+
&          S13*(S12*S23-S22*S13)
C      WRITE(UNIT=88,*) 'DETS = ', DETS
      CC(1,1) = (S22*S33-S23**2)/DETS
      CC(2,2) = (S11*S33-S13**2)/DETS
      CC(3,3) = (S11*S22-S12**2)/DETS
      CC(1,2) = (S13*S23-S33*S12)/DETS
      CC(1,3) = (S12*S23-S22*S13)/DETS
      CC(2,3) = (S12*S13-S11*S23)/DETS
      CC(3,2) = CC(2,3)
      CC(2,1) = CC(1,2)
      CC(3,1) = CC(1,3)
      CC(4,4) = GMOD1
      CC(5,5) = GMOD2
      CC(6,6) = GMOD3

C      WRITE(UNIT=88,*) 'CC11 = ', CC(1,1)
C      WRITE(UNIT=88,*) 'CC22 = ', CC(2,2)
C      WRITE(UNIT=88,*) 'CC33 = ', CC(3,3)
C      WRITE(UNIT=88,*) 'CC12 = ', CC(1,2)
C      WRITE(UNIT=88,*) 'CC13 = ', CC(1,3)
C      WRITE(UNIT=88,*) 'CC23 = ', CC(2,3)
C      WRITE(UNIT=88,*) 'CC11 = ', CC(1,1)
C      WRITE(UNIT=88,*) 'CC21 = ', CC(2,1)
C      WRITE(UNIT=88,*) 'CC31 = ', CC(3,1)
C      WRITE(UNIT=88,*) 'CC32 = ', CC(3,2)
C      WRITE(UNIT=88,*) 'CC44 = ', CC(4,4)
C      WRITE(UNIT=88,*) 'CC55 = ', CC(5,5)
C      WRITE(UNIT=88,*) 'CC66 = ', CC(6,6)

      RETURN
      END
C

      SUBROUTINE UMAT_EFFRAT_MATER(DSUBETOT,DT,TEMPC,DTEFF)
C
C      RENE 80 EXIBITS RATE INDEPENDENCE BELOW 1200 DEG F
C      A WAY TO INTRODUCE THIS RATE INDEPENDENCE INTO THE
C      VISCOPLASTIC LAW IS TO SCALE THE TIME INCREMENT FOR
C      A GIVEN INCREMENT TO A LEVEL THAT GIVES A STRAIN RATE
C      EQUAL TO THE REFERENCE RATE. THIS ROUTINE TAKES IN
C      THE UMAT SUPPLIED STRAIN INCREMENT DE, THE TEMPERATURE
C      TEMP, AND THE REAL TIME INCREMENT DT, AND CALCULATES AN

```

```

C   EFFECTIVE TIME INCREMENT DTEFF WHICH WILL GIVE A CONSTANT
C   STRAIN RATE.
C
C   *** DSUBETOT      : TOTAL STRAIN TENSOR
C   *** DEVSUBETOT    : DEVIATORIC STRAIN TENSOR
C   *** TZERO         : CUTOFF TEMPERATURE FOR RATE INDEPENDENCE
C   *** FRAC          : FRACTION WHICH SETS STEEPNESS OF STEP
C   ***              : FUNCTION AROUND TZERO
C   *** REFRAT        : REFERENCE STRAIN RATE DESCRIBED BELOW
C   *** SDELTEMP       : SCALED DIFFERENCE BETWEEN TEMP AND TZERO
C   *** DEVEFF         : EFFECTIVE DEVIATORIC STRAIN INCREMENT
C   *** DTEFF         : EFFECTIVE TIME INCREMENT
C
C   IMPLICIT REAL*8(A-H,O-Z)
C   REAL*8 KRONECKER(6)
C   DIMENSION DSUBETOT(6),DEVSUBETOT(6)
C   DATA KRONECKER/3*1.0,3*0.0/
C
C   DEFINE HYPERBOLIC TANGENT FUNCTION
C
C   TANF(X) = (DEXP(2.0*X)-1.0)/(DEXP(2.0*X)+1.0)
C
C   TZERO IS THE TEMPERATURE BELOW WHICH STRAIN-RATE
C   INDEPENDENCE OCCURS
C
C   TZERO = 1200 F = 649 C = 922 K
C   TZERO = 922.0
C   FRAC = 0.02
C
C   REFRAT IS EXPERIMENTALLY DETERMINED REFERENCE RATE AT
C   WHICH CONSTITUTIVE MODEL AGREES WITH EXPERIMENTAL DATA
C
C   REFRAT = 0.0008
C   CALL FIRSTINV(3,3,DSUBETOT,FINV)
C   DSUBETOTH=FINV
C
C   DO I=1,6
C     DEVSUBETOT(I) = DSUBETOT(I) - KRONECKER(I)*DSUBETOTH/3.0
C   END DO
C
C   CALCULATION OF EFFECTIVE STRAIN RATE
C
C   CALL SECONDINV(3,3,DEVSUBETOT,SINV)
C   DEVEFF=DSQRT(2./3.*SINV)
C   BZERO=DEVEFF/REFRAT
C
C   SDELTEMP = FRAC*(TEMPC-TZERO)
C
C   HYPERBOLIC TANGENT FUNCTION IS BASICALLY A STEP FUNCTION WHICH
C   ALLOWS A SMOOTH TRANSITION FROM RATE INDEPENDENT REGIME TO
C   RATE DEPENDENT REGIME. AT TEMPERATURES ABOVE TZERO THE EFFECTIVE
C   TIME INCREMENT EQUALS THE ACTUAL INCREMENT.
C
C   TANF = (DEXP(2.0*SDELTEMP)-1.0)/(DEXP(2.0*SDELTEMP)+1.0)
C   DTEFF=(TANF+1.)*DT/2.+BZERO*(1.
C   + -TANF)/2.
C
C   RETURN
C   END
C
C   PROGRAM NAME: UMAT_CONSTANT
C
C   AUTHOR: K.P. WALKER
C
C   ADDRESS: ENGINEERING SCIENCE SOFTWARE, INC.
C   315 LOG ROAD
C   SMITHFIELD, R.I. 02917
C
C   TELEPHONE: (401) 231-3182
C
C   PURPOSE: MATERIAL CONSTANTS FOR UNIFIED VISCOPLASTIC MODEL

```

```

C
C *****
C *** MATERIAL CONSTANTS FOR > RENE 80DS < ***
C *****
C
C UNITS: SI - TEMP=K
C           SIGMA=MPA
C           [L]=MM
C           [T]=SEC
C           [M]=KG
C
C INPUT: CURRENT TEMPERATURE, TEMPERATURE INCREMENT, CONSTANTS VS TEMPER
C
C OUTPUT: ARRAY OF CONSTANTS EVALUATED AT ENDSTEP TEMPERATURE
C
C CALLING ROUTINES: UMAT, UMAT_DIFF_MATER, UMAT_INT_MATER
C
C CALLED ROUTINES: UMAT_LOCATE
C
C
C SUBROUTINE UMAT_CON_MATER (TEMPC,DTEMPC,NCON,DNCON)
C
C *** MAXTEMP : MAX NUMBER OF TEMPERATURES IN TABLE (USER-DEFINED)
C *** MAXCONST: MAX NUMBER OF CONSTANTS IN TABLE (USER-DEFINED)
C *** TEMP    : TEMPERATURE FOR MATERIAL CONSTANTS EVALUATION
C *** NCON    : MATERIAL CONSTANTS
C *** DNCON   : CHANGE IN CONSTANTS W.R.T. TEMPERATURE
C *** MEXP    : MATERIAL EXPONENTS
C *** DMEXP   : CHANGE IN EXPONENTS W.R.T. TEMPERATURE
C
C PARAMETER (MAXTEMP = 10)
C PARAMETER (MAXCONST = 9)
C IMPLICIT REAL*8(A-H,O-Z)
C REAL*8 NCON(9)
C DIMENSION DNCON(9),TTEMP_N(MAXTEMP)
C
C *** LOCAL VARIABLES ***
C
C *** I      : LOOP INDICIES
C *** KMIN,KMAX : RANGE POINTERS
C *** DELTEMP : TEMPERATURE RANGE
C *** FRAC    : INTERPOLATION FRACTION
C
C *** TEMPERATURE TABLE (USER-DEFINED) - K SINCE USING RAD. FOR LOADING
C
C DIMENSION TTEMP_N(MAXTEMP)
C DATA TTEMP_N/273.,294.,700.,811.,922.,1033., 1144.,1255.,1366.,1477./
C
C *** MATERIAL CONSTANTS VS TEMP
C *** THERE ARE 9 CONSTANTS AT EACH OF 10 TEMPERATURES:
C *** [ K1, n2, n3, n6, Omega0, Beta, n9, n10, n11 ]
C *** ON WALKER'S B1900+Hf PAPER
C *** DATA TTEMP_N/273.,294.,700.,811.,922.,1033., 1144.,1255.,1366.,1477./
C DIMENSION TN(MAXCONST,MAXTEMP)
C DATA TN/12.4, 2.41E6, 4794.0, 0.0, 0.0, 1.73E11, 11.87, 0.0, 4.70E3,
1 12.4, 2.41E6, 4794.0, 0.0, 0.0, 1.73E11, 11.87, 0.0, 4.70E3,
2 12.4, 2.41E6, 4794.0, 0.0, 0.0, 1.73E11, 11.87, 0.0, 4.70E3,
3 12.4, 2.41E6, 4794.0, 0.0, 0.0, 1.73E11, 11.87, 0.0, 4.70E3,
4 12.4, 8.27E5, 1714.0, 0.0, 0.0, 3.862E10, 16.64, 0.0, 4.70E3,
5 13.8, 8.27E5, 1880.0, 0.0, 0.0, 2.55E10, 19.83, 2.44E-3, 4.70E3,
6 16.6, 2.36E6, 621.2, 8.73E-4, 0.0, 5.5E12, 59.33, 2.44E-3, 9.65E2,
7 13.8, 9.65E4, 400.0, 4.29E-4, 0.0, 4.20E10, 136.0, 2.44E-3, 0.0,
8 9.0, 2.36E4, 278.7, 4.83E-2, 0.0, 5.57E9, 136.0, 2.44E-3, 0.0,
9 5.87,5.77E3,194.0,5.44,0.0,7.39E8,136.0,2.44E-3,0.0/
C
C *** EVALUATE CONSTANTS AT TEMPERATURE ***
C
C DO I=1,MAXCONST

```

```

      NCON(I) = 0.0
      DNCON(I) = 0.0
    END DO

    KMIN = 0
    KMAX = 0
    FRAC = 0.0

C *** LOCATE ENDSTEP TEMPERATURE IN TTEMP TABLE ***
    TEMPL = TEMPC + DTEMPC

C *** VALUES COMPUTED ON A 10 TEMP. RANGE
    CALL UMAT_LOCATE (TTEMP_N,MAXTEMP,TEMPL,KMIN,KMAX,FRAC)
C    WRITE(UNIT=88,*) 'KMIN = ',KMIN
C    WRITE(UNIT=88,*) 'KMAX = ',KMAX
C    WRITE(UNIT=88,*) 'FRAC = ',FRAC
    DELTEMP = TTEMP_N(KMAX)-TTEMP_N(KMIN)

    DO I = 1, MAXCONST
      NCON(I) = TN(I,KMIN)*(1.-FRAC) + TN(I,KMAX)*FRAC
C    WRITE(UNIT=88,*) 'NCON = ',NCON(I)
      IF (DTEMPC .NE. 0.) THEN
        DNCON(I) = (TN(I,KMAX)-TN(I,KMIN))/DELTEMP
      ENDIF
    END DO
    RETURN

  END

```

APPENDIX J

PROGRAMS FOR THE DETERMINATION OF THE OPTIMAL FATIGUE-OXIDATION DAMAGE MODEL PARAMETERS

This Appendix presents the softwares developed for the determination of the parameters (constants and exponents) of the models of Coffin, of Ostergren, of Antolovich et al., and of Romanoski et al. which optimises the fitting of various isothermal fatigue data.

The program HTFDATA.BAS was first used to put into files the continuous frequency, the tensile strain hold time, the compressive strain hold time, the plastic strain range, the stress range, the maximum stress and the corresponding fatigue life for each fatigue test of a series of tests conducted at the same temperature. Each datafile has a generic name of the form of "HTF_DATA.AT" where A is the initial of the Author of the data set and T is the Test series number. The specific values of the variables and of the fatigue lives are given in Tables J.1 to J.6, for the six data sets obtained from IF tests on CC René 80 from Antolovich et al. [14] (data sets A1, A2, A3) and from Coffin et al. [5, 6] (data sets C1, C3, C4).

Then, the parameters of each of the four models which optimise the fitting of each data set were determined by iteration and by employing one of the two following criteria: the minimisation of the variance of the constant A' , C_2 , C , K , or K_0 of the different models, or the minimisation of the relative error (RE) of the fatigue life prediction. At the beginning of the execution, the user is asked to enter the Author initial, the Test series number, and the range for the exponents, when applicable. After execution, the values of the parameters which satisfy the best the criterion is printed as well as the associated RE. Predicted and experimental fatigue lives values ($N_{f\text{ cal}}$, $N_{f\text{ exp}}$) are also written in a file of generic name "MOD_C_AT" or "MOD_K_AT" or "MOD_RE_AT" for further statistical analysis or generation of $N_{f\text{ cal}}$ vs $N_{f\text{ exp}}$ plots, where MOD represents the three first letters of the model's Author. For each model, a program based on the first criterion named "MOD-C.BAS" or "MOD-K.BAS" and a program named "MOD-RE.BAS" which uses the second criterion, were written. Only

three of the 10 programs are listed for instance at the end of this Appendix with values of the resulting parameters given in Tables J.7 and J.8.

Listing of the Program HTFDATA.BAS

```

10 'PROGRAM HTFDATA.BAS
20 '
30 'READ AND WRITE IN FILE;
40 '     THE FREQUENCY, THE HOLD TIME IN TENSION AND IN COMPRESSION,
50 '     THE PLASTIC STRAIN RANGE, THE STRESS RANGE, THE MAXIMUM STRESS
AND
60 '     THE CORRESPONDING CYCLIC LIFE
70 '
80 CLS
90   INPUT "ENTER THE INITIAL OF THE AUTHOR AND PRESS ENTER: ", AS
100  INPUT "ENTER THE TEST NUMBER AND PRESS ENTER: ", TS
110  AT$ = LEFT$(AS,1) + LEFT$(TS,1)
120  DATAFILES$ = "HTF_DATA." + AT$
130  OPEN "O", #1, DATAFILES$
140  INPUT "ENTER THE NUMBER OF DATA TO CONSIDER AND PRESS ENTER: ", M%
150  PRINT "IF THE TIME AND FREQ. UNITS USED ARE IN seconds AND Hz,
      PRESS 1,"
160  INPUT "IF THEY ARE IN minutes AND cpm, PRESS 2 AND ENTER: ",
      TIMEUNIT%
170  PRINT "IF THE STRESS UNIT USED ARE IN MPa, PRESS 1,"
180  INPUT "IF THEY ARE IN ksi, PRESS 2 AND ENTER: ", SUNIT%
190  PRINT #1, M%, TIMEUNIT%, SUNIT%
200  CLS
210  MINSMAX = 1E+10
220  FOR I% = 1 TO M%
230    PRINT "ENTER v, thT, thC, eP(range, in %), S(range), Smax,
      NF,";
240    PRINT " AND PRESS ENTER"
250    INPUT V, THT, THC, EPR, SR, SMAX, NF
260    IF TIMEUNIT% = 2 THEN V = V/60: THT = THT*60: THC = THC*60 ELSE
270    PRINT #1, V, THT, THC, EPR/100, SR, SMAX, NF
280    IF SMAX < MINSMAX THEN MINSMAX = SMAX
290  NEXT I%
300  PRINT #1, MINSMAX
310  CLOSE #1
320  END

```

Table J.1 Data obtained from IF tests on CC René 80 at 871°C for various imposed strain range and continuous frequencies (data set A1 [14])

ν (cpm)	t_{hT} (min)	t_{hC} (min)	$\Delta\varepsilon_p$ (%)	$\Delta\sigma$ (MPa)	σ_{max} (MPa)	N_f
51.300	0.0	0.0	0.013	771	586	9780
0.530	0.0	0.0	0.048	650	340	1945
32.000	0.0	0.0	0.048	1095	677	1244
0.530	0.0	0.0	0.051	661	344	2682
34.000	0.0	0.0	0.051	1138	658	1417
31.250	0.0	0.0	0.051	1092	732	936
47.000	0.0	0.0	0.120	1172	627	710
46.700	0.0	0.0	0.135	1241	662	470
46.900	0.0	0.0	0.140	1241	669	330
20.000	0.0	0.0	0.230	1472	775	230
0.307	0.0	0.0	0.250	827	416	455
0.305	0.0	0.0	0.250	781	378	421
23.600	0.0	0.0	0.250	1360	710	202
0.604	0.0	0.0	0.255	965	428	485

Table J.2 Data obtained from IF tests on CC René 80 at 871°C for various imposed strain range and strain hold times (data set A2 [14])

ν (cpm)	t_{hT} (min)	t_{hC} (min)	$\Delta\varepsilon_p$ (%)	$\Delta\sigma$ (MPa)	σ_{max} (MPa)	N_f
53.800	1.5	0.0	0.050	776	239	7440
51.000	1.5	0.0	0.050	792	246	7008
0.342	1.5	0.0	0.250	607	258	580
0.357	1.5	0.0	0.250	709	317	662
29.100	1.5	0.0	0.250	1015	309	631
28.200	1.5	0.0	0.250	1085	377	665

Table J.3 Data obtained from IF tests on CC René 80 at 982°C for various imposed strain range and continuous frequencies (data set A3 [14])

ν (cpm)	t_{hr} (min)	t_{hc} (min)	Δe_p (%)	$\Delta\sigma$ (MPa)	σ_{max} (MPa)	N_f
0.745	0.0	0.0	0.046	355	186	9720
0.700	0.0	0.0	0.040	401	214	4772
56.700	0.0	0.0	0.040	622	341	2119
56.700	0.0	0.0	0.040	639	409	1525
43.300	0.0	0.0	0.136	731	374	752
43.300	0.0	0.0	0.140	706	374	753
0.432	0.0	0.0	0.184	485	252	523
0.432	0.0	0.0	0.192	476	245	473
0.693	0.0	0.0	0.084	381	168	1437
0.687	0.0	0.0	0.090	399	177	1499
56.700	0.0	0.0	0.104	611	182	835
56.700	0.0	0.0	0.110	585	189	984
0.432	0.0	0.0	0.196	495	226	526
0.432	0.0	0.0	0.212	496	234	331
43.400	0.0	0.0	0.222	654	241	405
43.300	0.0	0.0	0.230	705	258	378

Table J.4 Data obtained from IF tests on CC René 80 at 871°C for various imposed strain range and strain hold times (data set C1 [6])

ν (cpm)	t_{hT} (min)	t_{hC} (min)	$\Delta\epsilon_p$ (%)	$\Delta\sigma$ (ksi)	σ_{max} (ksi)	N_f
3.000	5.0	0.0	0.3200	158.65	69.93	450
3.000	0.0	5.0	0.3200	150.90	107.80	225
3.000	2.5	2.5	0.3200	165.80	84.10	280
3.000	30.0	0.0	0.3200	163.80	57.37	600
3.000	0.0	30.0	0.3200	165.32	105.82	170
3.000	15.0	15.0	0.3200	150.00	88.20	350

Table J.5 Data obtained from IF tests on CC René 80 (3 Stage Heat-Treatment) at 871°C for various imposed strain range and continuous frequencies (data set C3 [5])

ν (cpm)	t_{hr} (min)	t_{hc} (min)	$\Delta\epsilon_p$ (%)	$\Delta\sigma$ (ksi)	σ_{max} (ksi)	N_f
5.200	0.0	0.0	0.3770	214.90	107.45	270
1.090	0.0	0.0	0.3470	179.00	89.50	250
1.090	0.0	0.0	0.3379	165.00	82.50	325
0.210	0.0	0.0	0.3340	134.20	67.10	300
0.077	0.0	0.0	0.3379	128.50	64.25	350
5.940	0.0	0.0	0.0897	114.30	57.15	1300
1.090	0.0	0.0	0.0876	113.70	56.85	1450
0.200	0.0	0.0	0.0873	101.20	50.60	1800
1.150	0.0	0.0	0.0307	112.60	56.30	3200
31.100	0.0	0.0	0.0130	109.60	54.80	7600
5.800	0.0	0.0	0.0146	92.20	46.10	21750

Table J.6 Data obtained from IF tests on CC René 80 (4 Stage Heat-Treatment) at 871°C for various imposed strain range and continuous frequencies (data set C4 [5])

ν (cpm)	t_{hT} (min)	t_{hC} (min)	$\Delta \epsilon_p$ (%)	$\Delta \sigma$ (ksi)	σ_{max} (ksi)	N_f
5.100	0.0	0.0	0.3643	191.70	95.85	350
1.010	0.0	0.0	0.3395	161.00	80.50	275
0.220	0.0	0.0	0.3385	122.70	61.35	380
0.079	0.0	0.0	0.3386	119.90	59.95	325
0.034	0.0	0.0	0.3160	112.60	56.30	420
5.400	0.0	0.0	0.0895	143.40	71.70	1145
1.080	0.0	0.0	0.0834	116.20	58.10	1450
0.210	0.0	0.0	0.0882	83.60	41.80	3808
5.500	0.0	0.0	0.0243	126.80	63.40	2000
1.050	0.0	0.0	0.0253	88.40	44.20	7000
36.200	0.0	0.0	0.0163	143.90	71.95	5000
6.000	0.0	0.0	0.0133	105.50	52.75	6000

Listing of the program OST-RE.BAS

```

10 'PROGRAM OST-RE.BAS
20 '
30 'READ THE HTF DATA
40   GOSUB 1000
50 'COMPUTE THE AVERAGE AND THE STANDARD DEVIATION OF C
60 'FOR VARIOUS FAILURE LIFE EXPONENTS AND VARIOUS FREQUENCY EXPONENTS
70 MINSTDREN = 9.999999E+35
80 NUMITE% = 20: NUMITEK% = 20
90 DIM PL(NUMITE%+1,3), MINSTDRENL(NUMITE%+1,3)
100 VSTDKF0FILE$ = "V_REN_" + AT$ + ".123"
110 OPEN "O", #2, VSTDKF0FILE$
120 FOR PASSP% = 1 TO 3
130   DP = (PMAX-PMIN)/NUMITE%
140   FOR ITE% = 0 TO NUMITE%
150     MINSTDRENL = 9.999999E+35
160     BMIN = BMIN0: BMAX = BMAX0
170     PL = PMIN + ITE%*DP
180     FOR PASSK% = 1 TO 3
190       DB = (BMAX-BMIN)/NUMITEK%
200       MINSTDRENK = 9.999999E+35
210       FOR K% = 0 TO NUMITEK%
220         BK = BMIN + K%*DB
230         GOSUB 2000
240         IF STDREN < MINSTDREN THEN B=BK: KF0=AVGKF0: P=PL:
           MINSTDKF0 = STDKF0: MINSTDREN=STDREN
250         IF STDREN < MINSTDRENL THEN MINSTDRENL = STDREN
260         IF STDREN < MINSTDRENK THEN BOPT = BK:
           MINSTDRENK = STDREN
270       NEXT K%
280       BMIN = BOPT - DB
290       BMAX = BOPT + DB
300     NEXT PASSK%
310     PL(ITE%, PASSP%) = PL
320     MINSTDRENL(ITE%, PASSP%) = MINSTDRENL
330   NEXT ITE%
340   PMIN = P - DP: PMAX = P + DP
350 NEXT PASSP%
360 'PUT INTO FILE "V_REN_AT.123" THE (PL,MINSTDRENL) VALUES
370   FOR R% = 0 TO NUMITE%
380     PRINT #2, USING "  ##.####"; PL(R%,1);
390     PRINT #2, USING "  ##.####^"; MINSTDRENL(R%,1);
400     PRINT #2, USING "  ##.####"; PL(R%,2);
410     PRINT #2, USING "  ##.####^"; MINSTDRENL(R%,2);
420     PRINT #2, USING "  ##.####"; PL(R%,3);
430     PRINT #2, USING "  ##.####^"; MINSTDRENL(R%,3)
440   NEXT R%
450 CLOSE #2
460 'PRINT THE VALUE OF C, B AND
470 'THE VALUE OF k THAT MINIMIZES
480 'THE RELATIVE ERROR ON THE Nf PREDICTION
490   GOSUB 3000
500 'COMPUTE THE RELATIVE STANDARD DEVIATION OF Ncal FROM Nexp (RSTDNC)
510 'OR RELATIVE ERROR, AND SAVE Nfexp-Nfcal IN FILE "OST_E_AT"

```



```

520      GOSUB 4000
530 SOUND 1046.5, 20
540 END
550 '
1000 'SUBROUTINE 1000; READ THE HTF DATA
1005   CLS
1010   INPUT "ENTER THE INITIAL OF THE AUTHOR AND PRESS ENTER: "; A$
1020   INPUT "ENTER THE TEST NUMBER AND PRESS ENTER: "; T$
1030   AT$ = LEFT$(A$,1) + LEFT$(T$,1)
1040   DATAFILES = "HTF_DATA." + AT$
1050   OPEN "I", #1, DATAFILES$
1060   INPUT #1, M$, TIMEUNIT$, SUNIT$
1070   DIM V(M%), EPR(M%), SR(M%), SMAX(M%), NF(M%), NFCAL(M%), KF0(M%)
1080   IF SUNIT%=1 THEN SUNIT$="MPa" ELSE IF SUNIT%=2 THEN SUNIT$="ksi"
ELSE
    PRINT "SUNIT IS WRONG!"
1090 ' READ THE DATA (FREQUENCY, ..., PLAST. STRAIN RANGE,
    ..., LIFE TO FAILURE)
1100   FOR I% = 1 TO M%
1110     INPUT #1, V, THT, THC, EPR(I%), SR(I%), SMAX(I%), NF(I%)
1120     V(I%) = 60/(1/V + THT + THC)
    'THE EFF. FREQUENCY IS CONVERTED IN cpm
1130   NEXT I%
1140   INPUT #1, MINSMAX
1150   INPUT "ENTER THE MINIMAL VALUE OF THE FREQUENCY EXPONENT: "; PMIN
1160   INPUT "ENTER THE MAXIMAL VALUE OF THE FREQUENCY EXPONENT: "; PMAX
1180   INPUT "ENTER THE MINIMAL VALUE OF THE FAILURE LIFE EXPONENT: "
    ; BMINO
1190   INPUT "ENTER THE MAXIMAL VALUE OF THE FAILURE LIFE EXPONENT: "
    ; BMAXO
1200   PRINT "": PRINT "PLEASE WAIT"
1210 RETURN 50
1220 '
2000 'SUBROUTINE 2000; COMPUTE THE AVERAGE VALUE OF KF0 AND THE STDREN
2010 ' AVERAGE KF0
2020   SUMKF0 = 0!
2030   FOR J% = 1 TO M%
2040     KF0(J%) = SMAX(J%)*EPR(J%)*NF(J%)^BK*V(J%)^((PL-1!)*B)
2050     SUMKF0 = KF0(J%) + SUMKF0
2060   NEXT J%
2070   AVGKF0 = SUMKF0/M%
2080 ' STANDARD DEVIATION OF KF0
2090   SUMSTDKF0 = 0!
2100   FOR J% = 1 TO M%
2110     SUMSTDKF0 = ABS(KF0(J%)-AVGKF0) + SUMSTDKF0
2120   NEXT J%
2130   STDKF0 = SUMSTDKF0/M%
2140 ' STANDARD DEVIATION OF RENFC, STDREN
2150   SUMSTDREN = 0!
2160   FOR J% = 1 TO M%
2170     NFCAL(J%) = (AVGKF0/SMAX(J%)/EPR(J%))^(1/BK)*V(J%)^(1!-PL)
2180     SUMSTDREN = ABS((NFCAL(J%)-NF(J%))/NF(J%)) + SUMSTDREN
2190   NEXT J%
2200   STDREN = 100*SUMSTDREN/M%
2210 RETURN 240
2220 '
3000 'SUBROUTINE 3000; PRINT THE RESULTS
3010 PRINT " "

```

```

3020 PRINT "RESULTS:"
3030 PRINT ""
3040 PRINT USING "C = ###.###^"; KF0;
3050 PRINT USING " &_.mn_^(k-1)B_.cycle_^B"; SUNITS
3060 PRINT USING "STD(C) = ###.###^"; MINSTDKF0;
3070 PRINT USING " &_.mn_^(k-1)B_.cycle_^B"; SUNITS
3080 PRINT USING "B = ###.###"; B
3100 PRINT USING "k = ###.###"; P
3120 RETURN 500
3130 '
4000 'SUBROUTINE 4000; COMPUTE NFCAL AND THE RELATIVE STANDARD DEVIATION
      (RSTD) OF Ncal FROM Nexp OR STANDARD RELATIVE
      ERROR
4010 NCALFILE$ = "OST_E_" + AT$
4020 OPEN "O", #3, NCALFILE$
4030 SUMRSTDNC = 0!
4040 FOR J% = 1 TO M%
4050   NFCAL(J%) = (KF0/SMAX(J%)/EPR(J%))^(1/B)*V(J%)^(1!-P)
4060   PRINT #3, USING "#####"; NF(J%);
4070   PRINT #3, USING "#####"; NFCAL(J%)
4080   SUMRSTDNC = ABS((NFCAL(J%)-NF(J%))/NF(J%)) + SUMRSTDNC
4090 NEXT J%
4100 RSTDNC = 100*SUMRSTDNC/M%
4110 PRINT ""
4120 PRINT USING "Relative Error on NfCAL = #####.#_"; RSTDNC
4130 CLOSE #3
4140 RETURN 530

```

Listing of the program ROM-KF.BAS

```

10 'PROGRAM ROM-KF.BAS
20 '
30 'READ THE HTF DATA
40   GOSUB 1000
50 'COMPUTE THE AVERAGE AND THE STANDARD DEVIATION OF KF0
60 'FOR VARIOUS THRESHOLD STRESS AND VARIOUS FREQUENCY EXPONENTS
70   MINSTDKF0 = 9.999999E+35
80   NUMITE% = 20: NUMITEK% = 20
82   DIM PL(NUMITE%+1,3), MINSTDKF0L(NUMITE%+1,3)
85   VSTDKF0FILE$ = "V_KF_" + AT$ + ".123"
86   OPEN "O", #2, VSTDKF0FILE$
90   FOR PASSP% = 1 TO 3
120     DP = (PMAX-PMIN)/NUMITE%
130     FOR ITE% = 0 TO NUMITE%
140       MINSTDKF0L = 9.999999E+35
150       STHMIN = 0!: STHMAX = .999*MINSMAX
160       PL = PMIN + ITE%*DP
170       FOR PASSK% = 1 TO 3
180         DSTH = (STHMAX-STHMIN)/NUMITEK%
190         MINSTDKF0K = 9.999999E+35
200         FOR K% = 0 TO NUMITEK%
210           STHK = STHMIN + K%*DSTH
220           GOSUB 2000
230           IF STDKF0 < MINSTDKF0 THEN STH=STHK: KF0=AVGKF0: P=PL:
             MINSTDKF0=STDKF0
240           IF STDKF0 < MINSTDKF0L THEN MINSTDKF0L = STDKF0
250           IF STDKF0 < MINSTDKF0K THEN STHOPT = STHK:
             MINSTDKF0K = STDKF0
260         NEXT K%
270       STHMIN = STHOPT - DSTH: IF STHMIN < 0! THEN STHMIN = 0!
280       STHMAX = STHOPT + DSTH: IF STHMAX >= MINSMAX
             THEN STHMAX=.999*MINSMAX
290     NEXT PASSK%
300     PL(ITE%, PASSP%) = PL
310     MINSTDKF0L(ITE%, PASSP%) = MINSTDKF0L
320   NEXT ITE%
340   PMIN = P - DP: PMAX = P + DP
350 NEXT PASSP%
355 'PUT INTO FILE "VEXP_AT.123" THE (PL,MINSTDKF0L) VALUES
360   FOR R% = 0 TO NUMITE%
370     PRINT #2, USING "  ##.####"; PL(R%,1);
375     PRINT #2, USING "  ##.####^"; MINSTDKF0L(R%,1);
380     PRINT #2, USING "  ##.####"; PL(R%,2);
385     PRINT #2, USING "  ##.####^"; MINSTDKF0L(R%,2);
386     PRINT #2, USING "  ##.####"; PL(R%,3);
387     PRINT #2, USING "  ##.####^"; MINSTDKF0L(R%,3)
390   NEXT R%
395 CLOSE #2
400 'PRINT THE AVERAGE VALUE AND THE STANDARD DEVIATION OF KF0
410 'PRINT THE AVERAGE VALUE AND THE STANDARD DEVIATION OF KF0
420 'AND THE VALUE OF Sth AND 1/2n THAT MINIMIZES THE VARIANCE OF KF0
430   GOSUB 3000
440 'COMPUTE THE PREDICTED Nf, THE RELATIVE ERROR (ERRNC in %)
```

```

450 'AND SAVE Nfexp-Nfcal IN FILE "ROM_K_AT"
460   GOSUB 4000
470 SOUND 1046.5, 20
480 END
490 '
1000 'SUBROUTINE 1000; READ THE HTF DATA
1005   CLS
1010   INPUT "ENTER THE INITIAL OF THE AUTHOR AND PRESS ENTER: "; A$
1020   INPUT "ENTER THE TEST NUMBER AND PRESS ENTER: "; T$
1030   AT$ = LEFT$(A$,1) + LEFT$(T$,1)
1040   DATAFILES$ = "HTF_DATA." + AT$
1050   OPEN "I", #1, DATAFILES$
1060   INPUT #1, M$, TIMEUNIT$, SUNIT$
1070   DIM V(M%), EPR(M%), SR(M%), SMAX(M%), NF(M%), NFCAL(M%), KF0(M%)
1080   IF SUNIT$=1 THEN SUNIT$="MPa" ELSE IF SUNIT$=2 THEN SUNIT$="ksi"
ELSE
    PRINT "SUNIT IS WRONG!"
1090 ' READ THE DATA (FREQUENCY,..., MAX. STRESS, ..., LIFE TO FAILURE)
1100   FOR I% = 1 TO M%
1110     INPUT #1, V, THT, THC, EPR(I%), SR(I%), SMAX(I%), NF(I%)
1120     V(I%) = 60/(1/V + THT + THC)
    'THE EFF. FREQUENCY IS CONVERTED IN cpm
1150   NEXT I%
1160   INPUT #1, MINSMAX
1180   INPUT "ENTER THE MINIMAL VALUE OF THE FREQUENCY EXPONENT: "; PMIN
1190   INPUT "ENTER THE MAXIMAL VALUE OF THE FREQUENCY EXPONENT: "; PMAX
1200   PRINT "": PRINT "PLEASE WAIT"
1210 RETURN 50
1220 '
2000 'SUBROUTINE 2000; COMPUTE THE AVERAGE VALUE AND THE STD OF KF0
2010 ' AVERAGE KF0
2020   SUMKF0 = 0!
2030   FOR J% = 1 TO M%
2040     KF0(J%) = SMAX(J%)*(SMAX(J%)-STHK)*NF(J%)^-.5*V(J%)^(-PL)
2050     SUMKF0 = KF0(J%) + SUMKF0
2060   NEXT J%
2070   AVGKF0 = SUMKF0/M%
2080 ' STANDARD DEVIATION OF KF0
2090   SUMSTDKF0 = 0!
2100   FOR J% = 1 TO M%
2110     SUMSTDKF0 = ABS(KF0(J%)-AVGKF0) + SUMSTDKF0
2120   NEXT J%
2130   STDKF0 = SUMSTDKF0/M%
2140 RETURN 230
2150 '
3000 'SUBROUTINE 3000; PRINT THE RESULTS
3010 PRINT ""
3020 PRINT "RESULTS:"
3030 PRINT ""
3040 PRINT USING "KF0 = ###.###^^(1/2).mn^(1/2n)"; KF0;
3050 PRINT USING " &_ ^2_.cycle_^(1/2).mn_^(1/2n)"; SUNIT$
3060 PRINT USING "STD(KF0) = ###.###^^(1/2).mn^(1/2n)"; MINSTDKF0;
3070 PRINT USING " &_ ^2_.cycle_^(1/2).mn_^(1/2n)"; SUNIT$
3080 PRINT USING "StH = ###.###"; STH;
3090 PRINT USING " &"; SUNIT$
3100 PRINT USING "1/2n = ###.###"; P
3110 IF P <> 0! THEN PRINT USING "n = ###.###"; 1/2/P
3120 RETURN 440

```

```
3130 '
4000 'SUBROUTINE 4000; COMPUTE NFCAL AND THE RELATIVE ERROR (ERRNC)
4010 NCALFILES = "ROM_K_" + AT$
4020 OPEN "O", #3, NCALFILES
4030 SUMERRNC = 0!
4040 FOR J% = 1 TO M%
4050     NFCAL(J%) = (KF0*V(J%)^P/(SMAX(J%)*(SMAX(J%)-STH)))^2
4060     PRINT #3, USING "#####"; NF(J%);
4070     PRINT #3, USING "#####"; NFCAL(J%)
4080     SUMERRNC = ABS((NFCAL(J%)-NF(J%))/NF(J%)) + SUMERRNC
4090 NEXT J%
4100 ERRNC = 100*SUMERRNC/M%
4110 PRINT ""
4120 PRINT USING "RELATIVE ERROR on NfCAL = #####.#_%" ; ERRNC
4130 CLOSE #3
4140 RETURN 470
```

Listing of the program ROM-RE.BAS

```

10 'PROGRAM ROM-RE.BAS
20 '
30 'READ THE HTF DATA
40   GOSUB 1000
50 'COMPUTE THE AVERAGE AND THE STANDARD DEVIATION OF KF0
60 'FOR VARIOUS THRESHOLD STRESS AND VARIOUS FREQUENCY EXPONENTS
70 MINSTDREN = 9.999999E+35
80 NUMITE% = 20: NUMITEK% = 20
90 DIM PL(NUMITE%+1,3), MINSTDRENL(NUMITE%+1,3)
100 VSTDKF0FILE$ = "V_REN_" + AT$ + ".123"
110 OPEN "O", #2, VSTDKF0FILE$
120 FOR PASSP% = 1 TO 3
130   DP = (PMAX-PMIN)/NUMITE%
140   FOR ITE% = 0 TO NUMITE%
150     MINSTDRENL = 9.999999E+35
160     STHMIN = 0!: STHMAX = .999*MINSMAX
170     PL = PMIN + ITE%*DP
180     FOR PASSK% = 1 TO 3
190       DSTH = (STHMAX-STHMIN)/NUMITEK%
200       MINSTDRENK = 9.999999E+35
210       FOR K% = 0 TO NUMITEK%
220         STHK = STHMIN + K%*DSTH
230         GOSUB 2000
240         IF STDREN < MINSTDREN THEN STH=STHK: KF0=AVGKF0: P=PL:
           MINSTDKF0 = STDKF0: MINSTDREN=STDREN
250         IF STDREN < MINSTDRENL THEN MINSTDRENL = STDREN
260         IF STDREN < MINSTDRENK THEN STHOPT = STHK:
           MINSTDRENK = STDREN
270       NEXT K%
280       STHMIN = STHOPT - DSTH: IF STHMIN < 0! THEN STHMIN = 0!
290       STHMAX = STHOPT + DSTH: IF STHMAX >= MINSMAX
           THEN STHMAX=.999*MINSMAX
300     NEXT PASSK%
310     PL(ITE%, PASSP%) = PL
320     MINSTDRENL(ITE%, PASSP%) = MINSTDRENL
330   NEXT ITE%
340   PMIN = P - DP: PMAX = P + DP
350 NEXT PASSP%
360 'PUT INTO FILE "V_REN_AT.123" THE (PL,MINSTDRENL) VALUES
370   FOR R% = 0 TO NUMITE%
380     PRINT #2, USING "  ##.####"; PL(R%,1);
390     PRINT #2, USING "  ##.####^{}"; MINSTDRENL(R%,1);
400     PRINT #2, USING "  ##.####"; PL(R%,2);
410     PRINT #2, USING "  ##.####^{}"; MINSTDRENL(R%,2);
420     PRINT #2, USING "  ##.####"; PL(R%,3);
430     PRINT #2, USING "  ##.####^{}"; MINSTDRENL(R%,3)
440   NEXT R%
450 CLOSE #2
460 'PRINT THE VALUE OF KF0, Sth AND
470 'THE VALUE OF 1/2n THAT MINIMIZES
480 'THE RELATIVE ERROR ON THE Nf PREDICTION
490   GOSUB 3000
500 'COMPUTE THE RELATIVE STANDARD DEVIATION OF Ncal FROM Nexp (RSTDNC)

```

```

510 'OR RELATIVE ERROR, AND SAVE Nfexp-Nfcal IN FILE "ROM_E_AT"
520   GOSUB 4000
530 SOUND 1046.5, 20
540 END
550 '
1000 'SUBROUTINE 1000; READ THE HTF DATA
1005   CLS
1010   INPUT "ENTER THE INITIAL OF THE AUTHOR AND PRESS ENTER: "; A$
1020   INPUT "ENTER THE TEST NUMBER AND PRESS ENTER: "; T$
1030   AT$ = LEFT$(A$,1) + LEFT$(T$,1)
1040   DATAFILE$ = "HTF_DATA." + AT$
1050   OPEN "I", #1, DATAFILE$
1060   INPUT #1, M%, TIMEUNIT%, SUNIT%
1070   DIM V(M%), EPR(M%), SR(M%), SMAX(M%), NF(M%), NFCAL(M%), KF0(M%)
1080   IF SUNIT%=1 THEN SUNIT$="MPa" ELSE IF SUNIT%=2 THEN SUNIT$="ksi"
      ELSE PRINT "SUNIT IS WRONG!"
1090 ' READ THE DATA (FREQUENCY, ..., MAX. STRESS, ..., LIFE TO FAILURE)
1100   FOR I% = 1 TO M%
1110     INPUT #1, V, THT, THC, EPR(I%), SR(I%), SMAX(I%), NF(I%)
1120     V(I%) = 60/(1/V + THT + THC)
      'THE EFF. FREQUENCY IS CONVERTED IN cpm
1150   NEXT I%
1160   INPUT #1, MINSMAX
1180   INPUT "ENTER THE MINIMAL VALUE OF THE FREQUENCY EXPONENT: "; PMIN
1190   INPUT "ENTER THE MAXIMAL VALUE OF THE FREQUENCY EXPONENT: "; PMAX
1200   PRINT "": PRINT "PLEASE WAIT"
1210 RETURN 50
1220 '
2000 'SUBROUTINE 2000; COMPUTE THE AVERAGE VALUE OF KF0 AND THE STDREN
2010 ' AVERAGE KF0
2020   SUMKF0 = 0!
2030   FOR J% = 1 TO M%
2040     KF0(J%) = SMAX(J%)*(SMAX(J%)-STHK)*NF(J%)^-.5*V(J%)^(-PL)
2050     SUMKF0 = KF0(J%) + SUMKF0
2060   NEXT J%
2070   AVGKF0 = SUMKF0/M%
2080 ' STANDARD DEVIATION OF KF0
2090   SUMSTDKF0 = 0!
2100   FOR J% = 1 TO M%
2110     SUMSTDKF0 = ABS(KF0(J%)-AVGKF0) + SUMSTDKF0
2120   NEXT J%
2130   STDKF0 = SUMSTDKF0/M%
2140 ' STANDARD DEVIATION OF RENFC, STDREN
2150   SUMSTDREN = 0!
2160   FOR J% = 1 TO M%
2170     NFCAL(J%) = (AVGKF0*V(J%)^PL/(SMAX(J%)*(SMAX(J%)-STHK)))^2
2180     SUMSTDREN = ABS((NFCAL(J%)-NF(J%))/NF(J%)) + SUMSTDREN
2190   NEXT J%
2200   STDREN = 100*SUMSTDREN/M%
2210 RETURN 240
2220 '
3000 'SUBROUTINE 3000; PRINT THE RESULTS
3010 PRINT ""
3020 PRINT "RESULTS:"
3030 PRINT ""
3040 PRINT USING "KF0 = ##.###^####"; KF0;
3050 PRINT USING " &_2_.cycle_^(1/2)_.mn_^(1/2n)"; SUNIT$

```

```

3060 PRINT USING "STD(KF0) = ##.###^^^"; MINSTDKF0;
3070 PRINT USING " &^2_.cycle_^(1/2)_.mn_^(1/2n)"; SUNIT$
3080 PRINT USING "StH = ####.##"; STH;
3090 PRINT USING " &"; SUNIT$
3100 PRINT USING "1/2n = ##.###"; P
3110 IF P <> 0! THEN PRINT USING "n = ##.###"; 1/2/P
3120 RETURN 500
3130 '
4000 'SUBROUTINE 4000; COMPUTE NFCAL AND THE RELATIVE STANDARD DEVIATION
      (RSTD) OF Ncal FROM Nexp OR STANDARD RELATIVE
      ERROR
4010 NCALFILE$ = "ROM_E_" + AT$
4020 OPEN "O", #3, NCALFILE$
4030 SUMRSTDNC = 0!
4040 FOR J% = 1 TO M%
4050     NFCAL(J%) = (KF0*V(J%)^P/(SMAX(J%)*(SMAX(J%)-STH)))^2
4060     PRINT #3, USING "#####"; NF(J%);
4070     PRINT #3, USING "#####"; NFCAL(J%)
4080     SUMRSTDNC = ABS((NFCAL(J%)-NF(J%))/NF(J%)) + SUMRSTDNC
4090 NEXT J%
4100 RSTDNC = 100*SUMRSTDNC/M%
4110 PRINT ""
4120 PRINT USING "Relative Error on NfCAL = #####.##_%"; RSTDNC
4130 CLOSE #3
4140 RETURN 530

```


Table J.7 Values of the parameters of the Coffin models which minimise the RE on life prediction for the six TF data sets

Models	Cies	872°C									982°C
		Cont. Cycling			Hold Time						Cont. Cyl.
		A1	C3	C4	A2	C1	C1'	AVG	STD	STD (%)	A3
CoC. (EI)	E (MPa)	153000	154443	154443	152000	154443	154443	153795	960	0.6	140000
	A' (MPa)	2652	4231	3198	3293	10073	8239	5281	2829	53.6	2078
	B'	0.171	0.224	0.188	0.136	0.375	0.351	0.241	0.090	37.6	0.218
	k1'	0.086	0.082	0.105	0.528	0.017	-0.076	0.124	0.191	154.2	0.091
CoC. (PI)	C2	0.399	0.5705	1.035	0.1974	0.1175*	0.02322*	0.550	0.309	56.2	0.25
	B	0.855	0.886	0.973	0.667	0.6*	0.345*	0.845	0.112	13.2	0.776
	k	1.16	1.04	1.122	0.883	0.8*	1.191*	1.051	0.106	10.1	1.026
	C1	98.03	98.146	145.93	64.144	13.687*	*	101.563	29.124	28.7	157.72
	r	-0.3257	-0.1774	-0.285	-0.8474	0.4578*	*	-0.409	0.259	-63.3	-0.1992
	$v_{eff,cm}$ (cpm)	0.305	0.077	0.034	0.226	0.03297	0.03297	0.118	0.108	91.4	0.432
	$v_{eff,cm}$ (cpm)	51.3	31.1	36.2	0.659	0.1875	0.1875	20	21	102.9	56.7
	Nt ($v_{eff,cm}$)	144	155	382	226	3*	*	227	95	41.9	186
	Nt ($v_{eff,cm}$)	27	53	52	91	6*	*	56	23	41.0	71
	N_{cm}	202	250	275	580	170	170	275	142	51.7	331
	N_{cm}	9780	21750	7000	7440	600	600	7862	7106	90.4	9720

*: MARGINAL VALUES DISCARDED FOR THE DETERMINATION OF THE AVERAGE (AVG) AND THE STANDARD DEVIATION (STD) OF THE CONSTANTS

A1, A2, A3, C1, C3, C4: COMPUTED WITH THE EFFECTIVE FREQUENCY:

$$v_{eff} = 1/(1/v + t_{hT} + t_{hC})$$

C1': COMPUTED WITH THE MODIFIED EFFECTIVE FREQUENCY:

$$v_{eff} = 1/(1/v + t_{hT} - t_{hC}) \text{ for } t_{hT} > t_{hC}$$

$$v_{eff} = v \text{ for } t_{hT} \leq t_{hC}$$

Table J.8 Values of the parameters of the models of Ostergren, of Antolovich et al., and of Romanoski et al. which minimise the RE on life prediction for the six TF data sets

Models	Cns	872°C									982°C
		Cont. Cycling			Hold Time						Cont. Cyl.
		A1	C3	C4	A2	C1	C1'	AVG	STD	STD (%)	A3
Ost.	C (MPa)	301.500	1019.735	1232.783	311.100	50.4007	442.9883	559.751	421.535	75.3	63.84
	B	0.944	1.085	1.120	0.865	0.565	0.952	0.922	0.182	19.7	0.784
	k	1.000	0.953	1.023	0.530	0.964	1.070	0.923	0.180	19.5	1.003
Ant.	K (MPa)	98.1	2298.0	1280.4	1961.0	5562.0	1015.6	2035.9	1726.0	84.8	1018.0
	n/p	8.130	4.184	6.390	4.202	3.711	10.404	6.170	2.439	39.5	4.055
Rom.	K _{TD} (MPa ⁿ)	2.43e6	4.98e6	4.08e6	3.64e6	4.78e6	6.03e6	4.32e6	1.13e6	26.2	2.04e6
	S _{th} (MPa)	234.9	98.9	137.9	113.8	0.0	0.0	97.6	81.4	83.4	0.0
	n	1.436	2.714	1.848	0.606	-5.102*	3.906	2.102	1.129	53.7	7.299

*: MARGINAL VALUES DISCARDED FOR THE DETERMINATION OF THE AVERAGE (AVG) AND THE STANDARD DEVIATION (STD) OF THE CONSTANTS

A1, A2, A3, C1, C3, C4: COMPUTED WITH THE EFFECTIVE FREQUENCY:

$$v_{eff} = 1/(1/v + t_{hT} + t_{hC})$$

C1': COMPUTED WITH THE MODIFIED EFFECTIVE FREQUENCY:

$$v_{eff} = 1/(1/v + t_{hT} - t_{hC}) \text{ for } t_{hT} > t_{hC}$$

$$v_{eff} = v \text{ for } t_{hT} \leq t_{hC}$$

APPENDIX K

PROGRAMS FOR THE DETERMINATION OF THERMAL FATIGUE LIFE FROM IF AND TMF DAMAGE MODELS

This Appendix presents the softwares developed for the determination of thermal fatigue lives from IF damage models of Coffin, of Ostergren, of Antolovich et al., of Romanoski et al. and from the TMF damage model of Neu-Schitoglu.

K.1 Thermal Fatigue Prediction with IF Damage Models

In Subsection 5.3, the lives were determined along the leading edge (LE) of the DEW specimens tested in the burner rig using the IF damage models enumerated above. In order to put into files values of the variables of the models corresponding to each node considered along the LE, the program BRDATA.BAS was first used. The variables, which are the node position, Z (in mm), the plastic strain range, $\Delta\epsilon_p$ (in mm/mm), the pic value of the tensile stress during cooling, $\sigma_{US,max}$ (in MPa), the pic value of the compressive stress during heating, $\sigma_{US,min}$ (in MPa), the temperature corresponding to the tensile pic T_{US} (in °C), the plateau value of the tensile stress during heating, $\sigma_{SS,max}$ (in MPa), the plateau value of the compressive stress during cooling, $\sigma_{SS,min}$ (in MPa) and the maximum temperature reached during thermal cycling, $T_{SS,max}$ (in °C), were obtained from the thermal and stress-strain FE-analyses, presented in Subsections 5.1 and 5.2. The datafile has the generic name "BR-DATA.FEA" where FEA is a code specific to the FE analyses results employed. The specific values of the variables are given in Tables K.1.

For each model, a program was developed. Only the program of the model of Ostergren is listed at the end of this Appendix, as an example. The programs compute the fatigue-oxidation lives associated to the unsteady and the steady temperature-stress portions of the thermal cycles, according to the methodology exposed in Subsection 5.3.2.1. The total lives, resulting from damage accumulation during both US and SS portions of the cycles, are also obtained using a linear damage accumulation rule.

Listing of the Program BRDATA.BAS

```
10 'PROGRAM BRDATA.BAS
20 '
30 'READ AND WRITE IN FILE THE RESULTS OF THE FINITE ELEMENT ANALYSIS
   (FEA);
40 'FOR THE DEW SPECIMEN THERMALLY CYCLED IN THE BURNER RIG;
50 '   THE PLASTIC STRAIN RANGE,
60 '   THE MAXIMUM AND MINIMUM PIC STRESSES AND CORRESPONDING MAX
   TEMPERATURE,
70 '   THE MAXIMUM AND MINIMUM HOLD STRESSES AND THE MAXIMUM
   TEMPERATURE,
80 '
90 CLS
100  INPUT "ENTER THE FEA CODE (MAX 3 CHARACTERS) AND PRESS ENTER: ",
      FEAS
110  FEAS = LEFT$(FEAS,3)
120  DATAFILES$ = "BR-DATA." + FEAS
130  OPEN "O", #1, DATAFILES$
140  INPUT "ENTER THE NUMBER OF NODES TO CONSIDER AND PRESS ENTER: ", M%
150  PRINT "IF THE STRESS UNIT USED ARE IN MPa, PRESS 1,"
160  INPUT "IF THEY ARE IN ksi, PRESS 2 AND ENTER: ", SUNIT%
170  PRINT #1, M%, SUNIT%
180  CLS
190  FOR I% = 1 TO M%
200    PRINT "ENTER Z(in mm), DeP(in mm/mm), SmaxPIC, SminPIC,
      COR. T(in C),"
210    PRINT "SmaxHOLD, SminHOLD, Tmax, AND PRESS ENTER"
220    INPUT Z, EPR, SMAXP, SMINP, TCP, SMAXH, SMINH, TCH
230    PRINT #1, Z, EPR, SMAXP, SMINP, TCP+273, SMAXH, SMINH, TCH+273
240  NEXT I%
250  CLOSE #1
260  END
```

Table K.1 Values of the Variables_(σ) used in IF Damage Models for life prediction at Each Node along the LE of the DEW Specimens Tested in the Burner Rig

Z (mm)	Δe_p (mm/mm)	$\sigma_{US,max}$ (MPa)	$\sigma_{US,min}$ (MPa)	T_{US} (°C)	$\sigma_{SS,max}$ (MPa)	$\sigma_{SS,min}$ (MPa)	$T_{SS,max}$ (°C)
0.00	0	19.8	-8.4	338.0	8.2	-2.0	597.4
4.25	0	23.1	-88.3	618.0	0.0	0.0	619.1
8.50	0	53.8	-214.0	619.0	0.0	0.0	667.6
12.75	0	86.6	-296.0	724.0	0.0	0.0	734.3
17.00	0	134.0	-354.0	717.0	0.0	0.0	884.2
21.25	0	186.0	-381.0	836.0	0.0	0.0	1027.0
25.50	0.000088	253.0	-420.0	959.0	0.0	0.0	1209.0
29.75	0.000425	331.0	-422.0	1077.0	129.0	-135.7	1361.0
34.00	0.001048	348.0	-518.0	1117.0	110.7	-262.4	1402.0
38.25	0.001132	367.0	-560.0	1024.0	111.3	-300.3	1426.0
42.50	0.000988	391.0	-591.0	1034.0	69.5	-208.3	1434.0
46.75	0.000881	395.0	-604.0	1034.0	20.6	-128.1	1437.0
51.00	0.000908	393.0	-592.0	1030.0	48.7	-196.7	1434.0
55.25	0.000877	388.0	-563.0	1014.0	72.6	-211.2	1426.0
59.50	0.000969	353.0	-515.0	1095.0	74.1	-245.9	1402.0
63.75	0.000347	355.0	-415.0	1040.0	107.2	-118.9	1361.0
68.00	0.000076	246.0	-415.0	899.0	0.0	0.0	1217.0
72.25	0	146.0	-386.0	750.0	0.0	0.0	1042.0
76.50	0	99.8	-376.0	694.0	0.0	0.0	919.8
80.75	0	80.9	-341.0	692.0	0.0	0.0	800.3
85.00	0	71.0	-293.0	729.0	0.0	0.0	777.6
88.75	0	70.0	-208.0	693.0	0.0	0.0	778.1
92.50	0	53.4	-129.0	672.0	0.0	0.0	769.8
96.25	0	23.0	-52.5	689.0	0.0	0.0	764.1
100.00	0	11.3	-3.8	310.0	4.8	-1.9	761.8

*: Refer to the text for the signification of the symbols used in this Table.

Listing of the Program OST-NF.BAS

```

10 'PROGRAM OST-NF.BAS
20 '
30 'READ THE DATA
40   GOSUB 1000
50 'COMPUTE THE PREDICTED Nf, FOR BOTH FREQUENCIES
   (PIC AND HOLD STRESSES)
60 'AND SAVE NfPIC AND NfHOLD IN FILE "OST-NF.FE#"
70   GOSUB 2000
80 END
90 '
1000 'SUBROUTINE 1000; READ THE DATA
1010   INPUT "ENTER THE FEA CODE (3 CHARACTERS) AND PRESS ENTER: "; FEAS
1020   FEAS = LEFT$(FEAS,3)
1030   DATAFILES$ = "BR-DATA."+ FEAS
1040   OPEN "I", #1, DATAFILES$
1050   INPUT #1, M%, SUNIT%
1060   DIM Z(M%), EPR(M%), SMAXP(M%), SMINP(M%), TKP(M%), NFP(M%)
1070   DIM SMAXH(M%), SMINH(M%), TKH(M%), NFH(M%)
1080   IF SUNIT%=1 THEN SF!=1! ELSE IF SUNIT%=2 THEN SF! = 6.89476
       ELSE PRINT "SUNIT IS WRONG!"
1090 ' READ THE FREQUENCY, THE STRESS AND THE LIFE TO FAILURE
1100   FOR I% = 1 TO M%
1110     INPUT #1, Z(I%), EPR(I%), SMAXP(I%), SMINP(I%), TKP(I%),
       SMAXH(I%), SMINH(I%), TKH(I%)
1120     SMAXP(I%) = SMAXP(I%)*SF!: SMINP(I%) = SMINP(I%)*SF!
1130     SMAXH(I%) = SMAXH(I%)*SF!: SMINH(I%) = SMINH(I%)*SF!
1140   NEXT I%
1150 '
1160   PRINT "ENTER THE VALUE OF THE FREQUENCY (in cpm)"
1170   PRINT "CORRESPONDING TO THE PIC STRESSES"
1180   INPUT "AND PRESS ENTER: "; VP
1190   PRINT "ENTER THE VALUE OF THE FREQUENCY (in cpm)"
1200   PRINT "CORRESPONDING TO THE HOLD STRESSES"
1210   INPUT "AND PRESS ENTER: "; VH
1220   PRINT "": PRINT "PLEASE WAIT"
1230 RETURN 50
1240 '
2000 'SUBROUTINE 2000; COMPUTE NfPIC AND NfHOLD
2010 NFFILES$ = "OST-NF." + FEAS
2020 OPEN "O", #2, NFFILES$
2030 B = .784: K = 1.003: C0 = 2.275E-07: AR = 24412.92
2040 PRINT "  Z          NfPIC          NfHOLD"
2050 PRINT " (mm)      (cycles)      (cycles)"
2060 FOR J% = 1 TO M%
2070   IF SMAXP(J%)*EPR(J%) <= 0! THEN NFP(J%) = 9.999999E+37
       ELSE NFP(J%) =
         (C0*EXP(AR/TKP(J%))/SMAXP(J%)/EPR(J%))^(1/B)*VP^(1-K)
2080   IF SMAXH(J%)*EPR(J%) <= 0! THEN NFH(J%) = 9.999999E+37
       ELSE NFH(J%) =
         (C0*EXP(AR/TKH(J%))/SMAXH(J%)/EPR(J%))^(1/B)*VH^(1-K)
2090   PRINT #2, USING "###.##"; Z(J%);

```

```
2100     PRINT #2, USING "##.###^^^^"; NFP(J%);
2110     PRINT #2, USING "##.###^^^^"; NFH(J%)
2120     PRINT USING "###.##"; Z(J%);
2130     PRINT USING "  ##.###^^^^"; NFP(J%);
2140     PRINT USING "  ##.###^^^^"; NFH(J%)
2150 NEXT J%
2160 CLOSE #2
2170 RETURN 80
```


K.2 Thermal Fatigue Prediction with the TMF Damage Model

The TMF model of Neu-Sehitoglu was employed to compute the life at the location exposed to the most severe fatigue-oxidation conditions along the LE of DEW specimens. This model acknowledges the temperature variation, the phasing between the thermal and the mechanical strains during TMF cycling, the triaxiality of the principal stress tensor, and the effect of oxidation and creep on pure fatigue damage accumulation. Life associated to pure fatigue damage is given by the Manson-Hirshberg and lives associated to oxidation-fatigue and creep-fatigue damages interactions are determined with the models of Neu-Sehitoglu. These models were presented in Subsection 2.2.2.6.

The lives associated to the different damage processes involved during thermal fatigue in the burner rig and presented in Subsection 5.3.2, required the determination of effective parabolic rate constants, the phasing parameter for oxidation-fatigue damage which vary with temperature as for the terms in the creep-fatigue damage accumulation rule. These parameters and terms were obtained by numerical integration, for the particular case of the thermal cycle met in the burner rig at the LE nodes of interest, and implemented in the program NEU1-NF.BAS listed below. The parameters and constants were determined from TMF tests on MM-247 (CC) which is the closest case to that of DSR80 tested in the burner rig. The values of these are shown in Table K.2.

Table K.2 Values of the Parameters and Constants of the TMF Model of Neu-Sehitoglu

Pure Fatigue Damage Model	
C	0.0137
d	-0.149
Oxidation-Fatigue Damage Model	
b	0.75
β	1.5
B	$6.93 \times 10^{-3} \text{ s}^{-0.5}$
δ_0	$1.12 \times 10^{-10} \text{ } \mu\text{m} \cdot \text{s}^{-0.75}$
k_{p0}^{ox} (matrix)	$1.54 \times 10^4 \text{ } \mu\text{m}^2/\text{s}$
Q^{ox} (matrix)	175.9 kJ/mol
k_{p0}^{γ} (γ depletion)	$8.57 \times 10^3 \text{ } \mu\text{m}^2/\text{s}$
Q^{γ} (γ depletion)	163.3 kJ/mol
CF_{kp}	0.5
h_{cr}	461.4 μm
ξ^{ox}	0.44
Φ^{ox}	0.036
Creep-Fatigue Damage Model	
A	$7.0 \times 10^{25} \text{ s}^{-1}$
m	11.6
ΔH	536.4 kJ/mol
ξ^{creep}	0.34
Φ^{creep}	0.021
α_1	1/3
α_2	1
K	$886.1 \text{ MPa} - 0.376 \cdot T(^{\circ}\text{C})$

Note that the constants k_{p0} , Q and CF_{kp} have been introduced in Subsection 2.3 and 5.3. These constants are used in Equations 77, 78 and 149, which completely define the effective oxidation rate constant, $k_{p,\text{eff}}$, representative of an entire thermal cycle.

Listing of the Program NEU1-NF.BAS

```

10 'PROGRAM NEU1-NF.BAS
20 '
30 'COMPUTE THE DAMAGE ASSOCIATED TO PURE FATIGUE; OXIDATION AND CREEP
40 'DURING ONE CYCLE USING THE MODEL OF NEU-SEHITOGLU
50 '
60 'COMPUTE THE RESULTANT LIFE Nf
70 '
80 'THE MATERIAL CONSTANTS USED IN THE MODEL ARE THOSE OF MAR-M247(CC)
90 '
100 'READ THE VALUES OF THE VARIABLES AND DEFINE THE MATERIAL CONSTANTS
110   GOSUB 1000
120 'COMPUTE THE DAMAGE TERM ASSOCIATED TO FATIGUE; DFAT
130   GOSUB 2000
140 'COMPUTE THE DAMAGE TERM ASSOCIATED TO OXIDATION; DOX
150   GOSUB 2100
160 'COMPUTE THE DAMAGE TERM ASSOCIATED TO CREEP; DCREEP
170   GOSUB 2200
180 'COMPUTE THE RESULTANT LIFE Nf
190   NF = 1/(DFAT + DOX + DCREEP)
200 'PRINT THE RESULTS
210   PRINT ""
220   PRINT ""
230   PRINT "RESULTS:"
240   PRINT ""
250   PRINT USING "    NfFAT =    ##.###^ ^ ^ cycles"; NFFAT
260   PRINT USING "    NfOX =    ##.###^ ^ ^ cycles"; NFOX
270   PRINT USING "    NfCREEP = ##.###^ ^ ^ cycles"; NfCREEP
280   PRINT ""
290   PRINT USING "    Nf =    ##.###^ ^ ^ cycles"; NF
300 END
1000 'SUBROUTINE 1000; READ THE VARIABLES
1010   INPUT "ENTER THE TEMPERATURE (in degree C) AND PRESS ENTER: ", TC
1020   TK = TC + 273
1030   INPUT "ENTER THE STRESS S11 (in MPa) AND PRESS ENTER: ", S1
1040   INPUT "ENTER THE STRESS S22 (in MPa) AND PRESS ENTER: ", S2
1050   INPUT "ENTER THE STRESS S33 (in MPa) AND PRESS ENTER: ", S3
1060   PRINT "ENTER THE PRINCIPAL MECHANICAL STRAIN RANGE EMR
        (in mm/mm) "
1070   INPUT "AND PRESS ENTER: ", EMR
1080   INPUT "ENTER THE STRAIN RATE (in mm/mm/s) AND PRESS ENTER: ",
        EMDOT
1090 'COMPUTE THE EQUIVALENT STRESS SEQ AND THE HYDROSTATIC STRESS SH
1100   SEQ = 1/2^.5*((S1-S2)^2 + (S2-S3)^2 + (S3-S1)^2)^.5
1110   SH = (S1 + S2 + S3)/3
1120 'MATERIAL CONSTANTS
1130   'FOR THE FATIGUE DAMAGE TERM OF THE MODEL
1140   C = .0137
1150   D = -.149
1160   'FOR THE OXIDATION DAMAGE TERM OF THE MODEL
1170   BEXP = .75
1180   BETA = 1.5

```

```

1190      B = .00693
1200      DELTA0 = 1.12E-10
1210      KP0OX = 15400!
1220      QOX = 175.9
1230      KP0GP = 8570!
1240      QGP = 163.3
1245      CFKP = .5
1250      HCR = 461.4
1260      PHIOX = .0357
1270      'FOR THE CREEP DAMAGE TERM OF THE MODEL
1280      A = 7E+25
1290      M = 11.6
1300      DH = 536.4
1310      K0 = 886.1
1320      DKDT = -.376
1330      ALPHA1 = 1/3
1340      ALPHA2 = 1
1350      PHICREEP = .0206
1360      '
1370      'THE GAS CONSTANT
1380      R = 8.314001E-03
1390      RETURN 130
1400      '
2000      'SUBROUTINE 2000; COMPUTE THE FATIGUE DAMAGE TERM; DFAT
2010      NFFAT = .5*(EMR/(2*C))^(1/D)
2020      DFAT = 1/NFFAT
2030      RETURN 150
2040      '
2100      'SUBROUTINE 2100; COMPUTE THE OXIDATION DAMAGE TERM; DOX
2110      KPOX = KP0OX*EXP(-QOX/R/TK)
2120      KPGP = KP0GP*EXP(-QGP/R/TK)
2130      KPMAX = KPOX + KPGP
2135      KPEFF = CFKP*KPMAX
2140      DOX = (HCR*DELTA0/(B*PHIOX*KPEFF))^(1/BETA)*
              2*EMR^(2/BETA+1)/EMDOT^(1-BEXP/BETA)
2150      NFOX = 1/DOX
2160      RETURN 170
2170      '
2200      'SUBROUTINE 2200; COMPUTE THE CREEP DAMAGE TERM; DCREEP
2210      DCREEP = PHICREEP*A*EXP(-DH/R/TK)*
              ((ALPHA1*SEQ + ALPHA2*SH)/(K0 + DKDT*TC))^M
2220      NFCREEP = 1/DCREEP
2230      RETURN 190

```

APPENDIX L

PROGRAMS FOR THE DETERMINATION OF THE DEPLETION PROFILE AND THE ALLOY RECESSION INTERFACE IN UNCOATED AND COATED Ni-BASE ALLOYS

This Appendix presents the softwares developed for the determination of alloy depletion profile and alloy surface recession for bare and coated Ni-base alloys subjected to cyclic oxidation. The programs as well as the definition of the variables and constants used in the programs are listed below whereas the algorithm is given in Figure 5.42.

ZNO:	the position number along the LE (0-99);
TC1:	the temperature after heating (in Celcius);
TC2:	the Temperature after Cooling (in Celcius);
TK:	the temperature TC1 converted in Kelvin;
ENETM1:	the net strain of the substrate after heating (in mm/mm);
ENETM2:	the net strain of the substrate after cooling (in mm/mm);
NTOT:	the total number of thermal cycles;
PERIOD:	the heating period of the thermal cycles (in s);
CFKP:	the correcting factor of Kp;
YCO:	the coating thickness (in μm);
NB0:	nominal content of B in the substrate;
NBCOAT:	nominal content of B in the coating;
N:	number of nodes in the depletion zone;
I:	node position in the depleted zone;
NB(I):	content of B in the depleted zone at node I;
NBP(I):	content of B in the depleted zone at node I after increment of time dt;
NBTR:	alloy composition in B to get transition from internal to external oxidation of B;
YTOT:	maximum expected thickness of the depleted zone;
DY:	distance between nodes in the depleted zone;
YA:	alloy surface recession;
DT:	increment of time dt;

FAO:	number of increment of time dt for the growth of the AO oxide scale before its spalling;
FBO:	number of increment of time dt for the growth of the BO oxide scale before its spalling;
J:	counter;
VM:	equivalent molar volume of the alloy;
VA:	equivalent molar volume of the metal A in the depleted zone;
VAO:	equivalent molar volume of the AO oxide formed from the depleted zone;
VMO:	equivalent molar volume of the MO oxide formed from the substrate;
VCO:	equivalent molar volume of the CO oxide formed on the coating;
KPOA:	frequency factor of the parabolic oxidation rate constant for the metal A;
KPOM:	frequency factor of the parabolic oxidation rate constant for the alloy M;
KPOCO:	frequency factor of the parabolic oxidation rate constant for the coating C;
QAO:	activation energy for the oxidation of the metal A in the depleted zone;
QMO:	activation energy for the oxidation of the alloy M;
QCO:	activation energy for the oxidation of the coating C;
R:	the gas constant (8.314 J/mole/K);
KPA:	effective parabolic oxidation rate constant for the metal A;
KPM:	effective parabolic oxidation rate constant for the alloy M;
KPCO:	effective parabolic oxidation rate constant for the coating C;
XBOMIN:	minimal BO oxide scale thickness;
JBMAX:	maximal B flux in the depleted zone;
D0B:	frequency factor of the constant of diffusion of B in the depleted zone;
QB:	activation energy for the diffusion of B in the depleted zone;
DB:	constant of diffusion of B in the depleted zone;
F0:	adimensional regroupment of the variables DB, DT and DY;
BIMAX:	maximal value of the adimensional number BI;

GAO:	metal-oxide interface energy for the system A-AO;
GMO:	metal-oxide interface energy for the system M-MO;
GCO:	metal-oxide interface energy for the system C-CO;
EAO:	elastic modulus of the oxide AO;
EMO:	elastic modulus of the oxide MO;
ECO:	elastic modulus of the oxide CO;
NUAO:	Poisson's ratio of the oxide AO;
NUMO:	Poisson's ratio of the oxide MO;
NUCO:	Poisson's ratio of the oxide CO;
ALPHAAO:	linear coefficient of thermal expansion of the oxide AO;
ALPHAMO:	linear coefficient of thermal expansion of the oxide MO;
ALPHACO:	linear coefficient of thermal expansion of the oxide CO;
DENETM:	net strain range of the substrate;
DELTAT:	temperature range;
EMECHAO:	mechanical strain of the oxide AO after cooling;
EMECHMO:	mechanical strain of the oxide MO after cooling;
EMECHCO:	mechanical strain of the oxide CO after cooling;
XCAO:	critical AO oxide scale thickness for spalling;
XCMO:	critical MO oxide scale thickness for spalling;
XCCO:	critical CO oxide scale thickness for spalling;
FILE1\$:	output filename;
CYCLE:	cycle number;
SUBTIME:	time cumulation during one thermal cycle;
TIMEBO:	time cumulation during BO oxide growth before spalling;
TIME:	time cumulation during alloy depletion in B;
XBO:	BO oxide scale thickness;
JB:	flux of B at the alloy-oxide interface;
BI:	adimensional number regrouping the variables JB, DY, VM and DB;

M: index number;
SUBT: storage of the old value of SUBTIME
TIME0AO: time of AO oxide growth before the CYCLEth thermal cycle;
TIMEAO: time of AO oxide growth after the CYCLEth thermal cycle;
X0AO: AO oxide scale thickness before the CYCLEth thermal cycle;
XAO: AO oxide scale thickness after the CYCLEth thermal cycle;
DXAO: AO oxide scale growth thickness during the CYCLEth thermal cycle;
DYA: alloy surface recession thickness during the CYCLEth thermal cycle;
YA: cumulative alloy surface recession thickness.

Listing of the program DEPLETIO.BAS

```

10 'PROGRAM DEPLETIO.BAS
20 '*****
30 '          PROGRAM DEPLETIO.BAS
40 '**  COMPUTATION OF THE CONCENTRATION PROFILE OF THE LESS NOBLE METAL
50 '**          IN THE DEPLETION ZONE DURING CYCLIC OXIDATION
60 '*****
70 'VARIABLE DEFINITION
80   N = 10
90   DIM NB(N),NBP(N)
100 'INITIAL CONDITIONS
110   INPUT "ENTER the Position Number along the LE (0-99): ", ZNO
120   IF ZNO > 99 OR ZNO < 0 THEN GOTO 110
130   INPUT "ENTER the Temperature After Heating (in Celcius): ", TC1
140   INPUT "ENTER the Temperature After Cooling (in Celcius): ", TC2
150   TK = TC1 + 273
160   PRINT "ENTER the Net Strain of the Substrate after Heating"
170   INPUT "(+ for Tensile Strain; - for Compressive Strain): ", ENETM1
180   PRINT "ENTER the Net Strain of the Substrate after Cooling"
190   INPUT "(+ for Tensile Strain; - for Compressive Strain): ", ENETM2
200   INPUT "ENTER the Total Number of Thermal Cycles: ", NTOT
210   INPUT "ENTER the Heating Period of the Cycles (in s): ", PERIOD
220   INPUT "ENTER the Correcting Factor of Kp: ", CFKP
230 'NOMINAL ALLOY COMPOSITION
240   NBO = .22
250   FOR I = 0 TO N
260     NB(I) = NBO
270   NEXT I
280 'SPATIAL VARIABLES
290   YTOT = 100!
300   DY = YTOT/N
310 'TEMPORAL VARIABLES
320   DT = 1!
330   FBO = 0
340   J = 0
350   TIME = J*DT
360 'PHYSICAL CONSTANTS
370   VM = 7.02005E+12
380   VBO = 1.4589E+13
390   KP0B = 46211.4
400   QBO = 185621.6
410   R = 8.314
420   KPB = CFKP*KP0B*EXP(-QBO/R/TK)
430   XBOMIN = (2*KPB*DT)^.5
440   JBMAX = 1/VBO*KPB/XBOMIN
450   DOB = 5E+07: QB = 267770!
460   DB = DOB*EXP(-QB/R/TK)
470   F0 = DB*DT/DY^2
480   BIMAX = JBMAX*DY*VM/DB
490   PRINT "F0 = ", F0
500   IF F0 > .5 THEN PRINT "WARNING: F0 IS TOO BIG!!!": GOTO 1020
510 'COMPUTE THE CRITICAL SCALE THICKNESS
520   GBO = 5.800001E-12
530   EBO = 2.8E-07
540   NUBO = .29
550   ALPHABO = 9.600001E-06

```

```

560   DENETM = ENETM2 - ENETM1
570   DELTAT = TC2 - TC1
580   EMECHBO = DENETM - ALPHABO*DELTAT
590   XCBO = 2*GBO/(EBO*(1+NUBO)*EMECHBO^2)
600 'CREATE THE OUTPUT FILE
610   IF ZNO < 10 THEN Z$="0"+RIGHT$(STR$(ZNO),1)
        ELSE Z$=RIGHT$(STR$(ZNO),2)
620   FILE1$ = "NB-Z" + Z$
630   OPEN "O", #1, FILE1$
640   PRINT #1, "cycles,          MOLAR FRACTION (NB)
650   PRINT #1, USING "#####.### c.:"; 0;
660   FOR I = 0 TO N-1
670     PRINT #1, USING "###.####"; NB0;
680   NEXT I
690   PRINT #1, USING "###.####"; NB0
700   CLS
710   PRINT "cycles,          MOLAR FRACTION (NB)
720 '
730 'COMPUTE THE PROFILE NB-Y
740   FOR CYCLE = 1 TO NTOT
750     FOR SUBTIME = 1 TO FIX(PERIOD/DT+.5)
760       FBO = FBO + 1
770       TIMEBO = FBO*DT
780       J = J + 1
790       TIME = J*DT
800       XBO = (2*KPB*TIMEBO)^.5
810       JB = 1/VBO*KPB/XBO
820       BI = JB*DY*VM/DB
830       NBP(0) = 2*F0*(NB(1) - BI) + (1 - 2*F0)*NB(0)
840       IF NBP(0) <= 0! THEN PRINT "NB' = 0": GOTO 1020
850       FOR M = 1 TO N-1
860         NBP(M) = F0*(NB(M-1) + NB(M+1)) + (1-2*F0)*NB(M)
870       NEXT M
880       NBP(N) = 2*F0*NB(N-1) + (1 - 2*F0)*NB(N)
890       FOR I = 0 TO N
900         NB(I) = NBP(I)
910       NEXT I
920       GOSUB 10000
930     NEXT SUBTIME
940     GOSUB 1000
950     IF XBO > XCBO THEN FBO = 0
960   NEXT CYCLE
970 '
980   CLOSE #1
990   PRINT USING "JBox = ###.####^ ^ ^ ^"; JB
1000  JBM = DB*NBP(1)/VM/DY
1010  PRINT USING "JBM = ###.####^ ^ ^ ^"; JBM
1020  SOUND 1046.5, 20
1030  END
1040 '
1050 '
10000 'SUBROUTINE 10000; OUTPUT FILE
10010  PRINT #1, USING "#####.### c.:"; TIME/PERIOD;
10020  FOR I = 0 TO N-1
10030    PRINT #1, USING "###.####"; NBP(I);
10040  NEXT I
10050  PRINT #1, USING "###.####"; NBP(N)

```

```
10060 'PRINT SCREEN
10070   PRINT USING "#####.### c.: "; TIME/PERIOD
10080   FOR I = 0 TO N-1
10090     PRINT USING "##.####"; NBP(I);
10100   NEXT I
10110   PRINT USING "##.####"; NBP(N)
10120 RETURN
```

Listing of the program DEP-COAT.BAS

```

10 'PROGRAM DEP-COAT.BAS
20 '*****
30 '*
40 '*      PROGRAM DEP-COAT.BAS
50 '*      COMPUTATION OF THE CONCENTRATION PROFILE OF THE LESS NOBLE METAL
60 '*      IN THE DEPLETION ZONE OF A COATING DURING CYCLIC OXIDATION
70 '*****
70 'VARIABLE DEFINITION
80     N = 25
90     DIM NB(N),NBP(N)
100 'INITIAL CONDITIONS
110     INPUT "ENTER the Position Number along the LE (0-99): ", ZNO
120     IF ZNO > 99 OR ZNO < 0 THEN GOTO 110
130     INPUT "ENTER the Temperature after Heating (in Celcius): ", TC1
140     INPUT "ENTER the Temperature after Cooling (in Celcius): ", TC2
150     TK = TC1 + 273
160     PRINT "ENTER the Net Strain of the Substrate after Heating"
170     INPUT "(+ for Tensile Strain; - for Compressive Strain): ", ENETM1
180     PRINT "ENTER the Net Strain of the Substrate after Cooling"
190     INPUT "(+ for Tensile Strain; - for Compressive Strain): ", ENETM2
200     INPUT "ENTER the Total Number of Thermal Cycles: ", NTOT
210     INPUT "ENTER the Heating Period of the Cycles (in s): ", PERIOD
220     INPUT "ENTER the Correcting Factor of Kp: ", CFKP
230     INPUT "ENTER the Coating Thickness (in um): ", YCO
240 'NOMINAL COMPOSITION OF THE COATING AND THE SUBSTRATE
250     NB0 = .22: NBcoat = .6
260     FOR I = 0 TO N/5
270         NB(I) = NBcoat
280     NEXT I
290     FOR I = N/5+1 TO N
300         NB(I) = NB0
310     NEXT I
320 'SPATIAL VARIABLES
330     YTOT = 5*YCO
340     DY = YTOT/N
350 'TEMPORAL VARIABLES
360     DT = 1!
370     FBO = 0
380     J = 0
390     TIME = J*DT
400 'PHYSICAL CONSTANTS
410     VM = 7.02005E+12
420     VBO = 1.2795E+13
430     KP0CO = 167984.8
440     QCO = 237468.5
450     R = 8.314
460     KPB = CFKP*KP0CO*EXP(-QCO/R/TK)
470     XBOMIN = (2*KPB*DT)^.5
480     JBMAX = 1/VBO*KPB/XBOMIN
490     DOB = 5E+07: QB = 267770!
500     DB = DOB*EXP(-QB/R/TK)
510     F0 = DB*DT/DY^2
520     BIMAX = JBMAX*DY*VM/DB
530     PRINT "F0 = ", F0
540     IF F0 > .5 THEN PRINT "WARNING: F0 IS TOO BIG!!!": GOTO 1090
550 'COMPUTE THE CRITICAL SCALE THICKNESS

```

```

560   GBO = 7.700001E-12
570   EBO = 3.7E-07
580   NUBO = .24
590   ALPHABO = .0000081
600   DENETM = ENETM2 - ENETM1
610   DELTAT = TC2 - TC1
620   EMECHBO = DENETM - ALPHABO*DELTAT
630   XCBO = 2*GBO/(EBO*(1+NUBO)*EMECHBO^2)
640 'CREATE THE OUTPUT FILE
650   IF ZNO < 10 THEN Z$="0"+RIGHT$(STR$(ZNO),1)
        ELSE Z$=RIGHT$(STR$(ZNO),2)
660   FILE1$ = "NBCO-Z" + Z$
670   OPEN "O", #1, FILE1$
680   PRINT #1, "cycles,          MOLAR FRACTION (NB)
690   PRINT #1, USING "####.### c.:"; 0;
700   FOR I = 0 TO N/5
710     PRINT #1, USING "###.####"; NB0;
720   NEXT I
730   FOR I = N/5+1 TO N-1
740     PRINT #1, USING "###.####"; NB0;
750   NEXT I
760   PRINT #1, USING "###.####"; NB0
770   CLS
780   PRINT "cycles,          MOLAR FRACTION (NB)
790 '
800 'COMPUTE THE PROFILE NB-Y
810   FOR CYCLE = 1 TO NTOT
820     FOR SUBTIME = 1 TO FIX(PERIOD/DT+.5)
830       FBO = FBO + 1
840       TIMEBO = FBO*DT
850       J = J + 1
860       TIME = J*DT
870       XBO = (2*KPB*TIMEBO)^.5
880       JB = 1/VBO*KPB/XBO
890       BI= JB*DY*VM/DB
900       NBP(0) = 2*F0*(NB(1) - BI) + (1 - 2*F0)*NB(0)
910       IF NBP(0) <= 0! THEN PRINT "NB' = 0": GOTO 1090
920       FOR M = 1 TO N-1
930         NBP(M) = F0*(NB(M-1) + NB(M+1)) + (1-2*F0)*NB(M)
940       NEXT M
950       NBP(N) = 2*F0*NB(N-1) + (1 - 2*F0)*NB(N)
960       FOR I = 0 TO N
970         NB(I) = NBP(I)
980       NEXT I
990       GOSUB 10000
1000     NEXT SUBTIME
1010   '       GOSUB 1000
1020     IF XBO > XCBO THEN FBO = 0
1030   NEXT CYCLE
1040 '
1050 CLOSE #1
1060 PRINT USING "JBox = ###.####^ ^ ^ ^"; JB
1070 JBM = DB*NBP(1)/VM/DY
1080 PRINT USING "JBm = ###.####^ ^ ^ ^"; JBM
1090 SOUND 1046.5, 20
1100 END
1110 '

```

```
1120 '  
10000 'SUBROUTINE 10000; OUTPUT FILE  
10010   PRINT #1, USING "#####.### c.:"; TIME/PERIOD;  
10020   FOR I = 0 TO N-1  
10030     PRINT #1, USING "#####"; NBP(I);  
10040   NEXT I  
10050   PRINT #1, USING "#####"; NBP(N)  
10060 'PRINT SCREEN  
10070   PRINT USING "#####.### c.:"; TIME/PERIOD  
10080   FOR I = 0 TO N-1  
10090     PRINT USING "#####"; NBP(I);  
10100   NEXT I  
10110   PRINT USING "#####"; NBP(N)  
10120 RETURN
```

Listing of the program YA-REC.BAS

```

10 'PROGRAM YA-REC.BAS
20 '*****
30 '*               PROGRAM YA-REC.BAS
40 '*  COMPUTATION OF THE CONCENTRATION PROFILE IN THE DEPLETION ZONE *
50 '*  AND OF THE ALLOY INTERFACE RECESSION DURING CYCLIC OXIDATION *
60 '*****
70 'VARIABLE DEFINITION
80  N = 10
90  DIM NB(N),NBP(N)
100 'INITIAL CONDITIONS
110  INPUT "ENTER the Position Number along the LE (0-99): ", ZNO
120  IF ZNO > 99 OR ZNO < 0 THEN GOTO 110
130  INPUT "ENTER the Temperature after Heating (in Celcius): ", TC1
140  INPUT "ENTER the Temperature after Cooling (in Celcius): ", TC2
150  TK = TC1 + 273
160  PRINT "ENTER the Net Strain of the Substrate after Heating"
170  INPUT "(+ for Tension; - for Compression): ", ENETM1
180  PRINT "ENTER the Net Strain of the Substrate after Cooling"
190  INPUT "(+ for Tension; - for Compression): ", ENETM2
200  INPUT "ENTER the Total Number of Thermal Cycles: ", NTOT
210  INPUT "ENTER the Heating Period of the Cycles (in s): ", PERIOD
220  INPUT "ENTER the Correcting Factor of Kp: ", CFKP
230 'NOMINAL ALLOY COMPOSITION
240  NB0 = .22
250  FOR I = 0 TO N
260    NB(I) = NB0
270  NEXT I
280  NBP(0) = 1!
290  NBTR = .12
300 'SPATIAL VARIABLES
310  YTOT = 100!
320  DY = YTOT/N
330  YA = 0!
340 'TEMPORAL VARIABLES
350  DT = 5!
360  FAO = 0
370  FBO = 0
380  J = 0
390 'PHYSICAL CONSTANTS AND PARAMETERS OF KINETICS OF OXIDATION AND
    DIFFUSION
400  VM = 7.02005E+12
410  VA = 8.3865E+12
420  VAO = 1.383E+13
430  VBO = 1.4589E+13
440  KP0A = 7729.48
450  QAO = 165058.9
460  KP0B = 46211.4
470  QBO = 185621.6
480  R = 8.314
490  KPA = CFKP*KP0A*EXP(-QAO/R/TK)
500  KPB = CFKP*KP0B*EXP(-QBO/R/TK)
510  XBOMIN = (2*KPB*DT)^.5
520  JBMAX = 1/VBO*KPB/XBOMIN
530  D0B = 5E+07: QB = 267770!
540  DB = D0B*EXP(-QB/R/TK)

```



```

550     F0 = DB*DT/DY^2
560     BIMAX = JBMAX*DY*VM/DB
570     CLS
580     PRINT "F0 = ", F0
590     IF F0 > .5 THEN PRINT "WARNING: F0 IS TOO BIG!!!": GOTO 930
600     'COMPUTE THE CRITICAL SCALE THICKNESSES
610     GAO = 3.600001E-12
620     GBO = 5.800001E-12
630     EAO = .0000002
640     EBO = 2.8E-07
650     NUAO = .32
660     NUBO = .29
670     ALPHA AO = .0000135
680     ALPHA BO = 9.600001E-06
690     DENETM = ENETM2 - ENETM1
700     DELTAT = TC2 - TC1
710     EMECHAO = DENETM - ALPHA AO*DELTAT
720     EMECHBO = DENETM - ALPHA BO*DELTAT
730     IF EMECHAO >= 0! THEN EMECHAO = .000001 ELSE EMECHAO = -EMECHAO
740     IF EMECHBO >= 0! THEN EMECHBO = .000001 ELSE EMECHBO = -EMECHBO
750     XCAO = 2*GAO/(EAO*(1+NUAO)*EMECHAO^2)
760     XCBO = 2*GBO/(EBO*(1+NUBO)*EMECHBO^2)
770     'CREATE THE OUTPUT FILE
780     IF ZNO < 10 THEN Z$="0"+RIGHT$(STR$(ZNO),1)
           ELSE Z$=RIGHT$(STR$(ZNO),2)
790     FILE1$ = "YA-Z" + Z$
800     OPEN "O", #1, FILE1$
810     PRINT #1, "cycles,    YA (um),    NB'"
820     PRINT #1, USING "##### c: "; CYCLE;
830     PRINT #1, USING "#####.# um "; 0;
840     PRINT #1, USING "###.####"; NB0
850     '
860     'COMPUTE THE NB-Y PROFILE AND OF THE INTERFACE RECESSON YA
870     FOR CYCLE = 1 TO NTOT
880         IF NBP(0) > 0! THEN GOSUB 1000 ELSE GOSUB 2000
890         GOSUB 3000
900     NEXT CYCLE
910     CLOSE #1
920     SOUND 1046.5, 20
930 END
940 '
950 '
1000 'SUBROUTINE 1000; ALLOY DEPLETION IN B ASSOCIATED TO BO OXIDE GROWTH
1010     FOR SUBTIME = 1 TO FIX(PERIOD/DT+.5)
1020         FBO = FBO + 1
1030         TIMEBO = FBO*DT
1040         J = J + 1
1050         TIME = J*DT
1060         XBO = (2*KPB*TIMEBO)^.5
1070         JB = 1/VBO*KPB/XBO
1080         BI = JB*DY*VM/DB
1090         NBP(0) = 2*F0*(NB(1) - BI) + (1 - 2*F0)*NB(0)
1100         FOR M = 1 TO N-1
1110             NBP(M) = F0*(NB(M-1) + NB(M+1)) + (1-2*F0)*NB(M)
1120         NEXT M
1130         NBP(N) = 2*F0*NB(N-1) + (1 - 2*F0)*NB(N)
1140         IF NBP(0) <= 0! THEN NBP(0) = 0!

```

```

1150         FOR I = 0 TO N
1160             NB(I) = NBP(I)
1170         NEXT I
1180         SUBT = SUBTIME
1190     NEXT SUBTIME
1200     IF XBO >= XCBO THEN FBO = 0: FAO = 0
1210     RETURN
1220 '
2000 'SUBROUTINE 2000; INTERFACE RECESSION ASSOCIATED TO AO OXIDE GROWTH
2010 'INTERFACE RECESSION
2020     FAO = FAO + 1
2030     TIME0AO = (FAO-1)*PERIOD
2040     TIMEAO = FAO*PERIOD
2050     X0AO = (2*KPA*TIME0AO)^.5
2060     XAO = (2*KPA*TIMEAO)^.5
2070     DXAO = XAO - X0AO
2080     DYA = VA/VAO*DXAO
2090     YA = YA + DYA
2100     IF XAO >= XCAO THEN FAO = 0
2110 'RECESSION OF THE DEPLETION PROFILE NB-Y
2120     FOR I = 0 TO N-1
2130         NB(I) = DYA/DY*(NB(I+1)-NB(I)) + NB(I)
2140     NEXT I
2150     NB(N) = NB0
2160     IF NB(0) < NBTR THEN NBP(0) = 0! ELSE NBP(0) = 1!
2170     RETURN
2180 '
3000 'SUBROUTINE 3000; OUTPUT FILE FOR YA-Z-N
3010     PRINT #1, USING "##### c: "; CYCLE;
3020     PRINT #1, USING "#####.# um "; YA;
3030     PRINT #1, USING "###.####"; NB(0)
3040 'PRINT SCREEN
3050     PRINT USING "##### c: "; CYCLE;
3060     PRINT USING "#####.# um "; YA;
3070     PRINT USING "###.####"; NB(0)
3080     RETURN

```

Listing of the program YAR-COAT.BAS

```

10 'PROGRAM YAR-COAT.BAS
20 '*****
30 '*               PROGRAM YAR-COAT.BAS               *
40 '*  COMPUTATION OF THE CONCENTRATION PROFILE IN THE DEPLETION ZONE  *
50 '*  AND OF THE COATING SURFACE RECESSON DURING CYCLIC OXIDATION  •
60 '*****
70 'VARIABLE DEFINITION
80  N = 25
90  DIM NB(N),NBP(N)
100 'INITIAL CONDITIONS
110  INPUT "ENTER the Position Number along the LE (0-99): ", ZNO
120  IF ZNO > 99 OR ZNO < 0 THEN GOTO 110
130  INPUT "ENTER the Temperature after Heating (in Celcius): ", TC1
140  INPUT "ENTER the Temperature after Cooling (in Celcius): ", TC2
150  TK = TC1 + 273
160  PRINT "ENTER the Net Strain of the Substrate after Heating"
170  INPUT "(+ for Tension; - for Compression): ", ENETM1
180  PRINT "ENTER the Net Strain of the Substrate after Cooling"
190  INPUT "(+ for Tension; - for Compression): ", ENETM2
200  INPUT "ENTER the Total Number of Thermal Cycles: ", NTOT
210  INPUT "ENTER the Heating Period of the Cycles (in s): ", PERIOD
220  INPUT "ENTER the Correcting Factor of Kp: ", CFKP
230  INPUT "ENTER the Coating Thickness (in um): ", YCO
240 'NOMINAL ALLOY AND COATING COMPOSITION
250  NB0 = .22: NBcoat = .6
260  FOR I = 0 TO N/5
270    NB(I) = NBcoat
280  NEXT I
290  FOR I = N/5+1 TO N
300    NB(I) = NB0
310  NEXT I
320  NBP(0) = 1!
330  NBTR = .12
340 'SPATIAL VARIABLES
350  YTOT = 5!*YCO
360  DY = YTOT/N
370  YA = 0!
380 'TEMPORAL VARIABLES
390  DT = 5!
400  FAO = 0
410  FBO = 0
420  J = 0
430 'PHYSICAL CONSTANTS AND PARAMETERS OF KINETICS OF OXIDATION AND
    DIFFUSION
440  VM = 7.02005E+12
450  VA = 8.3865E+12
460  VAO = 1.383E+13
470  VMO = 1.4589E+13
480  VCO = 1.2795E+13
490  KP0A = 7729.48
500  QAO = 165058.9
510  KP0M = 46211.4
520  QMO = 185621.6
530  KP0CO = 167984.8
540  QCO = 237468.5

```

```

550   R = 8.314
560   KPA = CFKP*KPOA*EXP(-QAO/R/TK)
570   KPM = CFKP*KPOM*EXP(-QMO/R/TK)
580   KPCO = CFKP*KPCO*EXP(-QCO/R/TK)
590   XBOMIN = (2*KPCO*DT)^.5
600   JBMAX = 1/VCO*KPCO/XBOMIN
610   DOB = 5E+07: QB = 267770!
620   DB = DOB*EXP(-QB/R/TK)
630   F0 = DB*DT/DY^2
640   BIMAX = JBMAX*DY*VM/DB
650   CLS
660   PRINT "F0 = ",F0
670   IF F0 > .5 THEN PRINT "WARNING: F0 IS TOO BIG!!!": GOTO 1090
680 'COMPUTE THE CRITICAL SCALE THICKNESSES
690   GAO = 3.600001E-12
700   GMO = 5.800001E-12
710   GCO = 7.700001E-12
720   EAO = .0000002
730   EMO = 2.8E-07
740   ECO = 3.7E-07
750   NUAO = .32
760   NUMO = .29
770   NUCO = .24
780   ALPHA AO = .0000135
790   ALPHAMO = 9.600001E-06
800   ALPHACO = .0000081
810   DENETM = ENETM2 - ENETM1
820   DELTAT = TC2 - TC1
830   EMECHAO = DENETM - ALPHA AO*DELTAT
840   EMECHMO = DENETM - ALPHAMO*DELTAT
850   EMECHCO = DENETM - ALPHACO*DELTAT
860   IF EMECHAO >= 0! THEN EMECHAO = .000001 ELSE EMECHAO = -EMECHAO
870   IF EMECHMO >= 0! THEN EMECHMO = .000001 ELSE EMECHMO = -EMECHMO
880   IF EMECHCO >= 0! THEN EMECHCO = .000001 ELSE EMECHCO = -EMECHCO
890   XCAO = 2*GAO/(EAO*(1+NUAO)*EMECHAO^2)
900   XCMO = 2*GMO/(EMO*(1+NUMO)*EMECHMO^2)
910   XCCO = 2*GCO/(ECO*(1+NUCO)*EMECHCO^2)
920 'CREATE THE OUTPUT FILE
930   IF ZNO < 10 THEN Z$="0"+RIGHT$(STR$(ZNO),1)
          ELSE Z$=RIGHT$(STR$(ZNO),2)
940   FILE1$ = "YACO-Z" + Z$
950   OPEN "O", #1, FILE1$
960   PRINT #1, "cycles,    YA (um),    NB'"
970   PRINT #1, USING "##### c.: "; 0;
980   PRINT #1, USING "#####. # um "; 0;
990   PRINT #1, USING "###.####"; NBCOAT
1000 '
1010 'COMPUTE THE NB-Y PROFILE AND OF THE INTERFACE RECESSON YA
1020   FOR CYCLE = 1 TO NTOT
1030     IF YA <= YCO THEN VBO = VCO: KPB = KPCO: XCBO = XCCO
          ELSE VBO = VMO: KPB = KPM: XCBO = XCMO
1040     IF NBP(0) > 0! THEN GOSUB 10000 ELSE GOSUB 20000
1050     GOSUB 30000
1060     NEXT CYCLE
1070   CLOSE #1
1080   SOUND 1046.5, 20
1090   END

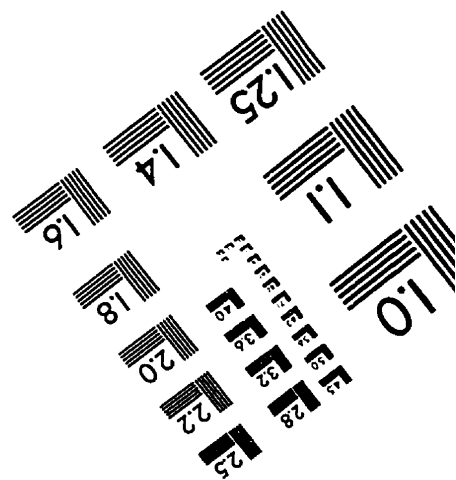
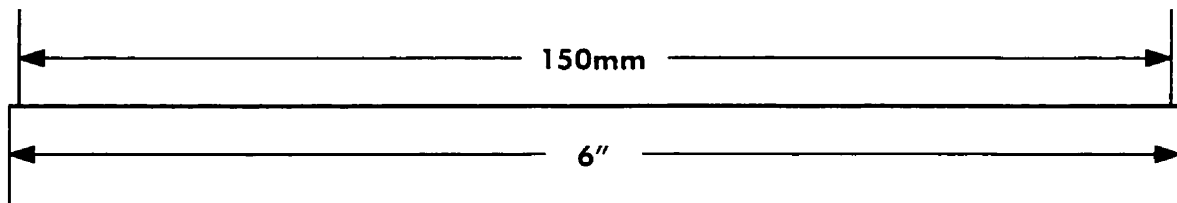
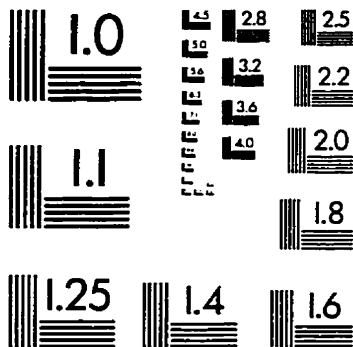
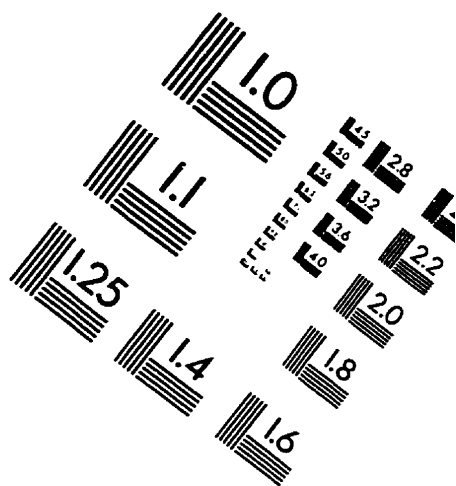
```

```

1100 '
1110 '
10000 'SUBROUTINE 10000; ALLOY DEPLETION IN B ASSOCIATED TO BO OXIDE
      GROWTH
10010   FOR SUBTIME = 1 TO FIX(PERIOD/DT+.5)
10020     FBO = FBO + 1
10030     TIMEBO = FBO*DT
10040     J = J + 1
10050     TIME = J*DT
10060     XBO = (2*KPB*TIMEBO)^.5
10070     JB = 1/VBO*KPB/XBO
10080     BI = JB*DY*VM/DB
10090     NBP(0) = 2*F0*(NB(1) - BI) + (1 - 2*F0)*NB(0)
10100     FOR M = 1 TO N-1
10110       NBP(M) = F0*(NB(M-1) + NB(M+1)) + (1-2*F0)*NB(M)
10120     NEXT M
10130     NBP(N) = 2*F0*NBP(N-1) + (1 - 2*F0)*NB(N)
10140   IF NBP(0) <= 0! THEN NBP(0) = 0!
10150     FOR I = 0 TO N
10160       NB(I) = NBP(I)
10170     NEXT I
10180     SUBT = SUBTIME
10190   NEXT SUBTIME
10200   IF XBO >= XCBO THEN FBO = 0: FAO = 0
10210   RETURN
10220 '
20000 'SUBROUTINE 20000; INTERFACE RECESSON ASSOCIATED TO AO OXIDE
      GROWTH
20010 'INTERFACE RECESSON
20020   FAO = FAO + 1
20030   TIME0AO = (FAO-1)*PERIOD
20040   TIMEAO = FAO*PERIOD
20050   X0AO = (2*KPA*TIME0AO)^.5
20060   XAO = (2*KPA*TIMEAO)^.5
20070   DXAO = XAO - X0AO
20080   DYA = VA/VAO*DXAO
20090   YA = YA + DYA
20100   IF XAO >= XCAO THEN FAO = 0
20110 'RECESSON OF THE DEPLETION PROFILE NB-Y
20120   FOR I = 0 TO N-1
20130     NB(I) = DYA/DY*(NB(I+1)-NB(I)) + NB(I)
20140   NEXT I
20150   NB(N) = NB0
20160   IF NB(0) < NBTR THEN NBP(0) = 0! ELSE NBP(0) = 1!
20170   RETURN
20180 '
30000 'SUBROUTINE 30000; OUTPUT FILE FOR YA-Z-N
30010   PRINT #1, USING "##### c: "; CYCLE;
30020   PRINT #1, USING "#####. # um "; YA;
30030   PRINT #1, USING "##.#####"; NB(0)
30040 'PRINT SCREEN
30050   PRINT USING "##### c: "; CYCLE;
30060   PRINT USING "#####. # um "; YA;
30070   PRINT USING "##.#####"; NB(0)
30080   RETURN

```

TEST TARGET (QA-3)



APPLIED IMAGE, Inc
1653 East Main Street
Rochester, NY 14609 USA
Phone: 716/482-0300
Fax: 716/288-5989

© 1993, Applied Image, Inc., All Rights Reserved